

AJNR

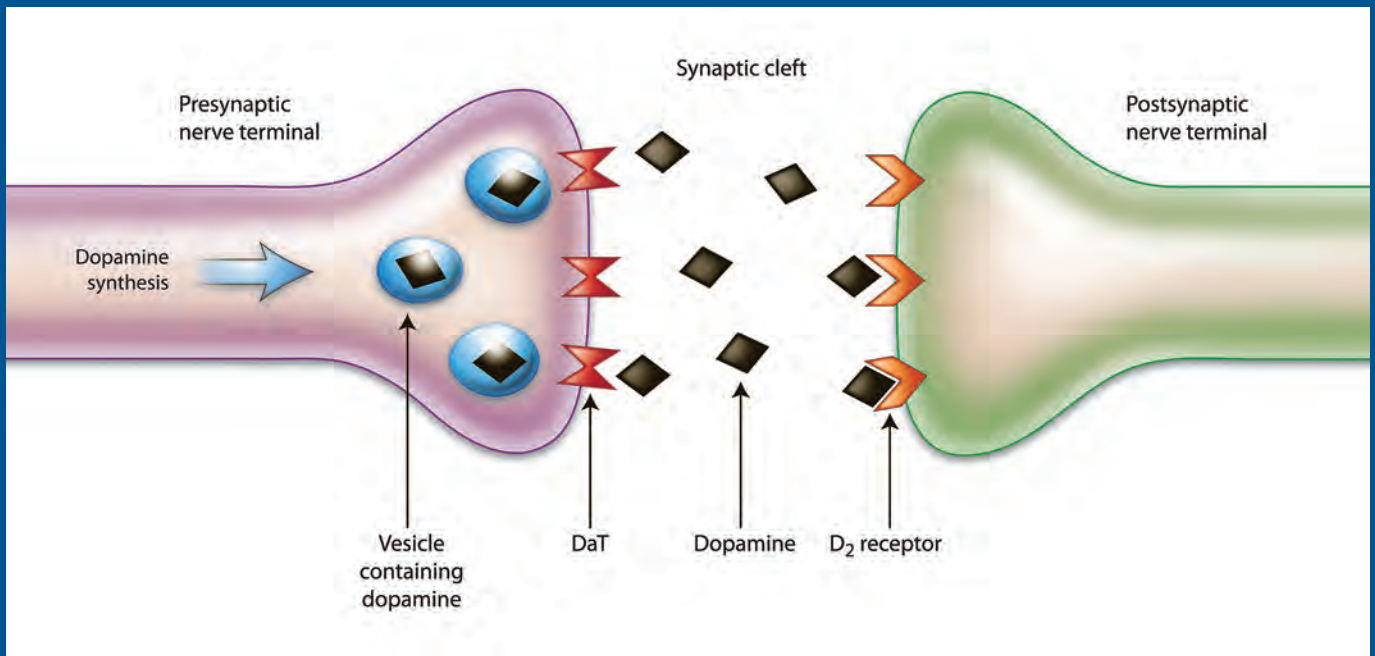
AMERICAN JOURNAL OF NEURORADIOLOGY

FEBRUARY 2015
VOLUME 36
NUMBER 2
WWW.AJNR.ORG

THE JOURNAL OF DIAGNOSTIC AND
INTERVENTIONAL NEURORADIOLOGY

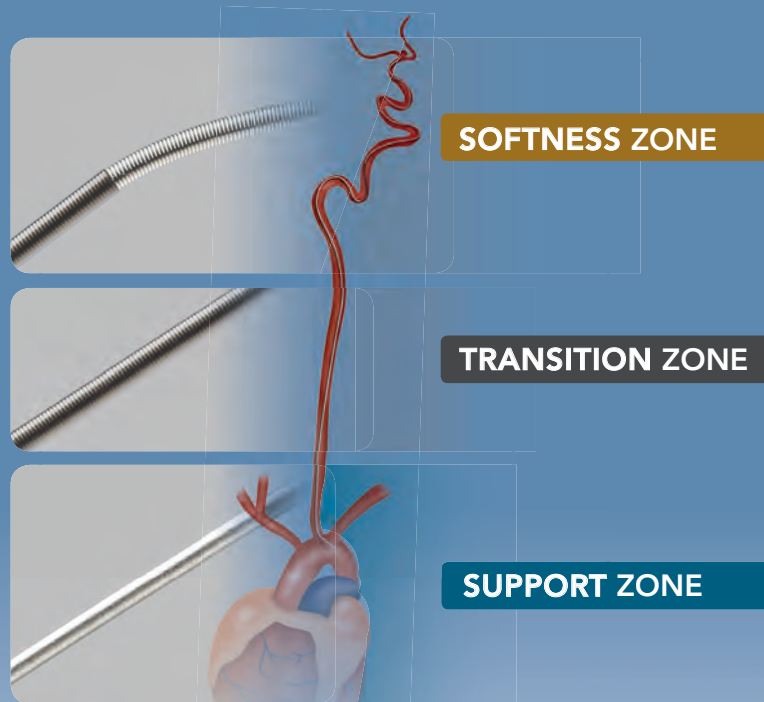
Acute flaccid paralysis due to enterovirus
Arch-to-vertex CTA in suspected acute stroke
Skull plain radiographs after coiling of aneurysms

Official Journal ASNR • ASFNR • ASHNR • ASPNR • ASSR



Advanced

by MicroVention



ENHANCED CONTROL TO MAXIMIZE COIL PERFORMANCE

The **V-Trak[®] Advanced Coil System**, the next generation to power the performance of our most technically advanced line of coils. Offering the optimal combination of support and flexibility.

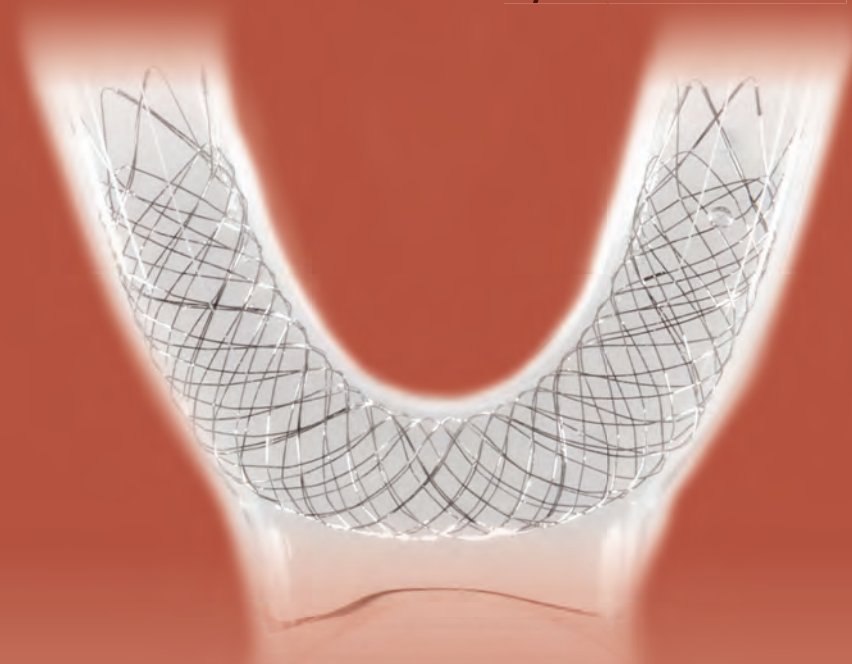
microvention.com

MICROVENTION, V-Trak, LVIS and Headway are registered trademarks of MicroVention, Inc. Scientific and clinical data related to this document are on file at MicroVention, Inc. Refer to Instructions for Use, contraindications and warnings for additional information. Federal (USA) law restricts this device for sale by or on the order of a physician. © 2015 MicroVention, Inc. 1/15

CE
0297

Support

by MicroVention



LOW-PROFILE VISUALIZED INTRALUMINAL SUPPORT

The **LVIS®** and **LVIS® Jr. devices** are the next generation technology for optimal intraluminal support and coverage for stent-assist coil procedures.

Used with  **Headway**
Microcatheter

RX only.

Humanitarian Device:

Authorized by Federal Law for use with bare platinum embolic coils for the treatment of unruptured, wide neck (neck \geq 4 mm or dome to neck ratio $<$ 2), intracranial, saccular aneurysms arising from a parent vessel with a diameter \geq 2.5 mm and \leq 4.5 mm. The effectiveness of this device for this use has not been demonstrated.

For more information or a product demonstration,
contact your local MicroVention representative:



MicroVention, Inc.

Worldwide Headquarters

1311 Valencia Avenue

Tustin, CA 92780 USA

MicroVention UK Limited

MicroVention Europe, S.A.R.L.

MicroVention Deutschland GmbH

PH +1.714.247.8000

PH +44 (0) 191 258 6777

PH +33 (1) 39 21 77 46

PH +49 211 210 798-0



BARRICADE™ COIL SYSTEM

PERFORMANCE AND VALUE DELIVERED



BLOCKADE
M E D I C A L

18 TECHNOLOGY DRIVE #169, IRVINE CA 92618 | P 949.788.1443
WWW.BLOCKADEMEDICAL.COM

 MADE IN AMERICA

CE
0297
MKTG-020 REV. B



AJNR

AMERICAN JOURNAL OF NEURORADIOLOGY

FEBRUARY 2015
VOLUME 36
NUMBER 2
WWW.AJNR.ORG

Publication Preview at www.ajnr.org features articles released in advance of print. Visit www.ajnrblog.org to comment on AJNR content and chat with colleagues and AJNR's News Digest at <http://ajnrdigest.org> to read the stories behind the latest research in neuroimaging.

EDITORIAL

PERSPECTIVES

- 227 **The Winds of Change** *M. Castillo*

REVIEW ARTICLES

- 229 **The Role of Functional Dopamine-Transporter SPECT Imaging in Parkinsonian Syndromes, Part 1** *T.C. Booth, M. Nathan, A.D. Waldman, A.-M. Quigley, A.H. Schapira, and J. Buscombe*
- 236 **The Role of Functional Dopamine-Transporter SPECT Imaging in Parkinsonian Syndromes, Part 2** *T.C. Booth, M. Nathan, A.D. Waldman, A.-M. Quigley, A.H. Schapira, and J. Buscombe*

EXPEDITED PUBLICATION

- 245 **MRI Findings in Children with Acute Flaccid Paralysis and Cranial Nerve Dysfunction Occurring during the 2014 Enterovirus D68 Outbreak** *J.A. Maloney, D.M. Mirsky, K. Messacar, S.R. Dominguez, T. Schreiner, and N.V. Stence*

BRAIN

- 251 **Double Inversion Recovery MR Sequence for the Detection of Subacute Subarachnoid Hemorrhage** *J. Hodel, R. Aboukais, B. Dutouquet, E. Kalsoum, M.A. Benadjaoud, D. Chechin, M. Zins, A. Rahmouni, A. Luciani, J.-P. Pruvo, J.-P. Lejeune, and X. Leclerc*

- 259 **Combining MRI with NIHSS Thresholds to Predict Outcome in Acute Ischemic Stroke: Value for Patient Selection** *P.W. Schaefer, B. Pulli, W.A. Copen, J.A. Hirsch, T. Leslie-Mazwi, L.H. Schwamm, O. Wu, R.G. González, and A.J. Yoo*

- 265 **Diagnostic Yield of Emergency Department Arch-to-Vertex CT Angiography in Patients with Suspected Acute Stroke** *A.R. Deipolyi, L.M. Hamberg, R.G. González, J.A. Hirsch, and G.J. Hunter*

- 269 **Do FLAIR Vascular Hyperintensities beyond the DWI Lesion Represent the Ischemic Penumbra?** *L. Legrand, M. Tisserand, G. Turc, O. Naggara, M. Edjlali, C. Mellerio, J.-L. Mas, J.-F. Méder, J.-C. Baron, and C. Oppenheim*

- 275 **Prediction of Infarction and Reperfusion in Stroke by Flow- and Volume-Weighted Collateral Signal in MR Angiography** *M. Ernst, N.D. Forkert, L. Brehmer, G. Thomalla, S. Siemonsen, J. Fiehler, and A. Kemmling*

- 283 **Effects of Agmatine on Blood-Brain Barrier Stabilization Assessed by Permeability MRI in a Rat Model of Transient Cerebral Ischemia** *S.S. Ahn, S.H. Kim, J.E. Lee, K.J. Ahn, D.J. Kim, H.S. Choi, J. Kim, N.-Y. Shin, and S.-K. Lee*

- 289 **Assessment of Intracranial Collaterals on CT Angiography in Anterior Circulation Acute Ischemic Stroke** *L.L.L. Yeo, P. Paliwal, H.L. Teoh, R.C. Seet, B.P. Chan, E. Ting, N. Venketasubramanian, W.K. Leow, B. Wakerley, Y. Kusama, R. Rathakrishnan, and V.K. Sharma*

-  Indicates Editor's Choices selection
-  Indicates Fellows' Journal Club selection
-  Indicates open access to non-subscribers at www.ajnr.org
-  Indicates article with supplemental on-line table
-  Indicates article with supplemental on-line photo
-  Indicates article with supplemental on-line video
-  Indicates Evidence-Based Medicine Level 1
-  Indicates Evidence-Based Medicine Level 2

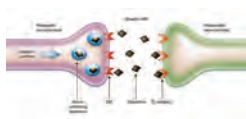


Diagram of dopaminergic pathway in the striatum.

Go Green!

AJNR urges American Society of Neuroradiology members to reduce their environmental footprint by voluntarily suspending their print subscription.

The savings in paper, printing, transportation, and postage not only help members cut down on clutter, but go to fund new electronic enhancements and expanded content.

The digital edition of *AJNR* presents the print version in its entirety, along with extra features including:

- Publication Preview
- Case of the Week
- Podcasts
- Special Collections
- The *AJNR* Blog
- Weekly Poll

It also **reaches subscribers much faster than print**. An **electronic table of contents** will be sent directly to your mailbox to notify you as soon as it publishes.

Readers can **search, reference, and bookmark** current and archived content 24 hours a day on www.ajnr.org, rather than thumb through stacks of accumulated paper issues for articles and images they need.



<http://www.ajnr.org/cgi/feedback>

ASNR members who wish to opt out of print can do so by using the Feedback form on the *AJNR* Website (<http://www.ajnr.org/cgi/feedback>). Just type "Go Green" in the subject line to stop print and spare our ecosystem.

-   **295 Regional Cerebral Arterial Transit Time Hemodynamics Correlate with Vascular Risk Factors and Cognitive Function in Men with Coronary Artery Disease** *B.J. MacIntosh, W. Swardfager, A.D. Robertson, E. Tchistiakova, M. Saleem, P.I. Oh, N. Herrmann, B. Stefanovic, and K.L. Lanctôt*
- 302 Meta-Analysis of Diffusion Metrics for the Prediction of Tumor Grade in Gliomas** *V.Z. Miloushev, D.S. Chow, and C.G. Filippi*
-    **309 Ultra-High-Field MR Imaging in Polymicrogyria and Epilepsy** *A. De Ciantis, A.J. Barkovich, M. Cosottini, C. Barba, D. Montanaro, M. Costagli, M. Tosetti, L. Biagi, W.B. Dobyns, and R. Guerrini*
- 317 Usefulness of Subtraction of 3D T2WI-DRIVE from Contrast-Enhanced 3D T1WI: Preoperative Evaluations of the Neurovascular Anatomy of Patients with Neurovascular Compression Syndrome** *Y. Masuda, T. Yamamoto, H. Akutsu, M. Shiigai, T. Masumoto, E. Ishikawa, M. Matsuda, and A. Matsumura*

INTERVENTIONAL *Published in collaboration with
Interventional Neuroradiology*

-   **323 Dual Stenting Using Low-Profile LEO Baby Stents for the Endovascular Management of Challenging Intracranial Aneurysms** *I. Akmangit, K. Aydin, S. Sencer, O.M. Topcuoglu, E.D. Topcuoglu, E. Daglioglu, M. Barburoglu, and A. Arat*
-  **330 Visual Outcomes with Flow-Diverter Stents Covering the Ophthalmic Artery for Treatment of Internal Carotid Artery Aneurysms** *A. Rouchaud, O. Leclerc, Y. Benayoun, S. Saleme, Y. Camilleri, F. D'Argento, M.-P. Boncoeur, P.-Y. Robert, and C. Mounayer*
-  **337 Efficacy of Skull Plain Films in Follow-up Evaluation of Cerebral Aneurysms Treated with Detachable Coils: Quantitative Assessment of Coil Mass** *S.J. Ahn, B.M. Kim, W.S. Jung, and S.H. Suh*
- 342 Parent Artery Curvature Influences Inflow Zone Location of Unruptured Sidewall Internal Carotid Artery Aneurysms** *K. Futami, H. Sano, T. Kitabayashi, K. Misaki, M. Nakada, N. Uchiyama, and F. Ueda*

EXTRACRANIAL VASCULAR

- 349 CT Angiographic Features of Symptom-Producing Plaque in Moderate-Grade Carotid Artery Stenosis** *A. Gupta, E.E. Mtui, H. Baradaran, G. Salama, A. Pandya, H. Kamel, A. Giambone, and P.C. Sanelli*

HEAD & NECK

- 355 Detection of Calcifications in Retinoblastoma Using Gradient-Echo MR Imaging Sequences: Comparative Study between In Vivo MR Imaging and Ex Vivo High-Resolution CT** *F. Rodjan, P. de Graaf, P. van der Valk, T. Hadjistilianou, A. Cerase, P. Toti, M.C. de Jong, A.C. Moll, J.A. Castelijns, and P. Galluzzi, on behalf of the European Retinoblastoma Imaging Collaboration*
- 361 MR Imaging Features of Acute Mastoiditis and Their Clinical Relevance** *R. Saat, A.H. Laulajainen-Hongisto, G. Mahmood, L.J. Lempinen, A.A. Aarnisalo, A.T. Markkola, and J.P. Jero*
- 368 Standardization of CT Depiction of Cochlear Implant Insertion Depth** *C.C. Colby, N.W. Todd, H.R. Harnsberger, and P.A. Hudgins*
- 372 Radiologic and Functional Evaluation of Electrode Dislocation from the Scala Tympani to the Scala Vestibuli in Patients with Cochlear Implants** *N. Fischer, L. Pinggera, V. Weichbold, D. Dejaco, J. Schmutzhard, and G. Widmann*
-  **378 Visualization of Human Inner Ear Anatomy with High-Resolution MR Imaging at 7T: Initial Clinical Assessment** *M.A. van der Jagt, W.M. Brink, M.J. Versluis, S.C.A. Steens, J.J. Briaire, A.G. Webb, J.H.M. Frijns, and B.M. Verbist*

CALL FOR AJNR EDITORIAL FELLOWSHIP CANDIDATES

ASNR and AJNR are pleased once again to join efforts with other imaging-related journals that have training programs on editorial aspects of publishing for trainees or junior staff (3–5 years after training), including Radiology (Olmsted fellowship), AJR (Figley and Rogers fellowships), and Radiologia.

2015 Candidate Information and Requirements

GOALS

- Increase interest in “editorial” and publication-related activities in younger individuals.
- Increase understanding and participation in the AJNR review process.
- Incorporate into AJNR’s Editorial Board younger individuals who have previous experience in the review and publication process.
- Fill a specific need in neuroradiology not offered by other similar fellowships.
- Increase the relationship between “newer” generation of neuroradiologists and more established individuals.
- Increase visibility of AJNR among younger neuroradiologists.

ACTIVITIES OF THE FELLOWSHIP

- Serve as Editorial Fellow for one year. This individual will be listed on the masthead as such.
- Review at least one manuscript per month for 12 months. Evaluate all review articles submitted to AJNR.
- Access to our electronic manuscript review system will be granted so that the candidate can learn how these systems work.
- Be involved in the final decision of selected manuscripts together with the Editor-in-Chief.
- Participate in all monthly Senior Editor telephone conference calls.
- Participate in all meetings of the Editors and Publications Committee during the annual meetings of ASNR and RSNA as per candidate’s availability. AJNR/ASNR will not provide funding for this activity but may offer a discounted fee for its annual meeting.
- Evaluate progress and adjust program to specific needs in biannual meeting or telephone conference with the Editor-in-Chief.
- Write at least one editorial for AJNR.
- Embark on an editorial scientific or bibliometric project that will lead to the submission of an article to AJNR or another appropriate journal as determined by the Editor-in-Chief. This project will be presented by the Editorial Fellow at the ASNR annual meeting.
- Serve as liaison between AJNR and ASNR’s Young Professionals Network and the 3 YPs appointed to AJNR as special consultants. Participate in meetings and telephone calls with this group. Design one electronic survey/year polling the group regarding readership attitudes and wishes.
- Recruit trainees as reviewers as determined by the Editor-in-Chief.
- Participate in Web improvement projects.
- Potentially become a member of AJNR’s Editorial Board at the end of the fellowship.
- Invite Guest Editors for AJNR’s News Digest to cover a variety of timely topics.

QUALIFICATIONS

- Be a fellow in neuroradiology from North America, including Canada (this may be extended to include other countries).
- Be a junior faculty neuroradiology member (< 3 years) in either an academic and private environment.
- Provide an “end” of fellowship report to AJNR’s Editor-in-Chief and ASNR’s Publications Committee.
- Be an “in-training” or member of ASNR in any other category.

APPLICATION

- Include a short letter of intent with statement of goals and desired research project. CV must be included.
- Include a letter of recommendation from the Division Chief or fellowship program director. A statement of protected time to perform the functions outlined is desirable.
- Applications will be evaluated by AJNR’s Senior Editors and the Chair of the Publications Committee prior to the ASNR meeting. The name of the selected individual will be announced at the meeting.
- Applications should be received by March 3, 2015 and sent to Ms. Karen Halm, AJNR Managing Editor, electronically at khalm@asnr.org.

  **384 Diffusion-Weighted Imaging of the Head and Neck in Healthy Subjects: Reproducibility of ADC Values in Different MRI Systems and Repeat Sessions** *A.S. Kolff-Gart, P.J.W. Pouwels, D.P. Noij, R. Ljumanovic, V. Vandecaveye, F. de Keyzer, R. de Bree, P. de Graaf, D.L. Knol, and J.A. Castelijns*

391 Impact of Model-Based Iterative Reconstruction on Image Quality of Contrast-Enhanced Neck CT *S. Gaddikeri, J.B. Andre, J. Benjert, D.S. Hippe, and Y. Anzai*

 **397 Radiology Reports for Incidental Thyroid Nodules on CT and MRI: High Variability across Subspecialties** *A.T. Grady, J.A. Sosa, T.P. Tanpitukpongse, K.R. Choudhury, R.T. Gupta, and J.K. Hoang*

PEDIATRICS

  **403 A Prospective Longitudinal Brain Morphometry Study of Children with Sickle Cell Disease** *R. Chen, M. Arkuszewski, J. Krejza, R.A. Zimmerman, E.H. Herskovits, and E.R. Melhem*

411 Comparison of Spin-Echo and Gradient-Echo T1-Weighted and Spin-Echo T2-Weighted Images at 3T in Evaluating Term-Neonatal Myelination
A.E. Tyan, A.M. McKinney, T.J. Hanson, and C.L. Truwit

SPINE

 **417 Time-Resolved Contrast-Enhanced MR Angiography of Spinal Vascular Malformations** *M. Amarouche, J.L. Hart, A. Siddiqui, T. Hampton, and D.C. Walsh*

ONLINE FEATURES (www.ajnr.org)

WHITE PAPER

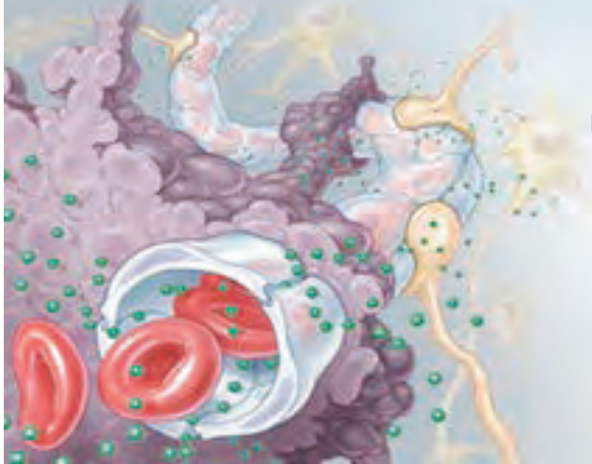
  **E1 Imaging Evidence and Recommendations for Traumatic Brain Injury: Advanced Neuro- and Neurovascular Imaging Techniques** *M. Wintermark, P.C. Sanelli, Y. Anzai, A.J. Tsiouris, and C.T. Whitlow, on behalf of the American College of Radiology Head Injury Institute*

BOOK REVIEWS *R.M. Quencer, Section Editor*

Please visit www.ajnrblog.org to read and comment on Book Reviews.

21st Annual Blood-Brain Barrier Consortium Meeting
March 19-21, 2015
Skamania Lodge in Stevenson, Washington

The 2015 Annual Blood-Brain Barrier Consortium Meeting will be held March 19-21 at Skamania Lodge in Stevenson, Washington. The meeting will include a state-of-the-art pre-clinical and clinical neuroimaging session titled "Imaging the Neurovascular Unit: Permeability, Blood Volume, and Functional Imaging". The meeting is partially funded by a National Institutes of Health R13 grant, with support from the National Cancer Institute, National Institute of Neurological Disorders and Stroke, and National Institute of Deafness and Communication Disorders, and is organized in collaboration with the International Brain Barriers Society.



For more information, please visit www.ohsu.edu/bbb



Simplify
the MOC Process

CMEgateway.org



Manage
your CME Credits Online



It's Easy and Free!

Log on to CME Gateway to:

- View or print reports of your CME credits from multiple societies from a single access point.
- Print an aggregated report or certificate from each participating organization.
- Link to SAMs and other tools to help with maintenance of certification.

American Board of Radiology (ABR) participation!

By activating ABR in your organizational profile, your MOC-fulfilling CME and SAM credits can be transferred to your own personalized database on the ABR Web site.

Sign Up Today!

go to CMEgateway.org

Available to Members of Participating Societies

American Board of Radiology (ABR)	Radiological Society of North America (RSNA)
American College of Radiology (ACR)	Society of Interventional Radiology (SIR)
American Roentgen Ray Society (ARRS)	SNM
American Society of Neuroradiology (ASNR)	The Society for Pediatric Radiology (SPR)
Commission on Accreditation of Medical Physics Educational Programs, Inc. (CAMPEP)	

Official Journal:

American Society of Neuroradiology
American Society of Functional Neuroradiology
American Society of Head and Neck Radiology
American Society of Pediatric Neuroradiology
American Society of Spine Radiology

EDITOR-IN-CHIEF

Mauricio Castillo, MD

Professor of Radiology and Chief, Division of Neuroradiology, University of North Carolina, School of Medicine, Chapel Hill, North Carolina

SENIOR EDITORS

Harry J. Cloft, MD, PhD

Professor of Radiology and Neurosurgery, Department of Radiology, Mayo Clinic College of Medicine, Rochester, Minnesota

Nancy J. Fischbein, MD

Professor of Radiology, Otolaryngology-Head and Neck Surgery, Neurology, and Neurosurgery and Chief, Head and Neck Radiology, Department of Radiology, Stanford University Medical Center, Stanford, California

Jeffrey S. Ross, MD

Staff Neuroradiologist, Barrow Neurological Institute, St. Joseph's Hospital, Phoenix, Arizona

Pamela W. Schaefer, MD

Clinical Director of MRI and Associate Director of Neuroradiology, Massachusetts General Hospital, Boston, Massachusetts, and Associate Professor, Radiology, Harvard Medical School, Cambridge, Massachusetts

Charles M. Strother, MD

Professor of Radiology, Emeritus, University of Wisconsin, Madison, Wisconsin

Jody Tanabe, MD

Professor of Radiology and Psychiatry, Chief of Neuroradiology, University of Colorado, Denver, Colorado

EDITORIAL BOARD

Ashley H. Aiken, *Atlanta, Georgia*
A. James Barkovich, *San Francisco, California*
Walter S. Bartynski, *Charleston, South Carolina*
Barton F. Branstetter IV, *Pittsburgh, Pennsylvania*
Jonathan L. Brisman, *Lake Success, New York*
Julie Bykowski, *San Diego, California*
Donald W. Chakeres, *Columbus, Ohio*
Alessandro Cianfoni, *Lugano, Switzerland*
Colin Derdeyn, *St. Louis, Missouri*
Rahul S. Desikan, *San Diego, California*
Richard du Mesnil de Rochemont, *Frankfurt, Germany*
Clifford J. Eskey, *Hanover, New Hampshire*
Massimo Filippi, *Milan, Italy*
David Fiorella, *Cleveland, Ohio*
Allan J. Fox, *Toronto, Ontario, Canada*
Christine M. Glastonbury, *San Francisco, California*

John L. Go, *Los Angeles, California*
Wan-Yuo Guo, *Taipei, Taiwan*
Rakesh K. Gupta, *Lucknow, India*
Lotfi Hacein-Bey, *Sacramento, California*
David B. Hackney, *Boston, Massachusetts*
Christopher P. Hess, *San Francisco, California*
Andrei Holodny, *New York, New York*
Benjamin Huang, *Chapel Hill, North Carolina*
Thierry A.G.M. Huisman, *Baltimore, Maryland*
George J. Hunter, *Boston, Massachusetts*
Mahesh V. Jayaraman, *Providence, Rhode Island*
Valerie Jewells, *Chapel Hill, North Carolina*
Timothy J. Kaufmann, *Rochester, Minnesota*
Kenneth F. Layton, *Dallas, Texas*
Ting-Yim Lee, *London, Ontario, Canada*
Michael M. Lell, *Erlangen, Germany*
Michael Lev, *Boston, Massachusetts*
Karl-Olof Lovblad, *Geneva, Switzerland*
Franklin A. Marden, *Chicago, Illinois*
M. Gisele Matheus, *Charleston, South Carolina*
Joseph C. McGowan, *Merion Station, Pennsylvania*
Kevin R. Moore, *Salt Lake City, Utah*
Christopher J. Moran, *St. Louis, Missouri*
Takahisa Mori, *Kamakura City, Japan*

Suresh Mukherji, *Ann Arbor, Michigan*
Amanda Murphy, *Toronto, Ontario, Canada*
Alexander J. Nemeth, *Chicago, Illinois*
Laurent Pierot, *Reims, France*
Jay J. Pillai, *Baltimore, Maryland*
Whitney B. Pope, *Los Angeles, California*
M. Judith Donovan Post, *Miami, Florida*
Tina Young Poussaint, *Boston, Massachusetts*
Joana Ramalho, *Lisbon, Portugal*
Otto Rapalino, *Boston, Massachusetts*
Álex Rovira-Cañellas, *Barcelona, Spain*
Paul M. Ruggieri, *Cleveland, Ohio*
Zoran Rumboldt, *Rijeka, Croatia*
Amit M. Saindane, *Atlanta, Georgia*
Erin Simon Schwartz, *Philadelphia, Pennsylvania*
Aseem Sharma, *St. Louis, Missouri*
J. Keith Smith, *Chapel Hill, North Carolina*
Maria Vittoria Spampinato, *Charleston, South Carolina*
Gordon K. Sze, *New Haven, Connecticut*
Krishnamoorthy Thamburaj, *Hershey, Pennsylvania*
Kent R. Thielen, *Rochester, Minnesota*
Cheng Hong Toh, *Taipei, Taiwan*
Thomas A. Tomsick, *Cincinnati, Ohio*
Aquila S. Turk, *Charleston, South Carolina*
Willem Jan van Rooij, *Tilburg, Netherlands*
Arastoo Vossough, *Philadelphia, Pennsylvania*
Elysa Widjaja, *Toronto, Ontario, Canada*
Max Wintermark, *Charlottesville, Virginia*
Ronald L. Wolf, *Philadelphia, Pennsylvania*
Kei Yamada, *Kyoto, Japan*

EDITORIAL FELLOW

Asim F. Choudhri, *Memphis, Tennessee*

YOUNG PROFESSIONALS ADVISORY COMMITTEE

Asim K. Bag, *Birmingham, Alabama*
Anna E. Nidecker, *Sacramento, California*
Peter Yi Shen, *Sacramento, California*

HEALTH CARE AND SOCIOECONOMICS EDITOR

Pina C. Sanelli, *New York, New York*

Founding Editor

Juan M. Taveras

Editors Emeriti

Robert I. Grossman, Michael S. Huckman,
Robert M. Quencer

Special Consultants to the Editor
Sandy Cheng-Yu Chen, Girish Fatterpekar,
Ryan Fitzgerald, Katherine Freeman,
Yvonne Lui, Greg Zaharchuk

INR Liaisons

Timo Krings, Karel terBrugge

Managing Editor

Karen Halm

Electronic Publications Manager

Jason Gantenberg

Editorial Assistant

Mary Harder

Executive Director, ASNR

James B. Gantenberg

Director of Communications, ASNR

Angelo Artemakis



AJNR (Am J Neuroradiol) (ISSN 0195–6108) is a journal published monthly, owned and published by the American Society of Neuroradiology (ASNR), 800 Enterprise Drive, Suite 205, Oak Brook, IL 60523. Annual dues for the ASNR include \$170.00 for journal subscription. The journal is printed by Cadmus Journal Services, 5457 Twin Knolls Road, Suite 200, Columbia, MD 21045; Periodicals postage paid at Oak Brook, IL and additional mailing offices. Printed in the U.S.A. POSTMASTER: Please send address changes to American Journal of Neuroradiology, P.O. Box 3000, Denville, NJ 07834, U.S.A. Subscription rates: nonmember \$380 (\$450 foreign) print and online, \$305 online only; institutions \$440 (\$510 foreign) print and basic online, \$875 (\$940 foreign) print and extended online, \$365 online only (basic), extended online \$790; single copies are \$35 each (\$40 foreign). Indexed by PubMed/Medline, BIOSIS Previews, Current Contents (Clinical Medicine and Life Sciences), EMBASE, Google Scholar, HighWire Press, Q-Sensei, RefSeek, Science Citation Index, and SCI Expanded. Copyright © American Society of Neuroradiology.

Trevo® XP ProVue Retrievers

See package insert for complete indications, complications, warnings, and instructions for use.

INDICATIONS FOR USE

The Trevo Retriever is intended to restore blood flow in the neurovasculature by removing thrombus in patients experiencing ischemic stroke within 8 hours of symptom onset. Patients who are ineligible for intravenous tissue plasminogen activator (IV t-PA) or who fail IV t-PA therapy are candidates for treatment.

COMPLICATIONS

Procedures requiring percutaneous catheter introduction should not be attempted by physicians unfamiliar with possible complications which may occur during or after the procedure. Possible complications include, but are not limited to, the following: air embolism; hematoma or hemorrhage at puncture site; infection; distal embolization; pain/headache; vessel spasm, thrombosis, dissection, or perforation; emboli; acute occlusion; ischemia; intracranial hemorrhage; false aneurysm formation; neurological deficits including stroke; and death.

COMPATIBILITY

3x20 mm retrievers are compatible with Trevo® Pro 14 Microcatheters (REF 90231) and Trevo® Pro 18 Microcatheters (REF 90238). 4x20 mm retrievers are compatible with Trevo® Pro 18 Microcatheters (REF 90238). Compatibility of the Retriever with other microcatheters has not been established. Performance of the Retriever device may be impacted if a different microcatheter is used. The Merci® Balloon Guide Catheters are recommended for use during thrombus removal procedures. Retrievers are compatible with the Abbott Vascular DOC® Guide Wire Extension (REF 22260)

WARNINGS

- Contents supplied STERILE, using an ethylene oxide (EO) process. Nonpyrogenic.
- To reduce risk of vessel damage, adhere to the following recommendations:
 - Take care to appropriately size Retriever to vessel diameter at intended site of deployment.
 - Do not perform more than six (6) retrieval attempts in same vessel using Retriever devices.
 - Maintain Retriever position in vessel when removing or exchanging Microcatheter.
- To reduce risk of kinking/fracture, adhere to the following recommendations:
 - Immediately after unsheathing Retriever, position Microcatheter tip marker just proximal to shaped section. Maintain Microcatheter tip marker just proximal to shaped section of Retriever during manipulation and withdrawal.
 - Do not rotate or torque Retriever.
 - Use caution when passing Retriever through stented arteries.
- Do not resterilize and reuse. Structural integrity and/or function may be impaired by reuse or cleaning.
- The Retriever is a delicate instrument and should be handled carefully. Before use and when possible during procedure, inspect device carefully for damage. Do not use a device that shows signs of damage. Damage may prevent device from functioning and may cause complications.
- Do not advance or withdraw Retriever against resistance or significant vasospasm. Moving or torquing device against resistance or significant vasospasm may result in damage to vessel or device. Assess cause of resistance using fluoroscopy and if needed resheath the device to withdraw.

- If Retriever is difficult to withdraw from the vessel, do not torque Retriever. Advance Microcatheter distally, gently pull Retriever back into Microcatheter, and remove Retriever and Microcatheter as a unit. If undue resistance is met when withdrawing the Retriever into the Microcatheter, consider extending the Retriever using the Abbott Vascular DOC guidewire extension (REF 22260) so that the Microcatheter can be exchanged for a larger diameter catheter such as a DAC® catheter. Gently withdraw the Retriever into the larger diameter catheter.
- Administer anti-coagulation and anti-platelet medications per standard institutional guidelines.

PRECAUTIONS

- Prescription only – device restricted to use by or on order of a physician.
- Store in cool, dry, dark place.
- Do not use open or damaged packages.
- Use by “Use By” date.
- Exposure to temperatures above 54°C (130°F) may damage device and accessories. Do not autoclave.
- Do not expose Retriever to solvents.
- Use Retriever in conjunction with fluoroscopic visualization and proper anti-coagulation agents.
- To prevent thrombus formation and contrast media crystal formation, maintain a constant infusion of appropriate flush solution between guide catheter and Microcatheter and between Microcatheter and Retriever or guidewire.
- Do not attach a torque device to the shaped proximal end of DOC® Compatible Retriever. Damage may occur, preventing ability to attach DOC® Guide Wire Extension.



Concentric Medical
301 East Evelyn
Mountain View, CA 94041



EMERGO Europe
Molenstraat 15
2513 BH, The Hague
The Netherlands



Stryker Neurovascular
47900 Bayside Parkway
Fremont, CA 94538

stryker.com/neurovascular
stryker.com/emea/neurovascular

Date of Release: JUN/2014

EX_EN_GL

The Winds of Change

M. Castillo, *Editor-in-Chief*

As of May 2014, the American Society of Neuroradiology (ASNR) had 702 women members. Although it is difficult to determine who the first women neuroradiologists were, ASNR's data base offers the possibility of determining who our initial female members were. Among the first 20, easily recognizable names due to their academic achievements include Drs Dietrich (#3), Davis (#4), Byrd (#12), Cohen (#13), Osborn (#19), and Donovan Post (#20). Of them, Dr Osborn is an ASNR Past President (1988–1989) and Dr Donovan Post, an ASSR Past President (1999–2000). From the time of its founding in 1962, ASNR has had only had 3 women Presidents apart from Dr Osborn as follows: Dr Hudgins (2005–2006), Dr Meltzer (2010–2011), and Dr Schaefer (2012–2013). In 2015, Dr Loevner will become its fifth female President. However, in ASNR, as in the rest of medicine, the winds of change are coming our way. At the time of this writing, I serve as the society's First Past President and 3 of the 6 members of the Administrative Committee are women and of 23 Executive Committee members 9 are women, the highest proportions ever. In *AJNR*, 3 out of 6 Senior Editors are women (Drs Schaefer, Fischbein, and Tanabe).

If one looks at medical school applicants in the United States, in 1969, 9% were women; however, by 2010, the American Association of Medical Colleges (AAMC) reported that 48% of medical degrees were awarded to women.¹ Nursing has always been a female vocation, and continues to be; 94.6% of registered nurses are women. In the past, pharmacology was mostly a man's occupation; however, today over 60% of pharmacists are female.² Women's participation in medicine did not significantly increase until the 1970s when our government banned discrimination on the grounds of sex and when the AAMC made a point of supporting their participation in medical education. In England, nearly 60% of current medical students are female (it reached 62% in 2003) and women make up 40% of physicians, 42% of general practitioners, and nearly 30% of specialists.³ British women seem to prefer general practices such as pediatrics (40%) more than surgical specialties (<10%) and similar statistics are found for Canadian physicians. The United States is catching up and nearly 44% of medical students are now female (in other countries the current female-to-male ratio is 3:2). In more liberal countries such as France and Spain, women make up 58% and 64% of doctors under the age 35, respectively.²

Warning: Before you continue reading, I must tell you that I am not casting judgment here, just summarizing what is found in the literature.

Some argue that women in medicine are less productive than men and debate if the rise of women in medicine will accentuate the shortage of physicians and access to health care. Workplace differences between males and females are consistent across different countries so culture and religion have little influence on

how medicine is practiced by either sex. In general, women are less likely to work excessive hours, they retire at the expected age (or at a younger age), and see lesser numbers of patients; conversely, they are better communicators and spend more time in preventive care. Because women patients seem to seek women physicians, more female doctors should equal better outcomes and life expectancies for women; however, studies have found that overall, the number of physicians per population regardless of sex has little to do with female life expectancy. In addition, countries such as Canada and Japan with a low physician density show longer lives for women than countries with higher densities of female physicians such as the United States and the Netherlands.⁴ However, because on the whole more physicians means more female physicians and more primary care practitioners, the overall benefits of adding more women to the medical workflow may eventually have a positive effect in prolonging life expectancy. The Organization for Economic Cooperation and Development has gathered data that support the notion that countries with the highest strength in primary care have better outcomes related to all-cause mortality, all-cause premature mortality, and cause-specific premature mortality. This report does not address the role of women in these outcomes, but because they represent a disproportionate presence in primary care, there must be some relationship.

In 2 controversial articles, the *British Medical Journal* discussed the issue of too many female medical graduates. Against female medical graduates, Dr McKinstry offered the following statements⁵:

- 1) Because females concentrate in family friendly specialties, their presence will tilt the balance between generalists and specialists, leading to a smaller number and shortage of the latter.
- 2) Females are more likely to work part-time and their work is disrupted by pregnancies and child rearing. Moreover, 50% of females continue to work part-time even when their children become older, while most men, regardless of age, work full-time.
- 3) Females generally retire earlier than age 60 (in psychiatry, they tend to retire on average at age 55).
- 4) Mothers tend to publish significantly less than men and childless women.

Arguing for the role of women in medicine, Dr Dacre stated⁶:

- 1) Medicine needs to attract the best and brightest, and women as a whole do better on undergraduate and postgraduate examinations (in reality these differences are minimal and of questionable significance as are the results of many other examinations).
- 2) Medicine is a caring profession and women are much more engaged in patient care than men.
- 3) Despite their large number in medicine, women are underrepresented in academia. Their numbers decrease with increasing ranks; in England and the United States, only 11% and 15% of professorships, respectively, are held by women. Only 10% of department Chairs are women in the United States.

Local politics may also favor the presence of women in medicine. In Europe, the current trend is to restrict the working week for health service professionals to 48 hours (The European Working Time Directive).¹ More female doctors working part-time will facilitate achieving these reduced schedules with enough physicians to support the needed workforce.

Increasing female participation in professional activities is occurring at all levels and in most countries, even the most conservative. Saudi Arabia now allows women to work in areas where women feel that communicating among each other is better. Most specialized women's apparel shops now must have female sales associates.⁷ In that country, women represent 17% of the current workforce and their participation increased 280% in the last 10 years, while nearly 60% of all university students are women. More than half of all PhDs in that country are now given to females.² Although Saudi professional women still make less money than their male counterparts, that is not the case everywhere. In Brazil, 30% of women make more money than their husbands.²

In December 2013, *Time* magazine published an article entitled: "2013: The Year Men Became Obsolete?"⁸ That short article offers a startling glimpse at the winds of change: In 2013, 57% of all bachelor's degrees were earned by women as well as 60% of master's degrees and 52% of doctorates. The number of women with degrees could be higher but many universities have chosen an arbitrary threshold of 60% as their cutoff for female admissions. While the participation of women in the workforce increased to 6.2% (1980–2012), men's participation went down by 7.2% during the same period. What are men doing? Well, according to that article they are pouring concrete, laying bricks, tarring roofs, and excavating sewage lines, among other dirty and dangerous métiers. These latter observations come from the famous Munk Debates on the obsolescence of males.*

But let us go back to women in medicine and particularly in radiology. Some 22 years ago when I came to the University of North Carolina, at least half of our residents were female, but after a few years, we had just men and now, out of 31 residents, 7 are female (roughly 23%). In the last 3 years, out of a total of 12 neuroradiology fellows, 4 have been female, so again roughly a similar proportion between specialty and subspecialty. These numbers match those reported in the literature, that is, about 24% of US radiologists are women. Why is that, when more than 50% of US medical students are female? The explanations offered follow: Fear of irradiation during childbearing age, too little patient contact, too many years of extra training, and a highly competitive specialty with decreasing job opportunities upon graduation. Curiously, females also find working in dark rooms unappetizing. The American College of Radiology is aware of this and has created a Commission for Women that is charged with researching and identifying ways to attract and retain more women in radiology. When compared with general medicine, the numbers of

women in radiology are decreasing. In 1995, 28% of radiology residents were women; however, by 2000, this number had decreased to 22%. A survey published in the *American Journal of Roentgenology* shows that after internal medicine (18%), radiology (15%) is the most popular specialty selected by female medical students.⁹ That article lists intellectual stimulation as one of the reasons that radiology is chosen by both women and men. Another reason that is not mentioned in that article may be regular hours. Another specialty with regular hours, gastroenterology, may shed some light onto this factor. The number of female gastroenterologists has gone up from 5% to 30% mostly due to its regular scheduled hours.² The changes being experienced by the medical profession are a subject of close scrutiny. From 1976 to 1979, only 6 articles exploring the role of women in medicine were published; between 2005 and 2009, there were 212.¹⁰

Of the 30 professions that will add the most jobs in the next 10 years, women already dominate 20.² The salaries for full-time men, when adjusted for inflation, have increased 28% from 1969 to date, but most women still make less money than men. Women, ages 25–35 make on average 20%–25% less than men (US \$37,000 versus \$49,000 in 2012). This may be, at least in part, because women still make up most low-paid workers. Unfortunately, the same pattern is seen in academia where female researchers earn US \$6000–\$13,000 less than men, and in departments of medicine where they on average earn US \$15,000 less than men across all ranks.¹¹ So although the winds of change are blowing our way, perhaps they need to blow stronger and more fairly.

REFERENCES

1. Women in medicine. http://en.wikipedia.org/wiki/Women_in_medicine. Accessed January 9, 2014
2. Pharm girls. How women remade the economy. In: Rossin H. *The End of Men and the Rise of Women*. New York: Riverhead Books; 2012:113–45
3. Elston MA. **Women in medicine. The future.** www.rcplondon.ac.uk/sites/default/files/women-and-medicine-summary.pdf. Accessed January 9, 2014
4. Phillips SP, Austin EB. **The feminization of medicine and population health.** *JAMA* 2009;301:863–64
5. McKinstry B. **Are there too many female medical graduates. Yes.** *BMJ* 2008;336:748–49
6. Dacre J. **Are there too many female medical graduates. No.** *BMJ* 2008;336:749–50
7. Zoepf K. **Shopgirls.** *The New Yorker*. December 23, 2013. http://www.newyorker.com/reporting/2013/12/23/131223fa_fact_zoepf. Accessed January 9, 2014
8. Paglia C. **2013: the year men became obsolete?** *Time*. December 30, 2013:26
9. Fielding JR, Major NM, Mullan BF, et al. **Choosing a specialty in medicine: female medical students and radiology.** *AJR Am J Roentgenol* 2007;188:897–900
10. Riska E. **Gender and medical careers.** *Maturitas* 2011;68:264–67
11. Mangan K. **Women in academic medicine: equal to men, except in pay.** *The Chronicle of Higher Education*. January 9, 2014. <http://chronicle.com/article/Women-in-Academic-Medicine-/64892/>. Accessed January 9, 2014

* The Munk Debates are held biannually in Toronto to discuss major policy issues. The organization was funded by Peter Munk (Chairman of the world's largest gold mining operation) in 2008.

The Role of Functional Dopamine-Transporter SPECT Imaging in Parkinsonian Syndromes, Part 1

T.C. Booth, M. Nathan, A.D. Waldman, A.-M. Quigley, A.H. Schapira, and J. Buscombe



ABSTRACT

SUMMARY: As we defeat infectious diseases and cancer, one of the greatest medical challenges facing us in the mid-21st century will be the increasing prevalence of degenerative disease. Those diseases, which affect movement and cognition, can be the most debilitating. Dysfunction of the extrapyramidal system results in increasing motor disability often manifest as tremor, bradykinesia, and rigidity. The common pathologic pathway of these diseases, collectively described as parkinsonian syndromes, such as Parkinson disease, multiple system atrophy, progressive supranuclear palsy, corticobasal degeneration, and dementia with Lewy bodies, is degeneration of the presynaptic dopaminergic pathways in the basal ganglia. Conventional MR imaging is insensitive, especially in early disease, so functional imaging has become the primary method used to differentiate a true parkinsonian syndrome from vascular parkinsonism, drug-induced changes, or essential tremor. Unusually for a modern functional imaging technique, the method most widely used in European clinics depends on SPECT and not PET. This SPECT technique (described in the first of 2 parts) commonly reports dopamine-transporter function, with decreasing striatal uptake demonstrating increasingly severe disease.

ABBREVIATIONS: DaT = dopamine transporters; ^{18}F = fluorine 18; ^{18}F -DOPA = 6- ^{18}F fluoro-L-3,4-dihydroxyphenylalanine; ^{123}I = iodine 123; ^{123}I -FP-CIT = ^{123}I -ioflupane (*N*- ω -fluoropropyl- β CIT); PD = idiopathic Parkinson disease; SWEDD = scans without evidence of dopaminergic deficit

Parkinsonian syndromes are a group of movement disorders characterized by tremor, bradykinesia, and rigidity. They are most frequently due to primary neurodegenerative disease, resulting in loss of dopaminergic nerve terminals along the nigrostriatal pathway, as occurs in idiopathic Parkinson disease (PD), multiple system atrophy, progressive supranuclear palsy, corticobasal degeneration, and dementia with Lewy bodies. Other causes of parkinsonism that do not involve nigrostriatal degeneration include drug-induced, vascular, or toxic insult and psychogenic disease. Patients with nigrostriatal degeneration may benefit from dopaminergic medication, whereas nondegenerative or postsynaptic etiologies do not.

The clinical diagnosis of PD, based on clinical signs, assessment of inclusion and exclusion criteria, and good response to levodopa,¹ can be straightforward. However, mild, atypical, or

ambiguous signs with unconvincing responses to levodopa can make the diagnosis inconclusive.² Lack of diagnosis may have adverse prognostic implications in the management of parkinsonism. Where there is clinical doubt, functional imaging may be decisive.

Pathophysiology of Parkinson Disease

PD accounts for approximately 75% of all cases of parkinsonism.³ Clinicopathologic studies have established the underlying cause of the dominant motor features of PD as dysfunction of the dopaminergic neurotransmitter system.⁴

Dopamine is a neurotransmitter that plays a central role in the regulation and control of movement, motivation, and cognition. Dopaminergic neurons are predominantly found in the midbrain and project from the substantia nigra pars compacta to the striatum (caudate nucleus and putamen). This is the presynaptic nigrostriatal dopaminergic pathway. The postsynaptic neurons lie in the striatum.

Dopamine is produced by the dopaminergic neurons and is stored in vesicles within the neuron, which protect it from oxidation by monoamine oxidase. Once the appropriate signal is received by the presynaptic neuron, dopamine is released into the synaptic cleft, where it interacts with dopamine receptors on the postsynaptic striatal neuron (Fig 1). To regulate dopamine levels and enable a response to the next signal, extracellular dopamine is actively pumped back into the presynaptic neuron by dopamine transporters

From the Department of Neuroradiology (T.C.B.), National Hospital for Neurology and Neurosurgery, London, UK; Department of Nuclear Medicine (M.N., A.-M.Q.), Royal Free Hospital National Health Service Trust, London, UK; Department of Imaging (A.D.W.), Imperial College Healthcare National Health Service Trust, London, UK; Department of Clinical Neurosciences (A.H.S.), Institute of Neurology, University College London, London, UK; and Department of Nuclear Medicine (J.B.), Addenbrooke's Hospital, Cambridge University Hospitals NHS Foundation Trust, Cambridge, UK.

Please address correspondence to Thomas C. Booth, MA, MBBS, MRCP, FRCP, Department of Neuroradiology, National Hospital for Neurology and Neurosurgery, Queen Square, London, WC1N 3BG, UK; e-mail: tombooth@doctors.org.uk

Indicates open access to non-subscribers at www.ajnr.org

<http://dx.doi.org/10.3174/ajnr.A3970>

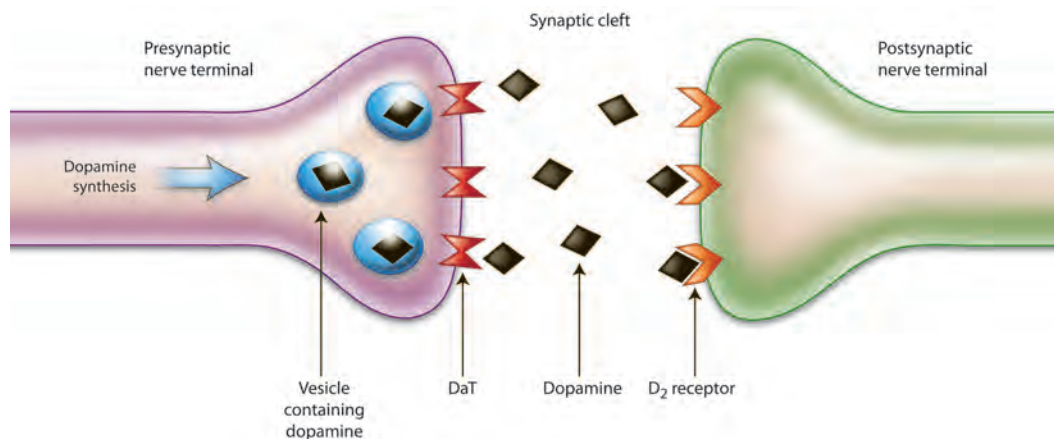


FIG 1. Schematic illustration of the dopaminergic pathway within the striatum. Dopamine is synthesized and stored in vesicles until released into the synaptic cleft in response to an action potential. After interacting with the postsynaptic dopamine receptors, dopamine is released back into the synaptic cleft, where it is actively taken up by dopamine transporters and carried into the presynaptic neuron.

(DaT) on the cell surface, where dopamine may either be re-stored in vesicles or catabolized into breakdown products.

PD is characterized neuropathologically by degeneration of the substantia nigra pars compacta within the midbrain with subsequent deposition of neuronal Lewy bodies. Nigrostriatal degeneration, with consequent DaT depletion and downregulation, has the effect of reducing the levels of dopamine within the striatum, manifesting clinically as resting tremor, rigidity, and bradykinesia. Nigrostriatal degeneration is asymmetric, with almost all patients diagnosed with PD presenting initially with unilateral signs.

An Overview of Imaging in Neurodegenerative Parkinsonian Syndromes

Conventional MR imaging alone is not sufficiently sensitive in diagnosing these disorders.⁵ Volumetric, spectroscopic, and diffusion MR imaging techniques and transcranial sonography show promise but are seldom used in routine clinical practice. Much of the evidence surrounding these methods derives from retrospective studies or small series. Moreover, differentiation among disease types is commonly demonstrated in group comparisons, rather than allowing a specific diagnosis in an individual patient. The most sensitive imaging techniques for an early diagnosis of parkinsonian syndromes are SPECT and PET, by using ligands that report nigrostriatal dopaminergic function.⁶ SPECT has proved useful in differentiating parkinsonism due to nigrostriatal degeneration and nondegenerative or postsynaptic causes. SPECT is, therefore, a valuable tool for the clinician in determining the correct management algorithm for the patient. However, other imaging modalities may exclude treatable nondegenerative etiologies and play a role in differentiating neurodegenerative parkinsonian disorders.

Imaging the Dopamine Transporter

DaT is a sodium chloride–dependent transmembrane protein localized to the presynaptic nigrostriatal cell surface,⁷ whose expression is not fixed but can be up- or downregulated by certain factors, by using membrane trafficking as the key mechanism.⁸ For example, insulin can increase DaT expression on the cell surface, while amphetamines or levodopa can decrease expression.^{9,10} In

vivo SPECT imaging of DaT with specific tracers provides a guide to the attenuation of functional dopaminergic neurons.

Postmortem studies have shown a severe reduction of presynaptic cocaine-binding dopamine receptors associated with DaT in patients with PD.⁷ Consequently, DaT selective radiotracers have been developed by using analogues of cocaine, of which iodine 123 (¹²³I)-β CIT (2β-carbomethoxy-3β-(4-iodophenyl) tropane) and ¹²³I-ioflupane (*N*-ω-fluoropropyl-β CIT; or FP-CIT) are the most widely used^{11,12} and are used in the DaT-SPECT clinical studies described below. Other ligand tracers include ^{99m}Tc-TRODAT [2-[[[3-(4-chlorophenyl)-8-methyl-8-azabicyclo[3.2.1]oct-2-yl]methyl](2-mercaptoethyl)amino]ethyl]-amino]ethanethiolato-(3-)-N₂,N₂'₂,S₂,S₂']oxo-[1R-(exo-exo)], which has a lower striatal uptake compared with background than ¹²³I probes¹³ and ¹²³I-IPT [N-(3-iodopropen-2-yl)-2β-carbomethoxy-3β-(4-chlorophenyl) tropane].¹⁴ ¹²³I-FP-CIT (trade name DaTSCAN; GE Healthcare, Buckinghamshire, United Kingdom) has been the preferred radiotracer due to the shorter interval (3–6 hours) between injection and image acquisition.¹⁵ In addition, its uptake is not competitive with dopamine products, so treatment with levodopa can be continued, though other drugs such as monoamine oxidase inhibitors can decrease uptake. ¹²³I-FP-CIT has been approved by the European Medicines Agency since 2000 and the US Food and Drug Administration since 2011.

The Role of DaT-SPECT Imaging in Parkinsonian Syndromes

DaT-SPECT imaging enables differentiation of neurodegenerative causes of parkinsonism, where typically patients will have abnormal scans, from other movement or tremor disorders where typically the DaT-SPECT study will be normal. Indications for DaT-SPECT imaging are given in the Table.

Before the use of functional imaging, the diagnosis of a neurodegenerative parkinsonian disorder depended on clinical evaluation with confirmation, when applicable, based on postmortem neuropathology. Even in specialized centers for movement disorders, where the positive predictive value of the final clinical diagnosis for all patients with parkinsonism was 85% (99% for PD

alone), 36% of patients were reclassified within a mean interval of 3.4 years from initial diagnosis.¹⁶ Since then, an industry-sponsored, prospective, 3-year longitudinal, multicenter study compared clinical scoring methods and DaT-SPECT findings in patients with clinical diagnostic uncertainty.¹⁷ Clinical scoring methods led to an overdiagnosis of PD, and it was suggested that DaT-SPECT should be implemented to reduce overdiagnosis in this population. In another recent, industry-sponsored, multicenter, randomized controlled trial, patients with a clinically uncertain parkinsonian syndrome or a monosymptomatic, atypical, or incomplete presentation of parkinsonian clinical features were randomized to DaT-SPECT imaging to see whether it led to a change in clinical diagnosis during 1 year.¹⁸ At 1 year, 54% of the patients randomized to DaT-SPECT imaging had a change in diagnosis, compared with 23% of the controls, and the imaging led to an increase in confidence in the clinicians' diagnoses. The most common change in management was initiation of medication,

Clinical indications for DaT-SPECT imaging

Indications
Only 1 of 3 cardinal clinical signs ^a with or without asymmetry
2 Signs without bradykinesia
Poor response to L-dopa
Lack of disease progression

^a Cardinal signs are resting tremor, rigidity, and bradykinesia. (An alternative classification adds a fourth cardinal sign as postural instability.)

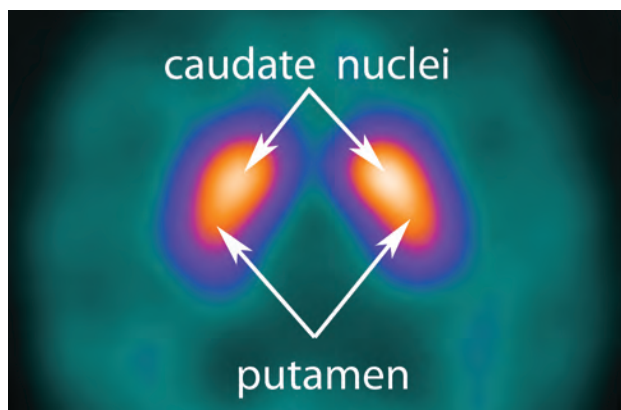


FIG 2. Normal study findings. The axial ¹²³I-FP-CIT DaT-SPECT image demonstrates symmetric tracer uptake in the caudate nuclei and putamina, with very low-grade, almost absent, background activity.

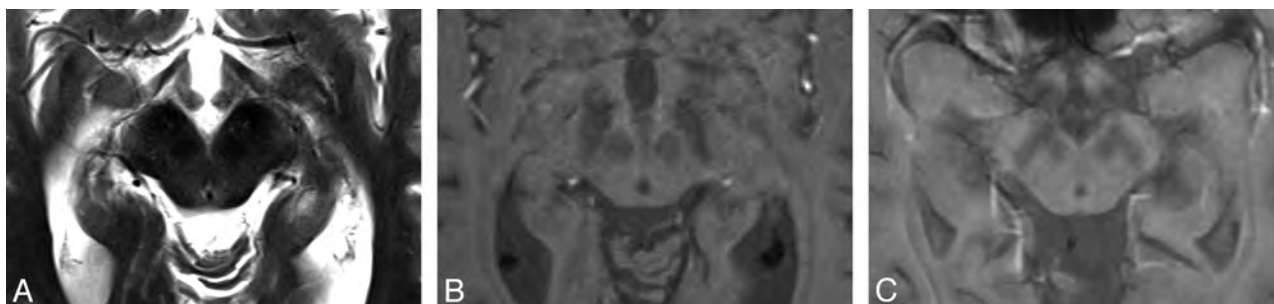


FIG 3. Axial T2-weighted MR imaging sequence in a patient with PD (A) demonstrating “smudging” of the hypointensity in the substantia nigra toward the red nucleus in the midbrain (right subtly more marked than the left, concordant with the contralateral clinical features). It is more easily visualized in the corresponding susceptibility-weighted image (B). Axial T2*-weighted MR imaging sequence also demonstrates the “smudging” sign as shown in another patient with PD (C) (left more than right concordant with worse contralateral clinical features). The “smudging” sign is nonspecific and seen in progressive supranuclear palsy, multiple system atrophy, and corticobasal degeneration. It is a subtle sign and often not used in routine clinical practice.

including dopaminergic therapy, confirming results from a previous multicenter trial.² Seventy-five percent of patients randomized to DaT-SPECT imaging treated by general neurologists had a change in diagnosis, as did 47% of those treated by a movement-disorder specialist, suggesting utility in both a general and specialist setting. The diagnostic stability of DaT-SPECT with time, together with a high interobserver agreement rate ($\kappa = 0.97$), demonstrates the reproducibility and reliability of the technique and highlights its value in adding objectivity to clinical scoring methods.¹⁷

DaT-SPECT imaging may be indicated at baseline or after a period of monitoring. The radiation dose is approximately equivalent to a head CT when using ¹²³I-FP-CIT.² Central nervous stimulants, such as amphetamines and other sympathomimetics, have a high affinity for DaT protein. Serotonin-reuptake inhibitors may upregulate or downregulate DaT. Therefore, these drugs can potentially confound DaT SPECT image interpretation and are usually stopped temporarily before imaging. Images are acquired by using standard gamma camera systems 3–4 hours after injection of 185-MBq ¹²³I-FP-CIT. The quality of the scan is dependent on optimization of the acquisition; it is essential that patient movement be minimized and that the rotational radius of the gamma camera detector head be as small as possible. Following reconstruction by using an iterative technique, images are usually displayed as axial sections parallel to a line drawn from a point where the anterior part of the frontal lobe is at its maximum distance from the posterior part of the occipital lobe. For diagnostic purposes, visual assessment of DaT binding appears to be comparable with semiquantitative analysis of ROIs normalized to reference brain (where there is absent or low background DaT expression).¹⁹ Detailed ¹²³I-FP-CIT practice guidelines have recently been published by the Society of Nuclear Medicine.²⁰

Because most dopaminergic transmission occurs in the striatum, this area will show the maximum uptake of DaT radiotracers, with minimal background activity in the remainder of the brain. In scans with normal findings, the striata appear as symmetric “comma” shapes (Fig 2). Any asymmetry or distortion of this shape, in the absence of patient motion, implies an abnormal scan finding.

Parkinson Disease

Structural abnormalities on MR imaging in PD are subtle and, other than nonspecific putaminal atrophy, are found in <20% of patients with PD.²¹ There may be nonspecific abnormalities of the substantia nigra, including “smudging” of the hypointensity in the substantia nigra toward the red nucleus on T2-weighted sequences (Fig 3)²² or increased signal with gray matter-suppressed T1-weighted inversion recovery sequences (Fig 4).²³ Voxel-based morphometry might reveal nonspecific gray matter loss of limbic, paralimbic, and prefrontal cortices.²⁴ Pathologic diffusion imaging findings in patients with PD are very rare⁵; however, elevated ADC may be seen in the region of the olfactory tracts in patients with PD compared with healthy controls.²⁵ ¹H-MRS studies are nonspecific, showing reduced NAA/Cr and NAA/choline ratios in the basal ganglia, reflecting neuronal loss.²⁶

Transcranial sonography reveals hyperechogenicity of the substantia nigra (Fig 5), which, together with normal echogenicity of the basal ganglia, has a positive predictive value of 93% for a prospective PD diagnosis.²⁷ An advantage of transcranial sonography is that these findings may also be premotor biomarkers.²⁸ However, a disadvantage is that up to 20% of white and 60% of Asians cannot be studied due to an inadequate temporal acoustic bone window.

6-[¹⁸F]fluoro-L-3,4-dihydroxyphenylalanine (fluorine 18 [¹⁸F]-DOPA) PET is a valuable functional technique that provides an

indirect measure of nigrostriatal neuron attenuation through evaluation of presynaptic dopa decarboxylase activity and intravesicular dopamine storage. With progressive nigrostriatal degeneration, there will be a consequent reduction in dopa decarboxylase activity and presynaptic dopamine storage. This is reflected on ¹⁸F-DOPA PET imaging as a reduction in uptake in the basal ganglia (Fig 6), similar to that in DaT SPECT imaging. With PD, there is a more pronounced reduction of radiotracer striatal binding in the putamen than in the caudate nucleus, which is asymmetric and correlated with disease severity.^{29,30} Most important, subclinical disease may also be identified on imaging.³¹ Other PET techniques are less informative.^{32,33} ¹⁸F-FDG PET measures regional metabolism and shows normal or increased uptake in the striatum contralateral to the initial clinical signs. Postsynaptic striatal neuron density can also be measured with ¹¹C-[(-)-(S)-3,5-dichloro-N-((1-ethyl-2-pyrrolidinyl) methyl)-6-methoxy-salicylamide tartrate; FLA 870(-); A40664] (raclopride) PET showing normal or increased dopamine receptor binding.

DaT-SPECT in Parkinson Disease

Like PET, SPECT reflects the typical asymmetric nigrostriatal degeneration with a reduction in striatal DaT binding contralateral to the initial signs. In keeping with PET and neuropathologic evidence, SPECT typically demonstrates preferential DaT loss in the putamen compared with the caudate nucleus,^{34,35} though

symmetric and somewhat uniform striatal loss of DaT may occur in genetic forms of parkinsonism such as those due to *parkin* (*PARK2*) mutations (the most commonly known cause of young-onset, autosomal recessive parkinsonism).³⁶

To categorize DaT-SPECT abnormality, the imaging findings from 3 prospective multicenter studies were visually classified into normal and abnormal, of which the latter was further subdivided into 3 different patterns.^{2,17,37} Studies with normal DaT findings demonstrated symmetric intense tracer uptake in both caudate nuclei and putamina. Abnormal patterns (Fig 7) are classified by Catafau and Tolosa² as the following:

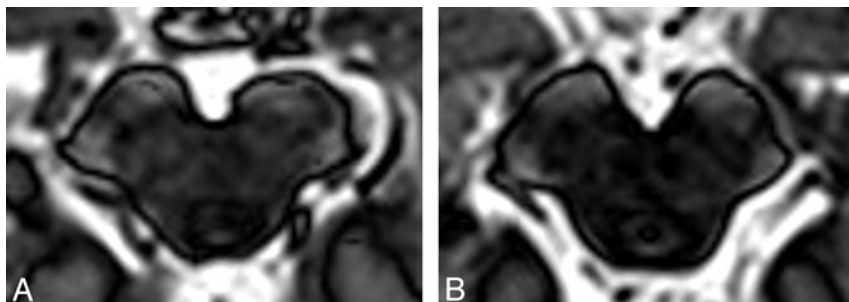


FIG 4. On these inversion-recovery T1-weighted images in which deep gray matter signal is suppressed, the substantia nigra in a patient with severe PD (A) appears both substantially shrunk and with altered contrast in comparison with a healthy control (B). There is a correlation between the substantia nigra area with the Unified Parkinson Disease Rating Scale score.²³ There is also a group difference between those with PD and controls; however, this metric has not been proved to be useful for individuals. Images courtesy of Dr Ludovico Minati, Scientific Department, Istituto Di Ricovero e Cura a Carattere Scientifico Foundation Neurologic Institute, Carlo Besta, Milan, Italy.

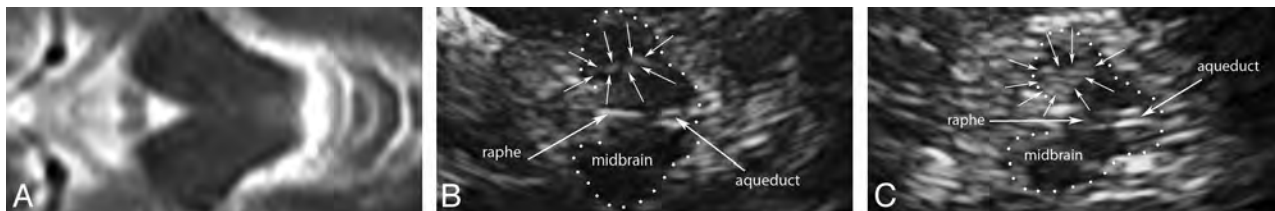


FIG 5. T2-weighted fast spin-echo MR image (A) and corresponding transcranial sonography images (B and C) of midbrain axial sections at the orbitomeatal line. B, Transcranial sonography image of the axial midbrain section in a healthy person depicting the hypoechoic midbrain (outlined) surrounded by the hyperechogenic basal cisterns. In the anatomic area of the ipsilateral substantia nigra, only small hyperechoic patches are visible (small arrows); the planimetrically measured area is <0.20 cm². The raphe is detected as a highly echogenic, continuous line; the aqueduct is shown at the dorsal part of the midbrain. C, Transcranial sonography of a patient with Parkinson disease showing a bilateral hyperechogenic substantia nigra (area ≥0.20 cm²). Small arrows indicate the substantia nigra. Images courtesy of Dr Rita CL Fernandes, Department of Neurodegeneration at Tübingen University Hospital and Hertie Institute of Clinical Brain Research, Tübingen, Germany.

asymmetric uptake with reduced putaminal activity in 1 hemisphere (type 1); clear symmetric reduction of putaminal uptake in both hemispheres (type 2); virtual absence of uptake in both the putamina and caudate nuclei in both hemispheres, resulting in a significant reduction in contrast, and the visualization of background activity throughout the rest of the image (type 3). Some centers use this classification as a routine descriptive system, but there is no clinical or outcome-measure correlation.

All studies in a meta-analysis on the diagnostic accuracy of DaT-SPECT demonstrated that patients with PD and healthy patients could be differentiated with 100% specificity.³⁸ However, the sensitivity varied from 38% to 100% among centers. This is reflected in 2 large multicenter clinical trials that used ¹²³I-β-CIT SPECT, which found that up to 15% of patients diagnosed as having PD had normal DaT-SPECT study findings classified as “scans without evidence of dopaminergic deficit” (SWEDD).^{10,39} It has been suggested that the discrepancy between clinical diagnosis and imaging findings is caused by reductions in striatal DaT availability in early PD that are below the detection threshold.¹ However, it is improbable that DaT imaging would have normal findings in initial early PD as the following combined evidence suggests: first, by the time PD clinically manifests, approximately 80% of striatal dopamine has been lost; this change is correlated to presynaptic nigrostriatal cell loss with a parallel reduction in DaT of 80%^{40,41}; second, studies suggest that DaT-SPECT is highly sensitive in detecting dopaminergic degeneration because there is a correlation between the extent of degeneration measured with DaT-SPECT and clinical severity.⁴² Furthermore, in asymptomatic but hyposmic first-degree relatives of patients with

PD, DaT-SPECT predicts subsequent PD.⁴³ Additionally, studies in patients with hemiparkinsonian disorders demonstrate a bilateral loss of striatal DaT.^{35,42} Follow-up of SWEDD cases has since shown that these patients neither deteriorate nor respond to levodopa and that their DaT-SPECT study findings remain normal.^{10,17} Some have since been diagnosed with dystonic tremor. In summary, it is thought highly likely that in the SWEDD cases, the initial clinical diagnosis of PD was incorrect and that DaT-SPECT may be more sensitive in diagnosing PD than some studies have shown.

Another potential role for DaT-SPECT imaging is in monitoring disease progression in patients with treated and untreated PD.^{39,44} Nigrostriatal loss in patients with PD is estimated to be at least 5% per year, which is substantially higher than the age-associated physiologic loss of nigrostriatal neurons, estimated to be 8% per decade.^{29,44} With this in mind, extending the role of DaT-SPECT to assess the efficacy of neuroprotective therapies in trials has been debated.³⁵ However, because there is no proved correlation between progressive decline in DaT and clinical outcome, its usefulness as a surrogate end point is questionable.⁴⁵ Furthermore, there is uncertainty about the pharmacodynamic interaction between neuroprotective therapies and radio-labeled ligands binding to DaT. In summary, while DaT-SPECT imaging could have a role in monitoring disease progression in PD, its role as a surrogate biomarker in neuroprotective therapy trials is less clear-cut.

Finally, although we have mentioned that PD may be detected subclinically, we emphasize that there remains no agreed-upon and clearly defined at-risk population to be screened.¹

In conclusion, conventional MR imaging alone is not sufficiently sensitive to differentiate neurodegenerative parkinsonian disorders from non-neurodegenerative parkinsonian disorders (disorders other than PD are covered in Part 2). Volumetric, spectroscopic, and diffusion MR imaging techniques and transcranial sonography are very promising but are seldom used in routine clinical practice.

As a screening tool for those at risk of PD and as a biomarker for monitoring disease progression, in particular in neuroprotective therapy trials, the role of DaT-SPECT has yet to be realized. What appears to be the strength of DaT-SPECT, like ¹⁸F-DOPA PET, is that nigrostriatal degeneration is observed in both clinically inconclusive parkinsonism and early, even premotor, disease. DaT-SPECT images are easy to interpret compared with advanced MR imaging techniques; the cost is low compared with PET; all compliant patients can be imaged, unlike in transcranial sonography; and at least in Europe, SPECT is widely available

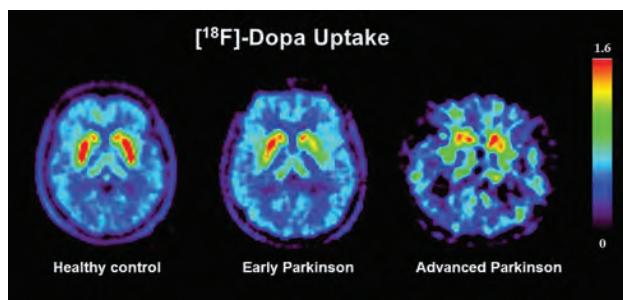


FIG 6. Axial ¹⁸F-DOPA PET images through the striatum. The patient with early Parkinson disease shows an asymmetric reduction in putaminal radiotracer uptake. With further disease progression, both putamina show a substantial reduction in radiotracer uptake. Images courtesy of Professor Philippe Remy, l’Hôpital Henri Mondor, Creteil, France.



FIG 7. Axial ¹²³I-FP-CIT DaT-SPECT sections depicting the different patterns of abnormality seen in PD as described by Catafau and Tolosa²—type 1: asymmetric activity with reduced putaminal uptake in 1 hemisphere (A); type 2: symmetric reduction in putaminal uptake in both hemispheres (B); and type 3: virtual absence of uptake in the putamina and caudate nuclei despite high gain as demonstrated by ample background activity (C).

compared with PET, advanced MR imaging, and transcranial sonography. DaT-SPECT is of unequivocal clinical value in carefully selected patients, aiding diagnosis and prognosis, as well as therapy. Nevertheless, any enthusiasm to use this technique should be tempered, as with most imaging tests, by the paucity of literature determining how DaT-SPECT actually affects patient outcomes.

Disclosures: Ann-Marie Quigley—RELATED: Other: Travel, hotel, and conference fees were paid by Novartis to attend the European Neuroendocrine Tumor Society 2013 meeting; travel and hotel paid by Nordion to attend the TheraSphere User Group in 2013; No fees were paid to me or my institution. Adam D. Waldman—UNRELATED: Consultancy: Bayer Healthcare, Payment for Lectures (including service on Speakers Bureaus): Bayer Healthcare, Siemens Healthcare, Comments: fees for lectures on education courses, Travel/Accommodations/Meeting Expenses Unrelated to Activities Listed: Bayer Healthcare, Comments: expenses for attendance at meetings for discussion groups and consultancy. John Buscombe—UNRELATED: Consultancy: Navidea, Comments: for work on Medicines and Healthcare Products Regulatory Agency submission, Travel/Accommodations/Meeting Expenses Unrelated to Activities Listed: BTG, Comments: to learn about TheraSpheres, Germany, February 2014. Anthony H. Schapira—RELATED: receives Medical Research Council and Wellcome Trust funding.

REFERENCES

- Scherfler C, Schwarz J, Antonini A, et al. **Role of DAT-SPECT in the diagnostic work-up of parkinsonism.** *Mov Disord* 2007;22:1229–38
- Catafau AM, Tolosa E. **Impact of dopamine transporter SPECT using ¹²³I-ioflupane on diagnosis and management of patients with clinically uncertain parkinsonian syndromes.** *Mov Disord* 2004;19:1175–82
- Hughes AJ, Daniel SE, Kilford L, et al. **Accuracy of clinical diagnosis of idiopathic Parkinson's disease: a clinicopathological study of 100 cases.** *J Neurol Neurosurg Psychiatry* 1992;55:181–84
- Booij J, Tissingh G, Winogrodzka A, et al. **Imaging of the dopaminergic neurotransmission system using single-photon emission tomography and positron emission tomography in patients with parkinsonism.** *Eur J Nucl Med* 1999;26:171–82
- Seppi K. **MRI for the differential diagnosis of neurodegenerative parkinsonism in clinical practice.** *Parkinsonism Relat Disord* 2007;13:S400–05
- Sitburana O, Ondo WG. **Brain magnetic resonance imaging (MRI) in parkinsonian disorders.** *Parkinsonism Rel Disord* 2009;15:165–74
- Kaufman MJ, Madras BK. **Severe depletion of cocaine recognition sites associated with the dopamine transporter in Parkinson's diseased striatum.** *Synapse* 1991;9:43–49
- Melikian HG, Buckley KM. **Membrane trafficking regulates the activity of the human dopamine transporter.** *J Neurosci* 1999;19:7699–710
- Garcia BG, Wei Y, Moron JA, et al. **Akt is essential for insulin modulation of amphetamine-induced human dopamine transporter cell-surface redistribution.** *Mol Pharmacol* 2005;68:102–09
- Fahn S, Oakes D, Shoulson I, et al. **Levodopa and the progression of Parkinson's disease.** *N Engl J Med* 2004;351:2498–508
- Neumeyer JL, Wang S, Gao Y, et al. **N-omega-fluoroalkyl analogues of (1R)-2 beta-carbomethoxy-3 beta-(4-iodophenyl)-tropane (beta-CIT): radiotracers for positron emission tomography and single photon emission computed tomography imaging of dopamine transporters.** *J Med Chem* 1994;37:1558–61
- Booij J, Andringa G, Rijks LJ, et al. **¹²³I-FP-CIT binds to the dopamine transporter as assessed by biodistribution studies in rats and SPECT studies in MPTP-lesioned monkeys.** *Synapse* 1997;27:183–90
- Mozley PD, Schneider JS, Acton PD, et al. **Binding of [^{99m}Tc]-TRODAT-1 to dopamine transporters in patients with Parkinson's disease and in healthy volunteers.** *J Nucl Med* 2000;41:584–89
- Kim HJ, Im JH, Yang SO, et al. **Imaging and quantification of dopamine transporters with iodine-123-IPT in normal and Parkinson's disease subjects.** *J Nucl Med* 1997;38:1703–11
- Booij J, Hemelaar TG, Speelman JD, et al. **One-day protocol for imaging of the nigrostriatal dopaminergic pathway in Parkinson's disease by [¹²³I]FP-CIT SPECT.** *J Nucl Med* 1999;40:753–61
- Hughes AJ, Daniel SE, Ben-Shlomo Y, et al. **The accuracy of diagnosis of parkinsonian syndromes in a specialist movement disorder service.** *Brain* 2002;125:861–70
- Marshall VL, Reiningner CB, Marquardt M, et al. **Parkinson's disease is overdiagnosed clinically at baseline in diagnostically uncertain cases: a 3-year European multicenter study with repeat [¹²³I]FP-CIT SPECT.** *Mov Disord* 2009;24:500–08
- Kupsch AR, Bajaj N, Weiland F, et al. **Impact of DaTscan SPECT imaging on clinical management, diagnosis, confidence of diagnosis, quality of life, health resource use and safety in patients with clinically uncertain parkinsonian syndromes: a prospective 1-year follow-up of an open-label controlled study.** *J Neurol Neurosurg Psychiatry* 2012;83:620–28
- Acton PD, Newberg A, Ploessl K, et al. **Comparison of region-of-interest analysis and human observers in the diagnosis of Parkinson's disease using [^{99m}Tc]TRODAT-1 and SPECT.** *Phys Med Biol* 2006;51:575–85
- Djang DS, Janssen MJ, Bohnen N, et al. **SNM practice guideline for dopamine transporter imaging with ¹²³I-ioflupane SPECT 1.0.** *J Nucl Med* 2012;53:154–63
- Yekhlief F, Ballan G, Macia F, et al. **Routine MRI for the differential diagnosis of Parkinson's disease, MSA, PSP, and CBD.** *J Neural Transm* 2003;110:151–69
- Savoio M. **Differential diagnosis of Parkinson's disease and atypical parkinsonian disorders by magnetic resonance imaging.** *Neurol Sci* 2003;24(Suppl 1):S35–37
- Aquino D, Contarino V, Albanese A, et al. **Substantia nigra in Parkinson's disease: a multimodal MRI comparison between early and advanced stages of the disease.** *Neurol Sci* 2014;35:753–58
- Nagano-Saito A, Washimi Y, Arahata Y, et al. **Cerebral atrophy and its relation to cognitive impairment in Parkinson disease.** *Neurology* 2005;64:224–29
- Scherfler C, Schocke MF, Seppi K, et al. **Voxel-wise analysis of diffusion weighted imaging reveals disruption of the olfactory tract in Parkinson's disease.** *Brain* 2006;129:538–42
- Clarke CE, Lowry M. **Systematic review of proton magnetic resonance spectroscopy of the striatum in parkinsonian syndromes.** *Eur J Neurol* 2001;8:573–77
- Gaenslen A, Unmuth B, Godau J, et al. **The specificity and sensitivity of transcranial ultrasound in the differential diagnosis of Parkinson's disease: a prospective blinded study.** *Lancet Neurol* 2008;7:417–24
- Berg D, Godau J, Walter U. **Transcranial sonography in movement disorders.** *Lancet Neurol* 2008;7:1044–55
- Morrish PK, Rakshi JS, Bailey DL, et al. **Measuring the rate of progression and estimating the preclinical period of Parkinson's disease with [¹⁸F]dopa PET.** *J Neurol Neurosurg Psychiatry* 1998;64:314–19
- Brooks DJ, Salmon EP, Mathias CJ, et al. **The relationship between locomotor disability, autonomic dysfunction, and the integrity of the striatal dopaminergic system in patients with multiple system atrophy, pure autonomic failure, and Parkinson's disease, studied with PET.** *Brain* 1990;113:1539–52
- Khan NL, Valente EM, Bentivoglio AR, et al. **Clinical and subclinical dopaminergic dysfunction in PARK6-linked parkinsonism: an 18F-dopa PET study.** *Ann Neurol* 2002;52:849–53
- Ghaemi M, Hilker R, Rudolf J, et al. **Differentiating multiple system atrophy from Parkinson's disease: contribution of striatal and mid-brain MRI volumetry and multi-tracer PET.** *J Neurol Neurosurg Psychiatry* 2002;73:517–23
- Antonini A, Leenders KL, Vontobel P, et al. **Complementary PET studies of striatal neuronal function in the differential diagnosis**

- between multiple system atrophy and Parkinson's disease. *Brain* 1997;120:2187–95
34. Innis RB, Seibyl JP, Scanley BE, et al. **Single photon emission computed tomographic imaging demonstrates loss of striatal dopamine transporters in Parkinson disease.** *Proc Natl Acad Sci U S A* 1993;90:11965–69
 35. Brücke T, Asenbaum S, Pirker W, et al. **Measurement of the dopaminergic degeneration in Parkinson's disease with [123I] beta-CIT and SPECT: correlation with clinical findings and comparison with multiple system atrophy and progressive supranuclear palsy.** *J Neural Transm Suppl* 1997;50:9–24
 36. Varrone A, Pellicchia MT, Amboni M, et al. **Imaging of dopaminergic dysfunction with [123I]FP-CIT SPECT in early-onset parkin disease.** *Neurology* 2004;63:2097–103
 37. Benamer TS, Patterson J, Grosset DG, et al. **Accurate differentiation of parkinsonism and essential tremor using visual assessment of [¹²³I]-FP-CIT SPECT imaging: the [¹²³I]-FP-CIT study group.** *Mov Disord* 2000;15:503–10
 38. Vlaar AM, van Kroonenburgh MJ, Kessels AG, et al. **Meta-analysis of the literature on the diagnostic accuracy of SPECT in parkinsonian syndromes.** *BMC Neurol* 2007;7:27
 39. **Dopamine transporter brain imaging to assess the effects of pramipexole vs levodopa on Parkinson disease progression.** *JAMA* 2002;287:1653–61
 40. Bernheimer H, Birkmayer W, Hornykiewicz O, et al. **Brain dopamine and the syndromes of Parkinson and Huntington: clinical, morphological and neurochemical correlations.** *J Neurol Sci* 1973;20:415–55
 41. Bezard E, Dovero S, Prunier C, et al. **Relationship between the appearance of symptoms and the level of nigrostriatal degeneration in a progressive 1-methyl-4phenyl-1,2,3,5-tetrahydropyridine-lesioned macaque model of Parkinson's disease.** *J Neurosci* 2001; 21:6853–61
 42. Tissingh G, Bergmans P, Booij J, et al. **Drug-naive patients with Parkinson's disease in Hoehn and Yahr stages I and II show a bilateral decrease in striatal dopamine transporters as revealed by [123I]beta-CIT SPECT.** *J Neurol* 1998;245:14–20
 43. Ponsen MM, Stoffers D, Wolters EC, et al. **Olfactory testing combined with dopamine transporter imaging as a method to detect prodromal Parkinson's disease.** *J Neurol Neurosurg Psychiatry* 2010;81:396–99
 44. van Dyck CH, Seibyl JP, Malison RT, et al. **Age-related decline in striatal dopamine transporter binding with iodine-123-beta-CIT SPECT.** *J Nucl Med* 1995;36:1175–81
 45. Ravina B, Eidelberg D, Ahlskog JE, et al. **The role of radiotracer imaging in Parkinson's disease.** *Neurology* 2005;64:208–15

The Role of Functional Dopamine-Transporter SPECT Imaging in Parkinsonian Syndromes, Part 2

T.C. Booth, M. Nathan, A.D. Waldman, A.-M. Quigley, A.H. Schapira, and J. Buscombe



ABSTRACT

SUMMARY: The functional imaging technique most widely used in European clinics to differentiate a true parkinsonian syndrome from vascular parkinsonism, drug-induced changes, or essential tremor is dopamine-transporter SPECT. This technique commonly reports dopamine-transporter function, with decreasing striatal uptake demonstrating increasingly severe disease. The strength of dopamine-transporter SPECT is that nigrostriatal degeneration is observed in both clinically inconclusive parkinsonism and early, even premotor, disease. In this clinical review (Part 2), we present the dopamine-transporter SPECT findings in a variety of neurodegenerative diseases, including multiple system atrophy, progressive supranuclear palsy, corticobasal degeneration, and dementia with Lewy bodies. The findings in vascular parkinsonism, drug-induced parkinsonism, and essential tremor are also described. It is hoped that this technique will be the forerunner of a range of routinely used, process-specific ligands that can identify early degenerative disease and subsequently guide disease-modifying interventions.

ABBREVIATIONS: CBD = corticobasal degeneration; DaT = dopamine transporters; ^{18}F = fluorine 18; IBF = ^{123}I -5-iodo-7-N-((1-ethyl-2-pyrrolidinyl)methyl)carboxamido-2,3-dihydrobenzofuran; IBZM = ^{123}I -5-(K)-N-[[1-ethyl-2-pyrrolidinyl)methyl]-2-hydroxy-3-iodo-6-methoxybenzamide; ^{123}I -FP-CIT = ^{123}I -ioflupane (N- ω -fluoropropyl- β CIT); MSA = multiple system atrophy; MSA-P = patients with multiple system atrophy with predominant parkinsonism; PSP = progressive supranuclear palsy

The dopamine transporter is a sodium chloride-dependent transmembrane protein localized to the presynaptic nigrostriatal cell surface. SPECT imaging of dopamine transporters (DaT) with specific tracers gives a guide to the attenuation of functional dopaminergic neurons. The technical concepts of DaT-SPECT were outlined in Part 1 (*The Role of Functional Dopamine Transporter SPECT Imaging in Parkinsonian Syndromes, Part 1*) of this 2-part Review Article and would be valuable reading as background to this article.

What appears to be the strength of DaT-SPECT, like 6- ^{18}F -fluoro-L-3,4-dihydroxyphenylalanine PET, is that nigrostriatal degeneration is observed in both clinically inconclusive parkinsonism and early, even premotor, disease. DaT-SPECT images are easy to interpret compared with advanced

MR imaging techniques; the cost is low compared with that of PET; all compliant patients can be imaged, unlike in transcranial sonography; and at least in Europe, SPECT is widely available compared with PET, advanced MR imaging, and transcranial sonography.

Parkinsonian syndromes are a group of movement disorders characterized by tremor, bradykinesia, and rigidity. They are most frequently due to primary neurodegenerative disease, resulting in loss of dopaminergic nerve terminals along the nigrostriatal pathway, as occurs in idiopathic Parkinson disease, multiple system atrophy (MSA), progressive supranuclear palsy (PSP), corticobasal degeneration (CBD), and dementia with Lewy bodies. Other causes of parkinsonism that do not involve nigrostriatal degeneration include drug-induced, vascular or toxic insult, and psychogenic disease. Patients with nigrostriatal degeneration may benefit from dopaminergic medication, whereas nondegenerative or postsynaptic etiologies do not.

The Table demonstrates the distinguishing clinical features of idiopathic Parkinson disease, MSA, PSP, CBD, and dementia with Lewy bodies. Due to its multisystem involvement, patients with MSA are typically subdivided into those who present with predominant parkinsonism (MSA-P) and those with predominant cerebellar ataxia (MSA-C). The clinical diagnosis of idiopathic Parkinson disease, based on clinical signs, assessment of inclusion and exclusion criteria, and good response to

From the Department of Neuroradiology (T.C.B.), National Hospital for Neurology and Neurosurgery, London, UK; Department of Nuclear Medicine (M.N., A.-M.Q.), Royal Free Hospital NHS Trust, London, UK; Department of Imaging (A.D.W.), Imperial College Healthcare NHS Trust, London, UK; Department of Clinical Neurosciences (A.H.S.), Institute of Neurology, University College London, London, UK; and Department of Nuclear Medicine (J.B.), Addenbrooke's Hospital, Cambridge University Hospitals NHS Foundation Trust, Cambridge, UK.

Please address correspondence to Thomas C. Booth, MA, MBBS, MRCP, FRCP, Department of Neuroradiology, National Hospital for Neurology and Neurosurgery, Queen Square, London, WC1N 3BG, UK; e-mail: tombooth@doctors.org.uk

Indicates open access to non-subscribers at www.ajnr.org

<http://dx.doi.org/10.3174/ajnr.A3971>

Distinguishing clinical features of the neurodegenerative and non-neurodegenerative causes of parkinsonism

	Clinical Features of Parkinsonism (Bradykinesia, Rigidity, Tremor)	Additional Helpful Clinical Features
Neurodegenerative Parkinsonism		
Parkinson disease	Yes	Nil
Multiple system atrophy	Yes	Pyramidal, autonomic, and cerebellar signs
Progressive supranuclear palsy	Yes	Supranuclear gaze palsy, increased axial tone, bulbar palsy, early postural instability
Corticobasal degeneration	Yes	Asymmetric cortical dysfunction
Dementia with Lewy bodies	Yes	Fluctuating dementia, visual hallucinations, hypersensitivity to neuroleptic medications
Non-neurodegenerative etiologies of parkinsonism		
Essential tremor	Tremor	Usually bilateral tremor that worsens on movement; tremor can affect head and voice
Vascular parkinsonism	Bradykinesia with at least one of resting tremor, rigidity, or postural instability	Cerebrovascular disease diagnosed clinically or on CT/MR imaging; temporal relationship between cerebrovascular infarcts near or within the basal ganglia and acute/progressive development of parkinsonism; insidious onset of parkinsonism with bilateral symptoms at onset, presence of early shuffling gait, or cognitive dysfunction and extensive subcortical white matter lesions on MRI
Drug-induced parkinsonism	Yes	Very difficult to distinguish clinically from neurodegenerative idiopathic Parkinson disease

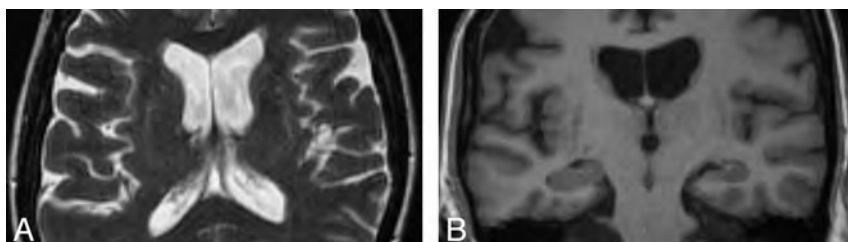


FIG 1. Axial T2-weighted MR imaging sequence at 1.5T in a patient with MSA-P (A) demonstrating hyperintense putaminal rims. The sign is 96% specific in differentiating patients with MSA from those with idiopathic Parkinson disease; however, it is only 56% sensitive according to 1 study.⁶ The corresponding coronal T1-weighted MR imaging sequence (B) shows that the putaminal rims are hypointense. The putaminal rim sign is nonspecific in the wider population—for example, it can be seen in Wilson disease or some spinocerebellar ataxia subtypes. It is also a normal finding at 3T.

levodopa,¹ can be straightforward. However, mild, atypical, or ambiguous signs with unconvincing responses to levodopa, can make the diagnosis inconclusive.² This may have adverse prognostic implications in the management of parkinsonism.

Another important clinical differential diagnosis is essential tremor. Typical cases of essential tremor are easily distinguished from idiopathic Parkinson disease, but diagnosis may be more of a challenge if the tremor is unilateral or if there is a dystonic upper limb tremor. Where there is clinical doubt, functional DaT-SPECT imaging may be decisive.

Multiple System Atrophy

Approximately 10% of patients with parkinsonism are diagnosed with MSA,³ which is characterized by widespread neurodegeneration, especially within the striatum, substantia nigra, pons, inferior olivary and vagal motor nuclei, cerebellum, and spinal cord.⁴

Structural MR imaging findings overlap in all MSA subtypes, independent of clinical presentation, though trends can be seen. In MSA-P, the putamen may demonstrate a rim of increased sig-

nal on T2-weighted sequences due to gliosis (Fig 1).⁵ In MSA with predominant cerebellar ataxia, pontocerebellar degeneration may result in visually apparent cerebellar and pontine atrophy, which, along with MSA-P to a lesser extent, is associated with increased signal on T2-weighted sequences in the middle cerebellar peduncles, cerebellum, and the pontine transverse fibers and raphe (“hot cross bun” sign) (Fig 2).

Atrophy is most evident in patients with well-established disease. If one uses a cutoff value of 8 mm, the middle cerebellar peduncle width allows differentiation

of patients with MSA compared with controls or those with idiopathic Parkinson disease with 100% positive predictive value (Fig 2).⁶ Volumetry and voxel-based morphometry group studies show striatal and cerebellar volume loss in patients with MSA-P compared with those with idiopathic Parkinson disease and controls.⁷⁻⁹ Voxel-based morphometry also demonstrates selective cortical atrophy in MSA-P, affecting the motor cortical targets of basal ganglia output pathways such as the primary sensorimotor and lateral premotor cortices and the prefrontal and insular cortices.⁸

Although validation in prospective studies is required, high regional ADC in patients with MSA-P appears discriminatory. With 100% positive predictive value, putaminal ADC differentiates MSA-P and idiopathic Parkinson disease,¹⁰ whereas middle cerebellar peduncle ADC distinguishes MSA-P from PSP and idiopathic Parkinson disease.¹¹ Similarly, when combined with DTI, high ADC and low fractional anisotropy in either the pons, cerebellum, or putamen are demonstrated in all patients with MSA-P, allowing this disease to be distinguished from idiopathic Parkinson disease.¹²

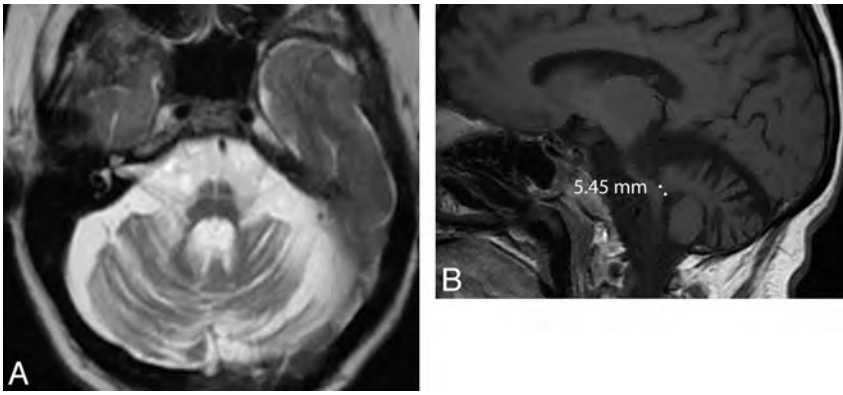


FIG 2. Axial T2-weighted MR imaging sequence in a patient with MSA with predominant cerebellar ataxia (A) demonstrating the “hot-cross bun” sign, which results from selective loss of myelinated pontine transverse fibers and raphe neurons. One study showed that the sign is 100% specific in differentiating patients with MSA from those with idiopathic Parkinson disease; however, it is only 50% sensitive.⁶ Marked pontine and cerebellar atrophy is also demonstrated. This olivopontocerebellar volume loss is shown on the sagittal T1-weighted sequences (B), where a middle cerebellar peduncle width <8 mm is demonstrated. All these signs are nonspecific in the wider population—for example, they can be seen in some spinocerebellar ataxia subtypes.

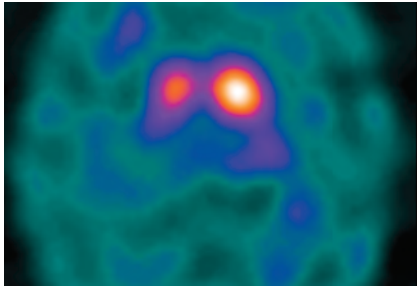


FIG 3. Axial ¹²³I-FP-CIT DaT-SPECT image in a patient with MSA. Note that imaging appearances are similar to those in idiopathic Parkinson disease, with asymmetric reduction in putaminal uptake. It is, therefore, difficult to differentiate MSA and idiopathic Parkinson disease on the basis of DaT-SPECT imaging alone.

Although less impressive than diffusion-based strategies, at 3T ¹H-MRS, combined assessment of the NAA/Cr ratio in the pontine base and putamen may be effective in differentiating MSA-P from idiopathic Parkinson disease.¹³

With transcranial sonography, a combination of lenticular hyperechogenicity and normal echogenicity of the substantia nigra distinguishes MSA-P from idiopathic Parkinson disease with a positive predictive value of 100%.¹⁴ With 6-[¹⁸F]fluoro-L-3,4-dihydroxyphenylalanine PET, MSA may be indistinguishable from idiopathic Parkinson disease or may show lower caudate uptake.^{15,16} PET studies also show reduced striatal dopamine-receptor binding and ¹⁸F-FDG uptake in MSA, with 1 study suggesting that MSA can be distinguished from idiopathic Parkinson disease with 100% positive predictive value.^{7,16}

DaT-SPECT in Multiple System Atrophy

There is no discernible difference in the pattern of nigrostriatal degeneration between idiopathic Parkinson disease and MSA. This is reflected in DaT-SPECT imaging in which abnormal scan findings demonstrating asymmetric reduction in DaT binding are consistent with either disease (Fig 3).^{17,18} Recently, DaT-SPECT

voxel-based morphometry has been used at the group level to distinguish MSA-P from idiopathic Parkinson disease.¹⁹ In the dorsal brain stem, there was greater signal reduction of patients with MSA-P compared with those with idiopathic Parkinson disease, and after a mean follow-up of 2.4 years, there was a greater signal reduction in the caudate and anterior putamen in patients with MSA-P compared with those with idiopathic Parkinson disease. This is in accordance with faster disease progression.

Similar to those who investigated PET, researchers have endeavored to distinguish idiopathic Parkinson disease and MSA by using SPECT dopamine D₂ receptor imaging. Most striatal D₂ receptors are located postsynaptically and function by facilitating cell-to-cell communication. They have a key role in modulating locomotion

and are a critical target for dopaminergic therapeutics.²⁰ SPECT radiolabeled ligands used to image D₂ receptors are dopamine-receptor antagonists such as ¹²³I-S-(K)-N-[(1-ethyl-2-pyrrolidinyl)methyl]-2-hydroxy-3-iodo-6-methoxybenzamide (IBZM)²¹ and ¹²³I-(S)-5-iodo-7-N-[(1-ethyl-2-pyrrolidinyl)methyl]carboxamido-2,3-dihydrobenzofuran (IBF).²² A neuropathologic study has demonstrated loss of striatal D₂ receptors in patients with MSA,²³ and there is corroborative evidence on SPECT²⁴ and PET as described above. Therefore, in contrast to patients with idiopathic Parkinson disease who do not have reduced D₂ receptor binding, patients with MSA may demonstrate a reduction in D₂ receptors.²⁵ This feature may also explain why patients with MSA do not show a noteworthy response to dopaminergic medication that binds to D₂ receptors. Several studies have sought to differentiate idiopathic Parkinson disease from MSA or PSP by combining presynaptic DaT-SPECT with postsynaptic D₂ imaging by using IBZM or IBF, and these are summarized below.

Progressive Supranuclear Palsy

PSP accounts for a small minority of patients with parkinsonism. Neuropathologically, this tauopathy is characterized by neuronal degeneration of the nigrostriatal pathway, basal ganglia, and brain stem nuclei with deposition of neurofibrillary tangles. A number of MR imaging features suggestive of PSP have been described, such as dilation of the third ventricle and signal increase of the midbrain.^{5,26} Although often absent, atrophy of the red nucleus, frontal and temporal lobe, and an anteroposterior midbrain diameter of <17 mm can each differentiate PSP from MSA with at least 75% positive predictive value (Fig 4). If one uses a “MR parkinsonism index” [(pons/midbrain) · (middle cerebellar peduncle/superior cerebellar peduncle)], PSP can be prospectively distinguished from idiopathic Parkinson disease, MSA-P, and controls with 100% positive predictive value.²⁷ Group studies additionally demonstrate that atrophy in the striatum and frontotemporal cortices, measured with volumetry and voxel-based mor-

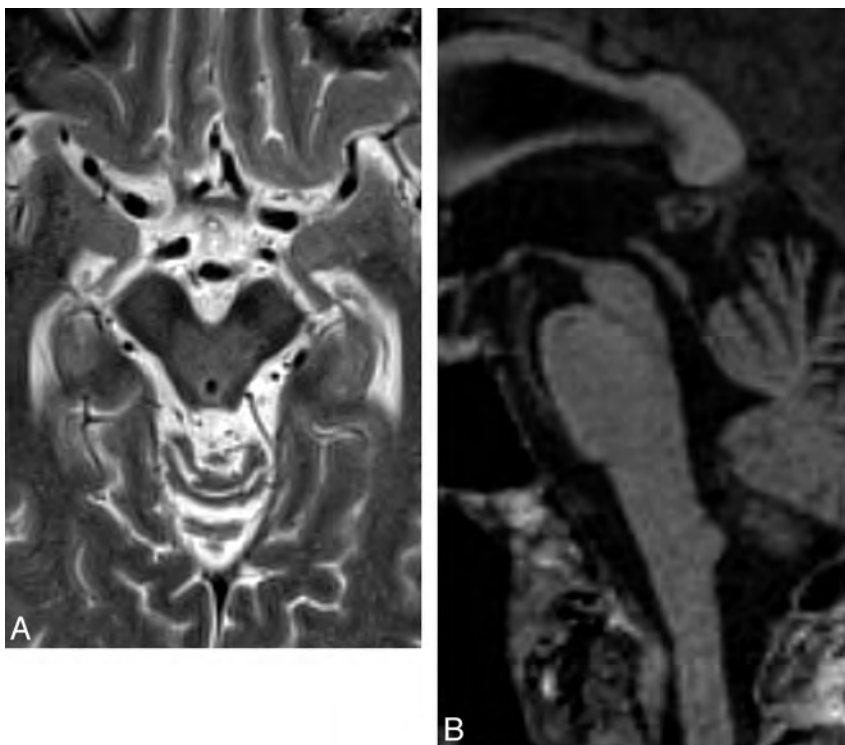


FIG 4. Axial T2-weighted MR imaging sequence in a patient with PSP (A) demonstrating increased midbrain signal intensity (which is only 60% sensitive and 70% specific compared with MSA) and an atrophic midbrain with an anteroposterior diameter of <17 mm (which is 23% sensitive and 96% specific compared with MSA).⁵ The signs are nonspecific in the wider population—for example, midbrain signal intensity can be seen in Wilson disease and a severely atrophic midbrain can be seen in CBD. The concave posterolateral borders of the atrophic midbrain give it a “morning glory” flower appearance. The corresponding sagittal T1-weighted sequence (B) shows tectal atrophy with a “hummingbird” appearance.

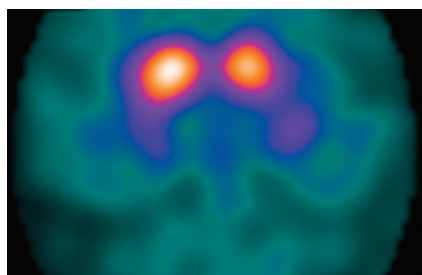


FIG 5. Axial ¹²³I-FP-CIT DaT-SPECT image in a patient with PSP, depicting a bilateral reduction in putaminal uptake. Note that the imaging features are similar to those of idiopathic Parkinson disease and MSA.

phometry, respectively, differentiate those with PSP from controls.^{9,28} Additionally, white matter atrophy in the subthalamic region can distinguish PSP from controls and idiopathic Parkinson disease when using voxel-based morphometry.²⁹

With similarities to MSA, diffusion imaging and PET may have roles in diagnosing PSP. ADC is increased in the decussation of the superior cerebellar peduncles compared with idiopathic Parkinson disease, MSA, and control groups,³⁰ and elevated putaminal ADC might discriminate PSP and idiopathic Parkinson disease with a positive predictive value of 100%.³¹ With PET, ¹¹C-raclopride demonstrates reduced striatal dopamine receptor binding,³² while ¹⁸F-FDG is reduced in the putamen, thalamus, frontal cortex, and midbrain.³³

DaT-SPECT in Progressive Supranuclear Palsy

In PSP, some DaT-SPECT studies show a predominant loss of DaT density in the putamen, comparable with idiopathic Parkinson disease,¹⁷ whereas others demonstrate more uniform DaT loss in both the caudate nucleus and putamen.³⁴ Overall, on the basis of DaT-SPECT results alone, it is not possible to reliably distinguish idiopathic Parkinson disease, MSA, and PSP (Fig 5).^{17,18} As with MSA, there appears to be D₂ receptor striatal loss in PSP, and the diagnostic accuracy of SPECT to differentiate MSA from PSP is low.²⁴

In some cases of MSA and PSP, the postsynaptic tracer has normal uptake. As such, a meta-analysis on the diagnostic accuracy of SPECT in parkinsonian syndromes found that postsynaptic and presynaptic tracers could not reliably distinguish idiopathic Parkinson disease and MSA or PSP.³⁵ Nonetheless, while negative postsynaptic SPECT scan findings do not exclude MSA or PSP, the positive predictive value of abnormal postsynaptic SPECT findings for the diagnosis of these conditions is very high; therefore, reduced postsynaptic radiotracer binding effectively excludes a diagnosis of idiopathic Parkinson disease.

Some studies combining DaT-SPECT with IBZM or IBF have shown that idiopathic Parkinson disease can be differentiated from MSA or PSP,^{36,37} whereas others have demonstrated otherwise.^{38,39} More promising is a recent prospective study, which, by using a combination of DaT-SPECT, ¹²³I-IBZM SPECT, and meta-¹²³I-iodobenzylguanidine scintigraphy (which probes myocardial adrenergic denervation seen in idiopathic Parkinson disease), reports a positive predictive value of 89%, and a negative predictive value of 97% (Fig 6).⁴⁰

Corticobasal Degeneration

CBD is a rare movement disorder presenting with rigidity, hypokinesia, and predominantly asymmetric cortical dysfunction. It is characterized by deposition of tau proteins in the form of neuronal inclusion bodies. On conventional MR imaging, asymmetric frontoparietal atrophy might distinguish patients with CBD from those with idiopathic Parkinson disease or MSA (Fig 7).²⁶ To differentiate CBD from PSP, another tauopathy with frontal atrophy, measuring cortical atrophy with voxel-based morphometry or volumetry appears promising,^{41,42} as does probing motor thalamic involvement with ADC.⁴³ With ¹⁸F-FDG there is asymmetric hypometabolism in the parietal lobe, while striatal dopamine-receptor binding is relatively preserved.⁴⁴ Transcranial sonography shows substantia nigra hyperechogenicity but does not allow discrimination between idiopathic Parkinson disease and CBD or dementia with Lewy bodies.¹⁴

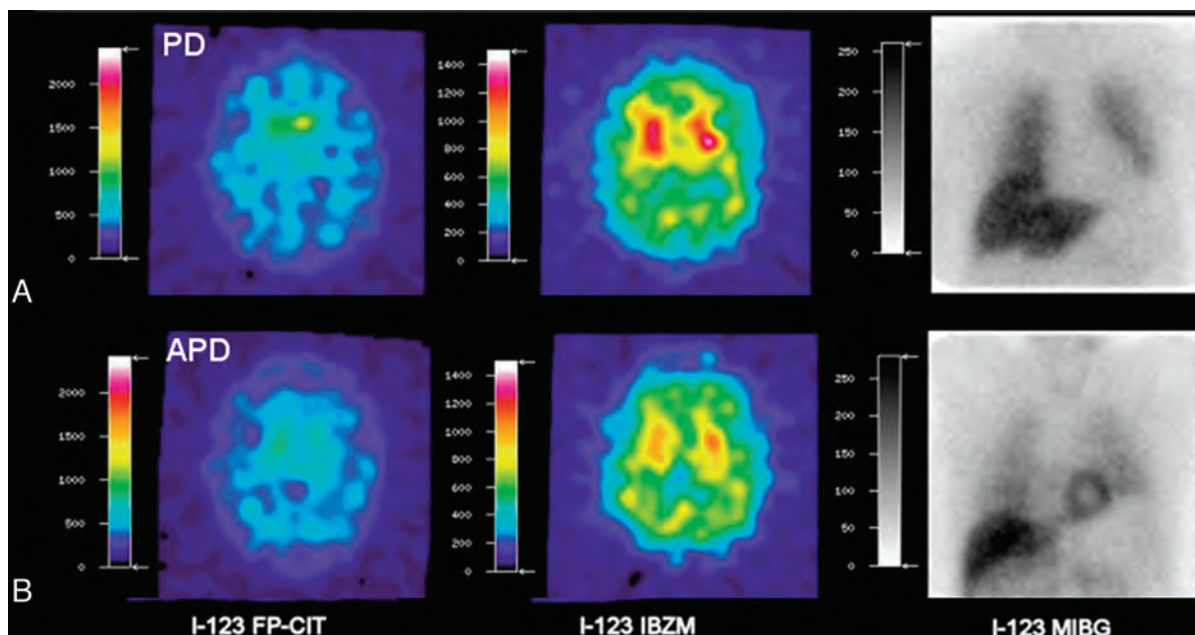


FIG 6. Axial ^{123}I -FP-CIT DaT-SPECT, ^{123}I -IBZM, and meta- ^{123}I -iodobenzylguanidine SPECT studies in idiopathic Parkinson disease (A) and atypical Parkinson disease (MSA or PSP) (B). Uptake patterns with all 3 radiopharmaceuticals are typical for idiopathic Parkinson disease with asymmetric striatal reduction using ^{123}I -FP-CIT, normal dopamine D_2 receptor binding with ^{123}I -IBZM, and reduction in myocardial uptake due to adrenergic denervation with meta- ^{123}I -iodobenzylguanidine (A). B, Images demonstrate findings of MSA or PSP: reduced striatal uptake with ^{123}I -FP-CIT and ^{123}I -IBZM but normal myocardial uptake with meta- ^{123}I -iodobenzylguanidine. Image courtesy of Dr M. Südmeyer. This was originally published in: Südmeyer M, Antke C, Zizek T, et al. Diagnostic accuracy of combined FP-CIT, IBZM, and MIBG scintigraphy in the differential diagnosis of degenerative parkinsonism: a multidimensional statistical approach. *J Nucl Med* 2011;52:733–40. © by the Society of Nuclear Medicine and Molecular Imaging, Inc.

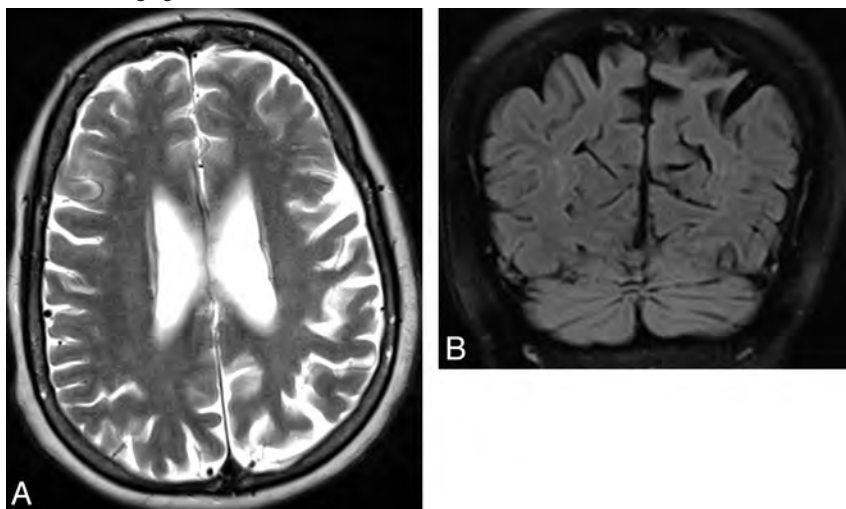


FIG 7. Axial T2-weighted MR imaging sequence in a patient with CBD (A) demonstrating asymmetric frontoparietal atrophy. The corresponding coronal FLAIR sequence (B) shows the asymmetric superior parietal lobules.

DaT-SPECT in Corticobasal Degeneration

In CBD, the dopaminergic neurons of 10% of cases appear to have preserved DaT density, whereas the remainder of cases that are affected tend to show a more uniform DaT reduction throughout the striatum and greater hemispheric asymmetry compared with idiopathic Parkinson disease (Fig 8).⁴⁵ However, DaT-SPECT does not allow CBD to be distinguished from idiopathic Parkinson disease, PSP, MSA, and dementia with Lewy bodies at the individual level.³⁹ SPECT imaging of the D_2 receptor is of limited value, with studies showing either normal or slightly reduced D_2 receptor binding.^{39,46}

Dementia with Lewy Bodies

Dementia with Lewy bodies is a form of dementia that is thought to be related to idiopathic Parkinson disease. In contrast to idiopathic Parkinson disease, Lewy bodies are found not only in the deep gray matter but diffusely throughout the brain including the cortex. It is the second most common cause of dementia after Alzheimer disease, and distinguishing the 2 diseases is often a diagnostic challenge because the clinical features can overlap. Alzheimer disease accounts for 31% of those with dementia, presenting with short-term memory decline, language dysfunction, neuropsychiatric features, and, in 5% of cases, parkinsonism.^{47–49} Dementia with Lewy bodies accounts for approximately 11% of patients with dementia and can present with falls or depression, which are also seen in Alzheimer disease; fluctuating dementia; and the more discriminatory presentations of visual hallucinations, multiple features, and, in 41% of cases, parkinsonism. Of note, the clinical features of parkinsonism in both forms of dementia are less severe than those seen in idiopathic Parkinson disease, presenting commonly with rigidity and bradykinesia and infrequently with resting tremor.⁵⁰

It is difficult to differentiate dementia with Lewy bodies from other dementias, though by using MR imaging to differentiate dementia with Lewy bodies from Alzheimer disease and vascular

dementia, the absence of medial temporal lobe atrophy is highly suggestive of dementia with Lewy bodies.⁵¹ With voxel-based morphometry, compared with Alzheimer disease, atrophy in the midbrain, hypothalamus, and substantia innominata is marked and the medial temporal lobe is relatively preserved.⁵² Nonetheless, medial temporal lobe atrophy often occurs in dementia with Lewy bodies, with volumetry showing the entorhinal cortex to be

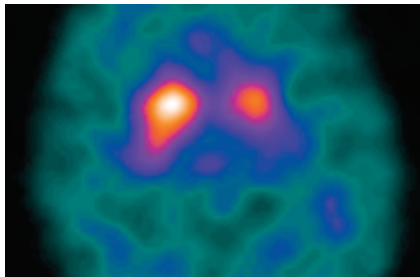


FIG 8. Axial ¹²³I-FP-CIT DaT SPECT image in a patient with cortico-basal degeneration. There is uniform striatal reduction in tracer activity with marked hemispheric asymmetry on the left. However, in many cases, imaging appearances can be indistinguishable from those in idiopathic Parkinson disease, MSA, or PSP. Image courtesy of Dr Roberto Ceravolo, Department of Neurosciences, University of Pisa, Italy.⁴⁵

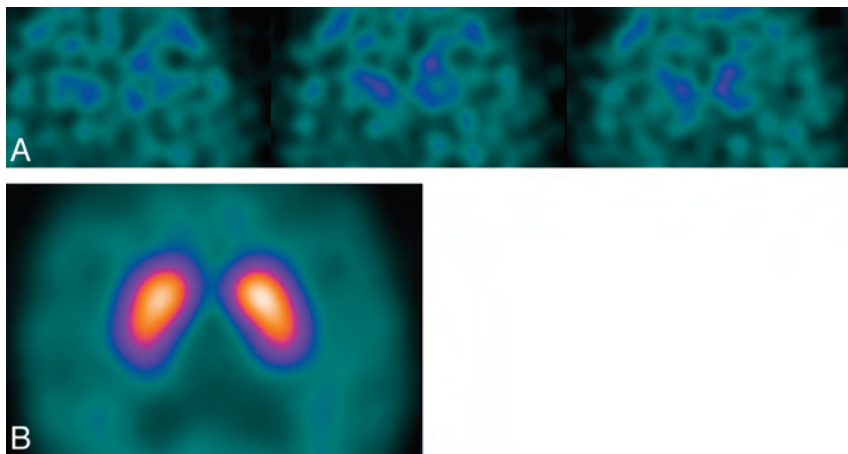


FIG 9. Axial ¹²³I-FP-CIT DaT-SPECT images in a patient with dementia with Lewy bodies (A) and a patient with Alzheimer disease (B). Note that the DaT-SPECT study helped to distinguish the 2 causes of dementia with the patient with dementia with Lewy bodies exhibiting a Catafau and Tolosa² type 3 pattern of abnormal striatal uptake; in contrast, the patient with Alzheimer disease demonstrates normal striatal uptake. Images from both patients have low gain as demonstrated by low background activity.

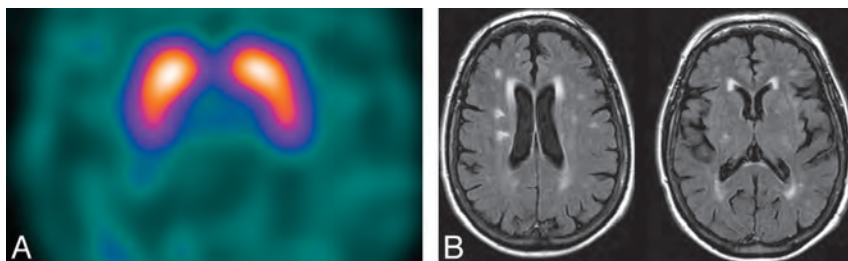


FIG 10. Axial ¹²³I-FP-CIT DaT-SPECT (A) and axial MR imaging FLAIR sequence (B) of the brain in the same patient with vascular parkinsonism. Note that the DaT-SPECT study has normal findings with symmetric, intense uptake in the caudate nuclei and putamina. This effectively excludes a nigrostriatal degenerative cause of parkinsonism. Consistent with ischemic disease, the MR imaging demonstrates diffuse T2-weighted hyperintensities in the striatum and in the periventricular and subcortical white matter.

smaller than that in control and idiopathic Parkinson disease groups.⁵³ In the parietal lobe of those with dementia with Lewy bodies, DTI appears to show reduced fractional anisotropy compared with control or Alzheimer disease groups.⁵⁴ While in the occipital lobe of patients with dementia with Lewy bodies, compared with patients with Alzheimer disease, hypoperfusion and hypometabolism are demonstrated by reduced hexamethylpropylene amine oxime and ¹⁸F-FDG uptake, respectively.^{55,56}

DaT-SPECT in Dementia with Lewy Bodies

Postmortem studies have shown normal levels of putaminal dopamine in Alzheimer disease compared with a 72% reduction in dementia with Lewy bodies.⁵⁷ This finding is reflected in DaT-SPECT studies that show an asymmetric reduction in DAT binding in dementia with Lewy bodies compared with a normal appearance in Alzheimer disease, allowing differentiation with 90% positive predictive value (Fig 9).^{39,58} It is particularly important to exclude dementia with Lewy bodies if the patient requires treatment for hallucinations. Otherwise, a parkinsonian crisis may be precipitated in a patient with dementia with Lewy bodies because some neuroleptic drugs block the postsynaptic D₂ receptor, thereby exacerbating the shortage of dopamine within the synaptic cleft.

More than half of such patients will have severe adverse reactions, some of which are fatal.⁴⁹

DaT-SPECT does not allow idiopathic Parkinson disease with dementia (an arbitrary definition of dementia developing at least 1 year after the diagnosis of idiopathic Parkinson disease) and dementia with Lewy bodies to be distinguished.⁵⁸

Other DaT SPECT Imaging Features

Idiopathic Parkinson Disease versus Vascular Parkinsonism. Because vascular lesions are often incidental findings in patients with idiopathic Parkinson disease, it is often difficult to diagnose parkinsonism secondary to vascular lesions (vascular parkinsonism). Criteria for the diagnosis of vascular parkinsonism have been described by Zijlmans et al⁵⁹ following a detailed clinical and neuropathologic analysis of the condition. The authors proposed that the diagnosis of vascular parkinsonism could be made if the following clinicoradiologic features were present: 1) bradykinesia with at least 1 of the following: resting tremor, rigidity, or postural instability; 2) cerebrovascular disease demonstrated either on CT/MR imaging or by the presence of focal clinical signs of stroke; and 3) a relationship between the 2 disorders: specifically, an acute or delayed progressive onset with infarcts in or near areas that can increase the basal ganglia motor output (globus

pallidus or substantia nigra pars compacta) or decrease the thalamocortical drive directly (thalamus or large frontal lobe infarct), or an insidious onset of parkinsonism with extensive subcortical white matter lesions, bilateral symptoms at onset, and the presence of an early shuffling gait or cognitive dysfunction.

These criteria, even when applied to the retrospective sample from which they were derived, are not 100% sensitive. DaT-SPECT has, therefore, been used to help establish the diagnosis of vascular parkinsonism because the nigrostriatal dopaminergic pathway is typically unaffected,⁵⁹ and consequently, the DaT binding will not be reduced as in idiopathic Parkinson disease.³⁹ The caveat is that occasionally a massive vascular infarct within the striatum can cause moderate nigrostriatal degeneration⁶⁰; therefore, though infrequent, marked asymmetry can be evident on DaT-SPECT. Nonetheless, in the absence of postsynaptic causes of parkinsonism (eg, drug-induced) and the presence of vascular lesions on CT/MR imaging (eg, a “punched out” lesion characteristic of an infarct or the diffuse white matter disease of ischemia), in an appropriate clinical context, normal DaT-SPECT

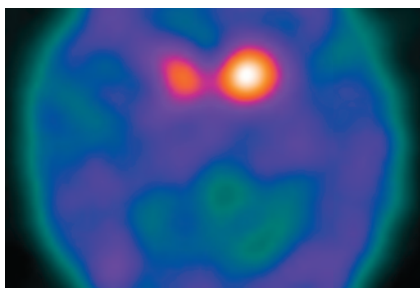


FIG 11. Axial ¹²³I-FP-CIT DaT-SPECT image from a patient with schizophrenia on neuroleptic medication. The patient presented with extrapyramidal signs. If the patient’s clinical signs were purely due to the side effects of neuroleptic medication, then the DaT-SPECT study findings would be normal. However, in this case, there is absent putaminal uptake bilaterally and asymmetric caudate nuclei uptake (Catafau and Tolosa² type 2), indicative of coexistent idiopathic Parkinson disease, MSA, or PSP.

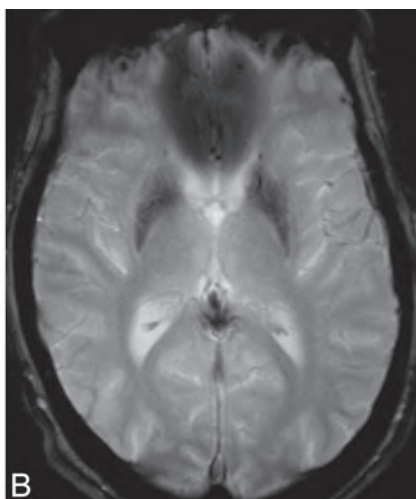
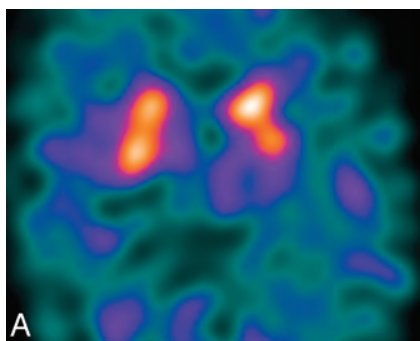


FIG 12. Axial ¹²³I-FP-CIT DaT-SPECT image (A) and axial T2*-weighted MR imaging sequence (B) in the same patient with neuroacanthocytosis. The patient presented with parkinsonian features. Note the asymmetric reduction of ¹²³I-FP-CIT uptake in the left putamen. MR imaging depicts marked hypointensity in the caudate nuclei and putamina, indicative of iron deposition, which is a feature of neuroacanthocytosis.

findings are diagnostic of vascular parkinsonism (Fig 10).¹ Overall, a meta-analysis of the diagnostic differentiation of idiopathic Parkinson disease and vascular parkinsonism by using DaT-SPECT demonstrated a sensitivity of 80%–100% and a specificity of 73%–100%.³⁸

Idiopathic Parkinson Disease versus Drug-Induced Parkinsonism. Drugs that have a competitive antagonistic effect on the postsynaptic D₂ receptors, such as neuroleptics (eg, olanzapine) and centrally acting antiemetics (eg, metoclopramide), can cause parkinsonism, which is usually reversible. Clinically, it can be very difficult to distinguish drug-induced parkinsonism from idiopathic Parkinson disease.¹ However, in contrast to idiopathic Parkinson disease, DaT-SPECT imaging has either normal findings or depicts increased striatal DAT activity, the latter suggesting a compensatory up-regulation of DaT in response to D₂ receptor blockade.^{38,61} Of clinical importance is the masking of early idiopathic Parkinson disease in patients with schizophrenia on neuroleptic medication. In these cases, the DaT-SPECT study findings will be abnormal, in keeping with coexistent idiopathic Parkinson disease (or another neurodegenerative parkinsonian syndrome) (Fig 11).

Idiopathic Parkinson Disease and Essential Tremor. Typically, the unilateral resting tremor of idiopathic Parkinson disease can be distinguished from the symmetric essential tremor on clinical grounds, especially when there are other signs of parkinsonism. However, clinical confusion may occur when the 2 diagnoses coexist or when there are equivocal parkinsonian features. In these cases, DaT-SPECT discriminates essential tremor and idiopathic Parkinson disease because patients with essential tremor consistently have, effectively, normal striatal DaT binding.^{18,38,39,62} Indeed, in a meta-analysis of the diagnostic differentiation of essential tremor and idiopathic Parkinson disease using DaT-SPECT, the study with the lowest sensitivity and specificity reported percentages of 80% and 95%, respectively.³⁵ Recently, DaT-SPECT has challenged the view that essential tremor has absolutely no pathophysiologic effect on dopaminergic transmission because a slight reduction in caudate DaT binding has been noted.⁶²

Rare Causes of Parkinsonism

Nigrostriatal degeneration may also be seen in other, rarer, causes of parkinsonism. Wilson disease demonstrates striatal DaT-SPECT reduction comparable with that in idiopathic Parkinson disease.⁶³ Similarly, reductions in DaT binding are seen in sporadic amyotrophic lateral sclerosis.⁶⁴ Neuroacanthocytosis encompasses a heterogeneous group of disorders characterized by the association of neurologic abnormalities with red cell acanthocytosis. They are categorized into 2 groups based on the presence or absence of movement disorders. In patients with neuroacanthocytosis presenting with movement disorders, there is underlying degeneration of the striatum.⁶⁵ There-

fore, it can be inferred that DaT-SPECT imaging is likely to be abnormal in these cases (Fig 12).

In conclusion, dopamine-transporter imaging, in particular DaT-SPECT, reliably distinguishes neurodegenerative causes of parkinsonism (idiopathic Parkinson disease, MSA, PSP, and CBD) from parkinsonism without nigrostriatal DaT loss (such as essential tremor, vascular parkinsonism, and drug-induced parkinsonism). DaT-SPECT alone cannot differentiate the disorders within the neurodegenerative group, whereas initial studies using a combination of radiotracers or other advanced imaging techniques appear promising. DaT-SPECT also helps to differentiate dementia secondary to Lewy body deposition and Alzheimer disease, thereby avoiding a potential treatment-induced parkinsonian crisis. It is hoped that this technique will be the forerunner of a range of routinely used, process-specific ligands that can identify early degenerative disease and subsequently guide disease-modifying interventions.

ACKNOWLEDGMENTS

The authors thank Dr Jonathan Hart for help in manuscript preparation.

Disclosures: Ann-Marie Quigley—RELATED: Other: Travel, hotel and conference fees were paid by Novartis to attend the European Neuroendocrine Tumor Society 2013 meeting; travel and hotel paid by Nordion to attend the TheraSphere User Group in 2013; No fees were paid to me or my institution. Adam D. Waldman—UNRELATED: Consultancy: Bayer Healthcare, Payment for Lectures (including service on Speakers Bureaus): Bayer Healthcare, Siemens Healthcare, Comments: fees for lectures on education courses, Travel/Accommodations/Meeting Expenses Unrelated to Activities Listed: Bayer Healthcare, Comments: expenses for attendance at meetings for discussion groups and consultancy. John Buscombe—UNRELATED: Consultancy: Navidea, Comments: for work on Medicines and Healthcare Products Regulatory Agency submission, Travel/Accommodations/Meeting Expenses Unrelated to Activities Listed: BTG, Comments: to learn about TheraSpheres, Germany, February 2014. Anthony H. Schapira—RELATED: receives Medical Research Council and Wellcome Trust funding.

REFERENCES

1. Scherfler C, Schwarz J, Antonini A, et al. **Role of DAT-SPECT in the diagnostic work-up of parkinsonism.** *Mov Disord* 2007;22:1229–38
2. Catafau AM, Tolosa E. **Impact of dopamine transporter SPECT using ^{123}I -Ioflupane on diagnosis and management of patients with clinically uncertain parkinsonian syndromes.** *Mov Disord* 2004;19:1175–82
3. Quinn N. **Multiple system atrophy: the nature of the beast.** *J Neurol Neurosurg Psychiatry* 1989(suppl):78–89
4. Papp MI, Lantos PL. **The distribution of oligodendroglial inclusions in multiple system atrophy and its relevance to clinical symptomatology.** *Brain* 1994;117:235–43
5. Schrag A, Good CD, Miszkiel K, et al. **Differentiation of atypical parkinsonian syndromes with routine MRI.** *Neurology* 2000;54:697–702
6. Nicoletti G, Fera F, Condino F, et al. **MR imaging of middle cerebellar peduncle width: differentiation of multiple system atrophy from Parkinson disease.** *Radiology* 2006;239:825–30
7. Ghaemi M, Hilker R, Rudolf J, et al. **Differentiating multiple system atrophy from Parkinson's disease: contribution of striatal and mid-brain MRI volumetry and multi-tracer PET.** *J Neurol Neurosurg Psychiatry* 2002;73:517–23
8. Brenneis C, Seppi K, Schocke MF, et al. **Voxel-based morphometry detects cortical atrophy in the Parkinson variant of multiple system atrophy.** *Mov Disord* 2003;18:1132–38
9. Schulz JB, Skalej M, Wedekind D, et al. **Magnetic resonance imaging-based volumetry differentiates idiopathic Parkinson's syndrome from multiple system atrophy and progressive supranuclear palsy.** *Ann Neurol* 1999;45:65–74
10. Schocke MF, Seppi K, Esterhammer R, et al. **Diffusion-weighted MRI differentiates the Parkinson variant of multiple system atrophy from PD.** *Neurology* 2002;58:575–80
11. Nicoletti G, Lodi R, Condino F, et al. **Apparent diffusion coefficient measurements of the middle cerebellar peduncle differentiate the Parkinson variant of MSA from Parkinson's disease and progressive supranuclear palsy.** *Brain* 2006;129:2679–87
12. Ito M, Watanabe H, Kawai Y, et al. **Usefulness of combined fractional anisotropy and apparent diffusion coefficient values for detection of involvement in multiple system atrophy.** *J Neurol Neurosurg Psychiatry* 2007;78:722–28
13. Watanabe H, Fukatsu H, Katsuno M, et al. **Multiple regional 1H-MR spectroscopy in multiple system atrophy: NAA/Cr reduction in pontine base as a valuable diagnostic marker.** *J Neurol Neurosurg Psychiatry* 2004;75:103–09
14. Berg D, Godau J, Walter U. **Transcranial sonography in movement disorders.** *Lancet Neurol* 2008;7:1044–55
15. Brooks DJ, Salmon EP, Mathias CJ, et al. **The relationship between locomotor disability, autonomic dysfunction, and the integrity of the striatal dopaminergic system in patients with multiple system atrophy, pure autonomic failure, and Parkinson's disease, studied with PET.** *Brain* 1990;113:1539–52
16. Antonini A, Leenders KL, Vontobel P, et al. **Complementary PET studies of striatal neuronal function in the differential diagnosis between multiple system atrophy and Parkinson's disease.** *Brain* 1997;120:2187–95
17. Brücke T, Asenbaum S, Pirker W, et al. **Measurement of the dopaminergic degeneration in Parkinson's disease with [^{123}I] beta-CIT and SPECT: correlation with clinical findings and comparison with multiple system atrophy and progressive supranuclear palsy.** *J Neural Transm Suppl* 1997;50:9–24
18. Benamer TS, Patterson J, Grosset DG, et al. **Accurate differentiation of parkinsonism and essential tremor using visual assessment of [^{123}I]-FP-CIT SPECT imaging: the [^{123}I]-FP-CIT study group.** *Mov Disord* 2000;15:503–10
19. Nocker M, Seppi K, Donnemiller E, et al. **Progression of dopamine transporter decline in patients with the Parkinson variant of multiple system atrophy: a voxel-based analysis of [^{123}I]beta-CIT SPECT.** *Eur J Nucl Med Mol Imaging* 2012;39:1012–20
20. Seeman P, Niznik H. **Dopamine receptors and transporters in Parkinson's disease and schizophrenia.** *FASEB J* 1990;4:2737–44
21. Costa DC, Verhoeff NP, Cullum ID, et al. **In vivo characterisation of 3-iodo-6-methoxybenzamide ^{123}I in humans.** *Eur J Nucl Med* 1990;16:813–16
22. Ichise M, Ballinger JR, Vines D, et al. **Simplified quantification and reproducibility studies of dopamine D_2 -receptor binding with iodine-123-IBF SPECT in healthy subjects.** *J Nucl Med* 1997;38:31–37
23. Churchyard A, Donnan GA, Hughes A, et al. **Dopa resistance in multiple-system atrophy: loss of postsynaptic D_2 receptors.** *Ann Neurol* 1993;34:219–26
24. van Royen E, Verhoeff NPLG, Speelman JD, et al. **Multiple system atrophy and progressive supranuclear palsy: diminished striatal D_2 -receptor activity demonstrated by ^{123}I -IBZM single photon emission computed tomography.** *Arch Neurol* 1993;50:513–16
25. Schwarz J, Tatsch K, Gasser T, et al. **^{123}I -IBZM binding compared with long-term clinical follow up in patients with de novo parkinsonism.** *Mov Disord* 1998;13:16–19
26. Yekhlief F, Ballan G, Macia F, et al. **Routine MRI for the differential diagnosis of Parkinson's disease, MSA, PSP, and CBD.** *J Neural Transm* 2003;110:151–69
27. Quattrone A, Nicoletti G, Messina D, et al. **MR imaging index for differentiation of progressive supranuclear palsy from Parkinson disease and the Parkinson variant of multiple system atrophy.** *Radiology* 2008;246:214–21
28. Brenneis C, Seppi K, Schocke MF, et al. **Voxel-based morphometry**

- reveals a distinct pattern of frontal atrophy in progressive supranuclear palsy. *J Neurol Neurosurg Psychiatry* 2004;75:246–49
29. Price S, Paviour D, Scahill R, et al. **Voxel-based morphometry detects patterns of atrophy that help differentiate progressive supranuclear palsy and Parkinson's disease.** *Neuroimage* 2004;23:663–69
 30. Blain CR, Barker GJ, Jarosz JM, et al. **Measuring brain stem and cerebellar damage in parkinsonian syndromes using diffusion tensor MRI.** *Neurology* 2006;67:2199–205
 31. Seppi K, Schocke MF, Esterhammer R, et al. **Diffusion-weighted imaging discriminates progressive supranuclear palsy from PD, but not from the Parkinson variant of multiple system atrophy.** *Neurology* 2003;60:922–27
 32. Brooks DJ, Ibanez V, Sawle GV, et al. **Striatal D² receptors in patients with Parkinson's disease, striatonigral degeneration, and progressive supranuclear palsy, measured with ¹¹C-raclopride and positron emission tomography.** *Ann Neurol* 1992;31:184–92
 33. Garraux G, Salmon E, Degueldre C, et al. **Comparison of impaired subcortico-frontal metabolic networks in normal aging, subcortico-frontal dementia, and cortical frontal dementia.** *Neuroimage* 1999;10:149–62
 34. Antonini A, Benti R, De NR, et al. **¹²³I-Ioflupane SPECT binding to striatal dopamine transporter (DAT) uptake in patients with Parkinson's disease, multiple system atrophy and progressive supranuclear palsy.** *Neuro Sci* 2003;24:149–50
 35. Vlaar AM, van Kroonenburgh MJ, Kessels AG, et al. **Meta-analysis of the literature on the diagnostic accuracy of SPECT in parkinsonian syndromes.** *BMC Neurol* 2007;1:27
 36. Koch W, Hamann C, Radau PE, et al. **Does combined imaging of the pre- and postsynaptic dopaminergic system increase the diagnostic accuracy in the differential diagnosis of parkinsonism?** *Eur J Nucl Med Mol Imaging* 2007;34:1265–73
 37. Kim YJ, Ichise M, Ballainger JR, et al. **Combination of dopamine transporter and D₂ receptor SPECT in the diagnostic evaluation of PD, MSA and PSP.** *Mov Disord* 2002;2:303–12
 38. Vlaar AM, de Nijs T, Kessels AG, et al. **Diagnostic value of ¹²³I-Ioflupane and ¹²³I-iodobenzamide SPECT scans in 248 patients with Parkinsonian syndromes.** *Eur Neurol* 2008;59:258–66
 39. Plotkin M, Amthauer H, Klaffke S, et al. **Combined [¹²³I]-FPCIT and [¹²³I]-IBZM SPECT for the diagnosis of parkinsonian syndromes: study on 72 patients.** *J Neural Transm* 2005;112:677–92
 40. Südmeyer M, Antke C, Zizek T, et al. **Diagnostic accuracy of combined FP-CIT, IBZM, and MIBG scintigraphy in the differential diagnosis of degenerative parkinsonism: a multidimensional statistical approach.** *J Nucl Med* 2011;52:733–40
 41. Gröschel K, Hauser TK, Luft A, et al. **Magnetic resonance imaging-based volumetry differentiates progressive supranuclear palsy from corticobasal degeneration.** *Neuroimage* 2004;21:714–24
 42. Boxer AL, Geschwind MD, Belfor N, et al. **Patterns of brain atrophy that differentiate corticobasal degeneration syndrome from progressive supranuclear palsy.** *Arch Neurol* 2006;63:81–86
 43. Erbetta A, Mandelli ML, Savoiardo M, et al. **Diffusion tensor imaging shows different topographic involvement of the thalamus in progressive supranuclear palsy and corticobasal degeneration.** *AJNR Am J Neuroradiol* 2009;30:1482–87
 44. Klaffke S, Kuhn AA, Plotkin M, et al. **Dopamine transporters, D2 receptors, and glucose metabolism in corticobasal degeneration.** *Mov Disord* 2006;21:1724–27
 45. Cilia R, Rossi C, Frosini D, et al. **Dopamine transporter SPECT imaging in corticobasal syndrome.** *PLoS One* 2011;6:e18301
 46. Pirker S, Perju-Dumbrava L, Kovacs GG, et al. **Dopamine D2 receptor SPECT in corticobasal syndrome and autopsy-confirmed corticobasal degeneration.** *Parkinsonism Relat Disord* 2013;19:222–26
 47. Stevens T, Livingston G, Kitchen G, et al. **Islington study of dementia subtypes in the community.** *Br J Psychiatry* 2002;180:270–76
 48. Ala TA, Yang KH, Sung JH, et al. **Hallucinations and signs of parkinsonism help distinguish patients with dementia and cortical Lewy bodies from patients with Alzheimer's disease at presentation: a clinicopathological study.** *J Neurol Neurosurg Psychiatry* 1997;62:16–21
 49. McKeith I, Fairbairn A, Perry R, et al. **Neuroleptic sensitivity in patients with senile dementia of Lewy body type.** *BMJ* 1992;305:673–78
 50. Ditter SM, Mirra SS. **Neuropathologic and clinical features of Parkinson's disease in Alzheimer's disease patients.** *Neurology* 1987;37:754–60
 51. Barber R, Gholkar A, Scheltens P, et al. **Medial temporal lobe atrophy on MRI in dementia with Lewy bodies.** *Neurology* 1999;52:1153–58
 52. Whitwell JL, Weigand SD, Shiung MM, et al. **Focal atrophy in dementia with Lewy bodies on MRI: a distinct pattern from Alzheimer's disease.** *Brain* 2007;130:708–19
 53. Kenny ER, Burton EJ, O'Brien JT. **A volumetric magnetic resonance imaging study of entorhinal cortex volume in dementia with Lewy bodies: a comparison with Alzheimer's disease and Parkinson's disease with and without dementia.** *Dement Geriatr Cogn Disord* 2008;26:218–25
 54. Firbank MJ, Blamire AM, Krishnan MS, et al. **Diffusion tensor imaging in dementia with Lewy bodies and Alzheimer's disease.** *Psychiatry Res* 2007;155:135–45
 55. Lobotesis K, Fenwick JD, Phipps A, et al. **Occipital hypoperfusion on SPECT in dementia with Lewy bodies but not AD.** *Neurology* 2001;56:643–49
 56. Gilman S, Koeppe RA, Little R, et al. **Differentiation of Alzheimer's disease from dementia with Lewy bodies utilizing positron emission tomography with [¹⁸F]fluorodeoxyglucose and neuropsychological testing.** *Exp Neurol* 2005;191:S95–S103
 57. Piggott MA, Marshall EF, Thomas N, et al. **Striatal dopaminergic markers in dementia with Lewy bodies, Alzheimer's and Parkinson's diseases: rostrocaudal distribution.** *Brain* 1999;122:1449–68
 58. O'Brien JT, Colloby S, Fenwick J, et al. **Dopamine transporter loss visualized with FP-CIT SPECT in the differential diagnosis of dementia with Lewy bodies.** *Arch Neurol* 2004;61:919–25
 59. Zijlmans JC, Daniel SE, Hughes AJ, et al. **Clinicopathological investigation of vascular parkinsonism, including clinical criteria for diagnosis.** *Mov Disord* 2004;19:630–40
 60. Forno L. **Reaction of the substantia nigra to massive basal ganglia infarction.** *Acta Neuropathol (Berl)* 1983;62:96–102
 61. Sjöholm H, Bratlid T, Sundsfjord J. **[¹²³I]-beta-CIT SPECT demonstrates increased presynaptic dopamine transporter binding sites in basal ganglia in vivo in schizophrenia.** *Psychopharmacology (Berl)* 2004;173:27–31
 62. Isaias IU, Marotta G, Hirano S, et al. **Imaging essential tremor.** *Mov Disord* 2010;25:679–86
 63. Jeon B, Kim JM, Jeong JM. **Dopamine transporter imaging with [¹²³I]-beta-CIT demonstrates presynaptic nigrostriatal dopaminergic damage in Wilson's disease.** *J Neurol Neurosurg Psychiatry* 1998;65:60–64
 64. Borasio GD, Linke R, Schwarz J, et al. **Dopaminergic deficit in amyotrophic lateral sclerosis assessed with [¹²³I] IPT single photon emission computed tomography.** *J Neurol Neurosurg Psychiatry* 1998;65:263–65
 65. Ichiba M, Nakamura M, Sano A. **Neuroanthocytosis update.** *Brain Nerve* 2008;60:635–41

MRI Findings in Children with Acute Flaccid Paralysis and Cranial Nerve Dysfunction Occurring during the 2014 Enterovirus D68 Outbreak

J.A. Maloney, D.M. Mirsky, K. Messacar, S.R. Dominguez, T. Schreiner, and N.V. Stence



ABSTRACT

BACKGROUND AND PURPOSE: Enterovirus D68 was responsible for widespread outbreaks of respiratory illness throughout the United States in August and September 2014. During this time, several patients presented to our institution with acute flaccid paralysis and cranial nerve dysfunction. The purpose of this report is to describe the unique imaging findings of this neurologic syndrome occurring during an enterovirus D68 outbreak.

MATERIALS AND METHODS: Patients meeting a specific case definition of acute flaccid paralysis and/or cranial nerve dysfunction and presenting to our institution during the study period were included. All patients underwent routine MR imaging of the brain and/or spinal cord, including multiplanar T1, T2, and contrast-enhanced T1-weighted imaging.

RESULTS: Eleven patients met the inclusion criteria and underwent MR imaging of the brain and/or spinal cord. Nine patients presented with brain stem lesions, most commonly involving the pontine tegmentum, with bilateral facial nerve enhancement in 1 patient. Ten patients had longitudinally extensive spinal cord lesions; those imaged acutely demonstrated involvement of the entire central gray matter, and those imaged subacutely showed lesions restricted to the anterior horn cells. Ventral cauda equina nerve roots enhanced in 4 patients, and ventral cervical nerve roots enhanced in 3, both only in the subacute setting.

CONCLUSIONS: Patients presenting with acute flaccid paralysis and/or cranial nerve dysfunction during the recent enterovirus D68 outbreak demonstrate unique imaging findings characterized by brain stem and gray matter spinal cord lesions, similar to the neuroimaging findings described in previous outbreaks of viral myelitis such as enterovirus 71 and poliomyelitis.

ABBREVIATIONS: AFP = acute flaccid paralysis; EV-D68 = enterovirus D68; EV-71 = enterovirus 71

Human enteroviruses are ubiquitous pathogens throughout the world and cause a variety of disease states, including respiratory infections, herpangina, hand-foot-and-mouth disease, and aseptic meningitis. Enterovirus D68 (EV-D68), first identified in California in 1962,¹ has been described primarily as a cause of respiratory illness.^{2,3} More recently, however, rare cases of CNS disease have been attributed to EV-D68.^{4,5}

In August and September 2014, EV-D68 was responsible for widespread outbreaks of respiratory disease throughout the

United States.⁶ Against this backdrop, Children's Hospital Colorado noted an unusual number of cases of acute flaccid paralysis (AFP) and cranial nerve dysfunction following a febrile upper respiratory illness. This association led the Centers for Disease Control and Prevention to issue a national Health Advisory,⁷ and it was subsequently described in the *Morbidity and Mortality Weekly Report*.⁸

Enteroviruses have been associated with neurologic syndromes previously, most notably enterovirus 71 (EV-71). EV-71 most commonly presents with nonneurologic manifestations but has been associated with multiple outbreaks of AFP and brain stem encephalitis throughout the world.⁹⁻¹⁵ MR imaging in affected patients typically reveals a rhombencephalitis affecting the dorsal pons and medulla, and a radiculomyelitis with a predilection for the anterior horn cells of the spinal cord and ventral nerve roots, findings that have also been described in poliomyelitis.¹⁶⁻¹⁹ Although EV-D68 has not been proved as the causative agent in this cluster, these cases demonstrate distinctive imaging features that are very similar to the neuroimaging presentation of both EV-71 and poliovirus.

Received October 15, 2014; accepted after revision October 25.

From the Departments of Radiology (J.A.M., D.M.M., N.V.S.) and Pediatrics, Section of Pediatric Infectious Disease (K.M., S.R.D.), Section of Hospital Medicine (K.M.), and Section of Child Neurology (T.S.), Children's Hospital Colorado, University of Colorado School of Medicine, Aurora, Colorado.

J.A. Maloney and D.M. Mirsky are co-first authors of this article.

Please address correspondence to John A. Maloney, MD, Department of Radiology, Children's Hospital Colorado, University of Colorado School of Medicine, 13123 E 16th Ave, Aurora, CO 80045; e-mail: john.maloney@childrenscolorado.org

 Indicates open access to non-subscribers at www.ajnr.org

 Indicates article with supplemental on-line table.

<http://dx.doi.org/10.3174/ajnr.A4188>

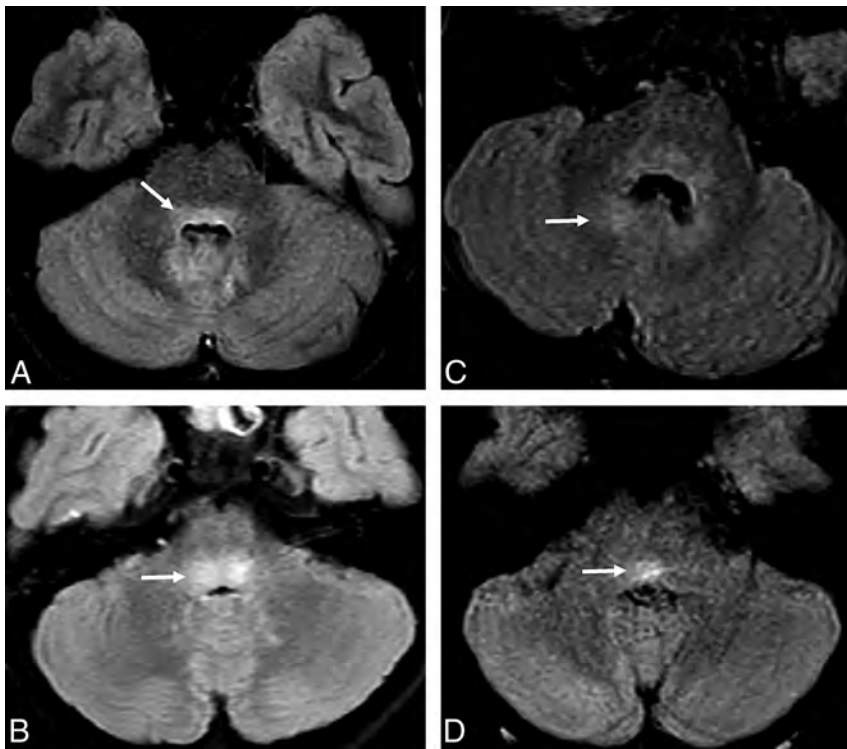


FIG 1. Noncontrast FLAIR images through the dorsal pons demonstrate a variety of types of T2 hyperintensity. *A*, In patient 4, T2 hyperintensity in the dorsal pons (*arrow*) extends into the dentate nuclei. *B*, In patient 2, more focal and intense T2 signal is localized in the dorsal pons (*arrow*). *C*, In patient 6, ill-defined and less intense signal in the dorsal pons extends to the dentate nuclei (*arrow*). *D*, In patient 10, more focal and T2 hyperintensity is seen within the dorsal pons (*arrow*).

We present an imaging-based report describing in detail the MR imaging findings of neurologic diseases associated with an EV-D68 outbreak.

MATERIALS AND METHODS

Patients

Patients who presented to our institution from August 1, 2014, to October 1, 2014, with symptoms of AFP and/or cranial nerve dysfunction and with lesions in the brain stem or spinal cord gray matter on MR imaging were included.

MR Imaging

Imaging was performed on a 1.5T or 3T Ingenia (Philips Healthcare, Best, the Netherlands) or a 1.5T Avanto unit (Siemens, Erlangen, Germany). Ten of 11 patients underwent MR imaging of the brain, 7 had MR imaging of the entire spine, 2 had MR imaging of the cervical and thoracic spine only, and 1 had MR imaging of the cervical spine only. One patient did not undergo dedicated spine imaging. Parameters and specific sequences of various MR imaging brain examinations were variable, though each patient underwent isometric 3D T1-weighted gradient-echo imaging be-

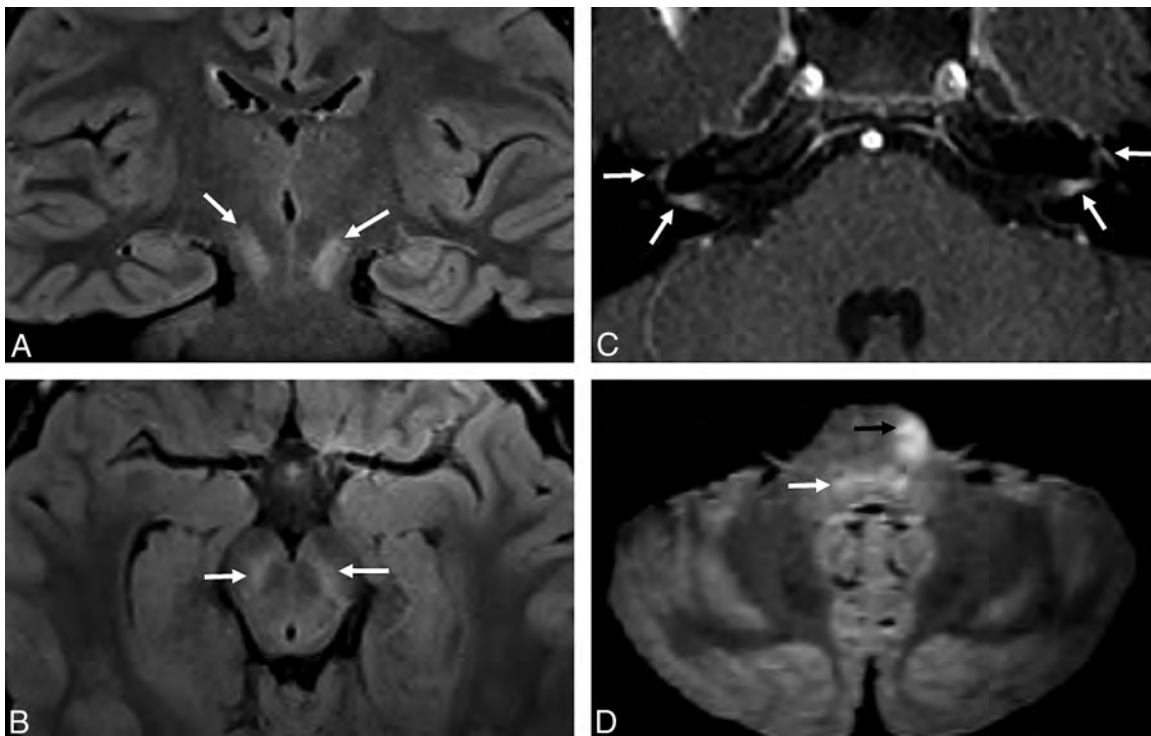


FIG 2. Atypical appearance of CNS disease includes T2 hyperintensity localized to the substantia nigra in patient 3 (*white arrows, A and B*). In patient 7, the facial nerves abnormally enhance bilaterally (*white arrows, C*) and the left ventral pons has an atypical T2 hyperintense focus (*black arrow, D*). There is also more ill-defined hyperintensity in the dorsal pons (*white arrow, D*).

fore and after intravenous administration of gadobenate dimeglumine (TR, 8.19–8.79 ms; TE, 3.77–4.60 ms; NEX, 1; section thickness, 1 mm), axial T2-weighted FSE (TR, 3500–10,000 ms; TE, 80–110 ms; NEX, 1 or 2; section thickness, 2–4 mm), FLAIR imaging (TR, 4800–11,000 ms; TE, 125–330 ms; NEX, 2; section thickness, 1 or 4 mm), and axial gradient echo T2*-weighted imaging (TR, 550–900 ms; TE, 23–26 ms; flip angle, 18°–20°; NEX, 1 or 2; section thickness, 4 or 5 mm), or SWI (TR, 18.36–19.34 ms; TE, 25–27 ms; NEX, 1; section thickness, 2 mm). Spinal imaging included precontrast axial and sagittal spin-echo T1-weighted (TR, 450–650 ms; TE, 8–10 ms; NEX, 2 or 3; section thickness, 3 mm), T2-weighted (TR, 3000–3500 ms; TE, 100–120 ms; NEX, 2 or 3; section thickness, 3 mm), and contrast-enhanced axial and sagittal T1-weighted images. All scans were reviewed independently by 3 fellowship-trained pediatric neuroradiologists.

RESULTS

Clinical Findings

Eleven patients met the inclusion criteria. The patient demographics, presenting symptoms, vaccination history, diagnostic work-up, and clinical course have been detailed elsewhere (K.M. et al, unpublished data, 2014) and are summarized in the On-line Table. Briefly, patients presented with neurologic symptoms following a febrile upper respiratory illness, including limb weakness in 8 patients and cranial nerve dysfunction in 9. Involved cranial nerves were VI, VII, IX, X, XI, and XII.

Eight patients tested positive for rhinovirus/enterovirus in the nasopharynx, 4 of which were subtyped as EV-D68 (On-line Table). Findings of enteroviral polymerase chain reaction of the CSF were negative in all patients. Testing for West Nile virus and other arboviruses, herpes viruses, *Mycoplasma pneumoniae*, parechoviruses, and poliovirus was also negative.

Imaging Findings

On MR imaging, lesions were identified in the brain stem in 9 patients. The pontine tegmentum was the most common site of brain stem involvement, showing increased T2 signal in 8 cases (Fig 1). A ventral pontine lesion in a ninth case was associated with bilateral facial nerve enhancement (patient 7, Fig 2). Lesions were identified in the midbrain in 2 cases, including the bilateral substantia nigra in 1 case (patient 3, Fig 2), and in the medulla in 5 cases. The dentate nuclei were abnormally T2 hyperintense in 2 cases. No supratentorial lesions were identified.

Ten patients had spinal cord lesions involving the central gray matter (On-line Table and Figs 3 and 4). The spinal cord lesions consisted of either ill-defined, nonenhancing T2 hyperintensity throughout the entire central spinal cord gray matter (Fig 3A–C) or a more well-defined T2 hyperintensity confined to the anterior horn cells (Fig 3D, –E). A single patient, patient 1, underwent both acute (day 3) and subacute (day 38) imaging. In this case, the pattern of spinal cord T2 hyperintensity evolved from diffuse central gray matter involvement acutely to an anterior horn cell pattern in the subacute phase (Fig 4). The cases with ill-defined diffuse central gray matter involvement were all imaged earlier than cases with well-defined anterior horn cell signal abnormality (median of 3 days after symptom onset versus 27.5 days, with no overlap between groups). Cord lesions uniformly affected the cer-

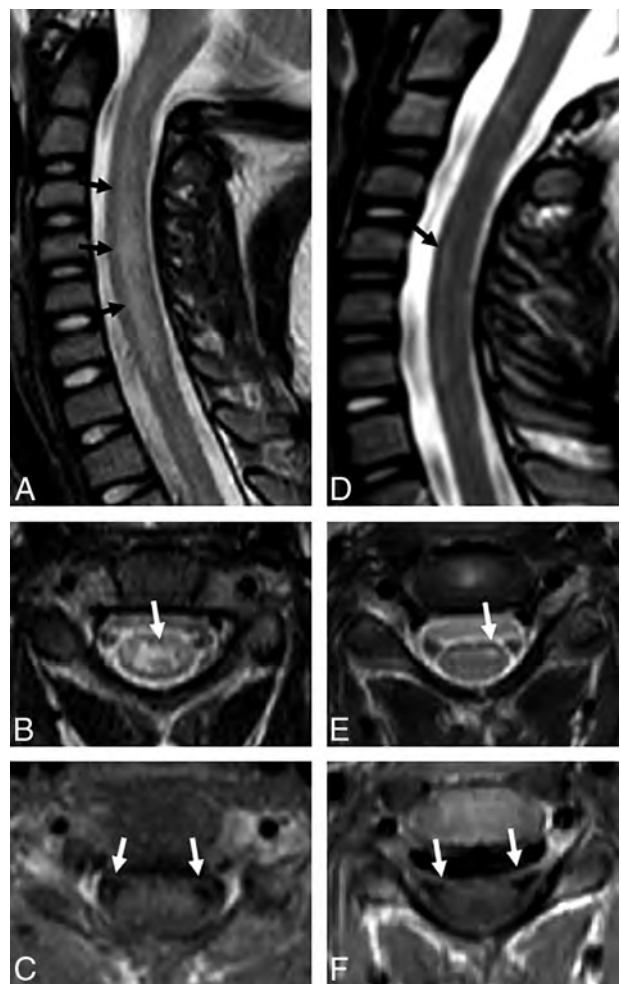


FIG 3. A–C, In Patient 2 scanned at 2 days, the central cord hyperintensity is more ill-defined and involves the entire central gray matter (black arrows, A; white arrow, B). Nerve roots do not enhance (white arrows, C). D–F, Patient 8, scanned at 25 days, demonstrates T2 hyperintensity confined to the anterior horn cells asymmetric to the left (black arrow, D; white arrow, E) and nerve root enhancement (white arrows, F).

vical spine, with decreasing involvement inferiorly. In 4 cases, the lesions extended the entire length of the cord, from the cervicomedullary junction to the conus medullaris (Fig 4). All brain and spinal cord lesions were nonenhancing.

Ventral cauda equina nerve root enhancement occurred in 4 patients (Fig 4), though only 3 had clinical findings of lower extremity weakness. Cervical nerve root enhancement at the levels of spinal cord gray matter T2 hyperintensity and clinical weakness was also detected in 3 patients. Those cases with nerve root enhancement were imaged later than those without (median of 27.5 days after neurologic symptom onset versus 3 days after symptom onset, with no overlap between groups).

DISCUSSION

Rhombencephalitis and AFP have been reported as uncommon complications of EV-71 infections.^{9–15} Multiple case series have described MR imaging findings in cases of EV-71 neurologic disease, including nonenhancing dorsal brain stem T2 hyperintensity,^{9,11,15,20–25} long-segment T2 hyperintensity of spinal



FIG 4. A–D, Acute imaging performed at 2–3 days in patient 1 demonstrates T2 hyperintensity in the right dorsal pons (*white arrow, A*) and more ill-defined central gray matter hyperintensity seen more commonly in the acute phase (*white arrows, B and C; black arrows, D*). E–I, Subacute imaging of the spine performed in the same patient at 38 days demonstrates contraction of the cord T2 hyperintensity to focally involve the anterior horn cells (*black arrows, E; white arrows, F and H*) and nerve root enhancement of ventral cervical roots (*white arrows, G*) and the cauda equina (*white arrows, I*).

cord anterior horn cells,^{11,15,20,23,25,26} nerve root enhancement,^{11,15,20–22,25} enhancement of anterior horn cells or brain stem,^{11,15,20,24} and substantia nigra involvement.¹¹ Similarly, several case reports of MR imaging findings in poliomyelitis have also described dorsal brain stem T2 hyperintensity,¹⁶ anterior horn cell T2 hyperintensity,^{17–19,27,28} anterior horn cell enhancement,¹⁹ and substantia nigra T2 hyperintensity.^{16,17,29} Some published cases of AFP caused by West Nile virus have also reported comparable imaging findings of anterior horn–predominant spinal cord lesions and ventral nerve root enhancement.^{30,31} The similarity of the MR imaging findings in this case series to these past reports of virally mediated myelitis suggests a similar direct viral pathogenic effect.

The brain stem was abnormal in most patients in our series, and all of these patients presented with symptoms of cranial nerve dysfunction (Fig 1 and On-line Table). This pattern of clinical involvement in EV-71 neurologic disease has often been described as brain stem encephalitis or rhombencephali-

tis.^{9,11,15,20–25} Almost all patients presented with cervical spinal cord T2 hyperintensities, and 9 reported weakness of ≥ 1 extremity (Fig 3 and On-line Table). This clinical and imaging pattern has been described as AFP in prior case series of EV-71 neurologic disease.^{11,15,20,23,25,26}

As mentioned, imaging performed shortly after the onset of CNS symptoms referable to the spinal cord usually demonstrated ill-defined signal abnormality involving the entire central spinal cord gray matter (Fig 3A–C), while the few patients who were imaged subacutely showed more well-defined signal abnormality confined to the anterior horn cells (Fig 3D, -E). We speculate that this difference reflects maturation of the disease process, possibly indicating permanent damage, which has been described previously in EV-71 infection.²³

Other patients with less stereotyped findings include a single patient with diplopia and cranial nerve VI palsies with bilateral substantia nigra T2 hyperintensities (patient 3, Fig 2), which has been described more frequently in poliomyelitis.^{16,17,29} Imaging

of another patient who presented with bilateral facial nerve palsies revealed a small, nonenhancing ventral pons lesion and bilateral facial nerve enhancement (patient 7, Fig 2). Although facial nerve palsies are frequently reported in EV-71 infections,²⁴ to our knowledge, this is the first report of both facial nerve enhancement and a unilateral ventral pontine lesion in the context of suspected enteroviral CNS disease.

Similar to the cases in our cluster, spinal nerve root enhancement has been previously described in cases of EV-71 neurologic disease.^{11,15,20–22,25} Nerve root enhancement is thought to result from either breakdown of the blood-nerve endothelial barrier³² or radicular vein enhancement.³³ In the case of EV-71 neurologic disease and the current series, possible etiologies could include direct viral infection, inflammation related to Wallerian degeneration from anterior horn cell damage, or a postinfectious autoimmune inflammatory process, as is suspected in Guillain-Barre-related enhancement.³⁴

Several imaging features argue against alternative, noninfectious differential diagnoses. None of these patients presented with supratentorial lesions, as are frequently seen in acute disseminated encephalomyelitis.³⁵ The restriction of involvement to the central gray matter in our series is not typical of the imaging or clinical findings of idiopathic acute transverse myelitis (admittedly a diagnosis of exclusion), which is typically described as central, extensive spinal cord T2 hyperintensity, swelling, and lesion enhancement.^{36,37} Nerve root enhancement is also not typical of either acute disseminated encephalomyelitis or transverse myelitis. While Guillain-Barre syndrome is characterized by nerve root enhancement, cord and brain stem lesions are not typical features.³⁴

Details on treatment of this cohort are described elsewhere (K.M. et al, unpublished data, 2014). To date, most of these patients have residual deficits. Long-term outcomes are unknown. Continued radiographic and neurologic follow-up will be critical to our understanding of the course of this condition.

CONCLUSIONS

This series of children presenting with neurologic disease after a respiratory illness during an EV-D68 outbreak shares a characteristic pattern of MR imaging findings previously described in past outbreaks of EV-71 neurologic disease, West Nile virus–associated AFP, and poliomyelitis. MR imaging findings in this series include brain stem lesions preferentially involving the pontine tegmentum, spinal cord lesions of the central gray matter acutely and anterior horn cells subacutely, and cranial and spinal nerve root enhancement. The marked similarity of these imaging findings in our cohort of patients to those reported in EV-71, poliomyelitis, and West Nile virus is very suggestive of a direct viral effect. Recognition of these findings is critical to aid clinicians as they consider therapeutic interventions.

Disclosures: Teri Schreiner—UNRELATED: Grants/Grants Pending: Environmental and Genetic Triggers of Pediatric MS,* Comments: This is a National Institutes of Health–funded study. I am in 1 of 14 sites that are participating in the study. Money was paid via contract to the University of Colorado; Payment for Lectures (including service on Speakers Bureaus): Consortium of MS Centers, Comments: I was paid \$500 (plus travel expenses) to provide a lecture at the annual meeting of the Consortium of MS Centers in May 2014. *Money paid to the institution.

REFERENCES

1. Committee on the Enteroviruses. **Classification of human enteroviruses.** *Virology* 1962;16:501–04
2. Oberste MS, Maher K, Schnurr D, et al. **Enterovirus 68 is associated with respiratory illness and shares biological features with both the enteroviruses and the rhinoviruses.** *J Gen Virol* 2004;85(pt 9): 2577–84
3. Centers for Disease Control and Prevention (CDC). **Clusters of acute respiratory illness associated with human enterovirus 68: Asia, Europe, and United States, 2008–2010.** *MMWR Morb Mortal Wkly Rep* 2011;60:1301–04
4. Kreuter J, Barnes A. **A fatal central nervous system enterovirus 68 infection.** *Arch Path Lab Med* 2011;135:793–96
5. Roux A, Lulu S, Waubrant E, et al. **A Polio-like syndrome in California: clinical, radiologic, and serologic evaluation of five children identified by a statewide laboratory over a twelve-month period.** *Neurology* 2014;82(10 suppl):P3.335
6. Midgley C, Jackson MA, Selvarangan R, et al. **Severe respiratory illness associated with enterovirus D68: Missouri and Illinois, 2014.** *MMWR Morb Mortal Wkly Rep* 2014;63:798–99
7. CDC Health Alert Network. **Acute neurologic illness with focal limb weakness of unknown etiology in children.** September 26, 2014. <http://www.bt.cdc.gov/han/han00370.asp>. Accessed October 6, 2014
8. Pastula DM, Aliabadi N, Haynes AK, et al. **Acute neurologic illness of unknown etiology in children: Colorado, August–September 2014.** *MMWR Morb Mortal Wkly Rep* 2014;63:3901–02
9. Wang SM, Liu CC, Tseng HW, et al. **Clinical spectrum of enterovirus 71 infection in children in southern Taiwan, with an emphasis on neurological complications.** *Clin Infect Dis* 1999;29:184–90
10. Ooi MH, Wong SC, Lewthwaite P, et al. **Clinical features, diagnosis, and management of enterovirus 71.** *Lancet Neurol* 2010;9:1097–105
11. Huang CC, Liu CC, Chang YC, et al. **Neurologic complications in children with enterovirus 71 infection.** *N Engl J Med* 1999;341:936–42
12. McMinn P, Stratov I, Nagarajan L, et al. **Neurological manifestations of enterovirus 71 infection in children during an outbreak of hand, foot, and mouth disease in Western Australia.** *Clin Infect Dis* 2001;32:236–42
13. McMinn PC. **Enterovirus 71 in the Asia-Pacific region: an emerging cause of acute neurological disease in young children.** *Neurol J Southeast Asia* 2003;8:57–63
14. Pérez-Vélez CM, Anderson MS, Robinson CC, et al. **Outbreak of neurologic enterovirus type 71 disease: a diagnostic challenge.** *Clin Infect Dis* 2007;45:950–57
15. Chen CY, Chang YC, Huang CC, et al. **Acute flaccid paralysis in infants and young children with enterovirus 71 infection: MR imaging findings and clinical correlates.** *AJNR Am J Neuroradiol* 2001;22:200–05
16. Wasserstrom R, Mamourian A, McGary C, et al. **Bulbar poliomyelitis: MR findings with pathologic correlation.** *AJNR Am J Neuroradiol* 1992;13:371–73
17. Choudhary A, Sharma S, Sankhyan N, et al. **Midbrain and spinal cord magnetic resonance imaging (MRI) changes in poliomyelitis.** *J Child Neurol* 2010;25:497–99
18. Haq A, Wasay M. **Magnetic resonance imaging in poliomyelitis.** *Arch Neurol* 2006;63:778
19. Kornreich L, Dagan O, Grunebaum M. **MRI in acute poliomyelitis.** *Neuroradiology* 1996;38:371–72
20. Chen F, Li JJ, Liu T, et al. **Clinical and neuroimaging features of enterovirus 71 related acute flaccid paralysis in patients with hand-foot-mouth disease.** *Asian Pac J Trop Med* 2013;6:68–72
21. Lee KY, Lee YJ, Kim TH, et al. **Clinico-radiological spectrum in enterovirus 71 infection involving the central nervous system in children.** *J Clin Neurosci* 2014;21:416–20
22. Jang S, Suh S, Ha SM, et al. **Enterovirus 71-related encephalomyelitis: usual and unusual magnetic resonance imaging findings.** *Neuroradiology* 2012;54:239–45
23. Shen WC, Chiu HH, Chow KC, et al. **MR imaging findings of enterovirus 71 infection in children.** *AJNR Am J Neuroradiol* 2004;23:1000–04

- viral encephalomyelitis: an outbreak in Taiwan.** *AJNR Am J Neuroradiol* 1999;20:1889–95
24. Zeng H, Wen F, Gan Y, et al. **MRI and associated clinical characteristics of EV71-induced brainstem encephalitis in children with hand-foot-mouth disease.** *Neuroradiology* 2012;54:623–30
 25. Li J, Chen F, Liu T, et al. **MRI findings of neurological complications in hand-foot-mouth disease by enterovirus 71 infection.** *Int J Neurosci* 2012;122:338–44
 26. Shen WC, Tsai C, Chiu H, et al. **MRI of Enterovirus 71 myelitis with monoplegia.** *Neuroradiology* 2000;42:124–27
 27. Rao DG, Bateman DE. **Hyperintensities of the anterior horn cells on MRI due to poliomyelitis.** *J Neurol Neurosurg Psychiatry* 1997;63:720
 28. Malzberg M, Rogg J. **Poliomyelitis: hyperintensity of the anterior horn cells on MR images of the spinal cord.** *AJR Am J Roentgenol* 1993;161:863–65
 29. França MC Jr, Schmutzler KM, Garibaldi SG, et al. **Bilateral substantia nigra involvement in vaccine-associated poliomyelitis.** *Neurology* 2006;66:1597–98
 30. Kraushaar G, Patel R, Stoneham GW. **West Nile virus: a case report with flaccid paralysis and cervical spinal cord MR imaging findings.** *AJNR Am J Neuroradiol* 2005;26:26–29
 31. Hainline ML, Kincaid JC, Carpenter DL, et al. **West Nile poliomyelitis in a 7-year-old child.** *Pediatr Neurol* 2008;39:350–54
 32. Nguyen C, Haughton V, Ho K, et al. **Contrast enhancement in spinal nerve roots: an experimental study.** *AJNR Am J Neuroradiol* 1995;16:265–68
 33. Georgy B, Snow R, Hesselink J. **MR imaging of spinal nerve roots: techniques, enhancement patterns, and imaging findings.** *AJR Am J Roentgenol* 1996;166:173–79
 34. Yikilmaz A, Doganay S, Gumus H, et al. **Magnetic resonance imaging of childhood Guillain-Barre syndrome.** *Childs Nerv Syst* 2010;26:1103–08
 35. Krupp LB, Banwell B, Tenenbaum S. **Consensus definitions proposed for pediatric multiple sclerosis and related disorders.** *Neurology* 2007;68(16 suppl 2):S7–12
 36. Andronikou S, Albuquerque-Jonathan G, Wilmshurst J, et al. **MRI findings in acute idiopathic transverse myelopathy in children.** *Pediatr Radiol* 2003;33:624–29
 37. Wolf VL, Lupo PJ, Lotze TE. **Pediatric acute transverse myelitis overview and differential diagnosis.** *J Child Neurol* 2012;27:1426–36

Double Inversion Recovery MR Sequence for the Detection of Subacute Subarachnoid Hemorrhage

J. Hodel, R. Aboukais, B. Dutouquet, E. Kalsoum, M.A. Benadjaoud, D. Chechin, M. Zins, A. Rahmouni, A. Luciani, J.-P. Pruvo, J.-P. Lejeune, and X. Leclerc



ABSTRACT

BACKGROUND AND PURPOSE: The diagnosis of subacute subarachnoid hemorrhage is important because rebleeding may occur with subsequent life-threatening hemorrhage. Our aim was to determine the sensitivity of the 3D double inversion recovery sequence compared with CT, 2D and 3D FLAIR, 2D T2*, and 3D SWI sequences for the detection of subacute SAH.

MATERIALS AND METHODS: This prospective study included 25 patients with a CT-proved acute SAH. Brain imaging was repeated between days 14 and 16 (mean, 14.75 days) after clinical onset and included MR imaging (2D and 3D FLAIR, 2D T2*, SWI, and 3D double inversion recovery) after CT (median delay, 3 hours; range, 2–5 hours). A control group of 20 healthy volunteers was used for comparison. MR images and CT scans were analyzed independently in a randomized order by 3 blinded readers. For each subject, the presence or absence of hemorrhage was assessed in 4 subarachnoid areas (basal cisterns, Sylvian fissures, interhemispheric fissure, and convexity) and in brain ventricles. The diagnosis of subacute SAH was defined by the presence of at least 1 subarachnoid area with hemorrhage.

RESULTS: For the diagnosis of subacute SAH, the double inversion recovery sequence had a higher sensitivity compared with CT ($P < .001$), 2D FLAIR ($P = .005$), T2* ($P = .02$), SWI, and 3D FLAIR ($P = .03$) sequences. Hemorrhage was present for all patients in the interhemispheric fissure on double inversion recovery images, while no signal abnormality was noted in healthy volunteers. Interobserver agreement was excellent with double inversion recovery.

CONCLUSIONS: Our study showed that the double inversion recovery sequence has a higher sensitivity for the detection of subacute SAH than CT, 2D or 3D FLAIR, 2D T2*, and SWI.

ABBREVIATIONS: IVH = intraventricular hemorrhage; DIR = double inversion recovery

Nontraumatic subarachnoid hemorrhage accounts for 3% of all strokes, and 85% are related to a ruptured intracranial aneurysm.¹ CT is highly sensitive for the diagnosis of SAH at the acute stage.² However, clinical symptoms may be atypical and result in delayed admission. In such patients, the diagnosis of subacute SAH is important because rebleeding may occur with subsequent life-threatening intracranial hemorrhage.³

When performed several days after symptom onset, CT does not appear reliable for the diagnosis of SAH^{4,5} and is outperformed by

brain MR imaging in this setting.⁶ Indeed, FLAIR MR imaging is more sensitive than CT for SAH detection at both acute⁷⁻⁹ and subacute¹⁰ stages. 3D FLAIR is even more specific than 2D FLAIR by reducing flow-related artifacts, which are known to provide false-positive findings on 2D FLAIR.¹¹ Nevertheless, SAH can still be misdiagnosed by using FLAIR imaging due to the time interval after onset¹² or artifacts.^{13,14} T2* gradient-echo sequences are useful for subacute or chronic SAH depiction.^{6,15,16} Susceptibility-weighted imaging uses tissue magnetic-susceptibility differences to generate a unique contrast, based on a 3D flow-compensated gradient-echo sequence.¹⁷ Previous studies have suggested that SWI could accurately detect small amounts of SAH and intraventricular hemorrhage (IVH).¹⁸⁻²⁰ A recent study focusing on the detection of microbleeds also demonstrated that SWI had a greater sensitivity for blood products than the conventional T2* sequence.²¹ However, no study available compares the diagnostic performance of T2* and SWI for the detection of spontaneous SAH, to our knowledge.

Double inversion recovery (DIR) MR imaging is useful for the detection of cortical lesions.²²⁻²⁴ This technique is based on a 3D

Received June 14, 2014; accepted after revision July 11.

From the Departments of Neuroradiology (J.H., B.D., E.K., J.-P.P., X.L.) and Neurosurgery (R.A., J.-P.L.), Hôpital Roger Salengro, Lille, France; Institut National De La Santé et De La Recherche Médicale (M.A.B.), Centre for Research in Epidemiology and Population Health, Villejuif, France; Philips Medical Systems (D.C.), Suresnes, France; Department of Radiology (J.H., M.Z.), Hôpital Saint Joseph, Paris, France; and Department of Radiology (A.R., A.L.), Centre Hospitalier Universitaire, Henri Mondor, Créteil, France.

Please address correspondence to Jérôme Hodel, MD, Department of Neuroradiology, Hôpital Roger Salengro, Rue Emile Laine, 59037 Lille, France; e-mail: jerome.hodel@gmail.com

Evidence-Based Medicine Level 2.

<http://dx.doi.org/10.3174/ajnr.A4102>

Table 1: Demographic and clinical data at admission

	Patients	Controls
No.	25	20
Sex	16 M/9 F	13 M/7 F
Age (yr) (mean) (range)	52 (28–71)	50 (26–69)
Fisher grading (mean)	3	
Grade 1 (No.)	5	
Grade 2 (No.)	2	
Grade 3 (No.)	6	
Grade 4 (No.)	12	
GCS (mean) (range)	14.1 (10–15)	
WFNS score (mean) (range)	1.5 (1–4)	
No vascular lesion (No.)	10	
Brain aneurysm (No.)	15	
Etiologic work-up (CTA and DSA)		
ACA (No.)	6	
MCA (No.)	(right 2, left 2)	
Right PcomA (No.)	2	
Left vertebral artery (No.)	1	
Left ICA (No.)	1	
Basilar artery (No.)	1	

Note:—GCS indicates Glasgow Coma Scale; WFNS, World Federation of Neurosurgical Societies; ACA, anterior communicating artery; PcomA, posterior communicating artery.

turbo spin-echo acquisition with variable refocusing flip angles (BrainView, Philips Healthcare, Best, the Netherlands; Cube, GE Healthcare, Milwaukee, Wisconsin; SPACE, Siemens, Erlangen, Germany). DIR includes 2 inversion recovery pulses designed for the suppression of both CSF and normal white matter.²⁴ Data are still not available on the value of 3D DIR for the detection of SAH. The purpose of our study was to determine the sensitivity of the 3D DIR sequence compared with CT, 2D and 3D FLAIR, 2D T2*, and 3D SWI sequences for the detection of subacute SAH.

MATERIALS AND METHODS

Patients and Brain Imaging

This prospective monocentric study was approved by our institutional review board, and informed consent was obtained from all patients or their representatives. The inclusion criteria were as follows: 1) patient admitted for suspected SAH, 2) acute SAH proved on the initial unenhanced CT scan or lumbar puncture performed at the admission, and 3) Glasgow Coma Scale score >10 (as required by the ethics committee). Patients with hydrocephalus or brain hematoma on the initial unenhanced CT scan were excluded.

From October to December 2013, 40 consecutive patients were diagnosed with acute and spontaneous SAH by using unenhanced CT. All CT scans were obtained at admission and were reviewed by a neuroradiologist with 20 years of experience. The diagnostic criterion for SAH on CT images was the presence of a high-attenuation area within the subarachnoid spaces. No diagnosis was based on lumbar puncture during the inclusion period. Of the 40 patients, 4 died and 11 had a Glasgow Coma Scale score of <10, including 4 with a brain hematoma. Finally, 25 patients fulfilled the inclusion criteria; demographic and clinical data are summarized in Table 1.

The etiologic work-up included CT angiography at admission and digital subtraction angiography (within the following 12 hours). Of the 25 patients, 15 presented with a ruptured intracranial aneurysm, which was successfully treated by coils within 48

hours after clinical onset. No patient was ventilated or received high-inspired oxygen.

From 14 to 16 days (mean, 14.75 days) after clinical onset, additional brain imaging was systematically performed, including 3T MR imaging (Achieva; Philips Healthcare) and repeated unenhanced CT (Somatom Sensation; Siemens) (median delay, 3 hours before MR imaging; range, 2–5 hours). Unenhanced spiral CT was performed from the first cervical vertebra to the vertex, with the following parameters: 120 kV; 350 mAs; collimation, 40 × 0.6 mm. To balance the study group, MR imaging was also performed in 20 healthy volunteers who served as controls. Healthy volunteers were scanned by using 3T MR imaging only, with the same protocol as that used in the included patients. All MR imaging examinations were performed at 3T by using a 32-channel array head coil, without gadolinium chelate injection. MR imaging protocol included diffusion-weighted imaging, 2D and 3D FLAIR, 3D SWI, 2D T2*, and 3D DIR MR imaging. The scan duration was 20 minutes. The parameters are summarized in Table 2. The parameters of the 3D FLAIR sequence used in this study were previously optimized for CSF suppression. We tested different TR and TI values (ranging from 4000 to 8000 ms and from 1500 to 2800 ms, respectively) in healthy volunteers. In this study, we also used a similar TE value for 3D DIR and 3D FLAIR sequences (near 260 ms) because high effective TE values are reported to be more sensitive to increases in CSF protein concentration.²⁵ The voxel size and acquisition time were also similar.

Image Analysis

First, MR images of healthy volunteers were randomly interspersed among the patient images. MR imaging interpretation was conducted independently by 3 blinded neuroradiologists with 25 (reader 1), 10 (reader 2), and 3 (reader 3) years of experience in neurovascular imaging.

For the detection of subacute SAH and IVH in each subject, the readers assessed each set of images (2D FLAIR, 3D FLAIR, 2D T2*, SWI, and DIR) separately in a randomized order. The independent sessions of image interpretation were 1 week apart to avoid recall bias. The readers were blinded to clinical data (patient with SAH or healthy volunteer) and to the results of other imaging modalities. Imaging criteria for hemorrhage at the subacute stage were the following: for CT images, increased attenuation values compared with the normal CSF; for DIR and FLAIR images, increased signal intensity compared with the normal CSF; and for T2* and susceptibility-weighted images, decreased signal intensity compared with the normal CSF. Multiplanar analysis was available for CT, 3D FLAIR, 3D SWI, and 3D DIR MR images, including axial, coronal, and sagittal reformations. The 3D susceptibility-weighted images were available in both average mode and minimum intensity projection.

For each subject and each set of images, the readers were asked to assess visually the presence or absence of hemorrhage according to a 2-point scale (0, no signal abnormality; 1, signal abnormality) within 4 subarachnoid areas (basal cisterns, Sylvian fissures, interhemispheric fissure, and brain convexity) and 1 ventricular area (including the fourth, the third, or the lateral ventricles). The basal cisterns included the perimesencephalic and prepontine cisterns and the cisterna magna.

Table 2: MR imaging sequence parameters

	2D FLAIR	2D T2*	3D FLAIR	3D SWI	3D DIR
Acquisition plane	Axial	Axial	Sagittal	Sagittal	Sagittal
TR/TE (ms)	11,000/125	1077/16	4800/267	13/19	5500/255
T1 (ms)	2800	—	1650	—	2600/625
Acquired voxel size (mm)	0.8 × 1.4 × 4	0.9 × 1.2 × 4	1.2 × 1.2 × 1.2	1.2 × 1.2 × 1.2	1.2 × 1.2 × 1.2
Bandwidth (Hz)	271	216	1433	172	1433
Echo-train length	31	—	182	—	173
No. of sections	36	36	280	280	280
SENSE	1.4	—	2.5	2.5	2.5
CLEAR	Yes	Yes	Yes	Yes	Yes
Fat suppression	No	No	SPIR	No	SPIR
Acquisition time	3 min	3 min	3 min 20 sec	3 min	4 min

Note:—SENSE indicates sensitivity encoding; CLEAR, inhomogeneity correction; SPIR, spectral presaturation with inversion recovery.

Table 3: Interobserver agreement among readers 1, 2, and 3 for each set of images according to the area considered

	CT	MRI				
		2D FLAIR	3D FLAIR	2D T2*	3D SWI	3D DIR
Total						
R1 vs R2 (95% CI)	1 (1–1)	0.85 (0.77–0.93)	0.79 (0.69–0.89)	0.84 (0.76–0.91)	0.79 (0.72–0.87)	0.94 (0.91–0.97)
R1 vs R3 (95% CI)	0.94 (0.85–1)	0.68 (0.57–0.79)	0.65 (0.53–0.76)	0.74 (0.65–0.83)	0.64 (0.55–0.73)	0.90 (0.87–0.93)
R2 vs R3 (95% CI)	0.94 (0.85–1.02)	0.70 (0.60–0.81)	0.70 (0.59–0.80)	0.72 (0.63–0.81)	0.73 (0.65–0.81)	0.93 (0.91–0.96)
Subarachnoid						
Interhemispheric						
R1 vs R2 (95% CI)	1 (1–1)	0.91 (0.74–1)	0.83 (0.60–1)	0.76 (0.54–0.98)	0.68 (0.44–0.92)	1 (1–1)
R1 vs R3 (95% CI)	1 (1–1)	0.83 (0.60–1.06)	0.76 (0.50–1.02)	0.87 (0.70–1.05)	0.44 (0.11–0.77)	1 (1–1)
R2 vs R3 (95% CI)	1 (1–1)	0.91 (0.74–1.08)	0.76 (0.50–1.02)	0.77 (0.56–0.99)	0.63 (0.39–0.88)	1 (1–1)
Sylvian fissures						
R1 vs R2 (95% CI)	1 (1–1)	1 (1–1)	1 (1–1)	0.94 (0.83–1)	0.82 (0.63–1)	0.95 (0.88–1)
R1 vs R3 (95% CI)	1 (1–1)	0.88 (0.66–1.11)	1 (1–1)	1 (1–1)	0.59 (0.31–0.86)	0.90 (0.81–1)
R2 vs R3 (95% CI)	1 (1–1)	0.88 (0.66–1.11)	1 (1–1)	0.94 (0.83–1.06)	0.73 (0.50–0.96)	0.95 (0.89–1.02)
Convexity						
R1 vs R2 (95% CI)	1 (1–1)	0.83 (0.68–0.98)	0.56 (0.27–0.84)	0.73 (0.57–0.89)	0.63 (0.43–0.84)	0.90 (0.85–0.95)
R1 vs R3 (95% CI)	0.83 (0.60–1.07)	0.61 (0.42–0.81)	0.48 (0.23–0.73)	0.60 (0.42–0.78)	0.63 (0.44–0.83)	0.87 (0.81–0.92)
R2 vs R3 (95% CI)	0.83 (0.60–1.07)	0.60 (0.40–0.79)	0.56 (0.33–0.80)	0.56 (0.37–0.74)	0.70 (0.55–0.86)	0.90 (0.85–0.95)
Basal cisterns						
R1 vs R2 (95% CI)	1 (1–1)	0.33 (–0.33–0.98)	0.70 (0.41–0.99)	0.74 (0.39–1)	0.64 (0.36–0.92)	0.94 (0.88–1)
R1 vs R3 (95% CI)	1 (1–1)	0.43 (–0.07–0.92)	0.25 (–0.20–0.70)	0.45 (–0.01–0.98)	0.25 (–0.13–0.62)	0.89 (0.82–0.97)
R2 vs R3 (95% CI)	1 (1–1)	0.39 (–0.29–1.07)	0.30 (–0.17–0.77)	0.74 (0.39–1.10)	0.41 (0.09–0.73)	0.95 (0.90–1)
Intraventricular						
R1 vs R2 (95% CI)	1 (1–1)	1 (1–1)	1 (1–1)	1 (1–1)	0.95 (0.85–1)	1 (1–1)
R1 vs R3 (95% CI)	1 (1–1)	0 (–1.12–1.12)	0 (–1.95–1.95)	0.66 (0.19–1.13)	0.86 (0.70–1.02)	0 (–1.38–1.38)
R2 vs R3 (95% CI)	1 (1–1)	0 (–1.12–1.12)	0 (–1.95–1.95)	0.66 (0.19–1.13)	0.82 (0.64–1)	0 (–1.38–1.38)

Note:—R1–R3 indicate readers 1–3; Total, all the subarachnoid and ventricular areas; Convexity, bilateral frontal, parietal, temporal, and occipital convexity areas; Basal cisterns, perimesencephalic and prepontine cisterns and cisterna magna.

Statistical Analysis

Statistical analyses were performed by using SAS software, Version 9.3 (SAS Institute, Cary, North Carolina). First, we evaluated the level of interobserver agreement for the detection of signal abnormalities by using CT and MR imaging (Cohen κ test). κ values between 0.4 and 0.6 suggested moderate agreement; κ values between 0.6 and 0.8, good agreement; and values higher than 0.8, excellent agreement. Comparison of κ values was performed. Second, disagreements between readers were resolved in consensus. Third, we compared the number of patients diagnosed with at least 1 subarachnoid and/or ventricular area with subacute hemorrhage (diagnosis of SAH and IVH, respectively) among CT, 2D FLAIR, 3D FLAIR, T2*, SWI, and DIR MR images by using the McNemar χ^2 test.

RESULTS

MR images were assessable for all subjects, with no motion artifacts.

Interobserver Agreement

Detailed results are shown in Table 3. Interobserver agreement was excellent with DIR for all the subarachnoid regions considered. Agreement between readers 1 and 2 was significantly better with DIR than with 2D FLAIR ($P = .03$), 3D FLAIR ($P = .002$), T2* ($P < .001$), and SWI ($P < .001$). Agreement between readers 1 and 3 and between readers 2 and 3 was significantly better with DIR than with the other MR images ($P < .001$). Agreement between readers 1 and 2 was significantly improved by the use of 2D FLAIR compared with 3D FLAIR for the detection of SAH at the brain convexity ($P = .02$). Agreement between readers 1 and 3 was significantly improved by the use of 3D FLAIR compared with 2D FLAIR for the detection of SAH at the basal cisterns ($P < .001$).

Detection of Subacute SAH

Consensus results are summarized in Table 4. In healthy volunteers, there was no signal abnormality detected by any of the readers by using DIR or other MR imaging.

Table 4: Number of patients with at least 1 subarachnoid and/or ventricular signal abnormality (diagnosis of SAH and IVH, respectively) for each imaging modality after consensus among readers

	CT	MRI				
		2D FLAIR	3D FLAIR	2D T2*	3D SWI	3D DIR
Patients with SAH	7	12	15	14	15	25
Interhemispheric ^a	0	6	7	13	15	25
Sylvian fissures ^a	4	4	4	9	8	17
Convexity ^a	3	8	8	10	11	19
Basal cisterns ^a	0	1	5	4	7	23
Patients with IVH	0	0	0	3	5	0

^aNumber of patients with at least 1 subarachnoid signal abnormality.

With DIR images, all patients presented with at least 2 subarachnoid areas of SAH. Conversely, there were no subarachnoid signal abnormalities in 15 patients on CT, 13 on 2D FLAIR, 11 on T2*, and 10 on 3D FLAIR and SWI. Indeed, for the diagnosis of SAH (ie, a patient with at least 1 area of subarachnoid signal abnormality), DIR was more sensitive than CT ($P < .001$), 2D FLAIR ($P = .005$), 2D T2* ($P = .02$), SWI ($P = .03$), and 3D FLAIR ($P = .03$). Regarding the diagnosis of SAH, there was no significant difference among T2*, SWI, and 2D and 3D FLAIR.

For the diagnosis of SAH, there were 17 disagreements among readers (ie, SAH detected by 1 reader but ruled out by the other 2 readers), including 2 disagreements with the T2* sequence, 5 with 2D FLAIR, 3 with 3D FLAIR, and 7 with 3D SWI. Reasons for disagreement included the following: hypointensity judged after consensus to be too faint or related to a vessel on T2* or SWI; hyperintensity that could be related to CSF flow-related artifacts on 2D FLAIR; and hyperintensity within the brain sulci judged too subtle to diagnose SAH on 3D FLAIR. There was no disagreement with the 3D DIR sequence.

Detection of Subacute IVH

On consensus analysis, T2* and SWI detected 3 and 5 patients, respectively, with a small amount of bleeding in both occipital horns of the lateral ventricles, while CT, 2D FLAIR, 3D FLAIR, and DIR did not. SWI was more sensitive than CT and all other MR imaging for the diagnosis of IVH ($P = .03$). However, T2* did not prove to be significantly better than 2D and 3D FLAIR ($P = .08$). The 5 patients with subacute IVH detected on SWI (4 men/1 woman; mean age, 52.6 years; range, 31–71 years) also had at least 2 subarachnoid areas with SAH on DIR images.

For the diagnosis of IVH (ie, at least 1 area with IVH), there were 7 disagreements among the readers: 1 each with T2*, 2D FLAIR, and 3D FLAIR MR images, and 2 each with 3D DIR and 3D SWI. Reasons for disagreement included hyperintensity on DIR and FLAIR images that could be related to CSF transependymal resorption.

Figure 1 shows the absence of artifacts or subarachnoid hyperintensities on DIR images in a healthy volunteer. Figures 2–4 illustrate the improved sensitivity of the 3D DIR sequence, in comparison with other MR images, for the detection of subacute SAH.

DISCUSSION

Our study showed that the DIR sequence had a higher sensitivity for the detection of subacute SAH than CT and conventional

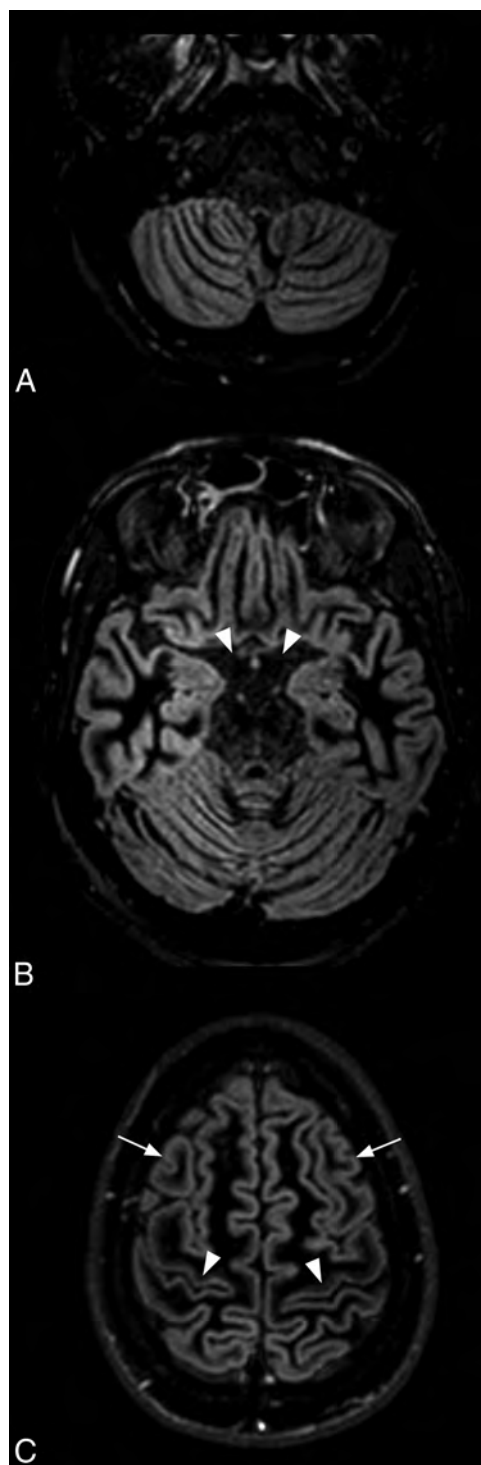


FIG 1. Axial DIR images in a 37-year-old healthy volunteer showing the basal cisterns (A and B) and the subarachnoid spaces at the brain convexity (C). In all the healthy volunteers scanned with the DIR sequence, the CSF appeared hypointense without CSF flow-related artifacts (B, arrowheads). Note the regional variation of gray matter signal intensity by using DIR, such as the difference between the prefrontal (C, arrows) and motor (C, arrowheads) cortices. The absence of CSF signal abnormality on DIR images in all the healthy volunteers and the strong agreement among readers suggest that the hyperintensities observed in patients with SAH by using DIR were not linked to artifacts.

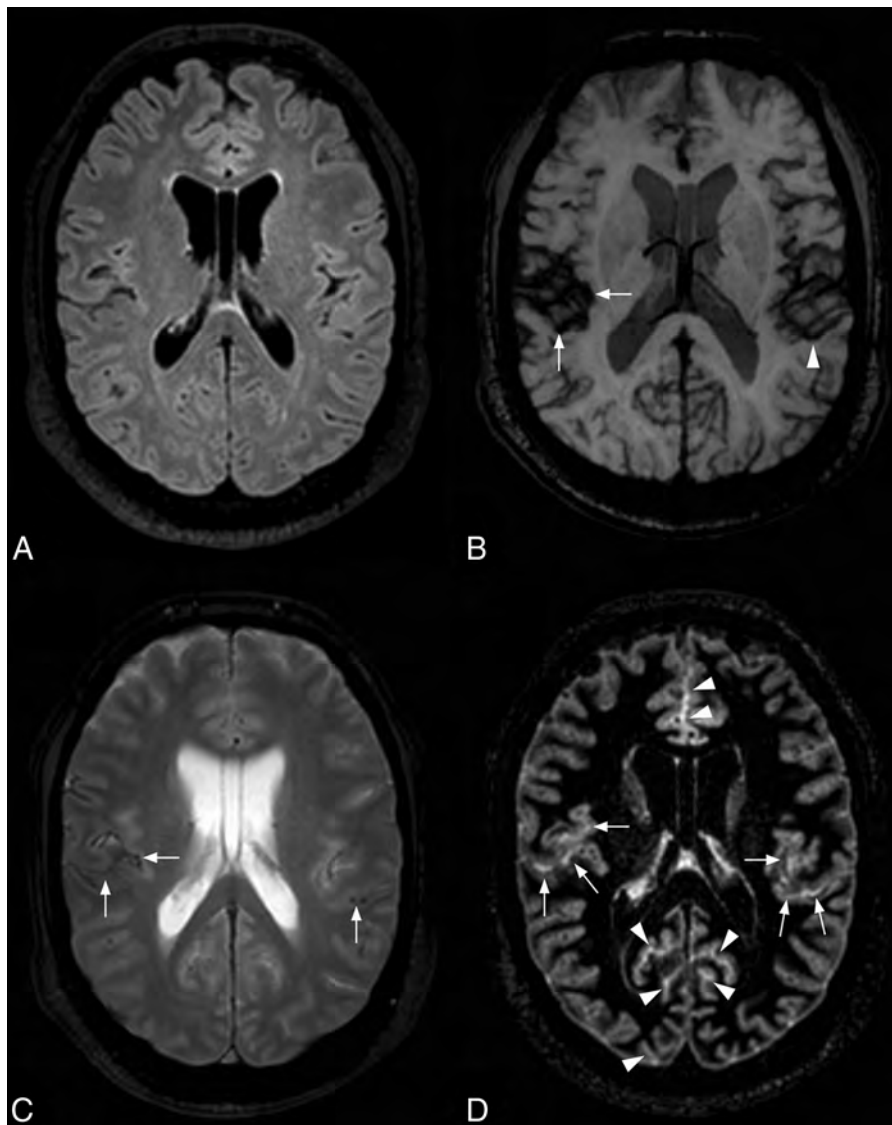


FIG 2. Subacute SAH related to an aneurysm of the anterior communicating artery in a 42-year-old woman. No signal abnormality is visible on 3D FLAIR (A). SAH is visible by using axial SWI minimum-intensity-projection reformations in the right Sylvian fissure (B, arrows). The hypointensity visible in the left Sylvian fissure on SWI was considered a cortical vein by the 3 blinded readers by using both average and minimum-intensity-projection reformations (B, arrowhead). On the axial T2* image, SAH is bilateral, involving the Sylvian fissures (C, arrows). The DIR sequence reveals extensive SAH prevailing in the Sylvian fissures (D, arrows) and interhemispheric and occipital sulci (D, arrowheads).

brain MR imaging, including 2D FLAIR, 3D FLAIR, 2D T2*, and 3D SWI. DIR appeared reliable for all the subarachnoid regions, while the sensitivity of the other imaging modalities was dependent on the anatomic distribution of hemorrhage.

In patients with subacute SAH, CT revealed subarachnoid high-attenuation abnormalities in only 7 of the 25 patients. This finding is in agreement with previous studies demonstrating the rapid attenuation changes according to the decreased concentration in hemoglobin in the time course of SAH.^{4,5} In our institution, CT is systematically performed 2 weeks after the onset to rule out potential hydrocephalus or rebleeding.

The MR imaging appearance of SAH differs from that of cerebral hematoma because the SAH signal results from blood combined with CSF.⁸ Detection of SAH is related to the difference of T1 and T2 relaxation times among blood, normal CSF, and brain parenchyma. FLAIR is the reference method for the diagnosis of

SAH at the subacute stage due to CSF suppression, which improves the image contrast. On FLAIR images, the subarachnoid signal intensity is directly related to cellularity and protein levels.¹⁴ The T1-shortening effects of higher protein concentrations in bloody CSF explain why SAH can be identified by using FLAIR.^{8,26} However, SAH can still be misdiagnosed by using FLAIR imaging due to the time interval between symptom onset and brain imaging¹² or image artifacts.^{13,14}

T2* is considered useful for the diagnosis of subacute or chronic SAH.^{6,16} This sequence appears effective in detecting a prior SAH indicating the location of a ruptured aneurysm.¹⁶ On T2* images, SAH signal is dependent on the state of oxygenation and the integrity of red blood cell walls. A limitation of the T2* sequence is detection of SAH, particularly at the skull base. Most interesting in the present study, SWI was not significantly better than conventional T2* for the diagnosis of SAH. Indeed, as pre-

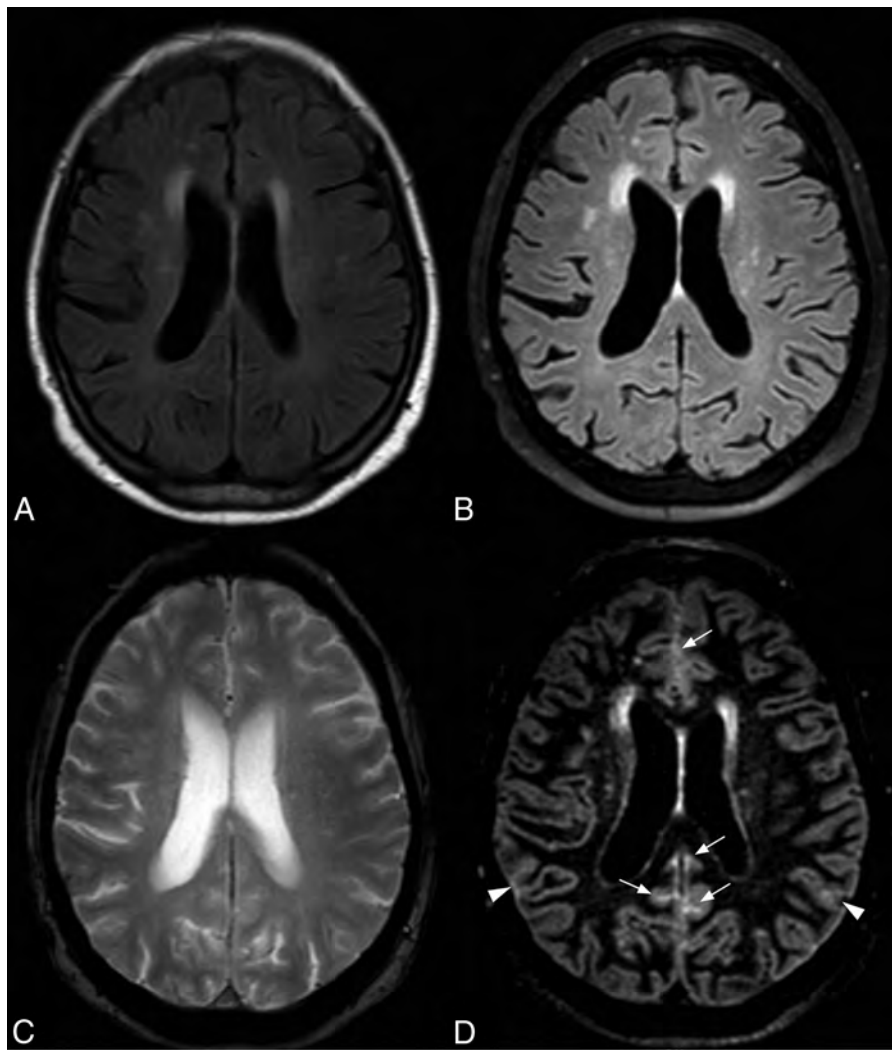


FIG 3. Subacute SAH related to an aneurysm of the anterior communicating artery in a 63-year-old man. With 2D FLAIR (A), 3D FLAIR (B), or T2* (C) images, no subacute hemorrhage is visible. Conversely, marked subarachnoid signal abnormalities along the anterior and posterior interhemispheric sulci are observed by using DIR (D, arrows). SAH involving the parietal lobes is also visible (D, arrowheads).

viously suggested,²⁰ hypointense cortical veins may be difficult to distinguish from SAH on both average and minimum-intensity-projection SWI. In addition, by using SWI, the signal of SAH may be similar to the low signal of CSF. This similarity may explain why the interobserver agreement was significantly lower by using T2* and SWI compared with DIR. However, in agreement with previous studies,^{19,20} T2* and SWI were particularly useful for detecting IVH, while FLAIR and DIR sequences failed to detect small amounts of intraventricular bleeding. Such findings may suggest that both SWI and DIR should be performed in patients with suspected SAH.

The detection of SAH may be improved in 3 ways: 1) by reducing vascular and CSF flow-related artifacts, 2) by enhancing SAH-to-background contrast, and 3) by improving spatial resolution. There are several potential advantages of using 3D sequences with thinner sections such as DIR for the detection of SAH. First, the decrease in section thickness may improve SAH detection by reducing the partial volume effects. Second, while 2D sequences are prone to flow-related artifacts,²⁷ 3D acquisition mode dramatically reduces them by using thicker volume.²⁸ In-

deed, subarachnoid signal abnormalities observed on DIR images cannot be related to slow arterial blood flow; this feature further improves the specificity of this technique for the diagnosis of SAH. Third, 3D sequences, with their higher SNR and isotropic voxel size, allow image postprocessing with reformations in arbitrary planes, which, in turn, may improve the conspicuity of signal abnormalities.

In our study, 3D DIR identified significantly more patients with SAH than 3D FLAIR and 3D SWI performed with the same voxel size, suggesting that DIR is inherently more sensitive for detecting subacute SAH. As with FLAIR, DIR suppresses the CSF signal, improving the depiction of local T1-shortening related to SAH. The additional inversion recovery pulse, designed for white matter suppression, may further improve the contrast between SAH and brain tissue. The increased signal intensity of SAH observed with DIR may also be related to a different dynamic range of the signal that automatically displays optimized predefined values for window width and window level, with subsequent maximization of contrast among tissues of interest. Indeed, the combination of 2 inversion recovery pulses with DIR appears

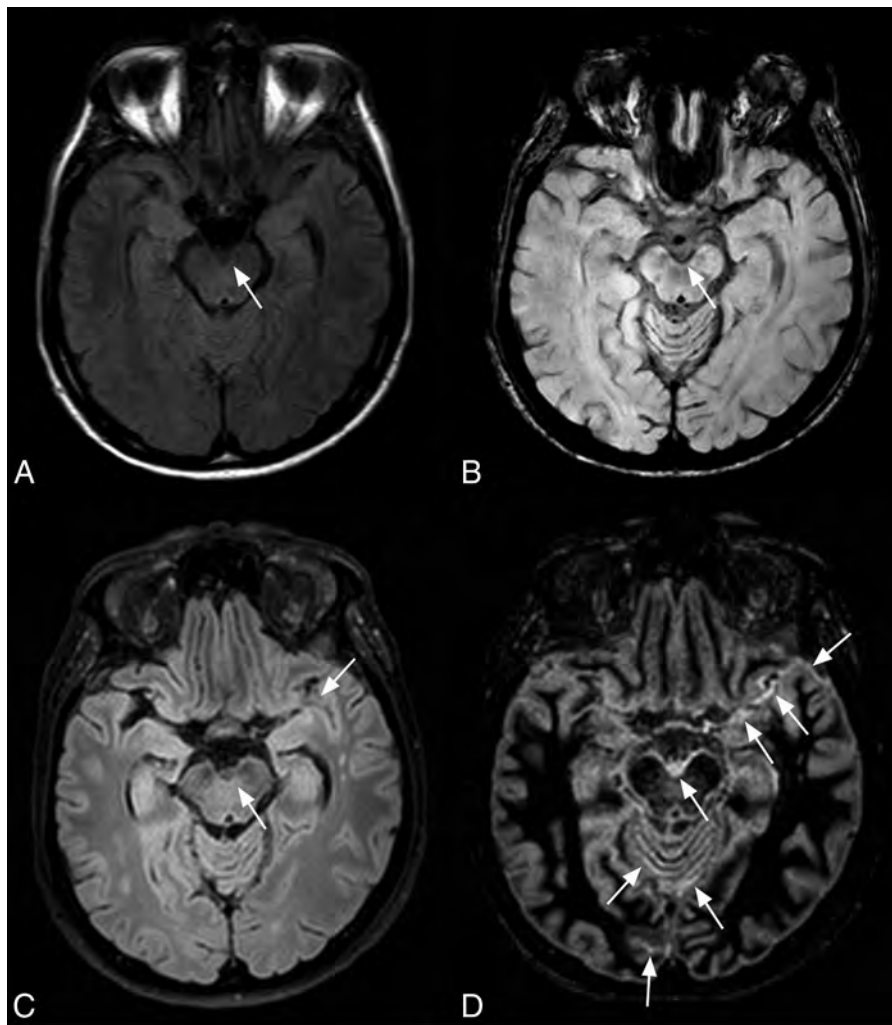


FIG 4. Subacute SAH related to an aneurysm of the left internal carotid artery in a 25-year-old woman. With 2D FLAIR images, the detection of SAH is challenging due to potential CSF flow-related artifacts (A, arrow). With an axial average SWI reformat, a slight rim of hemorrhage is visible within the interpeduncular fossa (B, arrow). On the 3D FLAIR image, SAH is subtle due to a lack of contrast (C, arrows). With DIR images, SAH is obvious, with a marked hyperintensity within the interpeduncular fossa, vermis, and left Sylvian fissure (D, arrows). Note the marked signal intensity of SAH with DIR compared with the other MR images.

particularly suitable for detecting SAH. Furthermore, DIR is also less prone to susceptibility artifacts than T2* or SWI because of the TSE readout used, explaining its reliability for detecting infra- and supratentorial SAH. Indeed, the excellent interobserver agreement with DIR may be related to an increased signal of SAH combined with reduced artifacts.

Our study has several limitations. First, the diagnosis of SAH relied on CT at admission, but there was no standard of reference to determine the exact distribution of SAH at the subacute stage. Therefore, we only analyzed the sensitivity for detecting subacute SAH, instead of standard accuracy parameters. The drastic improvement in SAH detection with DIR may raise doubts about the specificity of the subarachnoid signal abnormalities observed in patients. All the areas with SAH visible on FLAIR, T2*, and SWI were also detected with DIR. In addition, the absence of CSF signal abnormality on DIR images for all the healthy volunteers and the excellent agreement among readers strongly suggest that the DIR hyperintensities observed in patients were specific to SAH and thus not related to artifacts. Because the DIR sequence allows a clear delineation between the subarachnoid space and the cor-

tex, a cortical lesion would have been easily distinguished from SAH. In vitro or experimental studies could be required to confirm these findings. Second, due to the study design, only patients with Glasgow Coma Scale scores >10 at the time of admission were included; this choice explained the relatively small number of patients with subacute SAH. This drawback also explains the small amount of SAH (Fisher 1 or 2) detected on CT performed at admission in 7 of the 25 patients. However, such limited bleeding may further highlight the improved sensitivity of the 3D DIR sequence. Third, we did not evaluate the sensitivity of DIR at acute or more delayed stages. The marked SAH hyperintensity observed on DIR images may suggest that this sequence could also be useful at the chronic stage. Because 15 of the 25 patients underwent endovascular treatment, coils may have led to susceptibility artifacts, particularly when using T2* and SWI, which should temper the claim of a fully blinded assessment.

Differences in voxel size and the availability of multiplanar reformations were found among the 2D and 3D MR images. Indeed, each sequence was optimized before the study to improve the detection of SAH. Because we compared DIR with 2 other 3D

sequences with the same voxel size (3D FLAIR and 3D SWI), our results suggest that DIR may be inherently more sensitive for detecting subacute SAH. It would have been possible to reformat the 3D sequences (FLAIR, SWI, and DIR) into axial sections that matched the section thickness and acquisition plane of the 2D images (FLAIR and T2*). However, such an approach would have decreased the image quality and would not have fully used the ability of 3D sequences to acquire thin sections with an optimal signal-to-noise ratio.

CONCLUSIONS

Overall, the results of this study suggest that the DIR sequence provides a greater sensitivity for the detection of SAH than CT, 2D or 3D FLAIR, 2D T2*, and 3D SWI. DIR may be a promising tool for the diagnosis of SAH in patients admitted several days after the onset of symptoms.

Disclosures: David Chechin—UNRELATED: Employment: Philips Healthcare, Comments: As an employee of Philips Healthcare, I have supported this work. Alain Luciani—UNRELATED: Payment for Development of Educational Presentations: GE Healthcare, Comments: teaching on multienergy CT. Jean-Paul Lejeune—UNRELATED: Payment for Lectures (including service on Speakers Bureaus): BrainLab, Comments: lecture during the Congress of the Société de Neurochirurgie de Langue Française; Travel/Accommodations/Meeting Expenses Unrelated to Activities Listed: B. Braun, Comments: Congress of the Société Française de Neurochirurgie (accommodation expenses).

REFERENCES

- van Gijn J, Rinkel GJ. **Subarachnoid haemorrhage: diagnosis, causes and management.** *Brain* 2001;124:249–78
- Backes D, Rinkel GJ, Kemperman H, et al. **Time-dependent test characteristics of head computed tomography in patients suspected of nontraumatic subarachnoid hemorrhage.** *Stroke* 2012;43:2115–19
- Connolly ES Jr, Rabinstein AA, Carhuapoma JR, et al. **Guidelines for the management of aneurysmal subarachnoid hemorrhage: a guideline for healthcare professionals from the American Heart Association/American Stroke Association.** *Stroke* 2012;43:1711–37
- Fainardi E, Chierogato A, Antonelli V, et al. **Time course of CT evolution in traumatic subarachnoid haemorrhage: a study of 141 patients.** *Acta Neurochir (Wien)* 2004;146:257–63, discussion 263
- van Gijn J, van Dongen KJ. **The time course of aneurysmal haemorrhage on computed tomograms.** *Neuroradiology* 1982;23:153–56
- Mitchell P, Wilkinson ID, Hoggard N, et al. **Detection of subarachnoid haemorrhage with magnetic resonance imaging.** *J Neurol Neurosurg Psychiatry* 2001;70:205–11
- Noguchi K, Ogawa T, Inugami A, et al. **Acute subarachnoid hemorrhage: MR imaging with fluid-attenuated inversion recovery pulse sequences.** *Radiology* 1995;196:773–77
- Noguchi K, Seto H, Kamisaki Y, et al. **Comparison of fluid-attenuated inversion-recovery MR imaging with CT in a simulated model of acute subarachnoid hemorrhage.** *AJNR Am J Neuroradiol* 2000;21:923–27
- Woodcock RJ Jr, Short J, Do HM, et al. **Imaging of acute subarachnoid hemorrhage with a fluid-attenuated inversion recovery sequence in an animal model: comparison with non-contrast-enhanced CT.** *AJNR Am J Neuroradiol* 2001;22:1698–703
- Noguchi K, Ogawa T, Seto H, et al. **Subacute and chronic subarachnoid hemorrhage: diagnosis with fluid-attenuated inversion-recovery MR imaging.** *Radiology* 1997;203:257–62
- Lummel N, Schoepf V, Burke M, et al. **3D fluid-attenuated inversion recovery imaging: reduced CSF artifacts and enhanced sensitivity and specificity for subarachnoid hemorrhage.** *AJNR Am J Neuroradiol* 2011;32:2054–60
- Mohamed M, Heasley DC, Yagmurlu B, et al. **Fluid-attenuated inversion recovery MR imaging and subarachnoid hemorrhage: not a panacea.** *AJNR Am J Neuroradiol* 2004;25:545–50
- Stuckey SL, Goh TD, Heffernan T, et al. **Hyperintensity in the subarachnoid space on FLAIR MRI.** *AJR Am J Roentgenol* 2007;189:913–21
- Maeda M, Yagishita A, Yamamoto T, et al. **Abnormal hyperintensity within the subarachnoid space evaluated by fluid-attenuated inversion-recovery MR imaging: a spectrum of central nervous system diseases.** *Eur Radiol* 2003;13(suppl 4):L192–201
- Inoue T, Takada S, Shimizu H, et al. **Signal changes on T2*-weighted magnetic resonance imaging from the acute to chronic phases in patients with subarachnoid hemorrhage.** *Cerebrovasc Dis* 2013;36:421–29
- Imaizumi T, Chiba M, Honma T, et al. **Detection of hemosiderin deposition by T2*-weighted MRI after subarachnoid hemorrhage.** *Stroke* 2003;34:1693–98
- Haacke EM, Xu Y, Cheng YC, et al. **Susceptibility weighted imaging (SWI).** *Magn Reson Med* 2004;52:612–18
- Mittal S, Wu Z, Neelavalli J, et al. **Susceptibility-weighted imaging: technical aspects and clinical applications, part 2.** *AJNR Am J Neuroradiol* 2009;30:232–52
- Verma RK, Kottke R, Andereggen L, et al. **Detecting subarachnoid hemorrhage: comparison of combined FLAIR/SWI versus CT.** *Eur J Radiol* 2013;82:1539–45
- Wu Z, Li S, Lei J, et al. **Evaluation of traumatic subarachnoid hemorrhage using susceptibility-weighted imaging.** *AJNR Am J Neuroradiol* 2010;31:1302–10
- Cheng AL, Batool S, McCreary CR, et al. **Susceptibility-weighted MRI is more reliable than T2*-weighted gradient-recalled echo MRI for detecting microbleeds.** *Stroke* 2013;44:2782–86
- Geurts JJ, Pouwels PJ, Uitdehaag BM, et al. **Intracortical lesions in multiple sclerosis: improved detection with 3D double inversion-recovery MR imaging.** *Radiology* 2005;236:254–60
- Nelson F, Poonawalla AH, Hou P, et al. **Improved identification of intracortical lesions in multiple sclerosis with phase-sensitive inversion recovery in combination with fast double inversion recovery MR imaging.** *AJNR Am J Neuroradiol* 2007;28:1645–49
- Pouwels PJ, Kuijter JP, Mugler JP 3rd, et al. **Human gray matter: feasibility of single-slab 3D double inversion-recovery high-spatial-resolution MR imaging.** *Radiology* 2006;241:873–79
- Melhem ER, Jara H, Eustace S. **Fluid-attenuated inversion recovery MR imaging: identification of protein concentration thresholds for CSF hyperintensity.** *AJR Am J Roentgenol* 1997;169:859–62
- Bakshi R, Kamran S, Kinkel PR, et al. **Fluid-attenuated inversion-recovery MR imaging in acute and subacute cerebral intraventricular hemorrhage.** *AJNR Am J Neuroradiol* 1999;20:629–36
- Bakshi R, Caruthers SD, Janardhan V, et al. **Intraventricular CSF pulsation artifact on fast fluid-attenuated inversion-recovery MR images: analysis of 100 consecutive normal studies.** *AJNR Am J Neuroradiol* 2000;21:503–08
- Kallmes DF, Hui FK, Mugler JP 3rd. **Suppression of cerebrospinal fluid and blood flow artifacts in FLAIR MR imaging with a single-slab three-dimensional pulse sequence: initial experience.** *Radiology* 2001;221:251–55

Combining MRI with NIHSS Thresholds to Predict Outcome in Acute Ischemic Stroke: Value for Patient Selection

P.W. Schaefer, B. Pulli, W.A. Copen, J.A. Hirsch, T. Leslie-Mazwi, L.H. Schwamm, O. Wu, R.G. González, and A.J. Yoo



ABSTRACT

BACKGROUND AND PURPOSE: Selecting acute ischemic stroke patients for reperfusion therapy on the basis of a diffusion-perfusion mismatch has not been uniformly proved to predict a beneficial treatment response. In a prior study, we have shown that combining clinical with MR imaging thresholds can predict clinical outcome with high positive predictive value. In this study, we sought to validate this predictive model in a larger patient cohort and evaluate the effects of reperfusion therapy and stroke side.

MATERIALS AND METHODS: One hundred twenty-three consecutive patients with anterior circulation acute ischemic stroke underwent MR imaging within 6 hours of stroke onset. DWI and PWI volumes were measured. Lesion volume and NIHSS score thresholds were used in models predicting good 3-month clinical outcome (mRS 0–2). Patients were stratified by treatment and stroke side.

RESULTS: Receiver operating characteristic analysis demonstrated 95.6% and 100% specificity for DWI > 70 mL and NIHSS score > 20 to predict poor outcome, and 92.7% and 91.3% specificity for PWI (mean transit time) < 50 mL and NIHSS score < 8 to predict good outcome. Combining clinical and imaging thresholds led to an 88.8% (71/80) positive predictive value with a 65.0% (80/123) prognostic yield. One hundred percent specific thresholds for DWI (103 versus 31 mL) and NIHSS score (20 versus 17) to predict poor outcome were significantly higher in treated (intravenous and/or intra-arterial) versus untreated patients. Prognostic yield was lower in right- versus left-sided strokes for all thresholds (10.4%–20.7% versus 16.9%–40.0%). Patients with right-sided strokes had higher 100% specific DWI (103.1 versus 74.8 mL) thresholds for poor outcome, and the positive predictive value was lower.

CONCLUSIONS: Our predictive model is validated in a much larger patient cohort. Outcome may be predicted in up to two-thirds of patients, and thresholds are affected by stroke side and reperfusion therapy.

ABBREVIATIONS: AUC = area under the curve; IA = intra-arterial; PPV = positive predictive value; Tmax = time at which the scaled residue function reached its maximum

Reperfusion therapy improves outcomes of patients with acute ischemic stroke.^{1,2} The decision to treat is primarily determined by the time from symptom onset. Use of IV-rtPA is restricted to the 3-¹ or 4.5-hour² time window, resulting in only 1%–7% of patients receiving IV-rtPA.³ Advanced neuroimaging provides information about a patient's physiology that may be useful to guide treatment

decisions, especially in an extended time window. Selecting patients for reperfusion therapy on the basis of the mismatch between lesions in diffusion-weighted and perfusion images has been proposed,⁴ but this approach has not been uniformly proved to predict a beneficial treatment response.^{5–8} On the basis of findings that patients with DWI infarct volumes of >70 mL have poor outcome regardless of treatment^{9,10} and that the NIHSS score is a strong predictor of outcome,¹¹ we recently published a predictive model that combined DWI and mean transit time lesion volumes with NIHSS score thresholds to predict outcome in patients with anterior circulation acute ischemic stroke.¹² DWI lesion volume > 72 mL or NIHSS score > 20 predicted poor outcome (mRS, 3–6), while MTT lesion volume < 47 mL or NIHSS score < 8 predicted good outcome (mRS, 0–2) with a high positive predictive value (PPV) when used in combination, in two-thirds of patients.

In this study, we sought to validate our predictive model in a larger, independent cohort of patients and investigated the effects of reperfusion therapy and side of involvement on these thresholds.

Received June 27, 2014; accepted after revision July 21.

From the Departments of Radiology (P.W.S., B.P., W.A.C., J.A.H., T.L.-M., O.W., R.G.G., A.J.Y.) and Neurology (L.H.S.), Massachusetts General Hospital, Harvard Medical School, Boston, Massachusetts.

P.W. Schaefer and B. Pulli contributed equally to this work.

Please address correspondence to Pamela W. Schaefer, MD, Department of Radiology, Neuroimaging Division, Massachusetts General Hospital, 55 Fruit St, Boston, MA 02114; e-mail: pschaefer@partners.org

Indicates open access to non-subscribers at www.ajnr.org

Indicates article with supplemental on-line table.

Indicates article with supplemental on-line photo.

<http://dx.doi.org/10.3174/ajnr.A4103>

MATERIALS AND METHODS

Patient Selection and Assessment

We retrospectively examined the clinical and imaging data of consecutive patients with acute ischemic stroke admitted to our comprehensive stroke center. Inclusion criteria were the following: 1) DWI and PWI obtained within 6 hours of the patient being symptom-free, 2) acute MCA stroke, 3) NIHSS score > 2 , and 4) sufficient clinical follow-up to determine the mRS score at 90 days. This study was approved by our institutional review board. Records were maintained in compliance with the Health Insurance Portability and Accountability Act.

We identified 198 patients with acute ischemic stroke who underwent DWI and PWI within 6 hours. Seventy-five were excluded because of the lack of a follow-up mRS score ($n = 28$), posterior circulation infarction ($n = 29$), calculation of perfusion maps with a delay-sensitive deconvolution technique ($n = 9$), or image quality insufficient for analysis ($n = 9$). The remaining 123 patients were included for further analysis. This cohort was independent of the previously published cohort,¹² without overlap. In patients who received IV-tPA, treatment was started within 4.5 hours. In patients who received intra-arterial (IA) therapy, treatment was initiated within 8 hours after symptom onset.

Admission NIHSS score was determined by a stroke neurologist. Clinical outcome was evaluated by using the mRS score 90 days after stroke onset, which was determined by a stroke neurologist in 59 instances (48%) and was retrieved from a neurologic examination in the patient's medical record for the remaining patients. Patient outcomes were dichotomized into good (mRS 0–2) versus poor (mRS 3–6).

Image Acquisition, Postprocessing, and Analysis

MR imaging was performed on a 1.5T Signa scanner (GE Healthcare, Milwaukee, Wisconsin). DWI was performed with a single-shot echo-planar spin-echo sequence with two 180° radiofrequency pulses. Three images per section were acquired at $b=0$ s/mm², followed by 25 at $b=1000$ s/mm². Imaging parameters were TR/TE, 5000/80–110 ms; FOV, 22-cm; matrix, 128 × 128 zero-filled to 256 × 256; 5-mm thickness; 1-mm gap.

PWI was performed by using a dynamic-susceptibility technique. Serial echo-planar gradient-echo images were acquired with TR/TE, 1500/40 ms; FOV, 22 cm; matrix, 128 × 128; section thickness, 5 mm with a 1-mm gap. Twenty milliliters of gadopentetate dimeglumine, 0.5 mmol/mL (Bayer HealthCare Pharmaceuticals, Wayne, New Jersey), was injected intravenously at 5 mL/s, beginning 10 seconds after scanning started, followed by 20 mL of normal saline.

PWI data were processed by using locally written, automated software. Signal-versus-time curves for each pixel were converted to Δ -R2-versus-time curves. CBV was calculated by integrating the area under these curves; CBF, as the amplitude of the scaled residue function yielded by delay-insensitive singular-value deconvolution¹³; Tmax, as the time at which the scaled residue function reached its maximum; and MTT, as CBV/CBF.

For quantitative measurement, visually detected DWI and MTT abnormalities were segmented in randomized order by 2 experienced neuroradiologists blinded to clinical information by using a semiautomated commercial analysis program (Analyze, Version 7.0; (AnalyzeDirect, Overland Park, Kansas). Tmax maps

were thresholded to 6 seconds. Absolute mismatch was defined as MTT – DWI; percentage mismatch, as (MTT – DWI) / DWI × 100%.

Statistical Analysis

Statistical analysis was performed by using MedCalc for Windows, Version 11.2.1 (MedCalc Software, Mariakerke, Belgium). *P* values $< .05$ were considered significant. Clinical and imaging data were compared by using the Student *t* test or Mann-Whitney *U* test, and categorical data, by using the χ^2 test. Receiver operating characteristic curves were calculated for DWI, MTT, Tmax, and the NIHSS score relative to clinical outcome. Areas under the curve (AUCs) were compared and stratified by reperfusion therapy and stroke side. Prognostic yield was defined as the proportion of patients fulfilling at least 1 threshold criterion.

RESULTS

Baseline Clinical and Imaging Characteristics, Treatment, Outcomes, and Predictors of 3-Month mRS

Sixty-eight patients (55.3%) had good clinical outcome 90 days after stroke onset (Table 1). There were no significant differences in age, sex, right-hemisphere involvement, relative mismatch volume, or time from symptom onset to MR imaging between patients with good-versus-poor outcome. Median admission NIHSS score was significantly higher (16 versus 7, $P < .0001$), and mean DWI, MTT, Tmax, and absolute mismatch volumes were significantly larger (63.4 versus 16.3, 189.9 versus 80.6, 217.3 versus 89.5, and 127.1 versus 64.9 mL, respectively; all $P < .0001$) in patients with poor outcome. More patients with poor outcome than with good outcome had proximal occlusions (ICA or MCA M1) versus MCA M2/M3 or no identifiable occlusion ($P < .0001$). Sixty-one patients (49.6%) received IV-tPA, and 25 (20.3%) received IA thrombolysis. Thirty-seven (30.1%) patients did not receive IV or IA therapy.

Validation of the Previously Described Combined Thresholds to Predict Outcome in Acute Ischemic Stroke

When applying the previously reported thresholds of DWI > 70 mL or NIHSS score > 20 to predict poor outcome and MTT < 50 mL or NIHSS score < 8 to predict good outcome to our patient cohort, we found the following: Combining DWI with MTT (or Tmax) led to 88.3% (or 87.9%) PPV, with 48.8% (or 47.2%) prognostic yield (Table 2). For NIHSS score < 8 or > 20 , the PPV was 94.3% with a 43.1% yield. Combining the NIHSS score with imaging thresholds improved prognostic yield to 65.0%, higher than that for NIHSS or DWI and MTT alone ($P < .01$), with a high PPV (88.8%, 71/80 patients). Figure 1 shows scatterplots of all patients dichotomized into good-versus-poor outcome for the different thresholds. Receiver operating characteristic analysis revealed 95.6% (87.6%–99.1%) specificity and 36.4% (23.8%–50.4%) sensitivity to predict poor outcome for DWI volume > 70 mL. For MTT volume < 50 mL, 92.7% (82.4%–98.0%) specificity and 50.0% (37.6%–62.4%) sensitivity to predict good outcome were found. For Tmax volume < 50 mL, 92.7% (82.4%–98.0%) specificity and 46.2% (33.7%–59.0%) sensitivity to predict good outcome were found. AUCs were

Table 1: Baseline clinical and imaging characteristics, treatment, and predictors of 3-month mRS

	All Patients (n = 123)	mRS 0–2 (n = 68)	mRS 3–6 (n = 55)	P Value
Age (yr)	69.8 ± 15.9	68.9 ± 16.9	70.8 ± 14.7	.727 ^a
Baseline NIHSS score	11 (6–16)	7 (5–11.5)	16 (14–20.75)	<.0001 ^a
Female sex	55 (44.7%)	31 (45.6%)	24 (43.6%)	.973 ^b
Right hemisphere	74 (47.2%)	34 (50.0%)	24 (43.6%)	.602 ^b
Time to MRI	3:57 ± 1:26	3:45 ± 1:29	4:12 ± 1:20	.085 ^c
DWI volume (mL)	37.4 ± 47.7	16.3 ± 20.1	63.4 ± 58.2	<.0001 ^a
MTT volume (mL)	129.5 ± 101.3	80.6 ± 78.3	189.9 ± 94.1	<.0001 ^a
Tmax volume (mL)	148.1 ± 114.9	89.5 ± 86.5	217.3 ± 106.0	<.0001 ^a
Absolute mismatch (mL)	92.7 ± 81.4	64.9 ± 69.1	127.1 ± 82.9	<.0001 ^a
Relative mismatch	8.7 ± 21.6	10.9 ± 27.8	6.0 ± 8.8	.541 ^a
Reperfusion therapy	None: 37 (30.1%) IV-tPA: 61 (49.6%) IAT ± IV-tPA: 25 (20.3%)	22 (32.4%) 36 (52.9%) 10 (14.7%)	15 (25.4%) 25 (45.5%) 15 (27.3%)	.200 ^b
Occlusion level	ICA: 24 (19.5%) MCA M1: 39 (31.7%) MCA M2/3: 36 (29.3%) None: 24 (19.5%)	6 (8.8%) 15 (22.1%) 24 (35.3%) 23 (33.8%)	18 (32.7%) 24 (43.6%) 12 (21.8%) 1 (1.8%)	<.0001 ^b

Note:—IAT indicates intra-arterial thrombolysis.

^a Mann-Whitney U test.

^b χ^2 test.

^c Student t test.

Table 2: Validation of the previously described model combining clinical and imaging thresholds to predict outcome in acute ischemic stroke

Threshold	Positive Predictive Value (%)	Prognostic Yield (%)
Poor outcome		
DWI > 70 mL	86.4 ^a	17.9
NIHSS score > 20	100.0 ^a	11.4
Good outcome		
MTT < 0 mL	89.5 ^a	30.9
Tmax < 50 mL	88.9 ^a	29.3
NIHSS score < 8	92.3 ^a	31.7
Combined clinical thresholds (NIHSS score)	94.3 ^a	43.1
Combined imaging thresholds (DWI + MTT)	88.3 ^a	48.8
Combined imaging thresholds (DWI + Tmax > 6 seconds)	87.9 ^a	47.2
Combined clinical and imaging thresholds	88.8 ^a	65.0 ^b

^a No significant difference in PPV between any of the applied thresholds.

^b Significantly increased over use of single parameters ($P < .0001$) and combined clinical or imaging thresholds ($P = .01$).

0.802 ± 0.04 for DWI, 0.816 ± 0.039 for MTT, and 0.819 ± 0.039 for Tmax (all $P < .0001$).

Intravenous or Intra-Arterial Reperfusion Therapy Affects Clinical and Imaging Thresholds

Stratification by reperfusion therapy (no IV/IA therapy versus IV-tPA alone or IA recanalization ± preceding IV-tPA) resulted in similar NIHSS scores (11.0 ± 7.9 versus 12.5 ± 5.8, $P = .23$) as well as DWI (44.5 ± 55.0 versus 35.1 ± 44.4 mL, $P = .70$), MTT (110.3 ± 101.8 versus 137.8 ± 100.6 mL, $P = .17$), and Tmax mean lesion volumes (125.0 ± 108.2 versus 157.6 ± 116.9 mL, $P = .16$). However, significant differences in receiver operating characteristic curves and DWI and NIHSS score thresholds for poor outcome were found. Setting specificity to 95% resulted in optimal thresholds of >74.8 mL for DWI and >19 for the NIHSS score. For untreated patients, optimal thresholds were lower: >20.5 mL for DWI and >15 for the NIHSS score. The AUC was greater for DWI in untreated-versus-treated patients (0.935 versus 0.724, $P = .011$). Prognostic yield using DWI was higher

for untreated-versus-treated patients (42.3%–35.1% versus 19.5%–10.4%, Table 3). The mean DWI volume was lower in untreated-versus-treated patients with good outcome (9.2 ± 1.7 versus 19.8 ± 3.4 mL, $P = .033$), and the median NIHSS score (5 versus 9.5, $P = .004$, Fig 2A) was also lower. Probability plots for poor outcome based on logistic regression show a flatter curve for treated patients, which plateaus at approximately 100-mL DWI infarct volume. In contrast, the curve plateaus at approximately 50 mL for untreated patients (Fig 2B).

Side of Involvement Affects Clinical and Imaging Thresholds

The DWI threshold set at 95% specificity for poor outcome was lower with left-sided (>51.8 mL) than right-sided strokes (>98.5 mL), and NIHSS score thresholds were higher (<9 or >20 versus <5 or >16) when the left hemisphere was affected. Prognostic yield was higher with strokes involving the left side: For DWI, the yield was 40.0%–16.9% versus 20.7%–10.4%, and for NIHSS score, the yield was 66.2%–38.5% versus 29.3%–1.7% (Table 4). Furthermore, the AUC was higher for DWI with left-sided strokes (0.875 versus 0.706, $P = .043$), and there was a trend toward a higher AUC with the NIHSS score (0.911 versus 0.808, $P = .077$). The mean DWI volume in patients with good outcome was smaller in left- versus right-sided strokes (Fig 3A). A probability plot for poor outcome demonstrates better predictability for left-sided strokes (Fig 3B). Scatter-

plots for good-versus-poor outcome show that with left-sided strokes, no patient with an NIHSS score of >20 (or <8) had good (or poor) outcome, while for right-sided strokes, no patients with NIHSS scores of >17 had good outcome, and some patients with NIHSS scores of <8 had poor outcome (Fig 3B). PPV of our model was 97.4% for left-sided strokes, and 82.1% for right-sided strokes ($P = .028$).

Patients in Whom Imaging or Clinical Thresholds Predicted Clinical Outcome Incorrectly

Three patients had poor outcomes despite an admission NIHSS score of <8. All 3 had right-sided MCA strokes, and 2 had critical ICA stenoses with substantial infarct growth after initial evaluation (On-line Table and On-line Figure, patient 3). Three patients had MTT abnormalities of <50 mL, but poor outcome. All 3 had significant comorbidities and/or complicated recoveries. Also, patient 5 (On-line Figure) had an infarct in the precentral gyrus, a highly eloquent region strongly represented on the mRS score. Three patients had DWI abnormalities of >70 mL but

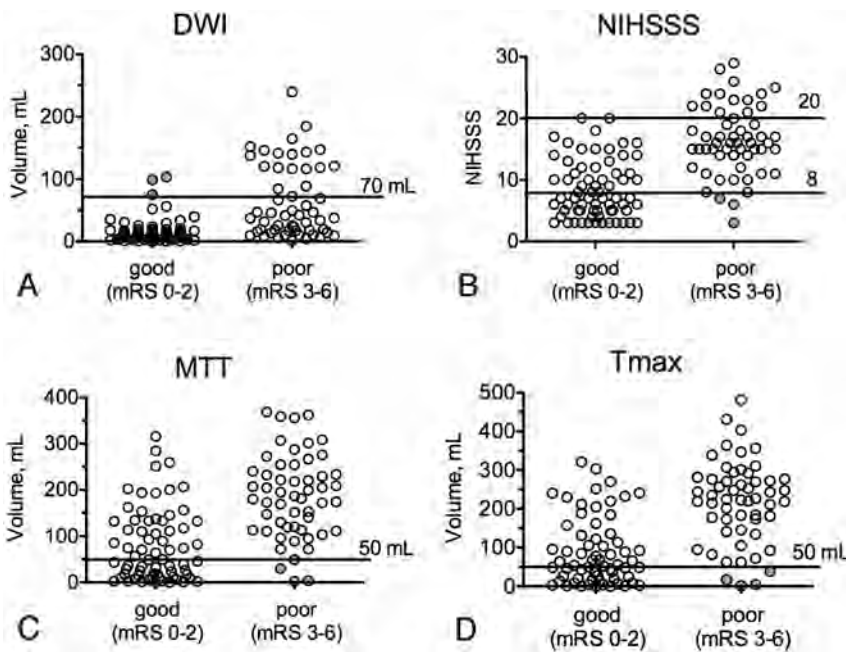


FIG 1. Baseline imaging volumes and NIHSS scores of patients with good (mRS 0–2) and poor (mRS 3–6) clinical outcome at 90 days after stroke. Horizontal lines indicate the thresholds used to predict outcome with DWI (A) (>70 mL MTT predicts poor outcome), NIHSS score (B) (<8 or >20 predicts good or poor outcome, respectively), MTT (C) (<50 mL predicts good outcome), and Tmax (D) (<50 mL predicts good outcome). The filled circles mark patients for whom prediction was incorrect.

Table 3: Differences of clinical and imaging thresholds in patients receiving thrombolysis versus untreated patients

	No Reperfusion Therapy	IV and/or IA Therapy	P Value
DWI			
AUC ± SE for predicting poor outcome	0.935 ± 0.06	0.724 ± 0.05	.011
90% Specificity for poor outcome (prognostic yield) (mL)	>19.7 (42.3%)	>51.8 (19.5%)	.016 ^a
95% Specificity for poor outcome (prognostic yield) (mL)	>20.5 (40.5%)	>74.8 (16.1%)	.007 ^a
	>30.6 (35.1%)	>103.1 (10.4%)	.003 ^a
NIHSS score			
AUC ± SE for predicting poor outcome	0.903 ± 0.06	0.827 ± 0.04	.314
90% Specificity for poor outcome (prognostic yield)	>12 (37.8%)	>16 (23.0%)	.142 ^a
95% Specificity for poor outcome (prognostic yield)	>15 (27.0%)	>19 (14.9%)	.182 ^a
100% Specificity for poor outcome (prognostic yield)	>17 (16.2%)	>20 (9.2%)	.414 ^a

^a P value for comparison among prognostic yields.

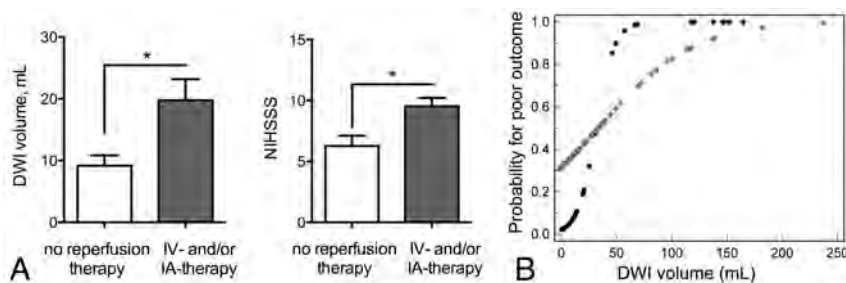


FIG 2. Baseline infarct volumes, clinical status, and probability for poor outcome in treated-versus-untreated patients. A, Mean DWI volume (left) and NIHSS score (right) in patients with good outcome stratified by treatment; asterisks indicate a significant difference. B, Probability (determined by logistic regression) for poor outcome versus DWI plots between untreated and treated patients (black circles represent untreated; gray circles, treated).

good outcome. These were relatively young patients (26–45 years of age) who all underwent reperfusion therapy (two-thirds had received IA thrombolysis and had uncomplicated

recoveries without significant infarct extension). Two also had right-sided strokes.

DISCUSSION

We have validated our previously described predictive thresholds of DWI > 70 mL or NIHSS > 20 for poor outcome of patients with acute ischemic stroke and of MTT < 50 mL or NIHSS score < 8 for good outcome, with a high PPV in this much larger, entirely independent cohort. In the 65% of patients who met at least 1 of these criteria, outcome was predictable with an 89% PPV. Indeed, we identified only 9 of 123 patients in whom an imaging or clinical threshold predicted clinical outcome incorrectly. Furthermore, we extended our previous results by comparing treated (with IV or IA therapy) versus untreated patients and by comparing right- versus left-sided strokes.

Factors involved in patient selection for reperfusion therapy are nuanced and are currently based on the time from onset and neurologic deficit. Advanced imaging may help to further refine these parameters and more appropriately select patients for intervention. Currently, the most frequently proposed advanced MR imaging method to select patients for intravenous reperfusion therapy is the mismatch between DWI and certain PWI lesion sizes.⁴ Although some evidence supports this strategy,^{14,15} it has not conclusively predicted a favorable treatment response.^{5–8} In addition, relative mismatch measurements fail to account for the absolute sizes of the infarct core and abnormally perfused areas.⁷ In the Echoplanar Imaging Thrombolytic Evaluation Trial (EPITHET), absolute Tmax and DWI lesion volumes influenced the response to reperfusion, but relative mismatch did not.¹⁶ Finally, DWI/PWI mismatch does not reflect the patient's clinical status. Clinical status, as measured by the NIHSS score, is an important independent predictor of outcome¹¹ and neurologic worsening.¹⁷ In general, in our predictive model, patients with DWI lesions of >70 mL or an NIHSS score of >20 have a high likelihood of poor outcome, and reperfusion therapy in these patients may offer minimal or no clinical

benefit. Patients with MTT lesions of <50 mL or an NIHSS score of <8 have a high likelihood of good outcome. Aggressive treatments may unnecessarily expose this group to the risks of invasive

Table 4: Differences of clinical and imaging thresholds in patients stratified by affected cerebral hemisphere

	Right Side	Left Side	P Value
DWI			
AUC ± SE	0.706 ± 0.07	0.875 ± 0.04	.043
90% Specificity for poor outcome (prognostic yield) (mL)	>39.6 (20.7%)	>23.4 (40.0%)	.034 ^a
95% Specificity for poor outcome (prognostic yield) (mL)	>98.5 (12.1%)	>51.8 (26.2%)	.082 ^a
100% Specificity for poor outcome (prognostic yield) (mL)	>103.1 (10.4%)	>74.8 (16.9%)	.435 ^a
NIHSS score			
AUC ± SE	0.808 ± 0.06	0.911 ± 0.03	.077
90% Specificity for poor or good outcome (prognostic yield)	>15 or <6 (29.3%)	>17 or <10 (66.2%)	<.001 ^a
95% Specificity for poor or good outcome (prognostic yield)	>16 or <5 (17.2%)	>20 or <9 (49.2%)	<.001 ^a
100% Specificity for poor or good outcome (prognostic yield)	>16 or <3 (1.7%)	>20 or <7 (38.5%)	<.001 ^a

^a P value for comparison between prognostic yields.

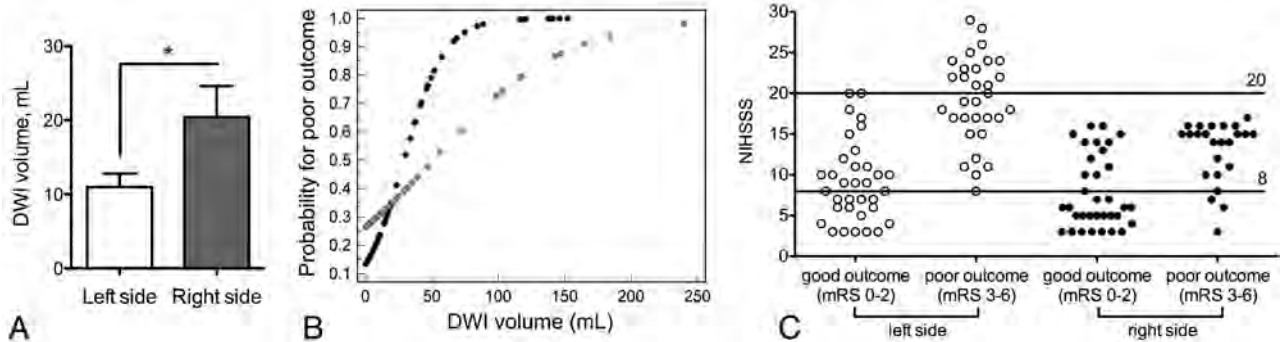


FIG 3. Baseline infarct volumes, probability for poor outcome, and NIHSS score thresholds in left- versus right-sided strokes. *A*, Mean DWI volume in patients with good outcome stratified by side of involvement. Asterisks indicate a significant difference. *B*, Probability (determined by logistic regression) for poor outcome versus DWI plots between left- and right-sided strokes (left = black circles, right = gray circles). *C*, NIHSS score scatterplots and thresholds stratified by side of involvement.

reperfusion therapy. The outcomes of the remaining 35% of patients, those with DWI volume of <70 mL, MTT volume of >50 mL, and an NIHSS score of >8 and <20, could not be predicted accurately by initial clinical and imaging assessments; this finding suggests that these patients may represent a group toward whom early invasive therapy may be directed.

We hypothesized that patients who received IV thrombolytic and/or IA recanalization therapy would have higher DWI and NIHSS score thresholds for poor outcome than untreated patients. Indeed, the 100% specific DWI threshold for poor outcome was 103 mL in treated compared with 31 mL in untreated patients, and the 100% specific NIHSS score thresholds were similarly 20 versus 17, respectively, suggesting that treated patients may tolerate larger baseline infarcts. This suggestion is also supported by significantly larger DWI lesions and higher NIHSS scores in treated-versus-untreated patients with good outcome. An explanation for this finding might be that in patients treated with reperfusion therapy, infarcts grow less than in untreated patients. When predicting good outcome with the NIHSS score, MTT, or Tmax, we did not find conclusive evidence for differences by treatment. We did not further stratify patients by different treatment strategies and recanalization status (eg, IV-versus-IA thrombolysis) because recanalization status was unknown in the 61 patients treated with IV therapy only and our sample size was too small.

Because the dominant (usually left) hemisphere has important functions represented in the mRS, we hypothesized that patients with right-sided strokes would tolerate larger DWI lesions and that our model would be less accurate. Indeed, the AUCs were significantly higher for DWI (0.88 versus 0.71, $P = .04$) with left-

sided strokes. The difference in AUC for the NIHSS score in left-versus right-sided strokes also approached significance (0.91 versus 0.81, $P = .08$). Moreover, patients with right-sided strokes could tolerate larger DWI lesions (100% specific DWI volume for poor outcome = 103 versus 75 mL), and on average, patients with right-sided strokes and good outcome had significantly larger DWI lesions (20 versus 10 mL, $P < .05$). No patient with an infarct affecting the right hemisphere had an NIHSS score of >17, making outcome prediction in these patients less reliable.

In the 9 patients for whom the above clinical or imaging thresholds predicted outcome incorrectly, we identified 4 scenarios: 1) Young patients undergoing reperfusion may do well with DWI lesion volumes of >70 mL, in accordance with studies suggesting better outcome in patients younger than 40 years of age.¹⁸ 2) Factors delaying rehabilitation or causing infarct growth, such as comorbidities, complicated recovery, and irregular clinical course, might lead to poor outcome despite MTT lesion volumes of <50 mL. 3) Infarcts in areas affecting functions highly represented in the mRS score (eg, motor function in the precentral gyrus) may result in poor outcome despite small MTT lesion volumes. This possibility is underscored by a recent study, in which infarct location on MR imaging correlated highly with outcome.¹⁹ 4) NIHSS score and mRS are strongly biased toward dominant (usually left) hemisphere functions. All patients with false prediction based on an NIHSS score of <8 had right-sided infarcts, and two-thirds of patients with infarct volumes of >70 mL and good outcome had right-sided strokes. The challenges to prediction represented by these variables are important to keep in mind when evaluating patients for therapy.

The limitations of our investigation are the consequences of the retrospective design and have been described elsewhere.¹² Briefly, we could not obtain data such as reperfusion status, final infarct volumes, and clinical status at day 30 for most patients. There were variable treatments and variable times from stroke onset to imaging and from imaging to follow-up clinical assessment. Potential selection bias was related to using MR imaging, the decision to offer thrombolysis, and our technical approach to performing IA therapy. While assessment of Tmax maps was based on a 6-second threshold, DWI and MTT lesions were outlined by visual estimation. Thresholds have been proposed to increase reliability, but most studies demonstrating a clinical benefit from perfusion imaging–based patient selection have used visual estimation.^{14,15} No thresholding software is universally accepted, and our data suggest that both methods can be used in our model with similar yield and PPV. Finally, our method for measuring DWI and PWI lesion volumes is too time-consuming for routine clinical use. The faster ABC/2 volume estimation method based on 3 orthogonal measurements, easily obtained on an MR imaging scanner console, could be a feasible substitute.²⁰

CONCLUSIONS

The previously proposed predictive model combining DWI, MTT, and NIHSS score thresholds is validated in a much larger patient cohort. For acute ischemic stroke, thresholds applied to acute DWI and MTT lesion volumes and NIHSS scores can be used to predict good and poor clinical outcomes with a high PPV. Our prediction model shows higher PPV in left-sided strokes. Younger patients, those treated with IV and/or IA therapy, and those with right-sided strokes may have good outcomes despite larger DWI infarcts. Those treated with reperfusion therapy may also tolerate a higher NIHSS score. These variables, alone and in combination, may help guide decisions related to patient selection for therapy. Patients who do not meet these thresholds have variable outcomes and may represent a target population for more aggressive revascularization approaches.

Disclosures: Joshua A. Hirsch—UNRELATED: Consultancy: CareFusion, Comments: In >24 months and <36 months, I received compensation related to vertebral augmentation; Royalties: CareFusion (as above); Stock/Stock Options: Intratech, Comments: development-stage company for interventional stroke products. Lee H. Schwamm—UNRELATED: Consultancy: Lundbeck, Comments: Member of data safety monitoring board for Desmoteplase In Acute Ischemic Stroke trial three-fourths trials of desmoteplase; Grants/Grants Pending: National Institute of Neurological Disorders and Stroke/Genentech,* Comments: Genentech provides drugs free of charge and some supplemental site payments for the MR WITNESS trial of extended window thrombolysis (Dr Schwamm is the Principal Investigator). Ona Wu—RELATED: Grant: National Institutes of Health,* Comments: R01NS059775, R01NS063925, P50NS051343, P41EB015896; UNRELATED: Consultancy: Penumbra, Comments: provided consultancy regarding digital imaging and communications in medicine servers and clients; Grants/Grants Pending: Genentech,* Comments: Genentech has provided funds to MR WITNESS to help per-subject reimbursement for each site; OTHER RELATIONSHIPS: I have a patent on "Delay-Compensated Calculation of Tissue Blood Flow," US Patent 7,512,435, March 31, 2009, and the patent has been licensed to GE Healthcare, Siemens, Imaging Biometric, and Olea Medical. Albert J. Yoo—UNRELATED: Grants/Grants Pending: Penumbra,* Comments: core imaging lab.* Money paid to the institution.

REFERENCES

1. Tissue plasminogen activator for acute ischemic stroke: the National Institute of Neurological Disorders and Stroke rt-PA Stroke Study Group. *N Engl J Med* 1995;333:1581–87
2. Hacke W, Kaste M, Bluhmki E, et al. Thrombolysis with alteplase 3 to 4.5 hours after acute ischemic stroke. *N Engl J Med* 2008;359:1317–29
3. Cocho D, Belvis R, Marti-Fabregas J, et al. Reasons for exclusion from thrombolytic therapy following acute ischemic stroke. *Neurology* 2005;64:719–20
4. Schlaug G, Benfield A, Baird AE, et al. The ischemic penumbra: operationally defined by diffusion and perfusion MRI. *Neurology* 1999;53:1528–37
5. Davis SM, Donnan GA, Parsons MW, et al. Effects of alteplase beyond 3 h after stroke in the Echoplanar Imaging Thrombolytic Evaluation Trial (EPITHET): a placebo-controlled randomised trial. *Lancet Neurol* 2008;7:299–309
6. Mishra NK, Albers GW, Davis SM, et al. Mismatch-based delayed thrombolysis: a meta-analysis. *Stroke* 2010;41:e25–33
7. Hacke W, Furlan AJ, Al-Rawi Y, et al. Intravenous desmoteplase in patients with acute ischaemic stroke selected by MRI perfusion-diffusion weighted imaging or perfusion CT (DIAS-2): a prospective, randomised, double-blind, placebo-controlled study. *Lancet Neurol* 2009;8:141–50
8. Kidwell CS, Jahan R, Gornbein J, et al. A trial of imaging selection and endovascular treatment for ischemic stroke. *N Engl J Med* 2013;368:914–23
9. Sanak D, Nosal V, Horak D, et al. Impact of diffusion-weighted MRI-measured initial cerebral infarction volume on clinical outcome in acute stroke patients with middle cerebral artery occlusion treated by thrombolysis. *Neuroradiology* 2006;48:632–39
10. Yoo AJ, Verduzco LA, Schaefer PW, et al. MRI-based selection for intra-arterial stroke therapy: value of pretreatment diffusion-weighted imaging lesion volume in selecting patients with acute stroke who will benefit from early recanalization. *Stroke* 2009;40:2046–54
11. Sato S, Toyoda K, Uehara T, et al. Baseline NIH Stroke Scale score predicting outcome in anterior and posterior circulation strokes. *Neurology* 2008;70:2371–77
12. Yoo AJ, Barak ER, Copen WA, et al. Combining acute diffusion-weighted imaging and mean transit time lesion volumes with National Institutes of Health Stroke Scale score improves the prediction of acute stroke outcome. *Stroke* 2010;41:1728–35
13. Wu O, Østergaard L, Weisskoff RM, et al. Tracer arrival timing-insensitive technique for estimating flow in MR perfusion-weighted imaging using singular value decomposition with a block-circulant deconvolution matrix. *Magn Reson Med* 2003;50:164–74
14. Furlan AJ, Eyding D, Albers GW, et al. Dose Escalation of Desmoteplase for Acute Ischemic Stroke (DEDAS): evidence of safety and efficacy 3 to 9 hours after stroke onset. *Stroke* 2006;37:1227–31
15. Hacke W, Albers G, Al-Rawi Y, et al. The Desmoteplase in Acute Ischemic Stroke Trial (DIAS): a phase II MRI-based 9-hour window acute stroke thrombolysis trial with intravenous desmoteplase. *Stroke* 2005;36:66–73
16. Parsons MW, Christensen S, McElduff P, et al. Pretreatment diffusion- and perfusion-MR lesion volumes have a crucial influence on clinical response to stroke thrombolysis. *J Cereb Blood Flow Metab* 2010;30:1214–25
17. DeGraba TJ, Hallenbeck JM, Pettigrew KD, et al. Progression in acute stroke: value of the initial NIH stroke scale score on patient stratification in future trials. *Stroke* 1999;30:1208–12
18. Galdiks N, Zaro-Weber O, Dohmen C, et al. Systemic thrombolysis with rt-PA in patients under 40 years of age: a subgroup analysis of the Cologne Stroke Experience. *Cerebrovasc Dis* 2010;30:514–18
19. Phan TG, Chen J, Donnan G, et al. Development of a new tool to correlate stroke outcome with infarct topography: a proof-of-concept study. *Neuroimage* 2010;49:127–33
20. Sims JR, Gharai LR, Schaefer PW, et al. ABC/2 for rapid clinical estimate of infarct, perfusion, and mismatch volumes. *Neurology* 2009;72:2104–10

Diagnostic Yield of Emergency Department Arch-to-Vertex CT Angiography in Patients with Suspected Acute Stroke

A.R. Deipolyi, L.M. Hamberg, R.G. Gonzaléz, J.A. Hirsch, and G.J. Hunter

ABSTRACT

BACKGROUND AND PURPOSE: Our aim was to investigate how often relevant diagnostic findings in an arch-to-vertex CTA scan, obtained specifically as part of the acute stroke CT protocol, are located in the head, neck, and upper chest regions.

MATERIALS AND METHODS: Radiology reports were reviewed in 302 consecutive patients (170 men, 132 women; median ages, 66 and 73 years, respectively) who underwent emergency department investigation of suspected acute stroke between January and July 2010. Diagnostic CTA findings relevant to patient management were recorded for the head, neck, and chest regions individually. Additionally, the contributions to the total CTA scan effective dose were estimated from each of the 3 anatomic regions by using the ImPACT CT Dose Calculator.

RESULTS: Of the 302 patients, 161 (54%) had relevant diagnostic findings in the head; 94 (31%), in the neck; and 4 (1%), in the chest. The estimated contributions to the total CTA scan dose from each body region, head, neck, and upper chest, were $14 \pm 2\%$, $33 \pm 5\%$, and $53 \pm 6\%$, respectively.

CONCLUSIONS: Most clinically relevant findings are in the head and neck, supporting inclusion of these regions in arch-to-vertex CTA performed specifically in patients with acute stroke in the emergency department. Further studies are required to investigate extending the scan to the upper chest because only 1% of patients in our study had clinically relevant findings in the mediastinum, yet half the CTA effective dose was due to scanning in this region.

In the evaluation of patients presenting to the emergency department within 4.5 hours of the onset of acute stroke or stroke-like symptoms, emphasis is placed on the immediate identification of inclusion and exclusion criteria for the administration of intravenous thrombolytic therapy.¹⁻⁶ Subsequent investigation of risk factors for stroke is an elective process and typically does not begin until after the acute event has passed.⁷⁻⁹

With improvement in CT technology, the limitations on scan coverage of neurovascular CTA have relaxed, and single-pass imaging from the aortic arch to the skull vertex has become commonplace.¹⁰⁻¹⁵ Nevertheless, we have found no studies that evaluated benefit to the patient from this practice. Furthermore, current guidelines for the emergency management of patients

with acute stroke remain focused on noncontrast head CT and CTA evaluation only of the intracranial circulation.^{1,16-17}

Our primary purpose was to investigate the incidence of diagnostically relevant findings reported in the head, neck, and chest components of an arch-to-vertex CTA performed in the emergency department as part of the immediate evaluation and triage of acute stroke. A secondary aim was to estimate the individual contributions to the total effective dose in these regions.

MATERIALS AND METHODS

Patient Population and Clinical Findings

This retrospective study was approved by our institutional review body, waiving consent in accordance with the Health Insurance Portability and Accountability Act. Included in the study were adult patients with signs and symptoms of acute stroke who presented to the emergency department between January 1 and July 31, 2010, and who underwent acute stroke CT imaging as part of their emergency diagnostic evaluation. There were no exclusion criteria. From the electronic medical record, age, weight, sex, NIHSS score at the time of presentation in the

Received April 23, 2014; accepted after revision August 5.

From the Department of Radiology (A.R.D., R.G.G., J.A.H., G.J.H.), Massachusetts General Hospital, Boston, Massachusetts; and Department of Radiology (L.M.H.), Brigham and Women's Hospital, Boston, Massachusetts.

Please address correspondence to George J. Hunter, MD, PhD, Department of Radiology, Massachusetts General Hospital, 55 Fruit St, Boston, MA 02114; e-mail: gjhunter@partners.org

<http://dx.doi.org/10.3174/ajnr.A4112>

emergency department, and the treatment received were recorded for each patient.

All patients were included in the determination of the diagnostic information from individual regions of the CTA. The radiology reports were reviewed, and the presence and number of relevant diagnostic findings in the head, neck, and chest portions of the CTA scan were identified. Relevant diagnostic findings were defined as follows: 1) in the head, any vascular pathology affecting the intracranial circulation, for example, >50% vessel stenosis, occlusion or partial occlusion of major vessels, loss of gray-white differentiation in a vascular territory, aneurysm, tumor, or hemorrhage; 2) in the neck, >50% stenosis of the common or internal carotid arteries, >70% stenosis of the vertebral arteries, or dissection of any vessel; and 3) in the chest, thrombus, dissection, or aneurysm of the aorta >5 cm. If there was uncertainty about the meaning of a report, joint review of both the report and the images was undertaken to resolve it. For the purposes of stenosis categorization, NASCET criteria were used.¹⁸

CTA Imaging

CTA scanning was performed as part of the acute stroke CT protocol on either a 64- or 16-section multidetector row CT scanner (LightSpeed VCT and LightSpeed Pro16; GE Healthcare, Milwaukee, Wisconsin). For the CTA, a single axial scan was acquired through the aortic root and a region of interest was placed in the ascending aorta for use with SmartPrep software (GE Healthcare), a manufacturer-specific bolus-tracking method that allows consistent timing of CTA imaging with respect to an individual patient's contrast hemodynamics. Contrast material (iopamidol, Isovue 370; Bracco Diagnostics, Princeton, New Jersey) was injected in 2 phases: first, 60 mL at 4 mL/s, immediately followed by 15 mL at 2 mL/s, followed by a 40-mL saline chase. The change in Hounsfield unit number in the aortic region of interest was monitored during injection; CTA imaging was triggered 10 seconds after this change exceeded 75 Hounsfield units. On the 64-section scanner, the scanning parameters for CTA were the following: 120 kV(peak) x-ray tube voltage, automatic tube-current modulation, 32-cm scan FOV, 64 × 0.625 mm detector configuration, 0.5-second gantry rotation time, a 0.52 pitch factor, and 40-mm beam width. On the 16-section scanner, the CTA scanning parameters were the following: either 120 or 140 kVp x-ray tube voltage, automatic tube current modulation, 25-cm scan FOV, 16 × 0.625 mm detector configuration, 0.5-second gantry rotation time, 0.94 pitch factor, and 10-mm beam width. For all protocols, 1.25-mm images were reconstructed at 0.625-mm intervals by using a 512 × 512 image matrix and the manufacturer's standard reconstruction kernel.

Effective Dose Estimation

Effective dose contributions for each protocol were estimated by using the ImpACT CT Patient Dosimetry Calculator (ImpACT, London, United Kingdom).¹⁹⁻²⁰ This software uses a mathematic, anthropomorphic phantom to represent an average-sized, 70-kg reference adult. If used for effective dose estimation in smaller patients, the software underestimates the

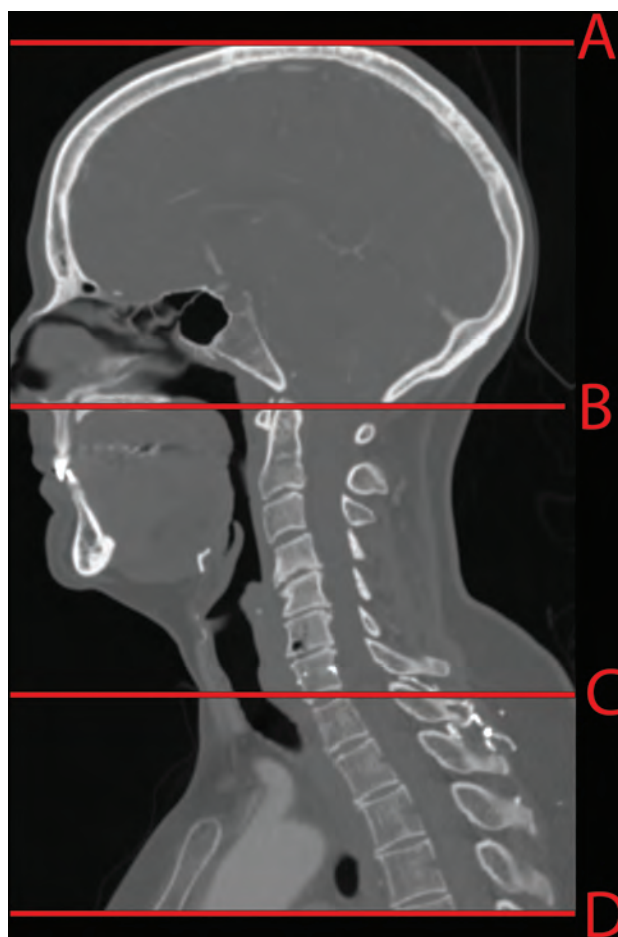


FIGURE. Template for the anatomic landmarks used to determine the head, neck, and chest regions. The red horizontal lines on the sagittal reformat demonstrate the location of the 4 landmarks used: the skull vertex (A), the top of the C1 arch (B), the bottom of the C7 vertebra (C), and the most inferior section scanned (D). The head region was defined as between A and B; the neck region, between B and C; and the chest region, between C and D.

effective dose, and in larger patients, it overestimates it. Thus, only those patients in our cohort with weights within 10 kg of the reference adult (60–80 kg) were included in the effective dose analysis.

Because all 3 CTA protocols had the tube current modulation option turned on, an average milliamperage value used for the head, neck, and upper chest region was determined for the patients studied. This was facilitated by writing custom software (Visual Studio 2010; Microsoft, Redmond, Washington) that obtained the milliamperage values for each section within a CTA series, together with their corresponding section location coordinates from the DICOM headers. From these data, a milliamperage value was individually determined for each body region for all patients.

The body regions were determined by using anatomic landmarks. The head region was counted from the skull vertex to the top of the C1 ring; the neck region was taken from the top of the dens to the bottom of the C7 vertebra; and the chest region, from the bottom of C7 to the lowest level scanned (Figure). The start and end locations for each body region were recorded on our institutional PACS system (Impax 5.3; Agfa-Gevaert, Mortsel,

Belgium) as the section location coordinates marking the relevant body region boundaries.

Descriptive and comparative statistics and significance testing (unpaired Student *t* test) were performed by using Excel 2010 (Microsoft).

RESULTS

Of the 302 patients identified in the study period, there were 170 men (mean age, 65 years; median age, 66 years; range, 19–90 years) and 132 women (mean age, 69 years; median age, 73 years; range, 23–100 years). Weight measurements were available in 267 patients (88%, 267/302) with a mean of 82 ± 19 kg. There were 111 patients weighing 60–80 kg (42%, 111/267), with a mean of 71 ± 6 kg. Data for these patients were used for estimation of effective dose contributions.

In all patients, the average NIHSS score at the time of presentation to the emergency department was 7.7 (range, 0–26). Ninety-three patients (31%, 93/302) were eligible for IV-tPA. Of these, 63% (59/93) received IV-tPA; 37% did not because they fell outside the time window for treatment (<4.5 hours), because their lesion was too large (more than one-third of the MCA territory), or there were medical contraindications such as recent trauma, systemic bleeding, or surgery; 6.6% of patients (20/302) proceeded to intra-arterial therapy. The mean NIHSS score in the intra-arterially treated group was 12.4, which was significantly higher than that in the remaining patients who had an average scale value of 7.3 ($P < .01$).

In the head portion of the CTA, 53% of patients (161/302) had significant vascular-related pathology. In 78% of these patients (129/161), the reported findings were directly relevant to the patient's ischemic stroke symptoms, with vessel cutoff in the territory of the patient's infarct.

In the neck portion of the CTA, relevant vascular pathology was found in 31% of patients (94/302). Of these, 64% (60/94) had at least moderate internal carotid artery stenosis, 30% (28/94) had significant vertebral artery stenosis, 6% (6/94) had both vertebral and internal carotid arterial stenosis, and 4% (4/94) had internal carotid or vertebral artery dissections.

In the upper chest, relevant vascular pathology was found in 1.3% of patients (4/302); this consisted of extensive aortic plaque associated with moderate or severe stenosis of a common carotid origin in all 4 cases.

The subset of 111 average-sized patients, for whom the body region contributions to the total effective dose were estimated, demonstrated a $14 \pm 2\%$, $33 \pm 5\%$, and $53 \pm 6\%$ contribution to the total effective dose from the head, neck, and chest regions, respectively.

DISCUSSION

We have found that a very small minority of findings on neurovascular CTA, performed expressly for the purposes of triage of patients with acute stroke symptoms, are in the chest. While some neurointerventional experts argue for the routine inclusion of the upper chest in an emergency department CTA, it is unclear how often 3D road maps from the scan are actually available before intra-arterial intervention. Increasing public awareness of potential radiation risks from medical x-rays has resulted in renewed

scrutiny of the radiation dose burden from CT scanning.²¹ We found that approximately half of the effective dose from arch-to-vertex CTA is due to the chest portion of the scan because of the high radiosensitivity of the lungs.²² On the basis of our observations, the chest portion of the CTA does not appear to contribute meaningfully to the management or triage of patients with acute stroke; thus, an approximately 50% reduction in effective dose could be achieved simply by limiting CTA to the vasculature above the shoulders, without compromising patient care.

The present study is limited by its retrospective nature because only the radiology report was used to determine the presence of relevant findings in the 3 regions of the CTA. In the acute setting, interpretation of the images by a neuroradiologist, as they appear on the scanner console, happens in real- or near-real-time, meeting the recommendations of the American Heart Association that stipulate interpretation of imaging studies within 45 minutes of patient arrival in the emergency department.¹ Discussion among neuroradiology, neurointerventional, and neurology personnel at that time will likely have a substantial impact on the chosen management pathway, yet it may not have been fully represented in the final radiology report and thus may have been unavailable for the present analysis. Thus, we may under-represent the actual findings used at the time of treatment. Addressing this issue and the issues of road-mapping before intra-arterial therapy and the management value of the intrathoracic component of the CTA would require prospective trials with appropriate power to answer these questions definitively. Another potential limitation is how well our study cohort represents the larger population of patients with acute stroke. Given the low number of relevant positive findings in the chest in 302 patients, we believe it is unlikely that substantially different results would be found in a larger study group.

CONCLUSIONS

In summary, we found that CT angiography of the head, neck, and upper chest performed in the emergency department, specifically to manage patients with acute stroke symptoms, provided diagnostically useful, potentially management-altering information only from the head and neck components of the scan. No information relevant to acute management of such patients was forthcoming from the chest portion of the CTA, yet this component accounted for approximately 50% of the effective dose of the CTA scan. Further evidence-based studies are needed to more fully evaluate these findings.

Disclosures: Joshua A. Hirsch—UNRELATED: Consultancy: CareFusion, Comments: Received fees related to vertebral augmentation; Stock/Stock Options: stroke development company.

REFERENCES

1. Jauch EC, Saver JL, Adams HP, et al. **Guidelines for the early management of adults with ischemic stroke: a guideline for healthcare professionals from the American Heart Association/American Stroke Association.** *Stroke* 2013;44:870–947
2. Del Zoppo GJ, Saver JL, Jauch EC, et al. **Expansion of the time window for treatment of acute ischemic stroke with intravenous tissue plasminogen activator: a science advisory from the American Heart Association/American Stroke Association.** *Stroke* 2009;40:2945–48

3. Wechsler LR. **Intravenous thrombolytic therapy for acute ischemic stroke.** *N Engl J Med* 2011;364:2138–46
4. Wardlaw JM, Murray V, Berge E, et al. **Recombinant tissue plasminogen activator for acute ischaemic stroke: an updated systematic review and meta-analysis.** *Lancet* 2012;379:2364–72
5. Adair G, Grant J, Pandhi N, et al. **Clinical inquires: when should patients with stroke receive thrombolytics?** *J Fam Pract* 2004;53:656, 658–59
6. Hacke W, Kaste M, Bluhmki E, et al. **Thrombolysis with alteplase 3 to 4.5 hours after acute ischemic stroke.** *N Engl J Med* 2008; 359:1317–29
7. Morris JG, Duffis EJ, Fisher M. **Cardiac workup of ischemic stroke: can we improve our diagnostic yield?** *Stroke* 2009;40:2893–98
8. Chung JH, Mitsumori LM, Ordovas KG, et al. **Heart as a source of stroke: imaging evaluation with computed tomography.** *J Thorac Imaging* 2012;27:W52–60
9. Boussel L, Cakmak S, Wintermark M, et al. **Ischemic stroke: etiologic work-up with multidetector CT of the heart and extra- and intracranial arteries.** *Radiology* 2011;258:206–12
10. Shrier DA, Tanaka H, Numaguchi Y, et al. **CT angiography in the evaluation of acute stroke.** *AJNR Am J Neuroradiol* 1997;18:1011–20
11. Knauth M, von Kummer R, Jansen O, et al. **Potential of CT angiography in acute ischemic stroke.** *AJNR Am J Neuroradiol* 1997; 18:1001–10
12. Hunter GJ, Hamberg LM, Ponzo JA, et al. **Assessment of cerebral perfusion and arterial anatomy in hyperacute stroke with three-dimensional functional CT: early clinical results.** *AJNR Am J Neuroradiol* 1998;19:29–37
13. Smith WS, Roberts HC, Chuang NA, et al. **Safety and feasibility of a CT protocol for acute stroke: combined CT, CT angiography, and CT perfusion imaging in 53 consecutive patients.** *AJNR Am J Neuroradiol* 2003;24:688–90
14. Latchaw RE, Alberts MJ, Lev MH, et al. **Recommendations for imaging of acute ischemic stroke: a scientific statement from the American Heart Association.** *Stroke* 2009;40:3646–78
15. Leiva-Salinas C, Wintermark M. **Imaging of acute ischemic stroke.** *Neuroimaging Clin N Am* 2010;20:455–68
16. Gentile NT, Cernetich J, Kanamalla US, et al. **Expedited computed tomography perfusion and angiography in acute ischemic stroke: a feasibility study.** *J Emerg Med* 2012;43:308–15
17. Kidwell CS, Wintermark M. **The role of CT and MRI in the emergency evaluation of persons with suspected stroke.** *Curr Neurol Neurosci Rep* 2010;10:21–28
18. Chang YJ, Golby AJ, Albers GW. **Detection of carotid stenosis: from NASCET results to clinical practice.** *Stroke* 1995;26:1325–28
19. Jones DG, Shrimpton PC. **Survey of CT Practice in the UK. Part 3: Normalized Organ Doses Calculated using Monte Carlo Techniques.** National Radiological Protection Board-250. London: Her Majesty's Stationery Office, 1991
20. Shrimpton PC, Jones DG, Hillier MC, et al. **Survey of CT Practice in the UK. Part 2: Dosimetric Aspects.** National Radiological Protection Board-R249. London: Her Majesty's Stationery Office; 1991
21. Boone JM, Hendee WR, McNitt-Gray MF, et al. **Radiation exposure from CT scans: how to close our knowledge gaps, monitor and safeguard exposure: proceedings and recommendations of the Radiation Dose Summit, sponsored by National Radiological Protection Board, February 24–25, 2011.** *Radiology* 2012;265:544–54
22. International Commission on Radiological Protection. **The 2007 Recommendations of the International Commission on Radiological Protection.** Stockholm: International Commission on Radiological Protection. ICRP Publication 103, Ann. ICRP 37 (2–4), 2007

Do FLAIR Vascular Hyperintensities beyond the DWI Lesion Represent the Ischemic Penumbra?

L. Legrand, M. Tisserand, G. Turc, O. Naggara, M. Edjlali, C. Mellerio, J.-L. Mas, J.-F. Méder, J.-C. Baron, and C. Oppenheim



ABSTRACT

BACKGROUND AND PURPOSE: In acute stroke with proximal artery occlusion, FLAIR vascular hyperintensities observed beyond the boundaries of the cortical lesion on DWI (newly defined “FLAIR vascular hyperintensity–DWI mismatch”) may be a marker of tissue at risk of infarction. Our aim was to compare the occurrence of FLAIR vascular hyperintensity–DWI mismatch relative to that of perfusion-weighted imaging–DWI mismatch in patients with proximal MCA occlusion before IV thrombolysis.

MATERIALS AND METHODS: In 141 consecutive patients with proximal MCA occlusion, 2 independent observers analyzed FLAIR images for the presence of FLAIR vascular hyperintensity–DWI mismatch before IV thrombolysis. PWI–DWI mismatch was defined as $\text{Volume}_{\text{hypoperfusion}} > 1.8 \times \text{Volume}_{\text{DWI}}$, with $\text{Volume}_{\text{hypoperfusion}} > 6$ seconds on time to maximum value of the residue function maps in the 94 patients with available PWI. The presence of FLAIR vascular hyperintensity–DWI mismatch, PWI–DWI mismatch, and infarct growth on 24-hour follow-up DWI was compared.

RESULTS: A FLAIR vascular hyperintensity–DWI mismatch was present in 102/141 (72%) patients, with an excellent interobserver reliability ($\kappa = 0.91$), and a PWI–DWI mismatch, in 61 of the 94 (65%) patients with available PWI. FLAIR vascular hyperintensity–DWI mismatch predicted PWI–DWI mismatch with a sensitivity of 92% (95% CI, 85%–99%) and a specificity of 64% (95% CI, 47%–80%). Patients with FLAIR vascular hyperintensity–DWI mismatch had smaller initial DWI lesion and larger infarct growth ($P < .001$) than patients without FLAIR vascular hyperintensity–DWI mismatch, even though their final infarcts remained smaller ($P < .001$).

CONCLUSIONS: Albeit being moderately specific, probably due to inclusion of oligemic tissue, the FLAIR vascular hyperintensity–DWI mismatch identifies large PWI–DWI mismatch with high sensitivity.

ABBREVIATIONS: DWI₁ = pretreatment lesions on DWI; DWI₂ = follow-up lesions on DWI; FVH = FLAIR vascular hyperintensity; Tmax = time to maximum value of the residue function

Advances in MR imaging have recently allowed better characterization of tissue and vessel status in acute stroke. FLAIR sequences are part of acute stroke MR imaging protocols in institutions using MR imaging as the first-line diagnostic tool.¹ In normal conditions, intracranial arteries are dark on FLAIR due to

the flow-void phenomenon caused by a loss of signal intensity produced by the movement of blood. After an intracranial arterial occlusion, FLAIR vascular hyperintensities (FVHs) are seen in 45%–100% of patients with stroke.^{1–14} Although their pathophysiologic and clinical significance is not fully understood, FVHs might help in the management of patients with acute stroke. Beyond their diagnostic value regarding the detection of arterial occlusion,^{11,14,15} FVHs may provide prognostic information, despite discrepancies among studies.¹ Some authors reported that FVHs have a good prognostic value^{3–6}; some, that they have a poor prognostic value^{7–10}; and others, that they have no prognostic value at all.¹¹ These discrepancies are likely due to differences among populations, end points, and FVH classifications.

Meanwhile, most groups agree that FVHs are related, to some extent, to hemodynamic impairment and represent slow retrograde flow in leptomeningeal collaterals.² These collaterals maintain some perfusion distal to the occlusion while awaiting revascularization.¹⁶ FVHs precede DWI abnormalities¹⁷ and can be

Received May 27, 2014; accepted after revision June 29.

From the Departments of Radiology (L.L., M.T., O.N., M.E., C.M., J.-F.M., C.O.) and Neurology (G.T., J.-L.M., J.-C.B.), Université Paris Descartes Sorbonne Paris Cité, Centre de Psychiatrie et Neurosciences, Institut National de la Santé et de la Recherche Médicale S894, Centre Hospitalier Sainte-Anne, Paris, France.

Laurence Legrand is supported by the Société Française de Radiologie; Marie Tisserand is supported by the Fondation de la Recherche Médicale.

Paper previously presented at: Annual Meeting of the American Society of Neuroradiology and the Foundation of the ASNR Symposium, May 17–22, 2014; Montreal, Quebec, Canada.

Please address correspondence to Catherine Oppenheim, MD, PhD, Service d'Imagerie, Centre Hospitalier Sainte-Anne, 1 Rue Cabanis, 75674 Paris Cedex 14, France; e-mail: c.oppenheim@ch-sainte-anne.fr

<http://dx.doi.org/10.3174/ajnr.A4088>

seen beyond the boundaries of the DWI lesion, and the final infarct volume falls between the initial DWI lesion and the area facing the FVHs.¹⁴ Furthermore, FVHs beyond the clot are associated with perfusion-weighted imaging–DWI mismatch^{3,8,13} and better outcome after IV-tPA.³ Taken together, these data suggest that prominent/extended FVHs indicate large areas of salvageable tissue and greater potential benefit from recanalization. In patients with stroke with acute proximal MCA occlusion, we tested the hypothesis that FVHs beyond the DWI cortical lesion boundaries (termed “FVH-DWI mismatch”) could be an easy and reproducible means to identify patients with a large penumbra area (ie, with a large PWI-DWI mismatch) and larger infarct growth.

MATERIALS AND METHODS

Patients

This retrospective analysis was based on a prospectively collected monocenter registry of consecutive patients exclusively treated by IV-tPA (0.9 mg/kg) for ischemic stroke between 2004 and 2013. MR imaging is systematically implemented in our center as a first-line pretherapeutic work-up in candidates for thrombolysis. They were treated within 3 hours from stroke onset until November 2008 and within 4.5 hours thereafter. Patients included in the present study were those who had the following: 1) an anterior circulation stroke due to proximal MCA occlusion (M1 segment); 2) pretreatment MR imaging; and 3) at least a PWI sequence before treatment or a 24-hour follow-up MR imaging, given that we searched for associations between FVH-DWI mismatch and PWI-DWI mismatch or between FVH-DWI mismatch and infarct growth. Internal carotid artery occlusion was not an exclusion criterion as long as the ipsilateral anterior cerebral artery remained visible on MRA. Patients with severe MR imaging artifacts or MR images not available in DICOM format were excluded.

Age, sex, hypertension, diabetes mellitus, hyperlipidemia, smoking, arterial blood pressure, serum glucose level at admission, and National Institutes of Health Stroke Scale score before and 24 hours after treatment were prospectively collected. Outcome at 3 months was assessed by using the mRS. Stroke etiology was assessed by using Trial of Org 10172 in Acute Stroke Treatment classification. The study was approved by the local ethics committee.

MR Imaging Protocol

Pretreatment and follow-up MR imaging was performed on 1.5T scanners (Signa Horizon EchoSpeed until November 2008 and Signa EchoSpeed thereafter; GE Healthcare, Milwaukee, Wisconsin) with a 33-mT/m gradient strength and an 8-channel head coil. The standard MR imaging protocol included FLAIR, DWI, T2*-weighted gradient-echo imaging, intracranial 3D time-of-flight MRA, and PWI whenever feasible with no delay. Total acquisition time was ≤ 10 minutes. The acquisition parameters of the axial 2D FLAIR sequence were as follows: TR/TE/TI, 8277–9802/155.5–159.4/2093–2300 ms; 24×24 cm² FOV; 256×192 matrix; 1 excitation; 24 sections; 6-mm contiguous section thickness; maximum duration, 2 minutes 18 seconds. DWI consisted of a single-shot echo-planar spin-echo sequence (3 directions, $b =$

1000 s/mm²). PWI was performed by using a T2*-weighted echo-planar sequence (TR/TE, 2000/60 ms; 24×24 cm² FOV; 64×96 matrix; 1 excitation; and repetition 50 times after a bolus [5–7 mL/s] of 20 mL of gadoteric acid). A follow-up MR imaging was scheduled ~ 24 hours after tPA and included the same set of sequences as that in the admission MR imaging except for PWI. All MR images were processed on a commercial workstation (Advantage Windows; GE Healthcare) by using an application for functional mapping calculation (READY View; GE Healthcare).

Image Analysis

FVHs were defined as focal, tubular, or serpentine hyperintensities in the subarachnoid space relative to CSF¹ and corresponding to the typical arterial course. Axial FLAIR and DWI were reviewed together to assess a FVH-DWI mismatch. FVH-DWI mismatch was considered present when FVHs extended beyond the boundaries of the cortical DWI lesion (ie, when ≥ 1 FVH was facing the isointense cortex on DWI). FVH-DWI mismatch was considered absent when there was no FVH or when all FVHs were facing the hyperintense cortex on DWI. Two radiologists (L.L. and C.O., with 3 and 17 years' experience in stroke imaging, respectively) independently reviewed the image datasets on a dedicated workstation for FVH-DWI mismatch evaluation. They were aware that all included patients had a proximal MCA occlusion; they had access to pretreatment DWI, MR angiography, and T2* images; but they were blinded to PWI, clinical data, and follow-up. Discordance between observers was resolved by consensus. One neuroradiologist (L.L.) reviewed the T2* images to ensure that FVHs did not correspond to blood clots and to evaluate FLAIR image quality (good-to-excellent or diagnostic quality despite artifacts).

Pretreatment (DWI₁) and follow-up DWI (DWI₂) lesions were segmented to compute initial and final DWI lesion volumes as detailed elsewhere,¹⁸ and DWI₁ lesion extent was evaluated semiquantitatively by using the 10-point DWI-ASPECTS. Relative infarct growth was defined as $\text{Volume}_{\text{DWI}_2} / \text{Volume}_{\text{DWI}_1} \times 100$. Critically hypoperfused tissue, defined as time to maximum value of the residue function (Tmax) > 6 seconds, was segmented from PWI maps (BrainStat AIF, READY View software; GE Healthcare). The PWI-DWI mismatch volume was defined as the Tmax > 6 -second volume without DWI₁ changes. On the basis of Diffusion and Perfusion Imaging Evaluation for Understanding Stroke Evolution (DEFUSE 2) criteria, a PWI-DWI mismatch was considered present when $\text{Volume}_{\text{hypoperfusion}} \text{exceeded } 1.8 \times \text{Volume}_{\text{DWI}_1}$.¹⁹ This stringent ratio was preferred to the classic 1.2 ratio to select patients with clinically meaningful PWI-DWI mismatch only. Pretreatment occlusion and recanalization (TICI score) were assessed on MRA.

For the per-region analysis, FVHs were rated by 2 readers according to their distribution based on the ASPECTS regions. Briefly, the 7 cortical divisions of ASPECTS (insula, M1–M6) were considered positive when they coincided with an FVH. Of note, as opposed to the original ASPECTS and its previous adaptation to FVHs in which only 2 axial sections were selected,^{5,10,20} we reviewed all FLAIR images here to ensure continuity of bright dots considered FVHs. Coregistered DWI₁, DWI₂, and PWI (Tmax > 6 -second maps) were analyzed visually by 1 reader for DWI hyperintensity, infarct progression, and hypoperfusion in each of the 7 ASPECTS regions. Each

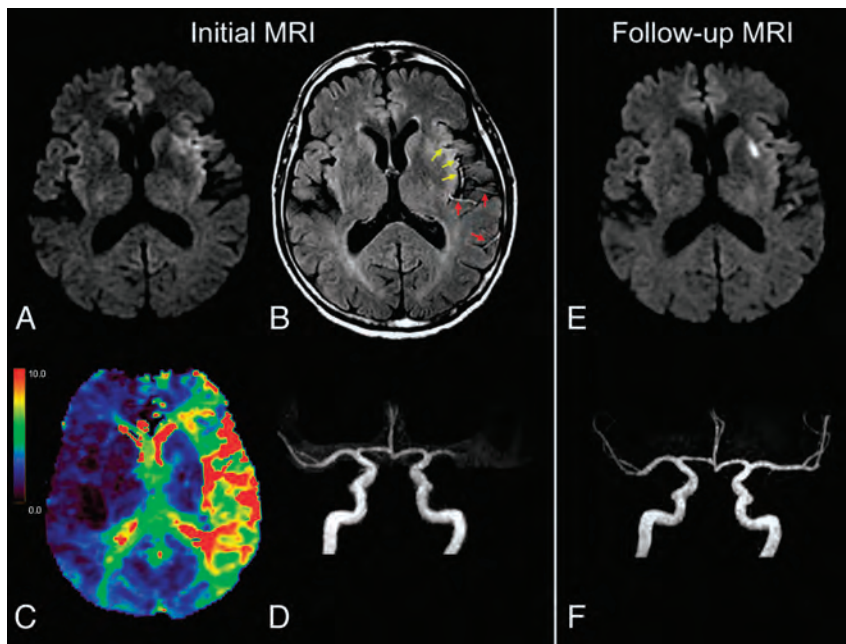


FIG 1. Illustrative case of FVH-DWI and PWI-DWI mismatch. MR images (A–D) of a 67-year-old man obtained 86 minutes after sudden onset of aphasia. Small hyperintense lesions are visible in the left MCA territory on admission DWI (A), with FVHs on FLAIR (B), some facing the DWI lesion (yellow arrows) and others located beyond the boundaries of DWI signal changes (red arrows), indicating a FVH-DWI mismatch. A large PWI-DWI mismatch on the Tmax map (C) with areas of Tmax of >6 seconds (yellow-to-red) topographically congruent with the FVHs. Proximal occlusion of left MCA on MRA (D, frontal view). On 24-hour follow-up MR images (E and F), there was no extension of the initial DWI lesion (E) and complete recanalization (F). IV-tPA was initiated 120 minutes after stroke onset.

ASPECTS region was subsequently classed as positive or negative for FVH-DWI and PWI-DWI mismatch.

Statistical Analysis

We compared continuous variables using the Student *t* test or Mann-Whitney *U* test, as appropriate. Categorical variables were compared by using the χ^2 or Fisher exact test as appropriate. The κ coefficient was used to assess interobserver agreement for FVH-DWI mismatch. We compared pre- and post-treatment characteristics in univariate analyses between patients with or without FVH-DWI mismatch and PWI-DWI mismatch. We finally searched for a model that would predict PWI-DWI mismatch on the basis of clinical and easily derivable imaging parameters available at admission (DWI-ASPECTS instead of DWI₁ volume). A multivariate binary logistic regression analysis was performed with PWI-DWI mismatch (present/absent) as the dependent variable. Variables were selected for entry into the model on the basis of results of the univariate analysis ($P < .20$) and were further excluded from the model with $P < .10$. The OR and 95% CI were obtained. A 2-tailed P -value $< .05$ was considered significant (SPSS for Windows, Version 19.0; IBM, Armonk, New York). Sensitivity, specificity, and positive and negative predictive values of the FVH-DWI mismatch for the detection of PWI-DWI mismatch were computed.

RESULTS

General Population

During the study period, 351 patients were treated with IV-tPA only. Two hundred ten (60%) patients were excluded for the fol-

lowing main reasons: non-MCA territory stroke ($n = 38$), CT scan at admission ($n = 32$), initial MR imaging not available in DICOM format ($n = 11$) or noninterpretable ($n = 11$, major artifacts), absence of M1 occlusion ($n = 110$), M1 occlusion combined with ipsilateral internal carotid and anterior cerebral artery occlusion ($n = 2$), and no PWI sequence or follow-up MR imaging ($n = 6$). One hundred forty-one patients (74 men) met the inclusion criteria, with a median (interquartile range) age and admission NIHSS score of 70 years (range, 57–79 years) and 17 (range, 12–21), respectively. They did not differ from the excluded patients on the basis of sex ($P = .34$) or age ($P = .81$) but had a higher NIHSS score of 17 (range, 12–21) versus 11 (range, 7–18) ($P < .001$). PWI was available in 94 (67%) patients. Median time-to-initial MR imaging and time to treatment were 117 minutes (range, 89–157 minutes) and 155 minutes (range, 123–194 minutes). Follow-up MR imaging (median [interquartile range] delay from onset = 25 hours [21–29 hours]) was available in 138 patients. Of these, complete recanalization (TICI 3) occurred in 41 patients (30%). The 3-month mRS score was available in 133 patients, with a median score of 3 (range, 1–4).

FVH-DWI Mismatch (Per-Patient Analysis)

The interobserver agreement for FVH-DWI mismatch (Figs 1 and 2) was $\kappa = 0.91$ (95% CI, 0.84–0.99). After consensus, 102 (72%) patients had a FVH-DWI mismatch. As shown in the Table, patients with FVH-DWI mismatch had a smaller DWI₁ volume and a higher PWI-DWI mismatch volume than patients without FVH-DWI mismatch. Patients with FVH-DWI mismatch had greater infarct progression at follow-up MR imaging, even though their follow-up infarct volume remained smaller and 3-month outcome was better than that of patients without FVH-DWI mismatch. All the above-mentioned associations remained significant when the analysis was restricted to patients with good-to-excellent FLAIR image-findings quality ($n = 105$ in the whole population, $n = 74$ in patients with PWI). The presence of FVH-DWI mismatch did not differ between patients treated before and after November 2008 ($37/52 = 71\%$ versus $65/89 = 73\%$, $P = .81$).

Per-Region Analysis

FVHs were visible in the insular region in all cases and were facing the M2, M5, M3, M6, M1, and M4 ASPECTS regions in 95%, 75%, 71%, 37%, 24%, and 15% of patients, respectively (average of 2 readers). Of the 987 ASPECTS regions (141 patients \times 7 regions), 60% were facing an FVH. In line with the per-patient

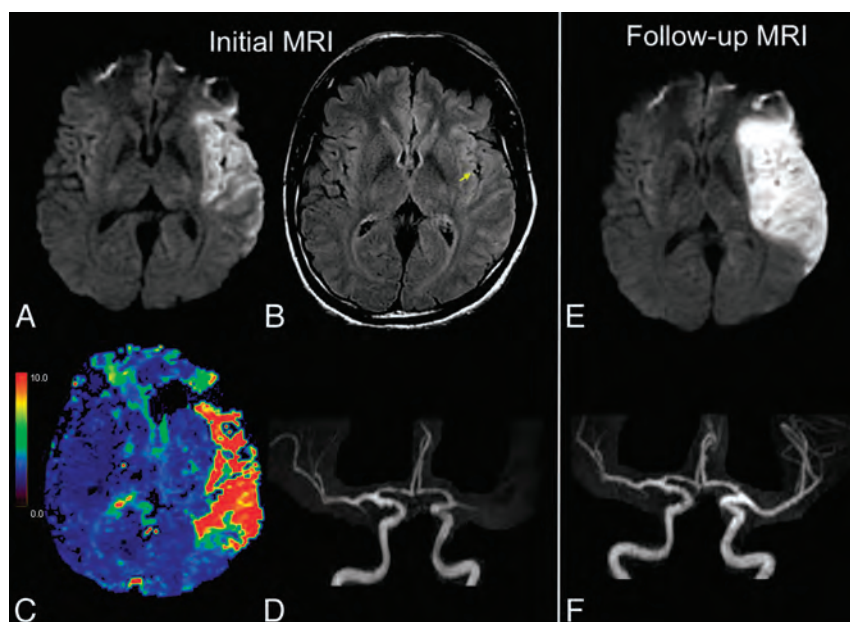


FIG 2. Illustrative case of no FVH-DWI or PWI-DWI mismatch. MR imaging (A–D) of a 47-year-old man obtained 81 minutes after sudden onset of right hemiparesis. Large hyperintense lesions in the left MCA territory on admission DWI (A) with FVH on FLAIR (B, arrow) only overlying the hyperintense parenchyma on DWI, indicating the absence of FVH-DWI mismatch. C, No significant PWI-DWI mismatch on the Tmax map is seen. Note proximal occlusion of the left MCA on MRA (D, frontal view). On 24-hour follow-up MR images (E and F), extension of the initial DWI lesion (E) is seen despite recanalization (F). IV-tPA was initiated 105 minutes after stroke onset.

analysis (see next paragraph), FVH-DWI mismatch was significantly associated with PWI-DWI mismatch: Eighty-two percent of regions positive for FVH-DWI mismatch were also positive for PWI-DWI mismatch versus only 17% of regions negative for FVH-DWI mismatch ($P < .001$). Infarcts progressed more often in brain tissue facing FVHs: Thirty-one percent of the areas with FVHs showed infarct progression versus 21% of the areas without it ($P < .001$).

Identification of PWI-DWI Mismatch

A PWI-DWI mismatch was present in 61 of the 94 (65%) patients with available PWI. In univariate analysis, patients with PWI-DWI mismatch had lower initial NIHSS scores (15 [range, 11–20] versus 19 [range, 16–23], $P = .003$), smaller DWI₁ lesion extent assessed by using volumes (17 mL [range, 7–35 mL] versus 108 mL [range, 63–149 mL], $P < .001$) or DWI-ASPECTS (7 [range, 6–8] versus 4 [range, 3–6], $P < .001$), shorter onset-to-initial MR imaging time (106 minutes [range, 84–137 minutes] versus 132 minutes [range, 97–178 minutes], $P = .01$), and lower serum glucose levels at admission (6.7 ± 1.2 versus 7.3 ± 1.8 mmol/L, $P = .04$). In multivariate analysis based on easily derivable admission variables, PWI-DWI mismatch was independently associated with FVH-DWI mismatch (OR, 7.63; 95% CI, 1.74–33.43; $P = .007$) after adjustment for onset-to-admission MR imaging time (OR, 0.98; 95% CI, 0.97–1.00; $P = .02$) and DWI-ASPECTS (OR, 1.76; 95% CI, 1.22–2.53; $P = .003$). Initial NIHSS score and serum glucose level were sequentially removed from the model.

Of the 94 patients with available PWI at admission, a FVH-DWI mismatch was present in 56/61 patients with a PWI-DWI mismatch (sensitivity = 92%; 95% CI, 85%–99%). There was no FVH-DWI mismatch in 21/33 patients without PWI-DWI mis-

match (specificity = 64%; 95% CI, 47%–80%). The positive and negative predictive values were 82% (95% CI, 73%–91%) and 81% (95% CI, 65%–96%), respectively. A post hoc analysis by using a less conservative threshold for the PWI-DWI mismatch profile (4-second Tmax threshold instead of 6-second) resulted in a similar sensitivity but a higher specificity (90% and 76%, respectively).

DISCUSSION

The present study revealed 3 salient points: 1) FVHs were consistently visualized in the insular region in patients with proximal MCA occlusion within 4.5 hours after symptom onset; 2) FVH-DWI mismatch was associated with a smaller initial infarct, the presence of PWI-DWI mismatch, and greater infarct growth after thrombolysis even though their final infarcts remained smaller; and 3) FVH-DWI mismatch predicted a large PWI-DWI mismatch with excellent sensitivity but moderate specificity.

The high prevalence of FVHs irrespective of their location is likely explained by the fact that patients were imaged within 4.5 hours and had proximal MCA occlusion. Indeed, a lower FVH prevalence has been reported in posterior strokes and in distal occlusions² or when onset-to-MR imaging time increased.^{1,17} Like others,^{10,20} we found fewer FVHs in borderzone areas (M4, M6) than in more proximal areas (insula, M2, M5). This FVH gradient is consistent with an increasing flow rate within leptomeningeal collaterals when moving toward borderzone areas.

Several approaches have been proposed to estimate the extent of FVHs. Some authors distinguished FVHs involving more or less than one-third of the MCA territory or of the hypoperfused area,^{3,6,21} but one has to acknowledge the well-known difficulties in determining this cutoff. Others proposed to count ASPECTS regions with FVH-matching boundaries^{10,20} or grade FVHs according to their sulcal location,²² without evaluating the reproducibility of these grading systems. Counting the number of axial FLAIR sections with FVHs⁵ only provides a rostrocaudal extension of FVHs and is dependent on the section number and thickness. FVH-DWI mismatch offers several advantages over previous estimates of FVH extent. It is simple, reproducible, and feasible at bedside and therefore compatible with timely treatment decisions in acute stroke. The FVH-DWI mismatch focuses on FVHs beyond the boundaries of the cortical DWI lesion, ignoring FVHs adjacent to the DWI lesion. Therefore, only FVHs facing potential tissue at risk of infarct expansion are considered in this definition. The presence of larger amounts of at-risk tissue in the presence of FVH-DWI mismatch is also supported by the results of our univariate analysis, with smaller initial DWI lesions and larger infarct progression after treatment, despite a similar

Univariate comparisons among patients according to FVH-DWI mismatch (n = 141)^a

	FVH-DWI Mismatch (n = 102)	No FVH-DWI Mismatch (n = 39)	P Value
Demographics/risk factors			
Age (yr)	68 ± 15	68 ± 14	.86
Male	51 (50%)	23 (59%)	.34
Hypertension	53 (52%)	23 (59%)	.46
Diabetes mellitus	6 (6%)	7 (18%)	.03
Hyperlipidemia	35 (34%)	15 (38%)	.65
Smoking	37 (36%)	11 (28%)	.37
Characteristics at admission			
Systolic BP (mm Hg)	153 ± 24	158 ± 18	.31
Diastolic BP (mm Hg)	83 ± 18	83 ± 17	.89
Serum glucose level (mmol/L)	6.8 ± 1.6	7.5 ± 1.9	.02
Initial NIHSS score	16 (12–20)	17 (15–22)	.054
Initial MRI			
Time from onset to initial MRI (min)	117 (87–144)	122 (96–159)	.16
Available PWI sequence	68 (67%)	26 (67%)	1.00
Terminal ICA occlusion	39 (38%)	11 (28%)	.27
Good-to-excellent FLAIR images	81 (79%)	24 (61%)	.03
DWI ₁ volume (mL)	18 (8–35)	108 (57–160)	<.001
PWI-DWI mismatch volume (mL) ^b	70 (40–105)	44 (33–64)	.03
PWI-DWI mismatch ^b	56 (82%)	5 (19%)	<.001
Cardioembolic stroke	61 (60%)	16 (41%)	.05
24-Hour evolution			
Follow-up NIHSS score	11 (5–18)	16 (10–22)	.004
DWI ₂ volume (mL) ^d	36 (19–66)	161 (95–230)	<.001
Relative infarct progression (%) ^d	195 (112–356)	133 (114–165)	.001
Complete recanalization ^{c,d}	29 (29%)	12 (32%)	.77
mRS score at 3 mo ^e	3 (1–4)	4 (3–6)	.001
mRS score ≤2 at 3 mo ^e	45 (47%)	9 (24%)	.02

Note:—BP indicates blood pressure.

^a Numbers (not %) are mean ± SD or median (interquartile range).

^b Ninety-four patients (PWI-DWI mismatch: >6-second Tmax, Volume_{hypoperfusion} > 1.8 × Volume_{DWI}).¹⁹

^c TIC1 3.

^d 24-hour MRI available in 138 patients.

^e mRS score at 3 months available in 133 patients.

rate of complete recanalization in both groups. These results closely match those from a previous series of 52 patients treated with thrombolysis for MCA occlusion.³ Similarly, others concluded that the extent of FVHs was associated with the presence of a PWI-DWI mismatch, though the definition used for the latter was qualitative^{1,3} or unspecified.^{8,10} Taken together with these previous findings, our results in turn reinforce the view that FVHs beyond the DWI lesion represent markedly impaired hemodynamics in patients with proximal occlusion.

The excellent sensitivity (92%) of FVH-DWI mismatch for a large PWI-DWI mismatch indicates that the former only rarely missed the latter. This could indicate that the absence of FVH-DWI mismatch may obviate PWI to identify patients with large penumbra. However, the moderate specificity (64%) means that FVH-DWI mismatch as implemented here captures hemodynamic compromises other than just the penumbra. Indeed, if bright vessels on FLAIR effectively represent slow flow in dilated leptomeningeal arterioles in response to cerebrovascular autoregulation, FVHs should overlie not just the penumbral cortex but also the less severely hypoperfused, not at-risk tissue (ie, the “benign” oligemia) and even perhaps surrounding normoperfused but autoregulated tissue.²³ This hypothesis was strengthened by the post hoc use of a deliberately defined less conservative Tmax threshold (>4 seconds). As expected, specificity increased while sensitivity held up, compared with the standard Tmax of >6

seconds. Thus, FVHs beyond the DWI lesion likely detect not just penumbral but also less severely hypoperfused areas. One should, however, keep in mind that the optimum Tmax cut-point separating the penumbra from the oligemia remains somewhat unclear.²⁴ However, even though the FVH-DWI mismatch likely overestimates the penumbra, it could serve as a surrogate for PWI-DWI mismatch whenever PWI is unavailable or degraded by artifacts or patients have difficult venous access or contraindications for gadolinium use such as renal failure or contrast hypersensitivity.

Our retrospective study has several limitations. First, our results cannot be generalized to all patients with stroke, especially those with no or distal occlusion. However, we deliberately selected a population of patients with proximal MCA occlusion and visible anterior cerebral artery origin to ensure homogeneity of the potential collateral supply, given the discrepant FVH findings in previous more heterogeneous populations. Second, we were unable to correlate FVHs with collateral flow because patients did not undergo digital subtraction or CT angiography. Third, we defined the PWI-DWI mismatch on the basis of stringent DEFUSE 2 criteria.

The accuracy of the FVH-DWI mismatch as a surrogate for PWI-DWI mismatch obviously depends on the definition of the latter, which is still debated. Fourth, slight differences in FLAIR parameters among patients in our study are unlikely to have induced major variability in FVH detection. We must, however, be careful in drawing any definite conclusion because differences in the FLAIR sequence, coil system, and magnetic field or among manufacturers may influence FVH visibility.

CONCLUSIONS

The FVH-DWI mismatch is a novel and promising approach that clearly contains important hemodynamic information, assessable by the naked eye. It could serve as a surrogate to PWI to identify patients with large PWI-DWI mismatches whenever perfusion data are missing. The criteria for the FVH-DWI mismatch model developed here require validation in an independent cohort. If validated, this straightforward MR imaging feature may prove useful for enriching trial cohorts with patients likely to benefit from reperfusion therapies.

Disclosures: Laurence Legrand—RELATED: Grant: Société Française de Radiologie. Marie Tisserand—RELATED: Grant: Fondation pour la Recherche Médicale. Myriam Edjlali—RELATED: Grant: Societe Française de Neurovasculaire. Jean-Louis Mas—UNRELATED: Board Membership: Bayer, Boehringer-Ingelheim, Bristol-Myers-Squibb, Daiichi-Sankyo. Comments: advisory boards; Payment for Lectures (including service on Speakers Bureaus): Bayer, Boehringer-Ingelheim, Bristol-Myers-Squibb, Daiichi-Sankyo.

REFERENCES

1. Azizyan A, Sanossian N, Mogensen MA, et al. **Fluid-attenuated inversion recovery vascular hyperintensities: an important imaging marker for cerebrovascular disease.** *AJNR Am J Neuroradiol* 2011; 32:1771–75
2. Sanossian N, Saver JL, Alger JR, et al. **Angiography reveals that fluid-attenuated inversion recovery vascular hyperintensities are due to slow flow, not thrombus.** *AJNR Am J Neuroradiol* 2009;30:564–68
3. Lee KY, Latour LL, Luby M, et al. **Distal hyperintense vessels on FLAIR: an MRI marker for collateral circulation in acute stroke?** *Neurology* 2009;72:1134–39
4. Huang X, Liu W, Zhu W, et al. **Distal hyperintense vessels on FLAIR: a prognostic indicator of acute ischemic stroke.** *Eur Neurol* 2012; 68:214–20
5. Olindo S, Chausson N, Joux J, et al. **Fluid-attenuated inversion recovery vascular hyperintensity: an early predictor of clinical outcome in proximal middle cerebral artery occlusion.** *Arch Neurol* 2012;69:1462–68
6. Pérez de la Ossa N, Hernandez-Perez M, Domenech S, et al. **Hyperintensity of distal vessels on FLAIR is associated with slow progression of the infarction in acute ischemic stroke.** *Cerebrovasc Dis* 2012;34:376–84
7. Girot M, Gauvrit JY, Cordonnier C, et al. **Prognostic value of hyperintense vessel signals on fluid-attenuated inversion recovery sequences in acute cerebral ischemia.** *Eur Neurol* 2007;57:75–79
8. Ebinger M, Kufner A, Galinovic I, et al. **Fluid-attenuated inversion recovery images and stroke outcome after thrombolysis.** *Stroke* 2012;43:539–42
9. Cheng B, Ebinger M, Kufner A, et al. **Hyperintense vessels on acute stroke fluid-attenuated inversion recovery imaging: associations with clinical and other MRI findings.** *Stroke* 2012;43:2957–61
10. Hohenhaus M, Schmidt WU, Brunecker P, et al. **FLAIR vascular hyperintensities in acute ICA and MCA infarction: a marker for mismatch and stroke severity?** *Cerebrovasc Dis* 2012;34:63–69
11. Schellinger PD, Chalela JA, Kang DW, et al. **Diagnostic and prognostic value of early MR imaging vessel signs in hyperacute stroke patients imaged <3 hours and treated with recombinant tissue plasminogen activator.** *AJNR Am J Neuroradiol* 2005;26:618–24
12. Kamran S, Bates V, Bakshi R, et al. **Significance of hyperintense vessels on FLAIR MRI in acute stroke.** *Neurology* 2000;55:265–69
13. Haussen DC, Koch S, Saraf-Lavi E, et al. **FLAIR distal hyperintense vessels as a marker of perfusion-diffusion mismatch in acute stroke.** *J Neuroimaging* 2013;23:397–400
14. Toyoda K, Ida M, Fukuda K. **Fluid-attenuated inversion recovery intraarterial signal: an early sign of hyperacute cerebral ischemia.** *AJNR Am J Neuroradiol* 2001;22:1021–29
15. Cosnard G, Duprez T, Grandin C, et al. **Fast FLAIR sequence for detecting major vascular abnormalities during the hyperacute phase of stroke: a comparison with MR angiography.** *Neuroradiology* 1999;41:342–46
16. Bang OY, Saver JL, Kim SJ, et al. **Collateral flow predicts response to endovascular therapy for acute ischemic stroke.** *Stroke* 2011;42: 693–99
17. Maeda M, Koshimoto Y, Uematsu H, et al. **Time course of arterial hyperintensity with fast fluid-attenuated inversion-recovery imaging in acute and subacute middle cerebral arterial infarction.** *J Magn Reson Imaging* 2001;13:987–90
18. Labeyrie MA, Turc G, Hess A, et al. **Diffusion lesion reversal after thrombolysis: a MR correlate of early neurological improvement.** *Stroke* 2012;43:2986–91
19. Lansberg MG, Straka M, Kemp S, et al. **MRI profile and response to endovascular reperfusion after stroke (DEFUSE 2): a prospective cohort study.** *Lancet Neurol* 2012;11:860–67
20. Kono T, Naka H, Nomura E, et al. **The association between hyperintense vessel sign and final ischemic lesion differ in its location.** *J Stroke Cerebrovasc Dis* 2014;23:1337–43
21. Gawlitza M, Gragert J, Quaschling U, et al. **FLAIR-hyperintense vessel sign, diffusion-perfusion mismatch and infarct growth in acute ischemic stroke without vascular recanalisation therapy.** *J Neuroradiol* 2014;41:227–33
22. Liu W, Xu G, Yue X, et al. **Hyperintense vessels on FLAIR: a useful non-invasive method for assessing intracerebral collaterals.** *Eur J Radiol* 2011;80:786–91
23. Muir KW, Buchan A, von Kummer R, et al. **Imaging of acute stroke.** *Lancet Neurol* 2006;5:755–68
24. Donnan GA, Baron JC, Ma H, et al. **Penumbra selection of patients for trials of acute stroke therapy.** *Lancet Neurol* 2009;8:261–69

Prediction of Infarction and Reperfusion in Stroke by Flow- and Volume-Weighted Collateral Signal in MR Angiography

M. Ernst, N.D. Forkert, L. Brehmer, G. Thomalla, S. Siemonsen, J. Fiehler, and A. Kemmling



ABSTRACT

BACKGROUND AND PURPOSE: In proximal anterior circulation occlusive strokes, collateral flow is essential for good outcome. Collateralized vessel intensity in TOF- and contrast-enhanced MRA is variable due to different acquisition methods. Our purpose was to quantify collateral supply by using flow-weighted signal in TOF-MRA and blood volume-weighted signal in contrast-enhanced MRA to determine each predictive contribution to tissue infarction and reperfusion.

MATERIALS AND METHODS: Consecutively (2009–2013), 44 stroke patients with acute proximal anterior circulation occlusion met the inclusion criteria with TOF- and contrast-enhanced MRA and penumbral imaging. Collateralized vessels in the ischemic hemisphere were assessed by TOF- and contrast-enhanced MRA using 2 methods: 1) visual 3-point collateral scoring, and 2) collateral signal quantification by an arterial atlas-based collateral index. Collateral measures were tested by receiver operating characteristic curve and logistic regression against 2 imaging end points of tissue-outcome: final infarct volume and percentage of penumbra saved.

RESULTS: Visual collateral scores on contrast-enhanced MRA but not TOF were significantly higher in patients with good outcome. Visual collateral scoring on contrast-enhanced MRA was the best rater-based discriminator for final infarct volume < 90 mL (area under the curve, 0.81; $P < .01$) and percentage of penumbra saved > 50% (area under the curve, 0.67; $P = .04$). Atlas-based collateral index of contrast-enhanced MRA was the overall best independent discriminator for final infarct volume of < 90 mL (area under the curve, 0.94; $P < .01$). Atlas-based collateral index combining the signal of TOF- and contrast-enhanced MRA was the overall best discriminator for effective reperfusion (percentage of penumbra saved > 50%; area under the curve, 0.89; $P < .001$).

CONCLUSIONS: Visual scoring of contrast-enhanced but not TOF-MRA is a reliable predictor of infarct outcome in stroke patients with proximal arterial occlusion. By atlas-based collateral assessment, TOF- and contrast-enhanced MRA both contain predictive signal information for penumbral reperfusion. This could improve risk stratification in further studies.

ABBREVIATIONS: AUC = area under the curve; CE = contrast-enhanced; CI = collateral index; CS = collateral score; CVA = collateral vessel abundance; FIV = final infarct volume; PPS = percentage of penumbra saved; ROC = receiver operating characteristic; Tmax = time-to-maximum; VOL = volume

In stroke patients with acute proximal artery occlusion, collateral blood supply is pivotal for functional outcome.¹ Collateral perfusion limits ischemic core expansion by maintaining oligemic

tissue-at-risk until reperfusion takes place and is an independent predictor of final infarct volume and clinical outcome.^{1–3} Collaterals enhance recanalization and avert hemorrhagic transformation by minimizing severe local perfusion impairment.^{4,5} For rapidly applicable and reproducible collateral assessment in the triage of acute stroke, several angiographic scoring methods have been introduced.^{2,6–8} Contrary to DSA, direct visualization of time-resolved collateral flow in the leptomeningeal arteries is not possible with conventional CTA or MRA. Instead, the visual abundance of contrasted, collateralized vessels distal to the occlusion has been used as a surrogate scoring system for leptomeningeal collateral supply in high-resolution CTA.^{1,7,9} In particular, a malignant CTA collateral profile is highly specific for poor outcome.⁹

Collateral assessment using TOF- or contrast-enhanced (CE)-MRA is less straightforward. Visualization of collateralized vessels

Received April 10, 2014; accepted after revision July 23.

From the Departments of Diagnostic and Interventional Neuroradiology (M.E., L.B., S.S., J.F., A.K.) and Neurology (G.T.), University Medical Center Hamburg-Eppendorf, Hamburg, Germany; Department of Radiology and Hotchkiss Brain Institute (N.D.F.), University of Calgary, Calgary, Canada; and Department of Neuroradiology (A.K.), University of Luebeck, Luebeck, Germany.

M. Ernst and N.D. Forkert contributed equally to this work.

Please address correspondence to André Kemmling, MD, Department of Diagnostic and Interventional Neuroradiology, University Medical Center Hamburg-Eppendorf, Haus Ost 22 (O 22), Martinistr 52, 20246 Hamburg, Germany; e-mail: a.kemmling@uke.de



Indicates article with supplemental on-line appendix.



Indicates article with supplemental on-line photo.

<http://dx.doi.org/10.3174/ajnr.A4145>

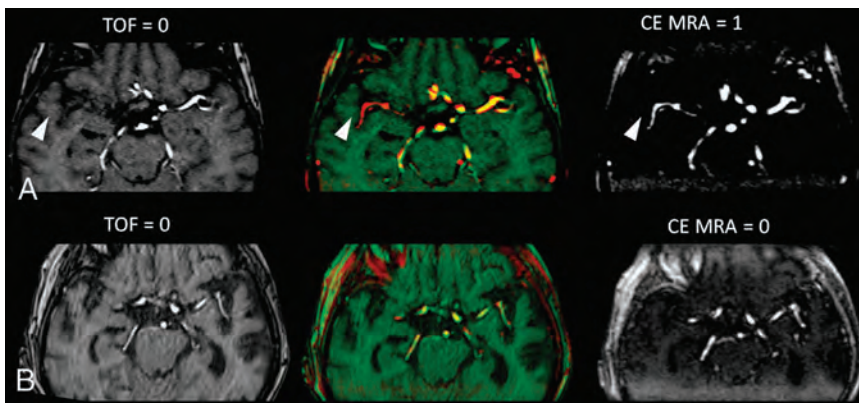


FIG 1. Illustration of visual collateral scores in TOF- and CE-MRA. *A*, Source images showing retrograde MCA filling in CE-MRA (scored 1) but not in TOF (scored 0) (arrowheads), with differing signal of collaterals as shown in red-green shift. *B*, No retrograde MCA filling in both, TOF- and CE-MRA (scored 0).

distal to mainstem occlusion is problematic in TOF-MRA, which is highly sensitive to low flow due to spin saturation.^{10,11} In CE-MRA, T1-shortening by gadolinium induces a vessel signal nearly independent of blood flow (for a sufficiently broad bolus) and primarily depends on blood volume (ie, intravascular volume). The different signal of collateralized vessels in both modalities may contain independent information; however, the efficacy of collateral assessment for outcome prediction attributed to each MRA technique has not been investigated in detail.¹¹⁻¹⁴ Our purpose was to differentially quantify collateralized vessels in proximal anterior circulation occlusive strokes, including both flow-weighted signal in TOF-MRA and volume-weighted signal in CE-MRA, and to determine each predictive contribution to tissue outcome.

MATERIALS AND METHODS

Patient Selection

Study data were acquired with institutional review board approval (Ethik-Kommission der Ärztekammer Hamburg). We screened consecutive patients with acute proximal occlusive stroke presenting to our department between January 2009 to August 2013 who met the study inclusion criteria: 1) occlusion of the intracranial ICA and/or the M1 segment of the MCA confirmed by DSA if available or CE-MRA; 2) pretreatment TOF-MRA, CE-MRA, DWI, and PWI within 6 hours after onset; 3) follow-up imaging within 72 hours; 4) NIHSS score of >4. Patients were excluded for poor image quality of MRA datasets or evidence of symptomatic intracranial hemorrhage with mass effect and signs of prior territorial stroke.

Image Acquisition

Patients were triaged with a standardized institutional acute stroke protocol for MR imaging independent of the study design. No extra contrast medium for CE-MRA was administered outside the routine clinical protocol. Admission stroke imaging was performed using a 1.5T MR imaging scanner (Magnetom Avanto; Siemens, Erlangen, Germany), including axial DWI, FLAIR, and TOF-MRA. Additional CE-MRA and PWI were performed in case of present proximal occlusion to guide and plan potential mechanical thrombectomy in light of current arguable evidence

for benefit.¹⁵ TOF- and CE-MRA covered the distal internal carotid artery and the anterior and middle cerebral arteries (MCA up to third-order branches). CE-MRA also covered the extracranial ICA. TOF-MRA was acquired with 2×40 section slabs; 0.9-mm section thickness; 0.47×0.47 mm in-plane resolution; 512×384 matrix; TE, 7 ms; TR, 27 ms; flip angle, 25°; acquisition time, 130 seconds. CE-MRA was acquired in a coronal 1×112 section slab with 0.7 mm per section; TE, 1.4 ms; TR, 3.8 ms; 0.6×0.63 mm in-plane resolution; 512×384 matrix; flip angle, 25°; 10-mL bolus of gadopentetate dimeglumine (Magnegraf; Marogra, Jena, Germany) at 3 mL/s triggered by Care Bolus (Siemens);

acquisition time, 2×45 seconds. Time-resolved perfusion raw data were acquired with 2D echo-planar imaging (22-mL bolus of gadopentetate dimeglumine; 5.0 mL/s; TE, 22 ms; TR, 1800 ms; flip angle, 80°; 26 sections; 4 mm per section) and an acquisition time of 113 seconds. Perfusion parameter maps (time-to-maximum [Tmax]) were calculated using an established in-house software (ANTONIA).¹⁶ The arterial input function for Tmax estimation was selected from the contralateral middle cerebral artery. Delay-corrected deconvolution for Tmax estimation was performed by standard singular value decomposition.

Image Analysis

The MRA signal intensity of MCA vasculature distal to the occlusion relative to the normal hemisphere was assessed as an indicator of leptomeningeal collateral supply to the MCA territory. This was accomplished by visual rater-based collateral scoring and automated-software-assisted quantification of collateral MRA signal in TOF- and CE-MRA.

Visual Collateral Scoring

Images of TOF-MRA and CE-MRA were evaluated independently by 2 raters (M.E. and A.K., certified neuroradiologists). Raters were blinded to clinical and concomitant admission and follow-up imaging data. MRA images were co-registered. Precise registration was checked by red-green shift, and images were presented as maximum intensity projections (20-mm slab thickness, 1-mm increment) (Fig 1).

The visual collateral score (CS) in each MRA dataset (CS_{TOF} and $CS_{\text{CE-MRA}}$) was rated by visual abundance of MCA vasculature distal to the occlusion in the ischemic hemisphere compared with the normal side by using a 3-point grading scale (0 = none/poor, 1 = fair, 2 = good/normal) as used previously.¹ The sinus and large veins were not included for scoring vasculature. Ratings were compared and decided by consensus if scores differed. A combined 5-point (0–4) collateral score, CS_{combined} , was a priori defined as the sum of each separate TOF- and CE-MRA subscore to further subdivide and rank collateral status using both MRA modalities in conjunction (On-line Appendix).

Automated Atlas-Based Collateral Quantification

To include objective rater-independent quantification of collaterals with a continuous imaging parameter, we used an automated method to determine the relative vascular signal intensity of MCA vasculature in the ischemic hemisphere compared to the normal side. For this purpose, collateral vessel abundance (CVA) was measured by the signal intensity of all MCA vascular voxels in each hemisphere distal to the M1-MCA segment. This measurement was accomplished by using a statistical cerebroarterial atlas derived from 700 normal MRA datasets published elsewhere (Online Appendix).¹⁷ The ratio of the MCA vascular intensities in the ischemic hemisphere compared to the normal hemisphere was defined as the collateral index (CI) (equation 1). The CI was determined in TOF- and CE-MRA datasets (CI_{TOF} and CI_{CE-MRA}). Any theoretical value of $CI > 1$ in equation 1 was truncated to 1.

$$1) \quad CI = \frac{CVA_{\text{ischemic hemisphere}}}{CVA_{\text{normal hemisphere}}}; 0 \leq CI \leq 1.$$

The combined collateral index, CI_{combined} , containing the collateral signal from TOF- and CE-MRA was defined by summing the CI of both MRA modalities. Any theoretical value of CI_{combined} of >2 in equation 2 was truncated to 2.

$$2) \quad CI_{\text{combined}} = CI_{TOF} + CI_{CE-MRA} = \left[\frac{CVA_{\text{ischemic hemisphere}}}{CVA_{\text{normal hemisphere}}} \right]_{TOF-MRA} + \left[\frac{CVA_{\text{ischemic hemisphere}}}{CVA_{\text{normal hemisphere}}} \right]_{CE-MRA}; 0 \leq CI_{\text{combined}} \leq 2.$$

Definition and Measurement of Tissue Outcome

End Points

Collateral measures were tested against 2 imaging-based tissue outcome parameters. Final infarct volume (FIV) quantifies the absolute amount of tissue damage that is directly related to clinical outcome. The percentage of tissue-at-risk spared from infarction (percentage of penumbra saved, [PPS]) quantifies reperfusion per volume of tissue-at-risk. It is related to the efficacy of recanalization normalized to the volume of penumbra present at admission imaging. Imaging lesion masks were segmented with semiautomated edge detection by using a standardized operational definition (Analyze 11.0 software; AnalyzeDirect, Overland Park, Kansas). FIV was segmented section-by-section in follow-up imaging (targeted at 48-hour onset to imaging). For PPS calculation (equation 3), volume (VOL) of ischemic lesions in Tmax MR-perfusion maps and DWI were segmented. Tissue-at-risk to infarct was classified by Tmax bolus delay ($VOL_{T_{\text{max}}}$) using a fixed window-level at the optimal threshold of 6 seconds with variable window width for optimal contrast (Online Appendix).¹⁸⁻²² Lesion masks of tissue-at-risk ($VOL_{T_{\text{max}}}$), initial ischemic core ($VOL_{D_{\text{WI}}}$), and final infarct volume were registered. PPS was calculated as follows:

$$3) \quad PPS = \frac{VOL_{T_{\text{max}}} - FIV}{VOL_{T_{\text{max}}} - VOL_{D_{\text{WI}}}}.$$

Statistical Analysis

Normally distributed continuous variables are shown as mean and SD or as median and interquartile range for non-normal dis-

tribution; discrete variables are reported as counts and percentages. Interrater agreement for visual CS was determined by κ statistics. Spearman rank correlation coefficients were used to analyze correlations between visual collateral scores and tissue outcomes. The level of significance was defined as a 2-tailed $P < .05$. Multiple linear regression analysis was performed to test for independent association of visual (CS_{CE-MRA} and CS_{TOF}) and automated (CI_{CE-MRA} and CI_{TOF}) collateral measures with respect to continuous tissue outcome parameters (FIV and PPS).

Patients were a priori stratified by dichotomizing tissue outcome (good-versus-poor). FIV was dichotomized at 90 mL, which has been shown to be most specific for poor clinical outcome in a patient population with major strokes with anterior proximal artery occlusion.²³ This highly specific cutoff for poor clinical outcome was chosen because it corresponds to a low rate of false-positives (low rate of falsely assuming poor outcome). A collateral measure that predicts FIV > 90 mL, therefore, indicates a high probability of futile recanalization with respect to clinical outcome, which is essential for treatment decisions when weighing benefits and risks.

PPS quantifies reperfusion in terms of tissue saved relative to ischemic core and penumbra. PPS was dichotomized at 50% to define effective reperfusion at the tissue level, which has been associated with good functional outcome in the Diffusion and Perfusion Imaging Evaluation for Understanding Stroke Evolution (DEFUSE) 2 trial.²⁴ Stratified patients (good-versus-poor outcomes) were compared by using an unpaired t test (normal distribution) and Mann-Whitney U rank sum test (non-normal distribution) for quantitative continuous or discrete variables and the Fischer exact test for qualitative categorical variables, respectively.

Receiver operating characteristic (ROC) curve analysis was performed to quantify the resolving power and optimal cutoff value of each collateral imaging measure, single and in combination, to classify patients into good and poor tissue outcome (FIV < 90 mL and PPS $> 50\%$). The collateral measures CS_{combined} and CI_{combined} were defined above to test whether the added vascular signal of both, TOF- and CE-MRA, has a higher discriminative power for outcome than either one by itself.

The best performing collateral measures for good tissue outcome were further used in stepwise multivariate logistic regression analysis including the 3 most relevant univariate predictors of infarct growth and penumbral loss (admission NIHSS score, DWI infarct volume, and age).²⁵⁻²⁷

To assess the relative benefit of recanalization dependent on collateral status, we calculated the odds ratio for good outcome in patients with and without recanalization (Online Appendix). Recanalization status was not included as a predictor in multivariate analysis because of statistical power.

The method of atlas-based collateral index to measure contrasted MCA vessels in CE-MRA secondary to retrograde filling via leptomeningeal collaterals was compared with DSA collateral scoring. DSA collateral scores were rated in intra-arterially treated patients and correlated with CI_{CE-MRA} . ROC curves between DSA and CI_{CE-MRA} for good outcome (FIV < 90 mL) were compared pair-wise (Online Appendix).

All data analysis was performed with SPSS Statistics 20.0 (IBM,

Table 1: Patient characteristics stratified by good and poor tissue-outcome parameters

Patient Characteristics ^a	Final			P	Penumbra		P
	All Patients	Infarct <90 mL	Infarct >90 mL		Saved >50%	Saved <50%	
Subjects (No.) (%)	44 (100.0)	29 (65.9)	15 (34.1)		33 (75.0)	11 (25.0)	
Age (yr) (mean ± SD)	69.3 (14.8)	65.9 (17.7)	71.0 (13.0)	.34	61.7 (18.1)	71.8 (12.8)	.05 ^b
Sex (female) (No.) (%)	28 (63.6)	18 (62.1)	10 (66.7)	1.00	21 (63.6)	7 (63.6)	1.00
Admit NIHSS (median, IQR)	14 (10.3–19.8)	14 (9.0–16.5)	18 (12.0–21.0)	.05 ^b	14 (9.5–19.0)	16 (14.0–20.0)	.13
Discharge NIHSS (median, IQR)	12 (4.0–19.3)	7 (3.0–14.0)	17 (9.0–23.0)	.01 ^b	9 (3.0–15.0)	17 (11.0–33.0)	.01 ^b
Left MCA infarction (No.) (%)	24 (54.5)	14 (48.3)	10 (66.7)	.34	16 (48.5)	8 (72.7)	.29
Vessel occlusion							
MI segment of MCA (No.) (%)	28 (63.6)	21 (72.4)	7 (46.6)	.11	22 (66.6)	6 (37.5)	.49
Carotid bifurcation/MI segment (No.) (%)	16 (36.4)	8 (27.6)	8 (53.3)	.11	11 (33.3)	5 (26.7)	.49
Treatment (No.) (%)	44 (100.0)						
Intravenous thrombolysis (No.) (%)	15 (34.1)	12 (41.4)	3 (20.0)	.19	12 (36.4)	3 (27.3)	.72
IA mechanical therapy (No.) (%)	29 (65.9)	17 (58.6)	12 (80.0)	.19	21 (63.6)	8 (72.7)	.72
Cardiovascular risk factors							
Hypertension (No.) (%)	30 (68.2)	19 (65.5)	11 (73.3)	.74	21 (63.6)	9 (81.8)	.46
Diabetes mellitus (No.) (%)	7 (15.9)	5 (17.2)	2 (13.3)	1.00	4 (12.1)	3 (27.3)	.34
Coronary heart disease (No.) (%)	8 (18.2)	6 (20.7)	2 (13.3)	.70	7 (21.2)	1 (9.1)	.66
Atrial fibrillation (No.) (%)	22 (50.0)	15 (51.7)	7 (46.7)	1.00	17 (51.5)	5 (45.5)	1.00
Smoking (No.) (%)	8 (18.2)	4 (13.8)	4 (26.7)	.41	6 (18.2)	2 (18.2)	1.00
Etiology							
Atherothrombotic (No.) (%)	16 (36.4)	12 (41.4)	4 (26.7)	.51	11 (33.3)	5 (45.5)	.49
Cardioembolic (No.) (%)	18 (40.9)	12 (41.4)	6 (40.0)	1.00	15 (45.5)	3 (27.3)	.48
Undetermined etiology (No.) (%)	5 (11.4)	3 (10.3)	2 (13.3)	.64	4 (12.1)	1 (9.1)	1.00
Other etiology (No.) (%)	5 (11.4)	2 (6.9)	3 (20.0)	.31	3 (9.1)	2 (18.2)	.59

Note:—IA indicates intra-arterial; IQR, interquartile range.

^a Continuous and discrete quantitative variables compared with the unpaired *t* test and Mann-Whitney *U* rank sum test, respectively. Qualitative categorical variables compared with the Fischer exact test.

^b Significant.

Table 2: Imaging parameters and collateral measures (visual and automated TOF- and CE-MRA)

Imaging Parameters ^a	Final			P	Penumbra		P
	All Patients	Infarct <90 mL	Infarct >90 mL		Saved >50%	Saved <50%	
Tissue imaging measurements							
Admit DWI infarct volume (mL) (mean ± SD)	30.8 (41.0)	16.3 (18.9)	59.0 (56.2)	.01 ^b	22.6 (27.0)	55.5 (63.3)	.12
Final DWI infarct volume (mL) (mean ± SD)	89.4 (114.9)	25.3 (26.3)	213.4 (119.1)	<.01 ^b	42.5 (47.8)	230.2 (142.8)	.01 ^b
Penumbra saved (%) (mean ± SD)	68.5 (39.2)	88.4 (22.2)	30.0 (36.5)	<.01 ^b	89.5 (14.2)	5.7 (12.9)	<.01 ^b
Admit Tmax volume (mL) (mean ± SD)	182.0 (97.0)	158.3 (70.5)	227.8 (124.7)	.06	189.5 (81.0)	159.5 (136.9)	.50
Successful recanalization (No.) (%)	32 (73)	25 (86)	7 (47)	.01 ^b	27 (82)	5 (45)	.05 ^b
Visual collateral score (range, 0–2)							
TOF-CS (mean ± SD)	.1 (.3)	.1 (.4)	.0 (.0)	.30	.0 (.2)	.2 (.6)	.39
CE-CS (mean ± SD)	1.0 (.8)	1.3 (.7)	.4 (.6)	<.01 ^b	1.1 (.8)	.6 (.8)	.01 ^b
Atlas-based collateral index (range, 0–1)							
TOF-CI (mean ± SD)	.39 (.09)	.42 (.07)	.35 (.09)	.01 ^b	.42 (.07)	.32 (.07)	<.01 ^b
CE-CI (mean ± SD)	.70 (.21)	.81 (.10)	.49 (.20)	<.01 ^b	.77 (.12)	.49 (.26)	.01 ^b

^a Continuous and discrete imaging parameters compared with the unpaired *t* test and Mann-Whitney *U* rank sum test, respectively.

^b Significant.

Armonk, New York) and Wolfram Mathematica 7.0 software (<http://www.wolfram.com/mathematica/>).

RESULTS

The study included 44 patients with anterior circulation proximal occlusive strokes. Patients stratified by good-versus-poor tissue outcome and reperfusion (FIV < 90 mL and PPS > 50%) were comparable and not significantly different with regard to sex, side of occlusion, treatment, risk factors, and stroke etiology. The discharge NIHSS score was significantly higher in patients with poor tissue outcome parameters; age was lower in patients with PPS > 50% (Table 1). With regard to group statistics of imaging parameters (Table 2), visual CS_{CE-MRA} but not CS_{TOF} was significantly higher in patients with good outcome (FIV < 90 mL and PPS > 50%). Atlas-based CI_{CE-MRA} and CI_{TOF} were both significantly higher in patients with good outcome.

Visual Collateral Scores

Visual CS_{TOF} and CS_{CE-MRA} were acquired with high interrater reliability (0.71 and 0.70, respectively). CS_{CE-MRA} correlated with FIV (Spearman $\rho = -0.48$, $P = .001$) but not PPS ($\rho = 0.26$, $P = .08$). CS_{TOF} did not correlate significantly with either tissue outcome parameter ($\rho = -0.25$, $P = .1$ and $\rho = 0.16$, $P = .3$, respectively). Accordingly, in multiple regression analysis, including both collateral scores, there was no independent predictive contribution of CS_{TOF} to tissue outcome and only CS_{CE-MRA} produced significant regression coefficients (FIV: $\beta = -65.97$, $P = .004$, $R^2 = 0.22$; PPS: $\beta = 0.21$, $P = .01$, $R^2 = 0.11$).

Atlas-Based Collateral Index

Atlas-based collateral signal significantly correlated with FIV and PPS. CI_{CE-MRA} was more strongly correlated with FIV ($\rho = -0.70$, $P < .001$) and PPS ($\rho = 0.59$, $P < .001$) than CI_{TOF} with

Table 3: ROC curve analysis of visual and automated collateral measured for discriminating good tissue outcome (FIV < 90 mL and PPS > 50%)

Collateral Measure	Final Infarct <90 mL						Penumbra Saved >50%					
	AUC (± SE)	P	Optimal Criterion	Youden Index	Sens. (%)	Spec. (%)	AUC (± SE) ^a	P	Optimal Criterion	Youden Index	Sens. (%)	Spec. (%)
Visual scoring (CS)												
CE-MRA	.81 (.07)	<.01 ^b	≥1	.53	86.2	66.7	.67 (.10)	.04 ^b	>1	.27	36.4	90.9
TOF	.53 (.02)	.15	≥1	–	–	–	.53 (.05)	.52	–	–	–	–
TOF + CE-MRA	.81 (.07)	<.01 ^b	≥1	.53	86.2	66.7	.65 (.10)	.16	–	–	–	–
Atlas-based collateral index (CI)												
CE-MRA	.94 (.04)	<.01 ^b	>.68	.76	89.7	86.7	.83 (.10)	<.01 ^b	>.64	.70	87.9	81.8
TOF	.74 (.08)	.01 ^b	>.37	.43	75.9	66.7	.86 (.06)	<.01 ^b	>.38	.58	75.8	81.8
TOF + CE-MRA	.95 (.03)	<.01 ^b	>1.13	.80	86.2	93.3	.89 (.08)	<.01 ^b	>1.05	.76	84.9	9.9

Note:—Sens. indicates sensitivity; Spec., specificity.

^a AUC indicates area under the ROC curve with associated significance level *P*. Optimal criterion defines collateral parameter cutoff for maximized sensitivity and specificity by the Youden index.

^b Significant.

FIV ($\rho = -0.49, P < .001$) and PPS (0.41, $P < .006$). Both modalities (CI_{TOF} and CI_{CE-MRA}) contributed independently in multiple regression to FIV (CI_{CE-MRA}: $\beta = -430.04, P < .001$; CI_{TOF}: $\beta = -430.51, P < .001$; $R^2 = 0.89$) and PPS (CI_{CE-MRA}: $\beta = 1.13, P < .001$; CI_{TOF}: $\beta = 1.16, P = .04$; $R^2 = 0.54$).

Visual CS_{CE-MRA} and atlas-based CI_{CE-MRA} correlated significantly (Spearman $\rho = 0.44, P = .003$). Visual CS_{TOF} and atlas-based CI_{TOF} did not correlate significantly (Spearman $\rho = 0.07, P = .67$).

CI_{CE-MRA} and DSA collateral scores correlated significantly with comparable discriminative power for good outcome (Online Appendix). Volume of Tmax ischemia in admission imaging was negatively correlated with CI_{CE-MRA} (Pearson correlation coefficient = $-0.33, P = .03$).

ROC Curve Analysis

According to ROC curve analysis (Table 3), the discriminative power of visual CS_{CE-MRA} for good infarct outcome (FIV < 90 mL) was high (AUC = 0.81; $P < .01$). Visual CS_{TOF} performed poorly (AUC = 0.53, $P = .15$) without benefit using CS_{combined} (AUC = 0.81, $P < .01$). The discriminative power of visual scoring for effective reperfusion (PPS > 50%) was overall low (CS_{CE-MRA}: AUC = 0.67, $P = .04$; CS_{TOF}: AUC = 0.53, $P = .52$). The discriminative power of atlas-based CI was higher for both tissue outcome parameters. For FIV < 90 mL, the overall best discriminator was CI_{CE-MRA} without significant benefit in combination with TOF (CI_{CE-MRA}: AUC = 0.94, $P < .01$; CI_{combined}: AUC = 0.95, $P < .01$). For effective reperfusion (PPS > 50%) both CI_{CE-MRA} and CI_{TOF} showed high AUC (AUC = 0.83, $P < .001$; AUC = 0.86, $P < .001$, respectively), and CI_{combined} performed best (AUC = 0.89, $P < .001$).

The best performing collateral measures by ROC curve analysis, CI_{CE-MRA} for infarct outcome (Fig 2A) and CI_{combined} for penumbral reperfusion (Fig 2B), were tested in multivariate logistic regression including admission NIHSS score, admission DWI volume, and age (Tables 4). For prediction of good infarct outcome, only CI_{CE-MRA} remained in the model, with significant independent predictive coefficients (Fig 2B). For prediction of good penumbral reperfusion, only CI_{combined} and age remained in the model with significant coefficients (Fig 2D).

Favorable odds for good outcome after recanalization was demonstrated in patients with good collaterals (defined by

CI_{CE-MRA} cutoff of >0.68 in Table 3). The odds ratio for good outcome in recanalizers with good collateral status versus recanalizers with poor collateral status was 7.9 ($P < .05$). The odds ratio for good outcome in nonrecanalizers with good collateral status versus nonrecanalizers with poor collateral status was not significant ($P = .11$).

DISCUSSION

In acute stroke triage, TOF-MRA and CE-MRA are frequently used sensitive methods for detecting large-vessel occlusion.^{11,12,14,28} Collateralized vessels distal to the proximal occlusion are visualized with higher intensity in CE-MRA than in flow-weighted TOF-MRA.¹¹ However, a systematic collateral assessment in MRA, taking into account the differing vessel signal information contained in each MR imaging protocol for prediction of tissue outcome, has not been reported so far.¹³ The main purpose of this study was to prove the hypothesis that the MRA imaging-based surrogate marker of collateral supply is a predictor of tissue outcome. We measured the MRA collateral signal by a rater-independent and reproducible method to show how TOF- and CE-MRA signal differentially predict outcome. This may be particularly useful in future studies that rely on objective measures of collateral supply. In terms of clinical feasibility and immediate impact on care, rater-based scores are fast and easily applied; therefore, we included the evaluation of visual scoring.

Consistent with prior angiographic studies, our dataset confirms that in stroke patients with acute proximal anterior arterial occlusion, the existence of good collateral status assessed by MRA is associated with a high percentage of penumbra saved (ie, greater reperfusion at the tissue level) and lower final infarct lesion volume (Table 2).^{1,6,29,30} However, this association depends on the MRA technique and method of collateral quantification.

For visual assessment, CE-MRA collateral scoring was the best discriminator for classifying patients into good and poor tissue outcome (FIV < 90 mL, best cutoff ≥ 1 ; AUC = 0.81). The results suggest that no visible collaterals in CE-MRA (CS_{CE-MRA} = 0) reliably identify patients with poor outcome and high probability of futile recanalization. CE-MRA scoring was only a moderate discriminator (best cutoff > 1, AUC = 0.67) for effective penumbral reperfusion (PPS > 50%). Collateral scoring by TOF-MRA

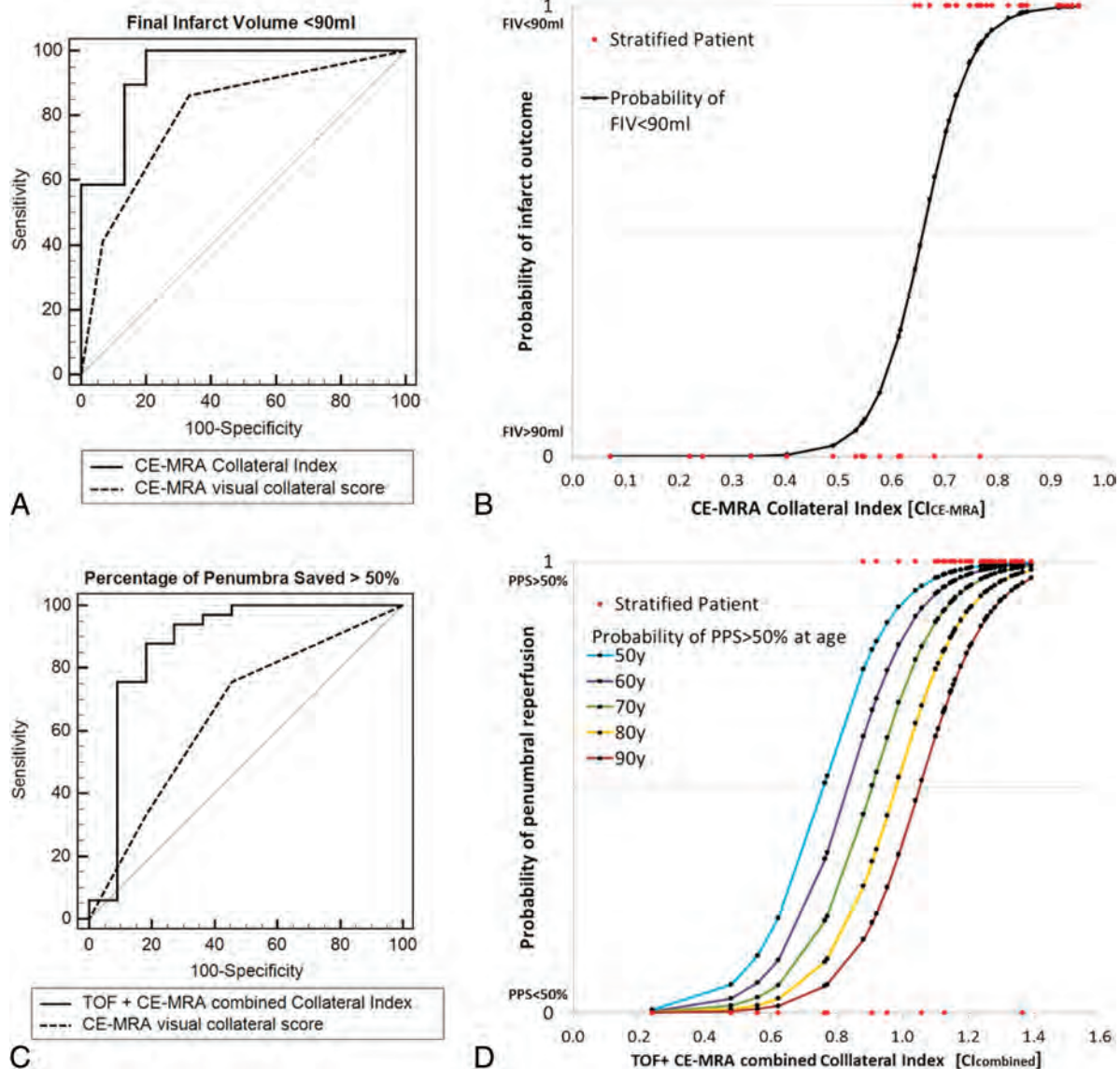


FIG 2. A and C, ROC curve analysis of best performing visual and atlas-based collateral measures (CS_{CE-MRA} and CI_{CE-MRA}) for discriminating good tissue outcome (FIV < 90 mL) and reperfusion (PPS > 50%). B, Probability curve of FIV < 90 mL with increasing CI_{CE-MRA} calculated from the logit model by using the retained significant coefficients in Table 4. D, Probability curves of PPS > 50% with increasing $CI_{combined}$ and age, calculated from the logit model by using the retained significant coefficients in Table 4.

Table 4: Multivariate logistic regression of best collateral measure, admission NIHSS score, admission DWI volume, and age for prediction of good tissue outcome

	Final Infarct <90 mL		Penumbra Saved >50%	
	β -Coefficient	P	β -Coefficient	P
CI_{CE-MRA}	22.05 (7.33)	<.01 ^a		
$CI_{combined}$			9.56 (3.09)	<.01 ^a
Admission DWI infarct volume	-.27 (.24)	.26	.01 (.02)	.73
Admission NIHSS score	.46 (.49)	.34	-.01 (.12)	.94
Age (yr)	-.09 (.10)	.35	.07 (.04)	.05 ^a
Intercept β_0	14.55		13.6	

^a Significant.

alone performed poorly, and there was no multivariate additive benefit when using combined visual TOF- and CE-MRA collateral scores.

The reason for the overall poor discriminative power of visual TOF-MRA collateral assessment for prediction of FIV and PPS

may be rooted within the inherent limitations of the TOF technique. The comparably long acquisition time more frequently leads to movement artifacts and degradation of image quality in comparison with CE-MRA.¹⁴ Among excluded screened cases due to poor image quality, 13 showed severe movement artifacts in TOF-MRA, but only 5 in CE-MRA. Further signal elimination in TOF-MRA may occur with a venous presaturation pulse saturating retrograde collateral arterial flow in the venous direction. Most important, TOF-MRA signal is highly susceptible to slow or in-plane blood flow due to saturation effects; therefore, slow collateral flow may not be displayed adequately, leading to an underestimation of collateral supply.^{7,10,11}

In CE-MRA, the paramagnetic effect of the contrast agent provides a nearly flow-independent signal with real luminal filling allowing a better delineation of slow-moving blood in distal intracranial arteries, even though the spatial resolution of CE-MRA

is lower compared with TOF.¹⁰ A disadvantage may be venous contamination of the CE-MRA signal. Large veins and sinus were excluded in visual scoring and were suppressed by low voxel probability in the atlas-based collateral index, but smaller draining veins may not be differentiated from arterial vasculature. However, this limitation may not be a disadvantage with respect to tissue outcome prediction. It is conceivable that signal from venous outflow could be indicative of collateralized tissue.

Computer-assisted image analysis was used to provide a continuous rater-independent imaging parameter for collateral status. In contrast to visual scoring, the overall discriminative power of atlas-based CI was higher for both tissue outcome parameters. The collateral index of CE-MRA was a reliable predictor of final infarct outcome (CI_{CE-MRA} : AUC = 0.94). Using the additional signal of TOF in combination with CE-MRA did not yield a significant predictive benefit ($CI_{combined}$: AUC = 0.95). However, the collateral index of TOF significantly contributed to prediction of penumbral reperfusion, which was best predicted by the combined TOF- and CE-MRA signal ($CI_{combined}$: AUC = 0.89). This observation may be linked to the physiologic concept of perfusion mismatch between low blood flow and blood volume for penumbral imaging.³¹ The apparent discrepancy of collateral signal when comparing TOF-MRA with CE-MRA may be a surrogate imaging feature for predicting tissue outcome. It is conceivable that a patient with adequate collateral signal in CE-MRA is likely to have better outcome if there is additional collateral signal in TOF-MRA (higher flow) compared with a patient who has a similarly adequate signal in CE-MRA but none in TOF-MRA (low flow). Thus, in analogy to “perfused tissue-at-risk,” a lower flow-weighted relative collateral signal in TOF concurrent with high blood volume-weighted collateral signal in CE-MRA could be an indicator for “collateralized tissue-at-risk.”

Only automated CI_{TOF} but not visual CS_{TOF} showed significant resolving power for penumbral reperfusion, and CS_{TOF} correlated poorly with CI_{TOF} . A reason may be that atlas-based analysis is not subject to rater variability and includes the signal intensity of all voxels with high vascular probability regardless of belonging to visual tubular structures. A further reason may be due to the type of data scale. The collateral index, being a continuous imaging parameter, has a higher scale-based precision than discrete collateral scoring. The significance of visual TOF- and CE-MRA collateral mismatch for tissue outcome may be proved with a larger study population.

The best-performing collateral measures, CI_{CE-MRA} for good infarct outcome (FIV < 90 mL) and $CI_{combined}$ for good penumbral reperfusion (PPS > 50%), were highly predictive against other known important prognostic factors (admission NIHSS score, age, admission DWI volume) by multivariate logistic regression. The curves from the logistic regression model (Fig 2B and 2D) show how the probability of good outcome increases with increasing favorable collateral measure independent of other variables included in the model. The results are important with respect to prior studies showing that collateral flow assessed by DSA or CTA is an independent predictor of outcome with respect to other known prognostic factors such as age, clinical stroke se-

verity, baseline imaging characteristics, occlusion site, treatment, and recanalization.^{1,3,7,29,32}

The treatment effect of recanalization on final infarct was dependent on collateral status (On-line Appendix). The odds for good tissue outcome were higher in recanalizers when good collaterals were present in CE-MRA compared with recanalizers with poor collaterals (odds ratio = 7.9, $P < .05$). Our results by odds ratios support the hypothesis that a favorable collateral status is required for good tissue outcome after recanalization. Thus, collateral assessment based on CE-MRA may augment patient selection in stroke triage and improve the benefit of treatment decisions.

Our study has limitations by design. For retrospective analysis, we defined a priori consecutively applied strict inclusion criteria. The inclusion criteria were chosen to focus on a homogeneous first-ever population of stroke patients with isolated proximal anterior circulation occlusions within definite imaging time windows. Consequently, the relatively small study size limited further multivariate analyses and stratification by recanalization status, stroke laterality, time to imaging, or treatment. Moreover, there may be selection bias inadvertently introduced by inclusion criteria of image technique and quality. Stratification by chosen imaging-based end points, even though specific for our study population, only indirectly relates to functional outcome.^{23,24} Further studies should include end points of long-term functional outcome. Rare cases with parenchymal hemorrhage and mass effect were a priori excluded to focus on prediction of ischemic tissue damage. Nonetheless, hemorrhagic infarction, if present, is a factor for poor clinical outcome in major strokes.

Results may not be translated to all types of TOF imaging protocols. For the 1.5T MR imaging scanner in this study, we used a standard TOF protocol for a fast clinical routine in stroke triage with sufficient visualization of major secondary and tertiary arterial branches. Collateral resolving power for outcome classification may improve considerably at higher field strengths with increased conspicuity of distal vessel segments combined with increased spatial imaging resolution.³³ Furthermore, at the expense of limited acquisition time in stroke imaging, additional contrast could be achieved by using a superior saturation band and magnetization transfer contrast or by variation of saturation flip angles.

CONCLUSIONS

In ischemic stroke patients with proximal anterior circulation occlusion, visual collateral scoring of CE- but not TOF-MRA is a reliable predictor of infarct outcome. CE- and TOF-MRA both contain predictive signal information for penumbral reperfusion by quantitative atlas-based collateral assessment. Further research should target and differentiate flow- and blood volume-dependent signal of collateralized vasculature in stroke MR imaging for outcome prediction and patient stratification.

Disclosures: Jens Fiehler—UNRELATED: Consultancy: Codman, Stryker, MicroVention; Grants/Grants Pending: Codman, Stryker, MicroVention; Payment for Lectures (including service on Speakers Bureaus): Penumbra, Philips, Covidien; Travel/Accommodations/Meeting Expenses Unrelated to Activities Listed: Covidien.* *Money paid to the institution.

REFERENCES

- Miteff F, Levi CR, Bateman GA, et al. **The independent predictive utility of computed tomography angiographic collateral status in acute ischaemic stroke.** *Brain* 2009;132:2231–38
- Christoforidis GA, Mohammad Y, Kehagias D, et al. **Angiographic assessment of pial collaterals as a prognostic indicator following intra-arterial thrombolysis for acute ischemic stroke.** *AJNR Am J Neuroradiol* 2005;26:1789–97
- Bang OY, Saver JL, Buck BH, et al. **Impact of collateral flow on tissue fate in acute ischaemic stroke.** *J Neurol Neurosurg Psychiatry* 2008;79:625–29
- Bang OY, Saver JL, Kim SJ, et al. **Collateral flow predicts response to endovascular therapy for acute ischemic stroke.** *Stroke* 2011;42:693–99
- Fiehler J, Remmele C, Kucinski T, et al. **Reperfusion after severe local perfusion deficit precedes hemorrhagic transformation: an MRI study in acute stroke patients.** *Cerebrovasc Dis* 2005;19:117–24
- Kim JJ, Fischbein NJ, Lu Y, et al. **Regional angiographic grading system for collateral flow: correlation with cerebral infarction in patients with middle cerebral artery occlusion.** *Stroke* 2004;35:1340–44
- Ishimaru H, Ochi M, Morikawa M, et al. **Accuracy of pre- and post-contrast 3D time-of-flight MR angiography in patients with acute ischemic stroke: correlation with catheter angiography.** *AJNR Am J Neuroradiol* 2007;28:923–26
- Maas MB, Lev MH, Ay H, et al. **Collateral vessels on CT angiography predict outcome in acute ischemic stroke.** *Stroke* 2009;40:3001–05
- Souza LC, Yoo AJ, Chaudhry ZA, et al. **Malignant CTA collateral profile is highly specific for large admission DWI infarct core and poor outcome in acute stroke.** *AJNR Am J Neuroradiol* 2012;33:1331–36
- Yang JJ, Hill MD, Morrish WF, et al. **Comparison of pre- and post-contrast 3D time-of-flight MR angiography for the evaluation of distal intracranial branch occlusions in acute ischemic stroke.** *AJNR Am J Neuroradiol* 2002;23:557–67
- Alfke K, Jensen U, Pool C, et al. **Contrast-enhanced magnetic resonance angiography in stroke diagnostics: additional information compared with time-of-flight magnetic resonance angiography?** *Clin Neuroradiol* 2011;21:5–10
- Schellinger PD, Jansen O, Fiebich JB, et al. **Feasibility and practicality of MR imaging of stroke in the management of hyperacute cerebral ischemia.** *AJNR Am J Neuroradiol* 2000;21:1184–89
- McVerry F, Liebeskind DS, Muir KW. **Systematic review of methods for assessing leptomeningeal collateral flow.** *AJNR Am J Neuroradiol* 2012;33:576–82
- Bash S, Villablanca JP, Jahan R, et al. **Intracranial vascular stenosis and occlusive disease: evaluation with CT angiography, MR angiography, and digital subtraction.** *AJNR Am J Neuroradiol* 2005;26:1012–21
- Broderick JP, Palesch YY, Demchuk AM, et al. **Endovascular therapy after intravenous t-PA versus t-PA alone for stroke.** *N Engl J Med* 2013;368:893–903
- Forkert ND, Cheng B, Kemmling A, et al. **ANTONIA perfusion and stroke: a software tool for the multi-purpose analysis of MR perfusion-weighted datasets and quantitative ischemic stroke assessment.** *Methods Inf Med* 2014;53:469–81
- Forkert ND, Fiehler J, Suniaga S, et al. **A statistical cerebroarterial atlas derived from 700 MRA datasets.** *Methods Inf Med* 2013;52:467–74
- Davis SM, Donnan GA, Parsons MW, et al. **Effects of alteplase beyond 3 h after stroke in the Echoplanar Imaging Thrombolytic Evaluation Trial (EPITHET): a placebo-controlled randomised trial.** *Lancet Neurol* 2008;7:299–309
- Albers GW, Thijs VN, Wechsler L, et al. **Magnetic resonance imaging profiles predict clinical response to early reperfusion: the diffusion and perfusion imaging evaluation for understanding stroke evolution (DEFUSE) study.** *Ann Neurol* 2006;60:508–17
- Wheeler HM, Mlynash M, Inoue M, et al. **Early diffusion-weighted imaging and perfusion-weighted imaging lesion volumes forecast final infarct size in DEFUSE 2.** *Stroke* 2013;44:681–85
- Campbell BC, Christensen S, Levi CR, et al. **Comparison of computed tomography perfusion and magnetic resonance imaging perfusion-diffusion mismatch in ischemic stroke.** *Stroke* 2012;43:2648–53
- Olivot JM, Mlynash M, Thijs VN, et al. **Optimal Tmax threshold for predicting penumbral tissue in acute stroke.** *Stroke* 2009;40:469–75
- Yoo AJ, Chaudhry ZA, Nogueira RG, et al. **Infarct volume is a pivotal biomarker after intra-arterial stroke therapy.** *Stroke* 2012;43:1323–30
- Lansberg MG, Straka M, Kemp S, et al. **MRI profile and response to endovascular reperfusion after stroke (DEFUSE 2): a prospective cohort study.** *Lancet Neurol* 2012;11:860–67
- König IR, Ziegler A, Bluhmki E, et al. **Predicting long-term outcome after acute ischemic stroke: a simple index works in patients from controlled clinical trials.** *Stroke* 2008;39:1821–26
- Yoo AJ, Barak ER, Copen WA, et al. **Combining acute diffusion-weighted imaging and mean transit time lesion volumes with National Institutes of Health Stroke Scale Score improves the prediction of acute stroke outcome.** *Stroke* 2010;41:1728–35
- Jung S, Gilgen M, Slotboom J, et al. **Factors that determine penumbral tissue loss in acute ischaemic stroke.** *Brain* 2013;136:3554–60
- Jauch EC, Saver JL, Adams HP Jr, et al. **Guidelines for the early management of patients with acute ischemic stroke: a guideline for healthcare professionals from the American Heart Association/American Stroke Association.** *Stroke* 2013;44:870–947
- Kucinski T, Koch C, Eckert B, et al. **Collateral circulation is an independent radiological predictor of outcome after thrombolysis in acute ischaemic stroke.** *Neuroradiology* 2003;45:11–18
- Liebeskind DS, Tomsick T, Foster LD, et al. **Collaterals at angiography and outcomes in the Interventional Management of Stroke (IMS) III trial.** *Stroke* 2014;45:645–51
- Bivard A, Spratt N, Levi C, et al. **Perfusion computer tomography: imaging and clinical validation in acute ischaemic stroke.** *Brain* 2011;134:3408–16
- Tan IY, Demchuk AM, Hopyan J, et al. **CT angiography clot burden score and collateral score: correlation with clinical and radiologic outcomes in acute middle cerebral artery infarct.** *AJNR Am J Neuroradiol* 2009;30:525–31
- Heverhagen JT, Bourekas E, Sammet S, et al. **Time-of-flight magnetic resonance angiography at 7 Tesla.** *Invest Radiol* 2008;43:568–73

Effects of Agmatine on Blood-Brain Barrier Stabilization Assessed by Permeability MRI in a Rat Model of Transient Cerebral Ischemia

S.S. Ahn, S.H. Kim, J.E. Lee, K.J. Ahn, D.J. Kim, H.S. Choi, J. Kim, N.-Y. Shin, and S.-K. Lee



ABSTRACT

BACKGROUND AND PURPOSE: BBB disruption after acute ischemic stroke and subsequent permeability increase may be enhanced by reperfusion. Agmatine has been reported to attenuate BBB disruption. Our aim was to evaluate the effects of agmatine on BBB stabilization in a rat model of transient cerebral ischemia by using permeability dynamic contrast-enhanced MR imaging at early stages and subsequently to demonstrate the feasibility of dynamic contrast-enhanced MR imaging for the investigation of new therapies.

MATERIALS AND METHODS: Thirty-four male Sprague-Dawley rats were subjected to transient MCA occlusion for 90 minutes. Immediately after reperfusion, agmatine (100 mg/kg) or normal saline was injected intraperitoneally into the agmatine-treated group ($n = 17$) or the control group, respectively. MR imaging was performed after reperfusion. For quantitative analysis, regions of interest were defined within the infarct area, and values for volume transfer constant, rate transfer coefficient, volume fraction of extravascular extracellular space, and volume fraction of blood plasma were obtained. Infarct volume, infarct growth, quantitative imaging parameters, and numbers of factor VIII–positive cells after immunohistochemical staining were compared between control and agmatine-treated groups.

RESULTS: Among the permeability parameters, volume transfer constant and volume fraction of extravascular extracellular space were significantly lower in the agmatine-treated group compared with the control group (0.05 ± 0.02 minutes⁻¹ versus 0.08 ± 0.03 minute⁻¹, $P = .012$, for volume transfer constant and 0.12 ± 0.06 versus 0.22 ± 0.15 , $P = .02$ for volume fraction of extravascular extracellular space). Other permeability parameters were not significantly different between the groups. The number of factor VIII–positive cells was less in the agmatine-treated group than in the control group (3-fold versus 4-fold, $P = .037$).

CONCLUSIONS: In ischemic stroke, agmatine protects the BBB, which can be monitored in vivo by quantification of permeability by using dynamic contrast-enhanced MR imaging. Therefore, dynamic contrast-enhanced MR imaging may serve as a potential imaging biomarker for assessing the BBB stabilization properties of pharmacologic agents.

ABBREVIATIONS: DCE = dynamic contrast-enhanced; K^{trans} = volume transfer constant

BBB disruption occurs within 1–2 hours after acute ischemic stroke by inflammatory cytokines and proteases.¹ Although thrombolysis has been increasingly used for the treatment of acute ischemic stroke, reperfusion after thrombolytic therapy has been reported to enhance BBB breakdown and, consequently, symptomatic hemorrhagic transformation, which is a fatal complica-

tion of ischemic stroke.^{2,3} Therefore, evaluation of the therapeutic effect of a BBB blocking agent is important to improve treatment outcomes in patients with stroke. One can estimate the permeability properties of the BBB by using various techniques; however, many of these methods are invasive or suitable only for animal models.⁴ Many studies have used MR imaging to measure BBB permeability to develop a feasible clinical technique for evaluating the integrity of the BBB and predicting hemorrhagic transformation in acute ischemic stroke.^{5–7} Dynamic contrast-enhanced (DCE)-MR imaging by using contrast agents, an emerging MR imaging technique based on kinetic modeling of microvascular permeability, enables quantification of BBB breakdown.⁸ A recent animal study reported that increased permeability measured by MR imaging correlates well with BBB disruption and hemorrhagic transformation on histology.⁹

A number of investigators have explored the use of neuroprotective drugs in animal experimental models to salvage regions of

Received April 28, 2014; accepted after revision July 31.

From the Department of Radiology and the Research Institute of Radiological Science (S.S.A., D.J.K., J.K., N.-Y.S., S.-K.L.), Department of Pathology (S.H.K.), Brain Research Institute, and Department of Anatomy (J.E.L.), Yonsei University College of Medicine, Seoul, Republic of Korea; and Department of Radiology (K.J.A., H.S.C.), The Catholic University College of Medicine, Seoul, Seoul, Republic of Korea.

Please address correspondence to Seung-Koo Lee, MD, PhD, Department of Radiology and the Research Institute of Radiological Science, Yonsei University College of Medicine, 50 Yonsei-ro, Seodaemun-gu, Seoul 120-752, Republic of Korea; e-mail: slee@yuhs.ac, lee.seungkoo@gmail.com

Evidence-Based Medicine Level 2.

<http://dx.doi.org/10.3174/ajnr.A4113>

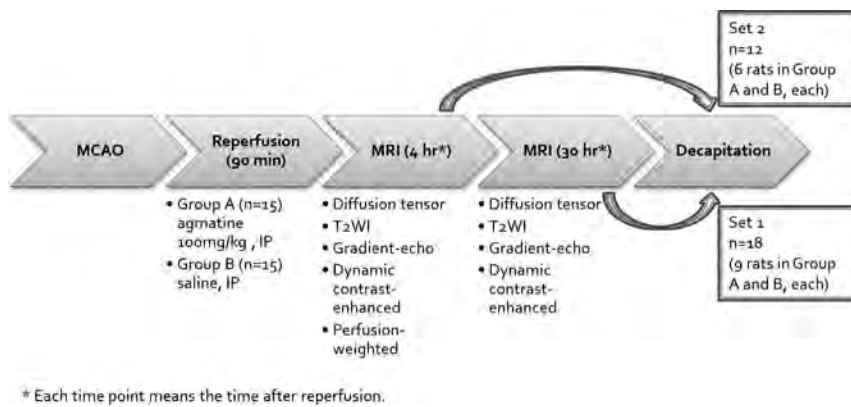


FIG 1. Flowchart overview of the experimental protocols.

ischemia and to minimize reperfusion injury.^{10–12} Agmatine is a primary amine formed by decarboxylation of L-arginine and has been shown to protect neurons by blocking the *N*-methyl-*D*-aspartate receptor or nitric oxide synthase.¹³ Because a previous animal study reported that agmatine showed a protective effect in rodent models of neurotoxic and ischemic brain injuries,¹⁴ many additional studies have also shown beneficial effects of agmatine and its mechanisms.^{15–17} Another recent study also suggested that agmatine attenuated BBB disruption and consequently reduced brain swelling when administered at the time of reperfusion.¹¹

Therefore, the aim of this study was to quantitatively evaluate the BBB stabilization effect of agmatine in rat models of transient cerebral ischemia by using DCE-MR imaging at early stages and subsequently to demonstrate the feasibility of DCE-MR imaging for the investigation of new therapies.

MATERIALS AND METHODS

Animal Preparation

All animal procedures were performed according to a protocol approved by the Institutional Animal Care and Use Committee in accordance with National Institutes of Health guidelines. Thirty-four male Sprague-Dawley rats (Orient Bio, Seongnam, Korea) weighing 250–300 g were subjected to transient middle cerebral artery occlusion. Animals were anesthetized with Xylazine, 10 mg/kg, and Zoletil, a combination of tiletamine and zolazepam, 30 mg/kg, intraperitoneally. Rectal temperature was maintained at 37°C by a heating pad during the operation. The depth of anesthesia was assessed by toe pinch every 15 minutes. Middle cerebral artery occlusion was induced by using the filament model as previously described.¹⁸ Briefly, under an operating microscope, an uncoated 23-mm segment of 4–0 polypropylene monofilament suture with the tip rounded by flame was inserted into the arteriotomy and advanced into the internal carotid artery approximately 19–20 mm from the bifurcation to occlude the ostium of the middle cerebral artery. After 90 minutes, the suture was withdrawn and surgical incisions were closed. The animal was allowed to awaken and recover with free access to food and water. We injected 100 mg/kg of agmatine mixed in normal saline solution intraperitoneally immediately after reperfusion in the agmatine-treated group ($n = 17$). In the experimental control group, the animals received an equivalent volume of normal saline ($n = 17$). The experimental design is shown in Fig 1. Four rats were excluded because they died before MR imaging acquisition (2 rats in the agmatine-

treated group and 2 rats in the control group). Seven rats died after MR imaging acquisition and before we obtained pathologic specimens (2 rats in the agmatine-treated group and 5 rats in the control group), and they were included only for image analysis.

Image Acquisition

After anesthesia with Rumpun, 10 mg/kg, and Zoletil, 30 mg/kg, intraperitoneally, MR imaging was performed by using a 3T system (Achieva; Philips, Best, Netherlands) and an 8-channel coil. Animals were divided into 2 sets to correlate MR

imaging with histopathology at 2 different stages. MR imaging was performed 4 and 30 hours after reperfusion in 18 rats (set 1: $n = 9$ agmatine-treated, $n = 9$ controls) and only 4 hours after reperfusion in 12 rats (set 2: $n = 6$ agmatine-treated, $n = 6$ controls) before obtaining the specimens. All images were obtained in the coronal plane with a 60-mm FOV. Pre- and postcontrast T1-weighted (TR/TE, 625/18 ms), T2-weighted (TR/TE, 2006/80 ms), and T2*-weighted (TR/TE, 549/16 ms) images were acquired with 2-mm section thickness, 0.2-mm section gap, and 192×192 matrix. Diffusion-tensor imaging was performed by applying 6 different directions of orthogonal diffusion gradients and b-values of 600 and 0 s/mm^2 (TR/TE, 3327/52 ms; 2-mm section thickness; 0.2-mm section gap; 128×128 matrix). To achieve quantitative hemodynamic measurements of cerebral permeability and perfusion, we injected 2 boluses via tail veins. The first bolus of contrast was administered to measure permeability and served as a preload bolus for the perfusion scans. For DCE-MR imaging, precontrast 3D T1-weighted images were obtained with the following parameters: TR/TE, 13.2/6.5 ms; 112×112 mm matrix; 2-mm section thickness; 0.2-mm section gap; and flip angle, 5°.

After the precontrast scan, 60 dynamic contrast-enhanced T1-weighted images were obtained with the same MR imaging parameters except for an increased flip angle of 15°. After acquisition of the fifth image volume, gadolinium-based contrast, gadobutrol (Gadavist, 0.2 mmol/kg; Bayer Schering Pharma, Berlin, Germany) was injected. The total scan time for DCE-MR imaging was 4 minutes 30 seconds with a temporal resolution of 4.5 seconds. Perfusion-weighted imaging (the rapid principles of echo shifting with a train of observations; TR/TE, 26.6/38.2 ms; 64×64 matrix) with 60 dynamic scans was performed following injection of the second bolus of Gadavist (0.2 mmol/kg) 4 hours after reperfusion. Relative cerebral blood volume maps were acquired by using commercially available postprocessing software (ViewForum; Philips), and reperfusion status was examined. All animals showed >90% relative cerebral blood volume of the contralateral hemisphere.

Image Analysis

Quantitative imaging analysis was performed by an investigator (a neuroradiologist with 4 years of experience) blinded to the treatments. First, DICOM data of diffusion-tensor imaging were transferred to a commercial software package (nordicICE;

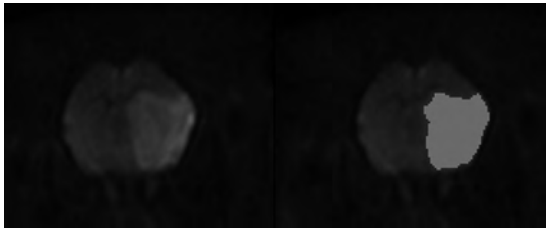


FIG 2. Semiautomatic measurement of infarct volume on diffusion-weighted imaging. The infarcted area with diffusion restriction is semiautomatically segmented (right) by using a commercial software package.

NordicNeuroLab, Bergen, Norway). On diffusion-weighted images, infarct volumes were calculated by using a semiautomated thresholding method to identify regions of interest with high signal intensity (Fig 2), and infarct volume fraction was expressed as a percentage of the ipsilateral hemisphere volume. Then, volumes of infarct growth were calculated in set 1.

All images were reviewed, and sections with the largest infarct area, near the sections of Bregma 1.60 mm, were selected for quantitative analysis of DCE-MR imaging.

All image data from DCE-MR imaging were transferred to an independent workstation for analysis. Permeability parameters for each pixel from DCE-MR imaging—volume transfer constant (K^{trans}), rate transfer coefficient, volume fraction of extravascular extracellular space, and volume fraction of blood plasma—were calculated, and color-coded parametric maps were generated by off-line Pride tools provided by Philips, which are based on the pharmacokinetic 2-compartment model of Tofts and Kermode.⁸ Postprocessing was composed of motion correction of pixels from dynamic images, T1 mapping by using different flip angles (5° and 15°), registration of pixels on the T1 map, arterial input function estimation, and pharmacokinetic modeling. All these processes were automatically performed by Pride tools except drawing ROIs for the arterial input function. Arterial input function was measured several times at the area of the left internal carotid artery, and the proper arterial input function showing high amplitude, early sharp rise, and fast decay was selected for processing. Each permeability parameter was obtained in the infarct area. Permeability maps were also used for estimating brain tissue volume with BBB disruption, which was measured by obtaining pixel values and counting the numbers of pixels with K^{trans} of >0 . Volume with BBB disruption was also expressed as a percentage of the ipsilateral hemisphere.

Pathologic Specimens

After performing MR imaging, the rats were anesthetized with Zoletil, 150 mg/kg, intravenously and perfused transcardially with 4% paraformaldehyde until the outflow fluid from the right atrium was colorless. The brain was rapidly removed and embedded in paraffin for histologic processing. Coronal sections (6- μ m thick) were taken at 2-mm intervals through the brain region corresponding to the MR imaging sections and stained with hematoxylin-eosin for histopathologic evaluation. Gross hemorrhage was defined as blood evident to the unaided eye on the hematoxylin-eosin-stained sections and confirmed by microscopy. Microscopic hemorrhage was defined as blood evident only by microscopy (original magnification $\times 40$).

Immunohistochemical Analysis

Seven rats were used in each group for immunohistochemical analysis. Paraffin-embedded sections were rehydrated. After permeabilization with proteinase K, sections were immunostained with primary antibodies against factor VIII (1:200 dilution) followed by biotinylated secondary antibodies. Sections were visualized by using horseradish peroxidase and then reacted with diaminobenzidine (DAB) as a substrate.

Images were observed and captured on an AX80 microscope equipped with a DP-72 digital camera (Olympus, Shinjuku, Tokyo, Japan). The stained cells were assessed in 2 consecutive coronal sections with the largest infarct areas from each rat. All data for immunohistochemistry were collected from 10 high-power fields (original magnification, $\times 200$) within the infarct area per slide. These included 5 regions from the striatum, 3 regions from the parietal cortex, and 2 regions from the border area of infarct showing the highest expression. Another 10 regions were selected in the corresponding area in the contralateral hemisphere.

The captured images from immunohistochemistry were analyzed by an investigator blinded to the treatments with the aid of ImageJ software (National Institutes of Health, Bethesda, Maryland). The numbers of factor VIII–positive cells were counted in 10 images from the infarct area and contralateral hemisphere and expressed as a ratio.

Statistical Analysis

Infarct volume and volume with BBB disruption showed interaction with groups and time; therefore, linear mixed modeling followed by Bonferroni correction was used for between-group comparisons and within-group comparisons at different time points. Otherwise, independent *t* tests were performed to compare infarct growth, quantitative imaging parameters, and numbers of factor VIII–positive cells between control and agmatine-treated groups on the basis of normality testing by the Kolmogorov-Smirnov test. All statistical analyses were performed by using statistical software (SAS, Version 9.2 m; SAS Institute, Cary, North Carolina). *P* values $< .05$ were considered significant.

RESULTS

Image Analysis

To investigate the effect of agmatine on ischemic damage, we assessed infarct volume by MR imaging and found that agmatine significantly reduced infarct volume. Absolute infarct volumes were 160.7 ± 69.4 mm³ in the agmatine-treated group and 250 ± 60.4 mm³ in the control group at 4-hour reperfusion ($P < .001$). Infarct-volume fractions to the ipsilateral brain volume were $36.1 \pm 10.8\%$ in the agmatine-treated group and $54.2 \pm 7.1\%$ in the control group at 4-hour reperfusion ($P < .001$). At 30-hour reperfusion in set 1, infarct volumes were $45.8 \pm 13\%$ in the agmatine-treated group and $73.9 \pm 10.8\%$ in the control group ($P < .001$). In addition, infarct growth was less in the agmatine-treated group than in the control group (60 ± 44.4 mm³ versus 130 ± 55.2 mm³, $P = .009$).

DCE-MR imaging showed an increase in permeability parameters in the ipsilateral hemisphere of the middle cerebral artery occlusion. There were no cases with positive values of permeability parameters in the contralateral hemisphere on DCE-MR im-

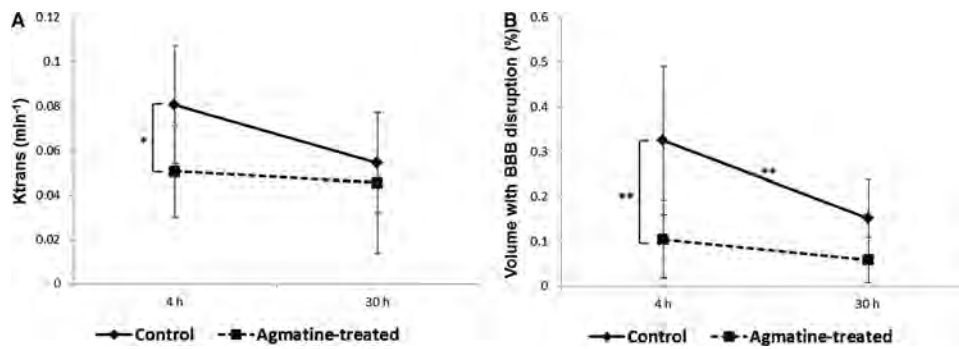


FIG 3. Permeability changes at 2 different time points. A, K^{trans} values. B, Brain tissue volume with BBB disruption expressed as a percentage of the ipsilateral hemisphere. Square and diamond-shaped dots are mean values; horizontal lines above and below the dots represent 95% confidence intervals. The asterisk indicates $P < .05$; 2 asterisks, $P < .01$.

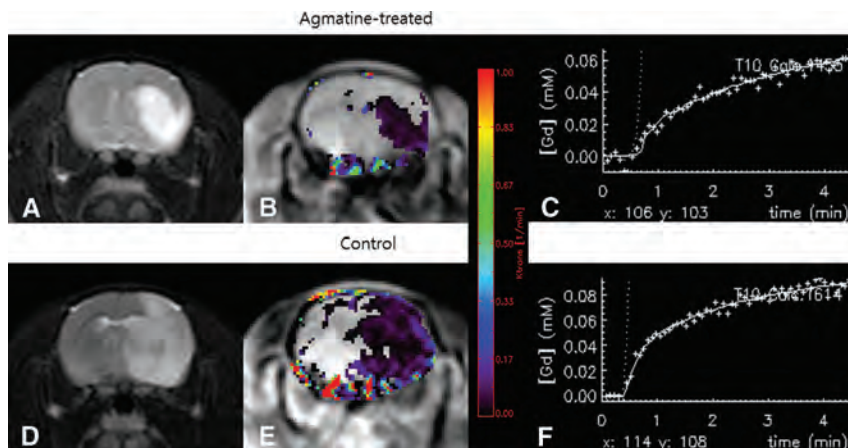


FIG 4. Representative MR images. Infarcted areas can be seen as hyperintensity on T2-weighted images (A and D). The color-coded permeability maps obtained 4 hours after reperfusion demonstrate increased permeability in the infarcted areas (B and E). The mean K^{trans} values were 0.05 ± 0.02 minutes $^{-1}$ in the agmatine-treated groups and 0.08 ± 0.03 minutes $^{-1}$ in the control group ($P = .012$). C and F, K^{trans} curves fit the data points (small plus sign) in the corresponding maps.

Permeability imaging parameters measured 4 hours after reperfusion^a

	Control Group (n = 15)	Agmatine-Treated Group (n = 15)	P Value
K^{trans} (min^{-1})	0.08 ± 0.03	0.05 ± 0.02	.012
K_{ep} (min^{-1})	0.46 ± 0.3	0.44 ± 0.28	.856
V_e	0.22 ± 0.15	0.12 ± 0.06	.02
V_p	0.042 ± 0.03	0.038 ± 0.02	.187
Volume of BBB disruption (%)	32.5 ± 16.5	10.4 ± 8.7	<.001

Note:— K_{ep} indicates rate transfer coefficient; V_e , volume fraction of extravascular extracellular space; V_p , volume fraction of blood plasma.

^a Data are means.

aging. Among the permeability parameters, K^{trans} and volume fraction of extravascular extracellular space were significantly lower in the agmatine-treated group compared with the control group (0.05 ± 0.02 minutes $^{-1}$ versus 0.08 ± 0.03 minutes $^{-1}$, $P = .012$, for K^{trans} and 0.12 ± 0.06 versus 0.22 ± 0.15 , $P = .02$, for volume fraction of extravascular extracellular space) 4 hours after reperfusion (Figs 3 and 4). However, K^{trans} and volume fraction of extravascular extracellular space measured 30 hours after reperfusion in set 1 were not significantly different between the 2 groups. Overall, there was a tendency of K^{trans} to decrease with time without statistical significance (0.06 ± 0.03 minutes $^{-1}$ at 4-hour reperfusion versus 0.05 ± 0.03 minutes $^{-1}$ at 30-hour rep-

erfusion, $P = .06$). Other permeability parameters were not significantly different between the groups at each time point (Table). The volume with BBB disruption estimated from the permeability map was significantly less in the agmatine-treated group than in the control group. The volumes were $10.4 \pm 8.7\%$ in the agmatine-treated group and $32.5 \pm 16.5\%$ in the control group at 4-hour reperfusion ($P < .001$) (Fig 3). At 30-hour reperfusion in set 1, the volumes with BBB disruption were $5.8 \pm 5.1\%$ in the agmatine-treated group and $15.2 \pm 8.6\%$ in the control group ($P = .367$). Overall, the volume with BBB disruption at 30-hour reperfusion was significantly less than that at 4-hour reperfusion ($22.4 \pm 15.4\%$ at 4-hour reperfusion versus $10.5 \pm 8.4\%$ at 30-hour reperfusion, $P < .001$).

Histopathologic Analysis

On histopathologic examination, gross hemorrhage was observed within the ischemic region of 2 rats in the agmatine-treated group and 2 rats in the control group. In addition, microscopic hemorrhage was observed in 1 agmatine-treated rat and 2 control rats.

The ratio of the number of factor VIII–positive cells in the ipsilateral to that in contralateral hemispheres was lower in the agmatine-treated group than in the control group (3.1-fold versus 4-fold, $P = .037$) (Fig 5). The ratio of the number of factor VIII–positive cells in the ipsilateral to that in contralateral hemispheres in set 2, from which histopathology was obtained after the first MR imaging acquisition, was lower than that in set 1 (2.8-fold versus 3.9-fold, $P = .021$).

DISCUSSION

In this study, we found that agmatine protects the BBB in ischemic stroke and the BBB stabilization effect of agmatine can be monitored in vivo by quantification of permeability by using DCE-MR imaging. K^{trans} , volume fraction of extravascular extra-

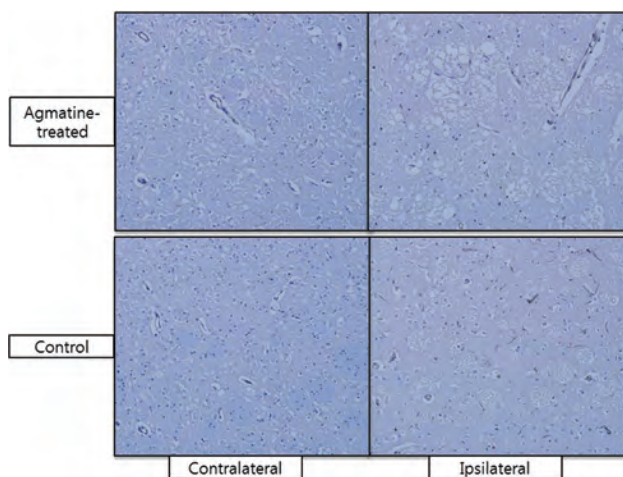


FIG 5. Immunohistochemical staining with primary antibodies against factor VIII. The ratio of the number of factor VIII–positive cells (brown) in the ipsilateral to that in contralateral hemisphere was lower in the agmatine-treated group (upper row) than in the control group (lower row) (3.1-fold versus 4-fold, $P = .037$) (original magnification $\times 200$).

cellular space, and brain tissue volume with BBB disruption were significantly less in the agmatine-treated group than in the control group at 4-hour reperfusion. Our results support a previous study that showed the protective effects of agmatine on the BBB by using Evans blue.¹¹ Moreover, in another previous study, decreased expression of matrix metalloproteinase by agmatine was suggested as a possible mechanism limiting BBB disruption because matrix metalloproteinases are known to be associated with BBB disruption and subsequent vasogenic edema after cerebral ischemia.¹⁹ Although Evans blue has been widely used to assess BBB disruption with its property of binding to serum albumin, it is only available for use in animal models.²⁰ DCE-MR imaging provides both permeability values and spatial maps of permeability changes without killing the animals, which enabled us to investigate the BBB blocking properties of pharmaceutical agents as a longitudinal study by acquiring multiple images at different time points. In addition, MR imaging is a more sensitive measure of BBB disruption because of the lower molecular weight of gadolinium compared with that of Evans blue as described in a previous experimental study (604.7 Da versus 75.8 kDa).²¹ Therefore, in the present study, DCE-MR imaging was used for monitoring the time course of focal cerebral ischemia and the BBB stabilization effects of agmatine.

Our results showed a significant increase of K^{trans} and brain-tissue volume with BBB disruption at 4-hour reperfusion, which may be attributed to increased inflammatory and oxidative stress on the BBB after reperfusion.^{20,22} There was a tendency of K^{trans} to decrease with time, and brain tissue volume with BBB disruption at 30-hour reperfusion was less than that at 4-hour reperfusion. Previous experimental studies have also shown a biphasic opening of the BBB after transient ischemic injury, which has been generally accepted.^{20,23,24} Even though the mechanisms of this partial recovery of the BBB at 30-hour reperfusion are not well-understood, the results suggest that the reverse of reactive oxygen species-mediated disassembly of tight junction proteins within 6 hours may contribute to a decrease in the extravasation

of gadolinium contrast agent.²³ On the other hand, recent animal studies have demonstrated continuous opening of the BBB.^{21,25} However, they also observed a nonsignificant drop in gadolinium enhancement and Evans blue extravasation at 24- and 36-hour reperfusion, which can be explained by microvascular plugging caused by infiltrating neutrophils, fibrin, and platelets. Therefore, longitudinal studies with a large number of subjects need to be conducted to investigate temporal changes of the BBB and its mechanisms.

We performed immunohistochemical staining with factor VIII to assess angiogenesis following cerebral ischemia and found that the expression of factor VIII–positive cells was less in the agmatine-treated group than in the control group. These results may be because BBB disruption in the agmatine-treated group was significantly less than that of the control group according to DCE-MR imaging. Because the formation of new microvessels is a hallmark tissue response to ischemic injury, reduced expression of factor VIII–positive cells in the agmatine-treated group may be attributed to the protective effect of agmatine on the BBB. Overall, the expression of factor VIII–positive cells was lower at 4-hour reperfusion than at 30-hour reperfusion. Although expression of angiogenesis-related factors begins within 1–2 hours after focal ischemia, it increases for up to 14 days¹; therefore, new vessels can be visualized better at later stages.

An increase in permeability measured by DCE-MR imaging may not directly reflect hemorrhagic transformation because the size of the gadolinium molecule is much smaller than that of red blood cells. Although BBB disruption was demonstrated in all cases of transient ischemic stroke, gross hemorrhage was observed in 2 rats of the agmatine-treated group and 2 rats of the control group. Therefore, on the basis of the results from this study, it is difficult to say whether agmatine would have a potential benefit preventing gross hemorrhage, which is clinically significant.

Agmatine was administered immediately after reperfusion because this timing is optimal for using agents with BBB blocking properties in a clinical setting. In addition, a previous animal experimental study reported that agmatine showed neuroprotective effects up to 4 hours after reperfusion.¹⁶ Further studies are needed to investigate functional recovery and ultimate stroke outcome when agmatine is administered early, late, or throughout the phase of ischemic injury because timely pharmacotherapy is important for dynamic temporal changes in BBB permeability.

If the treatment window for effective reperfusion therapy can be expanded with agmatine, considerably more patients with stroke would be eligible for therapy. The results of the present study suggest that DCE-MR imaging has the potential to provide imaging biomarkers that are valuable for adjunctive therapy to reduce complications associated with thrombolytic therapy in ischemic stroke.

There are several limitations in our study. First, spatial maps of permeability could not be correlated with images of immunohistochemical staining because it is not technically possible to match regions on both MR imaging and histopathology. Second, the long-term effects of agmatine could not be assessed because the rats were sacrificed to obtain pathologic specimens right after we performed MR imaging. Further studies are warranted to deter-

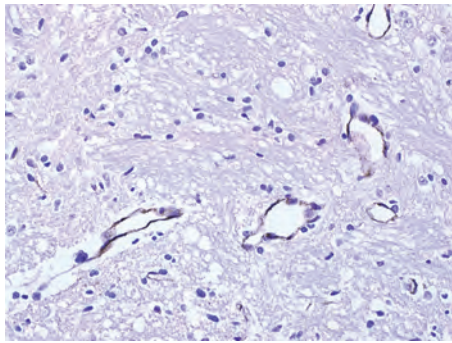


FIG 6. Immunohistochemical staining with high power (original magnification $\times 400$). Factor VIII is stained in the endothelium along the blood vessels.

mine the neuroprotective effects of agmatine, such as functional recovery, with serial follow-up. Third, a 3T MR imaging scanner, which is not dedicated for animal imaging, was used in this study. However, it is commonly used in clinical practice, and acceptable images can be obtained to evaluate permeability in rat stroke models. Thus, a 3T MR imaging scanner with the methods identical to those used in this study may possibly be applied in humans. Last, because we had tried to stain the brain tissue by immunoperoxidase, we did not perform reference staining such as 4',6-diamidino-2-phenylindole staining, which is necessary to prove that the factor VIII was stained in the cell. Instead, we confirmed that factor VIII was stained in the endothelium along the blood vessels with higher power magnification (original magnification $\times 400$) (Fig 6).

CONCLUSIONS

Agmatine protects the BBB in ischemic stroke, which can be monitored in vivo by quantification of permeability by using DCE-MR imaging. Therefore, DCE-MR imaging may serve as a potential imaging biomarker for assessing the BBB stabilization properties of pharmacologic agents, including agmatine, at early stages to reduce complications associated with thrombolytic therapy in ischemic stroke.

ACKNOWLEDGMENTS

Special thanks to Ah-Reum Yang and Jae Young Kim (Department of Anatomy, Yonsei University College of Medicine, Seoul, Korea), who helped us through the experimental processes from making the animal experimental models to obtaining pathologic specimens. The authors are grateful to Sei Young Kim (MR imaging technician, Severance Hospital, Seoul, Korea) for his help with the examinations and for his valuable suggestions.

Disclosures: Dong Joon Kim—UNRELATED: Grants/Grants Pending: Yonsei University College of Medicine faculty grant, Korea Healthcare Technology R&D Project; Patents (planned, pending or issued): stent delivery system.

REFERENCES

- del Zoppo GJ, Mabuchi T. Cerebral microvessel responses to focal ischemia. *J Cereb Blood Flow Metab* 2003;23:879–94
- Tissue plasminogen activator for acute ischemic stroke: the National Institute of Neurological Disorders and Stroke rt-PA Stroke Study Group. *N Engl J Med* 1995;333:1581–87
- Berger C, Fiorelli M, Steiner T, et al. Hemorrhagic transformation of ischemic brain tissue: asymptomatic or symptomatic? *Stroke* 2001;32:1330–35
- Sood R, Taheri S, Estrada EY, et al. Quantitative evaluation of the effect of propylene glycol on BBB permeability. *J Magn Reson Imaging* 2007;25:39–47
- Kassner A, Roberts T, Taylor K, et al. Prediction of hemorrhage in acute ischemic stroke using permeability MR imaging. *AJNR Am J Neuroradiol* 2005;26:2213–17
- Bang OY, Buck BH, Saver JL, et al. Prediction of hemorrhagic transformation after recanalization therapy using T2*-permeability magnetic resonance imaging. *Ann Neurol* 2007;62:170–76
- Wu S, Thornhill RE, Chen S, et al. Relative recirculation: a fast, model-free surrogate for the measurement of blood-brain barrier permeability and the prediction of hemorrhagic transformation in acute ischemic stroke. *Invest Radiol* 2009;44:662–68
- Tofts PS, Kermode AG. Measurement of the blood-brain barrier permeability and leakage space using dynamic MR imaging. 1. Fundamental concepts. *Magn Reson Med* 1991;17:357–67
- Hoffmann A, Bredno J, Wendland MF, et al. Validation of in vivo magnetic resonance imaging blood-brain barrier permeability measurements by comparison with gold standard histology. *Stroke* 2011;42:2054–60
- Nonaka Y, Tsuruma K, Shimazawa M, et al. Cilostazol protects against hemorrhagic transformation in mice transient focal cerebral ischemia-induced brain damage. *Neurosci Lett* 2009;452:156–61
- Kim JH, Lee YW, Park KA, et al. Agmatine attenuates brain edema through reducing the expression of aquaporin-1 after cerebral ischemia. *J Cerebr Blood Flow Metab* 2010;30:943–49
- Wang CC, Chio CC, Chang CH, et al. Beneficial effect of agmatine on brain apoptosis, astrogliosis, and edema after rat transient cerebral ischemia. *BMC Pharmacol* 2010;10:11
- Gilad GM, Gilad VH. Accelerated functional recovery and neuroprotection by agmatine after spinal cord ischemia in rats. *Neurosci Lett* 2000;296:97–100
- Gilad GM, Salame K, Rabey JM, et al. Agmatine treatment is neuroprotective in rodent brain injury models. *Life Sci* 1996;58:PL 41–46
- Feng Y, Piletz JE, Leblanc MH. Agmatine suppresses nitric oxide production and attenuates hypoxic-ischemic brain injury in neonatal rats. *Pediatric Res* 2002;52:606–11
- Kim JH, Yenari MA, Giffard RG, et al. Agmatine reduces infarct area in a mouse model of transient focal cerebral ischemia and protects cultured neurons from ischemia-like injury. *Exp Neurol* 2004;189:122–30
- Kim DJ, Kim DI, Lee SK, et al. Protective effect of agmatine on a reperfusion model after transient cerebral ischemia: temporal evolution on perfusion MR imaging and histopathologic findings. *AJNR Am J Neuroradiol* 2006;27:780–85
- Longa EZ, Weinstein PR, Carlson S, et al. Reversible middle cerebral artery occlusion without craniectomy in rats. *Stroke* 1989;20:84–91
- Kim JH, Lee YW, Kim JY, et al. The effect of agmatine on expression of MMP2 and MMP9 in cerebral ischemia. *Korean J Anatomy* 2008;41:97–104
- Belayev L, Busto R, Zhao W, et al. Quantitative evaluation of blood-brain barrier permeability following middle cerebral artery occlusion in rats. *Brain Res* 1996;739:88–96
- Strbian D, Durukan A, Pitkonen M, et al. The blood-brain barrier is continuously open for several weeks following transient focal cerebral ischemia. *Neuroscience* 2008;153:175–81
- Heo JH, Han SW, Lee SK. Free radicals as triggers of brain edema formation after stroke. *Free Radic Biol Med* 2005;39:51–70
- Pillai DR, Dittmar MS, Baldranov D, et al. Cerebral ischemia-reperfusion injury in rats: a 3 T MRI study on biphasic blood-brain barrier opening and the dynamics of edema formation. *J Cerebr Blood Flow Metab* 2009;29:1846–55
- Kuroiwa T, Ting P, Martinez H, et al. The biphasic opening of the blood-brain barrier to proteins following temporary middle cerebral artery occlusion. *Acta Neuropathol* 1985;68:122–29
- Durukan A, Marinkovic I, Strbian D, et al. Post-ischemic blood-brain barrier leakage in rats: one-week follow-up by MRI. *Brain Res* 2009;1280:158–65

Assessment of Intracranial Collaterals on CT Angiography in Anterior Circulation Acute Ischemic Stroke

L.L.L. Yeo, P. Paliwal, H.L. Teoh, R.C. Seet, B.P. Chan, E. Ting, N. Venketasubramanian, W.K. Leow, B. Wakerley, Y. Kusama, R. Rathakrishnan, and V.K. Sharma



ABSTRACT

BACKGROUND AND PURPOSE: Intracranial collaterals influence the prognosis of patients treated with intravenous tissue plasminogen activator in acute anterior circulation ischemic stroke. We compared the methods of scoring collaterals on pre-tPA brain CT angiography for predicting functional outcomes in acute anterior circulation ischemic stroke.

MATERIALS AND METHODS: Two hundred consecutive patients with acute anterior circulation ischemic stroke treated with IV-tPA during 2010–2012 were included. Two independent neuroradiologists evaluated intracranial collaterals by using the Miteff system, Maas system, the modified Tan scale, and the Alberta Stroke Program Early CT Score 20-point methodology. Good and extremely poor outcomes at 3 months were defined by modified Rankin Scale scores of 0–1 and 5–6 points, respectively.

RESULTS: Factors associated with good outcome on univariable analysis were younger age, female sex, hypertension, diabetes mellitus, atrial fibrillation, small infarct core (ASPECTS ≥ 8), vessel recanalization, lower pre-tPA NIHSS scores, and good collaterals according to Tan methodology, ASPECTS methodology, and Miteff methodology. On multivariable logistic regression, only lower NIHSS scores (OR, 1.186 per point; 95% CI, 1.079–1.302; $P = .001$), recanalization (OR, 5.599; 95% CI, 1.560–20.010; $P = .008$), and good collaterals by the Miteff method (OR, 3.341; 95% CI, 1.203–5.099; $P = .014$) were independent predictors of good outcome. Poor collaterals by the Miteff system (OR, 2.592; 95% CI, 1.113–6.038; $P = .027$), Maas system (OR, 2.580; 95% CI, 1.075–6.187; $P = .034$), and ASPECTS method ≤ 5 points (OR, 2.685; 95% CI, 1.156–6.237; $P = .022$) were independent predictors of extremely poor outcomes.

CONCLUSIONS: Only the Miteff scoring system for intracranial collaterals is reliable for predicting favorable outcome in thrombolized acute anterior circulation ischemic stroke. However, poor outcomes can be predicted by most of the existing methods of scoring intracranial collaterals.

ABBREVIATION: AAIS = acute anterior circulation ischemic stroke

Acute occlusion of an intracranial artery is responsible for the clinical manifestations in acute anterior circulation ischemic stroke (AAIS), and rapid dissolution of the offending arterial thrombi often leads to dramatic clinical recovery.¹ Therefore,

achieving timely recanalization remains the main aim of acute stroke care.²

Although the parenchymal ischemic injury is restricted to the vascular territories of the index artery, neuronal damage and its clinical manifestations are not uniform in patients with AAIS, especially during the first few hours after an acute intracranial occlusion. These phenomena are observed due to, at least to some extent, variations in the quality and quantity of collateral perfusion.³ Detailed imaging studies have shown that progression to complete infarction is highly variable and the process might take many hours or even days to complete.⁴

Irrespective of the mechanism of ischemia, various collateral pathways are recruited to limit ischemic injury to the brain.^{5–7} The wide variations in the clinical manifestations and the rates and extent of neurologic recovery in patients with AAIS may be attributable to these collateral pathways, comprising an intact circle of Willis, and the state of leptomeningeal collaterals connect-

Received June 17, 2014; accepted after revision July 27.

From the Division of Neurology, Department of Medicine (L.L.L.Y., P.P., H.L.T., R.C.S., B.P.C., N.V., B.W., Y.K., R.R., V.K.S.), and Department of Diagnostic Imaging (E.T.), National University Health System, Singapore; and Department of Computer Science (W.K.L.) and Yong Loo Lin School of Medicine (R.C.S., V.K.S.), National University of Singapore, Singapore.

This work was supported by the National Medical Research Council, Singapore, grant No. CNIG12nov001.

Please address correspondence to Leonard Leong Litt Yeo, MBBS, MRCP, Division of Neurology, Department of Medicine, National University Health System, Singapore, One E Kent Ridge Rd, Singapore 119228; e-mail: leonard_ll_yeo@nuhs.edu.sg

 Indicates open access to non-subscribers at www.ajnr.org

 Indicates article with supplemental on-line table.

<http://dx.doi.org/10.3174/ajnr.A4117>

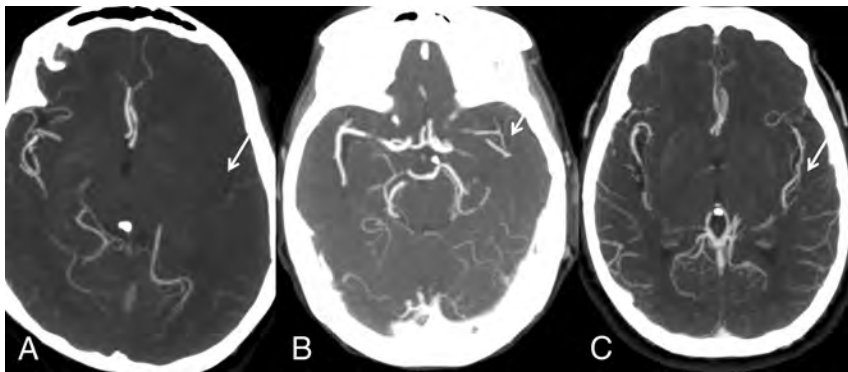


FIG 1. Miteff system. A, Contrast opacification is seen merely in the distal superficial branches. B, Vessels can be seen at the Sylvian fissure. C, Major vessels are reconstituted distal to the occlusion.

ing vascular territories. An acute intracranial occlusion produces an area of ischemic penumbra, the extent being dependent on residual and the collateral blood flow.⁸⁻¹⁰ Intravenously administered tissue plasminogen activator, the only approved drug therapy in AAIS, can salvage this penumbra if arterial recanalization is achieved in time. CT angiography of the brain is frequently performed for AAIS. Various methods have been described for the assessment of intracranial collaterals on CTA in patients with AAIS. However, there is no consensus on the best method to evaluate and grade collaterals. Current methods of assessment of collaterals are largely qualitative or semiquantitative, without any clear indication of the superiority of one technique over another. We compared various methods of scoring collaterals on the pretreatment CTA of the brain to determine their value in the prediction of functional outcome in our patients with AAIS treated with IV-tPA.

Ethics approval for this project was obtained from the institutional review board.

MATERIALS AND METHODS

We identified patients from our acute stroke data base; consecutive patients with AAIS treated with IV-tPA from January 2010 to December 2012 were considered for the study. Inclusion criteria were patients with AAIS who had a pretreatment CTA performed and then underwent IV-tPA. Patients who were pregnant, had poor-quality CTA scans, had only distal anterior cerebral artery occlusion, or were unable to come for follow-up appointments were excluded from the study. If consent could not be obtained from the patient or relatives, the patients were also excluded. We collected data for demographic characteristics and various vascular risk factors such as hypertension, diabetes mellitus types 1 and 2, dyslipidemia, atrial fibrillation, and smoking. Systemic blood pressure values were recorded for all patients at presentation, and levels were maintained during the first few days according to the recommended guidelines.¹¹ AAIS was classified into various subtypes by using the Trial of Org 10172 in Acute Stroke Treatment classification on the basis of the etiopathologic mechanisms.¹² National Institutes of Health Stroke Scale scores were recorded for all patients by credentialed neurologists before the IV-tPA bolus and at 2 and 24 hours after treatment initiation. Functional outcome was assessed by modified Rankin Scale at 3 months. Good and poor functional outcomes were defined by

mRS scores of 0–1 and 2–6, respectively. Extremely poor outcomes were defined by mRS scores of 5–6.

In addition to the noncontrast CT scan of the brain, high-resolution CTA was performed in all patients. In patients with no contraindication for the radiocontrast injection (specifically, contrast allergy or serum creatinine levels of >110 mol/L), high-resolution CTA was performed on a 64-section multidetector helical scanner (Brilliance; Philips Healthcare, Best, the Netherlands), and images were acquired with a 70-mL bolus injection of contrast at 3 mL/s followed by 30 mL of saline at 3 mL/s into the antecubital

vein. Scanning was triggered by using bolus tracking, with the region of interest placed in the posterior aortic arch with the trigger threshold set at 150 HU. Scan parameters at our institution were the following: section thickness, 1 mm; no section gap; FOV, 200 mm; matrix, 512 × 512; and 230–250 mAs. Coverage was from the base of the skull to the vertex, and the source images were reformatted into 3-mm-thick axial, coronal, and sagittal projections. MIPs were routinely provided as part of CTA; no 3D reconstructions were performed.

All CTA images were anonymized and reviewed at the same workstation, independently by 2 experienced neuroradiologists (E.T. and G.B.) blinded to the patient clinical information and results. Each CTA study was evaluated for intracranial collaterals according to the 4 following predefined criteria:

Miteff System. The system of Miteff et al¹³ is a 3-point score that grades middle cerebral artery collateral branches with respect to the Sylvian fissure and can be performed rapidly. The grades assigned are the following: 3 (if the vessels are reconstituted distal to the occlusion), 2 (vessels can be seen at the Sylvian fissure), or 1 (when the contrast opacification is merely seen in the distal superficial branches) (Fig 1).

Maas System. The system of Mass et al¹⁴ is a 5-point score that compares collaterals on the affected hemisphere against those on the unaffected side. It uses the Sylvian fissure vessels or leptomeningeal collaterals as internal controls. The score ranges are 5 (exuberant), 4 (more than those on the contralateral side), 3 (equal to those on the contralateral side), 2 (less than those on the contralateral side), and 1 (no vessel opacification) (Fig 2).

Modified Tan Scale. The modified scale of Tan et al¹⁵ is the simplest system that classifies the collaterals as “good” if seen in ≥50% of the MCA territory and “poor” when they are seen in <50% of the territory. This system allows a rapid assessment and is less prone to differences in opinion (Fig 3).

Alberta Stroke Program Early CT Score Methodology using a 20-Point Grading Scale. Collaterals are scored in regions corresponding to the ASPECTS system. Lenticulostriate arteries in the basal ganglia arising from retrograde-filling MCAs distal to an occlusion are included in the scoring. The system scores the extent of contrast opacification in arteries distal to the occlusion (0,

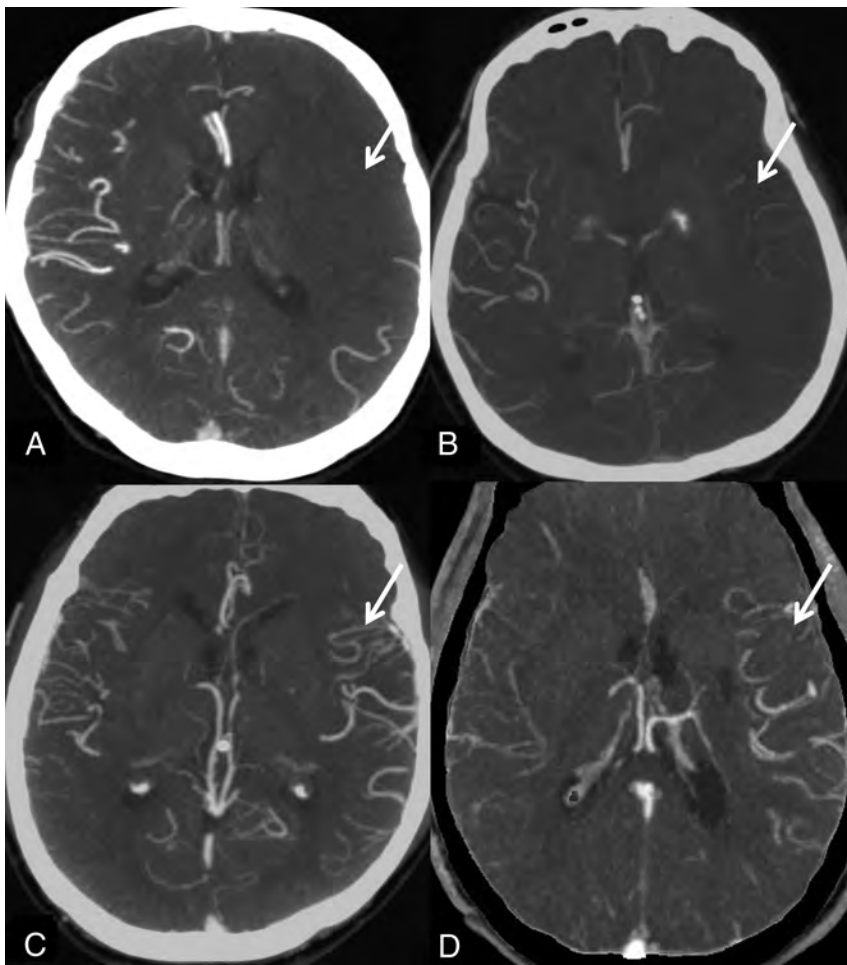


FIG 2. Maas system. *A*, No vessel opacification. *B*, Opacification less than that on the contralateral side. Opacification equal to that on the contralateral side is not shown. *C*, More opacification than that on the contralateral side. *D*, Exuberant.

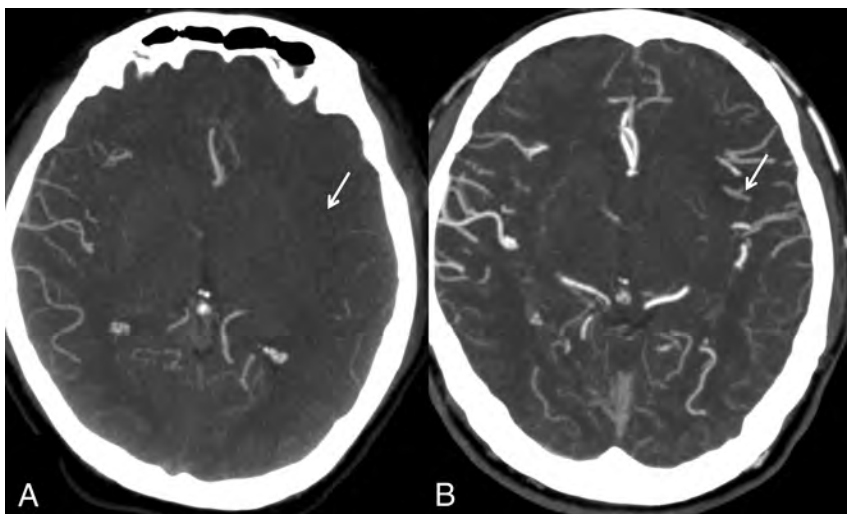


FIG 3. Modified Tan system. *A*, Less than 50% of the MCA territory. *B*, More than 50% of the MCA territory.

artery not seen; 1, less prominent; 2, equal or more prominent compared with a matching region in the opposite hemisphere) in the 6 ASPECTS cortical regions (M1–6), the caudate, insular ribbon,

grading of collaterals by other systems was the following: Mass system ($\kappa = 0.82$; 95% CI, 0.75–0.84 for leptomeningeal and $\kappa = 0.87$; 95% CI, 0.80–0.91 for Sylvian fissure vessels), Miteff system

internal capsule, and lentiform nucleus to form a score from 0 to 20 (Fig 4).^{16,17}

Statistical Methods

We present the numeric variables as mean and SD or median and range. Categorical variables are presented as percentages. Numeric predictors were tested by using a 2-sample *t* test or Mann-Whitney *U* test when applicable. Categorical variables were evaluated by using the χ^2 test or Fisher exact test when applicable. Variables found to have a significant association ($P < .05$) were entered into the multivariable model to perform logistic regression for determining the independent predictors of the prespecified good and bad functional outcomes at 3 months. To improve the robustness of our statistical model, we also included variables with $P < .10$ into a multivariable logistic regression model with a backward stepwise selection procedure. Associations are presented as odds ratios with corresponding 95% confidence intervals. Interobserver variability for the assessment of collateral status between the 2 observers was tested by using κ statistics. Statistical analyses were performed by using the Statistical Package for Social Sciences, Version 20 (IBM, Armonk, New York).

RESULTS

In the study time, 2409 patients with strokes were seen, and of these, 200 patients satisfied the inclusion criteria for this study. The median age was 63 years (range, 33–92 years), and 31.5% were women. The pre-tPA median NIHSS score was 19 points (range, 3–33). A relatively higher proportion (73, 36.5%) of patients had atrial fibrillation. Other factors are listed in Table 1. Overall, 93 (46.6%) patients achieved good functional outcome at 3 months, and extremely poor outcomes were noted in 34 (17%) patients (Fig 5). mRS 0–2 at 3 months was achieved in 107 (53.5%) patients.

The degree of agreement between the 2 independent neuroradiologists for interpreting the collaterals was best for the modified Tan system ($\kappa = 0.93$; 95% CI, 0.91–0.95). The level of agreement for the

($\kappa = 0.91$; 95% CI, 0.86–0.93), and ASPECTS-based grading system ($\kappa = 0.77$; 95% CI, 0.70–0.81).

On univariable analysis, younger age, female sex, hypertension, diabetes, atrial fibrillation, small infarct core on noncontrast CT (ASPECTS ≥ 8), recanalization of the vessel, lower pre-tPA NIHSS scores, and good collaterals according to Tan methodology, ASPECTS methodology, and Miteff methodology were found to be significantly associated with good functional out-

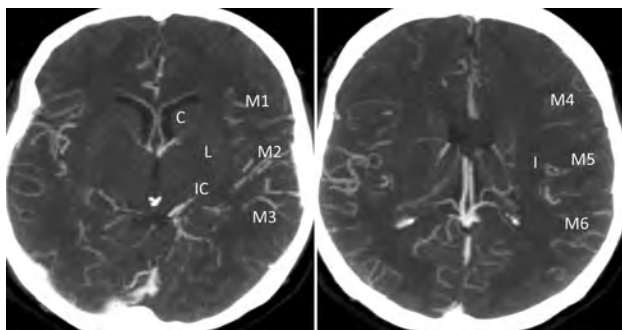


FIG 4. The ASPECTS system scores arteries distal to the occlusion (0, artery not seen; 1, less prominent; 2, equal or more prominent compared with a matching region in the opposite hemisphere) in the 6 ASPECTS cortical regions (M1–6), the caudate, insular ribbon, internal capsule, and lentiform nucleus to form a score from 0 to 20.

Table 1: Baseline characteristics of the study population (N = 200)

Variables	No.
Median age (range) (yr)	63 (35–92)
Female sex (%)	63 (31.5)
Hypertension (%)	131 (65.5)
Diabetes (%)	60 (30)
Dyslipidemia (%)	102 (51)
Smoker (%)	57 (28.5)
Atrial fibrillation (%)	73 (36.5)
Pre-tPA systolic BP (range)	152 (110–215)
Pre-tPA NIHSS score (range)	19 (3–33)
Median onset to treatment (range)	155 (73–275)
TOAST criteria	
Large-artery atherosclerosis	52 (26%)
Cardioembolic	96 (48%)
Lacunar	0 (0%)
Undetermined cause	42 (21%)
Stroke of other etiology	10 (5%)
Location of occlusion	
Tandem	6 (3%)
Terminal ICA	53 (26.5%)
M1	76 (38%)
Distal MCA	65 (32.5%)
Modified Rankin Scale 0–1 at 3 mo (%)	93 (46.6)
Modified Rankin Scale 5–6 at 3 mo (%)	34 (17)

Note:—TOAST indicates Trial of Org 10172 in Acute Stroke Treatment¹²; BP, blood pressure.

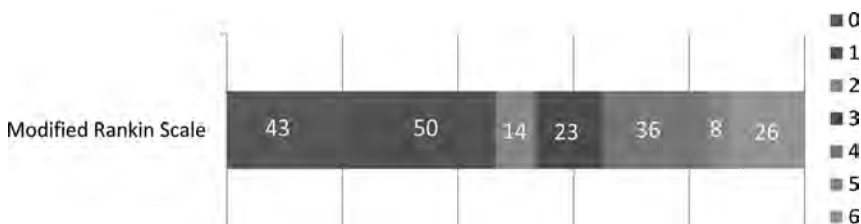


FIG 5. Three-month functional outcomes of patients by the modified Rankin Scale 0–6.

comes (Table 2). On multivariable logistic regression, only lower NIHSS (OR, 1.186 per NIHSS point; 95% CI, 1.079–1.302; $P = .001$), the presence of recanalization (OR, 5.599; 95% CI, 1.560–20.010; $P = .008$), and Miteff grading system for intracranial collaterals (OR, 3.341; 95% CI, 1.241–8.996; $P = .017$) were found to independently predict good functional outcome. While modified Tan and Maas methodologies failed to predict good functional outcome, ASPECTS methodology showed a trend toward statistical significance (OR, 1.784 per point; 95% CI, 0.820–9.761; $P = .068$). On ordinal regression analysis Miteff grading was still the most effective (On-line Table).

During the analyses for extremely poor outcome (mRS 5–6) at 3 months, the Miteff grading system with only distal superficial branches reconstituted (OR, 2.592; 95% CI, 1.113–6.038; $P = .027$), the Maas grading system with absent collaterals on the affected side (OR, 2.580; 95% CI, 1.075–6.187; $P = .034$), and ASPECTS methodology score ≤ 5 points (OR, 2.685; 95% CI, 1.156–6.237; $P = .022$) were significantly associated with poor outcome at 3 months. Other significant cofactors were higher NIHSS score (OR, 1.143 per point; 95% CI, 1.057–1.235; $P = .001$) and older age (OR, 1.040 per year increase; 95% CI, 1.003–1.079; $P = .034$). Symptomatic intracranial hemorrhage was observed in only 8 (4%) patients, while 26 (13%) patients died within the first 3 months after AAIS. None of the methods of collateral grading could predict mortality or symptomatic intracranial hemorrhage.

DISCUSSION

Our results show that the Miteff system of grading intracranial collaterals on CTA is the only method that could reliably predict good outcomes at 3 months in patients treated with IV-tPA. Extremely poor outcome was easier to predict by most (Maas, Miteff, and ASPECTS methodology) of the collateral grading systems.

Studies in mice with MCA occlusions have shown that infarction is significantly smaller if extensive collaterals develop.⁶ Similarly, in humans, the presence of robust collateral flow on conventional angiography is associated with smaller infarcts and better clinical outcome.^{18–21} The presence of effective collateral blood flow may influence the response to IV-tPA in AAIS by transporting fibrinolytics to both sides of the thrombus and facilitating its dissolution or limiting extension of the occlusion.^{20,22–24} Furthermore, patients with good collaterals might carry a lower risk of hemorrhagic complications.^{13,25} Therefore, information about collateral flow in AAIS may help in establishing early prognosis and in planning various therapeutic approaches. For example, in patients with a higher risk of bleeding or more associated comorbidities, a good Miteff score could lead

the treating physician to initiate treatment with IV-tPA. The converse can also be true in patients with poor Miteff scores, in whom one might withhold IV-tPA treatment.

Previous studies have demonstrated an association between the degree of leptomeningeal collaterals and good outcome in patients not treated with IV-tPA or endovascular intervention.²⁶ However,

Table 2: Determinants of functional outcome in patients with thrombolized acute ischemic stroke

Variable	mRS 0–1 (n = 93)	mRS 2–6 (n = 107)	P Value
Median age (yr) (range)	58 (33–89)	71 (34–92)	.040
Female sex (%)	20 (21.5)	43 (40.2)	.005
Hypertension (%)	51 (54.8)	80 (74.8)	.034
Diabetes (%)	22 (23.6)	38 (35.8)	.069
Dyslipidemia (%)	45 (48.4)	57 (53.3)	.491
Atrial fibrillation (%)	23 (24.7)	50 (46.9)	.001
Smoker (%)	33 (35.5)	24 (22.4)	.119
Median NIHSS pre-tPA (range)	14 (3–29)	21 (8–33)	.477
Mean SBP pre-tPA (range)	142 (110–209)	154 (110–210)	.777
Median onset-to-treatment time (range)	152 (91–275)	158 (73–265)	.199
ASPECTS <7	36 (38.7)	62 (57.9)	.010
Recanalization of vessel	70 (75.3)	76 (71)	.040
Good collaterals by Tan method	74 (79.6)	49 (45.8)	.001
Good collaterals by Miteff method	25 (26.9)	66 (61.7)	.001
Good collaterals by Maas method	42 (45.2)	23 (21.5)	.005
Median score by ASPECTS methodology (range)	11 (0–18)	8 (1–18)	.021

Note:—SBP indicates systolic blood pressure.

Rosenthal et al²⁷ reported that leptomeningeal collaterals showed only a minimal positive impact in patients who did not achieve arterial recanalization, and they did not show any impact if complete recanalization of the occluded intracranial artery was achieved. We hypothesized that a favorable pattern of leptomeningeal collaterals on the pre-tPA CTA would result in improved functional outcome. We evaluated the 4 most accepted methodologies to test our hypothesis and to identify the best collateral grading system for predicting outcome in our patients treated with IV-tPA.

Being a simple grading system, the modified Tan system is easily reproducible among readers.¹⁵ However, it was not found to be a useful predictor of good outcome. Similarly, the ASPECTS-based grading system and the Maas system failed to predict good functional outcome in our patients with thrombolized anterior circulation. Only the Miteff grading system could determine good functional outcomes at 3 months. Perhaps, this result is due to the focus on the Sylvian fissure, the insular region that is known to predict the penumbral mismatch in acute MCA infarcts.²⁸ Good collaterals in these anatomic regions improve perfusion, reduce final infarct size, and lead to better outcomes. Focus on the easily recognizable landmarks (Sylvian fissure and insula) and a high rate of reproducibility are the main strengths of the Miteff scoring system and enable it to be a reliable predictor of good outcome in patients with AAIS treated with IV-tPA.

Conventional angiography is considered the criterion standard for collateral-flow assessment, but its invasive nature limits its use in clinical practice. Noninvasive and safer methods, including transcranial Doppler and MR angiography, can evaluate larger arteries such as the circle of Willis. However, they do not have enough resolution to evaluate the leptomeningeal vascular bed.⁶ CTA is widely available and has a higher degree of spatial resolution, which enables the assessment of leptomeningeal collaterals. Furthermore, CTA can be performed with concurrent imaging of the cervical arteries and CT perfusion for the “multimodal” penumbral assessment.^{29,30} Despite these advantages, only a few studies have used CTA to assess the degree of collateral circulation in AAIS.^{6,27} With rapid advancements in technology, better methods for collateral assessment are evolving. Perhaps, a multiphasic

CTA that provides information about early and late arterial phases may serve as a better tool for the evaluation of intracranial collaterals in acute ischemic stroke and may serve as a surrogate for perfusion studies, eventually becoming a part of standard routine reporting of CTAs in patients with acute ischemic stroke. However, multiphasic CTA would need to be evaluated and validated in a larger prospective study.

Some limitations of our study need to be acknowledged. First, although we evaluated a moderate-sized cohort of 200 patients, this sample size may not be sufficient to analyze the subtle differences among various collateral grading systems. Second, despite their common aim of predicting the prognosis, various grading

systems have their own inherent limitations. For example, the Maas system is less accurate in patients with a previous intracranial occlusion due to a limited side-to-side comparison. This finding may be specifically relevant to our Asian cohort of patients with AAIS with a high prevalence of intracranial stenosis.³¹ Similarly, in the ASPECTS grading system, basal ganglia regions have less vasculature and result in a higher weighting for leptomeningeal vessels. The location of the occlusion may also affect the predictive ability of the collateral scoring system. Third, despite its high spatial resolution, CTA does not provide enough information about flow dynamics. Therefore, CTA may lead to an overestimation of the degree of collateral circulation.³² Perhaps, consideration of internal cerebral vein asymmetry in patients with severe occlusive disease of the ICA or MCA may add significant hemodynamic information to the preferred method of scoring the intracranial collaterals in AAIS.³³ Fourth, the retrospective design of our study could be a limitation. However, the collateral-grading readers were blinded to the clinical information and outcome. Fifth, as evident from a high NIHSS score at presentation (median, 19 points), our study included a larger proportion of patients with severe AAIS. Finally, none of the methods of collateral grading were associated with early mortality or symptomatic intracranial hemorrhage. We suspect that this observation is related to the sample size of our study, and a larger study is recommended to evaluate this association, especially between intracranial collateral grading and symptomatic intracranial hemorrhage.²⁵

CONCLUSIONS

Our study provides a comparative assessment of various grading methods for intracranial collaterals for establishing an early prognosis in patients with AAIS treated with IV-tPA. Only the Miteff system was found to be a reliable predictor of favorable outcome in IV-treated patients with AAIS. We believe that routine grading and reporting of intracranial collaterals will rapidly become a part of the standard stroke CTA reports as the clinical relevance becomes more and more apparent. Further larger scale prospective studies, with evaluation of additional information about cerebral

hemodynamics, are recommended to develop better grading criteria for intracranial collaterals in AAIS.

Disclosures: Leonard Yeo—RELATED: Grant: National Medical Research Council Singapore,* Comments: grant No. CNIGI2nov001. Benjamin Wakerley—UNRELATED: Travel/Accommodations/Meeting Expenses Unrelated to Activities Listed: Novartis, Comments: sponsored for the 2014 American Academy of Neurology meeting. *Money paid to the institution.

REFERENCES

1. Thomassen L, Waje-Andreassen U, Naess H, et al. **Doppler ultrasound and clinical findings in patients with acute ischemic stroke treated with intravenous thrombolysis.** *Eur J Neurol* 2005;12:462–65
2. Rha JH, Saver JL. **The impact of re-canalization on ischemic stroke outcome: a meta-analysis.** *Stroke* 2007;38:967–73
3. Liebeskind DS, Kim D, Changizi K, et al. **Collateral failure? Late mechanical thrombectomy after failed intravenous thrombolysis.** *J Neuroimaging* 2008;20:78–82
4. Liebeskind D. **Collaterals in acute stroke: beyond the clot.** *Neuroimaging Clin N Am* 2005;15:553–73
5. Liebeskind DS. **Understanding blood flow: the other side of an acute arterial occlusion.** *Int J Stroke* 2007;2:118–20
6. Liebeskind DS. **Collateral circulation.** *Stroke* 2003;34:2279–84
7. Liebeskind DS. **Neuroprotection from the collateral perspective.** *IDrugs* 2005;8:222–28
8. Sakoh M, Ostergaard L, Gjedde A, et al. **Prediction of tissue survival after middle cerebral artery occlusion based on changes in the apparent diffusion of water.** *J Neurosurg* 2001;95:450–58
9. Sobesky J, Weber OZ, Lehnhardt FG, et al. **Which time-to-peak threshold best identifies penumbral flow? A comparison of perfusion-weighted magnetic resonance imaging and positron emission tomography in acute ischemic stroke.** *Stroke* 2004;35:2843–47
10. Lin CS, Polsky K, Nadler JV, et al. **Selective neocortical and thalamic cell death in the gerbil after transient ischemia.** *Neuroscience* 1990;35:289–99
11. Jauch EC, Saver JL, Adams HP Jr, et al. **Guidelines for the early management of patients with acute ischemic stroke: a guideline for healthcare professionals from the American Heart Association/American Stroke Association.** *Stroke* 2013;44:870–947
12. Adams HP Jr, Bendixen BH, Kappelle LJ, et al. **Classification of subtype of acute ischemic stroke: definitions for use in a multicenter clinical trial: TOAST—Trial of Org 10172 in Acute Stroke Treatment.** *Stroke* 1993;24:35–41
13. Miteff F, Levi CR, Bateman GA, et al. **The independent predictive utility of computed tomography angiography collateral status in acute ischemic stroke.** *Brain* 2009;132:2231–38
14. Maas MB, Lev MH, Ay H, et al. **Collateral vessels on CT angiography predict outcome in acute ischemic stroke.** *Stroke* 2009;40:3001–05
15. Tan Y, Demchuk AM, Hopyan J, et al. **CT angiography clot burden score and collateral score: correlation with clinical and radiologic outcomes in acute middle cerebral artery infarct.** *AJNR Am J Neuroradiol* 2009;30:525–31
16. Menon BK, Smith EE, Modi J, et al. **Regional leptomeningeal score on CT angiography predicts clinical and imaging outcomes in patients with acute anterior circulation occlusions.** *AJNR Am J Neuroradiol* 2011;32:1640–45
17. Choi JY, Kim EJ, Hong JM, et al. **Conventional enhancement CT: a valuable tool for evaluating pial collateral flow in acute ischemic stroke.** *Cerebrovasc Dis* 2011;31:346–52
18. Bozzao L, Fantozzi LM, Bastianello S, et al. **Early collateral blood supply and late parenchymal brain damage in patients with middle cerebral artery occlusion.** *Stroke* 1989;20:735–40
19. von Kummer R, Holle R, Rosin L, et al. **Does arterial recanalization improve outcome in carotid territory stroke?** *Stroke* 1995;26:581–87
20. Ringelstein EB, Biniek R, Weiller C, et al. **Type and extent of hemispheric brain infarctions and clinical outcome in early and delayed middle cerebral artery recanalization.** *Neurology* 1992;42:289–98
21. Mohammad YM, Christoforidis GA, Bourekas EC, et al. **Qureshi grading scheme predicts subsequent volume of brain infarction following intra-arterial thrombolysis in patients with acute anterior circulation ischemic stroke.** *J Neuroimaging* 2008;18:262–67
22. Jo KD, Saver JL, Starkman S, et al. **Predictors of recanalization with mechanical thrombectomy for acute ischemic stroke (abstract).** *Stroke* 2008;39:599
23. Nogueira RG, Liebeskind DS, Sung G, et al. **Predictors of good clinical outcomes, mortality, and successful revascularization in patients with acute ischemic stroke undergoing thrombectomy: pooled analysis of the Mechanical Embolus Removal in Cerebral Ischemia (MERCi) and MultiMERCi trials.** *Stroke* 2009;40:3777–83
24. Jovin TG, Gupta R, Horowitz MB, et al. **Pretreatment ipsilateral regional cortical blood flow influences vessel recanalization in intra-arterial thrombolysis for MCA occlusion.** *AJNR Am J Neuroradiol* 2007;28:164–67
25. Bang OY, Saver JL, Kim SJ, et al. **Collateral flow averts hemorrhagic transformation after endovascular therapy for acute ischemic stroke.** *Stroke* 2011;42:2235–39
26. Lima FO, Furie KL, Silva GS, et al. **The pattern of leptomeningeal collaterals on CT angiography is a strong predictor of long-term functional outcome in stroke patients with large vessel intracranial occlusion.** *Stroke* 2010;41:2316–22
27. Rosenthal ES, Schwamm LH, Roccatagliata L, et al. **Role of recanalization in acute stroke outcome: rationale for a CT angiogram-based “Benefit of Recanalization” model.** *AJNR Am J Neuroradiol* 2008;29:1471–75
28. Kamalian S, Kemmling A, Borgie RC, et al. **Admission insular infarction >25% is the strongest predictor of large mismatch loss in proximal middle cerebral artery stroke.** *Stroke* 2013;44:3084–89
29. Zhao L, Barlinn K, Bag AK, et al. **Computed tomography perfusion prognostic maps do not predict reversible and irreversible neurological dysfunction following reperfusion therapies.** *Int J Stroke* 2011;6:544–46
30. Wintermark M, Meuli R, Browaeys P, et al. **Comparison of CT perfusion and angiography and MRI in selecting stroke patients for acute treatment.** *Neurology* 2007;68:694–97
31. De Silva DA, Woon FP, Pin LM, et al. **Intracranial large artery disease among OSCP subtypes in ethnic South Asian ischemic stroke patients.** *J Neurol Sci* 2007;260:147–49
32. Arnold M, Nedeltchev K, Mattle HP, et al. **Intra-arterial thrombolysis in 24 consecutive patients with internal carotid artery occlusions.** *J Neurol Neurosurg Psychiatry* 2003;74:739–42
33. Sharma VK, Yeo LL, Teoh HL, et al. **Internal cerebral vein asymmetry on follow-up brain computed tomography after intravenous thrombolysis in acute anterior circulation ischemic stroke is associated with poor outcome.** *J Stroke Cerebrovasc Dis* 2014;23:e39–45

Regional Cerebral Arterial Transit Time Hemodynamics Correlate with Vascular Risk Factors and Cognitive Function in Men with Coronary Artery Disease

BJ. MacIntosh, W. Swardfager, A.D. Robertson, E. Tchistiakova, M. Saleem, P.I. Oh, N. Herrmann, B. Stefanovic, and K.L. Lanctôt



ABSTRACT

BACKGROUND AND PURPOSE: Arterial transit time is the time needed for blood to travel from large arteries to capillaries, as estimated from arterial spin-labeling MR imaging. The purpose of this study was to determine whether vascular risk factors and cognitive performance are related to regional differences in cerebral arterial transit time in patients with coronary artery disease who are at risk for cognitive decline.

MATERIALS AND METHODS: Arterial transit time was estimated from multiple postlabel delay pseudocontinuous arterial spin-labeling images obtained from 29 men with coronary artery disease. Tests of memory, attention, processing speed, and executive function were administered. Principal component analysis was used to create separate models of cognition and vascular risk, which were related to brain regions through voxelwise analyses of arterial transit time maps.

RESULTS: Principal component analysis identified 2 components of vascular risk: 1) “pressor” (age, systolic blood pressure, and pulse pressure) and 2) “obesity” (body fat percentage and body mass index). Obesity was inversely related to arterial transit time in the posterior cingulate, precuneus, lateral occipital cortices, middle temporal gyrus, and frontal pole (P corrected $< .05$), whereas pressor was not significant. Cognitive scores were factored into a single component. Poor performance was inversely related to precuneus arterial transit time (P corrected $< .05$). The average arterial transit time in regions identified by obesity was associated with poorer cognitive function ($r^2 = 0.21$, $t = -2.65$, $P = .01$).

CONCLUSIONS: Altered cerebral hemodynamics, notably in nodal structures of the default mode network, may be one way that vascular risk factors impact cognition in patients with coronary artery disease.

ABBREVIATIONS: ASL = arterial spin-labeling; ATT = arterial transit time; BMI = body mass index; CAD = coronary artery disease; cog-PC = cognitive principal component; CVLT-LDFR = California Verbal Learning Test long-delay free recall; LATT = large-artery transit time; PC = principal component; SBP = systolic blood pressure

Obesity and hypertension are prevalent vascular risk factors among older adults, known to impact brain structure and function. Elevated body mass index (BMI), for example, has been associated with reduced gray matter volume.^{1,2} Furthermore,

overweight or obese classifications in midlife have been linked to decline in cognitive performance, involving memory, processing speed, verbal fluency, and visuospatial domains³ and an increased risk of Alzheimer disease and vascular dementia.⁴ Likewise, elevated systolic blood pressure (SBP) has been associated with reduced cerebral tissue, which appears to be more specific to men than women.⁵ Elevated SBP also has been associated with cognitive impairment, namely executive function, among older adults.⁶ Taking these findings into account, researchers have suggested that vascular risk factors contribute to cognitive impairment through cerebrovascular dysfunction itself.^{7,8}

In animal studies, hypertension and obesity lead to cerebrovascular remodeling, including thickened arteriolar walls, reduced lumen area, and rarefaction of the microcirculation.⁹ Ar-

Received May 28, 2014; accepted July 8.

From the Canadian Partnership for Stroke Recovery (B.J.M., W.S., A.D.R., E.T., N.H., B.S., K.L.L.), Physical Sciences (B.J.M., B.S.), and Neuropsychopharmacology Research Group (W.S., M.S., N.H., K.L.L.), Sunnybrook Research Institute, Toronto, Ontario, Canada; Departments of Medical Biophysics (B.J.M., E.T., B.S.), Pharmacology/Toxicology (K.L.L., W.S.), and Psychiatry (N.H., K.L.L.), University of Toronto, Toronto, Ontario, Canada; and Toronto Rehabilitation Institute (P.I.O., K.L.L.), Toronto, Ontario, Canada.

This work was funded by The Drummond Foundation (K.L.L., N.H.), Physicians' Services Incorporated Foundation (K.L.L., N.H.), and the Canadian Institutes of Health Research (K.L.L., N.H.: MOP-114913). W.S. was supported by the Canadian Partnership for Stroke Recovery, the Canadian Institutes of Health and Research and by the Toronto Rehabilitation Institute.

Please address correspondence to Bradley J. MacIntosh, PhD, Canadian Partnership for Stroke Recovery, Sunnybrook Research Institute, 075 Bayview Ave, M6-180, Toronto, ON, M4N 3M5, Canada; e-mail: bmac@sri.utoronto.ca; @HSFCSR

Indicates open access to non-subscribers at www.ajnr.org

Indicates article with supplemental on-line photo.

<http://dx.doi.org/10.3174/ajnr.A4094>

terial spin-labeling (ASL) is typically used to measure CBF as a single measure of perfusion; acquiring multiple postlabel delays permits more comprehensive hemodynamic estimates, including arterial transit time (ATT). Although ASL is a low SNR technique, considerable research has gone into modeling approaches that incorporate spatial and temporal information to produce robust voxel-level estimates.¹⁰⁻¹³ Mapping the ASL arterial transit time, for instance, is of interest because it reflects the time for labeled blood to travel from the labeling plane to the microvascular perfusion site. Previously, ATT has been used as an adjunct perfusion measure to study minor stroke and transient ischemic attack,¹⁴ large artery stenosis-occlusive disease,^{15,16} multiple sclerosis,¹⁷ and Alzheimer disease,^{18,19} but to date, it has not been used to examine the potential effects of vascular risk factors on cognition, to our knowledge.

We have recently reported gray matter perfusion findings in coronary artery disease (CAD) in the context of cerebrovascular health.²⁰ This population is relevant to the study of neurodegenerative disease risk because of the following: 1) They present with multiple vascular risk factors that impact both the heart and the brain, 2) have a propensity for small-vessel disease affecting the white matter, and 3) have a higher susceptibility to cognitive decline.^{21,22} In older adults, obesity was recently reported to affect the functional connectivity of the default mode network.²³ We hypothesized that regional ATT would be associated with aggregate measures of both vascular risk and cognitive function in men with CAD.

MATERIALS AND METHODS

Participants

Twenty-nine male patients with a history of CAD provided written informed consent and were recruited for this study. Sunnybrook Research Institute and University Health Network research ethics boards approved this study. After providing a detailed clinical history, patients underwent MR imaging and performed a battery of cognitive tests. Inclusion criteria were male sex, 55–80 years of age, and a documented history of CAD characterized by myocardial infarction, narrowing of at least 1 major coronary artery on angiography, prior percutaneous coronary intervention, or coronary artery bypass graft surgery. This study excluded women due to the low referral rate of women to the cardiac rehabilitation program²⁴ and reported differences in ATT between men and women,²⁵ which would have necessitated a larger sample to include sex as a covariate. Patients were excluded on the basis of a history of any neurodegenerative disorder. Demographic information, concomitant medications, anthropometrics, resting blood pressure, and history of hyperlipidemia, diabetes mellitus, hypertension, and smoking were ascertained, in addition to cardiac history.

MR Imaging

MR imaging was performed on a 3T system (Discovery MR750; GE Healthcare, Milwaukee, Wisconsin) by using a radiofrequency body coil for transmission and an 8-channel phased array radiofrequency head coil for signal detection. High-resolution T1-w images were collected by using 3D spoiled gradient-recalled echo (TR/TE/TI = 8.1/3.2/650 ms, flip angle = 8°, acquisition matrix = 256 × 192 × 186, nominal spatial resolution = 0.9 × 0.9 × 1 mm). Standard T2-weighted FLAIR images were acquired

to characterize white matter hyperintensities (2D axial images, TR/TE/TI = 9700/140/2200 ms, voxel dimensions = 0.9 × 0.9 × 3 mm, sections = 48). A semiautomated procedure was used to quantify the volume of white matter lesion burden (milliliter).²⁶ Pseudocontinuous ASL was performed with a label duration of 1.5 seconds, and the labeling plane was prescribed above the carotid bifurcation, aided by time-of-flight angiography images. Axial single-shot EPI was used to collect 25 sequential control and tag images. Seventeen slices were collected with a gap of 1.4 mm, section thickness of 4.2 mm, and nominal voxel dimensions of 3.4 × 3.4 × 5.6 mm³. The acquisition was repeated at 6 different postlabel delays (ie, 100, 500, 900, 1300, 1700, and 2100 ms) to produce an ASL kinetic time-series (On-line Figure), as reported previously.²⁷ In keeping with the recommended guidelines for clinical ASL, we did not use bipolar gradients to suppress large-artery flow signal.²⁸ Instead macrovascular signals were isolated, when appropriate, in the ASL model (see below).

Postprocessing

ASL images were processed by using the fMRI of the Brain Software Library tools (FSL; <http://www.fmrib.ox.ac.uk/fsl>). Postprocessing of ASL data included perfusion-weighted difference images, motion correction, and spatial smoothing by a Gaussian kernel of 5-mm full width at half maximum. Hemodynamic parameter estimates were generated by using the Bayesian Inference for Arterial Spin Labeling tool of FSL. ATT images were coregistered to the T1-w images by using transformation matrices established by CBF images, because both T1-w and CBF images contain good gray-to-white differentiation for registration purposes. T1-w images was subsequently aligned to a standard space template with 12 degrees of freedom.

ATT (seconds) was the primary cerebral gray matter hemodynamic outcome measure of interest in this study. ATT was estimated on the basis of the standard ASL model²⁹ and by using a fixed-label duration of 1.5 seconds. A 1-compartment model (tissue only) and a 2-compartment model (tissue and macrovascular compartments) were considered. The former produces ATT and CBF estimates, while the latter produces ATT, CBF, large artery transit time (LATT, seconds), and arterial blood volume estimates.¹² Most important, the 2-compartment model takes effect only in cases in which the voxel signal is deemed to be mixed between tissue and macrovascular compartments. This procedure is performed by using an automatic relevancy determination, whereby LATT and arterial blood volume macrovascular estimates are generated in addition to ATT and CBF.¹² The macrovascular estimates typically occur in voxels near large intracranial arteries, like the circle of Willis (LATT and arterial blood volume maps are shown in Fig 1). CBF and LATT data were included in secondary analyses.

Neuropsychological Testing

Cognitive assessments were chosen on the basis of the recommendations of the National Institute of Neurological Disorders and Stroke and Canadian Stroke Network harmonized standards.³⁰ The Trail-Making Test B (connecting a sequence of alternating letters and numbers) and the Victoria version of the Stroop interference task (color-word) were chosen for their sensitivity to ex-

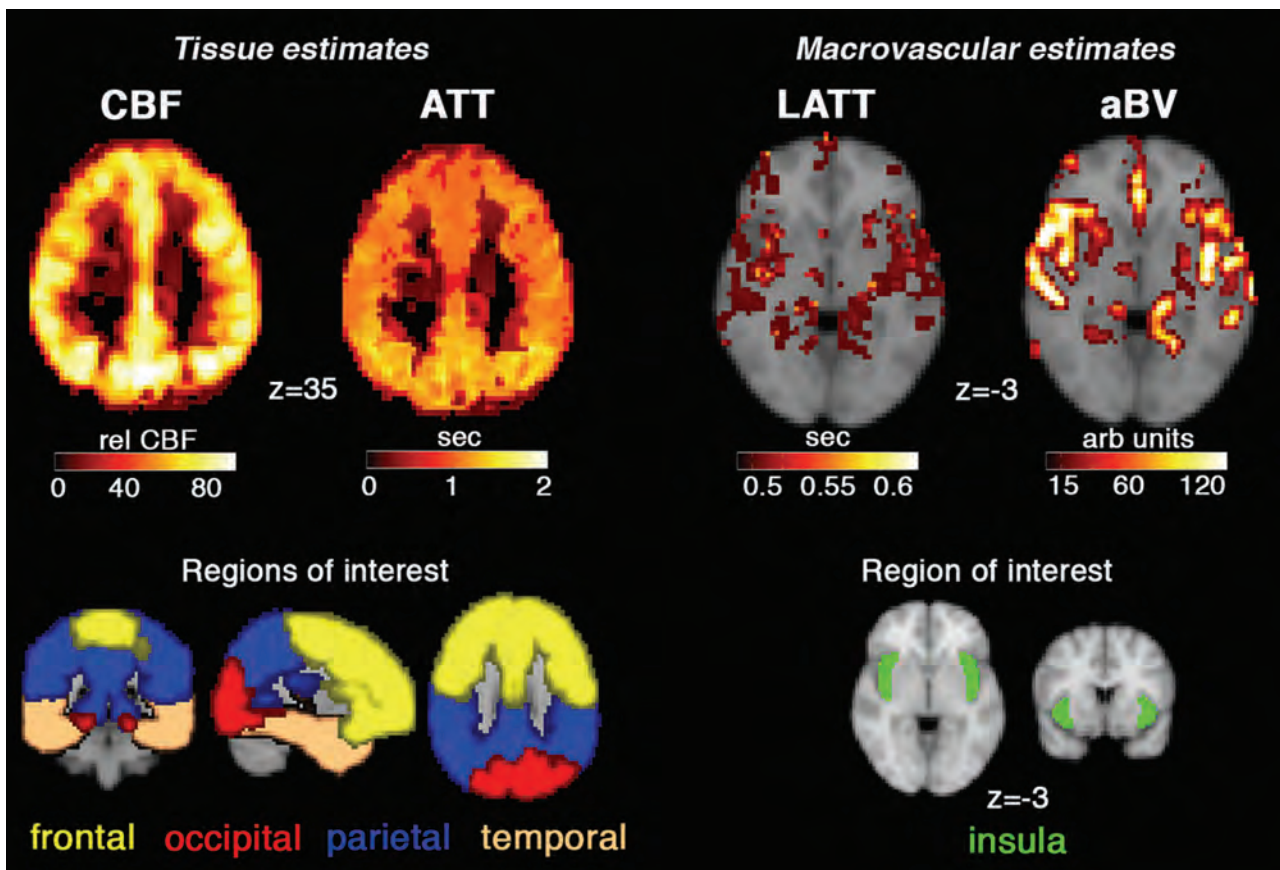


FIG 1. The top row of images shows cerebral blood flow (intensity-normalized units), arterial transit time, large-artery transit time, and arterial blood volume (arbitrary units) from a representative participant. In the ATT image, the posterior circulation tends to have a longer ATT compared with the middle cerebral artery vascular territory. LATT and arterial blood volume are macrovascular measures that are estimated from voxels containing large-artery/intravascular ASL signal. The bottom row shows 4 lobe-based regions of interest chosen for ATT (and CBF) analysis, while a middle cerebral artery/insula region of interest was chosen the LATT analysis.

ecutive function (eg, set shifting and overcoming interference between conflicting visual and lexical cognitive sets). These are timed tasks, with greater time to completion indicating poorer performance. The digit symbol-coding task from the Wechsler Adult Intelligence Scale, 3rd Edition, was chosen as a highly sensitive measure of complex attention and psychomotor processing speed. Digit symbol-coding performance is summarized by the number of symbols matched to digits based on a provided key within 2 minutes. Memory was assessed by the California Verbal Learning Test (CVLT) word list after a 20-minute delay (long-delay free recall [LDFR]). For the latter 2 tasks, greater scores indicate better performance. All cognitive testing was performed at 9:30 AM (± 30 minutes) after an 8-hour fast.

Statistics

Analyses of the 2-compartment ATT data were performed in standard space at 3-mm isotropic voxel dimensions (Montreal Neurological Institute standard atlas). ATT estimates from the 1-compartment model were also analyzed to assess the effect of the ASL model on the results. ATT was characterized by using the 4 bilateral lobes of the standard atlas brain (3-mm isotropic) as gray matter ROIs (frontal, occipital, parietal, temporal; Fig 1) and by using voxelwise approaches. LATT was analyzed from a single region of interest in the bilateral insula.¹² Two separate models

were constructed to explain between-subject variance in ATT, CBF, and LATT data: 1) a vascular risk factor model, and 2) a cognitive model. The vascular risk model consisted of the following variables: age, BMI, percentage body fat, SBP, and pulse pressure (ie, the difference between systolic and diastolic pressures). The cognitive model consisted of age and raw scores on the CVLT-LDFR, digit symbol-coding test, Stroop, and Trail-Making Test B. Principal component analysis was performed in R statistical computing software (<http://www.r-project.org/>) to extract uncorrelated vascular risk and cognitive predictors of ATT. Principal components (PCs) were considered in the model if individually they accounted for at least 10% of the total variance and collectively, $>80\%$ of the total explained variance.

General linear models were conducted by using R for the region-of-interest analyses and FSL for voxelwise group analyses. Explanatory variables in the general linear models were the demeaned vascular risk or cognitive PCs, and the 2 predictors were treated separately. For the region-of-interest analyses, a Bonferroni correction was performed to compute adjusted *P* values. For the voxelwise analyses, statistical maps were calculated by using permutation testing (ie, the FSL Randomise tool).³¹ Five thousand permutations were performed followed by threshold-free cluster enhancement³² to correct for multiple comparisons.

Significant voxels were reported at a corrected P value of .05 ($p_{\text{corrected}} = .05$).

RESULTS

Patient Characteristics

Patient demographics and characteristics are reported in Table 1. Evidence of severe symptomatic CAD was demonstrated by histories of myocardial infarction (41.4%), coronary artery bypass graft surgery (48.3%), and percutaneous coronary intervention (44.8%). All patients had a history of hyperlipidemia. Histories of diabetes mellitus (13.8%), hypertension (41.4%), and smoking (55.2%) were also common. All patients were using acetylsalicylic acid. The most common concomitant medications included cholesterol-lowering medication (96.6%),

Table 1: Patient demographics (N = 29)

Demographic	Mean (SD)	Minimum	Maximum
Age (yr)	65 (7)	55	78
BMI (kg/m ²)	28.2 (3.9)	20.5	35.3
Body fat (%)	26.0 (5.9)	13.3	38.7
SBP (mm Hg)	124 (15.4)	94.0	152.0
PP (mm Hg)	51 (13.0)	24.0	80.0

Note:—PP indicates pulse pressure.

Table 2: Vascular risk and cognitive model details

	Correlation Coefficient (r)		
	Component 1	Component 2	Component 3
Vascular model			
Age (yr)	-0.65	0.32	0.69
BMI (kg/m ²)	0.23	0.91	-0.06
Body fat (%)	0.24	0.91	-0.10
SBP (mm Hg)	-0.90	0.18	-0.32
PP (mm Hg)	-0.94	0.06	-0.21
Percentage of variance (%)			
Explained variance	0.45	0.36	0.13
Cumulative variance	0.45	0.81	0.94
Cognitive model			
Age (yr)	0.48	0.76	-0.39
CVLT-LDFR	-0.73	-0.37	-0.50
Digit symbol-coding	-0.70	0.53	0.30
Stroop	0.85	-0.06	-0.16
TMT B	0.82	-0.26	0.21
Percentage of variance (%)			
Explained variance	0.53	0.21	0.11

Note:—TMT indicates Trail-Making Test; PP, pulse pressure.

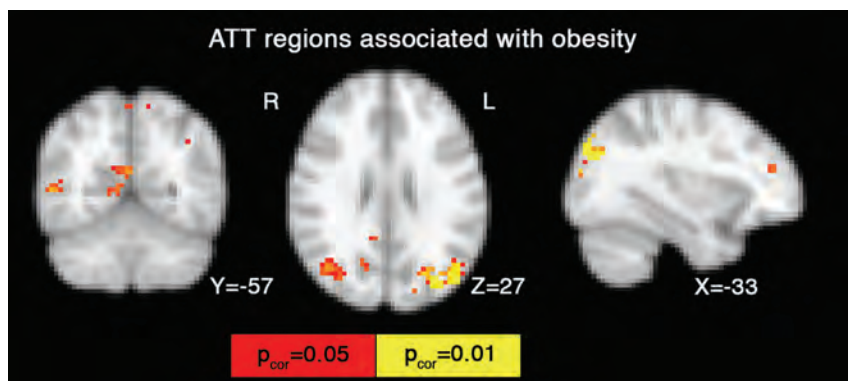


FIG 2. Voxelwise results from the regression analyses in which the vascular model (“pressor” and “obesity” factor) was used as an independent factor that influences ATT. The obesity factor produced a negative association with ATT, in the sense that the higher the BMI and/or body fat, the shorter the ATT. Significant voxels in red and yellow are corrected for multiple comparison ($p_{\text{corrected}} = .05$).

β -blockers (69.0%), antihypertensive agents (55.2%), and antidiabetic agents (13.8%). FLAIR white matter hyperintensities amounted to a median lesion burden of 2.63 mL (interquartile range = 1.54–6.76 mL).

Vascular Risk Factors versus Regional Hemodynamics

The first 3 PCs explained >80% of the vascular risk data and were subsequently used in this model. PC1, PC2, and PC3 explained 45%, 36%, and 13% of the variance, respectively (Table 2). PC1 was viewed as a “pressor” variable because SBP and pulse pressure contributed to this component with a correlation coefficient of $r < -0.9$. PC2 was viewed as an “obesity” variable because BMI and body fat contributed to this component with $r > 0.9$. PC3 was influenced by age to a lesser extent ($r = 0.69$).

The lobe region-of-interest analyses revealed that PC2 was significantly associated with ATT, while PC1 and PC3 were not. The obesity component (PC2) was inversely related to ATT—that is, higher body fat was associated with shorter ATT in the occipital lobe ($t = -3.2$, $P = .004$, Bonferroni-corrected $P = .015$), but none of the other lobes were significant (Bonferroni-corrected $P > .10$). Voxelwise ATT analysis revealed significant findings for the obesity component in the posterior cingulate, precuneus, lateral occipital cortices, right middle temporal gyrus, and the left frontal pole ($p_{\text{corrected}} < .05$, Fig 2 and Table 3). The insula region of interest had a LATT that was inversely associated with the pressor component (ie, LATT versus PC1, $t = -2.2$, $P = .034$), but not the obesity component, PC2, or PC3 ($P > .27$). The inverse association here suggests that higher pulse pressure and SBP were associated with prolonged ATT. Use of the more parsimonious ASL model (ie, with only a tissue compartment) did not influence the voxelwise associations between the vascular risk model and ATT.

Cognition versus Regional Hemodynamics

The first 3 cognitive PCs (cog-PCs) explained >80% of the cognitive data, and they were subsequently used in the cognitive model. Cog-PC1, cog-PC2, and cog-PC3 explained 53%, 21%, and 11% of the variance, respectively (Table 2). Cog-PC1 can be viewed as an indicator of cognitive dysfunction because the CVLT-LDFR and digit symbol-coding scores were negative associations, while the timed Stroop and Trail-Making Test B measures were positive associations. Each of the 4 cognitive measures contributed significantly to PC1 ($r > .82$ or $r < -0.70$). Less relevant cog-PCs were cog-PC2, which was influenced by aging, and cog-PC3, which did not contribute a meaningful cognitive effect.

Region-of-interest analyses revealed that cog-PC1 showed negative associations with ATT, indicating that individuals with poorer cognitive scores had shorter ATT, but these associations did not survive false discovery rate correction for multiple comparison (ie, 4 brain

lobes, adjusted $P > .054$). Voxelwise analysis was significant, however, with an association between cognitive decline and shorter ATT in the precuneus region ($p_{\text{corrected}} < .05$, Fig 3 and Table 3). The cog-PC2 and cog-PC3 did not show any significant associations. The insula LATT region of interest was not significant with any of the cognitive model parameters ($P > .086$). The use of the more parsimonious ASL model did not influence the voxelwise associations between the cognitive model and ATT.

Post Hoc Tests

Brain regions that were associated with the obesity component of the vascular model were used as a mask, and the average ATT in these regions was calculated for each participant. ATT in this obesity mask was significantly correlated with cognitive function ($r^2 = 0.21$, $t = -2.65$, $P = .013$).

CBF data produced no significant voxels related to components of vascular risk or cognition ($p_{\text{corrected}} > .05$) by using the same voxelwise analyses as used in the ATT data. However, within the ATT mask circumscribed by the vascular risk model results (PC2, Fig 2), CBF was negatively associated with obesity ($t = -2.43$, $P = .022$), and within the ATT mask circumscribed by the cognitive model results (PC1, Fig 3), CBF was negatively associated with cognitive PC1 ($t = -2.53$, $P = .018$).

The widely used BMI classifications (ie, healthy, overweight, obese)⁴ produced results similar to those of the obesity compo-

nent (PC2) in region-of-interest analyses, albeit with slightly reduced statistical significance (data not shown).

DISCUSSION

The current study demonstrates relationships among cerebral hemodynamics, obesity, and cognition. In older men with CAD, microvascular ATT decreased in association with obesity and poorer cognitive function. The implicated regions included areas of the lateral occipital, precuneus, angular gyrus, middle temporal, and frontal pole. In addition, the macrovascular LATT was significantly associated with hypertension, but not with obesity.

ATT differences associated with obesity occurred primarily in the parietal and occipital lobes. This result is notable for a few reasons. First, the regions identified are consistent with the default mode network, which is a network implicated in cognitive function in later life.^{33,34} Second, precuneus ATT was also found to be negatively associated with cognitive function. Third, ATT in brain regions identified by obesity explained 21% of the variance in cognitive function across the group.

The pressor component was defined by SBP and pulse pressure; however, it did not significantly correlate with regional ATT at a voxelwise level or in the lobe-based region-of-interest analyses. This finding was unexpected, given previous findings relating blood pressure with cerebral hemodynamics³⁵; however, the literature, to date, has focused primarily on large-artery hemodynamics, such as the middle cerebral artery pulsatility index or blood flow velocity. On the other hand, LATT provides macrovascular information and was significantly associated with the pressor component in the insula region of interest. These results suggest that vascular risk factors may have differential effects on cerebral hemodynamics, which appear to be region-specific.

While the ATT results were significant at a voxelwise level after a conservative correction for multiple comparisons, CBF analyses were not significant in stringent voxelwise analyses. However, post hoc tests suggested that CBF was decreased in proportion to both obesity and cognitive dysfunction in regions identified by ATT; this finding suggests complementary utility between ATT and CBF measures. The focus of the current study was on estimating hemodynamic ATT, which requires sampling multiple-postlabel delay acquisitions at the potential expense of the CBF estimate. Our choice of ASL parameters may therefore have contributed to the reduced sensitivity of CBF analyses.

Ischemic diseases, such as stroke and steno-occlusive large-artery disease, are known to produce prolonged ATT due to the necessity for collateral delivery of blood to tissue or narrowing of the large supplying arteries.^{15,16} In the current study, prolonged LATT and reduced ATT were associated with vascular risk factors. The reduced ATT may be attributed to altered pulsatile pressures, as reflected in the literature,^{35,36} and may be an indication of vessel wall hardening and thickening, which are arteriosclerosis processes consistent with higher BMI and body fat.⁹

Table 3: Summary of voxelwise findings

	No. of Voxels	MNI Coordinates		
		X	Y	Z
Vascular model				
1) Lateral occipital, R	540	-33	-78	30
2) Lateral occipital, L	38	39	-69	27
3) Middle temporal gyrus, R	36	54	-57	6
4) Precuneus	13	0	-60	60
5) Frontal pole, L	11	-36	45	18
6) Angular gyrus, L	11	-39	-51	42
7) Lateral occipital, L	4	-27	-63	48
Cognitive model				
1) Precuneus	189	0	-66	42

Note:—MNI indicates Montreal Neurological Institute; R, right; L, left.

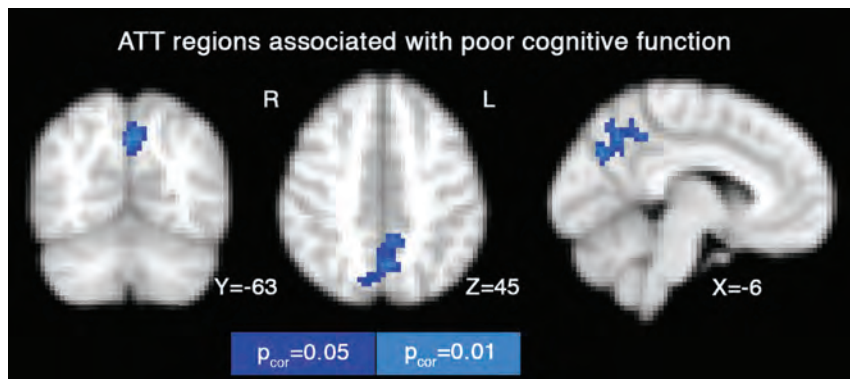


FIG 3. Voxelwise results from the regression analyses, in which the cognitive model was used as an independent factor that influences ATT. The first cognitive factor (ie, characterized by poor cognitive performance) was positively associated with ATT, in the sense that a lower cognitive score was associated with a shorter ATT. Significant voxels in blue and cyan are corrected for multiple comparison ($p_{\text{corrected}} = .05$).

This study was designed to detect only within-group differences, lacking comparisons between patients with CAD and age-matched controls without a history of CAD. Such normative data would be beneficial to determine whether similar associations are found in healthy age-related processes. The current study was limited to men, due to their relative over-representation in cardiac rehabilitation and the need to otherwise control for robust differences in ATT between men and women.²⁵ Future work should assess the extent to which both female and male patients with CAD show similar ATT changes in association with vascular and cognitive variables. The absence of uncontrolled diabetic symptoms and current smoking habits within the present cohort prevented these risk factors from being addressed. Furthermore, blood lipid levels were not available for all participants. These additional measures may have helped to explain a greater proportion of the variance and should be explored through future studies. Finally, principal component analysis was used to restrict the number of independent variables, which amounted to 2 vascular risk factors and 1 cognitive factor. This strategy proved useful in identifying voxelwise ATT associations with obesity and cognitive performance. Correlations with additional risk factors (eg, blood lipid levels and smoking habits) and, in particular, a mechanistic understanding of these relationships, including causality, should be addressed by studies that incorporate a longitudinal design.

CONCLUSIONS

We found that men with CAD have altered cerebral hemodynamics in proportion to both cardiometabolic risk factors and cognitive function. ATT was used as a microvascular measure, while LATT characterized macrovascular hemodynamics. We observed that ATT in nodes of the default mode network was associated with obesity and cognition, whereas LATT was associated with hypertension. The use of these ASL-derived hemodynamic measures produced novel associations that converge with other studies to implicate changes in the default mode network as markers of cognitive decline.^{34,37} Future studies might explore mechanisms potentially relating adiposity to cerebral hemodynamics and cognition, such as blood lipid levels associated with cognitive decline.³⁸

ACKNOWLEDGMENTS

We thank Dr Michael Chappell for useful discussion concerning the ASL model.

Disclosures: Nathan Herrmann—*RELATED: Grant:* The Drummond Foundation,* Physicians' Services Incorporated Foundation,* Canadian Institutes of Health Research,* *Comments:* peer-reviewed grants; *UNRELATED: Consultancy:* Sonexa Therapeutics, Wyeth Pharmaceuticals, Pivina Consulting, Sanofi-Aventis Canada; *Grants/Grants Pending:* Alzheimer Society of Canada,* Canadian Institute of Health Research,* Heart and Stroke Foundation,* Ontario Ministry of Health and Long-Term Care, Provincial Innovation Fund,* Ontario Brain Institute,* *Comments:* peer-reviewed grants; *Other:* Pfizer Canada,* F. Hoffman-La Roche Ltd,* Elan Pharma International Ltd,* Lundbeck Canada,* *Comments:* research contracts. Krista L. Lancôt—*RELATED: Grant:* Canadian Institutes of Health Research,* The Drummond Foundation,* Physicians' Services Incorporated Foundation*; *UNRELATED: Consultancy:* AbbVie, F. Hoffman-La Roche Ltd; *Grants/Grants Pending:* Alzheimer's Society Canada,* Alzheimer's Drug Discovery Foundation,* Canadian Institute of Health Research,* Heart and Stroke Foundation,* Consortium of Canadian Centres for Clinical Cognitive Research,* Canadian Consortium on Neurodegeneration in Aging,* *Other:* AbbVie,* F. Hoffman-La Roche Ltd,* Elan Pharma International Ltd,* Lundbeck Canada Inc.* *Comments:* research funding. *Money paid to the institution.

REFERENCES

1. Kurth F, Levitt JG, Phillips OR, et al. Relationships between gray matter, body mass index, and waist circumference in healthy adults. *Hum Brain Mapp* 2013;34:1737–46
2. Raschpichler M, Straatman K, Schroeter ML, et al. Abdominal fat distribution and its relationship to brain changes: the differential effects of age on cerebellar structure and function—a cross-sectional, exploratory study. *BMJ Open* 2013;3:pil: e001915
3. Hassing LB, Dahl AK, Pedersen NL, et al. Overweight in midlife is related to lower cognitive function 30 years later: a prospective study with longitudinal assessments. *Dement Geriatr Cogn Disord* 2010;29:543–52
4. Xu WL, Atti AR, Gatz M, et al. Midlife overweight and obesity increase late-life dementia risk: a population-based twin study. *Neurology* 2011;76:1568–74
5. Gianaros PJ, Greer PJ, Ryan CM, et al. Higher blood pressure predicts lower regional grey matter volume: consequences on short-term information processing. *Neuroimage* 2006;31:754–65
6. Kuo HK, Sorond F, Iloputaife I, et al. Effect of blood pressure on cognitive functions in elderly persons. *J Gerontol A Biol Sci Med Sci* 2004;59:1191–94
7. de la Torre JC. Alzheimer disease as a vascular disorder: nosological evidence. *Stroke* 2002;33:1152–62
8. Sato N, Morishita R. Roles of vascular and metabolic components in cognitive dysfunction of Alzheimer disease: short- and long-term modification by non-genetic risk factors. *Front Aging Neurosci* 2013;5:64
9. Joutel A, Monet-Lepretre M, Gosele C, et al. Cerebrovascular dysfunction and microcirculation rarefaction precede white matter lesions in a mouse genetic model of cerebral ischemic small vessel disease. *J Clin Invest* 2010;120:433–45
10. Asllani I, Borogovac A, Brown TR. Regression algorithm correcting for partial volume effects in arterial spin labeling MRI. *Magn Reson Med* 2008;60:1362–71
11. Groves AR, Chappell MA, Woolrich MW. Combined spatial and non-spatial prior for inference on MRI time-series. *Neuroimage* 2009;45:795–809
12. Chappell MA, MacIntosh BJ, Donahue MJ, et al. Separation of macrovascular signal in multi-inversion time arterial spin labelling MRI. *Magn Reson Med* 2010;63:1357–65
13. Francis ST, Bowtell R, Gowland PA. Modeling and optimization of look-locker spin labeling for measuring perfusion and transit time changes in activation studies taking into account arterial blood volume. *Magn Reson Med* 2008;59:316–25
14. MacIntosh BJ, Lindsay AC, Kyllintreas I, et al. Multiple inflow pulsed arterial spin-labeling reveals delays in the arterial arrival time in minor stroke and transient ischemic attack. *AJNR Am J Neuroradiol* 2010;31:1892–94
15. MacIntosh BJ, Marquardt L, Schulz UG, et al. Hemodynamic alterations in vertebralbasilar large artery disease assessed by arterial spin-labeling MR imaging. *AJNR Am J Neuroradiol* 2012;33:1939–44
16. Bokkers RP, van Laar PJ, van de Ven KC, et al. Arterial spin-labeling MR imaging measurements of timing parameters in patients with a carotid artery occlusion. *AJNR Am J Neuroradiol* 2008;29:1698–703
17. Paling D, Thade Petersen E, Tozer DJ, et al. Cerebral arterial bolus arrival time is prolonged in multiple sclerosis and associated with disability. *J Cereb Blood Flow Metab* 2014;34:34–42
18. Mak HK, Chan Q, Zhang Z, et al. Quantitative assessment of cerebral hemodynamic parameters by QUASAR arterial spin labeling in Alzheimer's disease and cognitively normal elderly adults at 3-Tesla. *J Alzheimers Dis* 2012;31:33–44
19. Yoshiura T, Hiwatashi A, Yamashita K, et al. Simultaneous measurement of arterial transit time, arterial blood volume, and cerebral blood flow using arterial spin-labeling in patients with Alzheimer disease. *AJNR Am J Neuroradiol* 2009;30:1388–93
20. MacIntosh BJ, Swardfager W, Crane DE, et al. Cardiopulmonary fitness correlates with regional cerebral grey matter perfusion and

- density in men with coronary artery disease. *PLoS One* 2014;9:e91251
21. Volonghi I, Pendlebury ST, Welch SJ, et al. **Cognitive outcomes after acute coronary syndrome: a population based comparison with transient ischaemic attack and minor stroke.** *Heart* 2013;99:1509–14
 22. Zheng L, Mack WJ, Chui HC, et al. **Coronary artery disease is associated with cognitive decline independent of changes on magnetic resonance imaging in cognitively normal elderly adults.** *J Am Geriatr Soc* 2012;60:499–504
 23. Kullmann S, Heni M, Veit R, et al. **The obese brain: association of body mass index and insulin sensitivity with resting state network functional connectivity.** *Hum Brain Mapp* 2012;33:1052–61
 24. Swardfager W, Herrmann N, Dowlati Y, et al. **Relationship between cardiopulmonary fitness and depressive symptoms in cardiac rehabilitation patients with coronary artery disease.** *J Rehabil Med* 2008;40:213–18
 25. MacIntosh BJ, Filippini N, Chappell MA, et al. **Assessment of arterial arrival times derived from multiple inversion time pulsed arterial spin labeling MRI.** *Magn Reson Med* 2010;63:641–47
 26. Gibson E, Gao F, Black SE, et al. **Automatic segmentation of white matter hyperintensities in the elderly using FLAIR images at 3T.** *J Magn Reson Imaging* 2010;31:1311–22
 27. Chaudhary S, Scouten A, Schwindt G, et al. **Hemodynamic effects of cholinesterase inhibition in mild Alzheimer’s disease.** *J Magn Reson Imaging* 2013;38:26–35
 28. Alsop DC, Detre JA, Golay X, et al. **Recommended implementation of arterial spin-labeled perfusion MRI for clinical applications: a consensus of the ISMRM perfusion study group and the European consortium for ASL in dementia.** *Magn Reson Med* 2014 Apr 8. [Epub ahead of print]
 29. Buxton RB, Frank LR, Wong EC, et al. **A general kinetic model for quantitative perfusion imaging with arterial spin labeling.** *Magn Reson Med* 1998;40:383–96
 30. Hachinski V, Iadecola C, Petersen RC, et al. **National Institute of Neurological Disorders and Stroke-Canadian Stroke Network vascular cognitive impairment harmonization standards.** *Stroke* 2006;37:2220–41
 31. Nichols TE, Holmes AP. **Nonparametric permutation tests for functional neuroimaging: a primer with examples.** *Hum Brain Mapp* 2002;15:1–25
 32. Smith SM, Nichols TE. **Threshold-free cluster enhancement: addressing problems of smoothing, threshold dependence and localization in cluster inference.** *Neuroimage* 2009;44:83–98
 33. Greicius MD, Srivastava G, Reiss AL, et al. **Default-mode network activity distinguishes Alzheimer’s disease from healthy aging: evidence from functional MRI.** *Proc Natl Acad Sci U S A* 2004;101:4637–42
 34. Celone KA, Calhoun VD, Dickerson BC, et al. **Alterations in memory networks in mild cognitive impairment and Alzheimer’s disease: an independent component analysis.** *J Neurosci* 2006;26:10222–31
 35. Webb AJ, Simoni M, Mazzucco S, et al. **Increased cerebral arterial pulsatility in patients with leukoaraiosis: arterial stiffness enhances transmission of aortic pulsatility.** *Stroke* 2012;43:2631–36
 36. Hirata K, Yaginuma T, O’Rourke MF, et al. **Age-related changes in carotid artery flow and pressure pulses: possible implications for cerebral microvascular disease.** *Stroke* 2006;37:2552–56
 37. Damoiseaux JS, Beckmann CF, Arigita EJ, et al. **Reduced resting-state brain activity in the “default network” in normal aging.** *Cereb Cortex* 2008;18:1856–64
 38. Saleem M, Ratnam Bandaru VV, Herrmann N, et al. **Ceramides predict verbal memory performance in coronary artery disease patients undertaking exercise: a prospective cohort pilot study.** *BMC Geriatr* 2013;13:135

Meta-Analysis of Diffusion Metrics for the Prediction of Tumor Grade in Gliomas

V.Z. Miloushev, D.S. Chow, and C.G. Filippi

ABSTRACT

BACKGROUND AND PURPOSE: Diffusion tensor metrics are potential *in vivo* quantitative neuroimaging biomarkers for the characterization of brain tumor subtype. This meta-analysis analyzes the ability of mean diffusivity and fractional anisotropy to distinguish low-grade from high-grade gliomas in the identifiable tumor core and the region of peripheral edema.

MATERIALS AND METHODS: A meta-analysis of articles with mean diffusivity and fractional anisotropy data for World Health Organization low-grade (I, II) and high-grade (III, IV) gliomas, between 2000 and 2013, was performed. Pooled data were analyzed by using the odds ratio and mean difference. Receiver operating characteristic analysis was performed for patient-level data.

RESULTS: The minimum mean diffusivity of high-grade gliomas was decreased compared with low-grade gliomas. High-grade gliomas had decreased average mean diffusivity values compared with low-grade gliomas in the tumor core and increased average mean diffusivity values in the peripheral region. High-grade gliomas had increased FA values compared with low-grade gliomas in the tumor core, decreased values in the peripheral region, and a decreased fractional anisotropy difference between the tumor core and peripheral region.

CONCLUSIONS: The minimum mean diffusivity differs significantly with respect to the World Health Organization grade of gliomas. Statistically significant effects of tumor grade on average mean diffusivity and fractional anisotropy were observed, supporting the concept that high-grade tumors are more destructive and infiltrative than low-grade tumors. Considerable heterogeneity within the literature may be due to systematic factors in addition to underlying lesion heterogeneity.

ABBREVIATIONS: Δ FA = fractional anisotropy difference; FA = fractional anisotropy; MD = mean diffusivity; minMD = minimum mean diffusivity or minimum ADC; ROC = receiver operator characteristic; WHO = World Health Organization

Diffusion tensor imaging is an MR imaging technique that can quantify diffusion of water in the brain and characterize the structural integrity of white matter tracts.¹⁻³ Multiple studies have examined the ability of basic diffusion tensor metrics such as mean diffusivity (MD) or the apparent diffusion coefficient and fractional anisotropy (FA) to discriminate the tumor grade of gliomas. Disruption of normal white matter structural integrity by primary glial neoplasms should theoretically reduce fractional anisotropy and increase mean diffusivity.

Mean diffusivity is positively correlated with decreased tumor cellular density and increased patient survival, and significant ef-

fects are reported in several studies with respect to discriminating tumor grade specifically by using minimum mean diffusivity (minMD).⁴⁻⁹ In contradistinction, there is no definitive consensus on the ability of fractional anisotropy to assess tumor grade, cellular density, and parenchymal infiltration or to prognosticate patient survival.^{7,10-21} We performed a quantitative meta-analysis of the existing literature to determine the statistical consensus of mean diffusivity and fractional anisotropy in distinguishing tumor grade of gliomas, separately examining the identifiable tumor core and region of peripheral signal abnormality.

MATERIALS AND METHODS

Articles were identified via PubMed and Science Citation Index query using the terms “diffusion” and “brain tumor.” This search produced 1657 articles from PubMed and 2158 articles from the Science Citation Index. Citations were imported into the End-Note citation manager (Thomson Reuters, New York, New York), which was used to remove duplicates, yielding 3128 citations. Articles were then restricted to those with publication dates between 2000 and 2013 and containing the word “glioma,” which yielded

Received May 8, 2014; accepted after revision July 17.

From the Department of Diagnostic Radiology, Columbia University, New York, New York.

Paper previously presented at: Mini-Symposiums on Tumor and Stroke at the Annual Meeting of the American Society of Neuroradiology and the Foundation of the ASNR Symposium, May 17–22, 2014; Montreal, Quebec, Canada.

Please address correspondence to Vesselin Z. Miloushev, MD, Department of Diagnostic Radiology, Columbia University, 622 West 168th St, PB 1-302C, New York, NY 10032; e-mail: vzml@columbia.edu

<http://dx.doi.org/10.3174/ajnr.A4097>

Study characteristics and technical factors^a

Attribute	MD	FA
Average no. of patients per tumor grade category	15.3 ± 12.0	13.4 ± 8.6
Average age of patients (yr)	49.3 ± 8.6	50.0 ± 7.6
Prospective design	79.1 %	69.4 %
Studies at 3T	34.5 %	41.7 %
Average maximum diffusion b-value	1103 ± 454	1111 ± 448
Average no. of noncollinear directions	–	21 ± 31

Note:— indicates not calculated.

^a SDs are reported for average values.

377 articles. An additional restriction to articles containing the phrase “fractional anisotropy” resulted in 242 articles. All studies (377 for mean diffusivity, 242 for fractional anisotropy) were read for relevance. Only studies that reported data for adult patients with histologic confirmation of treatment-naïve lesions were included. We could not control for sampling error associated with histologic sampling; with the exception of a few studies that performed stereotactic biopsies, it is possible that some lesions were inappropriately classified.²² Case reports were excluded.

FA and MD values were tabulated as mean values and SDs. The SDs and number of patients were used for weighting in the pooled analysis. Two articles displayed data in chart rather than numeric format; the chart images were analyzed by superimposing a finely decimated grid, which intersected the chart axis in the PowerPoint image manager (Microsoft, Redmond, Washington) to extract numeric values.

The World Health Organization (WHO) tumor grade and the range of histologic tumor types included were tabulated. Information on whether each study was prospective and/or retrospective, the number of patients, and the mean patient age, if provided, were recorded. The technical specifications for the diffusion acquisition, including main magnetic field strength, number of noncollinear gradient directions, number of b-values, and maximum b-value, were recorded. The MR imaging vendor and software used for analysis were noted.

We only included studies that separated diffusion metrics in the tumor core and tumor periphery, with the exception of 2 studies that reported the minimum mean diffusivity and included the entire region of signal abnormality.^{7,23} Studies that reported central necrotic regions for either tumor grade were excluded. Some studies separated tumor core values for enhancing and non-enhancing components, and these were recorded. Studies that reported values for the region of signal abnormality peripheral to the tumor core as either “edematous” or “infiltrated” were grouped into the peripheral region category; this was equated to the region of T2-prolongation on long-TR images, such as T2-weighted or FLAIR images. Critically, the peripheral region was distinguished from the “intermediary” or “boundary” region between the tumor core and the peripheral region, reported in some studies in the neighborhood of 1–2 mm from the tumor core. Also relevant for low-grade lesions, data from studies that only reported the white matter adjacent to the region of signal abnormality were not included.^{24,25} Summary statistics for the studies are provided in the Table.

Equations relating MD, equivalent to the apparent diffusion coefficient, and FA are provided below in terms of the 3 principal eigenvalues ($\lambda_1, \lambda_2, \lambda_3$).²⁶ However, 3 noncollinear diffusion gra-

dent directions suffice to calculate the mean diffusivity, without calculation of the individual eigenvalues. Adjustments were made if studies reported the trace instead of MD (trace = 3 MD).

$$1) \quad MD = \frac{\lambda_1 + \lambda_2 + \lambda_3}{3}$$
$$2) \quad FA = \sqrt{\frac{3(\lambda_1 - MD)^2 + (\lambda_2 - MD)^2 + (\lambda_3 - MD)^2}{(\lambda_1)^2 + (\lambda_2)^2 + (\lambda_3)^2}}$$

Statistical analysis was performed with R, Version 3.0.1 (<http://www.r-project.org>).²⁷ The metafor package (<http://cran.r-project.org/web/packages/metafor/index.html>) was used to implement a random-effects model, calculate I^2 as a measure of heterogeneity, perform meta-regression, and generate forest plots.²⁸ Standardized mean differences of mean diffusivity and fractional anisotropy between high-grade and low-grade gliomas were converted to odds ratios to simplify interpretation.²⁹ The mean difference was used to calculate the difference in fractional anisotropy (Δ FA) between the tumor core and peripheral region. The funnel plot asymmetry regression test was used to evaluate study sample size bias.³⁰ Approximate permutation tests for P values used 1000 iterations.³¹ The *pROC* package (<http://cran.r-project.org/web/packages/pROC/index.html>) was used to generate receiver operating characteristic (ROC) curves and calculate area under the curve via bootstrapping (10,000 replicates) for patient-level data.³² The binormal method was used for ROC curve smoothing. Confidence intervals were calculated at the 95% significance level.

RESULTS

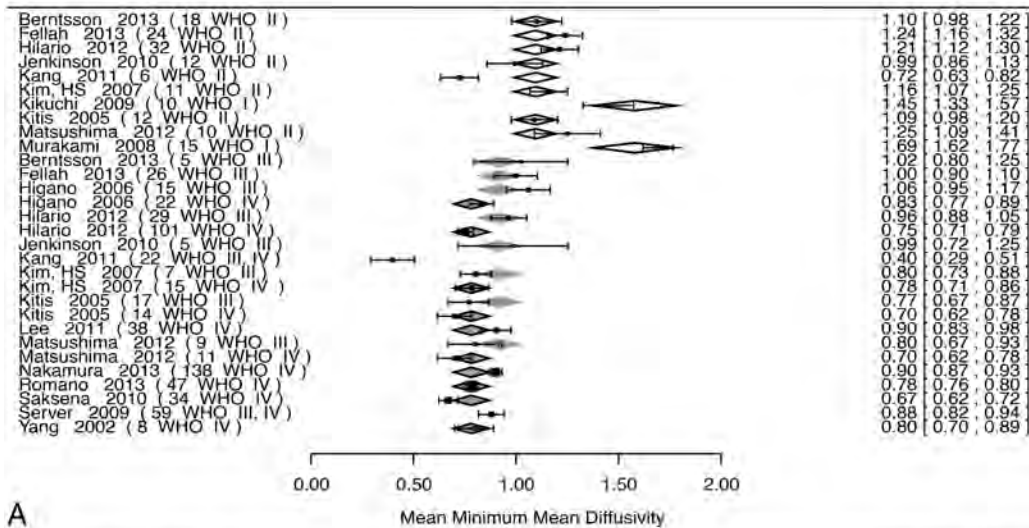
Minimum MD

Pooled analysis of minimum mean diffusivity (minMD) with respect to tumor grade was performed in 17 unique studies (772 patients) (Fig 1A). There was a significant effect of tumor grade (WHO I and II, III and IV) on minMD, with the higher tumor grade resulting in decreased minMD values ($P < .001$). Funnel plot asymmetry was not significant ($P = .96$). Considerable heterogeneity was present ($I^2 = 93\%$). Meta-regression models showed no significant effects for patient age, year of publication, MR imaging vendor, and main magnetic field strength ($P > .05$). Dichotomizing into high-grade (WHO III and IV) and low-grade (WHO grade I and II) groups was significant ($P < .001$); the mean minMD of low-grade gliomas was 1.19 ± 0.06 mm²/s, and the difference between the low-grade and high-grade groups was 0.37 ± 0.07 mm²/s.

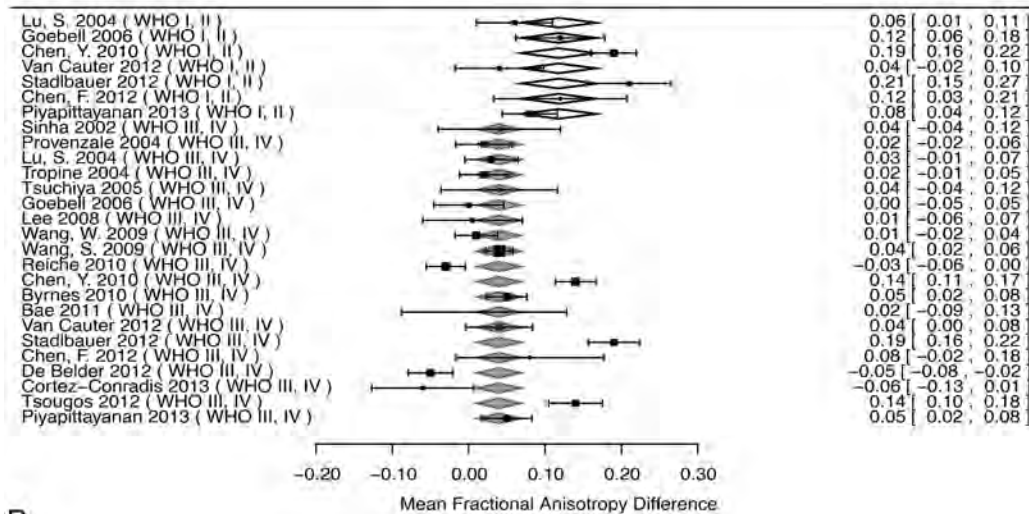
Patient-level data were available in 5 studies (105 patients) (Fig 1C). ROC analysis resulted in an area under the curve of 0.84 (95% CI, 0.76–0.91). The optimal threshold to distinguish low-grade and high-grade gliomas was minMD = 0.98 mm²/s, identified via the Youden Index. This threshold resulted in a specificity of 78.3% (95% CI, 66.7%–88.3%) and a sensitivity of 77.8% (95% CI, 64.4%–88.9%).

Average MD

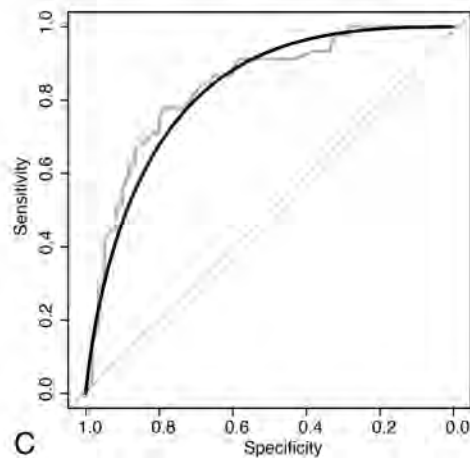
Pooled analysis of average values of MD was also performed for determination of tumor grade in the tumor core (26 studies, 996 patients) and the peripheral region of signal abnormality (10 studies, 207 patients) (Fig 2A, -B). The analysis was restricted to



A



B



C

FIG 1. Effects of tumor grade on minimum mean diffusivity and Δ fractional anisotropy. Moderator analysis was performed (A and B) with respect to tumor grade. In forest plots (A and B), the left column indexes each study by lead author and publication year, with the WHO tumor grade of the lesions in parentheses. WHO grade category means are shown by diamonds, with relative width corresponding to the standard error. The right column provides numeric mean values, with confidence intervals in brackets for each study. Pooled random-effects values are provided at the bottom of each plot. A, The forest plot of minMD and effect of WHO tumor grade are shown. *Open diamonds* indicate WHO II; *light-gray diamonds with gray borders*, WHO III; *dark gray diamonds with black borders*, WHO IV. B, The forest plot of Δ FA is shown. *Open diamonds* indicate WHO I, II; *light gray diamonds with gray borders*, WHO III, IV. C, An ROC plot of patient-level data for minMD is shown. *Gray step curve* indicates actual data; *black curve*, binormal smoothed curve; *dashed gray line*, 50:50 line.

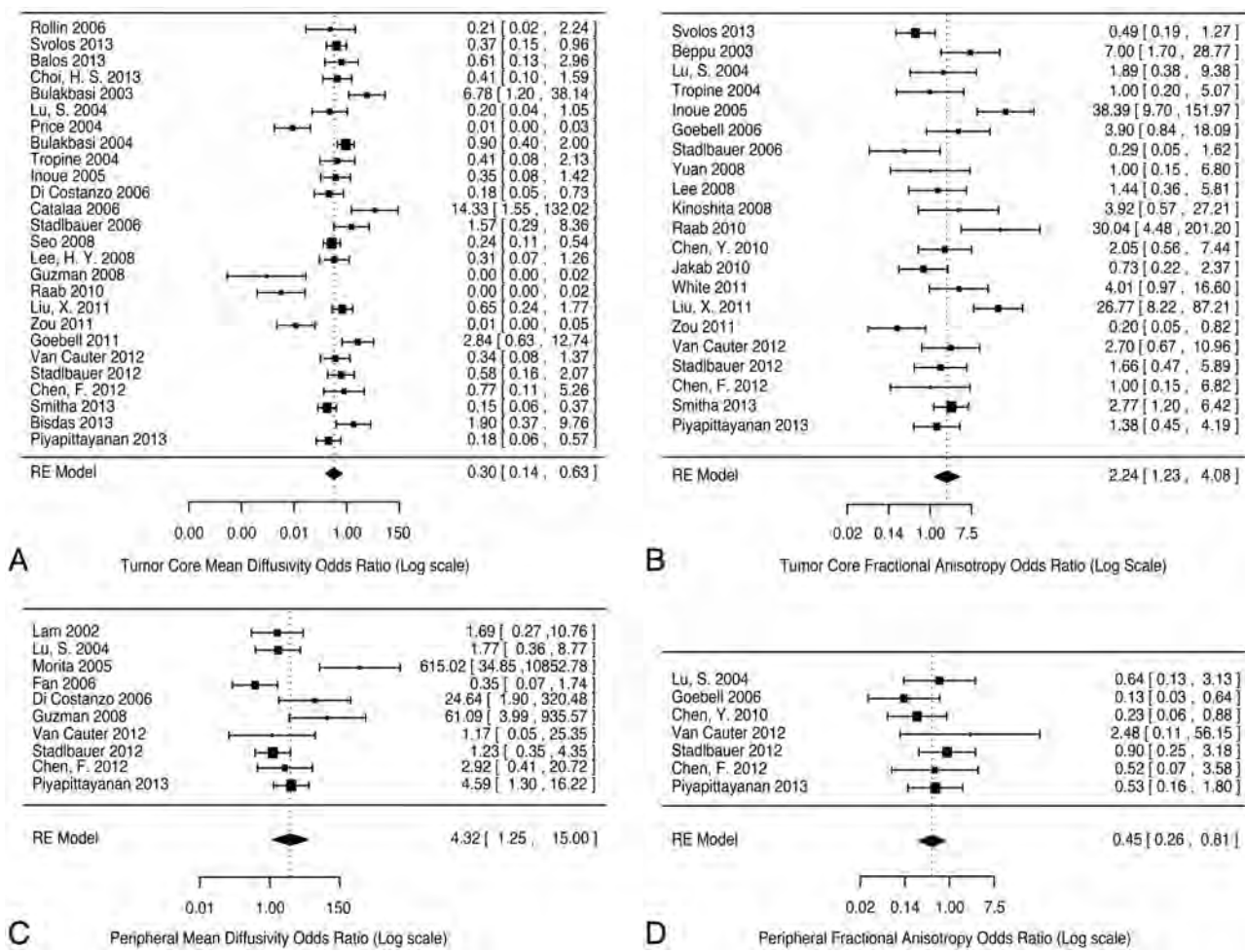


FIG 2. Forest plots of mean diffusivity and fractional anisotropy in the tumor core and peripheral region of signal abnormality, comparing differences between low-grade and high-grade categories (moderator analysis was not performed). The standardized mean difference between high-grade and low-grade lesions was converted to odds ratios as a measure of effect size. Mean diffusivity in the tumor core (A) and peripheral region (B) with fractional anisotropy in the tumor core (C) and peripheral region (D) are shown. For each forest plot, the left column indexes each study by lead author and publication year. The right column provides odds ratios, with confidence intervals in brackets for each study. Pooled random-effect odds ratios are provided at the bottom of each plot.

studies that provided data for both low-grade and high-grade gliomas, to provide internal controls. The odds ratio for high-grade versus low-grade lesions was 0.3 (95% CI, 0.14–0.63; permutation *P* value < .001) in the tumor core and 4.32 (95% CI, 1.25–15.0; permutation *P* value = .044) in the peripheral region; raw mean differences between high-grade and low-grade were, however, small (–0.16 and 0.14, respectively). Considerable significant heterogeneity was present for the tumor core, *I*² = 87.2% (95% CI, 80.3%–94.9%), less significantly in the peripheral region, *I*² = 76.8% (95% CI, 48.3%–94.6%).

ΔFA

Pooled analysis of the difference in fractional anisotropy (ΔFA) between the peripheral region of signal abnormality and the tumor core was performed in 20 unique studies (391 patients) (Fig 1B). High-grade gliomas had a significantly decreased ΔFA compared with low-grade gliomas (*P* = .007). The raw difference estimate between the 2 groups was 0.08 ± 0.03 (estimated ΔFA of low-grade gliomas = 0.12 ± 0.03). The permutation *P* value remained significant (*P* = .02), and the funnel plot asymmetry was

not significant (*P* = .6). Considerable heterogeneity was present, *I*² = 91% (95% CI, 84.3%–95.1%). A meta-regression model incorporating MR imaging vendor type (GE Healthcare, Siemens, Philips Healthcare, Toshiba) was not significant (*P* = .078); models incorporating patient age, year of publication, number of non-collinear DTI directions, and main magnetic field strength were also not significant.

Average FA

Pooled analysis of average values of FA was performed for determination of tumor grade in the tumor core (21 studies, 734 patients) and the peripheral region of signal abnormality (7 studies, 180 patients) (Fig 2C, -D). The analysis was restricted to studies that provided data for both low-grade and high-grade gliomas, to provide internal controls. The odds ratio for high-grade versus low-grade lesions was 2.24 (95% CI, 1.23–4.08, permutation *P* value = .006) in the tumor core and 0.45 (95% CI, 0.26–0.81, permutation *P* value = .032) in the peripheral region; raw mean differences between high-grade and low-grade were, however, small (0.02 and –0.02, respectively). Modest heterogeneity was

present for the tumor core, $I^2 = 74.9\%$ (95% CI, 56.2%–88.2%), without significant heterogeneity in the peripheral region, $I^2 = 0\%$ (95% CI, 0%–82.8%).

DISCUSSION

We performed a meta-analysis to explore the validity and consensus in the utility of mean diffusivity and fractional anisotropy for distinguishing tumor grade in gliomas. Pooled analysis was restricted to studies that internally compared low-grade and high-grade lesions, thus providing internal controls. Significant effects were observed, adding support to generalizations regarding tumor biology, though the raw effect sizes were small and significant heterogeneity was present in some of the cohorts of studies. In the identifiable tumor core, high-grade gliomas had decreased MD and increased FA values compared with low-grade gliomas. In the peripheral region of signal abnormality, high-grade gliomas had increased MD and decreased FA values. These observations suggest that high-grade gliomas have a more destructive effect on white matter tracts than low-grade gliomas in the peripheral region. In the tumor core, high-grade gliomas are expected to have increased extracellular-space volume and increased microvascular proliferation and are not expected to preserve white matter architecture, to account for the relatively greater fractional anisotropy.^{33,34} Theoretically, this effect may be a consequence of initial growth along the scaffold of white matter tracts. Alternatively, high-grade gliomas may have a less defined transition between the tumor core and periphery than is suggested by structural imaging.

We further analyzed the FA difference between the tumor core and peripheral region to provide additional insight into tumor biology. High-grade gliomas have a ΔFA that is approximately 0.08 ± 0.03 smaller than that in low-grade gliomas. The result may suggest that high-grade gliomas are more infiltrative than low-grade gliomas, as expected from mathematic modeling.³⁵ The results parallel those of Ferda et al,¹⁵ who observed that grade II gliomas have a sharper transition than grade III gliomas among the tumor core, intermediary region, and the peripheral region. We note, however, that their results also showed a sharp transition, presumably due to mass effect in grade IV gliomas, an observation that was not adequately testable in our meta-analysis.

The minMD was observed to be a significant diffusion imaging metric for distinguishing tumor grade in gliomas. While the minimum mean diffusivity is inherently subject to statistical noise and partial volume effects, it does not necessarily rely on precise lesion segmentation, thus eliminating a source of heterogeneity between studies. The ROC analysis of patient-level data suggested an optimal cutoff in minMD of $0.98 \text{ mm}^2/\text{s}$; minMD lower than this value favors a high-grade glioma. This suggested cutoff is within the range of previously published values.⁴⁻⁶ However, the lower bounds of the 95% CI for both sensitivity and specificity from our ROC analysis are approximately 65%, which limits clinical confidence in using this metric alone.

Several limitations of our study are inherent in its methods. First, more significant differences may not have been observed simply because mean diffusivity and fractional anisotropy are insufficient to discriminate tumor grade. Unfortunately, promising metrics such as diffusional kurtosis, p;q diffusion tensor decom-

position, and maximum SD of FA were provided in too few studies to be accessible by meta-analysis.^{19,36,37}

Considerable heterogeneity was observed in the cohort of studies for some of the metrics we tested. One source of heterogeneity was sampling error in pathologic specimens used for histologic grading. This error is expected to increase heterogeneity in the dataset because high-grade lesions may be mistakenly classified as low-grade lesions; unfortunately because most studies did not perform multiple biopsies, it is not possible to control for this source of heterogeneity. Variations in measurement precision are unavoidable, though in individual patients, measurements of the fractional anisotropy and mean diffusivity showed good reproducibility in at least 1 study.³⁸ However, measurement accuracy is difficult to account for among all studies. Nevertheless, technical factors such as the main magnetic field strength, MR imaging vendor, number of noncollinear diffusion gradient directions (in the case of FA), and number of b-values used were not found to significantly account for the heterogeneity among studies.

Nonquantitative aspects specifically related to segmentation of brain tumor components on imaging could not be adequately accounted for in our study. Discrimination of tumor components primarily relies on the expert opinion of neuroradiologists. Specific challenges arise for lesions lacking well-defined tumor core and peripheral region boundaries. Increased interest in semiautomated computer segmentation in the analysis of brain tumors, coupled with validation, may circumvent some subjectivity in delineating the image-definable components of glial tumors.³⁹ Standardization of segmentation techniques is expected to improve the utility of quantitative measurements.

Furthermore, in most studies, a range of values was observed among patients. Sources of this variation include different tumor locations and underlying patient-specific background tissue differences. However, there is likely additional heterogeneity within the low-grade and high-grade glioma groups. Within glioblastoma, 4 separate subtypes can be distinguished by molecular profiling, and these subtypes differ in the degree of infiltration.⁴⁰⁻⁴² For example, O6-methylguanine DNA methyltransferase promoter methylation has a significant effect on diffusion tensor metrics.^{43,44} WHO grade and single histologic designations are likely inadequate as sole descriptors of the biologic behavior of tumors.

CONCLUSIONS

Minimum mean diffusivity is an easily calculated diffusion tensor metric that differs significantly with respect to WHO tumor grade, though specific clinical recommendations cannot be made on the basis of this analysis. In the tumor core, high-grade gliomas have decreased MD and increased FA, while in the peripheral region high-grade gliomas have increased MD and decreased FA. However, considerable heterogeneity exists in the published literature, which is likely due to both systematic factors and the underlying biologic heterogeneity of gliomas. Standardization in terminology and segmentation of the regions of signal abnormality identifiable on imaging and standardization of DTI methodology are needed. However, to approach the underlying biologic heterogeneity of gliomas, future investigations may need to examine the correlation of diffusion tensor biomarkers with tumor genomic or expression profiles. Thus, diffusion tensor metrics can

be tested as quantitative biomarkers for tumor subtype and can be potentially used to report subpopulations within a given tumor subtype.

Disclosures: Christopher G. Filippi—UNRELATED: Consultancy: Syntactx Corporation, Regeneration Pharmaceuticals, Comments: For both of these consultant jobs, I help them organize MR imaging protocols for clinical drug trials, and I interpret MR images; Grants/Grants Pending: Coinvestigator on National Institutes of Health/National Cancer Institute (1R01CA161404-01A) and National Institutes of Health/National Heart, Lung, and Blood Institute (2R01HL071944-06).

REFERENCES

- Hajnal JV, Doran M, Hall AS, et al. MR imaging of anisotropically restricted diffusion of water in the nervous system. *J Comput Assist Tomogr* 1991;15:1–18
- Pierpaoli C, Jezzard P, Basser PJ, et al. Diffusion tensor MR imaging of the human brain. *Radiology* 1996;201:637–48
- Basser PJ, Pierpaoli C. Microstructural and physiological features of tissues elucidated by quantitative-diffusion-tensor MRI. *J Magn Reson B* 1996;111:209–19
- Higano S, Yun X, Kumabe T, et al. Malignant astrocytic tumors: clinical importance of apparent diffusion coefficient in prediction of grade and prognosis. *Radiology* 2006;241:839–46
- Murakami R, Hirai T, Kitajima M, et al. Magnetic resonance imaging of pilocytic astrocytomas: usefulness of the minimum apparent diffusion coefficient (ADC) value for differentiation from high-grade gliomas. *Acta Radiol* 2008;49:462–67
- Yamasaki F, Kurisu K, Aoki T, et al. Advantages of high b-value diffusion-weighted imaging to diagnose pseudo-responses in patients with recurrent glioma after bevacizumab treatment. *Eur J Radiol* 2012;81:2805–10
- Saksena S, Jain R, Narang J, et al. Predicting survival in glioblastomas using diffusion tensor imaging metrics. *J Magn Reson Imaging* 2010;32:788–95
- Zulfıqar M, Yousem DM, Lai H. ADC values and prognosis of malignant astrocytomas: does lower ADC predict a worse prognosis independent of grade of tumor? A meta-analysis. *AJR Am J Roentgenol* 2013;200:624–29
- Chen L, Liu M, Bao J, et al. The correlation between apparent diffusion coefficient and tumor cellularity in patients: a meta-analysis. *PLoS ONE* 2013;8:e79008
- Lu S, Ahn D, Johnson G, et al. Diffusion-tensor MR imaging of intracranial neoplasia and associated peritumoral edema: introduction of the tumor infiltration index. *Radiology* 2004;232:221–28
- Beppu T, Inoue T, Shibata Y, et al. Fractional anisotropy value by diffusion tensor magnetic resonance imaging as a predictor of cell density and proliferation activity of glioblastomas. *Surg Neurol* 2005;63:56–61, discussion 61
- Morita K, Matsuzawa H, Fujii Y, et al. Diffusion tensor analysis of peritumoral edema using lambda chart analysis indicative of the heterogeneity of the microstructure within edema. *J Neurosurg* 2005;102:336–41
- Stadlbauer A, Ganslandt O, Buslei R, et al. Gliomas: histopathologic evaluation of changes in directionality and magnitude of water diffusion at diffusion-tensor MR imaging. *Radiology* 2006;240:803–10
- Lee HY, Na DG, Song IC, et al. Diffusion-tensor imaging for glioma grading at 3-T magnetic resonance imaging: analysis of fractional anisotropy and mean diffusivity. *J Comput Assist Tomogr* 2008;32:298–303
- Ferda J, Kastner J, Mukensnabl P, et al. Diffusion tensor magnetic resonance imaging of glial brain tumors. *Eur J Radiol* 2010;74:428–36
- Kinoshita M, Goto T, Okita Y, et al. Diffusion tensor-based tumor infiltration index cannot discriminate vasogenic edema from tumor-infiltrated edema. *J Neurooncol* 2010;96:409–15
- Deng Z, Yan Y, Zhong D, et al. Quantitative analysis of glioma cell invasion by diffusion tensor imaging. *J Clin Neurosci* 2010;17:1530–36
- Jakab A, Molnar P, Emri M, et al. Glioma grade assessment by using histogram analysis of diffusion tensor imaging-derived maps. *Neuroradiology* 2011;53:483–91
- White ML, Zhang Y, Yu F, et al. Diffusion tensor MR imaging of cerebral gliomas: evaluating fractional anisotropy characteristics. *AJNR Am J Neuroradiol* 2011;32:374–81
- Zikou AK, Alexiou GA, Kosta P, et al. Diffusion tensor and dynamic susceptibility contrast MRI in glioblastoma. *Clin Neurol Neurosurg* 2012;114:607–12
- Sternberg EJ, Lipton ML, Burns J. Utility of diffusion tensor imaging in evaluation of the peritumoral region in patients with primary and metastatic brain tumors. *AJNR Am J Neuroradiol* 2014;35:439–44
- Stadlbauer A, Nimsky C, Buslei R, et al. Diffusion tensor imaging and optimized fiber tracking in glioma patients: histopathologic evaluation of tumor-invaded white matter structures. *Neuroimage* 2007;34:949–56
- Kang Y, Choi SH, Kim YJ, et al. Gliomas: histogram analysis of apparent diffusion coefficient maps with standard- or high-b-value diffusion-weighted MR imaging—correlation with tumor grade. *Radiology* 2011;261:882–90
- Chen Y, Shi Y, Song Z. Differences in the architecture of low-grade and high-grade gliomas evaluated using fiber density index and fractional anisotropy. *J Clin Neurosci* 2010;17:824–29
- Nilsson D, Rutka JT, Snead OC 3rd, et al. Preserved structural integrity of white matter adjacent to low-grade tumors. *Childs Nerv Syst* 2008;24:313–20
- Kingsley PB. Introduction to diffusion tensor imaging mathematics. Part II. Anisotropy, diffusion-weighting factors, and gradient encoding schemes. *Concepts in Magnetic Resonance Part A* 2006;28A:123–54
- R Development Core Team. R: A Language and Environment for Statistical Computing. Version 3.0.1. Vienna, Austria: R Foundation for Statistical Computing; 2013
- Viechtbauer W. Conducting meta-analyses in R with the metafor package. *Journal of Statistical Software* 2010;36:1–48
- Chinn S. A simple method for converting an odds ratio to effect size for use in meta-analysis. *Stat Med* 2000;19:3127–31
- Egger M, Davey Smith G, Schneider M, et al. Bias in meta-analysis detected by a simple, graphical test. *BMJ* 1997;315:629–34
- Higgins JP, Thompson SG. Controlling the risk of spurious findings from meta-regression. *Stat Med* 2004;23:1663–82
- Robin X, Turck N, Hainard A, et al. pROC: an open-source package for R and S+ to analyze and compare ROC curves. *BMC Bioinformatics* 2011;12:77
- Wesseling P, Vandersteenhoven J, Downey B, et al. Cellular components of microvascular proliferation in human glial and metastatic brain neoplasms. *Acta Neuropathol* 1993;85:508–14
- Vargová L, Homola A, Zamecnik J, et al. Diffusion parameters of the extracellular space in human gliomas. *Glia* 2003;42:77–88
- Swanson KR, Alvord EC Jr, Murray JD. A quantitative model for differential motility of gliomas in grey and white matter. *Cell Prolif* 2000;33:317–29
- Raab P, Hattingen E, Franz K, et al. Cerebral gliomas: diffusional kurtosis imaging analysis of microstructural differences. *Radiology* 2010;254:876–81
- Van Cauter S, Veraart J, Sijbers J, et al. Gliomas: diffusion kurtosis MR imaging in grading. *Radiology* 2012;263:492–501
- Paldino MJ, Barboriak D, Desjardins A, et al. Repeatability of quantitative parameters derived from diffusion tensor imaging in patients with glioblastoma multiforme. *J Magn Reson Imaging* 2009;29:1199–205
- Chow DS, Qi J, Guo X, et al. Semiautomated volumetric measurement on postcontrast MR imaging for analysis of recurrent and residual disease in glioblastoma multiforme. *AJNR Am J Neuroradiol* 2014;35:498–503
- Phillips HS, Kharbada S, Chen R, et al. Molecular subclasses of high-grade glioma predict prognosis, delineate a pattern of disease progression, and resemble stages in neurogenesis. *Cancer Cell* 2006;9:157–73
- Zinn PO, Majadan B, Sathyan P, et al. Radiogenomic mapping of

- edema/cellular invasion MRI-phenotypes in glioblastoma multiforme. *PLoS ONE* 2011;6:e25451
42. Verhaak RG, Hoadley KA, Purdom E, et al. **An integrated genomic analysis identifies clinically relevant subtypes of glioblastoma characterized by abnormalities in PDGFRA, IDH1, EGFR and NF1.** *Cancer Cell* 2010;17:98
43. Moon WJ, Choi JW, Roh HG, et al. **Imaging parameters of high grade gliomas in relation to the MGMT promoter methylation status: the CT, diffusion tensor imaging, and perfusion MR imaging.** *Neuroradiol* 2012;54:555–63
44. Romano A, Calabria LF, Tavanti F, et al. **Apparent diffusion coefficient obtained by magnetic resonance imaging as a prognostic marker in glioblastomas: correlation with MGMT promoter methylation status.** *Eur Radiol* 2013;23:513–20

Ultra-High-Field MR Imaging in Polymicrogyria and Epilepsy

A. De Ciantis, A.J. Barkovich, M. Cosottini, C. Barba, D. Montanaro, M. Costagli, M. Tosetti, L. Biagi, W.B. Dobyns, and R. Guerrini



ABSTRACT

BACKGROUND AND PURPOSE: Polymicrogyria is a malformation of cortical development that is often identified in children with epilepsy or delayed development. We investigated *in vivo* the potential of 7T imaging in characterizing polymicrogyria to determine whether additional features could be identified.

MATERIALS AND METHODS: Ten adult patients with polymicrogyria previously diagnosed by using 3T MR imaging underwent additional imaging at 7T. We assessed polymicrogyria according to topographic pattern, extent, symmetry, and morphology. Additional imaging sequences at 7T included 3D T2* susceptibility-weighted angiography and 2D tissue border enhancement FSE inversion recovery. Minimum intensity projections were used to assess the potential of the susceptibility-weighted angiography sequence for depiction of cerebral veins.

RESULTS: At 7T, we observed perisylvian polymicrogyria that was bilateral in 6 patients, unilateral in 3, and diffuse in 1. Four of the 6 bilateral abnormalities had been considered unilateral at 3T. While 3T imaging revealed 2 morphologic categories (coarse, delicate), 7T susceptibility-weighted angiography images disclosed a uniform ribbonlike pattern. Susceptibility-weighted angiography revealed numerous dilated superficial veins in all polymicrogyric areas. Tissue border enhancement imaging depicted a hypointense line corresponding to the gray-white interface, providing a high definition of the borders and, thereby, improving detection of the polymicrogyric cortex.

CONCLUSIONS: 7T imaging reveals more anatomic details of polymicrogyria compared with 3T conventional sequences, with potential implications for diagnosis, genetic studies, and surgical treatment of associated epilepsy. Abnormalities of cortical veins may suggest a role for vascular dysgenesis in pathogenesis.

ABBREVIATIONS: FSPGR = fast-spoiled gradient echo; GRE = gradient-recalled echo; IR = inversion recovery; SWAN = susceptibility-weighted angiography; TBE = tissue border enhancement

Polymicrogyria is a malformation of the cerebral cortex secondary to abnormal migration and postmigrational development.¹ It is characterized by an excessive number of abnormally small gyri separated by shallow sulci, associated with fusion of the

overlying molecular layer (layer 1) of the cerebral cortex.² This combination of features produces a characteristic appearance of irregularity at both the cortical surface and cortical–white matter junction.^{3,4} Its pathogenesis is still poorly understood, and its histopathology, clinical features, topographic distribution, and imaging appearance are heterogeneous. Deficiencies in the understanding of this malformation result from both causal heterogeneity (causative factors include destructive events such as congenital infections,^{5,6} *in utero* ischemia,⁷ metabolic disorders, and

Received June 9, 2014; accepted after revision August 1.

From the Pediatric Neurology Unit (A.D.C., C.B., R.G.), Meyer Children's Hospital, University of Florence, Florence, Italy; Department of Radiology and Biomedical Imaging (A.J.B.), University of California San Francisco, San Francisco, California; Department of Translational Research and New Technologies in Medicine and Surgery (M. Cosottini), University of Pisa, Pisa, Italy; IMAGO7 Foundation (M. Cosottini), Pisa, Italy; Fondazione Consiglio Nazionale delle Ricerche/Regione Toscana (D.M.), Unità Operativa Semplice Neuroradiologia, Pisa, Italy; Istituto di Ricovero e Cura a Carattere Scientifico Stella Maris Foundation (M. Costagli, M.T., L.B., R.G.), Pisa, Italy; and Center for Integrative Brain Research (W.B.D.), Seattle Children's Hospital, Seattle, Washington.

This work was supported by the Pisa Foundation (Project 133/11 "Ultra-high field MRI targeted imaging of dysplastic cortical lesions and dysembryoplastic tumours"), the European Research Project on Rare Diseases (E-Rare-2, TUB-GENCODEV, 11–027), and the European Union Seventh Framework Programme FP7/2007–2013 (under the project DESIRE: Development and Epilepsy: Strategies for Innovative Research to improve diagnosis, prevention and treatment in Children with difficult to treat Epilepsy, Grant Agreement: 602531).

Please address correspondence to Renzo Guerrini, MD, Pediatric Neurology and Neurogenetics Unit and Laboratories, Meyer Children's Hospital, Department of Neuroscience, Pharmacology and Child Health, University of Florence, Viale Pieraccini 24, 50139, Florence, Italy; e-mail: renzo.guerrini@unifi.it

Indicates open access to non-subscribers at www.ajnr.org

Indicates article with supplemental on-line tables.

Indicates article with supplemental on-line photos.

<http://dx.doi.org/10.3174/ajnr.A4116>

several gene mutations and copy number variations^{1,8,9}) and the limited number of postmortem examinations available.

The topographic distribution of polymicrogyria may be focal, multifocal, or diffuse; unilateral or bilateral; and symmetric or asymmetric.¹⁰⁻¹⁵ Polymicrogyria can occur as an isolated disorder or can be associated with other brain abnormalities such as corpus callosum dysgenesis, cerebellar hypoplasia, schizencephaly, and periventricular and subcortical heterotopia.^{16,17}

Clinical manifestations of patients with polymicrogyria have a large spectrum, ranging from isolated selective impairment of cognitive function¹⁸ to severe encephalopathy and intractable epilepsy.¹⁹ The severity of neurologic manifestations and the age at presentation are, in part, influenced by the extent and location of the cortical malformation but may also depend on its specific etiology.

Neuroimaging has a primary role in the diagnosis and classification of polymicrogyria due to its noninvasive nature. Imaging findings are variable and are primarily determined by the morphology of the malformed cortex itself but also by the maturity of myelination and imaging-related technical factors (section thickness, gray-white matter contrast).²⁰ In addition, polymicrogyria-like patterns can be seen in certain malformations, such as tubulinopathies²¹ and cobblestone malformations²²⁻²⁴; these have different histologic appearances but similar MR imaging appearances to polymicrogyria, which can lead to false diagnoses.

On the basis of morphologic characteristics, Barkovich^{2,20} described the variable appearance of polymicrogyria on MR imaging and suggested that the gyral-sulcal dysmorphisms may be roughly divided into 3 main categories: coarse with a thick, bumpy cortex and irregular surface on both the pial and gray-white junction sides; delicate with multiple small, fine gyri of thin cortex that remains thin even after myelination; and sawtooth, composed of thin microgyri separated by deep sulci (primarily seen in diffuse polymicrogyria and before myelination develops). However, numerous gradations of morphology exist within these groups. To date, neither functional nor etiologic associations have been inferred on the basis of this imaging categorization of a polymicrogyric cortex.

Over the past several years, ultra-high-field 7T MR imaging has been available for *in vivo* human brain imaging. *In vivo* 7T MR imaging can provide greater tissue-type identification than that obtained *in vitro* without stains.²⁵ As a result of an increased signal-to-noise ratio, enhanced image contrast, and improved resolution, MR imaging at 7T can visualize small anatomic structures not previously appreciated at lower fields.²⁵⁻²⁸ Because 7T MR imaging has already provided diagnostic benefits in different pathologies²⁸ such as multiple sclerosis,²⁹ cerebrovascular diseases (strokes, microbleeds),^{30,31} aneurysms,³² cavernous malformations,³³ brain tumors,³⁴ and degenerative brain diseases like dementia and Parkinson disease,^{35,36} we tested the added value of 7T MR imaging in providing details of structural changes and their extent in 10 patients with polymicrogyria with respect to conventional 3T imaging. We also addressed the limitations we encountered while exploring the polymicrogyric brain with 7T.

MATERIALS AND METHODS

Ethics Statement

Written informed consent was obtained from all patients and is recorded on file. The experimental protocol named "Evaluation of dysplastic cortical lesions and dysembryoplastic tumors by using ultra-high field MR imaging target imaging" Project 133/11 was funded by the Pisa Foundation and approved by the local competent ethics committee and the Italian Ministry of Health. The procedures followed were in accordance with institutional guidelines and included an adverse event form.

Subjects

Between June 2013 and October 2013, we enrolled, from our cortical malformation data base, 10 adult patients (4 men and 6 women) with polymicrogyria previously imaged at 3T. Exclusion criteria were age younger than 18 years and any contraindications to MR imaging. Polymicrogyria, as assessed by previous 3T MR imaging, had been classified as bilateral perisylvian in 2 patients, unilateral perisylvian in 7 patients, and diffuse in 1 patient. The mean age was 30.1 years (range, 21–53 years). Clinical details are described in On-line Table 1.

Data Acquisition

All 10 patients were imaged at both 3T (Excite HDx; GE Healthcare, Milwaukee, Wisconsin, equipped with a GE 8-channel head coil) and 7T (Discovery MR 950 scanner; GE Healthcare, equipped with a 2-channel transmit/32-channel-receive head coil, Nova Medical, Wilmington, Massachusetts). All participants received earplugs and a pair of pads covering the ears to limit acoustic noise.

The 3T MR imaging standard protocol included the following sequences: 3D T1-weighted fast-spoiled gradient echo (FSPGR), 2D T2 FLAIR, 2D T2-weighted FSE, and 2D white matter-suppressed FSE inversion recovery (IR). The 7T MR imaging protocol included the following sequences: 3D T1-weighted FSPGR, 3D susceptibility-weighted angiography (SWAN), 2D T2*-weighted targeted dual-echo gradient-recalled echo (GRE), 2D T2-weighted FSE, and 2D gray-white matter tissue border enhancement (TBE) FSE-IR. TBE is an IR sequence that uses an appropriate TI to produce images in which the interface between 2 neighboring tissues of interest is hypointense; therefore, tissue borders are clearly represented by dark lines. This effect is achieved by setting imaging parameters so that the neighboring tissues have magnetization with equal magnitude but out of phase; therefore, the voxels containing a mixture of each tissue (ie, the tissue interface) possess minimal net signal.³⁷ Therefore, the hypointense line-marking tissue interface produced by TBE does not reflect any specific fiber structure. Details of imaging parameters for 3T and 7T imaging are shown in On-line Table 2.

To limit specific absorption rate-related problems, image distortions and stronger susceptibility phenomena related to ultra-high-field, whole-brain 7T imaging included only SWAN and FSPGR sequences, with the remaining sequences targeting specific regions of interest by using small FOVs and a limited number of sections. To select the areas of interest for targeted imaging, we were guided by initial 7T whole-brain sequences.

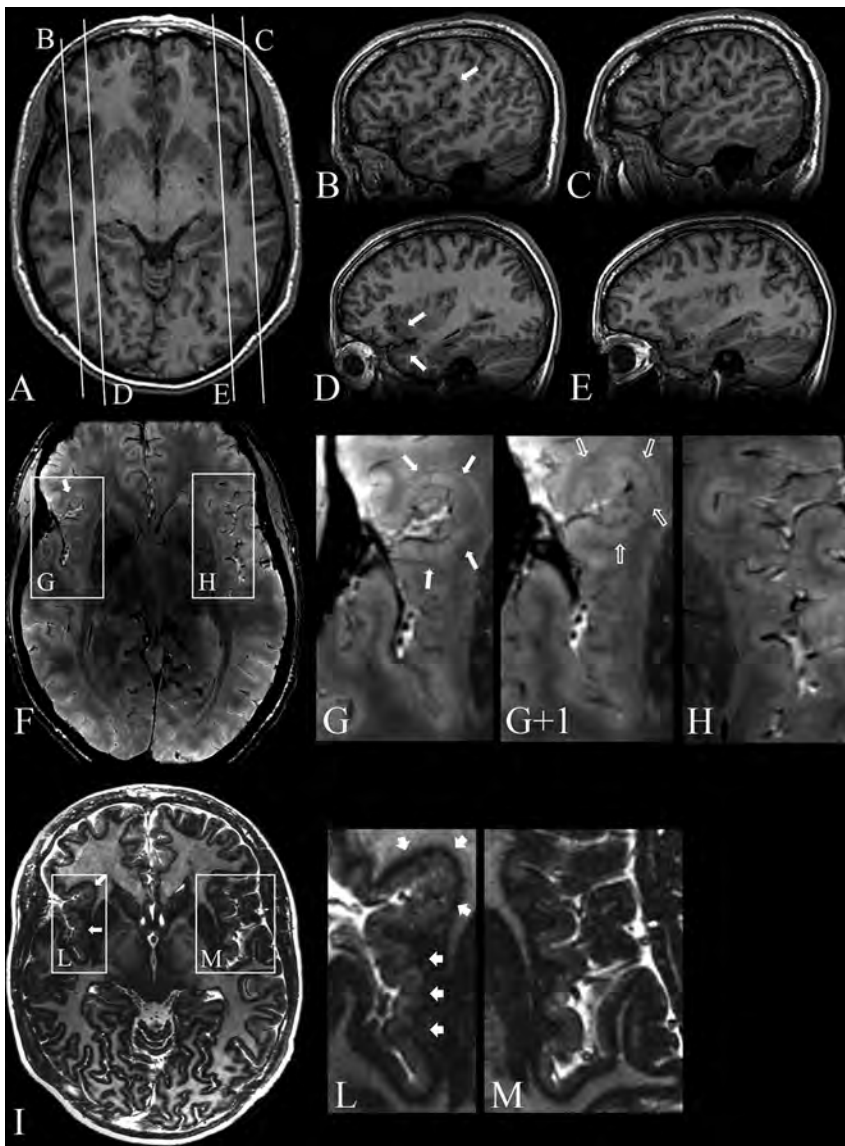


FIG 1. Patient 8. 3T axial (A) and sagittal (B–E) 3D FSPGR, 7T 3D SWAN (F), and magnified images (G, G+1, H), 7T axial 2D TBE FSE-IR (I) and magnified images (L and M). A, Mild cortical thickening in the right frontal operculum. Contiguous sagittal sections across the frontal operculum and the Sylvian fissure on the right (B and D) and left (C and E) sides provide a better comparative view of the morphologic characteristics of malformed-versus-normal cortex. B, An abnormal right Sylvian fissure (arrow), which is vertically oriented, shortened, and bordered by thick and irregular cortex. D, Thickening of the cortex in the inferior frontal gyrus and superior temporal gyrus (arrows). F, Two contiguous expanded views, from caudal (G) to rostral (G+1), provide ultra-high-resolution details of the right frontal operculum, which are not visible at 3T (A–E), substantiating the presence of a polymicrogyric cortex. H, A magnification of the homologous contralateral region clearly enhances the appreciation of the difference in folding of the polymicrogyric and normal cortex. I, Magnifications (L and M) show a hypointense line representing the gray-white matter interface and provide a high definition of the polymicrogyric (L, arrows) and normal (M) cortex, making it easier to appreciate irregularities in thickness and folding of the polymicrogyric cortex.

Data Analysis

All 7T images were independently assessed by 3 reviewers and later as a group to reach a consensus for eligibility. 3T and 7T images were assessed separately in each patient. Polymicrogyria was diagnosed with satisfaction of the combination of these characteristics: 1) the cortex had an irregular outer surface with an abnormal gyral pattern, 2) the cortex appeared thickened or overfolded, and 3) the cortical–white matter junction was irregular.³⁸

We reviewed all images for the following findings: 1) topo-

graphic pattern of polymicrogyria, 2) extent, 3) symmetry (if bilateral), 4) range of gyral-sulcal dysmorphisms, and 5) associated abnormalities. We classified the topographic pattern according to the different patterns described in the literature: focal, bilateral frontal, bilateral perisylvian (which varies in the extent of involvement), bilateral parieto-occipital, and diffuse polymicrogyria.

The 3T and 7T images were assessed digitally with a workstation (Advantage 4.1; GE Healthcare). 3D images were reformatted in orthogonal planes to better evaluate the cortical thickening and to rule out partial volume artifacts.

The postprocessing of SWAN images was performed by using the minimum intensity projection algorithm and multiplanar reformation techniques. The minimum intensity projection algorithm has the characteristic of enhancing the visualization of veins while attenuating the signal from the brain tissue. Conversely, tissue border enhancement images do not require additional postprocessing.

RESULTS

All imaging sessions were well-tolerated by the patients, and no adverse events occurred. Brain MR imaging findings and clinical details of all patients are summarized in On-line Table 1.

At 3T, we observed perisylvian polymicrogyria that was unilateral in 7 patients and bilateral in 2. Of the 7 patients with unilateral polymicrogyria, 6 had multilobar involvement, and in 1, only a portion of the Sylvian fissure was involved (Fig 1). One patient had diffuse polymicrogyria.

A range of gyral-sulcal dysmorphisms emerged at 3T (Fig 2A and On-line Fig 1A), all falling into the categorization formulated by Barkovich,² with 6 of 10 patients having dysmorphisms with a coarse appearance and the remaining 4 having a coarse together with a delicate appearance.

The thickness of the polymicrogyric cortex, measured with FSPGR imaging, ranged from 3.7 to 12 mm (the thickness

of the normal cortex at 3T ranged from 1.6 to 4 mm), with great variability even between adjacent cortical regions.

In 3 patients, polymicrogyria was an isolated abnormality, while in the remaining 7 patients, we detected additional subcortical abnormalities: unilaterally ($n = 1$) or bilaterally ($n = 4$) dilated ventricles, unilateral ($n = 2$) or bilateral ($n = 2$) hippocampal abnormalities, absence of the septum pellucidum ($n = 2$), cavum vergae ($n = 1$), unilateral periventricular nodular het-

erotopia ($n = 2$), and unilateral open-lip schizencephaly ($n = 1$). White matter volume reduction was apparent under the polymicrogyric cortex in all patients. One patient exhibited left intraor-

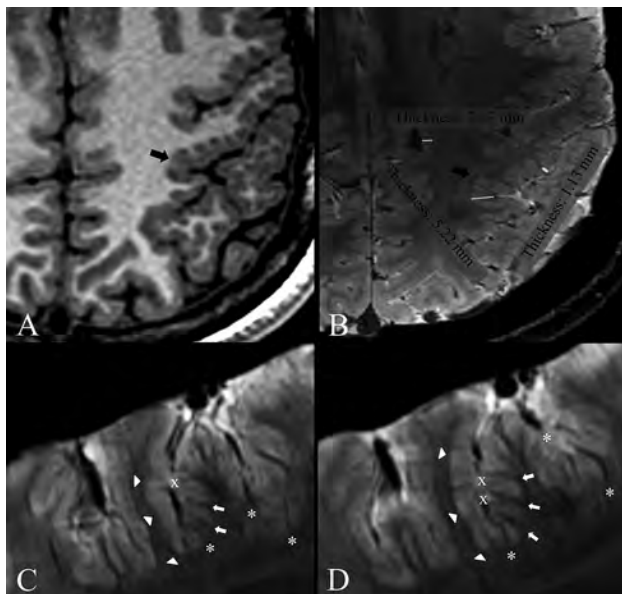


FIG 2. Patients 1 (A and B) and 9 (C and D). Comparison of 3T axial 3D FSPGR (A) and 7T axial 3D SWAN (B) images. Contiguous 7T axial 3D SWAN acquisitions show anatomic details of the polymicrogyric cortex (C and D). A, Delicate appearance of the polymicrogyric cortex in the left pre- and postcentral sulci, characterized by multiple small and delicate gyri of thin cortex (arrow). B, A thin and undulated polymicrogyric cortex, in which the spaces between microgyri are filled by thin white matter digitations, which have a low periodicity and are loosely packed. The gray-white matter junction is bordered by a thin hypointense line. 7T can, therefore, resolve the individual microgyri, revealing how grossly different morphologic characters (coarse or delicate) at 3T result, in fact, from variations of a common underlying morphologic pattern. C, Examples of cortical thickness measurements of normal (2.23 mm) and polymicrogyric cortex (1.13–5.22 mm) by using the straight-line distance measure between the surface and depth of the cortex. D, SWAN images show details of cortical structures and allow disentanglement of the structural units underlying the radiologic appearance of polymicrogyria. The typical undulated aspect is clearly detectable following the hypointense lines of the cortical border (arrowheads), which we assume represent arcuate white matter fibers, the white matter digitations within the gyri (arrows), the small vessels joining the pial veins (asterisks), and the fused molecular layer (crosses).

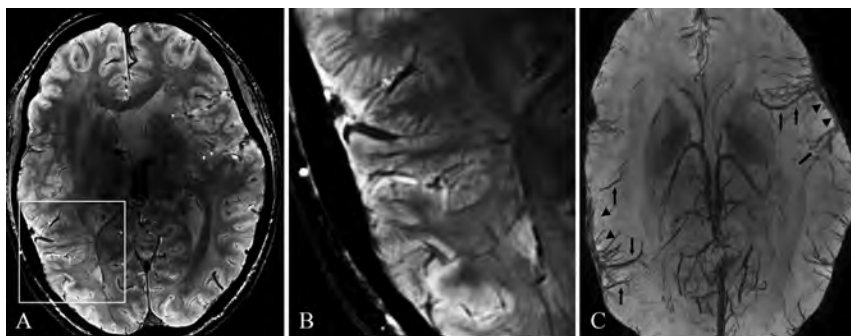


FIG 3. Patient 9. 7T axial 3D SWAN (A, magnified in B) and its minimum intensity projection reconstruction (C). A, Bilateral polymicrogyria involving the left frontal operculum and Sylvian fissure and the right Sylvian fissure and temporal lobe. B, Details of the polymicrogyric cortex in the right temporal lobe (magnified). C, Minimum intensity projection reconstruction shows dilated superficial veins in correspondence with the polymicrogyric areas (arrowheads); the large vascular structures running through the polymicrogyric sulci (arrows) define the location and the extent of the malformation.

bit cavernous hemangiomas and a left soft-tissue hemangioma and hypertrophy of the right Sylvian and medullary veins.

7T provided additional details to 3T findings and revealed more extensive areas of polymicrogyria in all patients. In particular, in 3 patients (patients 4, 7, and 8) in whom 3T FSPGR imaging had revealed unilateral polymicrogyria, 7T SWAN imaging confirmed a unilateral distribution but detected more extensive involvement (Fig 1). In 3 patients with bilateral polymicrogyria at 3T (patients 1, 3, and 9), 7T SWAN revealed more extensive involvement. Four patients (patients 2, 5, 6, and 10) who had been classified as having unilateral polymicrogyria at 3T exhibited bilateral involvement at 7T (On-line Fig 2). In patient 2, 3T FSPGR showed left posterior polymicrogyria engaging the left temporo-insuloparietal region and the medium and superior occipital gyri. 7T SWAN imaging disclosed that polymicrogyria also involved the right posterior insula. In patient 5, in whom 3T FSPGR showed left frontotemporoparietal polymicrogyria along the whole Sylvian fissure, 7T SWAN revealed polymicrogyria also in the right frontal operculum. In patients 6 and 10, the polymicrogyric cortex had right temporoparietal distribution at 3T FSPGR, while 7T disclosed abnormal infolding and thickening of the left frontal operculum. In patient 10, 7T SWAN also showed that polymicrogyria involved the area around the whole left Sylvian fissure, left anterior insula, and left anterior temporal region.

The increased signal-to-noise ratio and the increased sensitivity to magnetic susceptibility effects on SWAN sequences at 7T combined with high-resolution images with enhanced intracortical contrast provided improved polymicrogyria detailing by making it possible to identify details in the entire cortex: the lowest part of the sulcus, the intermediate zone, and the crown of the gyrus. The different categories of gyral and sulcal dysmorphisms seen at 3T (coarse, delicate, sawtooth) were not identifiable as such at 7T, in that SWAN images revealed a homogeneous morphologic character (Fig 2B and On-line Fig 1B). The malformed cortex, measured by using SWAN imaging, was 0.78- to 7-mm thick (the normal cortex was 1–2.89 mm), exhibiting an undulated profile at the gray-white matter junction and bordered by a thin hypointense line, which was considered to represent the arcuate white matter fibers. Within the abnormal cortex, small linear hypointense transcortical lines perpendicular to the cortical layers, probably representing the larger transcortical blood vessels, were present. The hypointense lines of the cortical border combined with those within the cortex contributed to generating the typical polymicrogyric appearance of the cortical ribbon at 7T (Fig 2C, -D).

In all patients, SWAN imaging revealed numerous dilated superficial veins draining the deeper infoldings of polymicrogyria, which were not visible at 3T by using conventional (FSPGR, FSE, and IR) sequences. These large venous structures, which have been described previously,³⁹ appeared to be roughly proportional to

the depth/size of the cortical infolding and extent of polymicrogyria (Fig 3).

In all patients, TBE imaging revealed a hypointense line corresponding to the gray-white matter interface, providing a high definition of the borders of the polymicrogyric cortex (On-line Figs 3 and 4). TBE imaging substantiated SWAN findings and, providing a precise topographic definition of the gray-white matter junction, made the examiner more confident about the extent of polymicrogyria, especially when the border between gray and white matter was poorly defined or the polymicrogyric cortex merged with a seemingly normal cortex (On-line Figs 3 and 4).

The diagnostic gain obtained at 7T originated from the improved image and contrast resolution of SWAN sequences and, to a lesser degree, from 2D GRE images. GRE sequences revealed cortical and pial veins and small vessels inside the cortex less precisely than SWAN. With GRE, cortical layering was less defined, the arcuate white matter fibers could not be visualized, and white matter digitations within the gyri were less conspicuous than those observed by using SWAN or TBE. GRE defined the complexity of cortical gyration better than FSPGR but worse than SWAN and TBE. T2-weighted FSE at 7T did not provide additional information with respect to the same sequence at 3T and had lower contrast and spatial resolution than GRE.

DISCUSSION

Accurate MR imaging depiction of polymicrogyria has important implications for correlating clinical severity with the extent of cortical abnormality,^{20,38,40} guiding genotyping of specific malformation patterns,¹ and delineating the resection margins in patients who are candidates for epilepsy surgery.⁴¹⁻⁴⁴

In this series, 7T SWAN imaging provided improved structural cortical details with more accurate information on cortical thickness, sulcal pattern, and cerebral veins. At 7T, the polymicrogyric cortex exhibited a highly variable thickness, ranging from 0.78 to 7 mm, close to pathology-specimen measures,²⁵ with bumpy inner and outer surfaces, broad gyri, and shallow sulci.

7T SWAN imaging also allowed better qualitative assessment of sulcal patterns compared with conventional 3T imaging. Due to high spatial resolution and increased contrast within the cortex of 7T SWAN imaging, the gyral-sulcal dysmorphisms of polymicrogyria² visible at 3T FSPGR appeared as a highly characteristic undulated pattern of contiguous densely packed microgyri. The polymicrogyric cortex, seen in some of the 3T FSPGR images as thick, rough, and blurred, was merely a poorly resolved image of more deeply undulating thin gyri, with the apparent cortical thickening generated by lower contrast and resolution that result from conventional sequences and field strengths. The significance of the deeper undulations remains to be determined.

Combining 7T high spatial resolution with 3D SWAN sequences, we uncovered bilateral involvement in 4 patients who had been diagnosed as exhibiting unilateral abnormalities at 3T. In addition to the SWAN imaging, we used a custom-designed TBE sequence, which produced a hypointense line along the gray-white matter interface, thereby providing a high definition of the undulating polymicrogyric borders and, together with improved resolution on SWAN images, allowed improved differentiation from adjacent normal cortex. TBE images substantiated the extent of

malformation observed by using SWAN imaging and revealed the borders of polymicrogyria in those areas where the gray-white matter junction was poorly defined or the polymicrogyric cortex merged with the normal cortex.

In addition to producing more accurate morphologic details of the polymicrogyric cortex, SWAN imaging at 7T detected deoxygenated venous blood that allowed visualization of the superficial and deep cerebral veins. Although 3T SWAN can also visualize venous abnormalities, there is no previous report emphasizing this finding at 3T, to our knowledge. At 7T, the polymicrogyric cortex was shown to harbor numerous dilated superficial veins, whose representation seemed to be roughly proportional to the extent and severity of the cortical malformation. The pial veins were visible as linear hypointensities, orthogonal to and penetrating into the cortex. Following the expected course of the sulci, the pial veins defined the complexity of cortical gyration, revealing the contour of polymicrogyria. SWAN–minimum intensity projection images, which enhance the visualization of veins while attenuating the signal from brain tissue, revealed large vascular structures running through the sulci, draining from the polymicrogyric cortex into the pial veins. These findings reinforce previous imaging observations indicating anomalous venous drainage in dysplastic cortical areas.^{39,45} On the other hand, although perfusion failure is a recognized cause of polymicrogyria, there is no reported neuropathologic evidence of vascular malformations associated with it.^{6,46-49}

Abnormal venous drainage might develop as a response to an event, such as cortical injury, during fetal development⁵⁰ and is probably the result of a lack of condensation of cortical veins with persistence of embryonic dural plexus tributaries.⁴⁵ Based on the prominence of vascular abnormalities in polymicrogyria, one may hypothesize that they are involved in its etiopathogenesis. For instance, a causative role of venous abnormalities has been suggested in patients with Sturge-Weber syndrome and polymicrogyria in the region underlying pial angiomas.^{38,51,52} One hypothesis concerning the cause of Sturge-Weber is that leptomeningeal vascular dysplasia leads to impaired perfusion, especially in regard to microvenular drainage, which produces blood stasis with progressive hypoperfusion and ischemia.⁵³ Alternatively, cortical dysgenesis could result from the abnormal expression of a factor playing a role in both vascular and cortical development.⁵⁴ On the basis of the observation that cryogenic lesions in the cortex of neonatal rats can produce focal microgyria and subsequent abnormal vascularization, it has also been suggested that cortical venous abnormalities in polymicrogyria might be the consequence, and not the cause, of abnormal cortical development.⁵⁵ However, it is not clear that lesion-induced polymicrogyria in the normally agyric rat cortex is the same malformation as the polymicrogyria found in gyrencephalic humans.

On the basis of the frequent location of polymicrogyria in watershed vascular territories and on evidence of laminar necrosis in brain specimens,^{7,49,56-59} some authors have suggested that polymicrogyria might result from arterial ischemia during the second trimester of gestation. Due to lack of arterial sequences in our study, however, we could not exclude the presence of arterial dysplasia in our patients and can only speculate on arterial dysgenesis as a possible cause of prenatal ischemia. In addition, we

studied adult patients with normal or nearly normal cognitive function whose main clinical problem was epilepsy. These clinical features might have characterized a subpopulation with a specific subtype of polymicrogyria or a specific etiology, which is certainly not representative of the larger population of individuals with polymicrogyria, in which varied etiologic factors other than vascular might be prevalent.

Polymicrogyria and polymicrogyria-like malformations have indeed been associated with mutations of various genes, including *COL18A1*, *PAX6*, *KIAA1279*, *RAB3GAP1*, *RAB3GAP2*, *TUBA1A*, *TUBB2B*, *TUBB3*, *TUBA8*, *TUBB5*, *TBR2*, and *WDR62* and different copy number variations.^{8,60–64} However, paucity of neuropathologic observations limits our ability to understand how comparable morphologic changes are in these conditions. Moreover, the large majority of cases of polymicrogyria are not caused by alterations of any known gene. 7T MR imaging will hopefully make it possible to better evaluate and classify specific polymicrogyria phenotypes and, by reducing sample heterogeneity, improve the approach to genetic studies, leading to a higher diagnostic yield. Genetic characterization of patients with polymicrogyria might ultimately lead to improved outcome prediction.⁶⁵ Quantitative measurements of abnormal sulcal patterns have made it possible to correlate morphologic abnormalities with language impairment.⁶⁶ Future 7T functional MR imaging studies are needed to clarify the correlation between abnormal sulcal patterns and functional impairment.

Approximately 78%–87% of patients with polymicrogyria have epilepsy.^{38,67} Associated epilepsy is often intractable, but only a limited number of patients are eligible for surgical treatment and invasive recordings are necessary in most to define eloquent cortex and the area to be removed.^{41,43,44} Although the final surgical margins are determined by the use of depth electrode recordings or by corticography in the operating theater, 7T MR imaging may help presurgical planning for patients with polymicrogyria-related epilepsy by providing a clearer assessment of the margins of the polymicrogyric cortex and revealing previously undetected bilateral abnormalities.

Although we demonstrated some obvious advantages offered by 7T, we also found limitations inherent its use. The protocols and acquisition methods we used for 3T and 7T MR imaging were different, and both relaxivity and susceptibility effects differ significantly at these various field strengths. In addition, optimal protocols at 7T have not yet been implemented. SWAN and TBE sequences were not included in our standard 3T MR imaging protocol and could not be directly compared with 7T acquisitions. When imaged at conventional field strengths, patients with polymicrogyria are not evaluated with GRE images but primarily with FSPGR, FSE, or IR sequences. At 7T, the inhomogeneous radiofrequency energy deposition and the increased susceptibility effect may cause signal inhomogeneity or image distortion. To remain within the specific absorption rate limits and reduce image distortion and stronger susceptibility phenomena, we acquired targeted images with small FOVs and a few sections focused on regions of interest at 7T. Therefore, we could not image the entire brain as instead it was feasible at lower field strengths. In particular, in order not to exceed the specific absorption rate limits imposed by regulations (International Electrotechnical Com-

mission Standards for Medical Electrical Equipment 60601–2–33), for FSE, it was possible to acquire 10 sections within 1 single acquisition, while for TBE, 10 sections were acquired during 2 separate series of 5 sections each.

An additional limitation of our study is that none of our patients had undergone epilepsy surgery and no pathology and post-operative outcome were available to be correlated with 7T imaging. Furthermore, our MR imaging comparison was based on visual, qualitative analysis. Nevertheless, we found substantially more and different information at 7T that we hope will be useful in future analyses of patients with polymicrogyria.

CONCLUSIONS

Ultra-high-field 7T imaging allows assessment of structural brain abnormalities that cannot be obtained from conventional MR imaging and represents an important tool for the diagnosis and characterization of polymicrogyria.

Disclosures: Alessio De Ciantis—*RELATED: Grant:* Pisa Foundation, Pisa, Italy (Project 133/11).* *Comments:* My salary was paid by Pisa Foundation through Meyer Children's Hospital; Carmen Barba—*RELATED: Grant:* Fondazione Cassa di Risparmio Pisa, Pisa, Italy (Project 133/11)*; European Union Seventh Framework Programme FP7/2007–2013 under the project DESIRE (Development and Epilepsy: Strategies for Innovative Research to improve diagnosis, prevention and treatment in Children with difficult to treat Epilepsy - Grant Agreement: 602531).* *Comments:* Grants allowed allocating human resources needed to perform the work for this article and comply with bureaucratic requirements; *Support for Travel to Meetings for the Study or Other Purposes:* Fondazione Cassa di Risparmio Pisa, Italy (Project 133/11)*; European Union Seventh Framework Programme FP7/2007–2013 under the project DESIRE (grant agreement No. 602531).* *Comments:* The reimbursement of travel expenses was made through my Institution. Mauro Costagli—*RELATED: Grant:* Fondazione Pisa.* *Comments:* My institution received a grant from "Fondazione Pisa" for this study. Michela Tosetti—*RELATED: Grant:* Pisa Foundation, Pisa, Italy.* *Comments:* My Institution, IRCCS Stella Maris Foundation, received a grant from "Fondazione Pisa" for a research project (Project 133/11) relating to the subject of this work. Laura Biagi—*RELATED: Pisa Foundation, Pisa, Italy (Project 133/11).** *Comments:* My institution received a grant from "Fondazione Pisa" for a research project relating to the subject of this work. William B. Dobyns—*RELATED: Grant:* National Institutes of Health.* *Comments:* grant No. R01NS058721; *Grants/Grants Pending:* National Institutes of Health*; *Payment for Lectures (including service on Speakers Bureaus):* Novartis Neuroscience Institute (Boston) in 2013. *Comments:* total less than US \$3000. Renzo Guerrini—*RELATED: Grant:* European Union Seventh Framework Programme FP7/2007–2013 under the project DESIRE (grant agreement No. 602531)*; Project 133/11" Fondazione Pisa.* *Money paid to the institution.

REFERENCES

1. Barkovich AJ, Guerrini R, Kuzniecky RI, et al. **A developmental and genetic classification for malformations of cortical development: update 2012.** *Brain* 2012;135:1348–69
2. Barkovich AJ. **MRI analysis of sulcation morphology in polymicrogyria.** *Epilepsia* 2010;51:17–22
3. Barkovich AJ, Kuzniecky RI, Jackson GD, et al. **A developmental and genetic classification for malformations of cortical development.** *Neurology* 2005;65:1873–87
4. Harding B, Copp AJ. **Malformations.** In: Graham DI, Lantos PL, eds. *Greenfield's Neuropathology*. 6th ed. London: Arnold; 1997:397–533
5. Barkovich AJ, Lindan CE. **Congenital cytomegalovirus infection of the brain: imaging analysis and embryologic considerations.** *AJNR Am J Neuroradiol* 1994;15:703–15
6. Crome L, France NE. **Microgyria and cytomegalic inclusion disease in infancy.** *J Clin Pathol* 1959;12:427–34
7. Barkovich AJ, Rowley H, Bollen A. **Correlation of prenatal events with the development of polymicrogyria.** *AJNR Am J Neuroradiol* 1995;16:822–27
8. Guerrini R, Parrini E. **Neuronal migration disorders.** *Neurobiol Dis* 2010;38:154–66
9. Robin NH, Taylor CJ, McDonald-McGinn DM, et al. **Polymicrogyria**

- and deletion 22q11.2 syndrome: window to the etiology of a common cortical malformation. *Am J Med Genet A* 2006;140:2416–25
10. Chang BS, Piao X, Bodell A, et al. **Bilateral frontoparietal polymicrogyria: clinical and radiological features in 10 families with linkage to chromosome 16.** *Ann Neurol* 2003;53:596–606
 11. Chang BS, Piao X, Giannini C, et al. **Bilateral generalized polymicrogyria (BGP): a distinct syndrome of cortical malformation.** *Neurology* 2004;62:1722–28
 12. Guerrini R, Dubeau F, Dulac O, et al. **Bilateral parasagittal parietooccipital polymicrogyria and epilepsy.** *Ann Neurol* 1997;41:65–73
 13. Guerrini R, Genton P, Bureau M, et al. **Multilobar polymicrogyria, intractable drop attack seizures, and sleep-related electrical status epilepticus.** *Neurology* 1998;51:504–12
 14. Guerrini R, Barkovich AJ, Sztriha L, et al. **Bilateral frontal polymicrogyria: a newly recognized brain malformation syndrome.** *Neurology* 2000;54:909–13
 15. Kuzniecky R, Andermann F, Guerrini R. **Congenital bilateral perisylvian syndrome: study of 31 patients.** *Lancet* 1993;341:608–12
 16. Barkovich AJ. **Morphologic characteristics of subcortical heterotopia: MR imaging study.** *AJNR Am J Neuroradiol* 2000;21:290–95
 17. Wieck G, Leventer RJ, Squier WM, et al. **Periventricular nodular heterotopia with overlying polymicrogyria.** *Brain* 2005;128:2811–21
 18. Galaburda AM, Sherman GF, Rosen GD, et al. **Developmental dyslexia: four consecutive patients with cortical anomalies.** *Ann Neurol* 1985;18:222–33
 19. Guerrini R, Dobyns WB, Barkovich AJ. **Abnormal development of the human cerebral cortex: genetics, functional consequences and treatment options.** *Trends Neurosci* 2008;31:154–62
 20. Barkovich AJ. **Current concepts of polymicrogyria.** *Neuroradiology* 2010;52:479–87
 21. Cushion TD, Dobyns WB, Mullins JG, et al. **Overlapping cortical malformations and mutations in TUBB2B and TUBA1A.** *Brain* 2013;136:536–48
 22. Bahi-Buisson N, Poirier K, Boddaert N, et al. **GPR56-related bilateral frontoparietal polymicrogyria: further evidence for an overlap with the cobblestone complex.** *Brain* 2010;133:3194–209
 23. Devisme L, Bouchet C, Gonzales M, et al. **Cobblestone lissencephaly: neuropathological subtypes and correlations with genes of dystroglycanopathies.** *Brain* 2012;135:469–82
 24. Singer K, Luo R, Jeong SJ, et al. **GPR56 and the developing cerebral cortex: cells, matrix, and neuronal migration.** *Mol Neurobiol* 2013;47:186–96
 25. Cho ZH, Kim YB, Han JY, et al. **New brain atlas—mapping the human brain in vivo with 7.0 T MRI and comparison with postmortem histology: will these images change modern medicine?** *Int J Imag Syst Tech* 2008;18:2–8
 26. Abosch A, Yacoub E, Ugurbil K, et al. **An assessment of current brain targets for deep brain stimulation surgery with susceptibility-weighted imaging at 7 Tesla.** *Neurosurgery* 2010;67:1745–56
 27. Metcalf M, Xu D, Okuda DT, et al. **High-resolution phased-array MRI of the human brain at 7 Tesla: initial experience in multiple sclerosis patients.** *J Neuroimaging* 2010;20:141–47
 28. van der Kolk AG, Hendrikse J, Zwanenburg JJ, et al. **Clinical applications of 7 T MRI in the brain.** *Eur J Radiol* 2013;82:708–18
 29. Tallantyre EC, Dixon JE, Donaldson I, et al. **Ultra-high-field imaging distinguishes MS lesions from asymptomatic white matter lesions.** *Neurology* 2011;76:534–39
 30. Conijn MM, Geerlings MI, Biessels GJ, et al. **Cerebral microbleeds on MR imaging: comparison between 1.5 and 7T.** *AJNR Am J Neuroradiol* 2011;32:1043–49
 31. Madai VI, von Samson-Himmelstjerna FC, Bauer M, et al. **Ultra-high-field MRI in human ischemic stroke: a 7 Tesla study.** *PLoS One* 2012;7:e37631
 32. Mönninghoff C, Maderwald S, Wanke I. **Pre-interventional assessment of a vertebralbasilar aneurysm with 7 Tesla time-of-flight MR angiography.** *Rofa* 2009;181:266–68
 33. Dammann P, Barth M, Zhu Y, et al. **Susceptibility weighted magnetic resonance imaging of cerebral cavernous malformations: prospects, drawbacks, and first experience at ultra-high field strength (7-Tesla) magnetic resonance imaging.** *Neurosurg Focus* 2010;29:E5
 34. Lupo JM, Li Y, Hess CP, et al. **Advances in ultra-high field MRI for the clinical management of patients with brain tumors.** *Curr Opin Neurol* 2011;24:605–15
 35. Cosottini M, Frosini D, Pesaresi I, et al. **MR imaging of the substantia nigra at 7 T enables diagnosis of Parkinson disease.** *Radiology* 2014;271:831–38
 36. Kwon DH, Kim JM, Oh SH, et al. **Seven-tesla magnetic resonance images of the substantia nigra in Parkinson disease.** *Ann Neurol* 2012;71:267–77
 37. Costagli M, Kelley DA, Symms MR, et al. **Tissue border enhancement by inversion recovery MRI at 7.0 Tesla.** *Neuroradiology* 2014;56:517–23
 38. Leventer RJ, Jansen A, Pilz DT, et al. **Clinical and imaging heterogeneity of polymicrogyria: a study of 328 patients.** *Brain* 2010;133:1415–27
 39. Barkovich AJ. **Abnormal vascular drainage in anomalies of neuronal migration.** *AJNR Am J Neuroradiol* 1988;9:939–42
 40. Guerrini R, Dravet C, Raybaud C, et al. **Epilepsy and focal gyral anomalies detected by MRI: electroclinico-morphological correlations and follow-up.** *Dev Med Child Neurol* 1992;34:706–18
 41. Chassoux F, Landre E, Rodrigo S, et al. **Intralesional recordings and epileptogenic zone in focal polymicrogyria.** *Epilepsia* 2008;49:51–64
 42. Guerrini R. **Polymicrogyria and epilepsy.** *Epilepsia* 2010;51:10–12
 43. Maillard L, Koessler L, Colnat-Coulbois S, et al. **Combined SEEG and source localisation study of temporal lobe schizencephaly and polymicrogyria.** *Clin Neurophysiol* 2009;120:1628–36
 44. Ramantani G, Koessler L, Colnat-Coulbois S, et al. **Intracranial evaluation of the epileptogenic zone in regional infrasylvian polymicrogyria.** *Epilepsia* 2013;54:296–304
 45. Thompson JE, Castillo M, Thomas D, et al. **Radiologic-pathologic correlation polymicrogyria.** *AJNR Am J Neuroradiol* 1997;18:307–12
 46. Friede RL. *Developmental Neuropathology.* Berlin: Springer-Verlag; 1989
 47. Golden JA, Harding BN. *Pathology and Genetics: Developmental Neuropathology.* Basel: ISN Neuropath Press; 2004
 48. Judkins AR, Martinez D, Ferreira P, et al. **Polymicrogyria includes fusion of the molecular layer and decreased neuronal populations but normal cortical laminar organization.** *J Neuropathol Exp Neurol* 2011;70:438–43
 49. Marques Dias MJ, Harmant-van Rijckevorsel G, Landrieu P, et al. **Prenatal cytomegalovirus disease and cerebral microgyria: evidence for perfusion failure, not disturbance of histogenesis, as the major cause of fetal cytomegalovirus encephalopathy.** *Neuropediatrics* 1984;15:18–24
 50. Pryor J, Setton A, Berenstein A. **Venous anomalies and associated lesions.** *Neurosurg Clin N Am* 1999;10:519–25
 51. Simonati A, Colamaria V, Bricolo A, et al. **Microgyria associated with Sturge-Weber angiomatosis.** *Childs Nerv Syst* 1994;10:392–95
 52. Terdjman P, Aicardi J, Sainte-Rose C, et al. **Neuroradiological findings in Sturge-Weber syndrome (SWS) and isolated pial angiomatosis.** *Neuropediatrics* 1991;22:115–20
 53. Cagneaux M, Paoli V, Blanchard G, et al. **Pre- and postnatal imaging of early cerebral damage in Sturge-Weber syndrome.** *Pediatr Radiol* 2013;43:1536–39
 54. Comi AM. **Pathophysiology of Sturge-Weber syndrome.** *J Child Neurol* 2003;18:509–16
 55. Dvorak K, Feit J, Juránková Z. **Experimentally induced focal microgyria and status verrucosus deformis in rats: pathogenesis and interrelation—histological and autoradiographical study.** *Acta Neuropathol* 1978;44:121–29
 56. Aeby A, Guerrini R, David P, et al. **Facial hemangioma and cerebral corticovascular dysplasia: a syndrome associated with epilepsy.** *Neurology* 2003;60:1030–32

57. Evrard P, Kadhim H, de Saint-Georges P, et al. **Abnormal development and destructive processes of the human brain during the second half of gestation.** In: Evrard P, Minkowski A, eds. *Developmental Neurobiology*. New York: Vevey-Raven Press; 1989:21–41
58. Richman DP, Stewart RM, Caviness VS Jr. **Cerebral microgyria in a 27-week fetus: an architectonic and topographic analysis.** *J Neuro-pathol Exp Neurol* 1974;33:374–84
59. Suzuki M, Choi BH. **Repair and reconstruction of the cortical plate following closed cryogenic injury to the neonatal rat cerebrum.** *Acta Neuropathol* 1991;82:93–101
60. Abdollahi MR, Morrison E, Sirey T, et al. **Mutation of the variant alpha-tubulin TUBA8 results in polymicrogyria with optic nerve hypoplasia.** *Am J Hum Genet* 2009;85:737–44
61. Breuss M, Heng JI, Poirier K, et al. **Mutations in the beta-tubulin gene TUBB5 cause microcephaly with structural brain abnormalities.** *Cell Rep* 2012;2:1554–62
62. Guerrini R, Dobyns WB. **Malformations of cortical development: clinical features and genetic causes.** *Lancet Neurol* 2014;13:710–26
63. Jaglin XH, Chelly J. **Tubulin-related cortical dysgeneses: microtubule dysfunction underlying neuronal migration defects.** *Trends Genet* 2009;25:555–66
64. Poirier K, Saillour Y, Bahi-Buisson N, et al. **Mutations in the neuronal ss-tubulin subunit TUBB3 result in malformation of cortical development and neuronal migration defects.** *Hum Mol Genet* 2010;19:4462–73
65. Shain C, Ramgopal S, Fallil Z, et al. **Polymicrogyria-associated epilepsy: a multicenter phenotypic study from the Epilepsy Phenome/Genome Project.** *Epilepsia* 2013;54:1368–75
66. Im K, Pienaar R, Paldino MJ, et al. **Quantification and discrimination of abnormal sulcal patterns in polymicrogyria.** *Cereb Cortex* 2013;23:3007–15
67. Guerrini R, Filippi T. **Neuronal migration disorders, genetics, and epileptogenesis.** *J Child Neurol* 2005;20:287–99

Usefulness of Subtraction of 3D T2WI-DRIVE from Contrast-Enhanced 3D T1WI: Preoperative Evaluations of the Neurovascular Anatomy of Patients with Neurovascular Compression Syndrome

Y. Masuda, T. Yamamoto, H. Akutsu, M. Shiigai, T. Masumoto, E. Ishikawa, M. Matsuda, and A. Matsumura

ABSTRACT

BACKGROUND AND PURPOSE: High-resolution 3D MR cisternography techniques such as 3D T2WI-driven equilibrium radiofrequency reset pulse (DRIVE) are used preoperatively to assess neurovascular anatomy in patients with neurovascular compression syndrome, but contrast between vessels and cranial nerves at the point of neurovascular contact is limited. The postprocessing technique subtraction of 3D T2WI-driven equilibrium radiofrequency reset pulse from contrast-enhanced 3D T1WI (sDRICE) provides both high spatial resolution and excellent contrast in depicting the neurovascular contact. We evaluated the usefulness of sDRICE compared with 3D T2WI-DRIVE.

MATERIALS AND METHODS: Twelve patients who underwent microvascular decompression for hemifacial spasm or trigeminal neuralgia were examined preoperatively with 3D T2WI-DRIVE and sDRICE. Two neuroradiologists retrospectively analyzed and scored lesion conspicuity, defined as the ease of discrimination between offending vessels and compressed nerves or the brain stem at the neurovascular contact. They also quantitatively analyzed the contrast and contrast-to-noise ratio at the neurovascular contact.

RESULTS: The lesion conspicuity scores of sDRICE images were significantly higher than those of 3D T2WI-DRIVE for all 12 patients ($P = .006$) and the 6 cases of hemifacial spasm ($P = .023$) but were not significantly higher in the 6 trigeminal neuralgia cases alone ($P = .102$). For all 12 patients, the contrast-to-noise ratio between the offending vessels and the brain stem and between the vessels and nerves on sDRICE images was significantly higher than that on 3D T2WI-DRIVE ($P = .003$ and $P = .007$, respectively). Among these structures, the contrast values were also significantly higher on the sDRICE than on the 3D T2WI-DRIVE ($P < .001$) images.

CONCLUSIONS: The postprocessing technique sDRICE is useful to evaluate neurovascular anatomy and to improve contrast and the contrast-to-noise ratio in patients with neurovascular compression syndrome.

ABBREVIATIONS: CE = contrast-enhanced; CN = cranial nerve; DRIVE = driven equilibrium radiofrequency reset pulse; HFS = hemifacial spasm; NVC = neurovascular contact; sDRICE = subtraction of 3D T2WI-DRIVE from contrast-enhanced 3D T1WI; SI = signal intensity; TN = trigeminal neuralgia

Neurovascular compression syndromes such as trigeminal neuralgia (TN) and hemifacial spasm (HFS) are characterized by hyperactive cranial nerve dysfunction. The most effective and standard treatment for this syndrome is microvascular decompression, which is capable of providing complete resolution of symptoms in most cases.¹⁻⁴ A preoperative determination of microvascular anatomy in terms of the exact localization and direction of the compressing vessel and the anatomic relationship between cranial nerves and vessels is of great value to neurosurgeons. Some authors have proposed that the presence of clear-cut

and marked vascular compression is a factor in good long-term prognosis^{5,6}; thus, the accurate preoperative radiologic evaluation of the neurovascular anatomy is crucial to achieve an excellent clinical outcome. High-resolution 3D MR cisternography, such as 3D T2-weighted imaging driven equilibrium radiofrequency reset pulse (3D T2WI-DRIVE),^{7,8} 3D FIESTA^{9,10} and 3D CISS,¹¹⁻¹³ is the method of choice to evaluate preoperative neurovascular anatomy in patients with neurovascular compression syndrome.

Although these sequences have excellent spatial resolution, the contrast between vessels and cranial nerves at the point of neurovascular contact (NVC) is limited in general; this poor contrast is a major drawback of these sequences for preoperative evaluations of vascular compression syndromes.^{14,15} On 3D TOF-MRA^{8,16-18} or 3D gadolinium-enhanced T1WI,^{8,13,18} vessels are clearly depicted but the nerves are too poorly seen to be depicted at the point of NVC. Fused images of 3D CTA or 3D TOF-MRA and 3D MR cisternography have been used to evaluate the NVC to

Received May 29, 2014; accepted after revision August 5.

From the Departments of Neurosurgery (Y.M., T.Y., H.A., E.I., M.M., A.M.) and Radiology (M.S., T.M.), Faculty of Medicine, University of Tsukuba, Tsukuba, Japan.

An earlier version of the article was previously presented at: Annual Meeting of the Japanese Society of Neuroradiology, February 24-26, 2011; Tokyo, Japan.

Please address correspondence to Hiroyoshi Akutsu, MD, 1-1-1 Tennodai, Tsukuba, Ibaraki 305-8575, Japan; e-mail: akutsuh@md.tsukuba.ac.jp

<http://dx.doi.org/10.3174/ajnr.A4130>



FIG 1. Method of image postprocessing. The first set of 3D T2WI-DRIVE source images (B) is subtracted from the second set of 3D CE T1WI (A) on a pixel-by-pixel basis by using workstations provided by the MR imaging system manufacturer. Then a third set of subtracted source images named sDRICE (C) is produced.

solve this problem,^{19–23} but making these fusion images is technically challenging and too time-consuming for daily clinical practice.

We report a simple postprocessing technique that we named subtraction of 3D T2WI-DRIVE from contrast-enhanced 3D T1WI (sDRICE), which provides both high spatial resolution and excellent contrast between vessels and cranial nerves. It is easy and simple to create sDRICE images on a console without the need for any fusion technique or special software. We evaluated the utility of sDRICE imaging for the radiologic evaluation of patients with neurovascular compression syndrome, and we compared its efficacy with that of 3D T2WI-DRIVE, which is used in standard 3D MR cisternography.

MATERIALS AND METHODS

Study Population

We studied 12 patients (9 women and 3 men; mean age, 53 years; range, 30–74 years) who underwent microvascular decompression for HFS or TN (6 cases of HFS and 6 cases of TN) at our institution between August 2009 and November 2013. All patients were examined with MR imaging by using both 3D T2WI-DRIVE and sDRICE before surgery. We retrospectively analyzed the patient data, including demographics, clinical history, and pre- and postoperative imaging findings. We analyzed the outcomes of the microvascular decompression in terms of cure and surgical complications on the basis of the criteria of the Japan Society for Microvascular Decompression Surgery.²⁴ The final clinical outcome of microvascular decompression was evaluated 1 year after surgery.

Image Acquisition

MR imaging was performed by using a 3T whole-body MR imaging system (Achieva 3T; Philips Healthcare, Best, the Netherlands) with a manufacturer-provided 32-channel head coil for reception and a body coil for transmission. The MR imaging protocol was implemented by 1 author (T.M., with 20 years of experience in MR imaging). The MR imaging technique was as follows: axial 3D T2-weighted-DRIVE: TR, 2000 ms; TE, 220 ms; FOV, 160 × 160 mm; voxel resolution, 0.63 × 0.63 × 1.0 mm³; sensitivity encoding for fast MR imaging factor, 2; number of

signals averaged, 1; echo-train length, 69; flip angle, 90°; acquisition time, 3 minutes 38 seconds. For the axial, contrast-enhanced 3D-T1-weighted fast-field echo images, we used the following parameters: TR, 30 ms; TE, 4.1 ms; FOV, 160 × 160 mm; voxel size, 0.63 × 0.63 × 1.0 mm³; sensitivity encoding for fast MR imaging factor, 2; number of signals averaged, 1; flip angle, 20°; acquisition time, 2 minutes 54 seconds. After a single intravenous Gd-DTPA (0.2 mmol/kg) injection was administered, a contrast-enhanced (CE) 3D T1-weighted sequence was run. We used 2 steps for simple and accurate subtraction after the acquisition: First, we matched the FOV and the voxel resolution between the 3D T2WI-DRIVE and CE 3D T1WI for the same scanning range. Second, to avoid misregistration, we shortened the interval time between the 2 sequences by scanning CE 3D T1WI in the train of 3D T2WI-DRIVE, and we asked the patients to stay still.

Image Postprocessing

After the data acquisition, the image data were transferred through a local area network for postprocessing by using the console software of the MR imaging system. The first set of 3D T2-weighted-DRIVE source images (Fig 1B) was subtracted from the second set of CE 3D T1WI (Fig 1A) on a pixel-by-pixel basis by using workstations provided by the manufacturers of the MR imaging system. This process produced the third set of subtracted source images of sDRICE (Fig 1C). All of the source and subtracted images were sent to the PACS of the hospital. There was no rudimentary image registration technique before the image subtraction in our postprocessing program. To control the possibility of misregistration, we checked whether the diameters of cranial nerves (CNs) V and VII and those of the offending vessels on sDRICE were similar on 3D T2WI-DRIVE and CE 3D T1WI side by side. Two-dimensional axial, coronal, and sagittal fusion images were obtained to evaluate the neurovascular relationship in the cerebellopontine angle cistern, and if necessary, oblique images were reconstructed.

Image Evaluation and Data Analysis

We analyzed 3D T2WI-DRIVE and sDRICE both qualitatively and quantitatively. The qualitative image analysis was performed

independently by 2 raters (T.M. and M.S. with 20 and 15 years of experience in neuroradiology, respectively) blinded to the hypothesis of the study and clinical data. The 3D T2WI-DRIVE and sDRICE images for each patient were independently evaluated in a random order of cases and sequences. Lesion conspicuity was defined as the ease of discrimination between offending vessels and compressed nerves or the brain stem at the NVC. To evaluate the lesion conspicuity, we used the following 3-point ordinal scoring system: 1, poor, not distinguishable due to no contrast; 2, good, distinguishable by slight contrast; and 3, excellent, easily distinguishable by clear contrast. The quantitative image analysis was performed by 2 authors (Y.M. and H.A.).

The contrast-to-noise ratios (CNRs) were calculated on the basis of signal intensity (SI) and SD measurements in manually drawn ROIs. The ROIs were placed in the areas of the offending vessels and compressed parenchyma of the brain stem and com-

pressed nerves at the NVC. Finally, the contrast and the CNRs of the offending vessels to brain stem and the offending vessels to compressed nerves were calculated by using the following equations: $Contrast_{a/b} = 2 (SI_a - SI_b)/(SI_a + SI_b)$, and $CNR_{a/b} = (SI_a - SI_b)/SD_a$, where a and b denote the tissues of interest.

Statistical Analysis

A statistical analysis was performed by using standard statistical software (SPSS Version 15.0 for Microsoft Windows; IBM, Armonk, New York). An analysis of the interobserver agreement regarding qualitative variables was assessed by the κ agreement test ($\kappa < 0$, poor agreement; $0 < \kappa < 0.2$, slight agreement; $0.2 < \kappa < 0.4$, fair agreement; $0.4 < \kappa < 0.6$, moderate agreement; $0.6 < \kappa < 0.8$, substantial agreement; and $0.8 < \kappa < 1$, almost perfect agreement).²⁵ Because there was substantial agreement between the scores given by the 2 raters at $\kappa = 0.660$ ($P < .001$), only the score data from 1 rater (rater 1) were used for the statistical analysis. The statistical significance of differences between 3D T2WI-DRIVE and sDRICE was established by using the Wilcoxon signed rank test in the qualitative evaluation. The data in the quantitative evaluation are presented as means and SDs. A paired *t* test was used to analyze observed differences.

RESULTS

All of the imaging examinations by using both 3D T2-weighted-DRIVE and sDRICE were successfully completed before surgery. The clinical results are shown in Table 1. In all 12 patients, the offending vessels and compressing point predicted by the sDRICE images matched the intraoperative findings. In all patients, the preoperative HFS or TN was completely resolved after the microvascular decompression, and no complication was encountered.

sDRICE images and the black/white-reversed 3D T2WI-DRIVE images of patients with HFS and TN are shown in Figs 2 (HFS) and 3 (TN), respectively. The results of the lesion conspicuity scoring by the 2 raters are shown in Table 2. In all except 1 of the 6 patients with HFS, the lesion conspicuity in sDRICE was scored better than that in 3D T2WI-DRIVE by both raters. In particular, in patients 1 and 2 (Fig 2A–D), the sDRICE images were scored 2 points better than the 3D T2WI-DRIVE images by both raters. There was only 1 patient (patient 6, Fig 2E, –F) for whom 1 rater scored the 3D T2WI-DRIVE and sDRICE images equally.

On the other hand, among the 6 patients with TN, there was only 1 patient for whom the sDRICE images were scored 2 points better than the 3D T2WI-DRIVE images by both raters (patient 7, Fig 3A, –B). In this patient, the offending vessel (the petrosal vein) was clearly depicted on the sDRICE images, in contrast to the 3D T2WI-DRIVE images. The 3D T2WI-

Table 1: Patient data and outcomes

Patient No.	Age (yr)/Sex	Disease	Side	Offending Vessel	Result	Complication
1	46/F	HFS	R	AICA-PICA	Cure	No
2	30/M	HFS	L	VA, AICA	Cure	No
3	53/F	HFS	L	PICA	Cure	No
4	60/M	HFS	L	VA, AICA	Cure	No
5	40/F	HFS	L	PICA	Cure	No
6	50/M	HFS	L	AICA	Cure	No
7	57/F	TN	L	Petrosal vein	Cure	No
8	61/F	TN	R	SCA	Cure	No
9	62/F	TN	L	SCA	Cure	No
10	74/F	TN	R	SCA	Cure	No
11	64/F	TN	L	SCA, AICA	Cure	No
12	33/F	TN	L	VA	Cure	No

Note:—AICA indicates anterior inferior cerebellar artery, PICA, posterior inferior cerebellar artery; SCA, superior cerebellar artery; VA, vertebral artery.

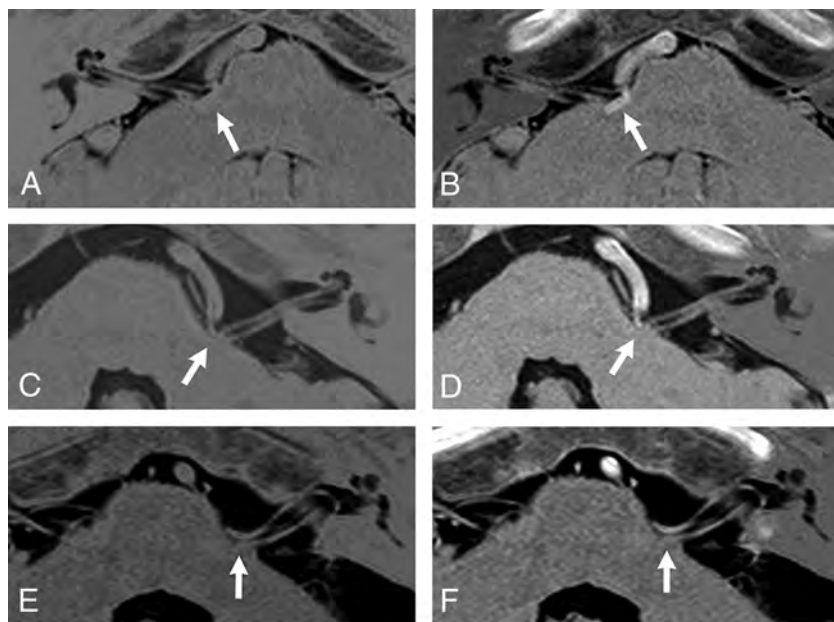


FIG 2. Comparison between the black/white-reversed 3D T2WI-DRIVE (A, C, E) and sDRICE images (B, D, F) at the NVC (arrow) in patients with HFS. In patients 1 (A and B) and 2 (C and D), the sDRICE images (B and D) clearly show that the offending vessel invaginates into the brain stem and compresses the root exit zone of CN VII, in contrast to the 3D T2WI-DRIVE images (A and C). In patient 6 (E and F), both images clearly show that the posterior cerebral artery compresses CN VII.

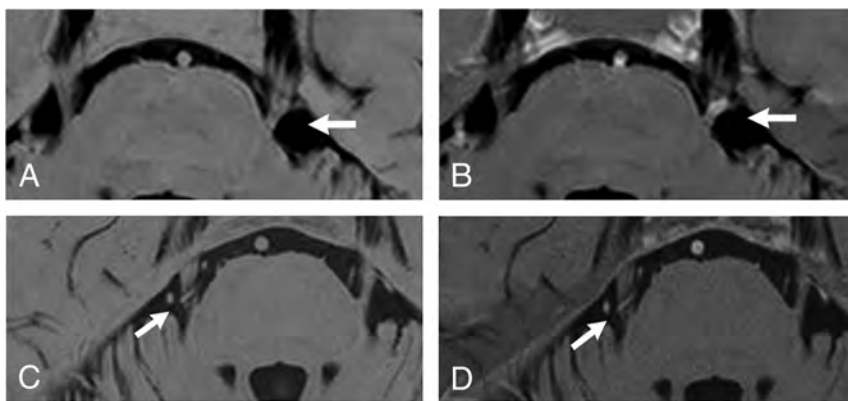


FIG 3. Comparison between the black/white-reversed 3D T2WI-DRIVE (A and C) and sDRICE images (B and D) at the NVC (arrow) in patients with TN. In patient 7 (A and B), the sDRICE image (B) clearly shows that the offending vessel (the petrosal vein) invaginates into CN V, in contrast to 3D T2WI-DRIVE (A). In patient 10 (C and D), the offending vessel is relatively easily discriminated from CN V even on 3D T2WI-DRIVE (D).

Table 2: The lesion conspicuity scoring by the 2 raters^a

Patient No.	Disease	Scores by Rater 1		Scores by Rater 2	
		3D T2WI-DRIVE	sDRICE	3D T2WI-DRIVE	sDRICE
1	HFS	1	3	1	3
2	HFS	1	3	1	3
3	HFS	1	2	1	3
4	HFS	2	3	2	3
5	HFS	2	3	2	3
6	HFS	2	3	2	2
7	TN	1	3	1	3
8	TN	1	2	1	3
9	TN	2	3	2	3
10	TN	3	3	2	3
11	TN	3	3	2	3
12	TN	3	3	3	3

^a Score 1, poor, not distinguishable due to no contrast; 2, good; distinguishable by slight contrast; 3, excellent, easily distinguishable by clear contrast.

DRIVE and sDRICE images were scored equally by rater 1 for patient 10 (Fig 3C, -D) and patient 11 and by both raters for patient 12. In those patients, the 3D T2WI-DRIVE and sDRICE images showed the offending vessel compressing CN V equally.

The results of the qualitative and quantitative analyses are summarized in Table 3. In the qualitative analysis, regarding the lesion conspicuity scored by rater 1, the sDRICE images received significantly higher scores than the 3D T2WI-DRIVE images in all 12 patients ($P = .006$) and in the patients with HFS ($P = .023$), but not in the patients with TN ($P = .102$).

In the quantitative analysis, the contrast values between the offending vessel and the brain stem and between the offending vessel and the compressed CN on sDRICE were significantly higher than those on 3D T2WI-DRIVE ($P < .001$). This difference supports the results of the qualitative analysis for lesion conspicuity. The CNRs between the offending vessel and the brain stem and between the offending vessel and the compressed CN on sDRICE were also significantly higher than those on 3D T2WI-DRIVE ($P = .003$ and $P = .007$, respectively).

DISCUSSION

MR cisternography performed with techniques such as 3D FIESTA,^{9,10} 3D CISS,¹¹⁻¹³ 3D T2-weighted-DRIVE sequences,^{7,8}

and reversed heavy T2WI²⁶ provides high spatial resolution and excellent visualization of vessels and cranial nerves and is thus a useful tool to depict cranial nerves and vessels in the cerebral cisterns. It is used for preoperative evaluations in cases of vascular compression syndrome, skull base tumors, and cerebrovascular disease. However, in these sequences, the contrast between vessels and cranial nerves is not always great enough, occasionally making a clear understanding of the anatomic structure difficult, especially in cases of neurovascular compression syndrome.^{9,14,15} Alternatives to standard MR cisternography (ie, image fusion between 3D CTA or 3D TOF-MRA and 3D MR cisternography) have been used to increase the contrast between vessels and cranial nerves.¹⁹⁻²³ However, several disadvantages of such image fusion techniques have been reported. First, some data may be lost through the segmentation process so that a signal defect in vessels or nerves occurs.²³ Second, artifacts are occasionally enhanced through the fusion process because artifacts of each technique are merged in the process.²⁰ Third, image fusion requires an extra software program and is time-consuming in most cases.

sDRICE can solve the above-mentioned limitations of the current standard MR cisternography because of its higher contrast without the use of any image fusion. In the present study, the lesion conspicuity of sDRICE was superior to that of 3D T2WI-DRIVE. Unlike fusion images, sDRICE images can be easily and quickly created on a console, and sDRICE presents no risk of data loss during the subtraction process. In addition, artifacts from CSF flow or chemical shifts are somewhat reduced by the subtraction process in sDRICE. Considering these advantages, sDRICE may be applicable for other intracranial lesions such as skull base tumors adjacent to cranial nerves.

On the basis of the results of the present study, we found that sDRICE is more useful for understanding the anatomy at the NVC in patients with HFS than in those with TN. The reasons for this are as follows: In patients with HFS, because CN VII and the offending artery are almost the same in diameter, the discrimination of these structures is difficult on 3D T2WI-DRIVE. In addition, the compressing point is generally at the root exit zone of CN VII; thus, an offending artery tends to run adjacent to the brain stem, occasionally invaginating into the brain stem, which also makes it difficult to discriminate the artery from the brain stem due to the lower contrast (patient 1, Fig 2A, -B). In fact, in all except 1 of the 6 patients with HFS, the lesion conspicuity of sDRICE was scored better than that of 3D T2WI-DRIVE by both raters. There was only 1 patient with HFS (patient 6, Fig 2E, -F) for whom 1 rater scored the 3D T2WI-DRIVE and sDRICE images equally, and this outcome was because the offending artery was easy to discriminate from CN VII and the brain stem on both images. In this case, the existing thin CSF space between the offending artery and CN VII or brain stem may help in the discrimination of these structures.

Table 3: Qualitative and quantitative analyses of 3D T2WI-DRIVE and sDRICE images

Parameter	3D		P Value
	T2WI-DRIVE	sDRICE	
Lesion conspicuity on the neurovascular contact point ^a			
Rater 1			
Overall (N = 12)	2.0 (1–3)	3.0 (2–3)	.006
HFS (n = 6)	1.5 (1–2)	3.0 (3–3)	.023
TN (n = 6)	2.5 (1–3)	3.0 (2–3)	.102
Rater 2			
Overall (N = 12)	2.0 (1–3)	3.0 (2–3)	.004
HFS (n = 6)	1.5 (1–2)	3.0 (2–3)	.038
TN (n = 6)	2.0 (1–3)	3.0 (3–3)	.038
Contrast (N = 12) ^b			
Vessel/nerve	-1.21 ± 0.72	0.28 ± 0.15	<.001
Vessel/brain stem	-1.08 ± 0.67	0.17 ± 0.88	<.001
CNR (N = 12) ^b			
Vessel/nerve	-1.80 ± 1.47	3.34 ± 1.99	.007
Vessel/brain stem	-0.97 ± 0.58	2.25 ± 1.57	.003

^a Scoring data are listed for both raters as rater 1/rater 2 and correspond to the median (with range) across patients. P values were calculated with the Wilcoxon signed rank test.

^b Contrast and CNR data are means ± SD. The P values were calculated with a paired t test. $Contrast_{a/b} = 2(SI_a - SI_b)/(SI_a + SI_b)$, and $CNR_{a/b} = (SI_a - SI_b)/SD_a$.

On the other hand, in the patients with TN, the offending artery (the superior cerebellar artery in most cases) was smaller in diameter than the trigeminal nerve, and it generally ran apart from the brain stem; thus, it was relatively easy to discriminate these structures, even on 3D T2WI-DRIVE without contrast enhancement. For the same reason, sDRICE may also be useful for cases of glossopharyngeal neuralgia, in which a cranial nerve and the offending vessel are similar in diameter.

As described in the “Materials and Methods” section, we used 2 steps for accurate subtraction without fusion to obtain the sDRICE images and controlled possible misregistration by using an internal check. First, we matched the FOV and the voxel resolution between 3D T2WI-DRIVE and CE 3D T1WI for the same scanning range. Second, we shortened the interval time between the 2 sequences by scanning CE 3D T1WI in the train of 3D T2WI-DRIVE, and we asked the patients to keep still. In this study, because all patients were without cognitive deficits and were stable in physical status, subtraction without fusion was successfully completed in all of them. However, this method might have possible subtle misregistration; thus, we checked and confirmed whether the diameter of CN V and VII and that of the offending vessels on sDRICE were similar on 3D T2WI-DRIVE and CE 3D T1WI side by side. Because of this possible misregistration, neuroradiologists separately evaluate 3D T2WI-DRIVE and CE 3D T1WI side by side for diagnostic purposes in clinical practice in our institution. Therefore, sDRICE images are used as adjuncts for more precise evaluation at neurovascular contact. On the other hand, for neurosurgeons, sDRICE has replaced the role of 3D T2-DRIVE and CE 3D T1WI for preoperative planning and intraoperative viewing.

Because sDRICE has excellent conspicuity at neurovascular contact and can depict both nerves and vessels on only 1 image set, it is more useful and practical for neurosurgeons than side-by-side-displayed 3D T2WI-DRIVE and CE 3D T1WI. Only 1 disadvantage of sDRICE compared with the standard noncontrast MR

cisternography was noted; with sDRICE, a contrast medium must be administered, which is contraindicated for patients with a history of allergy or renal dysfunction. However, an accurate preoperative evaluation of neurovascular anatomy is crucial for successful surgery in cases of neurovascular compression syndrome; thus, the use of contrast medium can be justified despite a possible-but-rare allergic reaction. In addition, contrast-enhanced images can depict not only arteries but also veins, in contrast to TOF imaging.¹² Adjacent veins can be an offending vessel in cases of TN. Moreover, the identification of venous anatomy in the surgical field, especially of the petrosal vein or its collateral veins, is crucial to avoid postoperative venous infarction. Therefore, an enhanced MR image is always mandatory for the precise preoperative evaluation in cases of vascular compression syndrome.

CONCLUSIONS

sDRICE is a novel, simple, and useful postprocessing technique to evaluate neurovascular anatomy in patients with neurovascular compression syndrome. It is useful especially in patients with HFS for discriminating offending vessels from cranial nerves or the brain stem due to the excellent contrast between these structures.

Disclosures: Tetsuya Yamamoto—UNRELATED: Grants/Grants Pending: Grant-in-Aid for Society Collaboration from the Ministry of Education, Science and Culture, Japan,* Comments: topic on radiation therapy. Tomohiko Masumoto—UNRELATED: Consultancy: Bayer, Comments: blinded review reader for clinical trial.*Money paid to the institution.

REFERENCES

- Jannetta PJ, Abbasy M, Maroon JC, et al. Etiology and definitive microsurgical treatment of hemifacial spasm: operative technique and results in 47 patients. *J Neurosurg* 1977;47:321–28
- Barker FG 2nd, Jannetta PJ, Bissonette DJ, et al. Microvascular decompression for hemifacial spasm. *J Neurosurg* 1995;82:201–10
- Barker FG 2nd, Jannetta PJ, Bissonette DJ, et al. The long-term outcome of microvascular decompression for trigeminal neuralgia. *N Engl J Med* 1996;334:1077–83
- Samii M, Günther T, Iaconetta G, et al. Microvascular decompression to treat hemifacial spasm: long-term results for a consecutive series of 143 patients. *Neurosurgery* 2002;50:712–18
- Sindou M, Leston J, Decullier E, et al. Microvascular decompression for primary trigeminal neuralgia: long-term effectiveness and prognostic factors in a series of 362 consecutive patients with clear-cut neurovascular conflicts who underwent pure decompression. *J Neurosurg* 2007;107:1144–53
- Zhang H, Lei D, You C, et al. The long-term outcome predictors of pure microvascular decompression for primary trigeminal neuralgia. *World Neurosurg* 2013;79:756–62
- Ciftci E, Anik Y, Arslan A, et al. Driven equilibrium (drive) MR imaging of the cranial nerves V–VIII: comparison with the T2-weighted 3D TSE sequence. *Eur J Radiol* 2004;51:234–40
- Leal PR, Hermier M, Souza MA, et al. Visualization of vascular compression of the trigeminal nerve with high-resolution 3T MRI: a prospective study comparing preoperative imaging analysis to surgical findings in 40 consecutive patients who underwent microvascular decompression for trigeminal neuralgia. *Neurosurgery* 2011;69:15–25
- Benes L, Shiratori K, Gurschi M, et al. Is preoperative high-resolution magnetic resonance imaging accurate in predicting neurovascular compression in patients with trigeminal neuralgia? A single-blind study. *Neurosurg Rev* 2005;28:131–36
- Zhou Q, Liu ZL, Qu CC, et al. Preoperative demonstration of neurovascular relationship in trigeminal neuralgia by using 3D FIESTA sequence. *Magn Reson Imaging* 2012;30:666–71

11. Yamakami I, Kobayashi E, Hirai S, et al. **Preoperative assessment of trigeminal neuralgia and hemifacial spasm using constructive interference in steady state-three-dimensional Fourier transformation magnetic resonance imaging.** *Neurol Med Chir (Tokyo)* 2000;40: 545–55; discussion 555–56
12. Yoshino N, Akimoto H, Yamada I, et al. **Trigeminal neuralgia: evaluation of neuralgic manifestation and site of neurovascular compression with 3D CISS MR imaging and MR angiography.** *Radiology* 2003;228:539–45
13. Tarnaris A, Renowden S, Coakham HB, et al. **A comparison of magnetic resonance angiography and constructive interference in steady state-three-dimensional Fourier transformation magnetic resonance imaging in patients with hemifacial spasm.** *Br J Neurosurg* 2007;21:375–81
14. Girard N, Poncet M, Caces F, et al. **Three-dimensional MRI of hemifacial spasm with surgical correlation.** *Neuroradiology* 1997;39: 46–51
15. Raslan AM, DeJesus R, Berk C, et al. **Sensitivity of high-resolution three-dimensional magnetic resonance angiography and three-dimensional spoiled-gradient recalled imaging in the prediction of neurovascular compression in patients with hemifacial spasm.** *J Neurosurg* 2009;111:733–36
16. Holley P, Bonafe A, Brunet E, et al. **The contribution of “time-of-flight” MRI-angiography in the study of neurovascular interactions (hemifacial spasm and trigeminal neuralgia).** *J Neuroradiol* 1996;23:149–56
17. Chang JW, Chang JH, Park YG, et al. **Microvascular decompression in trigeminal neuralgia: a correlation of three-dimensional time-of-flight magnetic resonance angiography and surgical findings.** *Stereotact Funct Neurosurg* 2000;74:167–74
18. Leal PR, Hermier M, Froment JC, et al. **Preoperative demonstration of the neurovascular compression characteristics with special emphasis on the degree of compression, using high-resolution magnetic resonance imaging: a prospective study, with comparison to surgical findings, in 100 consecutive patients who underwent microvascular decompression for trigeminal neuralgia.** *Acta Neurochir (Wien)* 2010;152:817–25
19. Satoh T, Onoda K, Date I. **Fusion imaging of three-dimensional magnetic resonance cisternograms and angiograms for the assessment of microvascular decompression in patients with hemifacial spasms.** *J Neurosurg* 2007;106:82–89
20. Naraghi R, Tanrikulu L, Troeschler-Weber R, et al. **Classification of neurovascular compression in typical hemifacial spasm: three-dimensional visualization of the facial and the vestibulocochlear nerves.** *J Neurosurg* 2007;107:1154–63
21. Satoh T, Omi M, Nabeshima M, et al. **Severity analysis of neurovascular contact in patients with trigeminal neuralgia: assessment with the inner view of the 3D MR cisternogram and angiogram fusion imaging.** *AJNR Am J Neuroradiol* 2009;30:603–07
22. González Sánchez JJ, Enseñat Nora J, Candela Canto S, et al. **New stereoscopic virtual reality system application to cranial nerve microvascular decompression.** *Acta Neurochir (Wien)* 2010;152: 355–60
23. Oishi M, Fukuda M, Hiraishi T, et al. **Interactive virtual simulation using a 3D computer graphics model for microvascular decompression surgery.** *J Neurosurg* 2012;117:555–65
24. Kondo A, Date I, Endo S, et al. **A proposal for standardized analysis of the results of microvascular decompression for trigeminal neuralgia and hemifacial spasm.** *Acta Neurochirurgica (Wien)* 2012; 154:773–78
25. Landis JR, Koch GG. **The measurement of observer agreement for categorical data.** *Biometrics* 1977;33:159–74
26. Morioka T, Hashiguchi K, Samura K, et al. **Detailed anatomy of intracranial venous anomalies associated with atretic parietal cephaloceles revealed by high-resolution 3D-CISS and high-field T2-weighted reversed MR images.** *Childs Nerv Syst* 2009;25:309–15

Dual Stenting Using Low-Profile LEO Baby Stents for the Endovascular Management of Challenging Intracranial Aneurysms

I. Akmangit, K. Aydin, S. Sencer, O.M. Topcuoglu, E.D. Topcuoglu, E. Daglioglu, M. Barburuglu, and A. Arat



ABSTRACT

BACKGROUND AND PURPOSE: Endovascular treatment of wide-neck, complex, and distally located cerebral aneurysms is a challenging issue. This study evaluated the safety and efficacy of dual stent placement by using a low-profile stent system (LEO Baby) for the treatment of challenging distal intracranial aneurysms.

MATERIALS AND METHODS: We retrospectively reviewed patients in whom at least 1 LEO Baby stent was used in the context of dual stent placement for the treatment of intracranial aneurysms. Patients who were treated with dual stent-assisted coil embolization and telescopic implantation of LEO Baby stents were included in the study. Clinical and angiographic findings, procedural data, and follow-up are reported.

RESULTS: Twelve patients were included in this study. Three patients presented with subarachnoid hemorrhage in the subacute-chronic phase, and the remaining patients had unruptured aneurysms. Nine patients were treated by using the dual stent-assisted coiling method. X- (nonintersecting), Y- (intersecting and reversible), T-, and parallel-stent configurations were performed for the dual stent-assisted coiling procedures. Three patients were treated by using telescopic stent placement for a flow diverter–like effect. The procedures were successful in all cases. Technical complications without a significant clinical adverse event developed in 2 patients. The 3- and 6-month control MRAs and DSAs demonstrated complete occlusion of the aneurysms in all patients except 1. All patients had good clinical outcomes on follow-up (mRS \leq 1).

CONCLUSIONS: The results of this small study showed the feasibility of dual stent placement by using low-profile LEO Baby stents to treat distally located complex intracranial aneurysms.

ABBREVIATION: AcomA = anterior communicating artery

Coiling of intracranial aneurysms is safe and effective, but endovascular treatment of wide-neck and anatomically complex aneurysms remains challenging.¹ Self-expandable intracranial stents have been used in the past decade to achieve successful and durable coil embolizations of these aneurysms.²⁻⁴ The placement of a stent bridging the ostium of a wide-neck aneurysm

creates a scaffold, which prevents the protrusion or herniation of coils into the parent artery and results in denser coil packing. In addition to the mechanical effect, intracranial stents have hemodynamic and biologic effects.⁵⁻⁸ Stent deployment across the orifice of an aneurysm is thought to redirect blood flow from the sac of the aneurysm toward the distal parent artery and decrease the hemodynamic stress that contributes to thrombosis of the aneurysmal sac.⁹ Furthermore, stent-induced neointimal overgrowth leads to the healing of the neck of the aneurysm.¹⁰ On the basis of these effects, stent monotherapy has been proposed as an alternative strategy for the endovascular treatment of uncoilable and complex intracranial aneurysms.⁹⁻¹¹ The telescopic placement of self-expandable intracranial stents can adequately divert the blood flow, especially for the treatment of blisterlike aneurysms.¹²

Recently, low-profile, self-expandable, braided intracranial stents (LEO Baby [Balt, Montmorency, France] and LVIS Jr. [MicroVention, Tustin, California]) have been available for the endovascular treatment of complex and/or distal aneurysms.^{13,14}

Received June 20, 2014; accepted after revision August 3.

From the Department of Radiology (I.A., E.D., A.A.), Ankara Numune Education and Research Hospital, Ankara, Turkey; Neuroradiology Division (K.A., S.S., M.B.), Department of Radiology, Istanbul Faculty of Medicine, Istanbul University, Istanbul, Turkey; Department of Radiology (I.A., O.M.T., A.A.), School of Medicine, Hacettepe University, Ankara, Turkey; and Department of Radiology (E.D.T.), School of Medicine, Ufuk University, Ankara, Turkey.

Please address correspondence to Anil Arat, MD, Department of Radiology, School of Medicine, Hacettepe University, Sıhhiye, Ankara, Turkey; e-mail: anilarat@hotmail.com

Indicates open access to non-subscribers at www.ajnr.org

Indicates article with supplemental on-line table.

<http://dx.doi.org/10.3174/ajnr.A4106>

These low-profile intracranial stents can be deployed into arteries with diameters of <3.5 mm and delivered through microcatheters with an internal diameter of 0.0165 inches, which allows easier navigation in small-sized, delicate vessels.

A single stent may not suffice for the endovascular treatment of wide-neck and geometrically complex bifurcation aneurysms with involvement of 1 or both side branches. Endovascular treatment of these complex aneurysms often necessitates the implantation of 2 stents (ie, dual stent placement) in various configurations, such as Y-, X-, or parallel configurations.¹⁴⁻¹⁶

This retrospective study evaluated the safety and efficacy of dual stent placement by using a low-profile stent system (LEO Baby) for the treatment of challenging intracranial aneurysms.

MATERIALS AND METHODS

Patient Population

We retrospectively reviewed interventional neuroradiology case records to identify patients in whom at least 1 LEO Baby stent was used in the context of dual stent placement for the treatment of intracranial aneurysms. Dual stent placement included Y-, X-, T-, or parallel configurations and the telescopic implantation of 2 low-profile stents without coiling (ie, telescopic stent monotherapy).

Interventional Procedures

All patients received 75 mg of clopidogrel and 300 mg of aspirin daily for at least 5 days before the procedure. In all cases, clopidogrel resistance was evaluated before the procedures (VerifyNow P2Y12 assay; Accumetrics, San Diego, California) to ensure a good response to clopidogrel. All endovascular procedures were performed with the patient under general anesthesia. Systemic anticoagulation was initiated immediately after the insertion of a femoral introducer sheath with a bolus dose of 5000 IU of IV heparin. The bolus dose was followed by a slow heparin infusion to maintain an activated clotting time of 2 times above the baseline value. A 6F guiding sheath was placed in the common carotid artery or the subclavian artery at the beginning of the procedure, and a distal-access catheter (Fargomax [Balt] or Neuron 070 delivery catheter [Penumbra, Alameda, California]) was navigated through the sheath into the intracranial internal carotid artery or to the V2 segment of the vertebral artery.

Stent-Assisted Coiling. Stent-assisted coil embolization of the aneurysms was performed by using the jailing technique. Aneurysm sacs were catheterized by using an Excelsior SL-10 (Stryker Neurovascular, Fremont, California) or Headway 17 microcatheter (MicroVention/Terumo) with a soft-tip 0.014-inch microguidewire before stent deployment. A second microcatheter (Vasco 21 [Balt] for the LEO stent, Prowler Select Plus [Codman & Shurtleff Neurovascular, Raynham, Massachusetts] for the Enterprise stent [Codman & Shurtleff], Excelsior SL-10 [Stryker Neurovascular] or Headway 17 for LEO Baby stents) was navigated across the aneurysm. For Y- and T-stents, including the temporary Y, the first stent was deployed and the microcatheter was navigated through the stent over the delivery wire. The delivery wire was exchanged with a microguidewire, the second side branch was accessed by using the same microcatheter, and the second stent was deployed (for the reversible Y, it was partially deployed and retrieved later). For X- and parallel-stent place-

ment, 2 microcatheters (Excelsior SL-10 or Headway 17) were placed from the ipsilateral A1 to the ipsilateral (parallel type) or contralateral A2 segments (X type). An exchange maneuver was performed after the deployment of the first stent to replace the larger microcatheters with an Excelsior SL-10 or Headway 17 when stents other than the LEO Baby were used as the first stent.

Coiling was performed with bare platinum detachable coils after the stents were deployed across the neck of the aneurysm. The aneurysms were coil-embolized until complete occlusion was achieved or no further coils could be safely deployed within the aneurysm sac.

Telescopic Dual Stent Placement with or without Coiling. We preferred to perform a dual stent monotherapy by using the telescopic implantation of 2 low-profile LEO Baby stents to achieve flow diversion. The microcatheter was navigated across the aneurysm neck during this procedure. Two LEO Baby stents were deployed telescopically within each other at the neck of aneurysms by using the same microcatheter. In 2 patients with dissecting aneurysms, stent monotherapy was performed; in 1 patient, subtotal coiling was performed.

Follow-Up

Immediate postprocedural angiograms were obtained at the end of the embolization procedures. Patients were asked to return at 3 months for MR angiography and at 6 months for a digital subtraction angiography follow-up. Patients' neurologic statuses were evaluated at the time of follow-up imaging by using the modified Rankin Scale. Postprocedural dual antiplatelet treatment, including 75 mg/day of clopidogrel and 300 mg/day of aspirin, was continued for 6 months. Then, dual antiplatelet therapy was switched to 300 mg/day of aspirin monotherapy.

RESULTS

Twelve patients, 9 women and 3 men, were included in the study. The mean age was 55.2 years (range, 30–69 years). Three patients presented with subarachnoid hemorrhage in the subacute (1–3 weeks) phase, and the remaining patients had unruptured aneurysms. Five of the 12 aneurysms were located at the anterior communicating artery (AcomA), 2 aneurysms were located at the basilar artery, 1 aneurysm was located at the posterior inferior cerebellar artery, 1 aneurysm was located at the A1 segment of the anterior cerebral artery, and 3 aneurysms were located at the MCA bifurcation. The mean aneurysm size was 9.8 mm (range, 3–22 mm). One patient had a previous coiling (patient 9), and another patient had a previous surgical clipping (patient 6) of the target aneurysm. Data on patient characteristics and procedures are summarized in detail in the On-line Table.

The dual stent-assisted coiling procedure was performed in 9 patients. Y-stent placement was performed in 5 patients (Fig 1), 1 of whom underwent temporary Y-stent placement. T- and non-intersecting X- (Fig 2) and parallel-stent placement were performed in 4 additional patients. The patient whose AcomA aneurysm (patient 4) was treated by using the nonintersecting X-stent-assisted coiling method also had 2 additional aneurysms located on the supraclinoid segment of left internal carotid artery. A flow-diverter stent (Silk; Balt) was implanted across the neck of these ICA aneurysms in the same session with X-stent placement

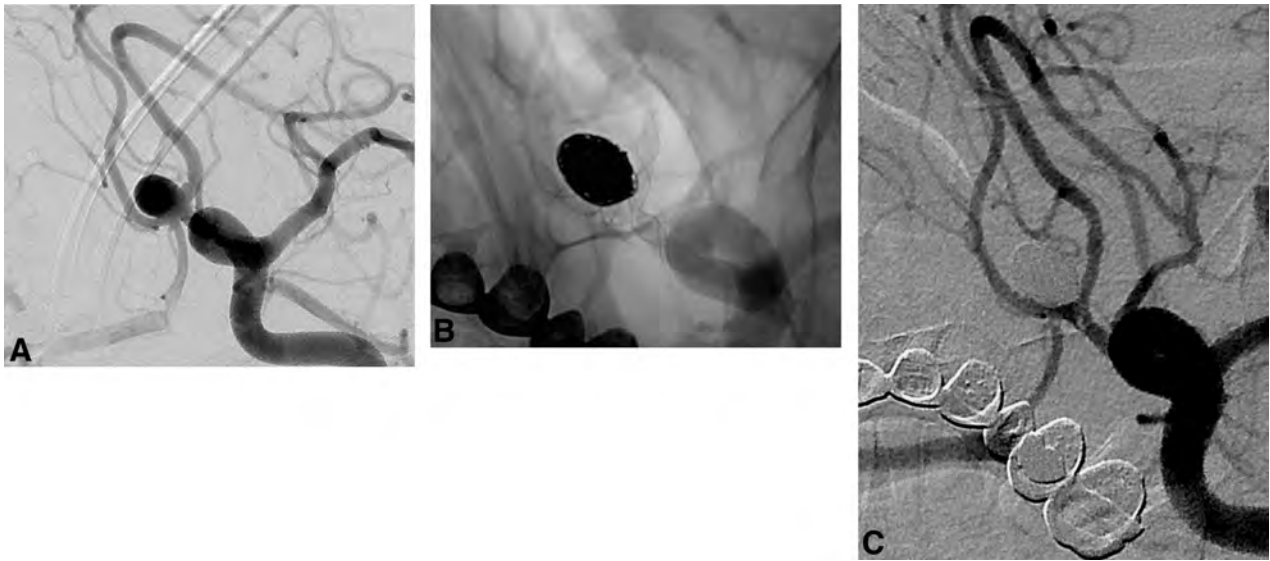


FIG 1. Procedural and follow-up DSAs of patient 3. *A*, DSA in the oblique-Waters projection revealing an 8-mm AcomA aneurysm with a wide neck extending to both A2 segments and a separate baby aneurysm at the left A1–A2 junction. *B*, The postprocedural native image from DSA shows that the aneurysm was well-embolized by stent-assisted coiling by using 2 LEO Baby stents in a Y-configuration. *C*, DSA in the 6-month angiogram shows no residual aneurysm and patent stents.

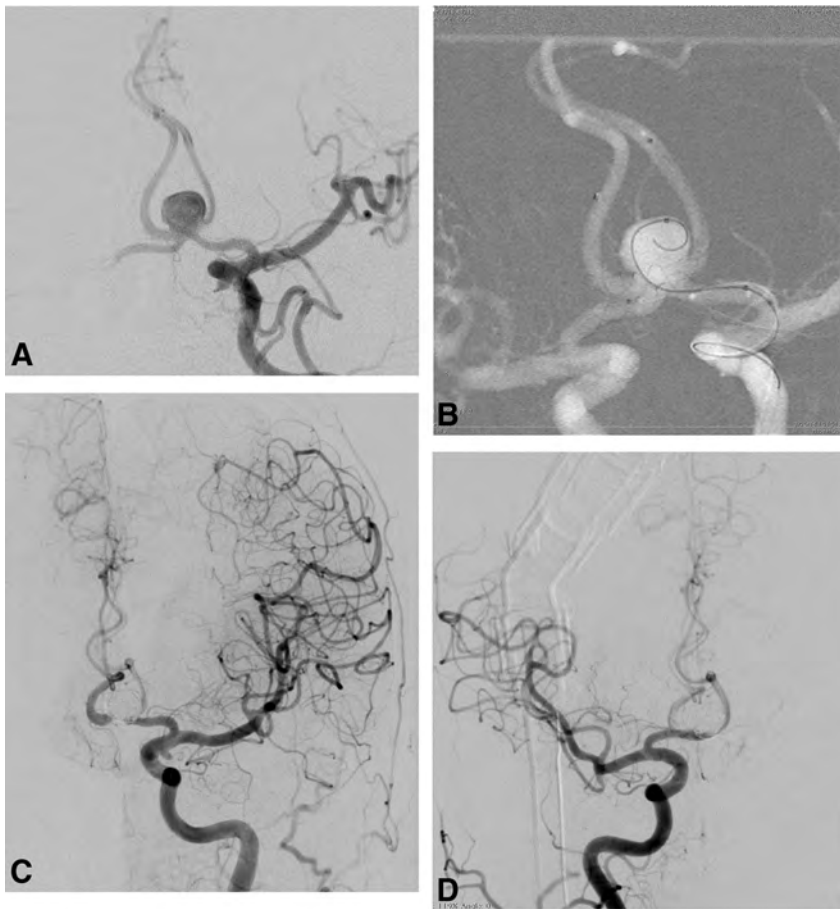


FIG 2. Procedural DSA images of patient 4. *A*, A 9-mm AcomA aneurysm with a wide neck extending to both A2 segments. *B*, A roadmap capture in the Waters projection obtained after bilateral simultaneous internal carotid artery injections. It shows nonintersecting X-stent placement and the jailed microcatheter within the aneurysm sac. *C* and *D*, The postprocedural DSA images after both left internal carotid artery injections show coiling by using 2 LEO Baby stents in an X-configuration.

(Fig 2). In 1 patient, telescopic stent placement following the partial coiling was performed in an effort to achieve flow diversion because stent-assisted coiling with a single stent was suboptimal due to recurrent microcatheter kickback from the shallow aneurysm (patient 11). Including patient 11, telescopic stent placement was performed in 3 patients (Fig 3). Only LEO Baby stents were used for dual stent placement in 8 patients. Enterprise and LEO stents were used as the first stent in 4 cases followed by the placement of LEO Baby stents. LEO Baby stents were successfully deployed in all patients except patient 7, in whom migration of the LEO Baby occurred during deployment. Immediate postprocedural DSA images demonstrated a complete or near-complete occlusion in 9 aneurysms that were treated by using dual stent-assisted coiling techniques (Fig 4). The immediate postprocedural DSA of patients who underwent telescopic stent placement, including patient 11, revealed a complete occlusion of the aneurysm in 1 patient and a stagnated filling of the neck in the 2 other patients.

Two technical complications without significant clinical adverse events were noted in this series. Stent placement with a reversed T-stent was attempted for the treatment of an MCA

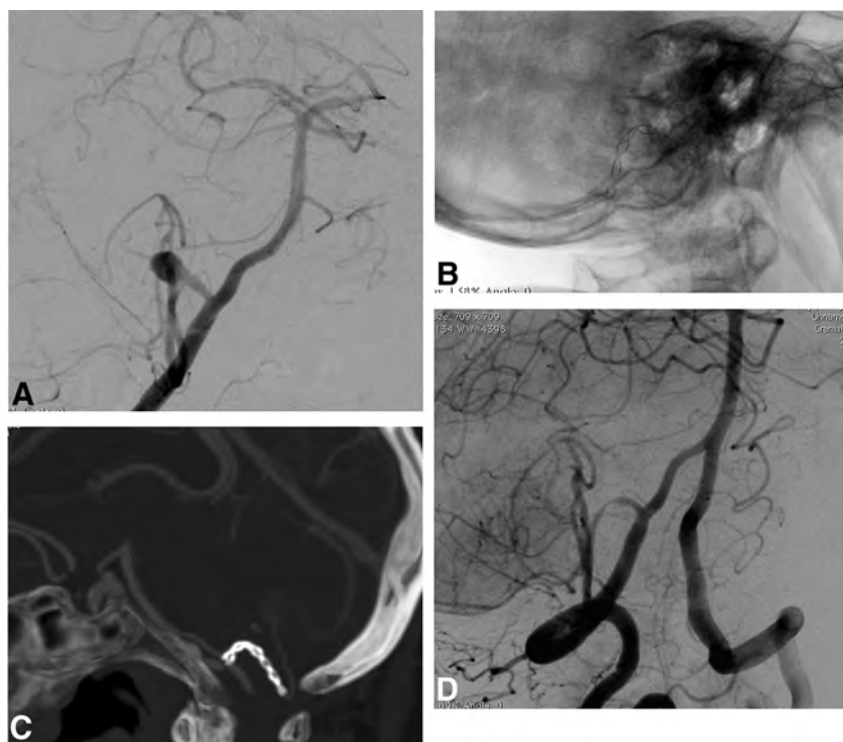


FIG 3. DSA and CT angiography images of patient 8. *A*, DSA image after the vertebral artery injection shows a 9-mm dissecting aneurysm located at the origin of the right posterior inferior cerebellar artery. *B*, Unsubtracted DSA image obtained during endovascular treatment shows 2 telescoped LEO Baby stents. *C*, Three-month follow-up CT angiogram shows the patent stents and no filling of the aneurysm. *D*, Six-month follow-up DSA image in the oblique position reveals no residual aneurysm filling and some neointimal growth within patent stents.

bifurcation aneurysm in patient 7. The first stent was deployed precisely during the procedure; the proximal tip of the stent ended exactly at the start of the superior MCA trunk, which originated from the aneurysm. However, we realized that the deployment system was stuck when we attempted to release the stent at the desired location, and the stent could not be released from the delivery wire despite being fully deployed. The stent was released from the delivery wire and migrated into the aneurysm sac following a gentle backward and forward manipulation of the wire, which was fixed to the stent. The aneurysm sac was catheterized by using the same microcatheter that was used for stent deployment, and the migrated stent was immobilized through the placement of several coils into the aneurysm sac. Two more stents in a Y-configuration were consecutively placed into the lower and upper MCA trunks to complete the coil embolization. Coiling was finalized in the usual manner without sequelae.

Temporary Y-stent placement was planned in 1 patient (patient 1) who had an MCA bifurcation aneurysm due to the high risk of a kickback of the microcatheter from the shallow aneurysm sac during coiling. A LEO Baby stent was deployed in the superior trunk of the MCA. A second LEO Baby stent was released in the inferior trunk for approximately 60% of the length of the stent with the intention of pulling it back after coiling. An instantaneous extravasation from the aneurysm was noted during the procedure, and coiling was continued with the assistance of both stents. However, the microcatheter kicked back from the

aneurysm sac. The partially opened second stent was withdrawn in response, and access to the aneurysm sac was attained with the microcatheter to complete the coiling. The patient awoke without neurologic deficits. Cerebral CT revealed that the contrast extravasation was confined to the Sylvian fissure.

Six-month follow up DSAs were available in 8 of the 12 patients. They demonstrated a stable occlusion of the aneurysms in all 8 patients. One patient (patient 7) had a 3-month follow-up DSA, which demonstrated the recurrence of the treated aneurysm. Two patients had 3-month follow-up MRAs that revealed a complete occlusion of the aneurysms in both. In 1 patient (patient 6), follow-up DSA at 6 months showed the occlusion of both A1 segments with robust retrograde opacification of the distal anterior cerebral arteries from the leptomeningeal collaterals. This patient did not reliably adhere to her antiplatelet medication regimen after discharge. The finding was incidental, and the patient did not have any neurologic signs or symptoms. We had not performed any follow-up imaging examination in 1 patient (patient 11) at the time of submission of this article. Neurologic control examinations at follow-ups revealed

good clinical outcomes in all patients (mRS scores ranged between 0 and 1).

DISCUSSION

Several endovascular techniques have been defined for the treatment of wide-neck intracranial aneurysms. Balloon-assisted coiling, stent-assisted coiling, dual or telescopic stent placement, and flow diversion by using dedicated flow diverters are the most commonly used methods for the endovascular treatment of wide-neck aneurysms. Balloon-assisted coiling is a relatively safe method, but it is associated with retreatment in the long term.^{17,18} Stent-assisted coiling addresses both the defective wall segment of the parent artery and the aneurysm sac.^{19,20} Stents may enable endovascular treatment in otherwise uncoilable aneurysms by providing a scaffold during coiling. Moreover, stents decrease aneurysm recurrence rates by altering hemodynamic effects and stimulating healing reactions.^{19,20}

Dual stent placement may be required for the endovascular treatment of some aneurysms, especially aneurysms located at the bifurcations and AcomA.²⁰⁻²³ Chow et al¹⁶ first defined stent-assisted coiling in the Y-configuration in 2004. Menendez and Harrigan¹⁵ described X-configuration stent placement, and dual stent placement is now widely used for the treatment of wide-neck complex aneurysms.²⁰⁻²³ Recently, several successful series of Y- or X-stent-assisted coiling by using low-profile stents have been

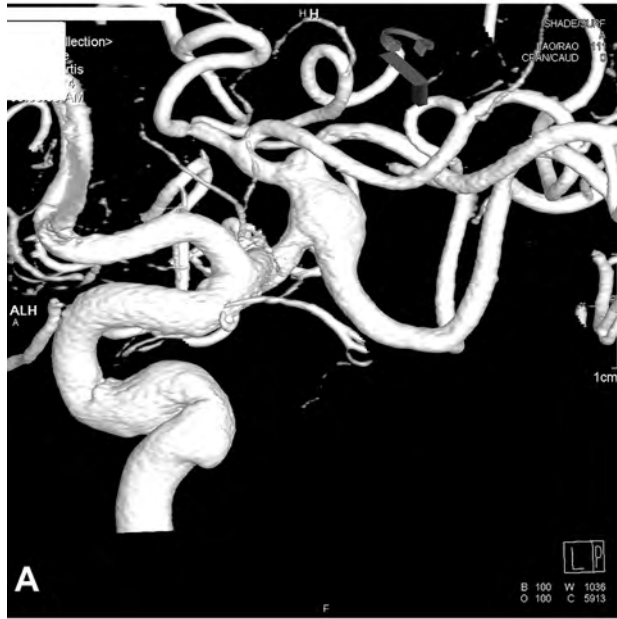


FIG 4. Procedural DSA images of patient 10. *A*, DSA image after the injection of left ICA reveals a fusiform 7-mm MCA bifurcation aneurysm extending to both MCA trunks. *B*, Roadmap-capture image in an oblique working projection shows the implantation of 2 LEO Baby stents in a T-configuration. *C*, The postprocedural DSA image in the working projection demonstrates the embolized aneurysm sac and the small residual “dog-ear” fillings at the origin of both trunks.

published.^{13,24} Möhlenbruch et al²⁴ reported 22 patients treated with LVIS Jr. stents, 9 of whom underwent dual stent placement. In another study, 11 of 34 aneurysms treated with LVIS Jr. stents underwent dual stent placement.¹³ However, only the first report provides details about the outcomes of dual stent placement by using low-profile stents, and this study suggested that these stents are safe to use in dual stent-assisted coiling. To our knowledge, there are no previous studies on dual stent placement by using the low-profile LEO Baby stent used in our series. We treated complex/distal intracranial aneurysms by using dual stent placement with the LEO Baby stent. Our case series demonstrates that favorable immediate and early follow-up angiographic results can be attained with dual stent placement by using low-profile intracranial stents that are deployed in various configurations, including telescopic stent placement for the treatment of wide-neck, complex aneurysms. We found that various dual stent placement configurations, such as Y-, nonintersecting X-, T-, and parallel-stent placement, could be successfully performed by using double LEO Baby stents or a single stent in combination with larger intracranial stents. To the best of our knowledge, there is only 1 case report of the use of LEO Baby stents for dual stent placement (nonintersecting X-stent placement) in the literature,¹⁴ and there are no reports on intersecting (ie, Y or reversible Y) or tangential dual stent placement (ie, T).

LEO Baby stents are self-expandable, low-profile stents composed of braided mesh nitinol wires. Two platinum wires enable radiographic visualization of the stent. LEO Baby stents, similar to the LVIS Jr. stents, exhibit several advantages over laser-cut stents. First, LEO Baby stents have a sliding-strut design, and this hybrid

design allows better wall apposition and scaffolding compared with open and closed cells. Second, LEO Baby stents are re-sheathable or re-positionable up to approximately 95% of their length.¹⁴ This feature is a major advantage over nonretrievable open-cell stents and Enterprise stents, which can be retrieved up to 70% of their length, and the LVIS Jr. stent, which can be withdrawn until it is 80% released.^{24,25} Finally, the LEO Baby stent fits inside microcatheters with luminal diameters of 0.0165 inches; therefore, these stents may exhibit improved navigation within arteries or through already-deployed stents. The struts of LEO Baby stents are not fixed (ie, the struts can move over each other); this feature makes room for the second stent and decreases the constraint on the second stent at the level of the stent intersection. Catheterization of the side branch through the stent is possible for the same reason. Similar to LEO stents, 2 radiopaque platinum markers of the LEO Baby stents produce linear artifacts, which would imitate an in-stent stenosis on the reconstructed MRA images.²⁶ However, the LEO Baby stents do not produce any significant artifacts outside the stent, and evaluation of residual or recurrent filling of the aneurysm is straightforward. Thus, we used contrast-enhanced MRA for 3-month follow-up imaging of our patients.

Several differences exist between the LVIS jr. stent and the LEO Baby stent. The major difference is the cell size. The LEO Baby stent has a cell size of approximately 0.9 mm, which is significantly smaller than that in the LVIS Jr. stent (1.5 mm).²⁴ We can cross the LEO Baby stent with small microcatheters (1.7F internal diameter) for Y-stentings, despite the very small cell size. However, every effort should be made to jail the microcatheter

before stent placement and to stent the harder-to-access branch first. Otherwise, the angle of entry through the attenuated stent mesh may not allow safe intra-aneurysmal or side-branch access. One advantage of this attenuated mesh is that the telescopic configuration may enhance healing by acting as a miniature flow diverter, as demonstrated in 2 of our telescopic configurations. Additionally, LEO Baby stent placement is intended for arteries as small as 1.5 mm (versus 2.0 mm), and it has been used in smaller arteries.^{14,27} The second difference is the presence of shorter flared ends in the LEO Baby stent, which potentially eases re-entry to the stent for dual stent placement once it is deployed. Finally, the LEO Baby stent is composed of 16 wires versus the 12 wires in the LVIS Jr., which increase its radial force.¹⁴ This difference may have prevented incomplete stent opening in the 20 stents deployed in this series. This adverse event occurs at a rate of 6%–7% with the LVIS Jr.^{24,25}

One technical complication, stent migration into the aneurysm after deployment, developed in 1 of our patients, but this complication did not result in any clinical consequences. Stent migration during deployment was reported by using other types of open-cell or closed-cell stents, but migration may be more of a concern with low-profile braided stents because they have a lower radial force. Not surprising, only 1 stent migration was reported in the 22 patients treated by Möhlenbruch et al.²⁴ The underlying cause for this technical complication was manipulation of the delivery wire, which was stuck in the stent. This adverse event, to the best of our knowledge, has not been reported previously by using low-profile stents. Another complication was occlusion of the parent artery without any clinical deficit at the 6-month follow-up. This patient did not adhere to the antiplatelet medication regimen after discharge. An early switch from dual antiplatelet therapy to aspirin monotherapy increases the risk of delayed thromboembolic complications in patients treated by stent-assisted coiling.²⁸ When we considered the distal locations of the aneurysms and relatively small sizes of the parent arteries in our cases, we continued the dual antiplatelet therapy for 6 months after the procedures. The newer versions of the LEO stents, including LEO Baby stents, undergo a new surface-modification procedure²⁹ to decrease thromboembolic events, but a higher risk of thromboembolic events is expected with the use of these stents in smaller stented arteries. Möhlenbruch et al.²⁴ reported that the risk of transient thromboembolic events was 14%, which is higher than normal for stents placed in large intracranial arteries. Intuitively, we anticipate a considerable thromboembolic risk for dual stent placement in small-caliber arteries and advocate heavy reliance on point-of-care testing and adenosine diphosphate/thrombin receptor agonist peptide values from the hospital laboratory to exclude patients with clopidogrel hyposensitivity.

Temporary stent placement with laser-cut intracranial stents has been described recently for ruptured aneurysms.³⁰ Our series demonstrated that this technique could be applied by using low-profile braided stents. Furthermore, this technique can also be used in unruptured aneurysms when there is a high risk of rupture or catheter kickback during dual stent placement, as shown in our series.

Our series reported successful results of telescopic dual-stent monotherapy for the treatment of 2 distally located, complex an-

eurysms. To the best of our knowledge, these patients are the first to have reports of telescopic low-profile stent implantation as stent monotherapy for the treatment of intracranial aneurysms. The aneurysms in these patients were distally located, partially thrombosed, and wide-neck. In another patient, we performed telescopic stent placement following an incomplete stent-assisted coiling to achieve complete occlusion. The placement of 2 LEO Baby stents inside one another telescopically may act as a flow diverter for distally located and/or dissecting aneurysms due to their attenuated mesh and higher wall coverage. The telescopic placement of low-profile braided stents may be an alternative to dedicated flow diverters and larger stents in parent arteries of <2 mm because these devices pass through larger and stiffer microcatheters with limited capacity during the catheterization of very distal aneurysms.

CONCLUSIONS

The short-term follow-up results of dual stent placement by using low-profile intracranial stents for the treatment of complex intracranial aneurysms in this small series are encouraging. This small study showed the feasibility of dual stent placement by using low-profile stents to treat distally located complex intracranial aneurysms. Moreover, the techniques were effective and were not associated with clinically significant adverse events.

REFERENCES

1. Molyneux A, Kerr R, Stratton I, et al. **International Subarachnoid Aneurysm Trial (ISAT) of neurosurgical clipping versus endovascular coiling in 2143 patients with ruptured intracranial aneurysms: a randomised trial.** *Lancet* 2002;360:1267–74
2. Wanke I, Doerfler A, Schoch B, et al. **Treatment of wide-necked intracranial aneurysms with a self-expanding stent system: initial clinical experience.** *AJNR Am J Neuroradiol* 2003;24:1192–99
3. Akpek S, Arat A, Morsi H, et al. **Self-expandable stent-assisted coiling of wide-necked intracranial aneurysms: a single-center experience.** *AJNR Am J Neuroradiol* 2005;26:1223–31
4. Lubicz B, Leclerc X, Levivier M, et al. **Retractable self-expandable stent for endovascular treatment of wide-necked intracranial aneurysms: preliminary experience.** *Neurosurgery* 2006;58:451–57
5. Wanke I, Forsting M. **Stents for intracranial wide-necked aneurysms: more than mechanical protection.** *Neuroradiology* 2008;50:991–98
6. Tateshima ST, Hakata Y, Tanoue SY, et al. **Alteration of intra-aneurysmal hemodynamics by placement of a self-expandable stent: laboratory investigation.** *J Neurosurg* 2009;111:22–27
7. Shobayashi Y, Tateshima S, Kakizaki R, et al. **Intra-aneurysmal hemodynamic alterations by a self-expandable intracranial stent and flow diversion stent: high intra-aneurysmal pressure remains regardless of flow velocity reduction.** *J Neurointerv Surg* 2013;5(suppl 3):iii38–42
8. Kono K, Terada T. **Hemodynamics of 8 different configurations of stenting for bifurcation aneurysms.** *AJNR Am J Neuroradiol* 2013;34:1980–86
9. Fiorella D, Albuquerque FC, Deshmukh VR, et al. **Endovascular reconstruction with the Neuroform stent as monotherapy for the treatment of uncoilable intradural pseudoaneurysms.** *Neurosurgery* 2006;59:291–99; discussion 299–300
10. Li C, Li Y, Jiang C, et al. **Stent alone treatment for dissections and dissecting aneurysms involving the basilar artery.** *J Neurointerv Surg* 2015;7:50–55
11. Bulsara KR, Kuzmik GA, Hebert R, et al. **Stenting as monotherapy for uncoilable intracranial aneurysms.** *Neurosurgery* 2013;73(1 suppl operative):ons80–85
12. Walsh KM, Moskowitz SI, Hui FK, et al. **Multiple overlapping stents**

- as monotherapy in the treatment of 'blister' pseudoaneurysms arising from the supraclinoid internal carotid artery: a single institution series and review of the literature. *J Neurointerv Surg* 2014; 6:184–94
13. Behme D, Weber A, Kowoll A, et al. **Low-profile Visualized Intraluminal Support device (LVIS Jr) as a novel tool in the treatment of wide-necked intracranial aneurysms: initial experience in 32 cases.** *J Neurointerv Surg* 2014 Apr 10. [Epub ahead of print]
 14. Cohen JE, Melamed I, Itshayek E. **X-microstenting and transmesh coiling in the management of wide-necked tent-like anterior communicating artery aneurysms.** *J Clin Neurosci* 2014;21:664–67
 15. Menendez JY, Harrigan MR. **X-configuration stent-assisted coiling.** *World Neurosurg* 2010;74:143–44
 16. Chow MM, Woo HH, Masaryk TJ, et al. **A novel endovascular treatment of a wide-necked basilar apex aneurysm by using a Y-configuration, double-stent technique.** *AJNR Am J Neuroradiol* 2004; 25:509–12
 17. Shapiro M, Babb J, Becske T, et al. **Safety and efficacy of adjunctive balloon remodeling during endovascular treatment of intracranial aneurysms: a literature review.** *AJNR Am J Neuroradiol* 2008; 29:1777–81
 18. Chalouhi N, Starke RM, Koltz MT, et al. **Stent-assisted coiling versus balloon remodeling of wide-neck aneurysms: comparison of angiographic outcomes.** *AJNR Am J Neuroradiol* 2013;34:1987–92
 19. Raymond J, Darsaut TE, Bing F, et al. **Stent-assisted coiling of bifurcation aneurysms may improve endovascular treatment: a critical evaluation in an experimental model.** *AJNR Am J Neuroradiol* 2013;34:570–76
 20. Thorell WE, Chow MM, Woo HH, et al. **Y-configured dual intracranial stent-assisted coil embolization for the treatment of wide-necked basilar tip aneurysms.** *Neurosurgery* 2005;50:1035–40
 21. Cho YD, Park SW, Lee JY, et al. **Nonoverlapping Y-configuration stenting technique with dual closed-cell stents in wide-neck basilar tip aneurysms.** *Neurosurgery* 2012;70:244–49
 22. Johnson AK, Heiferman DM, Lopes DK. **Stent-assisted embolization of 100 middle cerebral artery aneurysms.** *J Neurosurg* 2013; 118:950–55
 23. Akgul E, Aksungur E, Balli T, et al. **Y-stent assisted coil embolization of wide-neck intracranial aneurysms.** *Interv Neuroradiol* 2011; 17:36–48
 24. Möhlenbruch M, Herweh C, Behrens L, et al. **The LVIS Jr. microstent to assist coil embolization of wide-neck intracranial aneurysms: clinical study to assess safety and efficacy.** *Neuroradiology* 2014;56:389–95
 25. Poncyłjusz W, Biliński P, Safranow K, et al. **The LVIS/LVIS Jr. stents in the treatment of wide-neck intracranial aneurysms: multicentre registry.** *J Neurointerv Surg* 2014 May 14. [Epub ahead of print]
 26. Lövblad KO, Yilmaz H, Chouiter A, et al. **Intracranial aneurysm stenting: follow-up with MR angiography.** *J Magn Reson Imaging* 2006;24:418–22
 27. LEO + & LEO + Baby. Version DC015GB 2013/04 [brochure]. Mayabee Design Studio. Seoul: Balt Extrusion, 2013
 28. Hwang G, Kim JG, Song KS, et al. **Delayed ischemic stroke after stent-assisted coil placement in cerebral aneurysm: characteristics and optimal duration of preventative dual antiplatelet therapy.** *Radiology* 2014;273:194–201
 29. LEO +, next generation self-expanding intracranial stent. Version DC015GB 2010/03 [brochure]. Mayabee Design Studio. Seoul: Balt Extrusion, 2010
 30. Signorelli F, Gory B, Turjman F. **Temporary Solitaire stent-assisted coiling: a technique for the treatment of acutely ruptured wide-neck intracranial aneurysms.** *AJNR Am J Neuroradiol* 2014;35: 984–88

Visual Outcomes with Flow-Diverter Stents Covering the Ophthalmic Artery for Treatment of Internal Carotid Artery Aneurysms

A. Rouchaud, O. Leclerc, Y. Benayoun, S. Saleme, Y. Camilleri, F. D'Argento, M.-P. Boncoeur, P.-Y. Robert, and C. Mounayer



ABSTRACT

BACKGROUND AND PURPOSE: Flow-diverting stents can be used to treat intracranial aneurysms that are not amenable to treatment with coils. We analyzed ophthalmic consequences due to coverage of the origin of the ophthalmic artery by flow-diverting stents for the treatment of internal carotid artery aneurysms.

MATERIALS AND METHODS: From April 2009 to April 2013, the clinical and angiographic outcomes of all 28 patients treated for aneurysms with flow-diverting stents covering the origin of the ophthalmic artery were prospectively collected. The origin of the ophthalmic artery in relation to the target aneurysm was classified by using a 4-type classification. A complete ophthalmic examination was performed by a single ophthalmologist 48 hours before and 1 week after covering the ophthalmic artery.

RESULTS: Ophthalmic artery patency was normal at the end of endovascular treatment in 24/28 cases (85.7%). With extensive ophthalmic examinations, 11 patients (39.3%) showed new ophthalmic complications. Patients with the ophthalmic artery originating from the aneurysm sac were at high risk for retinal emboli (4/5, 80%). Patients with the ophthalmic artery originating from the inner curve of the carotid siphon were at high risk for optic nerve ischemic atrophy (3/4, 75%).

CONCLUSIONS: This prospective study shows that covering the ophthalmic artery with a flow-diverting stent is not without potential complications. Ophthalmic complications can occur but are often not diagnosed. The anatomic disposition of the ophthalmic artery in relation to the carotid siphon and aneurysm should be clearly understood because some configurations have a higher risk. When not required, covering of the ophthalmic artery by flow-diverting stents should be avoided.

ABBREVIATIONS: FDS = flow-diverting stent; OA² = ophthalmic artery aneurysm; PED = Pipeline Embolization Device

Flow-diverting stents (FDSs) are commonly used for the endovascular reconstruction of a segmentally diseased parent vessel and treatment of large-neck intracranial aneurysms, which can be difficult to reconstruct with coils, even when used with large-cell stents.¹⁻⁶ FDSs aim to maintain normal blood flow through parent and branch vessels while disrupting flow into the aneurysm, causing thrombosis, and eventually sealing the aneurysm ostium through neointimal proliferation across the device struts.⁶⁻⁸ Good angiographic and clinical results have been achieved in small series.^{4-6,9-12}

One issue concerning intracranial aneurysm treatment by an FDS is the patency of the perforating arteries and side branches

covered by the device.¹³ FDSs are designed to provide sufficient coverage across the aneurysm neck to exclude the lesion from circulation but to be porous enough to preserve the patency of any branch vessels covered by the construct through the interstices between the device strands.¹³ The flow into the regional perforators and branch arteries is governed by different factors from those that drive flow into an aneurysm, and the patency of the perforators is maintained by a suction effect due to lower pressure in those branches.¹⁴ This has been studied with histologic evaluation of the Pipeline Embolization Device (PED; Covidien, Irvine, California) in rabbit aorta, demonstrating rounded funnel-like defects into the homogeneous sheet of neointelium on the FDS in regard to the orifices of the regional branches.¹⁵

This pressure gradient may, however, be less important in vessels that have robust competitive collateral flow.¹⁵ This is most frequently seen when constructs are built over the ophthalmic artery, which occasionally becomes occluded when covered by multiple devices.⁸ In these situations, competitive collateral flow from the external carotid artery may create a "flow equalization

Received April 14, 2014; accepted after revision August 14.

From the Departments of Interventional Neuroradiology (A.R., S.S., Y.C., M.-P.B., C.M.) and Ophthalmology (O.L., Y.B., P.-Y.R.), Centre Hospitalier et Universitaire Dupuytren, Limoges, France; and Institute of Radiology (F.D.), Policlinico Agostino Gemelli, Catholic University, Rome, Italy.

Please address correspondence to Aymeric Rouchaud, MD, Department of Interventional Neuroradiology, CHU Dupuytren, 2 Ave Martin Luther King, Limoges, France; e-mail: aymeric.rouchaud@gmail.com

<http://dx.doi.org/10.3174/ajnr.A4129>

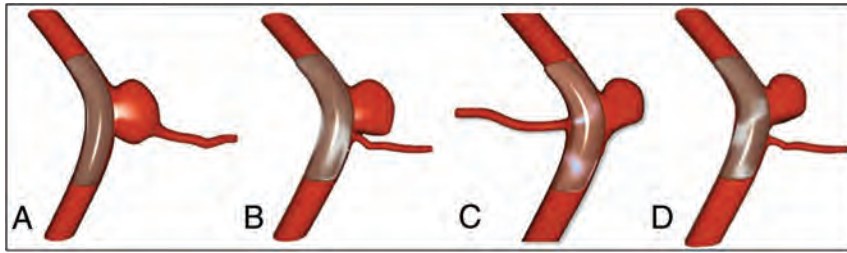


FIG 1. Classification according to the anatomy of the origin of the covered ophthalmic artery: the ophthalmic artery aneurysm classification. A, Type A: ophthalmic artery originating from the aneurysm sac. B, Type B: ophthalmic artery originating from the neck of the aneurysm. C, Type C: ophthalmic artery originating in the inner curve of the carotid siphon. D, Type D: ophthalmic artery not involved in the aneurysm but covered by the Pipeline Embolization Device.

point,” resulting in slow flow or proximal occlusion of the ophthalmic artery because of its retrograde supply from the external carotid artery circulation.^{15,16} Recently, a study evaluated the patency rate of the ophthalmic artery with standard digital subtraction angiography and any change in angiographic flow in the artery immediately after FDS placement across the arterial inlet for the treatment of 20 proximal ICA aneurysms.¹⁷ This study assessed 21% of ophthalmic artery occlusions and 11% of ophthalmic arteries with slow antegrade flow. In this small, retrospective series, no visual worsening was observed in case of flow change in the ophthalmic artery, but only 5 patients had a detailed ophthalmic examination.¹⁷ Because small visual field amputations due to ischemic lesions can be easily underdiagnosed and they are often asymptomatic, it appears mandatory to explore ophthalmic disorders with a complete examination to identify even small deficits.

In this study, we analyzed ophthalmic consequences due to coverage of the ophthalmic artery by the implantation of an FDS covering the origin of the ophthalmic artery for the treatment of terminal ICA aneurysms. This analysis focuses on the anatomy of the origin of the ophthalmic artery in relation to the target aneurysm.

MATERIALS AND METHODS

Patients

From April 2009 to April 2013, the clinical and angiographic outcomes of all patients treated at our institution for aneurysms with PEDs covering the origin of the ophthalmic artery were collected prospectively. Our institutional ethics committee approved the study. Written informed consent was obtained from each patient.

Procedures

All procedures were performed by an experienced neuroradiologist with the patient under general anesthesia, by using a triaxial approach. Accurate measurement of the parent artery was performed on 3D images, acquired with rotational angiography, with a dedicated workstation (XtraVision; Philips Healthcare, Best, the Netherlands) for vessel analysis before each procedure. The PEDs (Covidien) were deployed in the desired position to have a perfect wall apposition. Angiographic images were acquired in anteroposterior, lateral, and working projections before and immediately after treatment. To assess the wall positioning of the device, we performed a vaso-CT acquisition (Allura Xper FD20; Philips Healthcare) just after the deployment.¹⁸ In case of malpositioning, balloon remodeling was performed inside the device or a second overlaid PED was implanted.

The number of PEDs to be deployed was decided on the basis of flow reduction observed during the procedure or of anatomic circumstances. Additional coiling was performed in large aneurysms with a maximum diameter of >12 mm, by using the jailed microcatheter technique.

Periprocedural Medication

All patients were given dual antiplatelet therapy for 7 days before to 3 months after the intervention (clopidogrel, 75 mg; aspirin, 160 mg daily). Adequate platelet inhibition was verified the day

before treatment with the VerifyNow P2Y12 assay (Accumetrics, San Diego, California).

If there was resistance, the doses were increased.

During catheterization and PED placement, anticoagulation with heparin kept the activated clotting time at 2–3 times the normal value. In addition, 250 mg of aspirin was given intravenously just before PED deployment.

Imaging

MR imaging was performed to assess optic nerve compression and cerebral ischemic complications with a 3T system before and 1 day and 3 months after the procedure.

Data Collection and Image Analysis

Patient age, sex, aneurysm location and type (saccular or fusiform), the presence of previous treatment, size, rupture status at presentation, and compressive symptoms were collected. Procedural details (eg, number and size of implanted PEDs and associated coiling) were noted.

A single reader evaluated all angiograms. Aneurysm occlusion was assessed by using the O’Kelly-Marotta grading scale. The patency of the ophthalmic artery was reported as normal or slowed antegrade flow, occlusion, or retrograde filling.

Classification according to Anatomy of the Origin of the Covered Ophthalmic Artery

The origin of the ophthalmic artery correlated to the location of the aneurysm was assessed by using a 4-type ophthalmic artery aneurysm (OA²) classification as detailed in Fig 1.

Ophthalmologic Examination

A complete standardized ophthalmologic examination was performed by a single ophthalmologist 48 hours before and 1 week after covering the ophthalmic artery. At every visit, possible visual side effects of treatment (decrease of visual acuity, loss of visual field, diplopia, and ocular pain) were investigated.

A routine logarithm of the minimum angle of resolution best spectacle-corrected visual acuity assessment was performed, followed by a slit-lamp examination of the anterior segment, fluorescein staining, a dilated fundus examination, and applanation tonometry. The oculocephalic reflex and a Lancaster test searched the limitation of the extrinsic ocular motility.

Each patient underwent retinal photography and, in case of any abnormality, retinal fluorescein angiography to study retinal

Table 1: Demographics and aneurysm/procedure characteristics^a

	Overall (n = 28)	Type			
		A (n = 5)	B (n = 6)	C (n = 4)	D (n = 13)
Demographics					
Age (yr)	52 (19–81)	45 (25–73)	54 (36–79)	46 (38–66)	52 (19–81)
Men	9 (32.1)	3 (60.0)	1 (16.7)	2 (50.0)	3 (23.1)
Aneurysm					
Size (mm)	8 (3–17)	6 (3–14)	7 (6–10)	11 (5–15)	8 (4–17)
Fortuitous presentation ^b	19 (67.9)	4 (80.0)	6 (100.0)	0	9 (69.2)
Procedure					
FDS and coils	7 (25.0)	0	1 (16.7)	1 (25.0)	5 (38.5)
>1 FDS	12 (42.9)	1 (20.0)	2 (33.3)	2 (50.0)	7 (53.9)

^a Values reported are median (range) or count (percentage).

^b Other cases were recanalization or oculomotor palsy.

Table 2: Outcomes^a

	Overall (n = 28)	Type			
		A (n = 5)	B (n = 6)	C (n = 4)	D (n = 13)
Normal patency of ophthalmic artery ^b					
Immediately after procedure	24 (85.7)	5 (100)	5 (83.3)	2 (50.0)	12 (92.3)
At 3 mo	27 (96.4)	5 (100)	6 (100)	4 (100)	12 (92.3)
At 12 mo	27 (96.4)	5 (100)	6 (100)	4 (100)	12 (92.3)
Ophthalmic complications					
Retinal emboli	5 (17.9)	4 (80.0)	0	0	1 (7.7)
Optic atrophy	3 (10.7)	0	0	3 (75.0)	0
New clinical symptoms	11 (39.3)	4 (80.0)	1 (16.7)	3 (75.0)	3 (23.1)
Transient	6 (21.4)	1 (20.0)	1 (16.7)	1 (25.0)	3 (23.1)
Permanent	5 (17.9)	3 (60.0)	0	2 (50.0)	0

^a Values reported are count (percentage).

^b Other cases had occlusion or slowed blood flow.

side effects. A Topcon 50 IA camera (Topcon, Tokyo, Japan) coupled with the IMAGENet Lite (Topcon) digital imaging system was used to acquire the images. Mean retinal thickness in the central foveal area was measured by using optical coherence tomography (Stratus OCT, Version 4.0.1; Carl Zeiss Meditec, Dublin, California). To study the retinal nerve fiber layer, we scanned the optical discs of each patient by optical coherence tomography. For visual field assessment, the 24–2 central field SITA Fast program of the Humphrey 750 (Carl Zeiss Meditec) was performed.

Clinical Events

Any clinical events appearing in the postoperative course were noted. A neurologic assessment was performed before the treatment, at discharge, and at follow-up.

Angiographic Follow-Up

Angiographic images obtained immediately after endovascular treatment were compared with those obtained at each follow-up examination. Our standard angiographic follow-up protocol consisted of angiography 3–6 months after endovascular treatment and then 1 year later, by using standard projections and the working projection for PED placement.

Data Analysis

Continuous variables are expressed as median (range), and qualitative variables, as count (percentage). Baseline characteristics and outcomes are described according to the OA² classification without statistical comparisons regarding the study sample size. Data were analyzed with SAS, Version 9.3 (SAS Institute, Cary, North Carolina).

RESULTS

Patients

Twenty-eight internal carotid artery aneurysms in 28 patients (median age, 52 years; 32.1% men) were selected for treatment with the FDS covering the origin of the ophthalmic artery (Table 1). Median aneurysm size was 8 mm (range, 3–17 mm). Presentations were fortuitous in 67.9%, angiographic recurrence of previously endovascularly treated aneurysms in 17.9%, and acute oculomotor nerve palsy due to nerve compression by the aneurysm in 14.2%.

Aneurysms were treated with an FDS alone in 75% and with an FDS and coils in 25% (Table 1). In most cases (57.1%), only 1 FDS was implanted, 35.7% had 2, and 7.1% with giant aneurysms had 3 FDSs.

Anatomic configuration according to the origin of the covered ophthalmic artery was type A in 17.9%, B in 21.4%, C in 14.3%, and D in 46.4%, with no important differences among the 4 groups in terms of demographics, aneurysm characteristics, or adjunctive use of coils.

Outcomes

During endovascular treatment, 1 parenchymal embolism occurred in the territory of the right middle cerebral artery, which was treated with intra-arterial abciximab without any clinical symptoms at patient wake-up, as previously reported.¹⁹

Follow-up MR imaging, performed in all patients, showed 1 case of territorial parenchymal ischemia in the right frontal area without clinical symptoms and no case of hemorrhagic complications. There were no cases of oculomotor nerve compression due to aneurysm thrombosis, and no patients had optic nerve compression or enlargement of the aneurysm after FDS implantation.

At follow-up, there was a global aneurysm complete occlusion rate of 78.6% at 6 months, with no difference according to the OA² classification. No cases of stent thrombosis were observed, and there was no intrastent intimal hyperplasia on DSA. No patients were lost to follow-up.

Ophthalmic artery patency was normal at the end of endovascular treatment in 85.7% of patients (Table 2). We observed 1 case of ophthalmic artery occlusion in a type B anatomy just after implantation of 2 FDSs with no ophthalmic symptoms despite an exhaustive examination and with a normal antegrade flow at 3-month and 1-year follow-ups. We observed 3 cases of ophthalmic artery flow slowing just after FDS implantation. At 3-month and 1-year follow-ups, all except 1 case had a normal antegrade flow in the covered ophthalmic artery. The only case that was not angiographically normal was a stenosis at the origin of a type D ophthalmic artery.

With an extensive ophthalmic examination, 11 patients

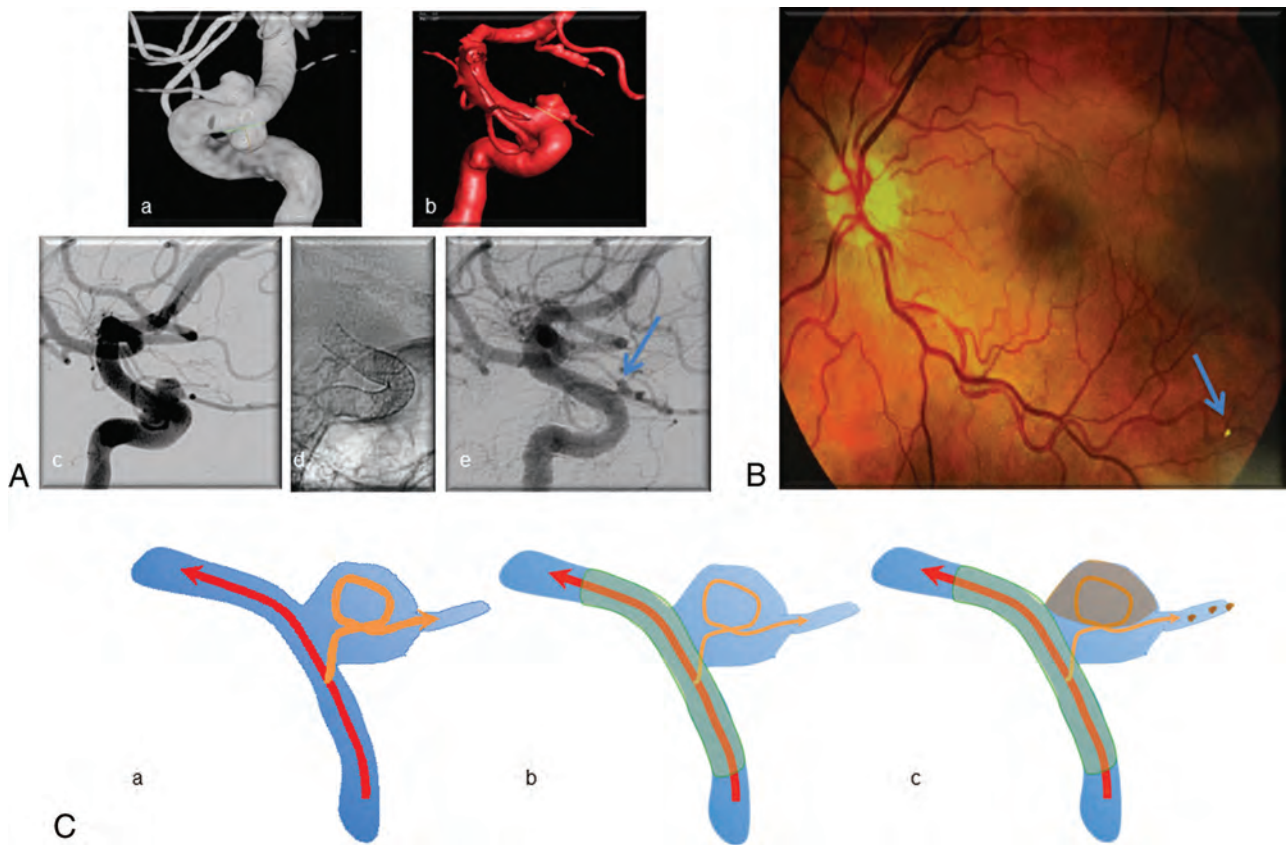


FIG 2. Illustrative case for type A. *A*, Left internal carotid artery angiograms: *a* and *b*, 3D angiograms with 2 carotid ophthalmic aneurysms with the ophthalmic artery originating from the aneurysm. *c–e*, Angiogram 3 months after flow-diverting stent implantation showing patency of the ophthalmic artery with a remnant of the upper aneurysm (arrow in *e*). *B*, Left eye funduscopy examination showing hyperattenuated embolic material in a retinal artery of the inferior retina (arrow). *C*, Explicative schema: *a*, The flow in the ophthalmic artery is turbulent due to the aneurysm. *b*, After placement of an FDS across the aneurysm neck, the turbulent flow is modified and may induce partial thrombosis of the aneurysm. *c*, The outflow channel that constitutes the ophthalmic artery may be the route for ophthalmic thromboemboli and subsequent retinal infarcts.

(39.3%) showed new ophthalmic complications: Six had visual blurring, 4 had visual field defects, and 1 had oculomotor palsy. New clinical complications were transient or asymptomatic in 6 (2 cases of visual field amputations were asymptomatic but were observed on visual field examinations). We observed 5 (17.9%) retinal emboli, all but 1 in type A anatomy, and 3 optic nerve atrophies in a type C anatomy (Table 2).

DISCUSSION

FDSs offer new opportunities for the treatment of aneurysms, extending the field of aneurysms eligible for endovascular approach and increasing long-term occlusion rates.^{1,4,15,20} They are considered effective and safe, especially before the level of the circle of Willis. Our findings support this finding because we observed only 1 case of parenchymal ischemic complication, no clinical symptoms, and 78.6% achieving complete occlusion at 6-month follow-up. However, the complications of FDSs are not well-known, and it seems important to detect them to understand their mechanisms and prevent them.

Our results show that coverage of the ophthalmic artery is not a harmless treatment because 17.9% of patients had permanent ophthalmic complications. These complications can be mild or severe, but some are only detected with a complete and extensive

ophthalmic examination, which was not performed in most previous studies.

Puffer et al¹⁷ reported that FDSs over the ophthalmic artery were clinically well-tolerated, because no patient experienced visual loss, even though 25% of the ophthalmic arteries covered with an FDS underwent ophthalmic artery occlusion with time. Some patients may have no clinical symptoms because of asymptomatic loss of the FOV, which highlights the importance of extensive ophthalmic examinations to detect retinal ischemia or subtle deficits.

The arterial flow of the ophthalmic artery, analyzed with DSA, may not be the only predictor of ophthalmic complications after coverage of the ophthalmic artery, especially because asymptomatic delayed ophthalmic artery thrombosis may be due to the development of an important collateral network.^{17,21} This mechanism is supported by several animal studies,^{8,22} suggesting that in cases of laminar flow with aspiration effect, due to a high pressure gradient in the covered side branch, the ophthalmic artery remains patent, but if the pressure gradient is low, as happens with the ophthalmic artery where an important collateral network develops, flow diversion may be increased and can result in side branch thrombosis. The aspirative flow mechanism to explain the patency of covered arteries has been described in a rabbit model

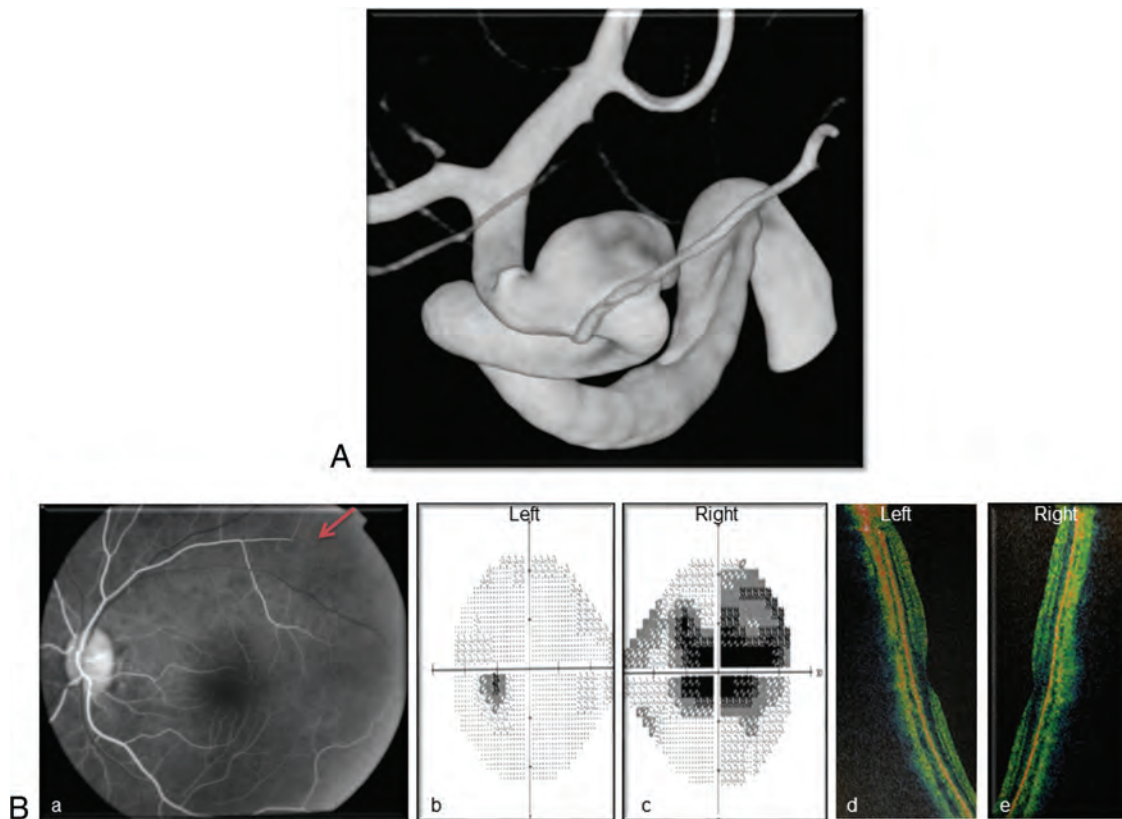


FIG 3. Illustrative case of type C. A, Right internal carotid artery 3D angiogram showing a carotid ophthalmic aneurysm with the ophthalmic artery originating from the inner curve of the ICA. B, Three-month ophthalmic examination: a, Right eye fluorescein retinal angiography showing an arterial flow defect in the upper part of the retina (arrow). b and c, Visual field assessment showing a large central scotoma in the right eye. d and e, Mean retinal thickness in the central foveal area, measured by using optical coherence tomography, proved right optic nerve atrophy (right eye, 55.03 μm ; left eye, 100.65 μm).

with coverage of the lumbar arteries; the authors reported excellent patency of small branch arteries covered by the device.¹⁵ This hypothesis, which has been confirmed in clinical practice, is that continued flow in these arteries permits ongoing patency, whereas aneurysm cavities, which lack an outflow channel, undergo thrombosis due to blood stagnation.^{8,22} It may be that this mechanism is not exactly applicable to all anatomic configurations; we therefore classified aneurysms into 4 groups according to the OA² classification (Fig 1).

In the case of an aneurysm at the origin of the covered side branches with the ophthalmic artery originating from the aneurysm sac (Fig 1A), the ophthalmic artery has turbulent flow after crossing the aneurysm rather than a rapid laminar flow. Thus, after placement of an FDS across the aneurysm neck, the turbulent flow in the aneurysm is modified and may induce partial thrombosis. Furthermore, the outflow channel that constitutes the ophthalmic artery may be the route for ophthalmic thromboemboli and subsequent retinal infarcts. Despite the small number of patients with type A aneurysms in our study ($n = 5$), we observed small retinal emboli in 80.0% of these cases. The hypothetical mechanism for this is illustrated in Fig 2. It may be that for these particular cases of a branched artery originating from the aneurysm sac, it would be necessary to restore a laminar flow in the branch with coiling before implantation of the FDS, but this strategy should be tested in animal models or with fluid computational analysis.

Another observation of this study is that patients with an ophthalmic artery originating in the inner curve of the carotid siphon (Fig 1C) have high rates of complications. This configuration only accounted for 14.3% of patients in our series, but 75.0% of them had new ophthalmic complications. Three of the 4 patients with type C anatomy presented with optic nerve atrophy, as described in Fig 3. The hypothesis to explain optic nerve atrophy is ischemia due to a drastic and rapid reduction of the blood flow in the ophthalmic artery. This could be explained by the tortuosity of the carotid siphon and the braided design of the FDS. In the inner part of a curve, the mesh attenuation of the device is higher than that in the outer curve because of tighter packing of the FDS.^{23,24} The free-cell space is consequently reduced across the origin of the ophthalmic artery, which leads to a rapid decrease of the inflow of the vessel.^{23,24} The persistency of an aspirative effect may allow patency of the ophthalmic artery, but it induces a defect of perfusion. If antegrade inflow by the ophthalmic artery decreases, its territory is taken over by the collaterals from the external carotid artery with a competitive flow through anastomosis, but this network develops with time.

In case of acute low perfusion and before any supply by collateral branches from the external carotid system, some territories vascularized by very tiny branches can be hypoperfused. This hypoperfusion might occur for the optic nerve head perfusion, which is ensured by perforators from short posterior ciliary arteries constituting the Zinn-Haller arterial ring.²⁵⁻²⁷ These territo-

ries can be injured in case of low flow after resuscitation or surgery and can cause optic nerve ischemia.^{28,29} This mechanism of acute low flow in the ophthalmic artery after implantation of an FDS with high mesh attenuation over the ophthalmic artery might explain optic nerve ischemia despite normal angiography findings. A type C aneurysm must be a concern before FDS implantation, and it appears mandatory to strictly adapt the FDS diameter to that of the carotid artery and choose an FDS of larger diameter to avoid excessive packing and reduce mesh attenuation in the inner curve.

Our study is limited by the small number of patients with each OA² classification, which lowers its power to identify differences among each type, and the study sample size is not large enough to exclude the possibility of confounding factors. However, the data of this series identify a large tendency for more ophthalmic complications (permanent or definitive) in groups A and C compared with other anatomy configurations. We did not observe an increased risk of ophthalmic complications related to the number of overlaid PEDs or in cases of associated coiling (data not shown), suggesting a real relationship between ophthalmic artery anatomy and ophthalmologic outcome, which should be confirmed in a larger population.

Furthermore, this observational study had no control group, and we did not perform detailed ophthalmic investigations in carotid-ophthalmic aneurysms treated with other devices or in the absence of coverage of the ophthalmic artery with the FDS. Nevertheless, the series of D'Urso et al³⁰ reported only 1 case of visual impairment in 126 unruptured paraclinoid aneurysms treated with coiling, suggesting that coiling (with or without associated stent) does not carry a high risk of ophthalmic complications and that the observations reported in our series could be related to coverage of the ophthalmic artery by the FDS.

Finally, the patency and flow velocity in the ophthalmic artery were estimated with angiography, which is not the most suitable tool. Further studies should analyze this flow by using Doppler sonography, before and after FDS placement, to correlate ophthalmic complications with subtle ophthalmic artery flow variations.

CONCLUSIONS

This prospective study shows that covering the ophthalmic artery with an FDS is not without potential complications. Ophthalmic complications are not rare but are usually underdiagnosed. The anatomic disposition of the ophthalmic artery regarding the carotid siphon and aneurysms should be clearly understood because some particular configurations may expose patients to a higher risk. When not required, covering the ophthalmic artery with an FDS should be avoided.

REFERENCES

1. Brinjikji W, Murad MH, Lanzino G, et al. **Endovascular treatment of intracranial aneurysms with flow diverters: a meta-analysis.** *Stroke* 2013;44:442–47
2. Fiorella D, Woo HH, Albuquerque FC, et al. **Definitive reconstruction of circumferential, fusiform intracranial aneurysms with the Pipeline embolization device.** *Neurosurgery* 2008;62:1115–20; discussion 1120–21
3. Pistocchi S, Blanc R, Bartolini B, et al. **Flow diverters at and beyond**

the level of the circle of Willis for the treatment of intracranial aneurysms. *Stroke* 2012;43:1032–38

4. Lylyk P, Miranda C, Ceratto R, et al. **Curative endovascular reconstruction of cerebral aneurysms with the Pipeline embolization device: the Buenos Aires experience.** *Neurosurgery* 2009;64:632–42; discussion 642–43
5. D'Urso PI, Lanzino G, Cloft HJ, et al. **Flow diversion for intracranial aneurysms: a review.** *Stroke* 2011;42:2363–68
6. Pierot L. **Flow diverter stents in the treatment of intracranial aneurysms: where are we?** *J Neuroradiol* 2011;38:40–46
7. Çinar C, Bozkaya H, Oran I. **Endovascular treatment of cranial aneurysms with the Pipeline flow-diverting stent: preliminary mid-term results.** *Diagn Interv Radiol* 2013;19:154–64
8. Dai D, Ding YH, Kadirvel R, et al. **Patency of branches after coverage with multiple telescoping flow-diverter devices: an in vivo study in rabbits.** *AJNR Am J Neuroradiol* 2012;33:171–74
9. Byrne JV, Beltechi R, Yarnold JA, et al. **Early experience in the treatment of intra-cranial aneurysms by endovascular flow diversion: a multicentre prospective study.** *PLoS One* 2010;5:e12492
10. Lubicz B, Collignon L, Raphaeli G, et al. **Flow-diverter stent for the endovascular treatment of intracranial aneurysms: a prospective study in 29 patients with 34 aneurysms.** *Stroke* 2010;41:2247–53
11. Leonardi M, Cirillo L, Toni F, et al. **Treatment of intracranial aneurysms using flow-diverting Silk stents (BALT): a single centre experience.** *Interv Neuroradiol* 2011;17:306–15
12. Lubicz B, Collignon L, Raphaeli G, et al. **Pipeline flow-diverter stent for endovascular treatment of intracranial aneurysms: preliminary experience in 20 patients with 27 aneurysms.** *World Neurosurg* 2011;76:114–19
13. Sadasivan C, Cesar L, Seong J, et al. **An original flow diversion device for the treatment of intracranial aneurysms: evaluation in the rabbit elastase-induced model.** *Stroke* 2009;40:952–58
14. Kulcsár Z, Ernemann U, Wetzel SG, et al. **High-profile flow diverter (Silk) implantation in the basilar artery: efficacy in the treatment of aneurysms and the role of the perforators.** *Stroke* 2010;41:1690–96
15. Fiorella D, Lylyk P, Szikora I, et al. **Curative cerebrovascular reconstruction with the Pipeline embolization device: the emergence of definitive endovascular therapy for intracranial aneurysms.** *J Neurointerv Surg* 2009;1:56–65
16. Albuquerque FC. **Visual impairment after endovascular treatment: does stent placement increase the incidence?** *World Neurosurg* 2012;78:222
17. Puffer RC, Kallmes DF, Cloft HJ, et al. **Patency of the ophthalmic artery after flow diversion treatment of paraclinoid aneurysms.** *J Neurosurg* 2012;116:892–96
18. Clarençon F, Piotin M, Pistocchi S, et al. **Evaluation of stent visibility by flat panel detector CT in patients treated for intracranial aneurysms.** *Neuroradiology* 2012;54:1121–25
19. Mounayer C, Piotin M, Baldi S, et al. **Intraarterial administration of abciximab for thromboembolic events occurring during aneurysm coil placement.** *AJNR Am J Neuroradiol* 2003;24:2039–43
20. Becske T, Kallmes DF, Saatci I, et al. **Pipeline for uncoilable or failed aneurysms: results from a multicenter clinical trial.** *Radiology* 2013;267:858–68
21. Szikora I, Berentei Z, Kulcsar Z, et al. **Treatment of intracranial aneurysms by functional reconstruction of the parent artery: the Budapest experience with the Pipeline embolization device.** *AJNR Am J Neuroradiol* 2010;31:1139–47
22. Kallmes DF, Ding YH, Dai D, et al. **A second-generation, endoluminal, flow-disrupting device for treatment of saccular aneurysms.** *AJNR Am J Neuroradiol* 2009;30:1153–58
23. Makoyeva A, Bing F, Darsaut TE, et al. **The varying porosity of braided self-expanding stents and flow diverters: an experimental study.** *AJNR Am J Neuroradiol* 2013;34:596–602
24. Maimon S, Gonen L, Nossek E, et al. **Treatment of intra-cranial aneurysms with the Silk flow diverter: 2 years' experience with 28 patients at a single center.** *Acta Neurochir (Wien)* 2012;154:979–87

25. Hayreh SS. **The 1994 Von Sallman Lecture: the optic nerve head circulation in health and disease.** *Exp Eye Res* 1995;61:259–72
26. Ohno-Matsui K, Futagami S, Yamashita S, et al. **Zinn-Haller arterial ring observed by ICG angiography in high myopia.** *Br J Ophthalmol* 1998;82:1357–62
27. Jonas JB, Holbach L, Panda-Jonas S. **Peripapillary arterial circle of Zinn-Haller: location and spatial relationships with myopia.** *PLoS One* 2013;8:e78867
28. Wirth CD, Leitner C, Perrig M. **Bilateral posterior ischaemic optic neuropathy after severe diabetic ketoacidosis, cardiopulmonary resuscitation and respiratory failure.** *BMJ Case Rep* 2013;2013:pii: bcr2012008291
29. Kudo D, Yamamura H, Nishiuchi T, et al. **Anterior and posterior ischemic optic neuropathy related to massive fluid resuscitation after blunt trauma.** *J Trauma* 2010;68:E67–70
30. D'Urso PI, Karadeli HH, Kallmes DF, et al. **Coiling for paraclinoid aneurysms: time to make way for flow diverters?** *AJNR Am J Neuro-radiol* 2012;33:1470–74

Efficacy of Skull Plain Films in Follow-up Evaluation of Cerebral Aneurysms Treated with Detachable Coils: Quantitative Assessment of Coil Mass

S.J. Ahn, B.M. Kim, W.S. Jung, and S.H. Suh



ABSTRACT

BACKGROUND AND PURPOSE: Skull plain films of coiled aneurysms have been used in a limited role, including morphologic comparison of the coil mass. We aimed to evaluate the efficacy of skull plain films in patients treated with detachable coils by using quantitative assessment.

MATERIALS AND METHODS: In this retrospective study, 78 pairs of the initial and follow-up skull anteroposterior and lateral images were reviewed independently by 2 neuroradiologists. The largest diameter, the perpendicular diameter, and area of the coil mass were measured separately on plain film, and quantitative changes of parameters were compared between subgroups, which were determined by consensus, depending on the need for retreatment. Subgroup analysis was also performed according to aneurysm size, packing attenuation, and ruptured status.

RESULTS: On skull lateral images, mean quantitative changes of the largest diameter (0.53 ± 0.43 mm versus 1.17 ± 0.91 mm, $P < .01$), the perpendicular diameter (0.56 ± 0.48 mm versus 1.20 ± 1.05 mm, $P < .01$), and the area of the coil mass (5.21 ± 7.51 mm² versus 10.55 ± 10.93 mm², $P < .02$) differed significantly between subgroups. Receiver operating characteristic analysis showed quantitative change of the largest diameter (>1.1 mm; sensitivity, 50.0%; specificity, 90.3%), the perpendicular diameter ($>.9$ mm; sensitivity, 62.5%; specificity, 85.5%), and the area (>8.5 mm²; sensitivity, 50.0%; specificity, 83.9%) on skull lateral films to be indicative of aneurysm recurrence, and the diagnostic accuracy of these parameters increased significantly in the high-packing-attenuation group.

CONCLUSIONS: Quantitative measurement of the coil mass by using skull plain lateral images has the potential to predict aneurysm recurrence in follow-up evaluations of intracranial aneurysms with coiling.

ABBREVIATIONS: A_{AP} = area on the anteroposterior view; A_{Lat} = area on the lateral view; AP = anteroposterior; L_{AP} = largest diameter of coil mass on the anteroposterior view; L_{Lat} = largest diameter on the lateral view; P_{AP} = diameter perpendicular to the L_{AP} ; P_{Lat} = diameter perpendicular to the L_{Lat}

Endovascular treatment with detachable coils has proved to be a safe and effective technique for patients with intracranial aneurysm.^{1,2} However, the major drawback is that 14%~33% of coiled aneurysms may be recanalized due to coil compaction, which will need retreatment.³⁻⁵

Therefore, follow-up imaging is essential for patients with coiled aneurysms. While DSA is still a criterion standard, MRA is becoming an alternative in follow-up imaging of coiled aneu-

rysms.^{6,7} However, these imaging studies have some disadvantages in reality.⁸⁻¹³

In contrast, skull plain films have been conventional imaging tools because they are simple, inexpensive, less invasive, and applicable to every patient under any circumstances. However, the efficacy of skull plain films has been infrequently reported in the follow-up imaging of coiled aneurysms,¹⁴⁻¹⁶ in which the detailed methods used for analysis were obscure and their reliability questionable.

We aimed to evaluate the efficacy of skull plain films as follow-up imaging tools of coiled aneurysms by using quantitative assessment and to compare the subgroups by clinical parameters.

MATERIALS AND METHODS

Patients

Our institutional review board did not require its approval or informed consent for this retrospective study. Seventy patients (18 men, 52 women; age range, 33–75 years; mean age, 53 years)

Received May 8, 2014; accepted after revision August 13.

From the Department of Radiology (S.J.A., W.S.J., S.H.S.), Gangnam Severance Hospital; Department of Radiology (B.M.K.); and Severance Institute of Vascular and Metabolic Research (S.H.S.), Yonsei University College of Medicine, Seoul, Korea.

This work was supported by a faculty research grant of Yonsei University College of Medicine for 2013 (6-2013-0051).

Please address correspondence to Sang Hyun Suh, MD, Department of Radiology, Gangnam Severance Hospital, Yonsei University, College of Medicine, 211 Eonju-ro, Gangnam-gu, Seoul 135-720, Korea; e-mail: SUHSH11@yuhs.ac

<http://dx.doi.org/10.3174/ajnr.A4121>

with 78 aneurysms (62 unruptured) from the institutional data base of 312 patients treated with detachable coils from 2005 to 2013 were enrolled in this study.

All treated aneurysms were the saccular type, neither fusiform nor dissection. The locations of aneurysms were the anterior communicating artery ($n = 3$), basilar tip ($n = 14$), cavernous ICA ($n = 8$), distal ICA ($n = 46$), posterior cerebellar artery ($n = 3$), superior cerebellar artery ($n = 3$), and vertebral artery ($n = 1$). Aneurysms ranged from 2 to 13 mm, with a mean diameter of 5.3 mm. The mean angiographic follow-up period was 24 months (range, 12–71 months).

Image Acquisition

Seventy-eight paired skull plain films (156 images of skull anteroposterior [AP] and lateral views, respectively) were finally included. The initial skull plain films, including AP and lateral views, were obtained within 1 week after completion of coil embolization, and the next ones were obtained once every year during the follow-up period.

The skull plain films were obtained in digital radiography with a flat panel detector system (Digital Diagnost; Philips Healthcare, Best, Netherlands). The conventional method with the patient in a sitting position was used for skull plain films,¹⁷ in which the same focus–film distance was used with a constant 70 kV and 400 mA. The diameters and area of coil mass were measured by using a workstation for the PACS (Centricity PACS; GE Healthcare, Milwaukee, Wisconsin). The phantom study by using the radiopaque measuring ruler was performed to avoid possible measurement error from the PACS, and the measurement on the PACS was in good agreement with the ruler.

Cerebral angiographies were performed immediately after coil embolization and were repeated at 12 and 24 months after the procedures and were used to confirm the recurrence of the coiled aneurysm.

Image Analysis

The initial skull plain films were compared with the final ones obtained during the follow-up period. In cases with retreatment, the initial ones were compared with the last ones before retreatment.

Two independent radiologists (W.S.J., S.J.A.) estimated the largest diameter of the coil mass (L_{AP}) and the diameter perpendicular to the L_{AP} (P_{AP}) on the skull AP view.¹⁸ On the skull lateral view, the largest diameter (L_{Lat}) and the diameter perpendicular to the L_{Lat} (P_{Lat}) were also measured in the same way. In measuring the area of the coil mass, a region of interest was drawn manually along the border of the coil mass on the skull plain films, and the areas on skull AP (A_{AP}) and lateral views (A_{Lat}) were automatically calculated from the same image workstation (Figure). Quantitative change in each parameter was defined as the absolute difference of each parameter measured in the paired skull plain films.

The size of the aneurysm was defined as the maximal diameter of those measured in 3 planes of 3D DSA images before coiling. Packing attenuation, which was defined as the percentage of aneurysm volume filled with coil mass, was calculated by

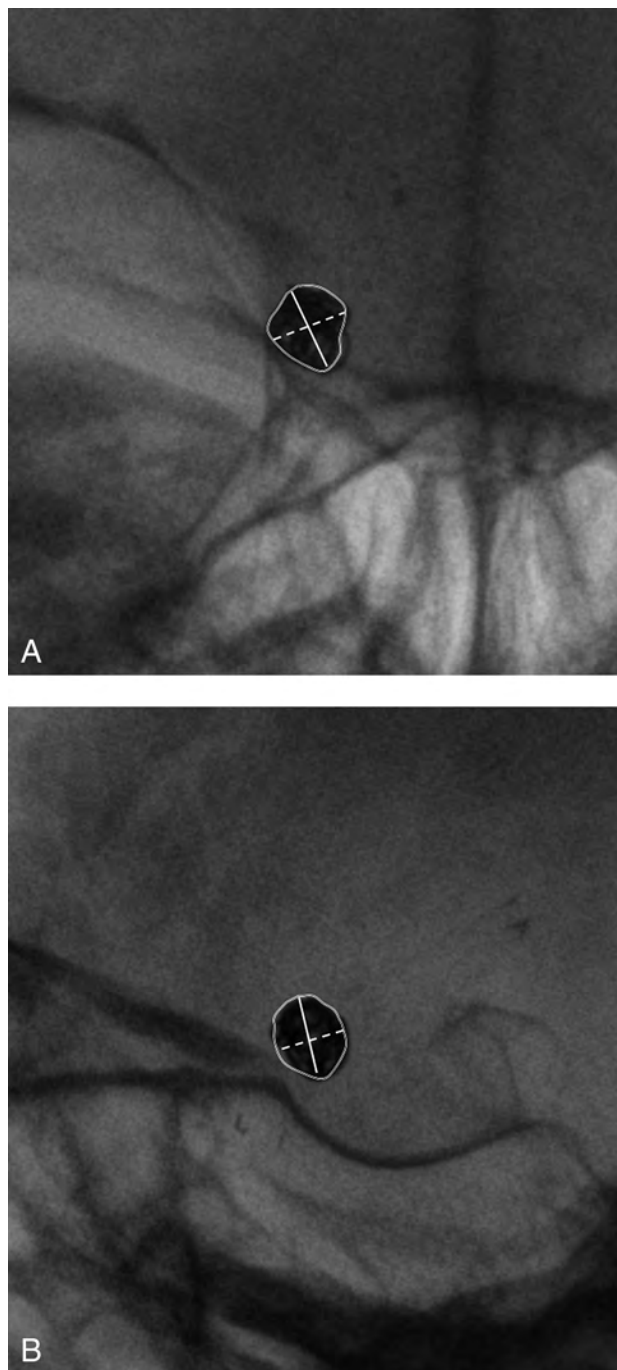


FIGURE. Quantitative measurement of a coiled aneurysm on the right distal ICA. The largest diameter, perpendicular diameter, and area of the coil mass are measured on skull AP (A) and lateral (B) views. The solid line indicates the largest diameter, and the dashed line is the perpendicular diameter. The area within the solid circle was automatically calculated.

using the software from the Web site AngioCalc (<http://www.angiocalc.com>).

Aneurysm recurrence was determined in consensus by 2 neuroradiologists (S.H.S., B.M.K.) by comparing the initial and last angiographies, and patients were divided into 2 groups: 1) Group A was defined as patients being stable or having minor morphologic changes of coiled aneurysms compared with the initial angiographies, and they did not need retreatment. On the follow-up

Table 1: Comparison of patient demographics between subgroups^a

	Group A Aneurysm (n = 62)	Group B Aneurysm (n = 16)	P Value
Sex (female)	49	6	<.01 ^b
Age (yr)	53.82 ± 8.83	52.62 ± 11.75	.65
Aneurysm size (mm)	5.10 ± 2.35	6.90 ± 1.91	<.01 ^b
Packing attenuation (%) ^c	27.35 ± 9.44 (n = 58)	24.01 ± 4.68 (n = 16)	.17
Follow-up (mo)	24.90 ± 19.95	20.43 ± 11.68	.39
Use of stent ^d	30 (48.3%)	3 (18.7%)	.06
Ruptured aneurysm ^d	11 (17.7%)	5 (31.2%)	.09
Initial angiographic result			
Complete	47 (75.8%)	11 (68.7%)	.92
Near-complete	15 (24.2%)	5 (31.3%)	.92
Incomplete	0	0	

^a Unless otherwise indicated, data are presented as mean ± SD.

^b Statistically significant ($P < .05$).

^c Packing attenuation (%) = (coil volume/aneurysm volume) × %. Seventy-four of 78 cases had the record of packing attenuation.

^d Data are presented as number of patients.

Table 2: Comparison of quantitative measurements on each skull plain film between subgroups^a

	Group A Aneurysm (n = 62)	Group B Aneurysm (n = 16)	P Value
AP image			
Differences in the largest diameter (mm)	0.54 ± 0.52	0.81 ± 0.57	.07
Differences in the perpendicular diameter (mm)	0.36 ± 0.29	0.47 ± 0.59	.30
Differences in area (mm ²)	2.82 ± 2.52	5.12 ± 9.26	.08
Lateral image			
Differences in the largest diameter (mm)	0.53 ± 0.43	1.17 ± 0.91	<.01 ^b
Differences in the perpendicular diameter (mm)	0.56 ± 0.48	1.20 ± 1.05	<.01 ^b
Differences in area (mm ²)	5.21 ± 7.51	10.55 ± 10.93	.02 ^b

^a Changes in each parameter mean the absolute difference of measurement from each skull view between the initial and follow-up periods.

^b Statistically significant ($P < .05$).

DSA, this group showed no interval change in the morphology of the coil mass. 2) Group B was defined as having major morphologic changes of the coil mass, such as significant coil compaction, contrast filling within the aneurysm sac, and coil loosening, compared with the initial treatment results. Most cases were retreated surgically or endovascularly.

Statistical Analysis

The interobserver agreement between 2 readers was evaluated by using the intraclass correlation coefficient,¹⁹ and an intraclass correlation coefficient > 0.75 was considered good agreement.²⁰

Continuous variables were presented as mean ± SD. Quantitative changes in each parameter were compared by using an unpaired *t* test between subgroups.

The diagnostic accuracy was measured by using the area under the receiver operating characteristic curves; and the area values of the largest diameter, the perpendicular diameter, and area of the coil mass were calculated in each skull plain film to predict aneurysm recurrence.

According to the aneurysm size, packing attenuation, use of stents, and the rupture status, the diagnostic accuracy of parameters was compared by using latent binomial alternative free-response receiver operating characteristic analysis. While the aneurysm size was subdivided by 5.3 mm of the reference size, the packing attenuation was classified by 24% of the aneurysm volume.⁴

Statistical analysis was performed by using commercial soft-

ware (MedCalc for Windows Version 10.1.2.0; MedCalc Software, Mariakerke, Belgium). A *P* value < .05 was considered to be statistically significant.

RESULTS

The patient demographics are summarized in Table 1, and sex and aneurysm size were significantly different between subgroups ($P < .01$).

In the skull lateral view, quantitative changes of 3 parameters (L_{Lat} , P_{Lat} , and A_{Lat}) were significantly different between subgroups ($P < .01$, $P < .01$, and $P = .02$, respectively, Table 2), but those of the skull AP view showed no significant difference.

In receiver operating characteristic analysis, the diagnostic accuracy of 3 parameters on the lateral view was higher than that on the AP view (Table 3). Among them, P_{Lat} had the highest accuracy of 0.74 with a sensitivity of 62.5%, specificity of 85.4%, positive predictive value of 45.4%, and negative predictive value of 89.2%. Only the accuracy of the L_{AP} (area under the curve value of 0.66, $P = .04$) was statistically significant in the AP view. However, there was no significant difference of diagnostic accuracy among L_{AP} , L_{Lat} , P_{Lat} , and A_{Lat} ($P > .05$).

While the diagnostic accuracy of L_{Lat} and P_{Lat} was dependent on high packing attenuation, P_{Lat} was a significant predictor in unruptured aneurysms (area under the curve value of 0.820, $P < .05$, Table 4). However, the diagnostic accuracy of both parameters was independent of aneurysm size and the use of a stent.

The interobserver agreement in all parameters was excellent between the 2 readers (intraclass correlation coefficients for L_{AP} , diameter perpendicular to L_{AP} , L_{Lat} , P_{Lat} , areas on skull AP, and A_{Lat} were 0.98, 0.99, 0.98, 0.99, 0.99, and 0.99, respectively).

DISCUSSION

In this study, all measurement parameters from skull plain lateral film achieved a feasible diagnostic performance. Quantitative changes of all parameters from the skull lateral view were significantly different between subgroups. In receiver operating characteristic analysis, 2 parameters from the lateral film may help to detect recanalization of the coiled aneurysms. The reason for this significant difference between the skull AP and lateral view is not clear, but we can extrapolate that the latter may be less affected by the following factors: 1) the direction of the aneurysm projection; 2) the aneurysm shape, such as spheric or ellipsoid; and 3) the patient position.

Few studies have shown the efficacy of skull plain films in the detection of aneurysm recurrence in patients with detachable coils.¹⁴⁻¹⁶ They focused mainly on the morphologic changes of coil mass and did not provide the quantitative information for

Table 3: Analysis of each quantitative parameter on the skull plain films for prediction of aneurysm recurrence^a

	AP Image			Lateral Image		
	L	P	A	L	P	A
AUC	0.66 (0.55~0.77)	0.50 (0.38~0.61)	0.54 (0.4~0.65)	0.69 (0.58~0.79)	0.74 (0.62~0.83)	0.66 (0.54~0.76)
Sensitivity	56.2 (29.9~80.2)	12.5 (1.9~38.4)	25.0 (7.4~52.4)	50.0 (24.7~75.3)	62.5 (35.5~84.7)	50.0 (24.7~75.3)
Specificity	79.0 (66.8~88.3)	98.4 (91.3~99.7)	90.3 (80.1~96.3)	90.3 (80.1~96.3)	85.5 (74.2~93.1)	83.9 (72.3~92.0)
Cutoff value	0.7	1.2	6.1	1.1	0.9	8.5
P value	.04 ^b	.99	.61	.01 ^b	<.01 ^b	.04 ^b

Note:—L indicates largest diameter; P, perpendicular diameter; A, area; AUC, area under the curve.

^a Data in parentheses are 95% confidence intervals.

^b Statistically significant ($P < .05$).

Table 4: Comparison of AUC values between the largest and perpendicular diameter in skull lateral films^a

Lateral Image	AUC		
	L	P	P Value ^b
Size			
<5.3 mm ($n = 38$)	0.76 (0.59~0.88) ^c	0.82 (0.66~0.92) ^c	.55
≥5.3 mm ($n = 40$)	0.77 (0.62~0.89) ^c	0.83 (0.68~0.93) ^c	.59
PD ^d			
<24% ($n = 36$)	0.61 (0.44~0.77)	0.64 (0.46~0.79)	.72
≥24% ($n = 38$)	0.79 (0.63~0.90) ^c	0.89 (0.74~0.96) ^c	.55
Stent			
(-) ($n = 45$)	0.69 (0.54~0.82) ^c	0.69 (0.53~0.82) ^c	.96
(+) ($n = 33$)	0.87 (0.71~0.96) ^c	0.88 (0.72~0.96) ^c	.80
Rupture status			
(-) ($n = 62$)	0.67 (0.53~0.78)	0.82 (0.70~0.91) ^c	.06
(+) ($n = 16$)	0.76 (0.49~0.93)	0.59 (0.32~0.83)	.21

Note:—PD indicates packing attenuation; (-), coil embolization without stent (in "Stent"), unruptured aneurysm (in "Rupture status"); (+), stent-assisted coil embolization (in "Stent"), ruptured aneurysm (in "Rupture status"); L, largest diameter; P, perpendicular diameter; AUC, area under the curve.

^a Data in parentheses are 95% confidence intervals.

^b AUC values between both diameters were compared.

^c Statistically significant ($P < .05$).

^d Seventy-four of 78 cases had the record of packing attenuation.

coiled aneurysms. Although Hwang et al¹⁶ first reported the usefulness of skull plain films in the prediction of aneurysm recurrence, they did not suggest the detailed morphologic criteria. Connor et al¹⁴ reported that morphologic changes of the coil mass showed an accuracy of 76% in the angiographic evaluation of aneurysm instability without quantitative information. In our study, P_{Lat} and L_{Lat} showed high accuracy (0.74 and 0.69) and specificity (85.5% and 90.3%) with cutoff values of 0.9 and 1.1 mm, respectively.

Several studies showed that MRA has moderate-to-high diagnostic performance for detecting recurrence of coiled aneurysms, and it is becoming an alternative diagnostic option to invasive DSA techniques.²¹⁻²³ Cottier et al¹⁵ proposed that the diagnostic performance of skull plain films was less accurate than TOF-MRA. This study also showed that P_{Lat} and L_{Lat} have relatively low sensitivities (62.5% and 50.0%, respectively), which means that these parameters might not be appropriate as screening tools. There are still controversies with regard to size variation in the coil mass,^{14,15} in which the instability of aneurysm occlusion depends mainly on thrombus in the aneurysm and healing of the arterial wall rather than the morphologic changes of coil mass.²⁴⁻²⁶ Thus, the diameter variation of the coil mass should be carefully interpreted on serial lateral films of the cranium. However, in patients with claustrophobia, anxiety disorder, or economic hardship, skull plain films may be a complement to MRA.^{10,11} Unlike MRA, the additional advantage of skull plain films is that their diagnos-

tic accuracy is not affected by the coil materials or device assistance, including stents.^{12,13}

There were some limitations in this study. First, the study design was retrospective for a small number of cases, which might not be enough to draw a conclusion in proving the efficacy of skull plain films. Second, selection bias was ineluctable in this study because only the patients with initial and second follow-up skull plain films were enrolled. Future prospective study with larger populations across multiple centers is needed.

CONCLUSIONS

Quantitative measurement of the coil mass by using skull plain lateral film has the potential to predict aneurysm recurrence in the follow-up evaluation of intracranial aneurysms with coiling. Although

a prospective study will be necessary for cost-effectiveness, skull plain films may be helpful in saving excessive medical expenses and reducing the radiation dose in patients without quantitative changes of the coiled mass by serial comparison of the skull plain films.

REFERENCES

1. Brilstra EH, Rinkel GJ, van der Graaf Y, et al. Treatment of intracranial aneurysms by embolization with coils: a systematic review. *Stroke* 1999;30:470-76
2. Molyneux A, Kerr R, Stratton I, et al. International Subarachnoid Aneurysm Trial (ISAT) of neurosurgical clipping versus endovascular coiling in 2143 patients with ruptured intracranial aneurysms: a randomised trial. *Lancet* 2002;360:1267-74
3. Sluzewski M, van Rooij WJ, Rinkel GJ, et al. Endovascular treatment of ruptured intracranial aneurysms with detachable coils: long-term clinical and serial angiographic results. *Radiology* 2003;227:720-24
4. Sluzewski M, van Rooij WJ, Slob MJ, et al. Relation between aneurysm volume, packing, and compaction in 145 cerebral aneurysms treated with coils. *Radiology* 2004;231:653-58
5. Raymond J, Guilbert F, Weill A, et al. Long-term angiographic recurrences after selective endovascular treatment of aneurysms with detachable coils. *Stroke* 2003;34:1398-403
6. Summers PE, Jarosz JM, Markus H. MR angiography in cerebrovascular disease. *Clin Radiol* 2001;56:437-56
7. Majoie CB, Sprengers ME, van Rooij WJ, et al. MR angiography at 3T

- versus digital subtraction angiography in the follow-up of intracranial aneurysms treated with detachable coils. *AJNR Am J Neuroradiol* 2005;26:1349–56
8. Hennemeyer CT, Wicklow K, Feinberg DA, et al. **In vitro evaluation of platinum Guglielmi detachable coils at 3 T with a porcine model: safety issues and artifacts.** *Radiology* 2001;219:732–37
 9. Shellock FG. **Biomedical implants and devices: assessment of magnetic field interactions with a 3.0-Tesla MR system.** *J Magn Reson Imaging* 2002;16:721–32
 10. Meléndez JC, McCrank E. **Anxiety-related reactions associated with magnetic resonance imaging examinations.** *JAMA* 1993;270:745–47
 11. Katznelson R, Djaiani GN, Minkovich L, et al. **Prevalence of claustrophobia and magnetic resonance imaging after coronary artery bypass graft surgery.** *Neuropsychiatr Dis Treat* 2008;4:487–93
 12. Lubicz B, Levivier M, Sadeghi N, et al. **Immediate intracranial aneurysm occlusion after embolization with detachable coils: a comparison between MR angiography and intra-arterial digital subtraction angiography.** *J Neuroradiol* 2007;34:190–97
 13. Takayama K, Taoka T, Nakagawa H, et al. **Usefulness of contrast-enhanced magnetic resonance angiography for follow-up of coil embolization with the Enterprise stent for cerebral aneurysms.** *J Comput Assist Tomogr* 2011;35:568–72
 14. Connor SE, West RJ, Yates DA. **The ability of plain radiography to predict intracranial aneurysm occlusion instability during follow-up of endosaccular treatment with Guglielmi detachable coils.** *Neuroradiology* 2001;43:680–86
 15. Cottier JP, Bleuzen-Couthon A, Gallas S, et al. **Follow-up of intracranial aneurysms treated with detachable coils: comparison of plain radiographs, 3D time-of-flight MRA and digital subtraction angiography.** *Neuroradiology* 2003;45:818–24
 16. Hwang GJ, Berenstein A, Niimi Y, et al. **The accuracy of plain skull x-ray examination as a predictor of recanalization following Guglielmi detachable coil embolisation in the treatment of cerebral aneurysms.** *Interv Neuroradiol* 2000;6:195–202
 17. Ballinger PW, Frank ED, Merrill V. *Merrill's Atlas of Radiographic Positions and Radiologic Procedures.* St. Louis: Elsevier Health Sciences; 2003
 18. Parlea L, Fahrig R, Holdsworth DW, et al. **An analysis of the geometry of saccular intracranial aneurysms.** *AJNR Am J Neuroradiol* 1999;20:1079–89
 19. Shrout PE, Fleiss JL. **Intraclass correlations: uses in assessing rater reliability.** *Psychol Bull* 1979;86:420–28
 20. Kim SY, Lee SS, Byun JH, et al. **Malignant hepatic tumors: short-term reproducibility of apparent diffusion coefficients with breath-hold and respiratory-triggered diffusion-weighted MR imaging.** *Radiology* 2010;255:815–23
 21. Farb RI, Nag S, Scott JN, et al. **Surveillance of intracranial aneurysms treated with detachable coils: a comparison of MRA techniques.** *Neuroradiology* 2005;47:507–15
 22. Gauvrit JY, Leclerc X, Caron S, et al. **Intracranial aneurysms treated with Guglielmi detachable coils: imaging follow-up with contrast-enhanced MR angiography.** *Stroke* 2006;37:1033–37
 23. Agid R, Willinsky RA, Lee SK, et al. **Characterization of aneurysm remnants after endovascular treatment: contrast-enhanced MR angiography versus catheter digital subtraction angiography.** *AJNR Am J Neuroradiol* 2008;29:1570–74
 24. Piotin M, Mandai S, Murphy KJ, et al. **Dense packing of cerebral aneurysms: an in vitro study with detachable platinum coils.** *AJNR Am J Neuroradiol* 2000;21:757–60
 25. Reul J, Spetzger U, Weis J, et al. **Endovascular occlusion of experimental aneurysms with detachable coils: influence of packing density and perioperative anticoagulation.** *Neurosurgery* 1997;41:1160–65, discussion 1165–68
 26. Byrne JV, Hope JK, Hubbard N, et al. **The nature of thrombosis induced by platinum and tungsten coils in saccular aneurysms.** *AJNR Am J Neuroradiol* 1997;18:29–33

Parent Artery Curvature Influences Inflow Zone Location of Unruptured Sidewall Internal Carotid Artery Aneurysms

K. Futami, H. Sano, T. Kitabayashi, K. Misaki, M. Nakada, N. Uchiyama, and F. Ueda

ABSTRACT

BACKGROUND AND PURPOSE: Future aneurysmal behaviors or treatment outcomes of cerebral aneurysms may be related to the hemodynamics around the inflow zone. Here we investigated the influence of parent artery curvature on the inflow zone location of unruptured sidewall internal carotid artery aneurysms.

MATERIALS AND METHODS: In 32 aneurysms, the inflow zone location was decided by 4D flow MR imaging, and the radius of the parent artery curvature was measured in 2D on an en face image of the section plane corresponding to the aneurysm orifice.

RESULTS: The inflow zone was on the distal neck in 10 (group 1, 31.3%), on the lateral side in 19 (group 2, 59.4%), and on the proximal neck in 3 (group 3, 9.4%) aneurysms. The radius in group 1 was significantly larger than that in group 2 (8.3 mm [4.5 mm] versus 4.5 mm [1.9 mm]; median [interquartile range]; $P < .0001$). All 7 aneurysms with a radius of >8.0 mm were in group 1. All 18 aneurysms with a radius of <6.0 mm were in group 2 or 3. In two group 3 aneurysms, the inflow zone was located in a part of the neck extending beyond the central axis of the parent artery.

CONCLUSIONS: The inflow zone locations of sidewall aneurysms can be influenced by the parent artery curvature evaluated in 2D on an en face image of the section plane corresponding to the aneurysm orifice.

ABBREVIATION: IQR = interquartile range

The hemodynamics around the inflow zone of cerebral aneurysms may be a principal cause of growth,¹⁻⁴ bleb formation resulting in rupture,^{1,2,5-8} and regrowth following clipping surgery or endovascular coiling.⁹⁻¹³ These sequelae are possibly related to the increased wall shear stress on the aneurysmal wall surrounding the inflow zone.^{2-6,14} Therefore, both identification of the exact location of the inflow zone and evaluation of the hemodynamics around this area may contribute to predicting future aneurysmal behaviors or obtaining good treatment outcomes.¹⁵ Previous studies have estimated that neck width and geometric relationship between an aneurysm and the parent artery are dominant factors in the determination of the inflow zone location.^{1,14,16-19}

4D flow MR imaging based on time-resolved 3D cine phase-contrast MR imaging techniques was recently used to evaluate the

hemodynamics of cerebral aneurysms²⁰⁻²⁴ and to identify the inflow zone of cerebral aneurysms.¹⁵ However, no previous studies have examined the correlation between the distribution of the inflow zone on the section plane corresponding to the aneurysm orifice and aneurysm morphology or the parent artery curvature in patient-specific imaging analysis, to our knowledge. Here we investigated the influence of morphologic factors or the parent artery curvature on the inflow zone location identified by using 4D flow MR imaging in unruptured sidewall ICA aneurysms.

MATERIALS AND METHODS

Materials

This study was approved by the ethics committee of Mattoh-Ishikawa Central Hospital, and written informed consent was obtained from all patients. Both conventional 3D TOF MRA and 4D flow MR imaging were performed for 41 sidewall unruptured saccular ICA aneurysms. The following 9 aneurysms were excluded from this study: 8 aneurysms that exhibited unstable and irregular streamline patterns irrelevant to the vascular shape on 4D flow MR images, possibly due to motion artifacts or limitations of spatial resolution; and 1 aneurysm with a complicated neck configuration for which the section plane corresponding to the aneurysm orifice could not be determined. Accordingly, this

Received May 21, 2014; accepted after revision August 13.

From the Department of Neurosurgery (K.F.), Mattoh-Ishikawa Central Hospital, Ishikawa, Japan; and Departments of Neurosurgery (H.S., T.K., K.M., M.N., N.U.) and Radiology (F.U.), Kanazawa University School of Medicine, Ishikawa, Japan.

Please address correspondence to Kazuya Futami, MD, Department of Neurosurgery, Mattoh-Ishikawa Central Hospital, 3-8 Kuramitsu, Hakusan, 920-8588 Ishikawa, Japan; e-mail: kfutami@mattothp.com

<http://dx.doi.org/10.3174/ajnr.A4122>

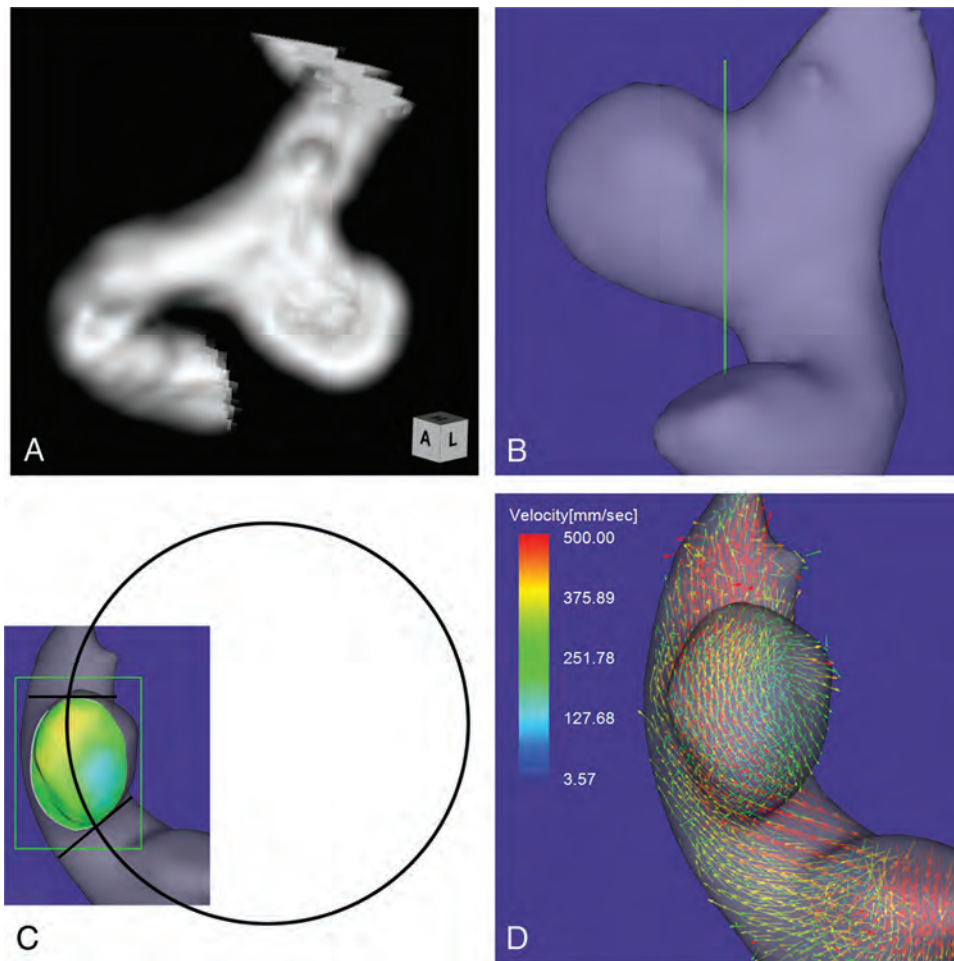


FIG 1. Case 1. A 64-year-old woman had an unruptured aneurysm at the medial C2 segment of the right ICA. *A*, 3D TOF MRA image. *B*, Image shows the section plane corresponding to the aneurysm orifice. *C*, En face image of the section plane. *A* 4D flow MR image demonstrates the inflow zone (orange) located on the distal neck and a circle in 2D fitting the central axis of the arterial part developing the aneurysm. The radius is 7.1 mm. *D*, A 4D flow MR image demonstrates a velocity vector map at peak systole.

study included 32 aneurysms (31 patients): Three were located on the cavernous segment; 3, on the paraclinoid segment; 16, on the medial C2 segment; and 10, on the bifurcation of the ICA and the posterior communicating artery. The maximum mean diameters of the aneurysms and the neck were 5.1 ± 1.7 mm (range, 2.6–10.7 mm) and 4.4 ± 1.3 mm (range, 2.1–7.8 mm), respectively.

MR Imaging

MR imaging was performed by a 1.5T MR imaging scanner (Magnetom Avanto; Siemens, Erlangen, Germany) with an 8-channel head array coil. The imaging parameters for 3D TOF MRA were as follows: TR/TE/NEX, 35/7.15 ms/average 1; flip angle, 22°; FOV, 150 × 123 mm; z-coverage, 45.6 mm; thickness, 0.6-mm; 3 slabs; 30 sections/slab; slab interval, -4.2 mm; matrix, 256 × 168 (512 × 336 with zero-filling interpolation processing); voxel size, 0.59 × 0.73 × 0.6 mm (0.295 × 0.365 × 0.6 mm with zero-filling); band width, 87 Hz/pixel; imaging time, 4 minutes 53 seconds; transaxial direction. For conventional 3D TOF MRA, vascular structures were constructed by using a volume-rendering method. The imaging parameters for 4D flow MR imaging were as follows: TR/TE/NEX, 33.05/5.63 ms/average 1; flip angle, 22°; FOV, 200 × 200 mm; 0.8-mm thickness; 1 slab; 24–26 sections/

slab; z-coverage, 19.2 mm; matrix, 192 × 192; no interpolation processing; voxel size, 1.04 × 1.04 × 0.8 mm; velocity encoding, 80 cm/s; band width, 434 Hz/pixel; parallel imaging with reduction factor, 2; imaging time, 2–30 minutes depending on each patient's heart rate; transaxial direction; retrospective gating with an electrocardiogram; 20 phases.

We used a commercially available software (Flova II, Version 2.9.5; R²tech, Hamamatsu, Japan) to visualize the vascular geometry and spatially registered blood flow. The vascular structures were segmented by using the region-growing method,²⁵ and vascular shapes were created by using the “marching cubes” method.²⁶ The 3D datasets were converted to pixel datasets at a spatial resolution of 0.5 × 0.5 × 0.5 mm. The inflow zone was defined as the orifice area where components vertical to the section plane of the inflow vectors exceeding 60% of the maximum inflow velocity at peak systole were depicted on a 4D flow MR image. Using a function of the software, we selected this 60% range to avoid both an opaque depiction on the higher range and an exceeding expansion of the inflow zone area on the lower range, because they make it difficult to classify the inflow zone location in each case. Three of the authors (K.F., M.N., and F.U.)

Aneurysm parameters: correlations between groups 1 and 2 and between group 1 and the other 2 groups^a

Parameters	Group 1 (n = 10)	Group 2 (n = 19)	Group 3 (n = 3)	P Value	
				Group 1 vs 2	Group 1 vs Others
MD	4.6 (1.7)	5.1 (2.5)	3.7 (0.5)	.491 (NS)	.714 (NS)
ND	4.3 (1.2)	4.2 (1.5)	4.0 (0.7)	.818 (NS)	.855 (NS)
MD/ND ratio	1.1 (0.1)	1.2 (0.4)	0.9 (0.0)	.383 (NS)	.745 (NS)
Maximum perpendicular height	3.4 (0.7)	4.3 (2.6)	3.4 (0.3)	.190 (NS)	.318 (NS)
Aspect ratio	1.1 (0.1)	1.2 (0.4)	0.7 (0.2)	.136 (NS)	.255 (NS)
Maximum height	3.9 (0.9)	4.4 (2.5)	3.4 (0.3)	.291 (NS)	.555 (NS)
Size ratio	1.1 (0.1)	1.4 (0.6)	0.8 (0.3)	.598 (NS)	.440 (NS)
Neck width	3.4 (0.6)	3.5 (1.5)	2.3 (0.3)	.335 (NS)	.699 (NS)
Maximum-orifice ratio	1.1 (0.3)	1.2 (0.6)	1.2 (0.2)	.568 (NS)	.502 (NS)
Width-orifice ratio	0.8 (0.2)	1.0 (0.4)	0.6 (0.3)	.215 (NS)	.350 (NS)
Radius of curvature	8.3 (4.5)	4.5 (1.9)	5.0 (0.3)	<.0001 (S)	<.0001 (S)

Note:—S indicates significant; NS, not significant by the comparison test adjusted for the P value; MD, maximum diameter; ND, neck diameter.

^aData are median (interquartile range). Units of parameters except for ratios are mm.

who have >15 years' experience in evaluating cerebral aneurysms on 3D TOF MRA images determined the window width and level of all the datasets and selected the section plane of the aneurysm orifice by consensus.

Using a function of a widely used software package (Keynote '09, Version 5.3; Apple, Cupertino, California), we drew a circle in 2D fitting the central axis of the parent artery segment that was developing the aneurysm on an en face image of the section plane corresponding to the orifice (Fig 1C). On the image, the circle to fit the midpoints of the parent artery width at both the proximal and distal ends of the aneurysm neck was selected. The radius of the curvature was measured on the image by comparison of the radius length of the circle with the length between 2 arbitrary points of which the actual length had been measured beforehand by using a function of Flova II. The radius of the curvature in this study is defined as the radius of the circle. Drawing the circle and measuring the radius were also performed on the basis of the consensus of 3 of the authors (K.F., M.N., and F.U.).

Data Analysis

According to the positional relationship to the central axis of the parent artery, we classified the locations of the inflow zones of cerebral aneurysms into the following 3 locations: distal neck, lateral side of the neck, and proximal neck. We investigated the correlation of the radius to the inflow zone location. We also compared the inflow zone location with respect to morphologic parameters, including the maximum diameters of the aneurysm and its neck, maximum perpendicular height, maximum height, aspect ratio, and aneurysm size ratio.²⁷⁻²⁹ These parameters were measured on conventional 3D TOF MRA.

Moreover, to clarify the correlation between neck size and inflow zone location, we measured the maximum orifice ratio obtained by the maximum neck diameter divided by the parent artery diameter and the width orifice ratio obtained by the maximum neck width divided by the parent artery diameter. The maximum neck width was measured on the direction perpendicular to the axis of the parent artery. Each numeric value of the various parameters was determined as the mean of the nearest 2 values independently estimated by the 3 readers.

Statistical analysis was performed by using the Mann-Whitney U test for continuous variables. P values < .05 were significant.

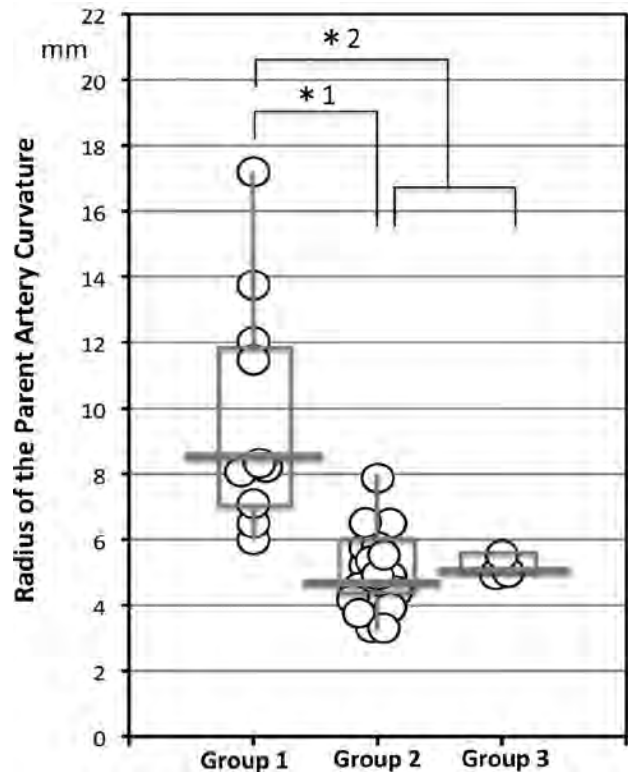


FIG 2. The distribution of the radius of the parent artery curvature measured in 2D on an en face image of the section plane corresponding to the orifice in group 1, 2, and 3 aneurysms. Group 1, 2, and 3 aneurysms have inflow zone locations on the distal neck, lateral side of the neck, and proximal neck, respectively. The radius in group 1 is significantly larger than that in group 2 (asterisk 1: 8.3 mm, median; interquartile range, 4.5 mm; versus 4.5 mm, median; IQR, 1.9 mm; $P < .0001$) or those in groups 2 and 3 (asterisk 2: 8.3 mm, median; IQR, 4.5 mm; versus 5.0 mm, median; IQR, 1.4 mm; $P < .0001$).

RESULTS

Of 32 sidewall aneurysms, 4D flow MR imaging revealed that the inflow zone location was the distal neck in 10 (group 1, 31.3%), the lateral side of the neck in 19 (group 2, 59.4%), and the proximal neck in 3 (group 3, 9.4%). Between groups 1 and 2 and between group 1 and the other 2 groups, there was no significant difference with respect to morphologic parameters, including the maximum and width orifice ratios (Table). Figure 2 shows the distribution of the radius in the aneurysms by group. The radius was 8.3 mm (median; IQR, 4.5 mm), 4.5 mm

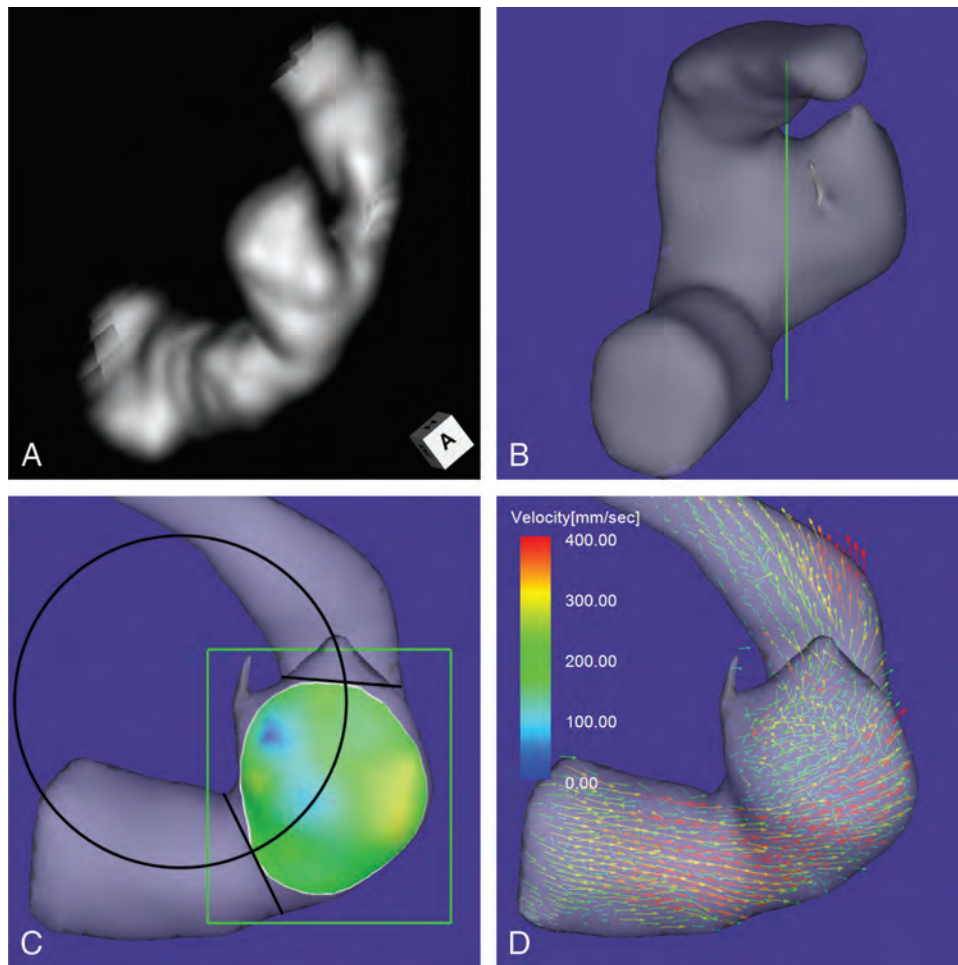


FIG 3. Case 2. An 80-year-old man had an unruptured aneurysm at the lateral C3 segment of the right ICA. *A*, A 3D TOF MRA image. *B*, Image shows the section plane corresponding to the aneurysm orifice. *C*, En face image of the section plane. A 4D flow MR image demonstrates the inflow zone (bright yellow) located on the lateral side of the neck and a circle in 2D fitting the central axis of the arterial part developing the aneurysm. The radius is 3.8 mm. *D*, A 4D flow MR image demonstrates a velocity vector map at peak systole, revealing that high-velocity vector components continue along the external side of the parent artery curvature.

(median; IQR, 1.9 mm), and 5.0 mm (median; IQR, 0.3 mm) in groups 1–3, respectively. The radius in group 1 was significantly larger than that in group 2 ($P < .0001$) and that in groups 2 and 3 (8.3 mm [median; IQR, 4.5 mm] versus 5.0 mm [median; IQR, 1.4 mm], $P < .0001$).

All 7 aneurysms with a radius of >8.0 mm were group 1 aneurysms. On the other hand, all 18 aneurysms with a radius of <6.0 mm were in group 2 or 3. In 2 of 3 group 3 aneurysms, the inflow zone was located in a part of the neck extending beyond the central axis of the parent artery.

Case Presentation

Case 1. A 64-year-old woman presented with an unruptured aneurysm at the medial C2 segment of the right ICA. Its maximum diameter and maximum neck diameter were 5.5 and 4.3 mm, respectively (Fig 1A). The inflow zone was located on the distal neck (Fig 1C). The radius was 7.1 mm. A velocity vector map at peak systole revealed that high-velocity vector components came from the internal side of the curvature of the proximal parent artery and went around the central axis of the arterial part developing the aneurysm (Fig 1D).

Case 2. An 80-year-old man presented with an unruptured aneurysm at the lateral C3 segment of the right ICA. Its maximum diameter and maximum neck diameter were 5.6 and 4.1 mm, respectively (Fig 3A). The inflow zone was located on the lateral side of the neck (Fig 3C). The radius was 3.8 mm. A velocity vector map at peak systole revealed that high-velocity vector components continued along the external side of the parent artery curvature (Fig 3D).

Case 3. A 73-year-old man presented with an unruptured aneurysm at the medial C2 segment of the right ICA. Its maximum diameter and maximum neck diameter were 4.6 and 5.0 mm, respectively (Fig 4A). The inflow zone was located in a part of the proximal neck that extended beyond the central axis of the parent artery (Fig 4C). The radius was 4.9 mm. A velocity vector map at peak systole revealed that high-velocity vector components continued along the external side of the parent artery curvature (Fig 4D).

DISCUSSION

The exact inflow zone location of sidewall aneurysms remains controversial.^{12,15,16,30-32} Previous studies have recognized that

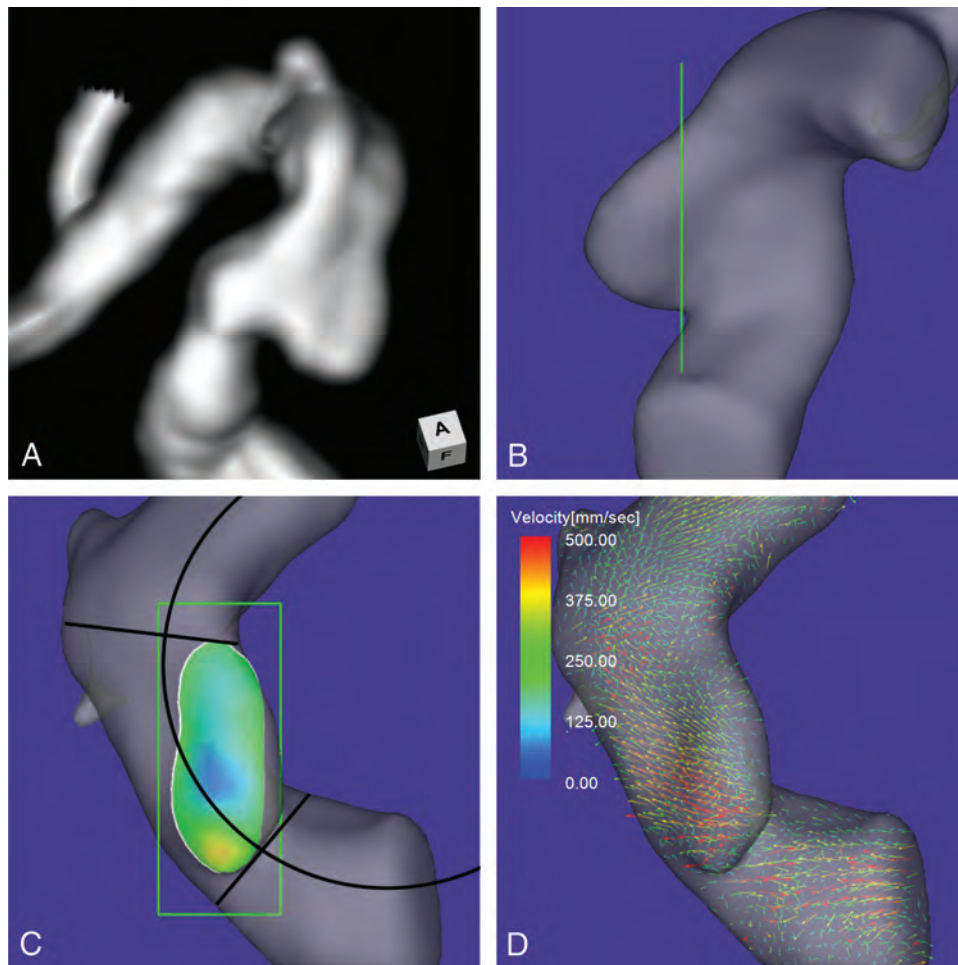


FIG 4. Case 3. A 73-year-old man had an unruptured aneurysm at the medial C2 segment of the right ICA. *A*, A 3D TOF MRA image. *B*, Image shows the section plane corresponding to the aneurysm orifice. *C*, En face image of the section plane. A 4D flow MR image demonstrates the inflow zone (orange) located in a part of the proximal neck extending beyond the central axis of the parent artery and a circle in 2D fitting the central axis of the arterial part developing the aneurysm. The radius is 4.9 mm. *D*, A 4D flow MR image demonstrates a velocity vector map at peak systole revealing that high-velocity vector components continue along the external side of the parent artery.

the inflow zone of sidewall aneurysms is consistently on the distal neck.^{30,31} In contrast, Szikora et al¹⁶ reported that the inflow zone could be on the proximal neck in most sidewall aneurysms with a wide neck. Sforza et al³² classified the locations of the inflow zones into the distal neck, side of the neck, and proximal neck by computational fluid dynamics analysis by using patient-specific models. However, they did not clarify the incidence of aneurysms in each location of the inflow zone and the factors for determining the location.³² Using 4D flow MR imaging, we recently reported that the inflow zone was not located on the distal neck in 25% of sidewall aneurysms.¹⁵ In this study, we defined the locations of the inflow zones more precisely by investigating the correlation between inflow zone location and parent artery central axis on the en face image of the section plane of the aneurysm orifice by using 4D flow MR imaging. Consequently, the inflow zone was located on the distal neck in 31.3%, the lateral side of the neck in 59.4%, and the proximal neck in 9.4% of unruptured sidewall ICA aneurysms.

Computational fluid dynamics analysis by using idealized models demonstrated that the parent artery curvature more closely influenced the inflow zone location than did aneurysm

shape or size.^{3,4,19,33-35} Imai et al¹⁹ and Sato et al³⁵ revealed that the inflow zone was on the distal neck when idealized aneurysms were located inside or outside the parent artery curvature and that the inflow zone was on the outer side of the curvature when the aneurysms were located lateral to the same curvature. Their observations indicated that the parent artery curvature evaluated in 2D on an en face image of the section plane corresponding to the aneurysm orifice may influence the inflow zone location.

In this study, the radius in group 1 (the inflow zone located on the distal neck) was significantly larger than that in group 2 (the lateral side of the neck) or in groups 2 and 3 (the proximal neck). These results indicate that the parent artery curvature on an en face image of the section plane corresponding to the aneurysm orifice influences the inflow zone locations of the sidewall aneurysms. As shown in Fig 3D, in aneurysms with a small radius, the main flow in the vessel cavity is shifted to the lateral side of the artery by the centrifugal effect, resulting in the lateral side inflow zone location in group 2 aneurysms. All 7 aneurysms with a radius of >8.0 mm of the parent artery curvature in this study were in group 1. Aneurysms with a radius of >8.0 mm on 3D TOF MRA can be determined to be on the distal neck without the need for

additional 4D flow MR imaging. These findings can help future investigators or clinicians infer the inflow zone location by using vascular curvature without having to perform flow imaging as in this study.

Szikora et al¹⁶ reported the possibility that neck size influences the inflow zone location and that in most sidewall aneurysms with a wide neck, the inflow zone could be in the proximal neck. In this study, we investigated the correlation between both the maximum and the width orifice ratios and the inflow zone location. However, there were no significant correlations. In addition, Sato et al³⁵ demonstrated that the inflow zone location was not dependent on the aneurysm shape by computational fluid dynamics analysis by using idealized models. Likewise, the morphologic parameters in this study did not influence the inflow zone location. In 2 of 3 aneurysms with an inflow zone on the proximal neck, the inflow zone was located in a part of the neck extending beyond the central axis of the parent artery. This specific neck shape and the centrifugal effect of the blood flow in the vessel may cause the inflow zone to be on the proximal neck.

This study has some limitations. 4D flow MR imaging requires an imaging time of 20–30 minutes for each patient. This relatively long time can result in motion artifacts. In addition, 4D flow MR imaging may have the limitation of spatial resolution.^{15,22} These disadvantages can cause unstable and irregular streamline patterns irrelevant to the vascular shape on 4D flow MR images. High-resolution MR imaging at >3T may decrease these artifacts.^{22,36} Here we investigated the correlation between inflow zone location and the curvature of the arterial part of developing aneurysms evaluated in 2D on an en face image of the section plane corresponding to the aneurysm orifice. However, the parent artery curvature proximal to the aneurysms can also influence the location of the main flow stream in the vessel cavity and the inflow zone.^{22,35} Further studies are needed to clarify the influence of the 3D parent artery curvature on the inflow zone location.

CONCLUSIONS

The inflow zone locations of sidewall aneurysms can be influenced by parent artery curvature evaluated in 2D on an en face image of the section plane corresponding to the aneurysm orifice. The inflow zone of all aneurysms with a radius of >8.0 mm was located on the distal neck, while that of all aneurysms with a radius of <6.0 mm was located on the lateral side of the neck or the proximal neck.

REFERENCES

1. Strother CM, Graves VB, Rappe A. **Aneurysm hemodynamics: an experimental study.** *AJNR Am J Neuroradiol* 1992;13:1089–95
2. Burleson AC, Strother CM, Turitto VT. **Computer modeling of intracranial saccular and lateral aneurysms for the study of their hemodynamics.** *Neurosurgery* 1995;37:774–82; discussion 782–84
3. Liou TM, Liou SN. **A review on *in vitro* studies of hemodynamic characteristics in terminal and lateral aneurysm models.** *Proc Natl Sci Counc Repub China B* 1999;23:133–48
4. Hoi Y, Meng H, Woodward SH, et al. **Effects of arterial geometry on aneurysm growth: three-dimensional computational fluid dynamics study.** *J Neurosurg* 2004;101:676–81
5. Liou TM, Chang WC, Liao CC. **LDV measurements in lateral**

model aneurysms of various sizes. *Experiments in Fluids* 1997; 23:317–24

6. Hassan T, Timofeev EV, Saito T, et al. **A proposed parent vessel geometry-based categorization of saccular intracranial aneurysms: computational flow dynamics analysis of the risk factors for lesion rupture.** *J Neurosurg* 2005;103:662–80
7. Cebal JR, Sheridan M, Putman CM. **Hemodynamics and bleb formation in intracranial aneurysms.** *AJNR Am J Neuroradiol* 2010;31:304–10
8. Russell JH, Kelson N, Barry M, et al. **Computational fluid dynamic analysis of intracranial aneurysmal bleb formation.** *Neurosurgery* 2013;73:1061–69
9. Gonzalez CF, Ortega HV, Moret J. **Intracranial aneurysms: flow analysis of their origin and progression.** *AJNR Am J Neuroradiol* 1992;13:181–88
10. Graves VB, Strother CM, Partington CR, et al. **Flow dynamics of lateral carotid artery aneurysms and their effects on coils and balloons: an experimental study in dogs.** *AJNR Am J Neuroradiol* 1992;13:189–96
11. Hayakawa M, Murayama Y, Duckwiler GR, et al. **Natural history of the neck remnant of a cerebral aneurysm treated with the Guglielmi detachable coil system.** *J Neurosurg* 2000;93:561–68
12. Tateshima S, Murayama Y, Villablanca JP, et al. **In vitro measurement of fluid-induced wall shear stress in unruptured cerebral aneurysms.** *Stroke* 2003;34:187–92
13. Schirmer CM, Malek AM. **Critical influence of framing coil orientation on intra-aneurysmal and neck region hemodynamics in a sidewall aneurysm model.** *Neurosurgery* 2010;67:1692–702
14. Steiger HJ, Poll A, Liepsch D, et al. **Haemodynamic stress in lateral saccular aneurysms: an experimental study.** *Acta Neurochir (Wien)* 1987;86:98–105
15. Futami K, Sano H, Misaki K, et al. **Identification of the inflow zone of unruptured cerebral aneurysms: comparison of 4D flow MRI and 3D TOF MRA data.** *AJNR Am J Neuroradiol* 2014;35:1363–70
16. Szikora I, Paal G, Ugron A, et al. **Impact of aneurysmal geometry on intra-aneurysmal flow: a computerized flow simulation study.** *Neuroradiology* 2008;50:411–21
17. Steiger HJ, Liepsch DW, Poll A, et al. **Hemodynamic stress in terminal saccular aneurysms: a laser-Doppler study.** *Heart Vessels* 1988;4:162–69
18. Castro MA, Putman CM, Cebal JR. **Computational fluid dynamics modeling of intracranial aneurysms: effects of parent artery segmentation on intra-aneurysmal hemodynamics.** *AJNR Am J Neuroradiol* 2006;27:1703–09
19. Imai Y, Sato K, Ishikawa T, et al. **Inflow into saccular cerebral aneurysms at arterial bends.** *Ann Biomed Eng* 2008;36:1489–95
20. Meckel S, Stalder AF, Santini F, et al. **In vivo visualization and analysis of 3-D hemodynamics in cerebral aneurysms with flow-sensitized 4-D MR imaging at 3 T.** *Neuroradiology* 2008;50:473–84
21. Bousset L, Rayz V, Martin A, et al. **Phase-contrast magnetic resonance imaging measurements in intracranial aneurysms in vivo of flow patterns, velocity fields, and wall shear stress: comparisons with computational fluid dynamics.** *Magn Reson Med* 2009;61:409–17
22. Isoda H, Ohkura Y, Kosugi T, et al. **Comparison of hemodynamics of intracranial aneurysms between MR fluid dynamics using 3D cine phase contrast MRI and MR-based computational fluid dynamics.** *Neuroradiology* 2010;52:913–20
23. Naito T, Miyachi S, Matsubara N, et al. **Magnetic resonance fluid dynamics for intracranial aneurysms: comparison with computed fluid dynamics.** *Acta Neurochir (Wien)* 2012;154:993–1001
24. Schnell S, Ansari SA, Vakil P, et al. **Three-dimensional hemodynamics in intracranial aneurysms: influence of size and morphology.** *J Magn Reson Imaging* 2014;39:120–31
25. Lorensen WE, Cline HE. **Marching cubes: a high resolution 3D surface construction algorithm.** *ACM Siggraph Computer Graphics* 1987;21:163–69
26. Shimai H, Yokota H, Nakamura S, et al. **Extraction from biological volume data of a region of interest with nonuniform intensity in-**

- teness. In: *Proceedings of Society of Photo-Optical Instrumentation Engineers, Optomechatronic Machine Vision*. 2005;6051:605115
27. Dhar S, Tremmel M, Mocco J, et al. **Morphological parameter for intracranial aneurysm rupture risk assessment.** *Neurosurgery* 2008;63:185–96; discussion 196–97
 28. Raghavan ML, Ma B, Harbaugh RE. **Quantified aneurysm shape and rupture risk.** *J Neurosurg* 2005;102:355–62
 29. Ujiie H, Tamano Y, Sasaki K, et al. **Is the aspect ratio a reliable index for predicting the rupture of a saccular aneurysm?** *Neurosurgery* 2001;48:495–502, discussion 502–03
 30. Hoh BL, Putman CM, Budzik RF, et al. **Combined surgical and endovascular techniques of flow alteration to treat fusiform and complex wide-necked intracranial aneurysms that are unsuitable for clipping or coil embolization.** *J Neurosurg* 2001;95:24–35
 31. Byun HS, Rhee K. **CFD modeling of blood flow following coil embolization of aneurysms.** *Med Eng Phys* 2004;26:755–61
 32. Sforza DM, Putman CM, Cebal JR. **Hemodynamics of cerebral aneurysms.** *Annu Rev Fluid Mech* 2009;41:91–107
 33. Oshima M, Torii R, Kobayashi T, et al. **Finite element simulation of blood flow in the cerebral artery.** *Computer Methods in Applied Mechanics and Engineering* 2001;191:661–71
 34. Meng H, Wang Z, Kim M, et al. **Saccular aneurysms on straight and curved vessels are subject to different hemodynamics: implications of intravascular stenting.** *AJNR Am J Neuroradiol* 2006;27:1861–65
 35. Sato K, Imai Y, Ishikawa T, et al. **The importance of parent artery geometry in intra-aneurysmal hemodynamics.** *Med Eng Phys* 2008;30:774–82
 36. Hollnagel DI, Summers PE, Poulidakos D, et al. **Comparative velocity investigations in cerebral arteries and aneurysms: 3D phase-contrast MR angiography, laser Doppler velocimetry and computational fluid dynamics.** *NMR Biomed* 2009;22:795–808

CT Angiographic Features of Symptom-Producing Plaque in Moderate-Grade Carotid Artery Stenosis

A. Gupta, E.E. Mtui, H. Baradaran, G. Salama, A. Pandya, H. Kamel, A. Giambone, and P.C. Sanelli

ABSTRACT

BACKGROUND AND PURPOSE: Emerging evidence indicates that plaque imaging can improve stroke risk stratification in patients with carotid artery atherosclerosis. We studied the association between soft and hard (calcified) plaque thickness measurements on CTA and symptomatic disease status (ipsilateral stroke or TIA) in patients with moderate-grade carotid artery stenosis.

MATERIALS AND METHODS: We measured soft-plaque and hard-plaque thickness on CTA axial source images in each carotid artery plaque in subjects with NASCET 50%–69% ICA stenosis. We used logistic regression and receiver operating characteristic analyses to assess the strength of the association between thickness measurements and prior stroke or TIA.

RESULTS: Twenty of 72 vessels studied (27.7%) had ischemic symptoms ipsilateral to the side of moderate-grade carotid stenosis. Each 1-mm increase in soft plaque resulted in a 3.7 times greater odds of a prior ipsilateral ischemic event (95% CI, 1.9–7.2). Conversely, for each 1-mm increase in hard plaque, the odds of being symptomatic decreased by approximately 80% (OR, 0.22; 95% CI, 0.10%–0.48%). Receiver operating characteristic analysis showed an area under the curve of 0.88 by using soft-plaque thickness measurements to discriminate between asymptomatic and symptomatic plaques. Sensitivity and specificity were optimized by using a maximum soft-plaque thickness of 2.2 mm, which provided a sensitivity of 85% and a specificity of 83%.

CONCLUSIONS: Simple CTA plaque-thickness measurements might differentiate symptomatic and asymptomatic moderate-grade carotid artery plaque. With further prospective validation, CTA plaque measures could function as an easily implementable tool for risk stratification in carotid artery disease.

ABBREVIATIONS: AUC = area under the curve; ROC = receiver operating characteristic

Moderate-grade carotid artery stenosis is a risk factor for stroke, with pooled analysis from randomized controlled trials, including the European Carotid Surgery Trial, NASCET, and Veterans Affairs Symptomatic Trial, suggesting that unoperated patients with moderate-grade stenosis face up to a 20% 5-year risk of stroke.¹ Data pooled from these randomized con-

trolled trials have also shown a modest stroke-risk-reduction benefit from carotid endarterectomy in patients with 50%–69% extracranial ICA stenosis.¹ However, the validity of these data has been questioned in the years since these trials were performed secondary to recent improvements in medical therapy, which have substantially reduced annual stroke rates in patients with carotid disease.^{2,3} Consequently, there has been significant recent effort to develop new imaging markers that can identify patients with carotid artery disease at highest risk for stroke beyond luminal-diameter stenosis measurements.

The 2 main pathophysiologic mechanisms underlying stroke risk in carotid artery disease are the propensity of plaque to locally embolize^{4,5} and downstream hemodynamic compromise (low flow).^{4,6,7} Although hypoperfusion and resultant slow flow from carotid disease likely play a role in a subset of strokes occurring in carotid stenosis, plaque instability causing distal embolus may be a relatively more influential etiologic factor for stroke in carotid disease in general.⁸ Although multisequence MR imaging characterization of plaque has allowed the *in vivo* discrimination of high-risk plaque tissue elements,^{9–11} its use in clinical practice has

Received June 18, 2014; accepted after revision July 14.

From the Departments of Radiology (A. Gupta, E.E.M., H.B., G.S., A.P., P.C.S.), Neurology (H.K.), and Healthcare Policy and Research (A.P., A. Giambone, P.C.S.) and Brain and Mind Research Institute (A. Gupta, H.K.), Weill Cornell Medical College, New York, New York.

Dr Gupta was supported, in part, by the Association of University Radiologists General Electric Radiology Research Academic Fellowship and the 2014–2015 Foundation of the American Society of Neuroradiology Scholar Award.

Paper previously presented in abstract form at: Annual Meeting of the American Society of Neuroradiology and the Foundation of the ASNR Symposium, May 17–22, 2014; Montreal, Quebec, Canada.

Please address correspondence to Ajay Gupta, MD, Department of Radiology, Weill Cornell Medical College 525 East 68th St, Starr 8A, Box 141, New York, NY 10065; e-mail: ajg9004@med.cornell.edu

<http://dx.doi.org/10.3174/ajnr.A4098>

been limited, given the time, expense, and challenge of performing multisequence carotid plaque MR imaging by using a dedicated carotid coil. CTA-based measurements of soft and hard (calcified) plaque determined on axial CTA source images have recently been proposed as potential simple alternative markers of vulnerable plaque in high-grade ICA stenosis.^{12,13} Because plaque volumes are relatively smaller in moderate-grade stenosis, it is unclear to what extent such techniques are capable of identifying symptom-producing plaque in this group of patients in whom optimal treatment guidelines are controversial. Therefore, we used a cross-sectional study design to assess the association between plaque thickness measurements obtained from neck CTA and previous stroke or TIA in patients with moderate-grade ICA stenosis.

MATERIALS AND METHODS

Subjects

This study was approved by the Human Subjects Institutional Review Board of our institution. We performed a retrospective study with a cross-sectional design by analyzing all CTA neck studies from our institution performed from May 2011 through March 2014. We applied the following inclusion criteria to determine our final cohort: 1) moderate-grade (50%–69%) extracranial internal carotid artery stenosis as measured on CTA neck examination; 2) adequate documentation in the electronic medical records to determine whether stroke or TIA had occurred before CTA, including review of brain MR imaging or CT; and 3) detailed medical record documentation of pre-existing vascular risk factors. We screened for eligible subjects for study inclusion if the clinical radiology report described a stenosis between 50% and 69%. We excluded nondiagnostic cases in which a NASCET-style carotid artery stenosis measurement could not be provided during the initial clinical interpretation secondary to significant motion artifacts or suboptimal contrast enhancement of the arterial vasculature.

Imaging Technique

The CTA neck examinations in this study were performed by using a standardized clinical protocol on one of several scanners at our imaging sites including LightSpeed Pro-16 or HD-750 (GE Healthcare, Milwaukee, Wisconsin). CT was performed in a helical mode with coverage extending from the aortic arch to the C1 ring. Collimation was performed at 0.625 mm, with a kV(peak) of 120, auto-milliamperes, and a rotation time of 0.5 seconds. Approximately 90 mL of nonionic iodinated contrast was administered to each patient via an 18-ga peripheral IV catheter at 4–5 mL/s by using a power injector and a SmartPrep software (GE Healthcare) region of interest on the aortic arch. In addition, maximum-intensity-projection reconstructions (8-mm thickness with 2-mm intervals) in both sagittal and coronal images were constructed as part of this protocol. To simulate clinical practice imaging conditions, we included, in our analysis, all studies with image quality sufficient to provide clinical interpretation at the time of original image acquisition.

Image Analysis

The details for CTA neck image analysis were adapted from a previously reported method.^{12,13} Briefly, a board-certified neuro-radiologist analyzed axial source images from the CTA examination and recorded 3 measurements for each carotid artery: 1)

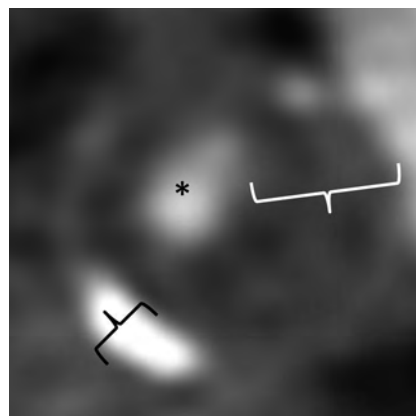


FIG 1. Representative magnified axial CTA image of the proximal internal carotid artery in a patient with predominantly soft plaque. The asterisk represents the residual patent ICA lumen. The white calipers represent maximum linear soft-plaque thickness, and black calipers represent maximum hard-plaque thickness measurements.

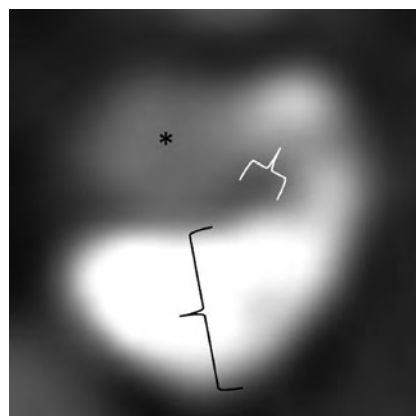


FIG 2. Representative magnified axial CTA image of the proximal internal carotid artery in a patient with predominantly calcified plaque. The asterisk represents the residual patent ICA lumen. The white calipers represent maximum linear soft-plaque thickness, and black calipers represent maximum hard-plaque thickness measurements.

NASCET stenosis measurements by using the normal distal ICA as the denominator for stenosis calculation; 2) maximum thickness of the noncalcified, soft-plaque component on the single axial section on which luminal diameter stenosis was greatest; and 3) maximum thickness of the calcified, hard-plaque component on the same single axial section on which luminal-diameter stenosis was greatest (see representative measurements in Figs 1 and 2). Plaques that were partially calcified and partially soft in attenuation had both maximum thickness measurements taken on the same single-axial section with the greatest luminal stenosis. These linear measurements were obtained by using the electronic caliper function of Centricity PACS (GE Healthcare), which allows measurements with a spatial resolution to 0.1 mm. Although the reported NASCET percentage stenosis in the existing clinical radiology report was used to screen for eligibility, all NASCET measurements used in the analysis of the included cohort were remeasured by a study investigator blinded to all clinical data to ensure strict compliance with NASCET methodology.^{14,15} These repeat study measurements were performed with care to avoid distal luminal denominator measurements in near-occlusion,

Table 1: Cohort demographics and risk-factor differences between main study groups^a

	Asymptomatic (n = 52)	Symptomatic (n = 20)	P Value
Demographic			
Age (yr)	74.1 ± 9.8	74.2 ± 11.6	.9786
Male	52% (27)	70% (14)	.1653
CT			
Stenosis	59.0 ± 3.4%	56.6 ± 6.1%	.1780
Cardiovascular risk factors			
Smoking history	62% (32)	45% (9)	.2043
Hypertension	90% (47)	80% (16)	.2327
Hyperlipidemia	73% (38)	65% (13)	.4994
Diabetes	25% (13)	20% (4)	.7640
Coronary artery disease	54% (28)	35% (7)	.1518
Atrial fibrillation	23% (12)	40% (8)	.1518
CTA imaging markers			
Max hard-plaque thickness (mm)	2.69 ± 1.04	1.19 ± 0.92	<.0001
Max soft-plaque thickness (mm)	1.41 ± 0.97	3.45 ± 1.54	<.0001
Ratio soft-/hard-plaque thickness	0.62 ± .57	2.73 ± 1.95	<.0001

Note:—Max indicates maximum.

^aMean values are shown with number of subjects shown in parentheses and SDs shown after ± signs.

which could incorrectly underestimate stenosis severity. In addition, in cases without near-occlusion, all distal luminal denominator measurements were obtained distal to the tapering carotid bulb in the segment of the extracranial ICA distal to parallel walls.

All measurements were obtained on source axial sections without additional postprocessing. We used these standard axial images instead of orthogonal reconstructions so that we could simulate routinely used clinical imaging protocols and also because excellent agreement between axial and orthogonal plaque element thickness measurements were previously found by using this technique.¹² We performed our analysis with window/level settings at approximately 800/200 with small adjustments made manually to optimize discrimination between soft and hard plaque. A second neuroradiologist with prior experience using this technique repeated thickness measurements on a subset of 20 subjects to assess measurement reproducibility.

Clinical Data Assessment

The history of ipsilateral TIA or stroke and pre-existing vascular risk factors were determined by a consensus of 2 study investigators after a detailed examination of the electronic medical record, with any disagreements in assessment resolved by consensus. All clinical data were determined blinded to CTA imaging analysis. We used American Heart Association definitions of TIA and stroke,¹⁶ with stroke and TIA defined as a permanent or transient episode, respectively, of neurologic dysfunction caused by focal brain or retinal ischemia. We classified stroke or TIA as being symptomatic disease only when events were referable to the stenotic ICA. We also recorded the days between qualifying ipsilateral ischemic events and CTA and the presence of a smoking history, diabetes (a hemoglobin A1C of >6.5% or on diabetic medication), hypertension (blood pressure of >140/90 mm Hg or on antihypertensive medication), atrial fibrillation, hyperlipidemia (LDL of >100 or on statins), and coronary artery disease.

Statistical Analysis

Multivariate logistic regression analysis was used to examine the association between each 1-mm increase in plaque-thickness measure and symptomatic disease status while adjusting for exact

stenosis percentage, sex, age, and any covariate risk factors found to be statistically significant ($P < .05$) in univariate analyses. The ratio of soft-to-hard plaque was also analyzed. Receiver operating characteristic (ROC) analyses were also performed for each CTA imaging feature (hard plaque, soft plaque, and ratio measurements), and optimum cut-offs were calculated for the plaque measurement shown to have the highest area under the curve (AUC) for the detection of symptomatic plaque. We also calculated operating characteristics of each plaque thickness measurement, including sensitivity, specificity, positive predictive value, and negative predictive value. An optimal cutoff for the plaque measurement shown to have the highest

AUC was also calculated. All statistical analyses were performed by using SAS 9.3 (SAS Institute, Cary, North Carolina).

RESULTS

Subject Characteristics

We screened 1376 patients and arrived at our final cohort of 68 subjects after excluding subjects who did not meet inclusion criteria. Four subjects with bilateral moderate-grade stenosis were included, resulting in 72 vessels eligible for analysis. Clinical indications for CTA included suspicion of an acute ischemic event in 32 subjects (47.1%), routine imaging for known carotid stenosis in 20 subjects (29.4%), work-up of abnormal findings on carotid sonography in 7 subjects (10.3%), altered mental status in 3 subjects (4.4%), neck pain in 2 subjects (2.9%), follow-up for a history of contralateral carotid endarterectomy in 2 subjects (2.9%), and follow-up for intracranial aneurysm in 2 subjects (2.9%).

Twenty of 72 vessels studied (27.7%) had ischemic symptoms ipsilateral to the side of moderate-grade carotid stenosis. Among the cerebrovascular events that had occurred, 19/20 occurred within 1 month of the CTA examination. Of the total events, 16 were ipsilateral strokes that occurred a median of 0 days before CTA (range, 0–621 days), while 4 were ipsilateral TIAs that occurred a median of 2.5 days before CTA (range, 0–16 days). All 20 patients with ischemic symptoms ipsilateral to the side of moderate-grade stenosis had imaging confirmation with either CT or MR which showed an infarct in all 16 patients with stroke and no evidence of infarct in the 4 subjects with TIA. Patient cohort characteristics are shown in Table 1. Vascular risk factors were not significantly different between groups.

CTA Plaque Imaging Results

Mean soft-plaque thickness was significantly higher in subjects with symptomatic disease, while mean hard-plaque thickness was significantly higher in asymptomatic subjects (Table 1). We found that each 1-mm increase in mean soft-plaque thickness was associated with a ~3.7 times greater likelihood of prior stroke or TIA ($P = .0001$), after adjusting for age, exact percentage stenosis, and

Table 2: Univariate and multivariate logistic regression odds ratios associating plaque characteristics with symptomatic carotid disease

Predictors of Interest	Univariate Logistic Regression				Adjusted Logistic Regression ^a				Difference in Univariate and Adjusted AUC
	OR	95% CI	AUC	P Value	OR	95% CI	AUC	P Value	P Value
Max hard-plaque thickness (mm)	0.22	0.10–0.47	0.85	.0001	0.22	0.10–0.48	0.87	.0001	.5205
Max soft-plaque thickness (mm)	3.98	2.02–7.81	0.87	<.0001	3.73	1.92–7.24	0.88	<.0001	.6193
Ratio soft-/hard-plaque thickness	6.40	2.44–16.80	0.87	.0002	6.12	2.34–16.02	0.86	.0002	.7146

Note:—Max indicates maximum.

^a Adjusted for age, stenosis (NASCET), and sex.

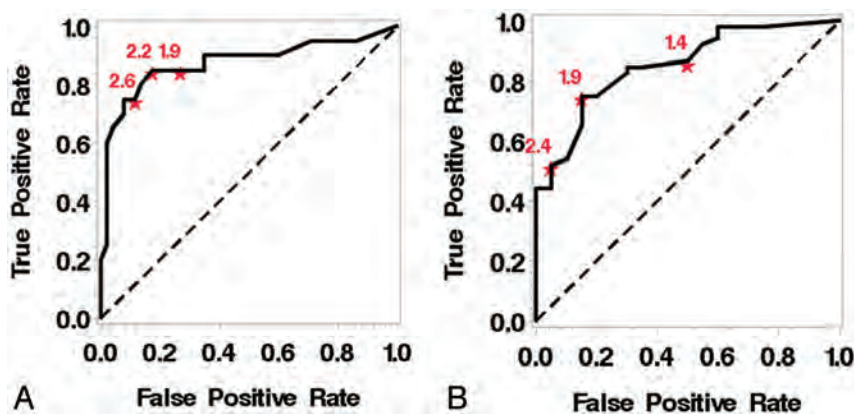


FIG 3. Receiver operating characteristic curves for maximum soft-plaque thickness (A) and maximum hard-plaque thickness (B).

sex (Table 2). Each 1-mm increase in hard-plaque thickness decreased the odds of having had a prior ipsilateral stroke or TIA by approximately 80% (OR = 0.22, $P = .0001$). The ratio between soft- and hard-plaque thickness was similarly predictive of symptomatic disease. Given the single outlier ischemic event occurring >30 days before CTA imaging (a stroke in 1 subject 621 days before CTA), in a post hoc sensitivity analysis excluding this subject, hard- and soft-plaque thickness adjusted-ORs were not significantly changed at 0.22 and 3.77, respectively. We calculated interreader correlation coefficients of 0.97 and 0.96 for soft- and hard-plaque thickness measurements, respectively, consistent with prior reports.^{12,13}

Diagnostic Accuracy Measures

In our ROC analysis adjusted for age, sex, and stenosis severity, soft-plaque thickness measures provided the greatest AUC (0.88) (Table 2 and Fig 3). Sensitivity and specificity were optimized by using a maximum soft-plaque thickness of 2.2 mm, which provided a sensitivity of 85%, specificity of 83%, positive predictive value of 65%, and negative predictive value of 93%. Hard-plaque thickness measurements provided a similar AUC of 0.87. Sensitivity and specificity were optimized by using a maximum hard-plaque thickness measurement of 1.9 mm, which provided a sensitivity of 75%, specificity of 85%, positive predictive value of 93%, and negative predictive value of 57%.

DISCUSSION

Using a simple and reproducible plaque measurement on CTA, we found a strong association between increasing soft-plaque thickness measurements and symptomatic carotid artery plaques. Previous studies have shown that CTA plaque thickness measures can predict high-risk plaque as defined on correlative MR imaging¹² or symptomatic plaque in high-grade stenosis.¹³ In the current study, we found that such CTA plaque measures can differ-

entiate asymptomatic and symptomatic carotid plaques despite the relatively smaller volume of plaque and lower absolute stroke risk present in moderate-grade stenosis. Moreover, we found no significant differences in traditional vascular risk factors in the asymptomatic and symptomatic groups, suggesting that plaque thickness measurements may be able to discriminate high-risk and stable plaque more accurately than clinical factors. This is the first report, to our knowledge, applying this CTA technique to patients with a tightly defined and clinically relevant NASCET stenosis category of 50%–69%. Although the ab-

absolute annual risk of stroke is lower in moderate-grade compared with high-grade carotid artery stenosis, the prevalence of 50%–69% stenosis is approximately 3 times higher in the general population¹⁷; therefore, the total population-based stroke risk attributable to moderate stenosis is substantial.

Although there are studies using alternative CTA imaging strategies to assess unstable or vulnerable carotid plaque, we believe that the technique we used has 3 significant advantages over previously studied CTA techniques. First, plaque thickness measurements require no additional postprocessing, unlike some prior methods^{18,19} that have required customized postprocessing software not routinely available or widely used in clinical practice. Similarly, the technique used in our study does not require the measurement of Hounsfield units, which have been shown to be poor discriminators among specific plaque elements, given overlapping attenuation of in vivo atherosclerotic plaque components such as hemorrhage, fibrosis, and lipids.^{20,21} Second, plaque thickness measurements do not require additional imaging acquisitions to be obtained as part of the CTA examination. Romero et al,²² for example, showed a correlation between arterial wall enhancement and symptomatic plaque, but their approach necessitated a noncontrast CT of the neck, an acquisition that is not part of most CTA neck studies. Third, plaque thickness measurements are highly reproducible, as evidenced by the excellent interobserver correlation coefficients we and others have found.¹² Although assessment of plaque morphology such as ulceration on CTA has been proposed as a high-risk plaque marker,^{20,23} the technique used in our study may be more desirable to implement in routine clinical image interpretation because it is less prone to observer subjectivity.

The mechanism underlying increased risk of symptomatic disease in carotid atheroma with greater soft plaque is not entirely

understood but is likely related to the low attenuation of high-risk elements of atherosclerosis, including a lipid-rich necrotic core and intraplaque hemorrhage.²⁴ The precise differentiation of tissue components within soft plaque may be of limited clinical significance, however, because most of these presumed tissue types are features of more advanced atherosclerotic lesions.¹¹ Understanding the relative importance of specific carotid plaque elements in predicting stroke risk has been made possible by high-resolution MR imaging. By allowing the accurate differentiation of tissue types in atherosclerotic lesions,¹² MR imaging provides important insights into the magnitude of risk that could potentially be conferred by increasing soft plaque on CTA. For example, a recent meta-analysis²⁵ of subjects with carotid stenosis followed after plaque MR imaging showed a lipid-rich necrotic core, intraplaque hemorrhage, and thinning or rupture of the fibrous cap as conferring 3-, 6-, and 4.5-fold higher risks of future stroke or TIA, respectively. Because lipid cores or hemorrhage together likely form a significant component of soft plaque,¹³ we hypothesize that soft-plaque measurements may represent a simple composite marker of vulnerable, high-risk plaque elements. Similarly, calcium in carotid plaque may be associated with relatively more stable plaque, which is likely to cause ischemic stroke. The apparent protective effect afforded by increasing calcium burden that we and other investigations^{12,13,26} have found might be explained by the decrease in fibrous cap inflammation or the increase in mechanical stability afforded by attenuated calcium deposition.²⁶

Limitations of this study require discussion. First, because it was a cross-sectional retrospective analysis, prior ischemic events were correlated with plaque imaging features rather than prediction of future stroke or TIA. Second, we were not able to precisely identify the tissue types constituting soft plaque on the basis of our study, which lacked histopathologic validation. Third, although the review of subject data makes carotid disease the most likely cause of stroke or TIA in our cohort, the possibility of tandem intracranial stenosis as a cause of ischemic symptoms in our cohort cannot be entirely excluded because we studied the neck arteries and not the intracranial circulation. We believe that our current study and prior work^{12,13} now justify a larger scale, appropriately powered prospective investigation of the ability of CTA plaque-thickness measurements to predict future stroke or TIA. Because plaque hemorrhage and lipid-rich necrotic core are powerful predictors of stroke on MR imaging,²⁵ it is likely that similar predictive information would be present in CTA attenuation measurements because we believe that hemorrhage and lipid are significant constituents of soft plaque. Moreover, although carotid atherosclerosis is a dynamic process, prospective evidence supports high-risk markers of plaque, such as intraplaque hemorrhage, as being relatively stable with time and conferring increased stroke risk for at least 5 years after their detection.⁵ An additional recent study²⁷ also showed that high-risk elements such as intraplaque hemorrhage, fibrous cap abnormalities, and lipid cores were generally not significantly changed during a 1-year follow-up period. Therefore, although further investigation is needed, it is reasonable to hypothesize that our results could translate into a prospective CTA-based stroke prediction tool in carotid artery disease.

CONCLUSIONS

By using simple single-axial source images from CTA, we were able to use soft- and hard-thickness measurements to discriminate between asymptomatic and symptomatic carotid artery plaque in a cohort of patients with moderate carotid artery stenosis. Ultimately, further prospective studies powered for stroke prediction are needed using this relatively simple and reproducible CT-based method.

Disclosures: Ajay Gupta—RELATED: Grant: Association of University Radiologists—GE Radiology Research Academic Fellowship Award,* Foundation of the American Society of Neuroradiology Scholar Award.* *Money paid to the institution.

REFERENCES

1. Rothwell PM, Eliasziw M, Gutnikov SA, et al. **Analysis of pooled data from the randomised controlled trials of endarterectomy for symptomatic carotid stenosis.** *Lancet* 2003;361:107–16
2. Abbott AL. **Medical (nonsurgical) intervention alone is now best for prevention of stroke associated with asymptomatic severe carotid stenosis: results of a systematic review and analysis.** *Stroke* 2009;40:e573–83
3. Raman G, Moorthy D, Hadar N, et al. **Management strategies for asymptomatic carotid stenosis: a systematic review and meta-analysis.** *Ann Intern Med* 2013;158:676–85
4. Caplan LR, Hennerici M. **Impaired clearance of emboli (washout) is an important link between hypoperfusion, embolism, and ischemic stroke.** *Arch Neurol* 1998;55:1475–82
5. Hosseini AA, Kandiyil N, Macsweeney ST, et al. **Carotid plaque hemorrhage on magnetic resonance imaging strongly predicts recurrent ischemia and stroke.** *Ann Neurol* 2013;73:774–84
6. Derdeyn CP. **Mechanisms of ischemic stroke secondary to large artery atherosclerotic disease.** *Neuroimaging Clin N Am* 2007;17:303–11, vii–viii.
7. Gupta A, Chazen JL, Hartman M, et al. **Cerebrovascular reserve and stroke risk in patients with carotid stenosis or occlusion: a systematic review and meta-analysis.** *Stroke* 2012;43:2884–91
8. Morgenstern LB, Fox AJ, Sharpe BL, et al. **The risks and benefits of carotid endarterectomy in patients with near occlusion of the carotid artery: North American Symptomatic Carotid Endarterectomy Trial (NASCET) group.** *Neurology* 1997;48:911–15
9. den Hartog AG, Bovens SM, Koning W, et al. **Current status of clinical magnetic resonance imaging for plaque characterisation in patients with carotid artery stenosis.** *Eur J Vasc Endovasc Surg* 2013;45:7–21
10. Cai JM, Hatsukami TS, Ferguson MS, et al. **Classification of human carotid atherosclerotic lesions with in vivo multicontrast magnetic resonance imaging.** *Circulation* 2002;106:1368–73
11. Stary HC, Chandler AB, Dinsmore RE, et al. **A definition of advanced types of atherosclerotic lesions and a histological classification of atherosclerosis: a report from the committee on vascular lesions of the council on arteriosclerosis, American Heart Association.** *Circulation* 1995;92:1355–74
12. Trelles M, Eberhardt KM, Buchholz M, et al. **CTA for screening of complicated atherosclerotic carotid plaque—American Heart Association type VI lesions as defined by MRI.** *AJNR Am J Neuroradiol* 2013;34:2331–37
13. Gupta A, Baradaran H, Kamel H, et al. **Evaluation of computed tomography angiography plaque thickness measurements in high-grade carotid artery stenosis.** *Stroke* 2014;45:740–45
14. Fox AJ, Symons SP, Aviv RI, et al. **Falsely claiming use of NASCET percentage stenosis method.** *Radiology* 2009;253:574–45, author reply 575
15. Fox AJ. **How to measure carotid stenosis.** *Radiology* 1993;186:316–18
16. Easton JD, Saver JL, Albers GW, et al. **Definition and evaluation of transient ischemic attack: a scientific statement for healthcare pro-**

- professionals from the American Heart Association/American Stroke Association Stroke Council; Council on Cardiovascular Surgery and Anesthesia; Council on Cardiovascular Radiology and Intervention; Council on Cardiovascular Nursing; and the Interdisciplinary Council on Peripheral Vascular Disease—the American Academy of Neurology affirms the value of this statement as an educational tool for neurologists. *Stroke* 2009;40:2276–93
17. de Weerd M, Greving JP, Hedblad B, et al. **Prevalence of asymptomatic carotid artery stenosis in the general population: an individual participant data meta-analysis.** *Stroke* 2010;41:1294–97
 18. Wintermark M, Jawadi SS, Rapp JH, et al. **High-resolution CT imaging of carotid artery atherosclerotic plaques.** *AJNR Am J Neuroradiol* 2008;29:875–82
 19. Wintermark M, Arora S, Tong E, et al. **Carotid plaque computed tomography imaging in stroke and nonstroke patients.** *Ann Neurol* 2008;64:149–57
 20. U-King-Im JM, Fox AJ, Aviv RI, et al. **Characterization of carotid plaque hemorrhage: a CT angiography and MR intraplaque hemorrhage study.** *Stroke* 2010;41:1623–29
 21. Walker LJ, Ismail A, McMeekin W, et al. **Computed tomography angiography for the evaluation of carotid atherosclerotic plaque: correlation with histopathology of endarterectomy specimens.** *Stroke* 2002;33:977–81
 22. Romero JM, Babiarz LS, Forero NP, et al. **Arterial wall enhancement overlying carotid plaque on CT angiography correlates with symptoms in patients with high grade stenosis.** *Stroke* 2009;40:1894–96
 23. Hokari M, Kuroda S, Yasuda H, et al. **Lumen morphology in mild-to-moderate internal carotid artery stenosis correlates with neurological symptoms.** *J Neuroimaging* 2011;21:348–54
 24. El-Barghouty NM, Levine T, Ladva S, et al. **Histological verification of computerised carotid plaque characterisation.** *Eur J Vasc Endovasc Surg* 1996;11:414–16
 25. Gupta A, Baradaran H, Schweitzer AD, et al. **Carotid plaque MRI and stroke risk: a systematic review and meta-analysis.** *Stroke* 2013;44:3071–77
 26. Kwee RM. **Systematic review on the association between calcification in carotid plaques and clinical ischemic symptoms.** *J Vasc Surg* 2010;51:1015–25
 27. Kwee RM, Truijman MT, van Oostenbrugge RJ, et al. **Longitudinal MRI study on the natural history of carotid artery plaques in symptomatic patients.** *PLoS One* 2012;7:e42472

Detection of Calcifications in Retinoblastoma Using Gradient-Echo MR Imaging Sequences: Comparative Study between In Vivo MR Imaging and Ex Vivo High-Resolution CT

F. Rodjan, P. de Graaf, P. van der Valk, T. Hadjistilianou, A. Cerase, P. Toti, M.C. de Jong, A.C. Moll, J.A. Castelijns, and P. Galluzzi, on behalf of the European Retinoblastoma Imaging Collaboration

ABSTRACT

BACKGROUND AND PURPOSE: Intratumoral calcifications are very important in the diagnosis of retinoblastoma. Although CT is considered superior in detecting calcification, its ionizing radiation, especially in patients with hereditary retinoblastoma, should be avoided. The purpose of our study was to validate T2*WI for the detection of calcification in retinoblastoma with ex vivo CT as the criterion standard.

MATERIALS AND METHODS: Twenty-two consecutive patients with retinoblastoma (mean age, 21 months; range, 1–71 months) with enucleation as primary treatment were imaged at 1.5T by using a dedicated surface coil. Signal-intensity voids indicating calcification on T2*WI were compared with ex vivo high-resolution CT, and correlation was scored by 2 independent observers as poor, good, or excellent. Other parameters included the shape and location of the signal-intensity voids. In 5 tumors, susceptibility-weighted images were evaluated.

RESULTS: All calcifications visible on high-resolution CT could be matched with signal-intensity voids on T2*WI, and correlation was scored as excellent in 17 (77%) and good in 5 (23%) eyes. In total, 93% (25/27) of the signal-intensity voids inside the tumor correlated with calcifications compared with none (0/8) of the signal-intensity voids outside the tumor. Areas of nodular signal-intensity voids correlated with calcifications in 92% (24/26), and linear signal-intensity voids correlated with hemorrhage in 67% (6/9) of cases. The correlation of signal-intensity voids on SWI was better in 4 of 5 tumors compared with T2*WI.

CONCLUSIONS: Signal-intensity voids on in vivo T2*WI correlate well with calcifications on ex vivo high-resolution CT in retinoblastoma. Gradient-echo sequences may be helpful in the differential diagnosis of retinoblastoma. The combination of funduscopy, sonography, and high-resolution MR imaging with gradient-echo sequences should become the standard diagnostic approach for retinoblastoma.

ABBREVIATIONS: HRCT = high-resolution CT; SIV = signal-intensity void

Retinoblastoma is generally treated on the basis of fundoscopic, sonography, and imaging findings without prior histopathologic confirmation of diagnosis. The prevalence of calcifications is approximately 85%¹ and is considered the key finding in differentiating retinoblastoma from simulating lesions (Coats disease, persistent hyperplastic primary vitreous, or toxocara en-

dophthalmitis) in young children.² Very rare lesions such as medulloepithelioma and retinocytoma may also have calcifications and hence occasionally cause difficulty with clinical and radiologic differentiation.³

Sonography is the most commonly used imaging technique for the evaluation of intraocular tumors. The combination of funduscopy and sonography allows the identification of calcifications in 91%–95% of all patients with newly diagnosed retinoblastoma.⁴ Sensitivity to small calcifications decreases, however, in the presence of massive retinal detachment, vitreous hemorrhage, and subretinal fluid, potentially hampering the confirmation of the diagnosis. In these complicated eyes, CT is generally the method of choice for studying intraocular calcifications, with reported sensitivities of 81%–96%.⁵ Its diagnostic performance in staging retinoblastoma disease extent is limited, however, and the theoretic increased risk of radiation-induced cataracts and fatal cancers in children who are exposed to ionizing radiation should

Received September 16, 2013; accepted after revision July 15, 2014.

From the Departments of Radiology (F.R., P.d.G., M.C.d.J., J.A.C.), Pathology (P.v.d.V.), and Ophthalmology (A.C.M.), VU University Medical Center, Amsterdam, the Netherlands; and Departments of Ophthalmology (T.H.), Neuroimaging and Neurointerventional Unit (A.C., P.G.), and Pathology (P.T.), Azienda Ospedaliera e Universitaria, Santa Maria alle Scotte, Siena, Italy.

This work was supported by grants from the ODAS Foundation, Delft, the Netherlands; National Foundation for the Blind and Visually Impaired, Utrecht, the Netherlands; and Blindenhulp Foundation, Gravenhage, the Netherlands.

Please address correspondence to F. Rodjan, MD, Department of Radiology, Room 0 X 112, VU University Medical Center, Postbox 7057, 1007 MB Amsterdam, the Netherlands; e-mail: firaziarodjan@slz.nl

<http://dx.doi.org/10.3174/ajnr.A4163>

be considered.⁶ Patients with hereditary retinoblastoma in particular are at an even higher risk of developing radiation-induced tumors compared with healthy children.

MR imaging is the noninvasive technique of choice for the evaluation of retinoblastoma. The combination of sonography and MR imaging is considered first-line diagnostic imaging in the evaluation of children with suspected retinoblastoma, surpassing CT.⁷ However, MR imaging does not allow reliable identification of tumoral calcifications on routinely used clinical sequences. The lack of spatial resolution with standard clinical sequences provides an additional challenge for the visualization of small punctate tumoral calcifications. Scarce data on high-resolution ocular MR imaging by using surface coils do, however, suggest that calcifications can be detected with reasonable diagnostic accuracy.⁸

Gradient-echo T2*-weighted imaging sequences are sensitive to susceptibility differences among tissues that cause magnetic field inhomogeneity leading to signal loss, and T2*WI is used to depict blood products, deoxygenated venous blood in dilated vessels (venous congestion), and calcifications.^{9,10} Previous work by Galluzzi et al¹¹ showed that T2*WI can be a feasible technique for detecting intraocular calcifications because calcified areas in retinoblastoma emerged as hypointense foci of signal-intensity voids (SIVs) within the soft-tissue mass. Most of the SIVs on T2*WI correlated with spots of intratumoral calcifications on CT. Whether the shape and spatial arrangement of the intraocular SIVs on MR imaging could be matched with calcifications on CT was not investigated.

The purpose of our study was to assess the performance of gradient-echo T2*WI in the visualization and morphologic evaluation of retinoblastoma calcifications and to compare T2*WI with ex vivo CT scans of the enucleated eyes as the criterion standard.

MATERIALS AND METHODS

Patient Population

This study included patients from 2 European retinoblastoma referral centers and was performed in agreement with recommendations of both local ethics committees, with a waiver of informed consent. From October 2009 to September 2011, patients with retinoblastoma diagnosed with funduscopy and sonography under general anesthesia were included under the following conditions: 1) Adequate pretreatment T2*WI was available, 2) enucleation of the eye was the primary treatment for retinoblastoma, and 3) high-resolution CT (HRCT) images of the enucleated eye were available. In patients with bilateral retinoblastoma, only the most affected eye was enucleated and included. Three patients were excluded because of inadequate T2*WI quality. The final study population included 22 patients. Patient records were reviewed for age at retinoblastoma diagnosis.

MR Imaging

Pretreatment MR imaging examinations were performed with the patient under general anesthesia on 1.5T systems (Avanto or Sonata; Siemens, Erlangen, Germany) by using a dedicated surface coil (loop or temporomandibular coils with a diameter of 4 and 7 cm, respectively) focused on the affected or most affected eye. Imaging was performed according to published guidelines.⁷ In all

patients, MR images included transverse and sagittal spin-echo T1WI (TR/TE, 300–420/13–15 ms; section thickness, 2 mm), transverse spin-echo T2WI (TR/TE, 1200–2470/120–166 ms; section thickness, 2 mm), and transverse 2D T2*WI (TR/TE, 300–650/15–25 ms; section thickness, 2 mm). Additionally, 5 patients underwent susceptibility-weighted imaging (TR/TE, 46/38 ms; matrix, 192 × 162; voxel size, 0.4 × 0.6 × 1 mm³; no gap; 35 sections; averages, 2; flip angle, 15°; acquisition time, 7.34 minutes). SWI datasets included phase images and minimum-intensity-projection images.

Ex Vivo HRCT

HRCT was performed immediately after enucleation by using either a BrightSpeed (GE Healthcare, Milwaukee, Wisconsin) or Somatom Sensation 64 (Siemens) system. Eyes were carefully positioned in a small cardboard tray supported with gauze in the same orientation as the transverse plane of the MR images. Axial images were acquired with a section thickness of 0.6 mm, collimation of 0.5 mm, pitch of 0.8, 120 kV, 250 mAs, FOV of 16 cm, and a 512 × 512 matrix. From the raw data, individual datasets were reformatted into images of 0.6-mm section thickness in all 22 eyes. Raw data remained available for additional multiplanar reconstructions, which were made afterward by 1 observer (F.R.) to provide accurate information of the obtained data in the axial plane. Finally, 2 datasets of CT images were reconstructed and were available for all patients; one with section thickness of 2 mm (the same orientation and section-thickness as the T2*WI) and one with very thin sections (0.6 mm).

Image Analysis

Retrospectively, 2 independent observers (P.G. and P.d.G., with 15 and 11 years of experience in ocular MR imaging, respectively) reviewed all T2*WI and HRCT images. Afterward, differences in scoring were resolved in consensus. Both observers were blinded to the results of clinical and histopathologic findings. Ex vivo HRCT was considered the criterion standard for detecting calcifications. The presence or absence of calcifications on HRCT was assessed. Calcifications were defined as hyperattenuated foci within the tumor on HRCT images. MR images were independently reviewed by the same observers. After analyzing the MR images, the observers confirmed detection of calcifications in correlation with HRCT images by using anatomic landmarks to adjust for section thicknesses, angulation, and obliquity. Criteria used to define calcifications on MR imaging were as follows: Calcifications were required to have the same morphologic pattern as that on the HRCT (same shape and same spatial arrangement) and were considered localized foci of marked hypointense SIV on T2*WI. Correspondence between intraocular hyperattenuated areas on CT and intraocular SIVs observed on MR imaging was scored as excellent, good, or poor. Excellent correspondence was scored if all calcifications on HRCT perfectly matched SIVs on T2*WI. Good correspondence was scored if there was an evident correlation between HRCT and MR imaging in some parts of the tumor but additional SIVs on MR imaging were present without an evident explanation on the basis of other MR images or hyperattenuated structures on CT. If no correlation could be observed at all, the correspondence was scored as poor. The location of SIVs

Patient findings and correlation of CT with MRI in calcium detection

Patient (Lat)	Age (mo) ^a	Int MRI-En (day)	Corr T2*WI-CT	SWI	Corr T2*WI-SWI
1 (U)	1	1	Moderate	No	NA
2 (U)	4	8	Moderate	No	NA
3 (U)	46	6	Moderate	No	NA
4 (U)	3	0	Moderate	No	NA
5 (U)	26	6	Moderate	No	NA
6 (U)	73	1	Good	No	NA
7 (B)	8	4	Good	No	NA
8 (U)	11	5	Good	No	NA
9 (U)	8	1	Good	No	NA
10 (U)	16	1	Good	No	NA
11 (U)	3	8	Good	No	NA
12 (B)	12	8	Good	No	NA
13 (B)	35	8	Good	No	NA
14 (U)	29	1	Good	No	NA
15 (B)	29	8	Good	No	NA
16 (B)	13	6	Good	No	NA
17 (U)	45	8	Good	No	NA
18 (U)	5	8	Good	Yes	Equal
19 (U)	9	7	Good	Yes	Better
20 (U)	38	1	Good	Yes	Better
21 (U)	5	8	Good	Yes	Better
22 (U)	37	5	Good	Yes	Better

Note:—Lat indicates tumor laterality; Int MRI-En, interval MRI and enucleation; Corr, correlation; U, unilateral; B, bilateral; NA, not applicable.

^a Median age, 12.5 mo; mean age, 20.72 mo.

in the tumor was categorized as central, peripheral, or a combination of both. The shape of SIVs was categorized as nodular or linear. SIVs on T2*WI secondary to intravitreal or subretinal hemorrhage were considered if fluid-fluid levels (in correspondence with T2WI) or a smooth hypointense outlining of the tumor or retina was present in the affected eye.

Eyes with good or poor correlation based on additional SIVs without corresponding calcification on HRCT or other explanations on conventional MR images were selected for additional correlation with histopathology. In 5 tumors, SIVs in SWI were evaluated and compared with the T2*WI and were scored as worse, equal, or better correlation with calcifications on HRCT. Furthermore, the feasibility of using phase images for the detection of calcifications in retinoblastoma was studied. Calcium undergoes a positive phase shift (paramagnetic susceptibility) and is displayed as a high signal-intensity area on the phase image, whereas a negative phase shift (diamagnetic susceptibility) occurs for veins, iron, and hemorrhage, making them appear uniformly dark.

Histopathologic Examination

Eyes were fixed in saline-buffered formalin, sampled, embedded in paraffin, and sectioned in the same orientation as the axial plane of the MR images (thickness, 4 μm) and stained with hematoxylin-eosin. Histopathologic sections were only evaluated in tumors with additional SIVs on T2*WI, without evident cause on other MR images or CT, by 2 pathologists (P.v.d.V. and P.T).

RESULTS

All 22 patients (22 eyes) in this study had histopathologically proved retinoblastoma (mean age, 21 months; range, 1–73

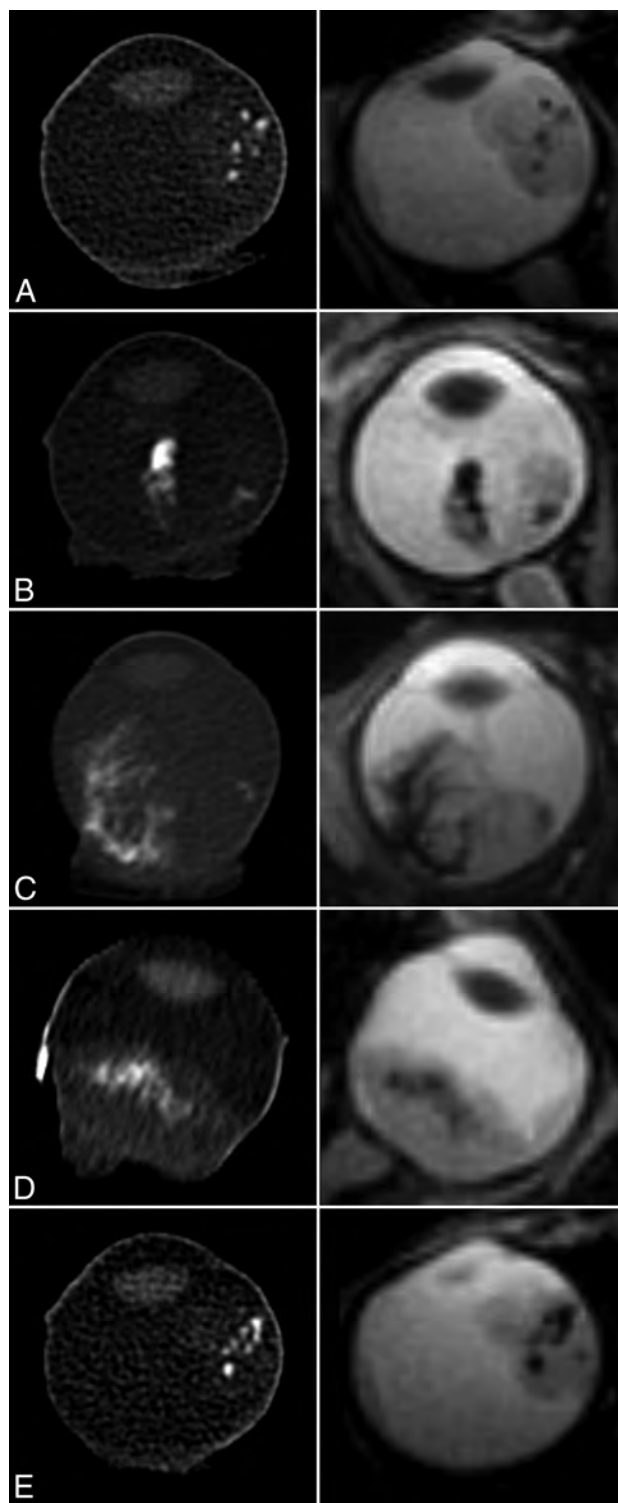


FIG 1. Excellent-matching hyperattenuated calcifications on ex vivo high-resolution CT (left column) with signal-intensity void spots on gradient-echo T2*-weighted MR images (right column) in patients 12 (A), 16 (B), 18 (C), 19 (D), and 14 (E).

months). The mean time interval between diagnosis and MR imaging was 5 days (range, 0–8 days). The mean time interval between MR imaging and CT was 5 days (range, 0–8 days). Patient characteristics are summarized in the Table.

Areas of calcification were present on HRCT in the tumors of

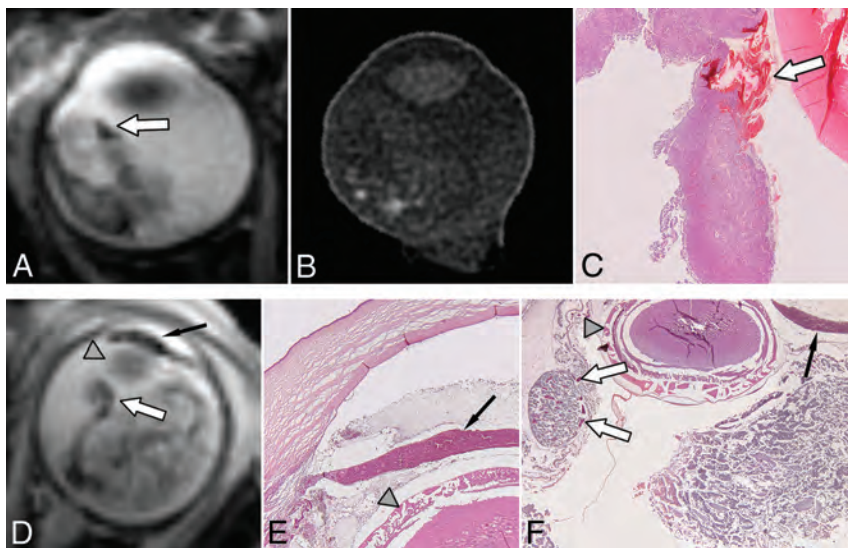


FIG 2. Examples of additional signal-intensity voids on T2*-weighted MR images without correspondence with ex vivo high-resolution CT. Patient 13 shows a hypointense nodular structure (A) in the anterior part of the eye (arrow) on T2*-weighted imaging without corresponding hyperattenuation on ex vivo high-resolution CT (B). Histopathology demonstrates a hemorrhage (arrow) precisely matching this additional SIV (C). Adjacent to this hemorrhage multiple linear-arranged spots match hyperattenuated spots on CT. In patient 11 (D), a linear band of SIV on T2*WI is shown outside the tumor along the detached retina (white arrow) and in the iris (black arrow). The gray arrowhead indicates the lens, which is dislocated. Histology (E and F) shows necrotic tumor with dilated vessels (venous congestion) (white arrow) and hemorrhagic necrosis of the iris combined with venous congestion (black arrow). The anterior chamber is infiltrated by neoplastic cells and cellular debris. (H&E staining, $\times 20$ magnification.)

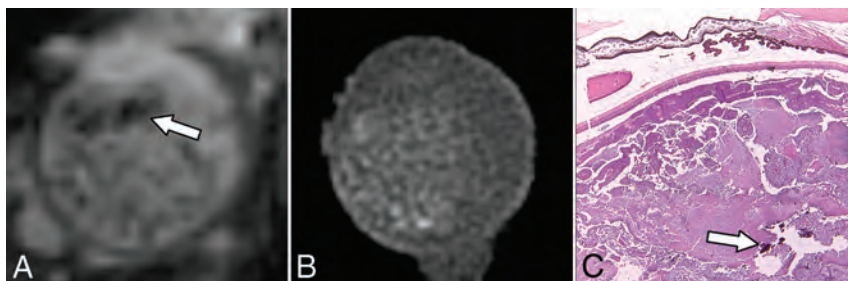


FIG 3. Extra signal-intensity void spots in the anterior part of the eye on gradient-echo T2*-weighted images (arrow, A) were observed in patient 21, with excellent correspondence with HRCT (B). However, a band of additional signal-intensity void spots was present in the anterior part of the tumor on the gradient-echo T2*-weighted MR image (arrow, A) without correspondence on ex vivo high-resolution CT. Histopathologic correlation (C) shows multiple foci of calcifications in the anterior part of the tumor (arrow). (H&E staining, $\times 20$ magnification.)

all 22 eyes. Furthermore, all eyes showed foci of SIVs on T2*WI. Thirty-five areas of SIVs were depicted, 27 areas of SIVs inside the tumor and 8 areas outside the tumor. Shape was classified as nodular ($n = 26$) and linear ($n = 9$). Nodular SIVs were predominantly located within the tumor (25 of 26 SIVs; 96%), and 19 (76%) were in the tumor center, whereas linear SIVs were predominantly located outside the tumor (7 of 9 SIVs; 78%). Of the 2 linear SIVs within the tumor, one was located at the periphery of the tumor, while the other was located centrally within the tumor.

Correlation between calcifications on CT and SIVs on T2*WI was scored as excellent in 17 (77%) and good in 5 (23%) eyes. Poor correlations were not observed. Of 27 areas of SIVs located inside the tumor, 25 areas (93%) correlated with calcifications; 1, with intratumoral hemorrhage; and 1, with a dilated venous vessel

(venous congestion). Of the 8 areas of SIVs located outside the tumor, 6 (75%) correlated with hemorrhage (5 subretinal and 1 intratumoral), and 2, with susceptibility artifacts secondary to air-tissue interface. Areas of nodular SIVs correlated with calcifications in 92% (24/26), and linear SIVs correlated with hemorrhage in 67% (6/9).

The 17 excellent-corresponding eyes showed a perfect match (same shape and same spatial arrangement) between hyperattenuated structures on CT and areas of SIVs on T2*WI (Fig 1). Additional SIVs in excellent-corresponding tumors were mostly located outside the tumor, with a linear aspect corresponding with artifacts or hemorrhage (Fig 2). In 3 excellent-corresponding tumors, additional SIVs were observed on T2*WI and did not have any corresponding hyperattenuation on HRCT. However on histopathology, these SIVs did correlate with spots of calcification (Fig 3).

In 5 good-corresponding eyes, the hypointense areas on MR imaging could only be correlated in part with hyperattenuated areas on CT. Additional SIVs were all located outside the tumor and correlated with hemorrhage and venous congestion.

Discrepancies between observers occurred in 2 excellent-corresponding cases. In one case, a linear hypointense structure that indicated hemorrhage caused confusion. In the other case, more SIVs were observed on MR imaging compared with the poor resolution of CT. The spots of calcification on CT, however, matched those on T2*WI well.

In 5 patients, SWI datasets were available and all eyes were excellent-corresponding. In 4 eyes, the correlation

between SIVs on SWI and the calcifications on HRCT was better compared with that on T2*WI (Fig 4), and in 1 eye, the correlation showed no difference between the 2 gradient-echo techniques. In 2 patients, the quality of the phase images was diminished due to image distortions. Phase images showed the hyperintense signal intensity of calcification in the other 3 eyes, which was confirmed on HRCT. None of these eyes showed intraocular or intratumoral hemorrhage clinically or on histopathology.

DISCUSSION

T2*WI allows accurate identification of calcified areas in retinoblastoma. In our study, all calcifications seen on ex vivo HRCT could be matched with SIVs on T2*WI, and this technique even depicted small SIVs better than HRCT. SIVs located in the tumor

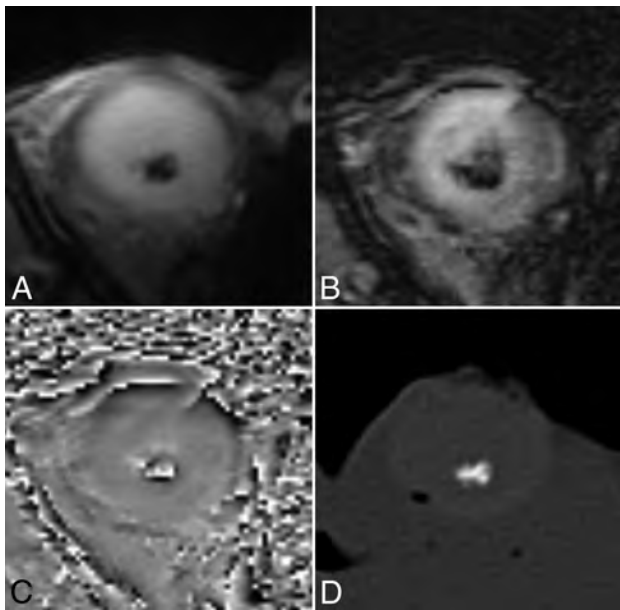


FIG 4. The value of phase imaging in identifying calcification in retinoblastoma (patient 22). Signal-intensity void spots can be seen on the T2*-weighted (A) and SWI minimum intensity projection (B). A phase image (C) shows high signal intensity centrally identifying calcification, confirmed on the ex vivo high-resolution CT image (D).

center are more likely to be calcification, whereas peripheral SIVs and other intraocular SIVs can also indicate hemorrhage, slow-flowing blood in venous congestion, or artifacts.

Detection of calcifications is critical for the differential diagnosis of retinoblastoma. After funduscopy, the first-line diagnostic tool is always ocular sonography. Experienced ophthalmologists find calcifications in most patients. When calcifications are not detected, cross-sectional imaging studies can be used as a problem-solving technique.^{12,13} MR imaging is the technique of choice for the evaluation of intraocular pathology, especially in children presenting with leukocoria.

The guidelines for imaging retinoblastoma by de Graaf et al⁷ serve as a checklist for minimal requirements for pretreatment diagnostic evaluation of retinoblastoma or mimicking lesions. They concluded that with sonography, high-resolution MR imaging is the most important technique for retinoblastoma diagnosis and the evaluation of associated intracranial abnormalities. CT was highly discouraged in children with retinoblastoma because of ionizing radiation and no added diagnostic value.

Historically, MR imaging has been considered an inferior technique for the detection of calcifications compared with CT. However, successful depiction of small foci of calcifications by T2*WI has already been reported in other studies.^{14,15} Galluzzi et al¹¹ showed that T2*WI is a feasible technique for detecting calcifications in retinoblastoma. In their study, all SIVs matched calcifications. SIVs on T2*WI could, however, also represent pathology other than calcifications. In our study, we further characterized SIVs as calcification, hemorrhage, or artifacts by discussing different accompanying patterns.

We were able to confirm the capability of T2*WI for calcification detection. In some tumors, T2*WI was even more sensitive in depicting small intraocular calcifications in vivo compared with

HRCT ex vivo. The HRCT protocol in this study is considered more sensitive for the detection of small punctate calcifications than commonly used clinical protocols for pediatric orbital CT.

Additional hypointense areas on MR imaging can, however, cause confusion. Intratumoral hemorrhage is the most important cause of false-positive SIVs.¹⁶ Hemorrhage is more likely to appear in large necrotic tumors and can cause extensive intraocular complications such as massive subretinal or intravitreal hemorrhage with a subsequent increase in intraocular pressure. Smooth and linear SIVs in retinoblastoma on T2*WI are indicative of intratumoral hemorrhage and are predominantly located in the tumor periphery, whereas calcifications more frequently present as hypointense SIVs in the tumor center. Massive subretinal or intravitreal hemorrhage can easily be diagnosed on conventional T2WI with fluid-fluid (sedimentation) levels. We considered smooth and linear SIVs on T2*WI indicative of intraocular hemorrhage. They are predominantly on the surface of the tumors or aligning with the usually detached retina. Close correlation with findings during funduscopy and sonography might further help in the interpretation of SIVs on the tumor surface.

Advanced disease with massive tumor necrosis can also present with secondary neovascular glaucoma, uveitis, and/or aseptic orbital cellulitis. These conditions are associated with venous congestion (ie, extremely dilated intraocular venous structures). Susceptibility effects in venous blood are caused by the presence of deoxyhemoglobin and become more pronounced in venous congestion with increased intravascular space and slow-flowing venous blood (Fig 4).¹⁷ Susceptibility artifacts due to air beneath the eyelid or within the paranasal sinuses can also cause SIVs on T2*WI. These artifacts can be distinguished from calcifications by their linear aspect and location. Susceptibility artifacts caused by air are usually located in or near the anterior eye segment.

SWI was available for review in a small subset of patients, which allowed us to explore, for the first time, the potential value of this sequence in retinoblastoma. This technique was more sensitive than T2*WI in detecting calcifications or microcalcifications and differentiating them from intratumoral hemorrhage or microhemorrhage, necrosis, and artifacts in oligodendroglioma, vestibular schwannoma, and diffuse infiltrating pontine glioma.^{10,18,19} In contrast to T2*WI, SWI is based on a long TE, high-resolution, flow-compensated 3D gradient-echo imaging technique with filtered phase information in each voxel. The combination of magnitude and phase data creates an enhanced contrast magnitude image that is particularly sensitive to hemorrhage, calcium, iron storage, and slow-flowing venous blood, therefore allowing a significant improvement in sensitivity and specificity compared with T2*WI.^{18,20} Preliminary results in our study showed that correlations between SWI and HRCT in retinoblastoma are equal to or even better compared with T2*WI. Therefore, further studies with more patients are required to determine the diagnostic accuracy of SWI in the detection of microcalcifications in retinoblastoma.

Our study has some limitations. First, we did not perform histopathologic correlation to confirm the presence of calcifications in all eyes but only of SIVs for which a corresponding hyperattenuation on HRCT was lacking. However, the accuracy of CT in depicting calcifications in soft tissues is well-accepted, and

this technique was used as a reference in several studies in the past.^{5,11,21} Second, the lesions studied were all retinoblastomas, without a number of simulating lesions for comparison. It is thus impossible to determine whether the absence or theoretic absence of SIVs on T2*WI or SWI in simulating diseases can be a reliable parameter to narrow the differential diagnosis. Third, all included patients required enucleation, which resulted in selection bias because small tumors are usually treated with conservative (eye-sparing) treatment options. The amount of calcifications might be higher in larger tumors, which makes detection of calcification by CT and MR imaging easier. A potential reduction in sensitivity might become apparent for both techniques by adding smaller tumors.

We recommend further research on this topic, in which retinoblastoma and simulating lesions are studied with T2*WI or SWI to evaluate the presence of SIVs in these diseases. Ideally, these studies should include close correlation with histopathology to explore possible false-positive findings in simulating lesions. The small sample size of SWI studies in retinoblastoma is another limitation in our study. However, these initial positive findings warrant further research, especially because SWI, by including information provided by the phase images, has the potential to be a sensitive and specific technique for detecting or excluding calcifications in retinoblastoma.

CONCLUSIONS

Our study shows an excellent correlation between SIVs as detected on in vivo T2*WI or SWI sequences and calcifications on ex vivo HRCT in retinoblastoma. The combination of funduscopy, sonography, and high-resolution MR imaging with gradient-echo sequences should become the standard diagnostic approach for retinoblastoma and removes potentially harmful ionizing radiation from the study protocol.

Disclosures: Paolo Galluzzi—RELATED: Support for Travel to Meetings for the Study or Other Purposes: ODAS Foundation (from Italy to the Netherlands, for the European Retinoblastoma Imaging Collaboration meeting in Amsterdam).

REFERENCES

1. Levy J, Frenkel S, Baras M, et al. Calcification in retinoblastoma: histopathologic findings and statistical analysis of 302 cases. *Br J Ophthalmol* 2011;95:1145–50
2. Chung EM, Specht CS, Schroeder JW. From the archives of the AFIP: pediatric orbit tumors and tumorlike lesions—neuroepithelial lesions of the ocular globe and optic nerve. *Radiographics* 2007;27:1159–86
3. Saunders T, Margo CE. Intraocular medulloepithelioma. *Arch Pathol Lab Med* 2012;136:212–16
4. Roth DB, Scott IU, Murray TG, et al. Echography of retinoblastoma: histopathologic correlation and serial evaluation after globe-con-

5. serving radiotherapy or chemotherapy. *J Pediatr Ophthalmol Strabismus* 2001;38:136–43
5. Beets-Tan RG, Hendriks MJ, Ramos LM, et al. Retinoblastoma: CT and MRI. *Neuroradiology* 1994;36:59–62
6. Brenner D, Elliston C, Hall E, et al. Estimated risks of radiation-induced fatal cancer from pediatric CT. *AJR Am J Roentgenol* 2001;176:289–96
7. de Graaf P, Göricke S, Rodjan F, et al. Guidelines for imaging retinoblastoma: imaging principles and MRI standardization. *Pediatr Radiol* 2012;42:2–14
8. Lemke AJ, Kazi I, Mergner U, et al. Retinoblastoma: MR appearance using a surface coil in comparison with histopathological results. *Eur Radiol* 2007;17:49–60
9. Chavhan GB, Babyn PS, Thomas B, et al. Principles, techniques, and applications of T2*-based MR imaging and its special applications. *Radiographics* 2009;29:1433–49
10. Zulfiqar M, Dumrongpisutikul N, Intrapromkul J, et al. Detection of intratumoral calcification in oligodendrogliomas by susceptibility-weighted MR imaging. *AJNR Am J Neuroradiol* 2012;33:858–64
11. Galluzzi P, Hadjistilianou T, Cerase A, et al. Is CT still useful in the study protocol of retinoblastoma? *AJNR Am J Neuroradiol* 2009;30:1760–65
12. de Graaf P, van der Valk P, Moll AC, et al. Retinal dysplasia mimicking intraocular tumor: MR imaging findings with histopathologic correlation. *AJNR Am J Neuroradiol* 2007;28:1731–33
13. Mafee MF, Goldberg MF, Cohen SB, et al. Magnetic resonance imaging versus computed tomography of leukocoric eyes and use of in vitro proton magnetic resonance spectroscopy of retinoblastoma. *Ophthalmology* 1989;96:965–75
14. Fatemi-Ardekani A, Boylan C, Noseworthy MD. Identification of breast calcification using magnetic resonance imaging. *Med Phys* 2009;36:5429–36
15. Tsushima Y, Endo K. Hypointensities in the brain on T2*-weighted gradient-echo magnetic resonance imaging. *Curr Probl Diagn Radiol* 2006;35:140–50
16. Atlas SW, Grossman RI, Hackney DB, et al. Calcified intracranial lesions: detection with gradient-echo-acquisition rapid MR imaging. *AJR Am J Roentgenol* 1988;150:1383–89
17. Kvistad KA, Rydland J, Vainio J, et al. Breast lesions: evaluation with dynamic contrast-enhanced T1-weighted MR imaging and with T2*-weighted first-pass perfusion MR imaging. *Radiology* 2000;216:545–53
18. Löbel U, Sedlacik J, Sabin ND, et al. Three-dimensional susceptibility-weighted imaging and two-dimensional T2*-weighted gradient-echo imaging of intratumoral hemorrhages in pediatric diffuse intrinsic pontine glioma. *Neuroradiology* 2010;52:1167–77
19. Thamburaj K, Radhakrishnan VV, Thomas B, et al. Intratumoral microhemorrhages on T2*-weighted gradient-echo imaging helps differentiate vestibular schwannoma from meningioma. *AJNR Am J Neuroradiol* 2008;29:552–57
20. Gasparotti R, Pinelli L, Liserre R. New MR sequences in daily practice: susceptibility weighted imaging: a pictorial essay. *Insights Imaging* 2011;2:335–47
21. Brisse HJ, Guesmi M, Aerts I, et al. Relevance of CT and MRI in retinoblastoma for the diagnosis of postlaminar invasion with normal-size optic nerve: a retrospective study of 150 patients with histological comparison. *Pediatr Radiol* 2007;37:649–56

MR Imaging Features of Acute Mastoiditis and Their Clinical Relevance

R. Saat, A.H. Laulajainen-Hongisto, G. Mahmood, L.J. Lempinen, A.A. Aarnisalo, A.T. Markkola, and J.P. Jero

ABSTRACT

BACKGROUND AND PURPOSE: MR imaging is often used for detecting intracranial complications of acute mastoiditis, whereas the intratemporal appearance of mastoiditis has been overlooked. The aim of this study was to assess the imaging features caused by acute mastoiditis in MR imaging and their clinical relevance.

MATERIALS AND METHODS: Medical records and MR imaging findings of 31 patients with acute mastoiditis (21 adults, 10 children) were analyzed retrospectively. The degree of opacification in the temporal bone, signal and enhancement characteristics, bone destruction, and the presence of complications were correlated with clinical history and outcome data, with pediatric and adult patients compared.

RESULTS: Most patients had $\geq 50\%$ of the tympanic cavity and 100% of the mastoid antrum and air cells opacified. Compared with CSF, they also showed intramastoid signal changes in T1 spin-echo, T2 TSE, CISS, and DWI sequences; and intramastoid, outer periosteal, and perimastoid dural enhancement. The most common complications in MR imaging were intratemporal abscess (23%), subperiosteal abscess (19%), and labyrinth involvement (16%). Children had a significantly higher prevalence of total opacification of the tympanic cavity (80% versus 19%) and mastoid air cells (90% versus 21%), intense intramastoid enhancement (90% versus 33%), outer cortical bone destruction (70% versus 10%), subperiosteal abscess (50% versus 5%), and perimastoid meningeal enhancement (80% versus 33%).

CONCLUSIONS: Acute mastoiditis causes several intra- and extratemporal changes on MR imaging. Total opacification of the tympanic cavity and the mastoid, intense intramastoid enhancement, perimastoid dural enhancement, bone erosion, and extracranial complications are more frequent in children.

ABBREVIATIONS: AM = acute mastoiditis; SI = signal intensity; SNHL = sensorineural hearing loss

Acute mastoiditis (AM) is a complication of otitis media in which infection in the middle ear cleft involves the mucoperiosteum and bony septa of the mastoid air cells. It can be divided into coalescent and noncoalescent mastoiditis. In coalescent AM, infection causes osteolysis of the bony septa or cortical bone, which can further lead to intra- and extracranial complications.

AM diagnosis is usually based on clinical findings, with imaging useful for detecting complications or ruling out other disease

entities mimicking AM.^{1,2} Treatment is mainly conservative, with mastoidectomy reserved for those with complications or no response to adequate antimicrobial treatment.^{3,4} However, generally accepted guidelines for the treatment of AM are lacking, and treatment algorithms vary by institution.

CT is usually the initial technique of choice for imaging patients with AM. Intravenous contrast agent is advisable for better evaluation of perimastoid soft tissues and because some intracranial complications like venous sinus thrombosis are detectable only from contrast-enhanced images. MR imaging is mainly reserved for detection or detailed evaluation of intracranial complications or both.

While the usefulness of MR imaging in diagnosing intracranial AM spread has been demonstrated many times over,^{1,5-9} intratemporal findings of AM on MR imaging tend to be overlooked and information on their clinical relevance is scarce. Problems exist with overdiagnosing “mastoiditis” on MR imaging if it is based on intramastoid fluid signal alone.^{10,11} Because MR imaging use in clinical practice is increasing, precise information on

Received April 24, 2014; accepted after revision August 7.

From the Department of Radiology, HUS Medical Imaging Center (R.S., G.M., A.T.M.), and Department of Otorhinolaryngology and Head and Neck Surgery (A.H.L.-H., L.J.L., A.A.A., J.P.J.), Helsinki University Central Hospital and University of Helsinki, Helsinki, Finland; and Department of Radiology (R.S.), East Tallinn Central Hospital, Tallinn, Estonia.

The study was supported by the Helsinki University Central Hospital Research Funds.

Please address correspondence to Riste Saat, MD, Department of Radiology, HUS Medical Imaging Center, POB 340, Haartmaninkatu 4, HUS 00029 Helsinki, Finland; e-mail: riste.saat@hus.fi

<http://dx.doi.org/10.3174/ajnr.A4120>

Table 1: Distribution of intramastoid signal intensity and enhancement

	No.	No. of Patients per Category (Valid %)		
SI in T2 FSE and CISS		Isointense to CSF	Hypointense to CSF, hyperintense to WM	Iso- or hypointense to WM
CISS	25	1 (4)	14 (56)	10 (40)
T2 FSE	31	3 (10)	24 (77)	4 (13)
SI in T1 SE		Isointense to CSF	Hyperintense to CSF, not to WM	Hyperintense to WM
T1 SE	31	0 (0)	22 (71)	9 (29)
SI in DWI (<i>b</i> =1000)		Hypointense to WM	Isointense to WM	Hyperintense to WM
	27	2 (7)	9 (33)	16 (59)
SI in ADC		Not lowered	Lowered	
	26	10 (38)	16 (62)	–
Enhancement		None	Faint, thin	Intense, thick
	31	3 (10)	12 (39)	16 (52)

Note:—No. indicates the number of patients with a specific sequence available.

the spectrum of MR imaging features of AM is essential. Our aim was to describe MR imaging findings resulting from AM and to clarify their clinical relevance.

MATERIALS AND METHODS

Patients

All 153 patients with a discharge diagnosis of AM (International Classification of Diseases-10 code H70.0) in the Ear, Nose, and Throat Department of our institution (a tertiary referral center providing health care for approximately 1.5 million people) during a 10-year period (2003–2012) were retrospectively identified from the hospital data base. Based on recent reports,^{12,13} the diagnostic criteria for AM in our institution were the following: either intraoperatively proved purulent discharge or acute infection in the mastoid process, or findings of acute otitis media and at least 2 of these 6 symptoms: protrusion of the pinna, retroauricular redness, retroauricular swelling, retroauricular pain, retroauricular fluctuation, or abscess in the ear canal, with no other medical condition explaining these findings. Those with MR imaging of the temporal bones available (*n* = 34) were selected for this study. We excluded 3 patients: 1 with recurrent disease after previous mastoidectomy, 1 with secondary inflammation due to an underlying tumor, and 1 in whom an intraoperative biopsy revealed middle ear sarcoidosis. The final analysis covered 31 patients. The study protocol was approved by the institutional ethics committee.

Clinical Data

Clinical data were collected from electronic patient records and consisted of the following variables: age and sex, side of the AM, duration of symptoms, duration of intravenous antibiotic treatment, presence or absence of retroauricular signs of infection (redness, swelling, pain, fluctuation, protrusion of the pinna), sensorineural hearing loss (SNHL), decision for operative treatment, mastoidectomy, and duration of hospitalization.

MR Imaging Protocol

MR imaging examinations were performed on a 1.5T unit (Magnetom Avanto; Siemens, Erlangen, Germany) with a 12-channel head and neck coil in 30 patients and on a 3T unit (Achieva; Philips Healthcare, Best, Netherlands) with an 8-channel head coil in 1 patient. The standard MR imaging protocol for mastoiditis consisted of axial and coronal T2 FSE and axial T1 spin-echo images, axial EPI DWI (*b* factors of 0 and 1000 s/mm²) and an

ADC map with 3-mm section thickness, high-resolution T2-weighted CISS images with 0.7-mm section thickness, and T1 MPRAGE images after intravenous administration of 0.1 mmol/kg of body weight of gadoterate meglumine (Dotarem; Guerbet, Aulnay-sous-Bois, France), obtained in the sagittal plane and reconstructed as 1-mm sections in axial and coronal planes.

Image Interpretation

The MR images were independently analyzed for their consensus diagnosis by 2 board-certified radiologists (R.S. and G.M. with 6 and 3 years of experience in reading temporal bone MR images and each holding a Certificate of Added Qualification in, respectively, head and neck radiology and neuroradiology). For every patient, only 1 ear was evaluated. In the 1 case with bilateral mastoiditis, only the first-involved ear was included.

Opacification degree in the tympanic cavity, mastoid antrum, and mastoid air cells; signal intensity in T1 spin-echo, T2 FSE, CISS, and DWI (*b*=1000); and intramastoid enhancement were recorded and scored into 3–4 categories of increasing severity by the principles shown in Table 1 and Fig 1. The following imaging findings were reported as being either present or absent: drop in signal intensity on the ADC map, blockage of the aditus ad antrum, bone destruction, signs of intratemporal abscess, signs of inflammatory labyrinth involvement, enhancement of the outer periosteum, perimastoid dural enhancement, epidural abscess, subperiosteal abscess, subdural empyema, generalized pachymeningitis, leptomeningeal enhancement, soft-tissue abscess, or sinus thrombosis.

Mastoid pneumatization is variable among patients and its contents inhomogenous, making objective signal intensity (SI) measurements complicated. Therefore, the intramastoid MR imaging SI was evaluated subjectively from the most abnormal regions in comparison with the SI of cerebellar WM in the same image and with the CSF in the location with no pulsation artifacts. It was scored according to the highest on T1WI and DWI (*b*=1000) or the lowest on T2WI detectable SI that involved a substantial part of the mastoid process. Additionally, ADC values were subjectively estimated as being either lowered or not lowered.

Destruction of bony structures was estimated from T2 FSE images as loss of morphologic integrity of bony structures or clear signal transformation inside the otherwise signal-voided cortical bone. This was evaluated at 3 subsites: the intercellular

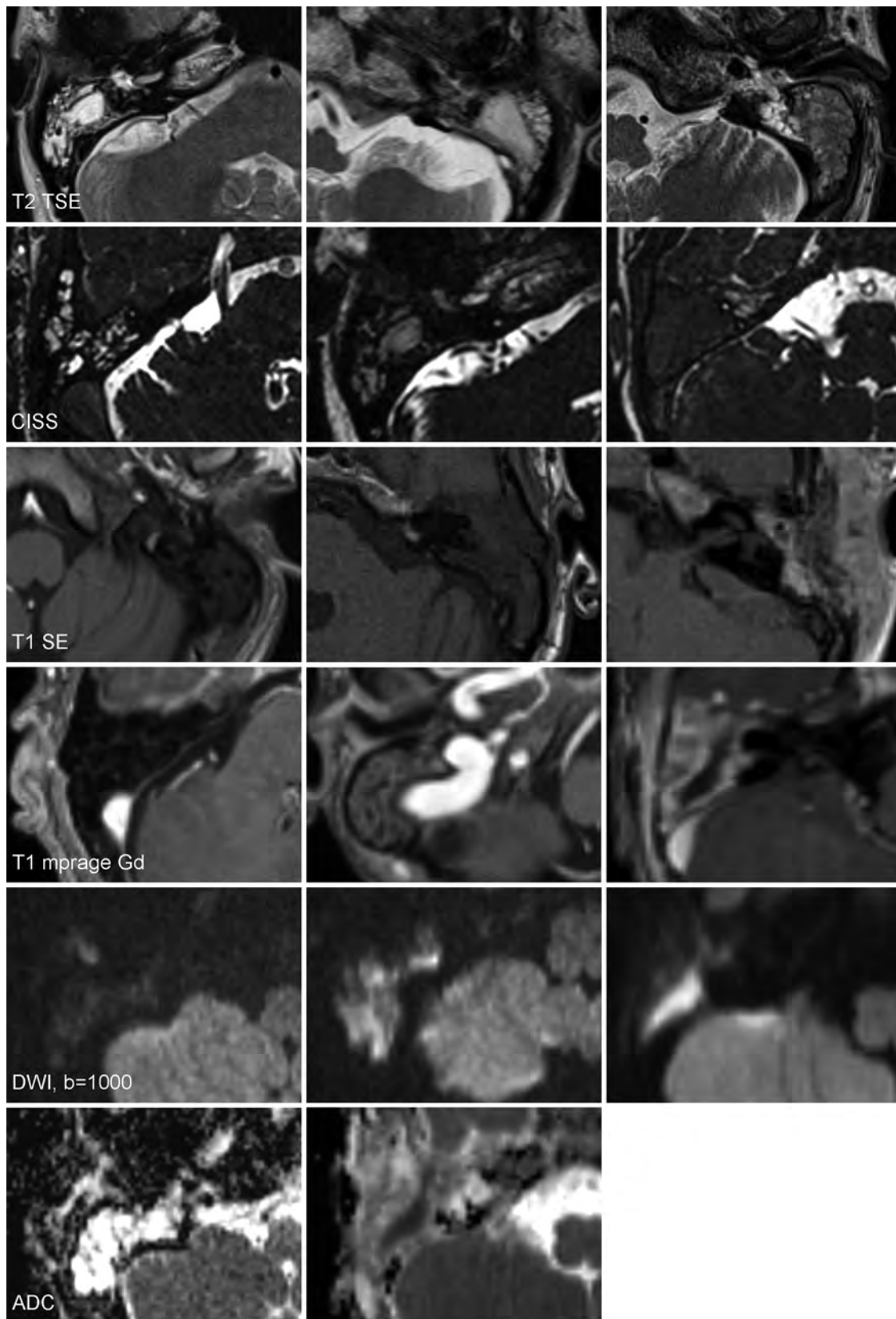


FIG 1. Image examples of each scoring category according to signal intensities. Categories are displayed in columns from left to right in increasing severity.

bony septa of the mastoid, inner cortical bone toward the intracranial space, and outer cortical bone toward the extracranial soft tissues.

Blockage of the aditus ad antrum was defined as filling of the aditus lumen by enhanced tissue. Signs of inflammatory labyrinth involvement were either diffuse intralabyrinthine en-

hancement or perilymph signal drop in CISS. Intratemporal abscess was defined as a nonanatomic cavity inside the temporal bone with an enhanced wall and marked diffusion restriction inside it. Criteria for generalized pachymeningitis (in contrast to perimastoid dural enhancement) were extensive thickening and enhancement of the dura that extended past the borders of the temporal bone.

Statistical Analysis

Due to the relatively small number of patients, the original MR imaging scoring groups were dichotomized by summation of the original scoring groups into groups of comparable sizes before statistical analysis. Associations between dichotomized MR imaging findings and background or outcome parameters were determined with the Fisher exact test for categorical data and the Mann-Whitney *U* test for numeric data. Clinical aspects and imaging findings between pediatric and adult patient groups were compared with the Fisher exact test. Statistical analysis was conducted by a biostatistician with NCSS 8 software (NCSS, Kaysville, Utah). A *P* value of $< .05$ was considered statistically significant.

RESULTS

Patients and Clinical Data

Thirty-one patients were analyzed (11 male and 20 female); mean age, 33.4 years (range, 3–81 years). Age distribution showed 2 peaks between 10 and 20 and between 40 and 50 years. Pediatric patients (16 years of age or younger) numbered 10.

The average duration of symptoms before MR imaging was 12.9 days (range, 0–90 days). Classic retroauricular signs of mastoid infection were present in 18 patients (58%); and SNHL in 15 (48%). Intravenous antibiotics had been initiated for at least 24 hours before MR imaging in 18 patients (58%); and the mean duration of this treatment was 2.8 days (range, 0–22 days).

Operative treatment was chosen for 20 patients (65%), and mastoidectomy was performed for 19 (61%) because of parent refusal in 1 patient.

The average length of hospitalization was 6.7 days (range, 1–26 days). Six patients had recurrent symptoms within the 3-month follow-up.

MR Imaging Findings

Opacification of the Middle Ear and Mastoid. Most patients had at least a 50% opacification in the tympanic cavity and total opacification of the mastoid antrum and air cells (Fig 2). A significant correlation appeared between $\geq 50\%$ opacification in the tympanic cavity and longer intravenous antibiotic treatment (mean, 5.0 versus 2.0 days; $P = .031$).

Intramastoid Signal Intensities. Findings regarding intramastoid signal intensities are demonstrated in Table 1. On T2 FSE, among 31 patients, the SI was hypointense to CSF in 28 (90%) and iso- or hypointense to WM of the brain in 4 (13%). On CISS, among 25 patients, SI was hypointense to CSF in 24 (96%) and iso- or hypointense to WM in 10 (40%). On unenhanced T1 spin-echo, SI was hyperintense to CSF in all 31 patients and hyperintense to

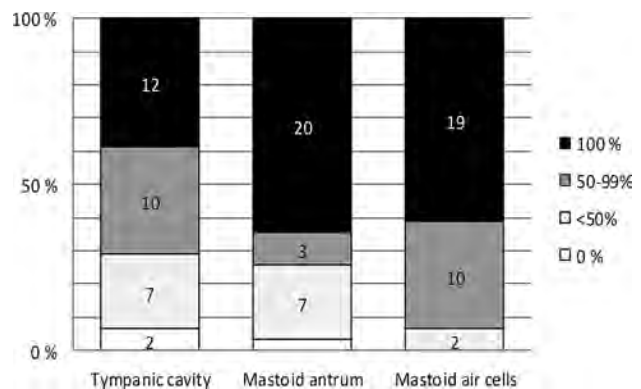


FIG 2. Obliteration degree in different temporal bone subregions ($n = 31$).

WM in 9 (29%). On DWI ($b=1000$), among 27 patients, SI was iso- or hyperintense to WM in 25 (93%) and hyperintense to WM in 16 (59%). Lowered SI in the ADC was detectable in 16 of 26 patients (62%). Hyperintense-to-WM SI in DWI was associated with a shorter duration of intravenous antibiotic treatment (mean, 1.9 versus 5.0 days; $P = .029$).

Enhancement Characteristics. Intramastoid enhancement was detectable in 28 patients (90%) and was thick and intense in 16 (52%) (Fig 3). Intense enhancement was associated with younger age (mean, 24.6 versus 42.7 years; $P = .019$). Enhancement of the outer periosteum occurred in 21 patients (68%); and perimastoid dural enhancement, in 15 (48%). Outer periosteal enhancement correlated with shorter duration of symptoms (7.1 versus 25.1 days, $P = .009$). Obliteration of the aditus ad antrum by enhanced tissue was detected in 11 patients (36%).

Bone Destruction. Destruction of the intramastoid bony septa was suspected in 11 (35%); of inner cortical bone, in 4 (13%); and of outer cortical bone, in 9 (29%) patients. Destruction of outer cortical bone was associated with younger age (mean, 34.0 versus 48.7 years; $P = .004$), shorter duration of symptoms before MR imaging (mean, 11.0 versus 24.5 days; $P = .031$), and the presence of retroauricular signs of infection ($P = .045$).

Complications. Intratemporal and extracranial complications predominated over intracranial complications (Table 2). Intratemporal abscess formation was suspected in 7 patients (23%). Subperiosteal abscesses were detectable in 6 (19%) and were correlated with younger age (mean, 6.0 versus 25.0 years; $P = .010$) and with retroauricular signs of infection ($P = .028$). Labyrinth involvement was detectable in 5 patients (16%). The prevalence of other complications was low in our cohort: 2 (7%) with epidural abscess, generalized pachymeningitis, leptomeningitis, or soft-tissue abscess; 1 (3%) with sinus thrombosis; and none with subdural empyema.

Outcome. Opacification of the tympanic cavity of 100% was associated positively with the decision for operative treatment ($P = .020$).

All patients with labyrinth involvement on MR imaging had SNHL ($P = .043$). Additionally, SNHL was associated with obliteration of the aditus ad antrum by enhanced tissue ($P = .023$) and outer cortical bone destruction ($P = .015$).

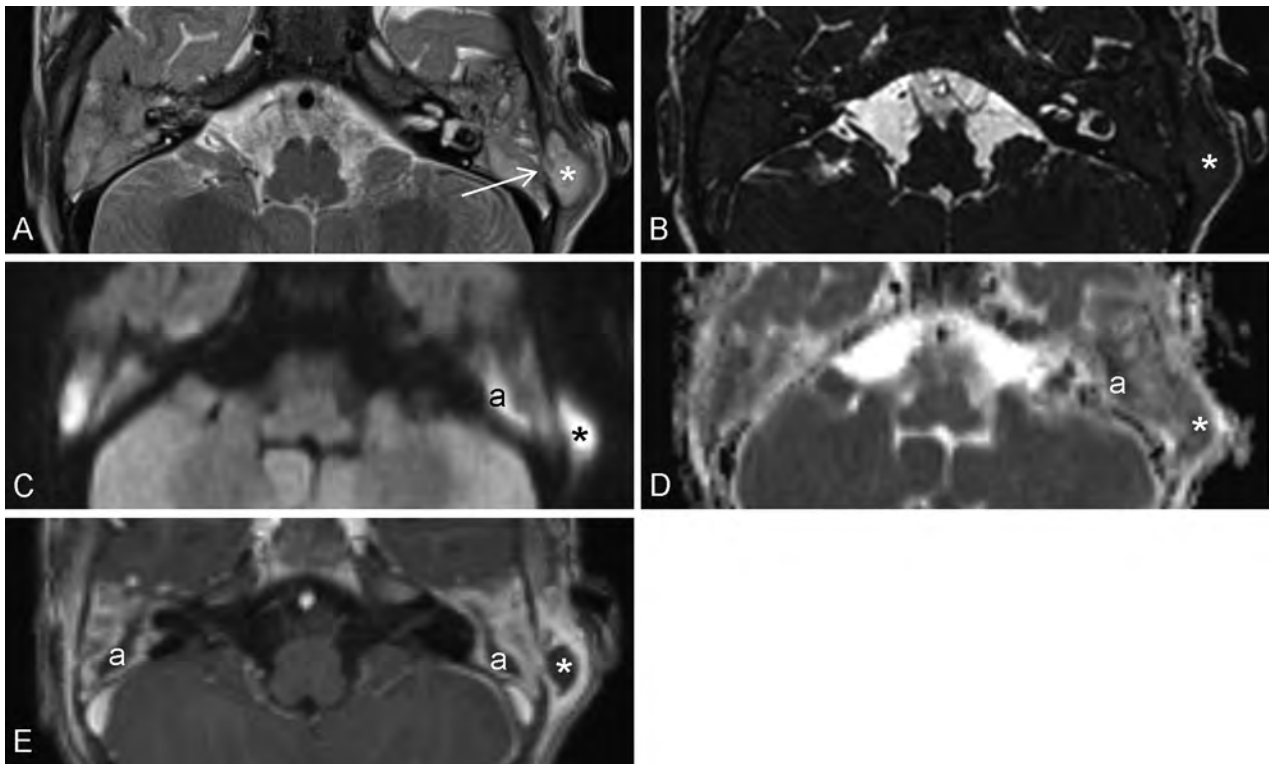


FIG 3. MR images of bilateral AM with duration of symptoms of 12 days on the left and fewer than 6 days (3–6 days) on the right side. T2 FSE image (A) shows total obliteration of middle ear and mastoid air spaces. SI is comparable with that of brain parenchyma. Especially on the right side, delineation of intramastoid bony septa is no longer detectable. On the left, outer cortical bone is destroyed (*arrow*) with subperiosteal abscess formation (*asterisk*). Intramastoid signal decrease, compared with CSF, becomes even more evident in CISS (B). In postgadolinium T1 MPRAGE (E), intense, thick enhancement surrounds the fluid-filled mastoid antra (a) and fills the peripheral mastoid cells. On the left, intense soft-tissue enhancement around the subperiosteal abscess and, on the right, periosteal enhancement surrounding the mastoid are visible. DWI $b=1000$ (C) and ADC (D) show diffusion restriction in the whole mastoid region bilaterally with foci of markedly elevated SI inside both antra (a) and the left subperiosteal abscess (*asterisk*).

Table 2: Prevalence of AM complications detected on MRI (N = 31)

Complication	No. (%)		
	All	Children	Adults
Septal destruction	11 (35)	5 (45)	6 (30)
Inner cortical bone destruction	4 (13)	2 (18)	2 (10)
Outer cortical bone destruction	9 (29)	7 (64) ^a	2 (10) ^a
Intratemporal abscess	7 (23)	3 (27)	4 (20)
Subperiosteal abscess	6 (19)	5 (45) ^a	1 (5) ^a
Labyrinth involvement	5 (16)	0 (0)	5 (25)
Epidural abscess	2 (6)	2 (18)	0 (0)
Soft-tissue abscess	2 (6)	1 (9)	1 (5)
Generalized pachymeningitis	2 (6)	1 (9)	1 (5)
Leptomeningitis	2 (6)	1 (9)	1 (5)
Sinus thrombosis	1 (3)	1 (9)	0 (0)
Subdural empyema	0 (0)	0 (0)	0 (0)

^a Significant differences between adult and pediatric subgroups ($P < .05$).

Pediatric versus Adult Patients. In pediatric patients, a significantly higher prevalence of total opacification occurred in the tympanic cavity (80% versus 19%, $P = .002$) and mastoid air cells (90% versus 21%, $P = .046$). Children more frequently showed intense intramastoid enhancement (90% versus 33% $P = .006$), enhancement of the perimastoid dura (80% versus 33%, $P = .023$), possible outer cortical bone destruction (70% versus 10%, $P = .001$), and subperiosteal abscess (50% versus 5%, $P = .007$). Accordingly, among children, the prevalence of retroauricular signs of infection was also higher (90% versus 43%, $P = .020$).

DISCUSSION

Imaging plays an important role in AM diagnostics, especially in complicated cases. The imaging technique of choice usually is CT for its sensitivity in detecting opacification and bone destruction. Its capability to differentiate among causes of opacification is poor.

In comparison with CT, MR imaging performs better in differentiating among soft tissues and in showing juxtaosseous contrast medium uptake, due to the natural MR signal void in bone. In the context of AM, evidence indicates the superiority of MR imaging over CT in the detection of labyrinth involvement and intracranial infection.^{1,6,14} Little focus has, however, been on intratemporal MR imaging findings, with most reports only of intramastoid high signal intensity on T2WI, reflecting fluid retention—a finding evidently nonspecific and leading to mastoiditis overdiagnosis.^{10,11}

During mastoiditis, variable signal intensities of retained fluid and intratemporal enhancement can appear, explained by desiccation of fluids and overgrowth of granulation tissue, especially under chronic conditions.⁸ According to Platzek et al¹⁵ (2014) a sensitivity of 100% and specificity of 66% in diagnosing AM are possible, with ≥ 2 of these intramastoid findings: fluid accumulation, enhancement, or diffusion restriction. In most of our patients with AM, $>50\%$ opacification of air spaces occurred in all temporal bone subregions (Fig 2). Total opacification of the tym-

panic cavity was the only imaging finding significantly associated with treatment options. Although opacification degree in the tympanic cavity usually was lower than that in the distal parts of the temporal bone, when 100%, it indicated a decision to perform surgery. All our patients had, before the MR imaging, either existing tympanic membrane perforation or myringotomy or a tympanostomy tube in place. In patients with an intact tympanic membrane, opacification of the tympanic cavity may have a different prognostic impact.

Trends toward predicting operative treatment were also detectable in regard to total opacification of mastoid air cells ($P = .056$) and thick and intense intramastoid enhancement ($P = .066$). In larger cohorts, these may still prove valuable markers of severe disease.

In most patients ($\geq 90\%$), intramastoid signal intensity on T2 TSE and even more on CISS was lower than that of CSF and even reached the values of the white matter SI (Table 1), most likely due to the increased protein content of the obliterating material. On T1WI, SI of the intramastoid substance, in comparison with CSF, was increased in all patients.

In some patients, marked signal changes and intense intramastoid enhancement were detected early in AM, even on the second symptomatic day, and therefore cannot be related to chronic conditions only.⁸

DWI was included in our protocol to detect purulent secretions and possible intratemporal abscesses.¹⁶⁻²⁰ On DWI, most patients (93%) showed variable degrees of signal increase in their mastoid effusions (Table 1). Nearly two-thirds (59%) had intramastoid signal intensity higher than that in their brain parenchyma on DWI and low signal on ADC, confirming the true diffusion restriction.

In contrast to cholesteatoma, diffusion restriction in AM is usually more diffuse.²¹ In cases of cholesteatoma underlying mastoiditis or in mastoiditis complicated by intratemporal abscess, difficulties may arise, calling for either surgical exploration or follow-up imaging. Differentiation among cholesteatoma, infected cholesteatoma, and intratemporal abscess may be possible, based on their ADC values, though large-study evidence is still lacking.²²

Imaging findings associated with either a clinically rapid course and shorter duration of symptoms or shorter duration of IV antibiotic treatment before MR imaging were outer periosteal enhancement, destruction of outer cortical bone, and hyperintense-to-WM SI on DWI. Outer cortical destruction and subperiosteal abscesses were associated with clinical signs of retroauricular infection.

Compared with adults, children, especially at a younger age (younger than 2 years) generally tend to develop so-called classic AM—usually of short duration and rapid course, with distinct clinical symptoms and signs.^{12,13} Our pediatric patients more often showed total opacification of the tympanic cavity and mastoid, strong intramastoid enhancement, outer cortical bone destruction, and subperiosteal abscesses. Intracranial complications were no more numerous among children when compared with adults, but these were very rare in each subgroup.

Our limitations are the small size and inhomogeneity of the patient cohort. For patients with AM, MR imaging was performed

rarely, usually for severe disease or unsatisfactory treatment response. Our imaging series thus does not reflect the average AM population. It includes both hyperacute cases and patients with a longer history and antibiotic treatment for variable durations. Drawing firm conclusions regarding the prognostic value of these MR imaging findings is thus difficult.

Traditionally in our institution, imaging was performed to confirm suspicion of AM complications necessitating surgery. In other circumstances, treatment decisions were based solely on clinical evidence of progressive disease, failure to respond to IV antibiotics within 48 hours, or underlying cholesteatoma.²³

In clinical practice, contrast-enhanced CT is still the preferable, first-line imaging technique due to better availability in urgent situations. Otolologists are more familiar with CT images as their preoperative map. In addition to detecting intracranial complications, MR imaging could be recommended for pediatric patients due to its lack of ionizing radiation. In young children, however, CT may be preferred over MR imaging when anesthesia is inadvisable. MR imaging provides an alternative diagnostic tool for patients with contraindications for contrast-enhanced CT and could benefit decision-making concerning surgery in conservatively treated patients with insufficient clinical response.

Thus far, radiologic markers for aggressive AM have been either bone destruction in CT or intra- and extracranial complications. Now MR imaging provides additional imaging markers reflecting soft-tissue reaction to infection: major intramastoid signal changes; diffusion restriction; or intramastoid, periosteal, or dural enhancement. These may serve in the assessment of AM severity. Their accuracy in detecting clinically relevant AM and their true prognostic value remain to be clarified by larger studies.

CONCLUSIONS

Acute mastoiditis causes several intra- and perimastoid changes visible on MR imaging, with $>50\%$ opacification of air spaces, non-CSF-like signal intensity of intramastoid contents, and intramastoid and outer periosteal enhancement detectable in most patients. In children, total opacification of the tympanic cavity and mastoid, intense intramastoid enhancement, perimastoid dural enhancement, bone erosion, and extracranial complications are more frequent.

ACKNOWLEDGMENTS

The authors thank Timo Pessi, MSc, for his assistance with statistics and Carolyn Brimley Norris, PhD, for her linguistic expertise.

Disclosures: Anu H. Laulajainen-Hongisto—RELATED: Grant: Helsinki University Central Hospital (research funds); Support for Travel to Meetings for the Study or Other Purposes: Finnish Society of Ear Surgery, Comments: Politzer Society meeting. Jussi P. Jero—RELATED: Grant: Helsinki University Hospital.* *Money paid to the institution.

REFERENCES

1. Minks DP, Porte M, Jenkins N. **Acute mastoiditis: the role of radiology.** *Clin Radiol* 2013;68:397–405
2. Psarommatas IM, Voudouris C, Douros K, et al. **Algorithmic management of pediatric acute mastoiditis.** *Int J Pediatr Otorhinolaryngol* 2012;76:791–96
3. Bakhos D, Trijolet J, Morniere S, et al. **Conservative management of acute mastoiditis in children.** *Arch Otolaryngol Head Surg* 2011;137:346–50

4. Chesney J, Black A, Choo D. **What is the best practice for acute mastoiditis in children?** *Laryngoscope* 2014;124:1057–58
5. Luntz M, Bartal K, Brodsky A, et al. **Acute mastoiditis: the role of imaging for identifying intracranial complications.** *Laryngoscope* 2012;122:2813–17
6. Dobben GD, Raofi B, Mafee MF, et al. **Otogenic intracranial inflammations: role of magnetic resonance imaging.** *Top Magn Reson Imaging* 2000;11:76–86
7. Hughes DC, Raghavan A, Mordekar SR, et al. **Role of imaging in the diagnosis of acute bacterial meningitis and its complications.** *Postgrad Med J* 2010;86:478–85
8. Maroldi R, Farina D, Palvarini L, et al. **Computed tomography and magnetic resonance imaging of pathologic conditions of the middle ear.** *Eur J Radiol* 2001;40:78–93
9. Vazquez E, Castellote A, Piqueras J, et al. **Imaging of complications of acute mastoiditis in children.** *Radiographics* 2003;23:359–72
10. Polat S, Aksoy E, Serin GM, et al. **Incidental diagnosis of mastoiditis on MRI.** *Eur Arch Otorhinolaryngol* 2011;268:1135–38
11. Meredith J, Boyev K. **Mastoiditis on MRI: fact or artifact?** *Ear Nose Throat J* 2008;87:514–18
12. Groth A, Enoksson F, Hultcrantz M, et al. **Acute mastoiditis in children aged 0–16 years: a national study of 678 cases in Sweden comparing different age groups.** *Int J Pediatr Otorhinolaryngol* 2012;76:1494–500
13. Stalfors J, Enoksson F, Hermansson A, et al. **National assessment of validity of coding of acute mastoiditis: a standardised reassessment of 1966 records.** *Clin Otolaryngol* 2013;38:130–35
14. Kuczkowski J, Dubaniewicz-Wybieralska M, Przewozny T, et al. **Otitic hydrocephalus associated with lateral sinus thrombosis and acute mastoiditis in children.** *Int J Pediatr Otorhinolaryngol* 2006;70:1817–23
15. Platzek I, Kitzler H, Gudziol V, et al. **Magnetic resonance imaging in acute mastoiditis.** *Acta Radiol Short Rep* 2014;3:2047981614523415
16. Schaefer PW. **Applications of DWI in clinical neurology.** *J Neurol Sci* 2001;186(suppl 1):S25–35
17. Lai PH, Ho JT, Chen WL, et al. **Brain abscess and necrotic brain tumor: discrimination with proton MR spectroscopy and diffusion-weighted imaging.** *AJNR Am J Neuroradiol* 2002;23:1369–77
18. Mukherji SK, Chenevert TL, Castillo M. **Diffusion-weighted magnetic resonance imaging.** *J Neuroophthalmol* 2002;22:118–22
19. Stadnik TW, Chaskis C, Michotte A, et al. **Diffusion-weighted MR imaging of intracerebral masses: comparison with conventional MR imaging and histologic findings.** *AJNR Am J Neuroradiol* 2001;22:969–76
20. Unal O, Koparan HI, Avcu S, et al. **The diagnostic value of diffusion-weighted magnetic resonance imaging in soft tissue abscesses.** *Eur J Radiol* 2011;77:490–94
21. Vercruyse JP, De Foer B, Pouillon M, et al. **The value of diffusion-weighted MR imaging in the diagnosis of primary acquired and residual cholesteatoma: a surgical verified study of 100 patients.** *Eur Radiol* 2006;16:1461–67
22. Thariat S, Riehm S, Kremer S, et al. **Apparent diffusion coefficient values of middle ear cholesteatoma differ from abscess and cholesteatoma admixed infection.** *AJNR Am J Neuroradiol* 2009;30:1123–26
23. Leskinen K, Jero J. **Acute complications of otitis media in adults.** *Clin Otolaryngol* 2005;30:511–16

Standardization of CT Depiction of Cochlear Implant Insertion Depth

C.C. Colby, N.W. Todd, H.R. Harnsberger, and P.A. Hudgins

ABSTRACT

BACKGROUND AND PURPOSE: Imaging a cochlear implant with CT is challenging because of implant-induced artifacts, anatomic cochlear variations, and lack of standard terminology for cochlear anatomy. The purposes of this project were to determine whether the cochlear implant tip was more accurately located on oblique CT reformations than on standard images, to review radiology reports for accurate cochlear implant locations, and to assess agreement between an implant surgeon and neuroradiologist by using standardized cochlear anatomy terminology for cochlear implant depth.

MATERIALS AND METHODS: In this retrospective study, a neuroradiologist and an implant surgeon independently viewed temporal bone CT images of 36 ears with cochlear implants. Direct axial images, standard coronal reformations, and oblique reformations parallel to the cochlea were compared to determine implant tip location, which was described by using a proposed standardized quadrant terminology. Implant locations were compared with the initial formal report generated by the original interpreting neuroradiologist.

RESULTS: Thirty-six temporal bones with cochlear implants underwent CT interpretation for implant location. Interobserver agreement was similar when comparing cochlear implant tip location by using a quadrant nomenclature on axial and coronal images and on oblique reformations. Clinical radiology reports all were imprecise and ambiguous in describing the location of the cochlear implant tip.

CONCLUSIONS: Accurate determination of insertion depth of the cochlear implant array can be determined by assessment of the implant tip on axial, coronal, and oblique CT images, but description of the tip location can be inaccurate due to lack of standardized terminology. We propose using a standardized terminology to communicate tip location by using the round window as the zero reference and quadrant numbering to describe cochlear turns. This results in improvement in radiology report accuracy and consistency regarding the cochlear implant insertion depth.

ABBREVIATION: CI = cochlear implant

Imaging of the cochlea is difficult due to its small size, oblique axis, and anatomic variations within the temporal bone. When a cochlear implant (CI) is in place, CT can be especially difficult because of artifacts from the implant. Furthermore, the absence of standard cochlear turn nomenclature renders radiology reports

regarding CI insertion depth difficult to understand. Anatomic descriptions of the cochlea vary throughout the basic science, radiology, pathology, and otolaryngology literature. Otolaryngology textbooks typically describe a basal turn, medial turn, and apical turn, but cochlear turn language is not standardized across all texts. Occasionally angle degrees, assuming 360° in a circle, are used as a descriptor for the multiple turns, with the round window niche as the zero-degree reference.¹

It is important to be able to describe the CI tip location because electrode-array insertion depth and location are relevant factors when considering hearing and speech outcomes following CI insertion.¹⁻⁴ Audiologic outcomes are better when the electrode array is inserted into the scala tympani, allowing better stimulation of the spiral ganglion neural elements. Multidetector CT can detect the scala tympani in cadaveric specimens,⁵ but application to routine clinical postimplantation imaging is limited. Multiple imaging methods have been used to determine CI electrode depth

Received September 23, 2013; accepted after revision July 30, 2014.

From the Department of Otolaryngology and Head and Neck Surgery (C.C.C.), University of Minnesota, Minneapolis, Minnesota; Department of Otolaryngology and Head and Neck Surgery (N.W.T.), and Head and Neck Imaging Section (P.A.H.), Department of Radiology and Imaging Sciences, Emory University School of Medicine, Atlanta, Georgia; and Division of Neuroradiology (H.R.H.), Department of Radiology, University of Utah School of Medicine, Salt Lake City, Utah.

Preliminary data previously presented as a poster at: Annual Meeting of the Triologic Society at Combined Otolaryngology Spring Meetings, April 28–30, 2011; Chicago, Illinois.

Please address correspondence to Patricia A. Hudgins, MD, Department of Radiology and Imaging Sciences, Emory University Hospital, 1364 Clifton Rd, NE, Atlanta, GA 30322; e-mail: phudgin@emory.edu

<http://dx.doi.org/10.3174/ajnr.A4105>

postoperatively, including conventional radiology,⁴ fluoroscopy,³ conebeam CT,⁶ fusion of conventional radiography and CT images,⁷ and multidetector CT.^{5,8} Lecerf et al⁹ showed that midmodiolar reconstructed CT on cadaver temporal bones can be used as an effective method for neuroradiologists to assess the location of CIs in either the scala vestibuli or scala tympani with high sensitivity and specificity. Ideally, the radiology report would routinely include objective measures of the CI tip insertion depth and a scalar chamber assignment so that these can be compared against the clinically desired position of the electrode tip.

In 2010, a consensus panel comprising radiologists, otologists, and researchers developed a cochlear coordinate system¹⁰ to have an objective method for comparing study and research outcomes by using a standard description of the cochlea. The consensus terminology developed for describing cochlear anatomy uses the round window as the zero-degree point.¹¹ This 3D cylindrical coordinate system uses the basal turn of the cochlea as the x and y planes and the center of the modiolus as the z-axis, with the zero-degree point described as the round window.

In our experience, this standard description of cochlear anatomy is not routinely used in the radiology report and, in fact, has not been emphasized in the radiology scientific literature. The lack of standard terminology when describing cochlear anatomy makes it nearly impossible to know from reading a radiology report how far the electrode array extends into the cochlea. Current clinical reports from radiologists often ambiguously describe how far the electrode array extends into the cochlea, and they lack consistent descriptions of the cochlea and implant array from one radiologist to the next.

We had 3 goals: first, to determine whether the CI tip was more accurately determined on direct axial images, standard coronal reformations, or oblique CT reformations obtained parallel to the basal portion of the first cochlear turn; second, to review the formal CT interpretations to see whether the CI tip location was accurately reported; and third, to assess agreement between an implant surgeon and neuroradiologist when asked to identify the CI-array depth by using the 2010 consensus terminology.

MATERIALS AND METHODS

This institutional review board–approved retrospective study included children younger than 18 years of age with CIs who underwent CT of the temporal bones during a 5-year period. Thirty-six temporal bones (33 children) with CIs were identified. Eighteen of the patients were male; 15 were female. The average age at the time of CT imaging was 8.4 years (range, 16 months to 16 years). The imaging was performed, on average, 3 years following implantation, with a range of 11 months to 11 years. Most of the implants were Cochlear Corporation devices (Englewood, Colorado) (25/36), with the remaining being MED-EL (Durham, North Carolina) (6/36) and Advanced Bionics (Valencia, California) (5/36) devices.

All patients included had undergone cochlear implantation for bilateral sensorineural hearing loss and were included regardless of cochlear anatomy. All CIs had been placed through a standard posterior tympanotomy, either through the round window or within millimeters of the round window. All had complete insertion achieved. The children underwent CT of the temporal bone due to concern for implant function or in preparation for

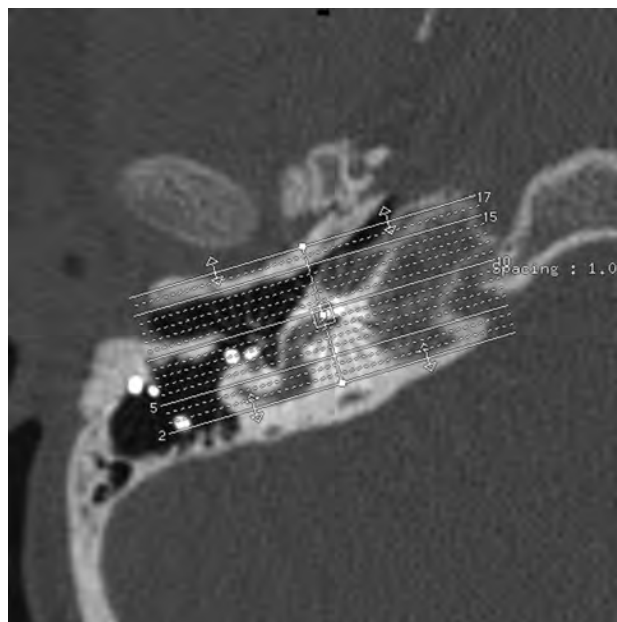


FIG 1. Oblique reformations along the plane of quadrant I. Axial CT, right temporal bone, through the first cochlear turn, quadrant I, showing the slab thickness for oblique reformations.

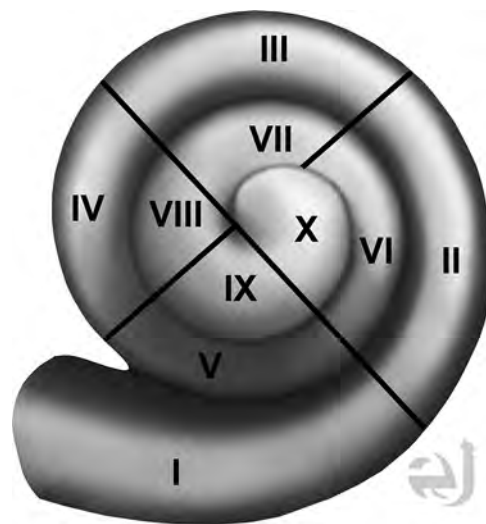


FIG 2. Drawing of the cochlea with quadrants numbered. Drawing of all cochlear turns, with the quadrants numbered I–X. Use of this approach in reporting the CI tip will standardize discussion of implant tip location. Courtesy of Eric Jablonowski, medical illustrator.

contralateral implantation. Images were obtained without intravenous contrast in the axial plane from immediately beneath the mastoid tip to the top of the petrous apex (110 kV[peak]; 120 mA; FOV, 17–18 cm; 0.625-mm section thickness). Axial source images were used to reconstruct coronal and oblique (along the plane of the basal portion of the first turn of the cochlea, Fig 1) CT images. If multiple scans were obtained in the study period, only the most recent imaging was used for study purposes. Exclusion criteria were imaging not performed at our tertiary care facility and images with motion artifacts precluding adequate reformations.

A neuroradiologist and an implant surgeon independently reviewed 3 sets of images: the axial images, coronal reformations, and oblique reformations along the plane of the basal portion of

the first cochlear turn. All images were interpreted on a PACS. Coronal reformations perpendicular to the axial images were performed by the CT technologist and were submitted directly to the PACS. The oblique reformations were created by the implant surgeon and the neuroradiologist, by using a postprocessing function of the workstation. Both readers were blinded to implant function and the implant tip location regarding the depth of the implant as described on surgical notes. The location of the implant position within the cochlea was described by using an approach based on consensus terminology for standard terms regarding cochlear anatomy.¹⁰ Results were recorded by using a 4-quadrant system for each 360° turn of the cochlea (noted as numerals I–X), with the round window as a zero-degree reference point (Fig 2). For exam-

ple, insertion into only the inferior quadrant of the first turn would be termed “quadrant I,” insertion into the inferior quadrant of the second turn would be termed “quadrant V,” and insertion into the posterior quadrant of the second turn would be termed “quadrant VIII” insertion. The data obtained were then compared with the original report that had been generated at the time of imaging by a neuroradiologist with a Certificate of Added Qualification. Interobserver agreement between the implant surgeon and neuroradiologist was determined for axial and coronal images, and for oblique reformations within the plane of the basal turn of the cochlea.

A consensus approach was used to resolve any cases in which the reading of the implant tip differed by >2 quadrants.

Statistical Analysis. Interobserver agreement was determined by using the Spearman rank correlation coefficient (Spearman *r*).

RESULTS

Interobserver agreement was excellent for the 3 planes assessed: axial, coronal, and oblique reformations (Fig 3). Interobserver agreements by expression of agreement among quadrants (Spearman *r*) are shown in Table 1. The implant surgeon’s and neuroradiologist’s readings did not differ by >2 quadrants in any given patient. Readings that differed were usually because the implant tip was near the interface between 2 quadrants.

Radiology reports for each CT study, written before the new consensus terminology, ambiguously described how far the electrode array extended into the cochlea. Examples of the description of the CI array from radiology reports are demonstrated in Table 2.

DISCUSSION

Using consensus terminology, we sought to evaluate agreement between an implant surgeon and neuroradiologist when asked to identify CI insertion depth. Interobserver agreement was excellent for direct axial and reformatted coronal planes and oblique reformations in the plane of the basal portion (quadrant I) of the first cochlear turn. Although CI tip location could be determined by using the axial and coronal planes, the oblique images reformatted in the plane of the basal portion of the first cochlear turn helped to confirm tip location, usually on a single image. Both the otologic surgeon and the neuroradiologist subjectively thought that the implant tip was easier and faster to determine on the oblique reformations, though this opinion was not objectively measured. We believe the use of standardized terminology allowed the observers to more accurately describe the location of the implant array and resulted in less uncertainty when describing cochlear anatomy.

Clinical radiology reports written without using consensus terminology have ambiguously described how far the

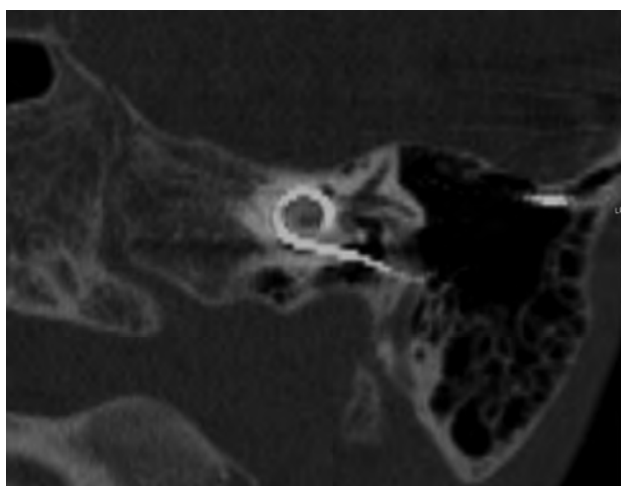


FIG 3. A 7-year-old boy with a left-sided cochlear implant. Single oblique reformation shows the CI tip in quadrant IV.

Table 1: Agreement about quadrant of cochlear implant depth in 36 ears (33 patients)

Agreement of Concern	Spearman <i>r</i>	Expression of Agreement			
		Same Quadrant	1-Quadrant Difference	2-Quadrant Difference	3-Quadrant Difference
Rdr 1: axial-coronal vs reformatted images	.90, <i>P</i> < .001	21	13	2	0
Rdr 2: axial-coronal vs reformatted images	.89, <i>P</i> < .001	20	15	1	0
Rdr 1 vs 2: axial-coronal images	.88, <i>P</i> < .001	16	18	2	0
Rdr 1 vs 2: reformatted images	.90, <i>P</i> < .001	16	16	4	0

Note:—Rdr indicates reader.

Table 2: Examples from dictations by neuroradiologists interpreting temporal bone CT obtained for CI position

Examples
“Enters the cochlea at the basal turn via the cochlear promontory and extends to the apical half turn.”
“Left cochlear implant in place.”
“Implant lead then enters the round window, passes into the cochlea and terminates near the apical half turn.”
“Electrode intact and normal in course.”
“Electrode continues to the cochlea where it has appropriate turns.”
“Enters the basal turn of the cochlea, looping within the cochlea, and terminating near the apex.”
“It extends to, but does not go through, the aperture.”
“Through the round window and filling the basal and middle turns of the cochlea.”

electrode array extended into the cochlea (Table 2), making it nearly impossible for the reader to consistently determine the exact location of the CI insertion depth. The electrodes on the CI can often be seen and even counted on the CT scan, but it may be difficult to see each electrode, depending on the manufacturer. The CI tip, however, can always be appreciated on CT. The complex anatomy of the cochlea and individual differences in size, form, and location within the temporal bone often add to the level of difficulty in accurately describing the location of the electrode array. Most implant surgeons probably review the CT scans themselves, but a more accurate written interpretation in the medical record is obviously necessary.

Factors that affect CI function include both patient and implant variables. For example, the duration of hearing loss and the age of implantation are patient-related factors that affect CI outcomes.¹² While early research suggested that the depth of insertion of the CI was an important variable affecting function, more recent data show that consideration of depth alone is an oversimplification of assessing CI function. In fact, one article has shown poorer function as the depth of insertion increases.² Implant function may be affected by whether the implant is in the scala tympani, as opposed to the scala vestibuli or if it hugs the modiolus, as opposed to being lateral in the cochlea. High-resolution CT has been able to predict the scala location of the implant.^{5,9} Although this has been described in postmortem temporal bones on CT, it is possible that the scalar location will be routinely determined in vivo. Therefore, as understanding of variables affecting CI function progresses, imaging interpretation will likely go beyond simply describing the location of the implant tip.

Use of the consensus terminology enables multiple experienced viewers to communicate implant-array location with less ambiguity than previous methods.¹⁰ Throughout the literature, especially when comparing otolaryngologic and radiologic textbooks, descriptions of cochlear anatomy vary significantly. This variation is especially seen when the cochlea is malformed, without the usual number of turns. Our population did not include severely malformed cochleas, and the quadrant nomenclature could not be used in severely malformed cochleas because it would not be directly applicable. Along with consensus terminology, we have found that easier determination of the insertion depth of CI arrays and more effective description of insertion depth are enabled by cochlea-specific reformation planes set in the plane of the cochlea and by using the round window niche as the zero reference. As implant technology progresses, the neuro-radiologist may be asked to be more precise about implant location in the cochlea, and a quadrant approach to describe implant tip location can serve as the basis for those interpretations.

CONCLUSIONS

CT reformations parallel to the cochlear turns and use of standardized terminology regarding cochlear anatomy facilitated consistent reporting of the depth of the CI insertion. We propose

universal use of standard terminology by using a numeric quadrant approach instead of naming individual cochlear turns. Until such a system of standard terminology for reporting CI insertion depth is adopted, comparisons regarding insertion depth and clinical outcomes among various research articles will remain problematic.

ACKNOWLEDGMENTS

The authors wish to acknowledge Eric Jablonowski, artist.

Disclosures: Patricia A. Hudgins—UNRELATED: Consultancy: Amirsys, Comments: medical education company (I am a consultant and author); Royalties: Amirsys, Comments: royalties for medical education company publishing; Ownership Interest: Amirsys. H. Ric Harnsberger—UNRELATED: Ownership Interest: CEO, Amirsys. Norman W. Todd—UNRELATED: Consultancy: National Institutes of Health, Comments: Data Safety Monitoring Board member for study of Auditory-Verbal teletherapy; Grants/Grants Pending: MED-EL.* Comments: clinical study about the potential usefulness of electrically elicited stapedius reflexes in cochlear implant recipients; Patents (planned, pending or issued): Force Threshold Gauge.* Comments: Patent application submitted. *Money paid to the institution.

REFERENCES

- Verbist BM, Ferrarini L, Briaire JJ, et al. **Anatomic considerations of cochlear morphology and its implications for insertion trauma in cochlear implant surgery.** *Otol Neurotol* 2009;30:471–77
- Finley CC, Holden TA, Holden LK, et al. **Role of electrode placement as a contributor to variability in cochlear implant outcomes.** *Otol Neurotol* 2008;29:920–28
- Roland JT Jr, Fishman AJ, Alexiades G, et al. **Electrode to modiolus proximity: a fluoroscopic and histologic analysis.** *Am J Otol* 2000; 21:218–25
- Xu J, Xu SA, Cohen LT, et al. **Cochlear view: postoperative radiography for cochlear implantation.** *Am J Otol* 2000;21:49–56
- Lane JJ, Driscoll CL, Witte RJ, et al. **Scalar localization of the electrode array after cochlear implantation: a cadaveric validation study comparing 64-slice multidetector computed tomography with microcomputed tomography.** *Otol Neurotol* 2007;28:191–94
- Schuman TA, Noble JH, Wright CG, et al. **Anatomic verification of a novel method for precise intrascalar localization of cochlear implant electrodes in adult temporal bones using clinically available computed tomography.** *Laryngoscope* 2010;120:2277–83
- Whiting BR, Bae KT, Skinner MW. **Cochlear implants: three-dimensional localization by means of coregistration of CT and conventional radiographs.** *Radiology* 2001;221:543–49
- Verbist BM, Joemai RM, Teeuwisse WM, et al. **Evaluation of 4 multisection CT systems in postoperative imaging of a cochlear implant: a human cadaver and phantom study.** *AJNR Am J Neurorad* 2008;29:1382–88
- Lecerf P, Bakhos D, Cottier JP, et al. **Midmodiolar reconstruction as a valuable tool to determine the exact position of the cochlear implant electrode array.** *Otol Neurotol* 2011;32:1075–81
- Verbist BM, Skinner MW, Cohen LT, et al. **Consensus panel on a cochlear coordinate system applicable in histologic, physiologic, and radiologic studies of the human cochlea.** *Otol Neurotol* 2010; 31:722–30
- Verbist BM, Joemai RM, Briaire JJ, et al. **Cochlear coordinates in regard to cochlear implantation: a clinically individually applicable 3 dimensional CT-based method.** *Otol Neurotol* 2010;31:738–44
- Holden LK, Finley CC, Firszt JB, et al. **Factors affecting open-set word recognition in adults with cochlear implants.** *Ear Hear* 2013; 34:342–60

Radiologic and Functional Evaluation of Electrode Dislocation from the Scala Tympani to the Scala Vestibuli in Patients with Cochlear Implants

N. Fischer, L. Pinggera, V. Weichbold, D. Dejaco, J. Schmutzhard, and G. Widmann

ABSTRACT

BACKGROUND AND PURPOSE: Localization of the electrode after cochlear implantation seems to have an impact on auditory outcome, and conebeam CT has emerged as a reliable method for visualizing the electrode array position within the cochlea. The aim of this retrospective study was to evaluate the frequency and clinical impact of scalar dislocation of various electrodes and surgical approaches and to evaluate its influence on auditory outcome.

MATERIALS AND METHODS: This retrospective single-center study analyzed a consecutive series of 63 cochlear implantations with various straight electrodes. The placement of the electrode array was evaluated by using multiplanar reconstructed conebeam CT images. For the auditory outcome, we compared the aided hearing thresholds and the charge units of maximum comfortable loudness level at weeks 6, 12, and 24 after implantation.

RESULTS: In 7.9% of the cases, the electrode array showed scalar dislocation. In all cases, the electrode array penetrated the basal membrane within 45° of the electrode insertion. All 3 cases of cochleostomy were dislocated in the first 45° segment. No hearing differences were noted, but the charge units of maximum comfortable loudness level seemed to increase with time in patients with dislocations.

CONCLUSIONS: The intracochlear dislocation rate of various straight electrodes detected by conebeam CT images is relatively low. Scalar dislocation may not negatively influence the hearing threshold but may require an increase of the necessary stimulus charge and should be reported by the radiologist.

ABBREVIATIONS: CI = cochlear implant; CBCT = conebeam CT

The number of cochlear implantations is increasing rapidly, with improved hearing performance and speech recognition with time. Nevertheless, the auditory outcome varies among individuals, with the causes of this variability investigated in many studies with different results.¹⁻⁶

The duration and cause of deafness are probably the most important factors contributing to the variability of outcomes.^{2,3,6} Additionally, motivation and cooperation of the patients have a strong influence on hearing performance.⁷ The electrode-modiolus distance and the preservation of inner ear structures are also important factors.⁸⁻¹⁰

In patients with adequate hearing in the low-frequency spectrum, the preservation of inner ear structures is important. Therefore, electrodes for atraumatic insertion were developed in recent years. Furthermore, different insertion techniques have been compared. Rajan et al⁹ showed that a slow electrode insertion speed can promote preservation of residual hearing. The favored operation technique is electrode access through the round window membrane. Alternatively, the electrode can be placed through a cochleostomy.

After surgery, the final placement of the electrode array within the cochlea can be documented with conebeam CT (CBCT). Due to the high resolution and low influence of metal artifacts, CBCT has emerged as a reliable technique in scalar localization of the electrode array, showing a sensitivity of 100% and specificity of 90%.¹¹

According to Aschendorff et al,¹ the intracochlear localization of the electrode has a significant impact on speech recognition. Insertion of the electrode array in the scala tympani is associated with a better outcome than insertion in the scala vestibuli. In

Received April 30, 2014; accepted after revision August 6.

From the Departments of Otorhinolaryngology (N.F., L.P., D.D., J.S.), Hearing, Speech and Voice Disorders (V.W.), and Radiology (G.W.), Medical University Innsbruck, Innsbruck, Austria.

Please address correspondence to Joachim Schmutzhard, MD, Department of Otorhinolaryngology, Medical University Innsbruck, Anichstraße 35, 6020 Innsbruck, Austria; e-mail: Joachim.Schmutzhard@i-med.ac.at

<http://dx.doi.org/10.3174/ajnr.A4189>

Table 1: Summary the electrode arrays used

Electrode Array Name	Length (mm)	Flexibility
FLEXsoft	31	Soft, single contact tip
FLEX 28	28	Soft, single contact tip
FLEX 24	24	Soft, single contact tip
Standard	31	Double contact tip

addition, an intracochlear dislocation from the scala tympani to the scala vestibuli is related to decreased function. According to Shepherd et al,¹² terminal sensorineural structures and spiral ganglia are more likely to be damaged when the electrode array is located in the scala vestibuli. In contrast to the 2 previous studies, Wanna et al¹³ could not find a correlation between the electrode location and auditory performance. More information on the frequency and clinical impact of the radiologic findings of a scalar dislocation of various electrodes and surgical approaches is needed.

The aim of this study was to analyze the intracochlear dislocation rate of various Med-EL electrodes (Innsbruck, Austria) and insertion depth by using CBCT and to correlate the relationship between electrode position in the cochlea and influence on aided hearing performance after implantation.

MATERIALS AND METHODS

Basic Settings and Enrolled Patients

We analyzed cochlear implantations with various straight electrodes of different lengths and flexibility manufactured by Med-EL at the Department of Otorhinolaryngology, Medical University Innsbruck, in a retrospective manner. The electrode arrays used are listed in Table 1.

Radiologic Evaluation

In all patients, the placement of the electrode array was evaluated the day after surgery, using CBCT, by a head and neck radiologist with 10 years' experience.

The system used was a CBCT scanner, KaVo 3D eXam (KaVo Dental, Biberach/Riß, Germany), by using the following protocol: 120 kVP; 37.07 mAs; voxel, 0.2 (0.2 × 0.2 × 0.2 mm); matrix, 768 × 768; FOV, 16 × 8 cm; rotation time, 26.9 seconds. The images were exported in DICOM format to a PACS and viewed by using Impax EE software (Agfa-Gevaert, Mortsel, Belgium) on a high-resolution diagnostic color LCD monitor CCL254i (Totoku Europe, Mönchengladbach, Germany). Multiplanar reconstructions were obtained by using the basal cochlear turn as a horizontal reference plane and a perpendicular vertical plane through the cochlear apex.

The location of the electrode array entry was evaluated as follows: 1) round window, 2) cochleostomy.

The position of the electrode array within the cochlea was described according to the intended positioning within the tympanic scala: 0 = tympanic scala, no dislocation, 1 = dislocation into the vestibular scala at 0°–45°, 2 = dislocation into the vestibular scala at 46°–90°, 3 = dislocation into the vestibular scala at 91°–135°, and so forth. Other dislocations, such as into the internal auditory canal or hypotympanic space, were morphologically described.

The insertion depth of the electrode array was evaluated in the

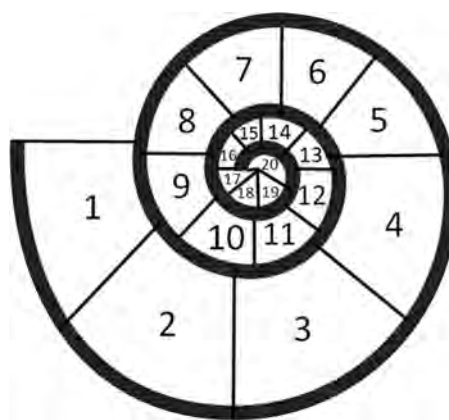


FIG 1. Definition of the insertion depth of the CI according to the radial position of the tip: 1 = 0°–45°, 2 = 46°–90°, 3 = 91°–135°, 4 = 136°–180°, 5 = 181°–225°, 6 = 226°–270°, 7 = 271°–315°, 8 = 316°–360°, 9 = 361°–405°, 10 = 406°–450°, 11 = 451°–495°, 12 = 496°–540°, 13 = 541°–585°, 14 = 586°–630°, 15 = 631°–675°, 16 = 676°–720°, 17 = 721°–765°, 18 = 766°–810°, 19 = 811°–855°, 20 = 856°–900°.

horizontal reference plane by using maximum intensity projection reconstructions with a 5-mm section thickness. The insertion depth was defined according to the radial position of the tip. Therefore, the cochlea was divided into 20 segments of 45° each (Fig 1).

Evaluation of Hearing Performance

The hearing thresholds of the cochlear implant (CI)-aided ear were assessed at frequencies 0.125/0.250/0.500/0.750/1/1.5/2/4/6/8 kHz under free field conditions. Patients were situated in a soundproof room with their CI in the tested ear activated and the device in the contralateral ear (if present) deactivated. Narrow band noises or warble tones with the above center frequencies were delivered from an audiometer via a loudspeaker located at a distance of 1 m in front of the patient. The level of the stimuli was calibrated according to European standards of EN 8253–3. The hearing thresholds were determined according to standard procedures used in audiometry.

For this study, we evaluated hearing threshold measurements obtained at 3 subsequent fitting sessions:

- 1) Six weeks after implantation (ie, 2 weeks after first activation of the speech processor)
- 2) Three months after implantation
- 3) Six months after implantation.

In a second step, the charge units of maximum comfortable loudness level of the 2 groups were compared. The charge units after 6 weeks and 3 and 6 months were analyzed.

Furthermore, a retrospective evaluation was performed of the speech recognition tests used.

Statistical Analysis

In the group of patients with regular electrode insertions, statistics were calculated and used for comparison. Expecting a low number of dislocations, we planned an individual data evaluation.

Each frequency of the aided hearing threshold was analyzed separately. Frequency-specific thresholds of controls were averaged and depicted as a boxplot, indicating the median, the second

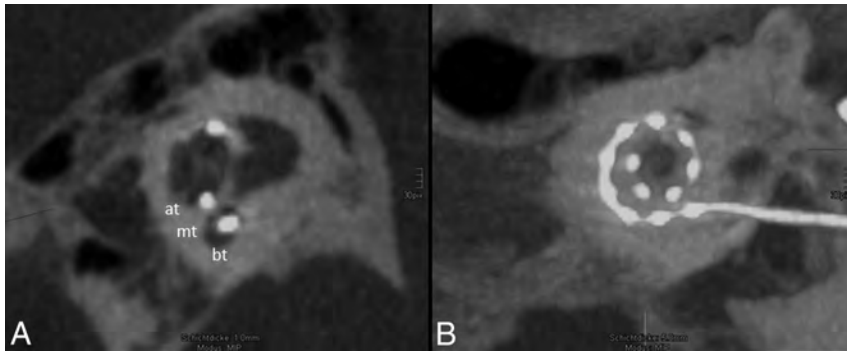


FIG 2. Regular position of the electrode array. *A*, One-millimeter MIP reconstruction of the cochlea shows the basal turn (bt), medial turn (mt), and apical turn (at). The position of the electrode array is clearly identified in the scala tympani (the scala tympani is basal; the scala vestibuli is apical). *B*, The insertion depth by using 5-mm MIP reconstruction in the horizontal reference plane reaches position 11, which refers to 451°–495° (Fig 1). All 12 electrodes (dots) can be identified on the electrode array.

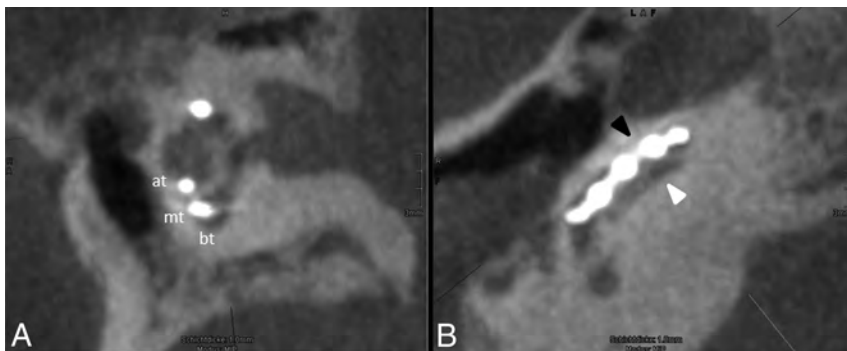


FIG 3. Scalar dislocation. *A*, One-millimeter MIP reconstruction of the cochlea showing the basal turn (bt), medial turn (mt), and apical turn (at). The position of the electrode array is clearly identified in the scala tympani. *B*, A cut along the basal turn demonstrates the scalar dislocation from the scala tympani (basal, white arrowhead) into the scala vestibuli (apical, black arrowhead) within the first 45° of insertion.

and third quartiles (the box), and the range between the upper and lower extremes (the error bars).

Hearing thresholds of patients with electrode dislocation were individually compared with the findings from the control group. Their frequency-specific thresholds were added as points beside the boxplots to show their positions in relation to those of the group with regular inserted electrodes. Hearing thresholds were considered normal (ie, corresponding to those of the controls) if lying within the lower and upper extremes (ie, the error bars of the boxplot). Hearing thresholds beyond the extremes were considered abnormal.

RESULTS

Sixty-three cochlear implantations of 59 adult patients were analyzed in this study. The patients were 7–85 years of age at implantation (mean, 51 ± 19.8 years). In the group with electrode dislocation, the mean age was 57 years; in the other group, it was 51 years; 52.5% were male and 47.5% female. The duration of deafness before implantation showed a large variability and ranged from >50 years to <1 year. In most cases, it was a progressive process, so the duration of deafness could not be determined exactly, but in both groups, the duration of deafness was similar. All patients had received the CI for the first time (no re-implantation) and

were equipped with a CI system including an electrode: either the FLEX 28 (63.5%), FLEX 24 (3.2%), FLEXsoft (11.1%), or Standard (22.2%; Med-EL).

Radiologic Evaluation

CBCT allowed clear visualization of the electrode array in the cochlea. The 12 electrodes on the array could be identified in all examinations (Fig 2B). On radiologic examination, in 5 of these implantations, an electrode dislocation was verified. The remaining 58 showed no signs of electrode misplacement and hence served as a control group for the assessment of the effects of a displaced electrode.

Electrode Dislocations

In 5 patients (7.9%), the electrode array was dislocated from the scala tympani to the scala vestibuli (Fig 3). The electrode array penetrated the basal membrane in the first 45° segment of the cochlea in all cases. The electrode was the FLEX 28 in all dislocated cases.

In the 3 included cochleostomy cases, the electrode dislocated from the scala tympani to the scala vestibuli (Fig 4).

Electrode Depth

In 95.2% ($n = 60$), the electrode was inserted through the round window, and in 4.8% ($n = 3$), a cochleostomy was

performed. The shortest insertion depth was between 226° and 270°, and the deepest was nearly up to the helicotrema (855°). The mean insertion depth was between 451° and 495°, which refers to approximately 1 and one-half turns. Figure 2 shows the regular placement of the electrode.

Auditory Performance

In patients with a scalar dislocation of the electrode array, the mean hearing threshold 12 weeks after implantation at 1000 Hz was 38.8 ± 10.3 dB; in patients with a regularly positioned electrode array, the mean hearing threshold was 40.8 ± 10.0 dB.

After 24 weeks, the mean hearing threshold at 1000 Hz in patients with scalar dislocation was 34.0 ± 10.2 dB, and without dislocation, 38.2 ± 7.9 dB.

Table 2 shows the mean hearing thresholds at weeks 6, 12, and 24 after implantation in all patients.

Frequency-specific hearing thresholds of controls at 6, 12, and 24 weeks are shown by the boxplots in Fig 5A–C. The hearing thresholds of the 5 patients with electrode dislocation are added as points. Fewer than 5 points (eg, Fig 5B) indicate missing data.

The graphic visualizations show that the hearing thresholds of the 5 ears with dislocation are within the extremes of the control group. This means that the hearing thresholds in ears with elec-

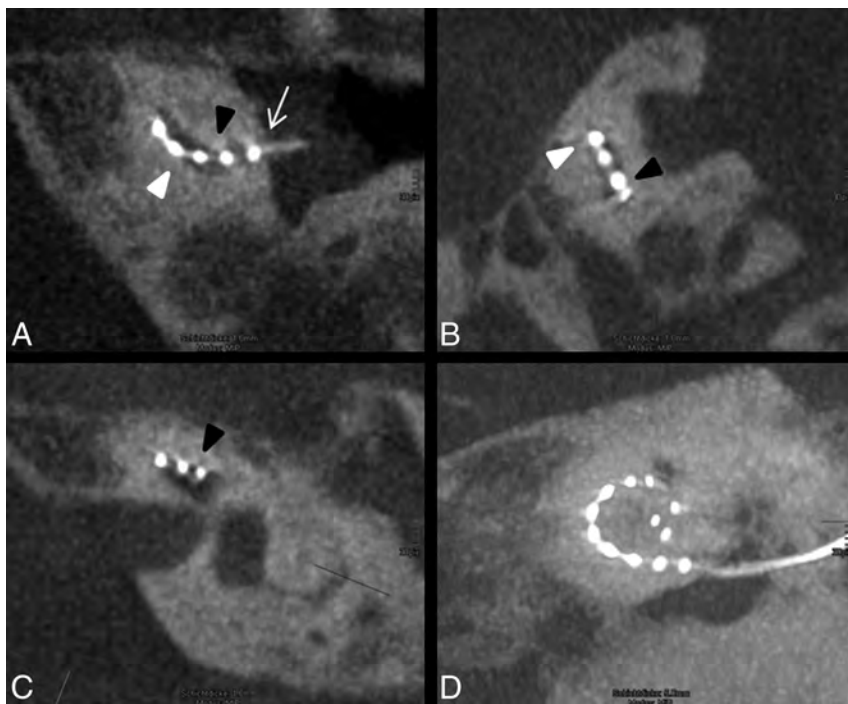


FIG 4. Atypical position of the electrode array. *A*, The electrode is inserted via cochleostomy (white arrow) and enters the basal cochlear turn from the scala vestibuli (apical, black arrowhead) into scala tympani (basal, white arrowhead). *B*, In the following course of the basal turn, the electrode array dislocates into the scala vestibuli. *C*, In the middle turn, the electrode array is clearly identified in the scala vestibuli. *D*, The insertion depth reaches position 8, which refers to 316°–360°, and the tip shows a kinking at the last electrode element.

Table 2: Mean hearing thresholds at weeks 6, 12, and 24 after implantation

	250 Hz	1000 Hz	4000 Hz	8000 Hz
After 6 weeks	38.8 ± 10.3 dB	43.6 ± 11.1 dB	44.6 ± 44.6 dB	47.0 ± 15.0 dB
After 12 weeks	35.2 ± 9.9 dB	41.0 ± 10.1 dB	40.0 ± 10.1 dB	44.5 ± 16.6 dB
After 24 weeks	33.9 ± 8.8 dB	37.8 ± 8.2 dB	38.1 ± 9.8 dB	38.6 ± 12.5 dB

trode dislocation do not differ from those in the ears with correct electrode positions.

At week 6, the mean values of the charge units of maximum comfortable loudness were equal in both groups (13.6 ± 6.4 versus 13.5 ± 3.1). After 12 weeks, the charge units increased in patients without dislocation to 17.4 ± 7.1 , and in patients with an electrode displacement, to 21.5 ± 11.2 . At week 24, the differences between the 2 groups were even higher: 19.6 ± 10.3 without dislocation and 26.2 ± 11.7 in the other group (Fig 5D–F).

A reliable evaluation of the speech recognition tests was not possible in the selected test population because of the variety of patients. One of the included patients had bilateral implantation. One side was positioned adequately in the scala tympani, and the other side was dislocated in the scala vestibuli. The results are shown in Fig 6.

DISCUSSION

This study investigated the electrode array location after cochlear implantation on multiplanar reconstructed CBCT images by using the basal cochlear turn as the horizontal reference plane and a perpendicular vertical plane through the cochlear apex. Accord-

ing to the histologic study of Marx et al,¹¹ the electrode position within the cochlea can be reliably identified. When one knows that in multiplanar reconstructions, the tympanic scala is basal and the vestibular scala is apical, the liquid-filled space is seen above the electrode array when the electrode is located correctly in the scala tympani.

The electrodes investigated are known for the variety of soft, flexible arrays that were optimized for structure preservation. In 5 of 63 implantations (7.9%), however, the electrode array dislocated from the scala tympani to the scala vestibuli. In 3 of the 5 dislocated cases, the electrode array had been inserted through a cochleostomy; only 3.3% of all electrodes dislocated following round window insertion. This finding suggests that electrode insertion through a cochleostomy has a higher risk for electrode array dislocation.

These data support the results of Adunka et al,¹⁴ who showed, in 2004, that cochleostomy has a higher risk of destructive basal trauma (48%) compared with performing round window membrane insertions (15%).

In all cases, the electrode array penetrated the basal membrane in the first 45° segment of the cochlea. Choosing the wrong angle during insertion of the electrode array could be the underlying cause.

Trauma to inner ear structures ranges from displacement of the basilar membrane to fracture of the osseous spiral lamina, tearing of the basilar membrane or spiral ligament, and deviation of the electrode array into the scala media or scala vestibuli. Rebscher et al,¹⁵ who tested the insertion damage in correlation to the stiffness of 8 different models of electrode arrays, showed that electrode arrays with proportionately greater stiffness in the vertical plane were less likely to produce severe trauma during insertion. Severe damage, defined as an electrode array dislocation from the scala tympani into the scala media or scala vestibuli, varied in straight electrodes from 0% to 37.5% and in spiral types from 0% to 38.9%.

Compared with these dislocation rates, the electrode dislocation rate of the straight electrodes analyzed in this study was relatively low.

All 5 dislocations involved the FLEX 28 array, which was the most represented electrode in our cases (63.5%). Furthermore, the standard approach is a round window insertion. An electrode insertion via cochleostomy is the second choice only if an adequate exposure of the round window cannot be achieved. The predominance of the dislocations in cochleostomy cases can be explained by a more difficult surgical approach, resulting in a steeper insertion angle. The dislocation rate did not significantly correlate with the insertion depth.

The hearing threshold after cochlear implantation depends on the comprehensive postoperative fitting and tuning of the audio pro-

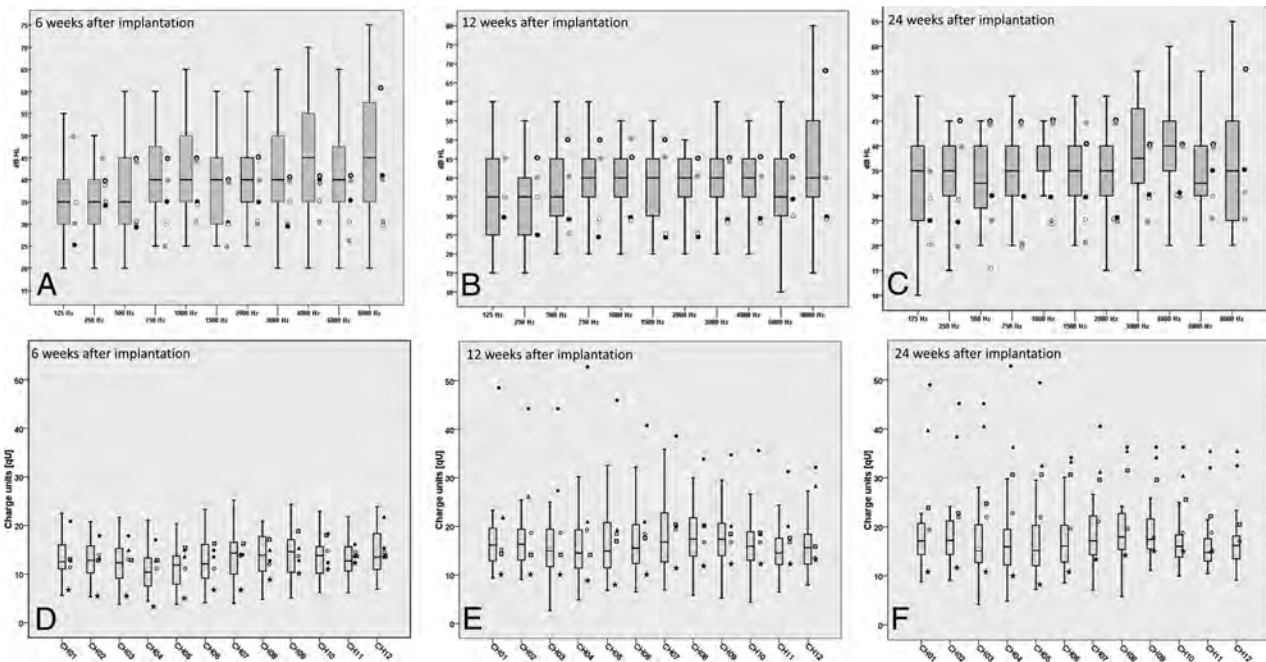


FIG 5. A–C, The boxplots represent the hearing thresholds of the control group. The hearing thresholds of the 5 patients with electrode dislocation are added as points beside the boxplots. Frequency-specific hearing thresholds of controls at 6 weeks after implantation (A), at 3 months after implantation (B), and at 6 months after implantation (C). D–F, The boxplots show the charge units of maximum comfortable loudness levels. The symbols beside the boxplots show the 5 patients with electrode dislocation. The charge units after 6 weeks (D), 12 weeks (E), and 24 weeks (F).

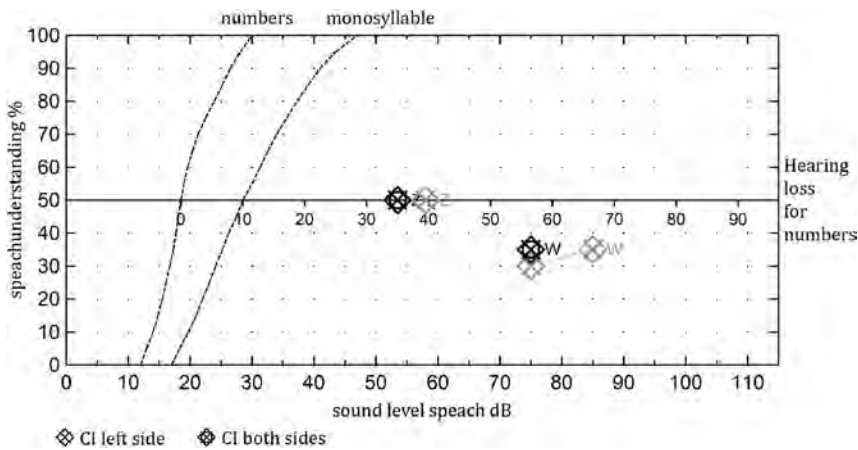


FIG 6. The speech audiometry of a patient with a dislocated CI on the left side 9 months after surgery and a normally inserted electrode array on the right side 18 months after surgery. No differences in the speech performance could be noted in either ear for the understanding of numbers and monosyllables.

cessor by experienced clinical personnel. The loudness has to be adapted in small steps, by the decreasing the thresholds with time. Some patients will not tolerate a hearing threshold <40 dB even after intensive training for years. The reason is mostly unknown. According to Aschendorff et al,¹ the electrode dislocation, which is associated with a rupture of the basal membrane, has an impact on the postoperative hearing threshold. However, in our study, patients with a dislocation of the electrode array had approximately the same hearing threshold compared with patients without a dislocation (38.8 versus 40.8 dB after 12 weeks, 34.0 versus 38.2 dB after 24 weeks) (Fig 5A–C).

stimulus charge increased in patients with dislocation compared with the control group (Fig 5). The reason could be that the damage of the delicate inner ear structures creates a higher fibrosis.

These findings show that a postoperative control of the electrode position is also important for the fitting, because an increase of the necessary stimulus charge sometimes can be explained by the electrode array dislocation.

Of course, for the patient, the speech recognition is more important than the hearing threshold. However, previous research has shown that lower sound field thresholds with CIs correlate significantly with better speech recognition.^{18–20}

The efficiency of an intracochlear electrode is considered higher if the stimulating elements are positioned close to the site of neural activation. Electrode arrays designed to position stimulating contacts near the modiolus appear to operate with lower current thresholds than previous devices that were located closer to the lateral wall of the scala tympani.^{15–17} The charge units of maximum comfortable loudness level of the 2 groups were compared to determine whether an electrode dislocation was associated with higher stimulus charges.

The graphic visualizations (Fig 5D–F) show that charge units of maximum comfortable loudness levels of the 5 ears with dislocation at the first fitting are within the extremes of the control group. However, it seems that after 6 months, the required

A critical reflection on the study design reveals the lack of speech data. Because of the retrospective study design, speech recognition tests were not performed in all patients at the same time. A second reason was that some patients did not reach open-set speech recognition within the evaluated time. The preoperative speech recognition varied greatly within the study population. Because of the complex pathophysiologic interrelations of speech recognition, which are influenced by many factors such as duration and cause of deafness, the age of patients, and, in particular, nonobjectified factors such as motivation and cooperation and factors not yet fully known at the time, a larger study population is necessary to analyze the effects of the electrode dislocation on speech recognition. Therefore, it is very difficult to have 2 matched reference groups that have the same basic comparable conditions. This factor could be the reason for the variability of results published.^{2,3,6}

An interesting finding is that in 1 patient who had bilateral implantation, CBCT showed that the electrode array inserted into the left cochlea was dislocated into the scala vestibuli and the tip showed a kinking at the last electrode element. On the right side, the electrode was located correctly in the scala tympani. No difference could be observed between the 2 ears. Neither the speech recognition test results nor the hearing thresholds varied. Most interesting, the charge units of the maximum comfortable loudness level at the first fitting in the dislocated ear were slightly higher and increased further after 6 months.

Wanna et al¹³ compared the audiologic outcomes of patients with bilateral implants. No differences of speech recognition between both ears could be found, even when the electrode array was dislocated on 1 side. A limiting factor of this study was the small number of included individuals. Nevertheless, this study supports our findings.

Precise localization of the electrode array may only be obtained in the basal turn of the cochlea and decreases along the medial and apical turns.²¹ Normal cochlear anatomy should not be obscured by the underlying disease process.²² Advantages of CBCT over multisection CT are lower radiation dose, less influence of metal artifacts, higher spatial resolution, and better visualization of the individual electrodes.²³

CONCLUSIONS

CBCT multiplanar reconstruction imaging is an excellent tool for assessing cochlear implants and may show scalar dislocation of the CI electrode arrays within the first 45° segment. Various straight flexible electrodes have a low risk of dislocation into the scala vestibuli. However, patients requiring a cochleostomy for the electrode insertion may have a higher risk of experiencing a dislocation compared with patients with round window membrane insertions. Electrode array dislocation may have no negative effect on the hearing threshold but may require an increase of the necessary stimulus charge. The insertion and position of the electrode array in the cochlea should be reported by the neuroradiologist.

REFERENCES

- Aschendorff A, Kromeier J, Klenzner T, et al. **Quality control after insertion of the nucleus contour and contour advance electrode in adults.** *Ear Hear* 2007;28:75S–79S
- Blamey P, Arndt P, Bergeron F, et al. **Factors affecting auditory performance of postlinguistically deaf adults using cochlear implants.** *Audiol Neurootol* 1996;1:293–306
- Blamey P, Artieres F, Baskent D, et al. **Factors affecting auditory performance of postlinguistically deaf adults using cochlear implants: an update with 2251 patients.** *Audiol Neurootol* 2013;18:36–47
- Finley CC, Holden TA, Holden LK, et al. **Role of electrode placement as a contributor to variability in cochlear implant outcomes.** *Otol Neurotol* 2008;29:920–28
- van Wermeskerken GK, van Olphen AF, Graamans K. **Imaging of cochlear position in relation to electrode functioning after cochlear implantation.** *Eur Arch Otorhinolaryngol* 2009;266:1527–31
- Wilson BS, Dorman MF. **Cochlear implants: a remarkable past and a brilliant future.** *Hear Res* 2008;242:3–21
- Fu QJ, Galvin JJ 3rd. **Perceptual learning and auditory training in cochlear implant recipients.** *Trends Amplif* 2007;11:193–205
- Esquia Medina GN, Borel S, Nguyen Y, et al. **Is electrode-modiolus distance a prognostic factor for hearing performances after cochlear implant surgery?** *Audiol Neurootol* 2013;18:406–13
- Rajan GP, Kontorinis G, Kuthubutheen J. **The effects of insertion speed on inner ear function during cochlear implantation: a comparison study.** *Audiol Neurootol* 2013;18:17–22
- Tamir S, Ferrary E, Borel S, et al. **Hearing preservation after cochlear implantation using deeply inserted flex atraumatic electrode arrays.** *Audiol Neurootol* 2012;17:331–37
- Marx M, Risi F, Escude B, et al. **Reliability of cone beam computed tomography in scalar localization of the electrode array: a radio histological study.** *Eur Arch Otorhinolaryngol* 2014;271:673–79
- Shepherd RK, Hatsushika S, Clark GM. **Electrical stimulation of the auditory nerve: the effect of electrode position on neural excitation.** *Hear Res* 1993;66:108–20
- Wanna GB, Noble JH, McRackan TR, et al. **Assessment of electrode placement and audiological outcomes in bilateral cochlear implantation.** *Otol Neurotol* 2011;32:428–32
- Adunka O, Gstoettner W, Hambek M, et al. **Preservation of basal inner ear structures in cochlear implantation.** *ORL J Otorhinolaryngol Relat Spec* 2004;66:306–12
- Rebscher SJ, Hetherington A, Bonham B, et al. **Considerations for design of future cochlear implant electrode arrays: electrode array stiffness, size, and depth of insertion.** *J Rehabil Res Dev* 2008;45:731–47
- Cords SM, Reuter G, Issing PR, et al. **A silastic positioner for a modiolus-hugging position of intracochlear electrodes: electrophysiologic effects.** *Am J Otol* 2000;21:212–17
- Dorman MF, Spahr T, Gifford R, et al. **An electric frequency-to-place map for a cochlear implant patient with hearing in the nonimplanted ear.** *J Assoc Res Otolaryngol* 2007;8:234–40
- Davidson LS, Skinner MW, Holstad BA, et al. **The effect of instantaneous input dynamic range setting on the speech perception of children with the nucleus 24 implant.** *Ear Hear* 2009;30:340–49
- Firszt JB, Holden LK, Skinner MW, et al. **Recognition of speech presented at soft to loud levels by adult cochlear implant recipients of three cochlear implant systems.** *Ear Hear* 2004;25:375–87
- Holden LK, Finley CC, Firszt JB, et al. **Factors affecting open-set word recognition in adults with cochlear implants.** *Ear Hear* 2013;34:342–60
- Güldner C, Wiegand S, Weiss R, et al. **Artifacts of the electrode in cochlea implantation and limits in analysis of deep insertion in cone beam tomography (CBT).** *Eur Arch Otorhinolaryngol* 2012;269:767–72
- Lane JI, Witte RJ, Driscoll CL, et al. **Scalar localization of the electrode array after cochlear implantation: clinical experience using 64-slice multidetector computed tomography.** *Otol Neurotol* 2007;28:658–62
- Ruivo J, Mermuys K, Bacher K, et al. **Cone beam computed tomography, a low-dose imaging technique in the postoperative assessment of cochlear implantation.** *Otol Neurotol* 2009;30:299–303

Visualization of Human Inner Ear Anatomy with High-Resolution MR Imaging at 7T: Initial Clinical Assessment

M.A. van der Jagt, W.M. Brink, M.J. Versluis, S.C.A. Steens, J.J. Briaire, A.G. Webb, J.H.M. Frijns, and B.M. Verbist



ABSTRACT

BACKGROUND AND PURPOSE: In many centers, MR imaging of the inner ear and auditory pathway performed on 1.5T or 3T systems is part of the preoperative work-up of cochlear implants. We investigated the applicability of clinical inner ear MR imaging at 7T and compared the visibility of inner ear structures and nerves within the internal auditory canal with images acquired at 3T.

MATERIALS AND METHODS: Thirteen patients with sensorineural hearing loss eligible for cochlear implantation underwent examinations on 3T and 7T scanners. Two experienced head and neck radiologists evaluated the 52 inner ear datasets. Twenty-four anatomic structures of the inner ear and 1 overall score for image quality were assessed by using a 4-point grading scale for the degree of visibility.

RESULTS: The visibility of 11 of the 24 anatomic structures was rated higher on the 7T images. There was no significant difference in the visibility of 13 anatomic structures and the overall quality rating. A higher incidence of artifacts was observed in the 7T images.

CONCLUSIONS: The gain in SNR at 7T yielded a more detailed visualization of many anatomic structures, especially delicate ones, despite the challenges accompanying MR imaging at a high magnetic field.

ABBREVIATION: SNHL = sensorineural hearing loss

Patients with sensorineural hearing loss (SNHL) have malfunction of the inner ear, cochlear nerve, or central auditory pathway. Treatment consists of amplification of sound or, in case of severe-to-profound SNHL, direct electrical stimulation of the cochlear nerve by a cochlear implant. MR imaging of patients with SNHL focuses on the integrity of the auditory pathways from the cochlea to the auditory cortex in the brain. In particular, the fluid-filled spaces of the labyrinth and internal auditory canal and the cerebellopontine angle are of interest because the most com-

monly identified pathologies that cause SNHL are found in these regions.¹⁻⁵

One clear trend in the development of MR imaging systems has been the drive to higher magnetic field strengths.⁶ For clinical inner ear scanning, MR imaging scanners with a magnetic field strength of 1.5T or 3T are routinely used. The relatively recent introduction of commercial 7T scanners potentially enables an increased SNR, resulting in more detailed imaging of anatomic structures. Concerning inner ear imaging, the visualization of delicate and small-sized inner ear structures might benefit from such high-resolution imaging. This may result in new opportunities for obtaining normative measurements and evaluating pathologic alterations within the inner ear or associated nerves. Such detailed anatomic depiction has caused particular interest for assessment of candidates for cochlear implants because it gives decisive information on implantation feasibility, possible surgical risks, and choice of implant device. As such, it would aid in patient-specific preoperative planning of cochlear implantation and could provide valuable information for individualized assessment of insertion.

Transition from a conventional 3T scanner to a stronger 7T scanner is challenging, however, due to technical complexities accompanying the higher magnetic field strength.⁶ One of these technical complexities is the increased inhomogeneity of the static

Received April 28, 2014; accepted after revision June 9.

From the Departments of Otorhinolaryngology (M.A.v.d.J., J.J.B., J.H.M.F.) and Radiology (W.M.B., M.J.V., A.G.W., B.M.V.), C.J. Gorter Center for High-Field MRI (W.M.B., M.J.V., A.G.W.), and Leiden Institute for Brain and Cognition (J.H.M.F.), Leiden University Medical Center, Leiden, the Netherlands; and Department of Radiology (S.C.A.S., B.M.V.), Radboud University Medical Center, Nijmegen, the Netherlands.

This work was supported by Advanced Bionics.

Paper previously presented as a poster at: Conference on Implantable Auditory Prostheses, July 14–19, 2013; Lake Tahoe, California; as an oral presentation in Dutch at: Annual Ear, Nose, and Throat meeting, November 15, 2013; Maastricht, the Netherlands.

Please address correspondence to Johan H.M. Frijns, MD, PhD, Department of Otorhinolaryngology, Leiden University Medical Center, PO Box 9600, 2300 RC Leiden, the Netherlands; e-mail: J.H.M.Frijns@lumc.nl

Indicates open access to non-subscribers at www.ajnr.org

<http://dx.doi.org/10.3174/ajnr.A4084>

Demographic details of studied patients (N = 17)

	No.
Sex	
Male	8
Female	9
Pathologic imaging reporting	
Cochlea malformation	1 ^a
Hypoplasia acoustic nerve	1 ^a
Fenestrel otosclerosis	1
Labyrinthitis ossificans	1
None	14
Etiology	
Congenital	
Pendred syndrome	1
Of unknown origin	5
Acquired	
Sudden deafness	2
MIDD	1
Otosclerosis	2
Rubella infection	2
Unknown	4
Duration of deafness, years (mean)	23.2

Note:—MIDD indicates maternally inherited diabetes and deafness.

^a Same patient.

(B_0) and radiofrequency (B_1) fields, typically featuring areas of low B_1 close to the temporal lobes. The B_0 inhomogeneities are caused primarily by the susceptibility difference between inner ear fluids and the surrounding bone, and the B_1 inhomogeneities, by the elliptic shape of the head.⁷ Both of these effects can result in loss of signal in the inner ear region as previously described by Takahara et al⁸ and van Egmond et al.⁹ Additionally, the specific absorption rate, for which regulatory safety limits are defined, scales approximately quadratic with field strength, ultimately limiting the imaging speed at high fields in vivo. Recently, we introduced geometrically tailored dielectric pads to locally tailor the B_1 distribution. These improved contrast homogeneity and transmit efficiency in the region of the inner ear without increasing the specific absorption rate, which contributed to the development of a high-resolution imaging protocol at 7T.¹⁰

The aim of this study was the following: 1) to investigate the feasibility of clinical inner ear imaging at 7T MR imaging, and 2) to compare the visibility of inner ear structures and nerves within the internal auditory canal with images acquired at 3T.

MATERIALS AND METHODS

Patients

This prospective study was approved by the hospital institutional review board (P07.096). Patients with SNHL, eligible for cochlear implantation and referred for 3T imaging between December 2012 and May 2013, were asked to participate in the study. Exclusion criteria were age younger than 18 years and contraindications for exposure to the magnetic field. Seventeen candidates for cochlear implantation were enrolled in the study, 9 women and 8 men between 27 and 78 years of age. Etiology and the duration of hearing loss are described in the Table. All patients underwent MR imaging at 3T as part of the standard work-up for cochlear implantation. After giving written informed consent, 16 patients underwent an examination at 7T; 1 patient was excluded due to an intracranial foreign body of unknown composition. Three other patients were excluded after the scanning procedure due to the

following reasons: Scans of 2 patients were incomplete due to premature termination of the scanning procedure due to an unspecified technical defect, and the scanning procedure of 1 patient had to be aborted due to claustrophobia. After the procedure, patients were asked if they had dizziness because this is a frequently reported but temporary side effect of scanning at 7T.

Imaging Technique

All patients underwent examination on an Achieva or Ingenia 3T system (Philips Healthcare, Best, the Netherlands) as part of the standard preoperative work-up. The following scan parameters were used for the T2-weighted TSE sequence: FOV = 130 × 130 × 24 mm, 0.6-mm³ isotropic voxels, TR/TE/TSE factor = 2400 ms/200 ms/73, and 80 sections, resulting in an acquisition time of approximately 6 minutes. In addition, all patients were scanned on an Achieva 7T system (Philips Healthcare) as described by Brink et al,¹⁰ by using a quadrature transmit and 32-channel receive coil (NM008A-7P-012; Nova Medical, Wilmington, Massachusetts). To improve contrast homogeneity and transmit efficiency, we positioned 2 sex-specific high-permittivity pads containing a suspension of barium titanate and deuterated water next to both ears.¹⁰ High-resolution T2-weighted images were acquired by using the following parameters: FOV = 180 × 180 × 24 mm, 0.3-mm³ isotropic voxels, TR/TE/TSE factor = 3000 ms/200 ms/69, tip angle/refocusing angle = 90°/135°, parallel imaging reduction factor = 2.5 × 1.5, and 160 sections. These resulted in an acquisition time of approximately 10 minutes.

Image Analysis

The high-resolution T2-weighted images acquired at both 3T and 7T were transferred to an OsiriX DICOM viewer (<http://www.osirix-viewer.com>).¹¹ The images were anonymized and presented in randomized order. Evaluation was performed by 2 head and neck radiologists with 5 and 13 years of experience, respectively. Twenty-four anatomic structures of the inner ear were assessed by using a 4-point grading scale for the degree of visibility for diagnostic evaluation: 1 = not assessable, 2 = poor, 3 = adequate, 4 = excellent. The structures selected were those most relevant for cochlear implantation. In addition, we designated an overall score for diagnostic image quality: 1 = not diagnostic, 2 = poor, 3 = adequate, 4 = excellent. Both ears were evaluated separately. Subsequently, the scores of the 2 ears and 2 observers were averaged and normalized into a parameter between 0 and 1. An overview of the anatomic structures and their difference in rating is shown in Fig 1. The numbers I, II, and III refer to the basal, mid-, and apical turns, respectively.

Statistical Analysis

Statistical analysis was performed by using SPSS (IBM, Armonk, New York). To study the influence of observed asymmetric signal intensity between the right and left inner ears on the 7T images, we performed a linear mixed model. Statistical differences per anatomic structure between the 3T and 7T scanners were determined by using a Wilcoxon signed rank test. The interrater variability was determined by the Cohen κ coefficient. All tests were 2-tailed, and $P < .05$ was considered a statistically significant difference.

Score differences 7 Tesla - 3 Tesla

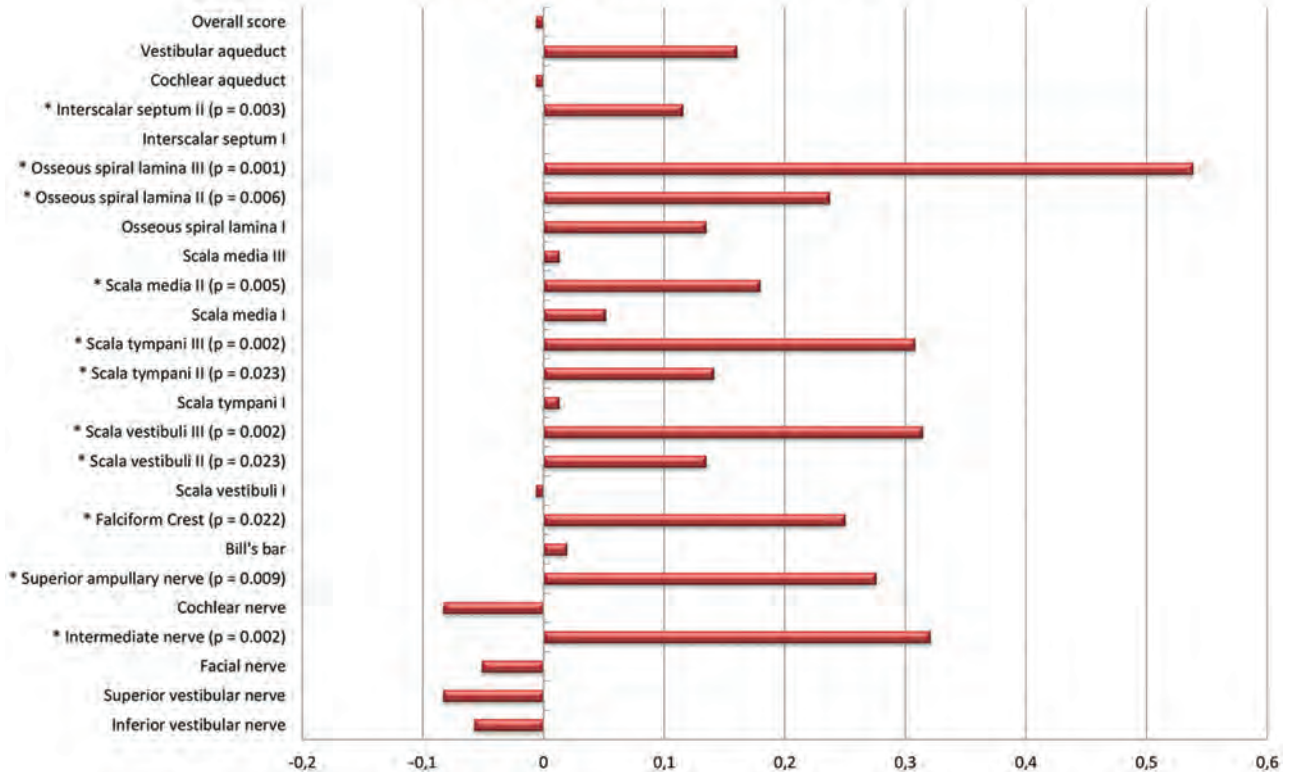


FIG 1. Mean differences in scoring of anatomic structures depicted at 3T and 7T. The bars on the right side of the zero line indicate differences in favor of the 7T images. The bars on the left side indicate differences in favor of the 3T images. The structures showing significant differences are marked with an asterisk on the left, and P values are mentioned if significant.

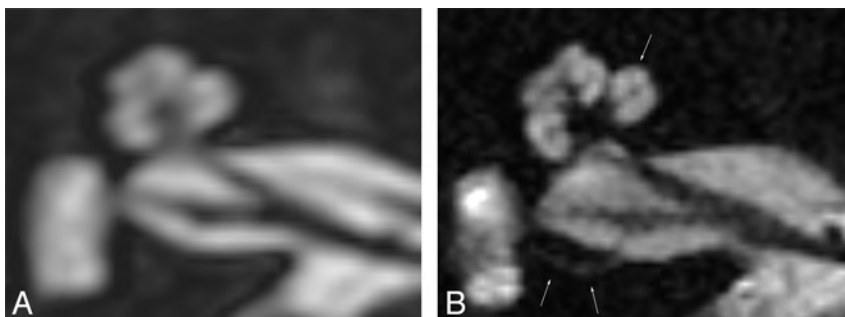


FIG 2. Axial cross-section of a right inner ear, rendered at 3T (A) and 7T (B); improved discrimination of the intracochlear structures and compartments is shown. In addition, sharper delineation of the nerves in the internal auditory canal is demonstrated. The single arrow indicates the scala media at the first turn. The double arrows indicate the superior ampullary nerve.

RESULTS

Twenty-six inner ears of 13 patients were available for image analysis. The occasionally observed asymmetric signal intensity on some of the 7T images did not result in a significantly different rating of the right and left inner ears ($P = .215$). Therefore, no distinction between inner ear sides was used for analysis. Because 24 anatomic structures per inner ear were evaluated on T2-weighted images acquired on 3T and 7T scanners plus an additional score for overall image quality, this process resulted in 2600 ratings applied by the 2 observers together. The ratings were averaged over ear and observer, leaving 650 ratings for statistical analysis. The visibility of 11 of the 24 anatomic structures was

rated higher on the 7T images. None of the anatomic structures were better depicted on the 3T images. There was no significant difference in the visibility of 13 anatomic structures and the overall diagnostic image-quality rating. The interobserver agreement was moderate with a κ value of 0.55. None of the patients reported excessive or extended dizziness during or after the scan procedure.

Cochlea

Figure 2 shows the cochlea on an axial cross-section image, clearly illustrating the improved resolution of the 7T image contributing to a more detailed depiction

of the inner ear anatomy. Evaluated cochlear structures included the scala vestibuli, scala tympani, scala media, osseous spiral lamina, and interscalar septa. All structures were evaluated separately for each cochlear turn. Significant differences in favor of the 7T images were found for the scala tympani and vestibuli in the second and third turns, with a mean difference of 0.13 ($P = .023$) and 0.31 ($P = .023$) for the second turn and 0.14 ($P = .002$) and 0.31 ($P = .002$) for the third turn. The scala media in the first turn could be distinguished in 7 of 52 ratings on the 7T images, but in none of the inner ears on the 3T images. Visualization of the distinguished scala media was 6 times evaluated as “poor” and 1

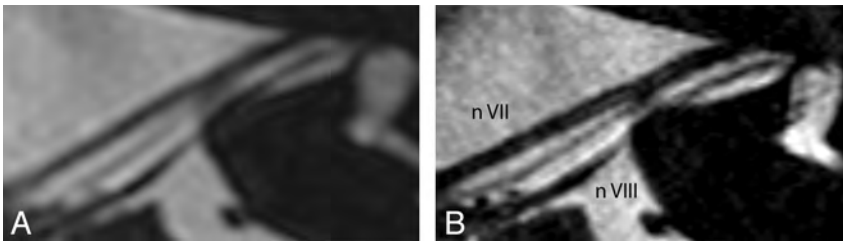


FIG 3. Axial cross-section along the course of the facial nerve of a left inner ear, rendered at 3T (A) and 7T (B). A sharp delineation of the neural structures and clear depiction of the intermediate nerve between cranial nerves VII and VIII are demonstrated on the 7T image.

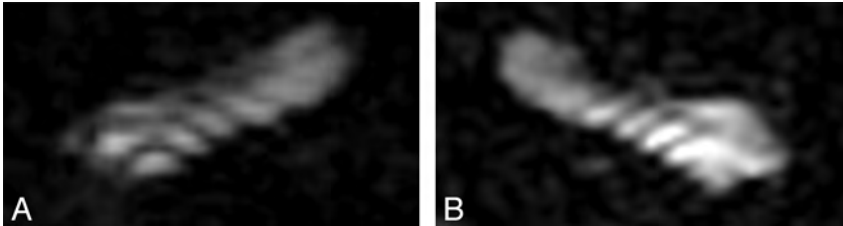


FIG 4. In 2 different patients, 7T images showing stripelike-artifacts at the level of the first turn of right (A) and left (B) cochleas, disturbing the quality of the representation and impeding the distinction of the scala vestibuli and tympani.

time as “adequate.” The resulting score difference of 0.05 was not significant ($P = .066$). In the second turn, the scala media was visible in 21 inner ears on the 7T images, compared with none on the 3T images. The degree of visibility of these structures was rated “poor” in 16 cases, “adequate” in 3 cases, and “very good” in 2 cases. The score difference of 0.18 was significant for this turn ($P = .005$). In the second and third turns, the depiction of the osseous spiral lamina was better on the 7T images, resulting in a sharp delineation of the scala tympani and vestibuli ($P = .006$ for the second turn and $P = .001$ for the third turn). The visibility of the interscalar septum between the second and third turns also significantly benefited from high-resolution imaging at 7T ($P = .003$).

Internal Auditory Canal

Statistical differences in visualization of the facial ($P = .259$), superior ($P = .131$), inferior vestibular ($P = .242$), and cochlear nerves ($P = .151$) through the internal auditory canal could not be demonstrated. On the 3T images, the intermediate nerve was observed 5 of 52 times, compared with 31 times on the 7T images. On the 7T images, the visibility of the intermediate nerve was evaluated as “poor” in 14 cases, “adequate” in 8 cases, and “excellent” in 9 cases. This evaluation resulted in a significant difference of 0.32 ($P = .002$). An example of the clear depiction of an intermediate nerve is shown in Fig 3. In addition, a sharper delineation of the other neural structures was obtained. The superior ampullary nerve is indicated in Fig 2B by 2 white arrows. This small neural structure is not regularly visualized on 3T scans. In this study, it was observed 10 of 52 times on the 3T scans, 7 times as “poor” and 3 times as “adequate,” compared with 28 times on the 7T scans, 11 times as “poor,” 6 times as “adequate,” and 11 times as “excellent.” These findings resulted in a significant difference of 0.28 ($P = .009$).

The visualization of the falciform crest was significantly improved on the 7T images; it was identified in 47 of 52 read-

ings on the 7T images, compared with 41 readings on the 3T images. This finding led to a score difference of 0.25 ($P = .022$). Bill’s bar was only occasionally observed at either magnetic field strength.

Cochlear and Vestibular Aqueducts

Visualization of the vestibular and cochlear aqueducts did not differ significantly among the 3T and 7T images. A score difference of 0.16 ($P = .107$) of the vestibular aqueduct and 0.01 ($P = .836$) of the cochlear aqueduct was found.

Artifacts

A higher incidence of image artifacts was observed on the 7T images: 9 of the 13 scans versus none of the 3T scans. These artifacts included motion artifacts likely due to the prolonged scan duration compared with 3T. Also, off-resonance effects due to the increased B_0 inhomogeneities causing signal loss, and stripelike artifacts

likely due to B_1 inhomogeneities were observed. An example of their appearances is shown in Fig 4.

Overall Image Quality

Image quality can be expressed as either the mean of scores per magnetic field strength or the actual applied score for image quality. First, we calculated the sum of scores separately for each magnetic field strength. Comparison of these values resulted in a significant difference of 0.11 per anatomic structure in favor of the 7T scanner ($P < .001$). Second, the score for overall image quality as rated directly was analyzed. This score for overall image quality was applied in the context of diagnostic value, meaning distortion of the image quality by artifacts was taken into account. Comparing these scores did not show a significant difference between the 2 field strengths ($P = .631$).

An overview of all the described outcomes is presented in Fig 1.

DISCUSSION

In patients with profound SNHL eligible for cochlear implantation, 7T MR imaging of the inner ear was successfully performed. Comparison with 3T images demonstrated improved visualization of a large number of anatomic structures of the inner ear and internal auditory canal with high-resolution 7T imaging and emphasized the potential of clinical imaging at 7T.

Regarding the cochlear structures, the benefit of increased SNR was most pronounced for visualization of the microstructures of the second and third turns. The accurate distinction of the different turns and compartments is essential to accurately diagnose and localize pathologies and support surgical planning. One specific development during the past years that has emphasized the role of radiologic evaluation of cochlear implant candidates is the expanded criteria for cochlear implant recipients. A malformed cochlea is no longer an absolute contraindication for im-

plantation; this change is important because as many as 20% of the patients with SNHL show some degree of inner ear malformation.¹² However, when a malformation is present, the surgical procedure carries a higher risk for complications such as CSF gusher, and often a different surgical approach and electrode type must be chosen to ensure a good outcome.¹³ These considerations require precise preoperative planning; an increase in anatomic information as achieved with 7T could be beneficial in such patients.

Another example in which an increase in anatomic information could be extremely relevant includes patients with obliterated cochleas. This fibrotic or osseous obliteration of the cochlear lumen is usually caused by meningitis-induced labyrinthitis. When parts of the cochlea are not patent, a different surgical approach should be followed with, in some cases, the use of a split array electrode.¹⁴ This device was developed to maximize the coverage of spiral ganglion cells by inserting 2 separate arrays through different cochleostomies. To precisely guide this procedure, comprehensive details of the cochlea anatomy are required. For electroacoustic stimulation, cochlear trauma needs to be minimized and preoperative delineation of the cochlear anatomy should be as accurate as possible. In addition, a gain in detailed anatomic information of the cochlea enables further research on morphologic characteristics, their influence on electrode position, and the relation of this position to the cochlear implant recipient's performance.^{15,16}

At the internal auditory canal, smaller nerve branches such as the superior ampullary nerve and the intermediate nerve were, in general, better depicted at 7T. The fact that larger neural structures did not benefit from the increased resolution at 7T can be explained by motion artifacts, off-resonance and stripelike artifacts, and the scoring system. The internal auditory canal where these structures are housed was particularly vulnerable to patient-induced motion artifacts. It was observed that the neural structures in the internal auditory canal were more frequently affected than the cochlear structures when motion of the head occurred during the scan procedure. An explanation for this observation is not well-defined yet, but one can realistically hypothesize a combination of the direction of the motion and the dimensions of the internal auditory canal that makes image quality more vulnerable. Scanner-related artifacts such as the stripelike artifacts and off-resonance were only pronounced at the higher field strength, as might be expected from the implicit larger absolute change in resonance frequency. Another contributing factor might have been the chosen 4-point grading scale. In most cases, the visibility of nerves was rated "excellent" on the basis of delineation of the neural structures in both the 3T and 7T images. Consequently, a distinction in visualization between the 2 scanners was then hardly detectable and the presence of artifacts became decisive. Yet, although not evaluated systematically, one observer reported more confident assessment on cochlear nerve hypoplasia at 7T.

With respect to the clinical relevance, many etiologies causing SNHL cannot be seen in vivo with current techniques. Increasing the SNR and resolution, however, may demonstrate more anatomic changes related to SNHL. Showing the capability of 7T MR imaging to visualize anatomic structures such as the distinguished scalas of the second and third turn, scala media, intermediate

nerve, and superior vestibular nerve is a first step toward that expectation. When etiologies are known, treatment and prognosis can be tailored more accurately.

Improved image quality does however, come with a number of drawbacks and limitations. An example of such a limitation is the prolonged scan duration. In our study, scan duration was prolonged from 6 to 10 minutes. This prolongation together with the lack of communication possibilities for this specific patient population caused an increased susceptibility to subject-induced artifacts; therefore, the use of communicative visual signaling during scanning is recommended. Additionally, the likelihood of motion artifacts could be reduced by shortening the scan duration through reduced-FOV imaging techniques.¹⁷ Another important issue is the presence of possible side effects during 7T examinations. Previous research reported a slightly higher incidence of dizziness than at 3T, discomfort from the gradient noise, and a metallic taste.¹⁸⁻²⁰ Nevertheless, these side effects are widely accepted, and in general, 7T examinations are well-tolerated. In our study population, none of the patients mentioned excessive discomfort during the scan procedure.

Another limitation of our study is the difference in background of the observers. One observer normally evaluates MR images acquired at 3T, whereas the second observer normally evaluates MR images acquired at 1.5T only. This difference may have resulted in overvaluation of the 3T images by the second observer, thereby diminishing the difference between the 3T and 7T images and decreasing the κ value.

CONCLUSIONS

We report progress toward the use of 7T MR imaging for inner ear scanning in a clinical setting. The gain in SNR resulted in a more detailed visualization of a large number of relevant anatomic structures despite the remaining difficulties accompanying high-magnetic-field imaging. The findings of this study are encouraging for continued research on technical adjustments to push the limits of 7T MR imaging to reach its full potential and make it suitable for clinical applications.

Disclosures: Annerie van der Jagt—*RELATED: Grant: Advanced Bionics, Comments: Advanced Bionics financially supports my PhD trajectory; Support for Travel to Meetings for the Study or Other Purposes: Advanced Bionics, Comments: Advanced Bionics paid for the expenses of attending the Conference of Implantable Auditory Prostheses in 2013 at Lake Tahoe, California, where these data were presented.* Wyger M. Brink—*RELATED: Grant: Nederlandse Organisatie voor Wetenschappelijk Onderzoek (No. 176.010.2005.030; A.G. Webb).** Jeroen J. Briaire—*RELATED: Grant: Advanced Bionics,* Comments: continuing-research grant for cochlear implant research; Support for Travel to Meetings for the Study or Other Purposes: Advanced Bionics,* Comments: travel to a conference; Grants/Grants Pending: Advanced Bionics,* Comments: grant on cochlear implant research.* Andrew G. Webb—*RELATED: Grant: Organisation for Scientific Research Netherlands,* Comments: funded project to develop applications for high-permittivity materials.* Johan H. M. Frijns—*RELATED: Grant: Advanced Bionics,* Comments: a research grant paying the salary of M.A.v.d. Jagt; UNRELATED: Board Membership: Advanced Bionics, Comments: Medical Advisory Board; Consultancy: Advanced Bionics; Expert Testimony: as an ear, nose, and throat surgeon in the LUMC;* Grants/Grants Pending: Advanced Bionics,* STW,* MED-EL,* ZonMW,* Heinsius-Houbolt Fund,* Comments: research grants in the field of cochlear implants; Royalties: STW,* Comments: from my predecessor's work on middle ear implants.* Berit M. Verbist—*RELATED: Other: Advanced Bionics,* Comments: financial support for PhD (Dr van der Jagt); UNRELATED: Payment for Lectures (including service on Speakers Bureaus): Bayer, ESMRMB, Comments: lectures/workshops on diagnostic imaging in the field of head and neck radiology; Royalties: LWW, Comments: coauthor of 2 books on head and neck radiology. *Money paid to the institution.*

REFERENCES

1. Verbist BM. **Imaging of sensorineural hearing loss: a pattern-based approach to diseases of the inner ear and cerebellopontine angle.** *Insights Imaging* 2012;3:139–53
2. Casselman JW. **Diagnostic imaging in clinical neuro-otology.** *Curr Opin Neurol* 2002;15:23–30
3. St Martin MB, Hirsch BE. **Imaging of hearing loss.** *Otolaryngol Clin North Am* 2008;41:157–78, vi-vii
4. Mohan S, Hoeffner E, Bigelow DC, et al. **Applications of magnetic resonance imaging in adult temporal bone disorders.** *Magn Reson Imaging Clin N Am* 2012;20:545–72
5. Davidson HC. **Imaging evaluation of sensorineural hearing loss.** *Semin Ultrasound CT MR* 2001;22:229–49
6. Robitaille P, Berliner L. *Ultra High Field Magnetic Resonance Imaging (Biological Magnetic Resonance)*, Vol. 26. Berlin: Springer; 2006
7. Sled JG, Pike GB. **Standing-wave and RF penetration artifacts caused by elliptic geometry: an electrodynamic analysis of MRI.** *IEEE Trans Med Imaging* 1998;17:653–62
8. Takahara T, Hoogduin H, Visser F, et al. **Imaging of the inner ear at 7T: initial results.** In: *Proceedings of the Annual Meeting of International Society of Magnetic Resonance in Medicine*, Stockholm, Sweden. May 1–7, 2010:4448. Vol 17
9. van Egmond SL, Visser F, Pameijer FA, et al. **Ex vivo and in vivo imaging of the inner ear at 7 Tesla MRI.** *Otol Neurotol* 2014;35:725–29
10. Brink WM, van der Jagt AM, Versluis MJ, et al. **High permittivity dielectric pads improve high spatial resolution magnetic resonance imaging of the inner ear at 7 T.** *Invest Radiol* 2014;49:271–77
11. Rosset A, Spadola L, Ratib O. **OsiriX: an open-source software for navigating in multidimensional DICOM images.** *J Digit Imaging* 2004;17:205–16
12. Sennaroglu L. **Cochlear implantation in inner ear malformations: a review article.** *Cochlear Implants Int* 2010;11:4–41
13. Sennaroglu L, Sarac S, Ergin T. **Surgical results of cochlear implantation in malformed cochlea.** *Otol Neurotol* 2006;27:615–23
14. Millar DA, Hillman TA, Shelton C. **Implantation of the ossified cochlea: management with the split electrode array.** *Laryngoscope* 2005;115:2155–60
15. van der Marel KS, Briaire JJ, Wolterbeek R, et al. **Diversity in cochlear morphology and its influence on cochlear implant electrode position.** *Ear Hear* 2014;35:e9–20
16. Holden LK, Finley CC, Firszt JB, et al. **Factors affecting open-set word recognition in adults with cochlear implants.** *Ear Hear* 2013;34:342–60
17. Wargo CJ, Moore J, Gore JC. **A comparison and evaluation of reduced-FOV methods for multi-slice 7T human imaging.** *Magn Reson Imaging* 2013;31:1349–59
18. Heilmaier C, Theysohn JM, Maderwald S, et al. **A large-scale study on subjective perception of discomfort during 7 and 1.5 T MRI examinations.** *Bioelectromagnetics* 2011;32:610–19
19. Theysohn JM, Maderwald S, Kraff O, et al. **Subjective acceptance of 7 Tesla MRI for human imaging.** *MAGMA* 2008;21:63–72
20. Versluis MJ, Teeuwisse WM, Kan HE, et al. **Subject tolerance of 7 T MRI examinations.** *J Magn Reson Imaging* 2013;38:722–25

Diffusion-Weighted Imaging of the Head and Neck in Healthy Subjects: Reproducibility of ADC Values in Different MRI Systems and Repeat Sessions

A.S. Kolff-Gart, P.J.W. Pouwels, D.P. Noij, R. Ljumanovic, V. Vandecaveye, F. de Keyzer, R. de Bree, P. de Graaf, D.L. Knol, and J.A. Castelijns



ABSTRACT

BACKGROUND AND PURPOSE: DWI is typically performed with EPI sequences in single-center studies. The purpose of this study was to determine the reproducibility of ADC values in the head and neck region in healthy subjects. In addition, the reproducibility of ADC values in different tissues was assessed to identify the most suitable reference tissue.

MATERIALS AND METHODS: We prospectively studied 7 healthy subjects, with EPI and TSE sequences, on 5 MR imaging systems at 3 time points in 2 institutions. ADC maps of EPI (with 2 b-values and 6 b-values) and TSE sequences were compared. Mean ADC values for different tissues (submandibular gland, sternocleidomastoid muscle, spinal cord, subdiaphragmatic lymph node, and tonsil) were used to evaluate intra- and intersubject, intersystem, and intersequence variability by using a linear mixed model.

RESULTS: On 97% of images, a region of interest could be placed on the spinal cord, compared with 87% in the tonsil. ADC values derived from EPI-DWI with 2 b-values and calculated EPI-DWI with 2 b-values extracted from EPI-DWI with 6 b-values did not differ significantly. The standard error of ADC measurement was the smallest for the tonsil and spinal cord (standard error of measurement = $151.2 \times 10^{-6} \text{ mm}^2/\text{s}^2$ and $190.1 \times 10^{-6} \text{ mm}^2/\text{s}^2$, respectively). The intersystem difference for mean ADC values and the influence of the MR imaging system on ADC values among the subjects were statistically significant ($P < .001$). The mean difference among examinations was negligible (ie, $<10 \times 10^{-6} \text{ mm}^2/\text{s}^2$).

CONCLUSIONS: In this study, the spinal cord was the most appropriate reference tissue and EPI-DWI with 6 b-values was the most reproducible sequence. ADC values were more precise if subjects were measured on the same MR imaging system and with the same sequence. ADC values differed significantly between MR imaging systems and sequences.

ABBREVIATIONS: 2b = 2 b-values; 6b = 6 b-values; IQR = interquartile range; LoA = limits of agreement; SEM = standard error of measurement

Almost 3% of all malignancies are head and neck cancer, 95% of which are squamous cell carcinomas.¹ MR imaging is one of the modalities used in the work-up of patients with head and neck cancer.² DWI is an MR imaging technique by which diffusion properties of water can be quantified as an ADC value.³ Changes in ADC are inversely correlated with changes in cellularity.⁴ In tissues with high cellularity, diffusion of extracellular water in particular is limited by cell membranes, which

give low ADC values. In tissues with low cellularity, when diffusion is facilitated (eg, in edematous or necrotic tissue), ADC values are high.

Indications for DWI in head and neck cancer include tissue characterization of primary tumors and nodal metastases, prediction and monitoring of treatment response after chemotherapy or radiation therapy, and differentiation of radiation changes and residual or recurrent disease.⁵

Neither the optimal DWI sequence for assessment of the head and neck region nor its reproducibility has been clearly established, to our knowledge. DWI can be performed with either EPI or TSE sequences, of which the EPI sequence is most commonly used in the head and neck area.^{6,7} On EPI-DWI, more malignant lesions can be detected and lesion delineation is facilitated. However, the interobserver agreement of ADC values is reported to be higher on TSE-DWI, probably due to the frequent occurrence of artifacts and geometric distortions in EPI-DWI.⁸

Currently the use of DWI in head and neck imaging is mostly confined to research protocols and advanced academic centers.

Received May 6, 2014; accepted after revision July 28.

From the Departments of Radiology and Nuclear Medicine (A.S.K.-G., D.P.N., R.L., P.d.G., J.A.C.), Physics and Medical Technology (P.J.W.P.), Otolaryngology-Head and Neck Surgery (R.d.B.), and Clinical Epidemiology and Biostatistics (D.L.K.), VU University Medical Center, Amsterdam, the Netherlands; and Department of Radiology (V.V., F.d.K.), University Hospitals Leuven, Leuven, Belgium.

Please address correspondence to Jonas A. Castelijns, MD, PhD, Department of Radiology and Nuclear Medicine, VU University Medical Center, PO Box 7057, 1007 MB Amsterdam, the Netherlands; e-mail: j.castelijns@vumc.nl



Indicates article with supplemental on-line appendix.



Indicates article with supplemental on-line photo.

<http://dx.doi.org/10.3174/ajnr.A4114>

Before DWI can be used in multicenter studies, its reproducibility across different centers and MR imaging systems should be validated.⁹ ADC values may be affected by the selected technique and MR imaging system (eg, due to differences in gradient systems, coils, pulse-sequence designs, imaging parameters, and artifacts related to susceptibility effects or eddy currents).¹⁰ Information on variance is needed.¹¹ Furthermore, the use of reference tissues might help ascertain the variability among different MR imaging systems and could potentially help correct for differences in ADC values among MR imaging systems.

The purpose of this prospective study was to determine the reproducibility of ADC values in the head and neck region obtained from DWI on the basis of both EPI and TSE sequences in repeated measurement on different MR imaging systems in healthy subjects. In addition, we assessed which tissue shows the highest reproducibility in ADC values, so that it could function as a reference tissue in future studies.

MATERIALS AND METHODS

Subjects

The study population consisted of 7 healthy subjects, 5 men and 2 women (age range, 27–54 years; median age, 30 years). The subjects were examined in 2 institutions: VU University Medical Center and University Hospitals Leuven. All examinations were performed in 2011, after obtaining approval from the relevant institutional review boards and written informed consent from all subjects. We used the

following MR imaging systems: I) Avanto (Siemens, Erlangen, Germany), II) Sonata (Siemens), III) Signa HDxt (GE Healthcare, Milwaukee, Wisconsin), and IV) Aera (Siemens), all at 1.5T, and V) Achieva (Philips Healthcare, Best, the Netherlands) at 3T. All examinations were performed with a dedicated head and neck radiofrequency coil in combination with a spine-array coil.

All subjects were examined on all MR imaging systems at 3 time points per MR imaging system, yielding a total of 15 sessions per subject. Two examinations were performed on the same day (between examinations, the subject was removed from the MR imaging system), and 1 examination, at least 1 month later.

Imaging Protocol

Each session included an anatomic T2-weighted sequence through the neck and up to 3 DWI sequences, with acquisition parameters as similar as possible among the MR imaging systems. Due to technical limitations, no EPI-DWI with 6 b-values (6b) was performed on 1 MR imaging system (Signa HDxt), and on 2 MR imaging systems (Aera and Achieva), no separate EPI-DWI with 2 b-values (2b) was performed. The sequences used per MR imaging system are shown in Table 1 and Fig 1.

All imaging was acquired with 21 transverse sections centered on the epiglottis (section thickness, 4 mm; intersection gap, 0.4 mm). The imaging protocol consisted of both conventional T2-weighted (TR/TE, at least 3700/90–110 ms; in-plane pixel size, 0.95 × 0.95 mm) and EPI-DWI (TR/TE, at least 4300/59–98 ms; in-plane pixel size, 1.5–1.9 × 1.5–1.9 mm; interpolated in-plane pixel size, 0.75–0.95 mm) or TSE-DWI (TR/TE, 900–3000/84–113 ms; in-plane pixel size, 1.3 × 1.3 mm). B-values for the 3 DWI series were as follows: 1) EPI-DWI obtained with 6 b-values of 0, 50, 100, 500, 750 and 1000 s/mm², 2) EPI-DWI obtained with 2 b-values of 0 and 1000 s/mm², and 3) TSE-DWI obtained with 2 b-values also of 0 and 1000 s/mm².

Table 1: Specification of DWI sequences obtained at each MRI system

	I	II	III	IV	V
Manufacturer	Siemens	Siemens	GE	Siemens	Philips
Model	Avanto	Sonata	Signa HDxt	Aera	Achieva
Center	Amsterdam	Amsterdam	Amsterdam	Leuven	Leuven
Field strength	1.5T	1.5T	1.5T	1.5T	3T
Conventional T2	+	+	+	+	+
EPI-DWI-2b	+	+	+	o	o
EPI-DWI-6b	+	+	–	+	+
TSE-DWI-2b	+	+	+	–	–

Note:—Amsterdam indicates VU University Medical Center; Leuven, University Hospitals Leuven; +, sequence performed; –, sequence not performed, not available; o, data extracted from 6b.

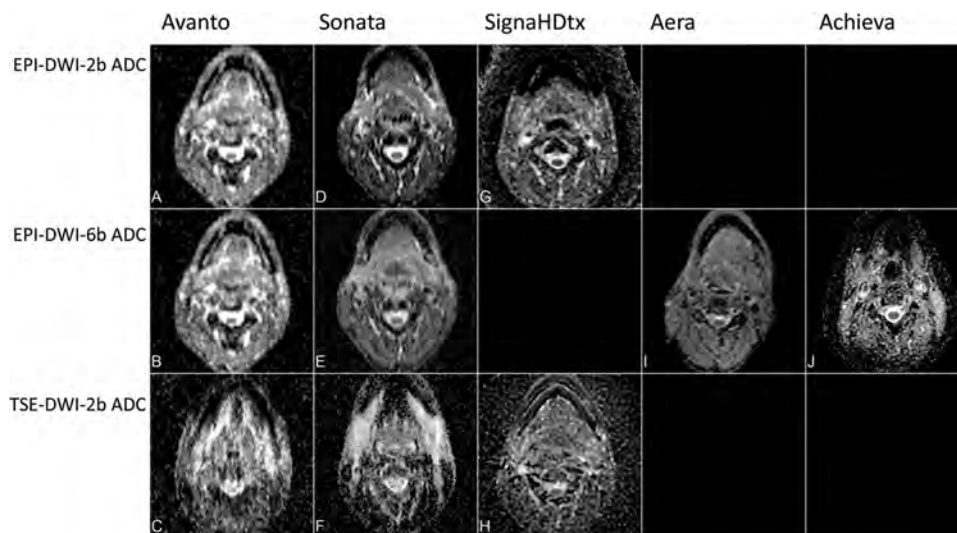


FIG 1. ADC maps of all DWI sequences on all MR imaging systems. On Signa HDxt (GE Healthcare), EPI-DWI-6b ADC was not performed. On Aera (Siemens) and Achieva (Philips Healthcare), EPI-DWI-2b ADC was extracted from EPI-DWI-6b and TSE-DWI-2b was not performed.

Table 2: Number of placed ROIs per tissue and per sequence^a

	Tonsil	Spinal Cord	SCM	SMG	SDG LN	Total
EPI-DWI-2b (No.) (%)	58 (90)	74 (96)	75 (97)	76 (99)	74 (99)	357 (96)
EPI-DWI-6b (No.) (%)	57 (89)	76 (99)	76 (99)	76 (99)	74 (99)	359 (97)
TSE-DWI-2b (No.) (%)	50 (83)	76 (97)	77 (97)	76 (96)	72 (97)	351 (95)
Total	165 (87)	226 (97)	228 (98)	228 (98)	220 (98)	1067 (96)

Note:—SCM indicates sternocleidomastoid muscle; SMG, submandibular gland; SDG LN, subdigastic lymph node.
^a The percentage of the maximum number of possible ROIs displayed is in parentheses. Elimination is due to poor image quality or artifacts.

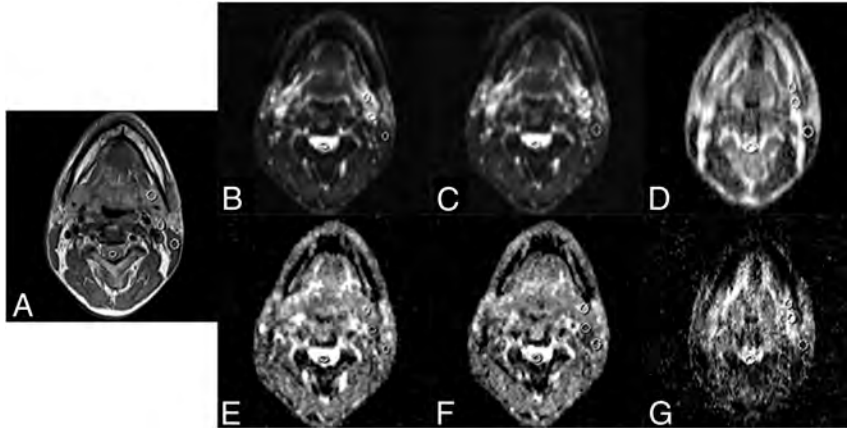


FIG 2. Examples of regions of interest drawn on T2 (A), EPI-DWI-2b B0 (B), EPI-DWI-6b B0 (C), TSE-DWI-2b B0 (D), EPI-DWI-2b ADC (E), EPI-DWI-6b ADC (F), and TSE-DWI-2b ADC (G). The tonsils are not visible at this level. Images were acquired with Avanto (Siemens).

Data Analysis

All ADC maps were calculated on-line or off-line by using the MR imaging system software of the respective vendor. EPI-DWI-6b was analyzed assuming a monoexponential ADC. ADC values for EPI-DWI-2b on the 2 MR imaging systems without EPI-DWI-2b were derived from EPI-DWI-6b by selecting only the images acquired by using $b=0$ s/mm² and $b=1000$ s/mm².¹² These “generated” EPI-DWI-2b data were compared with the other EPI-DWI-2b data. Data were transferred to a DICOM viewer.

For each examination, 1 elliptic region of interest per tissue was manually drawn on the section that contained the bulk of the tissue of interest by 1 observer (R.L.) with 7 years of experience in head and neck imaging. ADC values were determined for each of the following 5 tissues in the head and neck: 1) submandibular gland, 2) sternocleidomastoid muscle, 3) spinal cord, 4) subdigastic lymph node, and 5) tonsil. For the selection of a subdigastic lymph node, either the left or right one was selected consistently within each subject. The size (range, 20–50 mm²) and the position of the region of interest were identified on T2-weighted images. ROIs were drawn on corresponding B0 images by visual comparison with the anatomic T2WI. ROIs drawn on $b=0$ s/mm² images were copied to the corresponding ADC maps.

Statistical Analysis

First, it was determined whether ADC values of the EPI-DWI-2b sequences can be replaced with ADC maps obtained by selecting only the $b=0$ and $b=1000$ s/mm² images from the EPI-DWI-6b (for MR imaging systems IV and V), because they are theoretically equivalent. We used a linear mixed model, with fixed effects for subjects,

MR imaging systems, sequences, and an MR imaging system × sequences interaction.^{13,14} Random effects were all possible interactions with the subjects (On-line Appendix). This possibility was tested by using data from MR imaging systems I and II, these being the only MR imaging systems on which both sequences had been performed.

For the main variance analysis, 5 MR imaging systems and 3 sequences were compared by using the same statistical modeling approach and reasoning as those used for the linear mixed model and by incorporating tissues as fixed effects (On-line Appendix). All 3 examinations of each subject were assumed pure replications and were nested within subject × MR imaging system combinations. Models with sequence-specific error variances were compared by using the Akaike Information Criterion.¹⁵ The standard error of measurement (SEM) for ADC values per tissue was expressed as the square root of the sum of residual variance (σ^2_E) and the variance expressing the interaction between replication and subjects at different MR imaging systems ($\sigma^2_{R:IM}$), sequences ($\sigma^2_{SR:IM}$), and tissues ($\sigma^2_{TR:IM}$) (On-line Appendix):

$$SEM = \sqrt{\sigma^2_{R:IM} + \sigma^2_{SR:IM} + \sigma^2_{TR:IM} + \sigma^2_E}$$

Differences in mean ADC values for all systems and the between-subjects effects were tested by using a Levene Test of Equality of Error Variances; an α -level of .05 was used for statistical significance.¹⁶ All missing data or images with poor quality of DWI were specifically labeled for statistical analysis. Boxplots were created by using SPSS (Version 20.0; IBM, Armonk, New York). All other analyses were performed with Proc NL MIXED of SAS (Version 9.2; SAS Institute, Cary, North Carolina).

RESULTS

DWI

All subjects underwent multiple DWI sessions with multiple sequences on all MR imaging systems. For MR imaging system III, EPI-DWI-6b was unavailable; for MR imaging systems IV and V, ADC maps for EPI-DWI-2b were constructed by using only the $b=0$ and $b=1000$ s/mm² images from the EPI-DWI-6b, yielding a total of 12 DWI sequences per subject (Table 1). Two subjects underwent 2 instead of 3 replications. One subject had prior bilateral tonsillectomies. Therefore, the maximum number of possible ROIs was 1104. For a detailed overview of the number of possible ROIs, see On-line Figure. Further elimination was due to technically failed images and image-specific poor quality, and in 37 cases, it was impossible to place a region of interest: In 95% of tissues, region-of-interest placement was possible on TSE-DWI-2b; in 96%, on EPI-DWI-2b; and in 97%, on EPI-DWI-6b (Table 2). Examples of ADC maps on different MR

imaging systems and sequences are shown in Fig 1. An example of drawn ROIs is shown in Fig 2.

When combining the results of the 3 DWI sequences, region-of-interest placement was possible in 96% of tissues (Table 2). However, in only 87% (range, 83%–90%) of images could a region of interest be placed on the tonsil. In the other regions, ROIs could be placed in 97%–98% of cases. These data indicate that the tonsil is probably not a good reference tissue for future evaluations.

A variance component analysis was performed for MR imaging systems I and II to test potential differences between ADC values derived from the EPI-DWI-2b sequence and the calculated EPI-DWI-2b extracted from EPI-DWI-6b (Table 3). The lowest bias was found in the subdiaphragmatic lymph node ($0.7 \times 10^{-6} \text{ mm}^2/\text{s}$), and the highest bias was found in the tonsil ($-23.2 \times 10^{-6} \text{ mm}^2/\text{s}$). Furthermore, this analysis showed a small range of limits of agreement (LoA) (range, $-307.0 \times 10^{-6} \text{ mm}^2/\text{s}$ to $302.4 \times 10^{-6} \text{ mm}^2/\text{s}$) for all tissues combined. This finding implies that both ADC values are not significantly different. Therefore, we used calculated EPI-DWI-2b ADC values extracted from EPI-DWI-6b on systems if EPI-DWI-2b was not available for further analysis.

The intersystem difference between the MR imaging systems, with mean ADC values as a dependent variable, was statistically significant ($P < .001$). The influence of the sequence, the MR imaging system, and the interaction between these 2 parameters was significant ($P = .011$). The influence of the MR imaging system on the ADC values among the subjects ($P < .001$) was also significant.

Main Variance Analysis

For the main analysis, the actual median ADC values and the results of the main variance component analysis per tissue are shown in Table 4 and are visualized in a boxplot (Fig 3). The 3 DWI sequences used showed some difference: The EPI-DWI-6b sequence demonstrated the smallest interquartile range (IQR)

Table 3: Comparison of ADC values derived from calculated EPI-DWI-2b extracted from EPI-DWI-6b and EPI-DWI-2b for MRI systems I and II

	Bias ($10^{-6} \text{ mm}^2/\text{s}$)	LoA ($10^{-6} \text{ mm}^2/\text{s}$)
Tonsil	-23.2 (-2.9)	-307.0–260.7
Spinal cord	-12.7 (-1.2)	-296.6–271.1
SCM	10.8 (1.1)	-273.1–294.6
SMG	18.6 (1.3)	-265.3–302.4
SDG LN	0.7 (0.1)	-283.2–284.5

Note:—SCM indicates sternocleidomastoid muscle; SMG, submandibular gland; SDG LN, subdiaphragmatic lymph node.

^a In parentheses, the bias is displayed as a percentage of the mean ADC from EPI-DWI-2b for MRI systems I and II.

Table 4: Actual ADC values ($10^{-6} \text{ mm}^2/\text{s}$) and standard error of ADC measurement ($10^{-6} \text{ mm}^2/\text{s}$) for all subjects and MRI systems

	EPI-DWI-2b		EPI-DWI-6b		TSE-DWI-2b		Total per Tissue	
	Median (IQR)	SEM						
Tonsil	791 (675–876)	134.2	746 (674–857)	119.6	1089 (839–1272)	203.0	813 (694–980)	151.2
Spinal cord	950 (868–1053)	194.4	950 (865–1016)	170.6	1076 (908–1303)	204.2	976 (873–1100)	190.1
SCM	990 (782–1276)	221.6	1084 (810–1317)	210.5	534 (286–822)	285.0	872 (611–1171)	237.8
SMG	1257 (1090–1462)	247.0	1233 (1066–1362)	222.5	1392 (1030–1638)	431.2	1271 (1066–1468)	295.5
SDG LN	1042 (809–1211)	307.9	1027 (870–1174)	242.9	1393 (1124–1709)	322.0	1099 (910–1360)	291.0
Total per sequence	1000 (815–1226)	216.6	1000 (830–1217)	190.3	1082 (812–1414)	284.5	1020 (819–1273)	238.3

Note:—SCM indicates sternocleidomastoid muscle; SMG, submandibular gland; SDG LN, subdiaphragmatic lymph node.

values ($830\text{--}1217 \times 10^{-6} \text{ mm}^2/\text{s}$) and lowest SEM (190.3) in ADC for all tissues. The TSE-DWI-2b sequence demonstrated the broadest IQR ($812\text{--}1414 \times 10^{-6} \text{ mm}^2/\text{s}$) and largest SEM ($284.5 \times 10^{-6} \text{ mm}^2/\text{s}$) for all tissues, while EPI-DWI-2b and EPI-DWI-6b showed a narrower IQR ($815\text{--}1226 \times 10^{-6} \text{ mm}^2/\text{s}$ and $830\text{--}1217 \times 10^{-6} \text{ mm}^2/\text{s}$, respectively) and a smaller SEM ($216 \times 10^{-6} \text{ mm}^2/\text{s}$ and $190.3 \times 10^{-6} \text{ mm}^2/\text{s}$, respectively). Therefore measurements on EPI-DWI-2b and EPI-DWI-6b are more precise. Note that with TSE-DWI-2b, the lowest number of ADCs was available for analysis (95%, Table 2).

The spinal cord and tonsil showed the smallest IQR ($873\text{--}1100 \times 10^{-6} \text{ mm}^2/\text{s}$ and $694\text{--}980 \times 10^{-6} \text{ mm}^2/\text{s}$, respectively) and lowest SEM ($190.1 \times 10^{-6} \text{ mm}^2/\text{s}$ and $151.2 \times 10^{-6} \text{ mm}^2/\text{s}$, respectively) (Table 4 and Fig 4). These tissues have the lowest SEM, indicating that ADC measurements in these tissues are the most precise and the best reproducible ones. However, even though the SEM is low for the spinal cord (SEM = $190.1 \times 10^{-6} \text{ mm}^2/\text{s}$), with a median ADC of $976 \times 10^{-6} \text{ mm}^2/\text{s}$, the range of normal values is still broad (IQR = $873\text{--}1100 \times 10^{-6} \text{ mm}^2/\text{s}$).

Variance caused by time is limited (Fig 5). The mean difference in ADC values of the second examination compared with the first, which were on the same day, was $6 \times 10^{-6} \text{ mm}^2/\text{s}$ (SD = $310 \times 10^{-6} \text{ mm}^2/\text{s}$). For the third examination, 1 month after the first, the mean difference in ADC values was $-5 \times 10^{-6} \text{ mm}^2/\text{s}$ (SD = $310 \times 10^{-6} \text{ mm}^2/\text{s}$) compared with the first measurement.

DISCUSSION

Before quantitative DWI can be applied in a multicenter study, knowledge is required about the reproducibility of ADC values within a subject, among different MR imaging systems, and among sequences.¹⁰ This study is a first step to obtaining that knowledge.

In this study, we assessed the reproducibility of ADC values for different DWI sequences, MR imaging systems, and tissues in the head and neck. As expected, the variance in ADC values per subject per tissue is the smallest if the subject is measured on the same MR imaging system with the same sequence. The EPI-DWI-6b sequence showed the best reproducibility for all compared tissues, though this sequence was not available on all MR imaging systems. The EPI-DWI-2b sequence had a slightly lower reproducibility than the EPI-DWI-6b. Advantages of EPI-DWI-2b are a shorter acquisition time and being more widely clinically available. ADC measurements in the spinal cord and tonsil were the most precise and reproducible. Because the spinal cord is almost always present in the FOV during a head and neck study, this tissue can potentially be used as a reference. It also has the advantage of being rarely affected by malignancy; this advantage is in

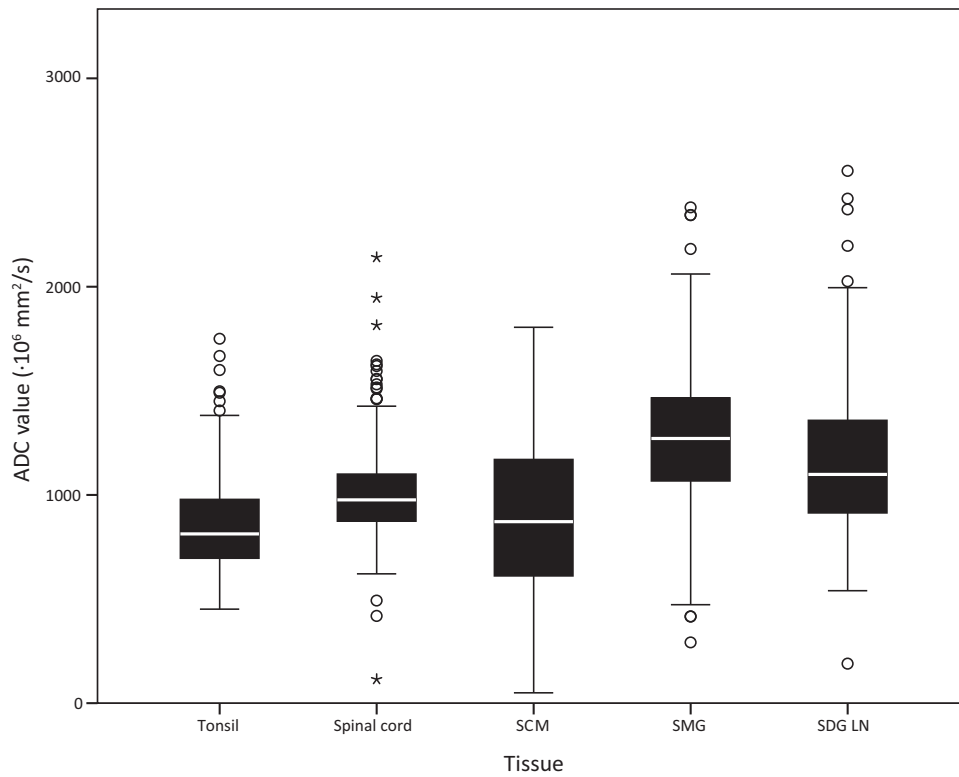


FIG 3. Boxplots showing the distribution of ADC values ($\times 10^{-6} \text{ mm}^2/\text{s}$) per sequence. The *points* are outliers (ie, >1.5 IQRs away from the 25th or 75th percentile). The *asterisk* is an extreme outlier (ie, >3 IQRs away from the 25th or 75th percentile).

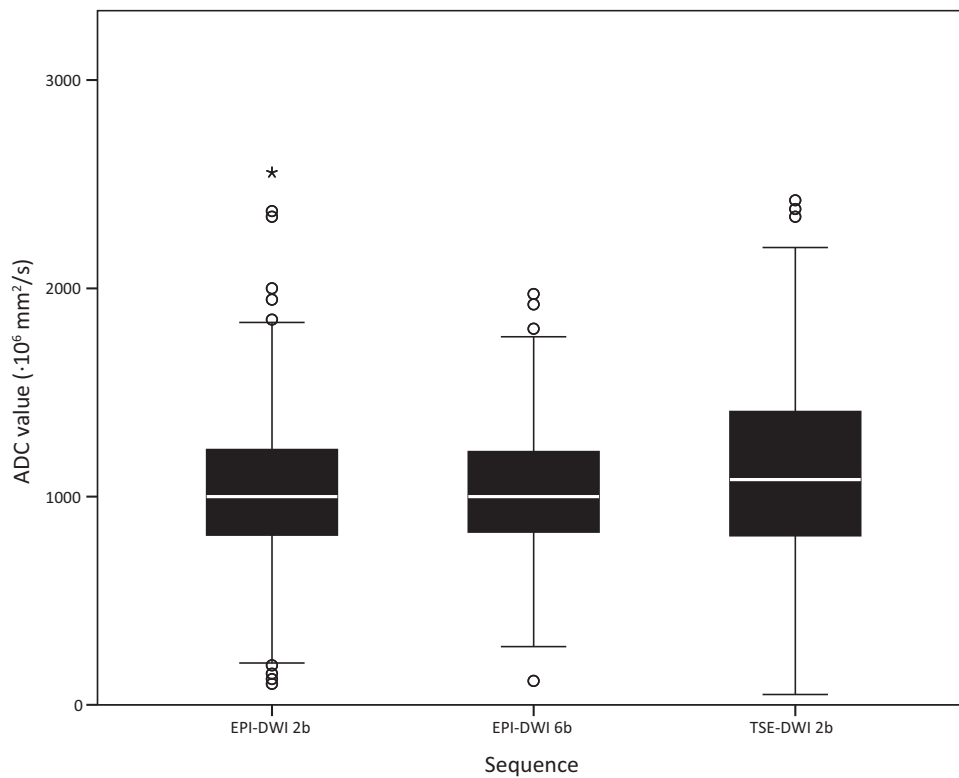


FIG 4. Boxplots showing the distribution of ADC values ($\times 10^{-6} \text{ mm}^2/\text{s}$) per tissue. The *points* are outliers (ie, >1.5 IQRs away from the 25th or 75th percentile). The *asterisks* are extreme outliers (ie, >3 IQRs away from the 25th or 75th percentile).

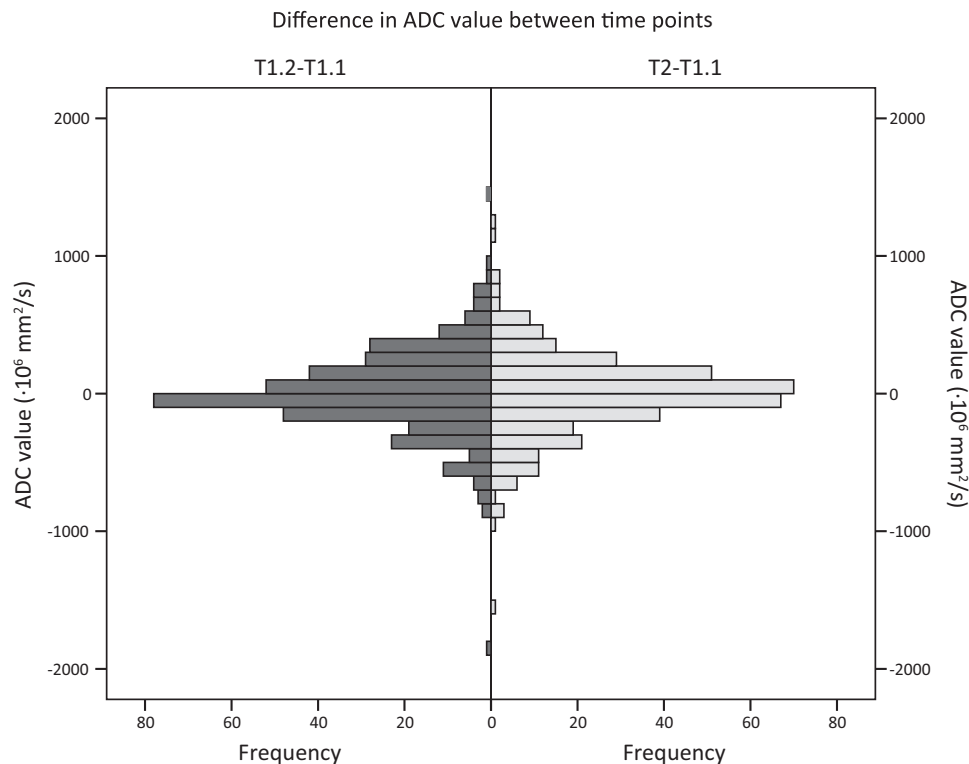


FIG 5. Histograms showing the difference in ADC values ($\times 10^{-6} \text{ mm}^2/\text{s}^2$) compared with the first scan (T1.1). T1.1 and T1.2 were obtained on the same day. T2 was 1 month later. T1.2–T1.1: mean, $6 \times 10^{-6} \text{ mm}^2/\text{s}^2$; SD, $310 \times 10^{-6} \text{ mm}^2/\text{s}^2$. T2–T1.1: mean, $-5 \times 10^{-6} \text{ mm}^2/\text{s}^2$; SD, $310 \times 10^{-6} \text{ mm}^2/\text{s}^2$.

contrast to the tonsils, which are absent in case of tonsillectomy and frequently prove to be the location of an initially unknown primary tumor.¹⁷ Therefore, the spinal cord seems to be the most suitable to serve as reference tissue.

DWI is frequently used in oncologic imaging.^{18,19} Previous studies have shown the potential of DWI in diagnosing malignancies in the head and neck area, response prediction, and differentiation between treatment-induced tissue changes and residual or recurrent disease.^{6,20,21} However, these studies were conducted in a single institution, without variance in MR imaging systems and protocol. Quantitative MR imaging parameters (eg, ADC) can differ substantially among MR imaging systems and imaging protocols.²² This difference was also confirmed in the present study. We performed 3 examinations on 5 MR imaging systems on healthy subjects. This study validates differences in ADC values being statistically significant for sequences, MR imaging systems, and the interaction between MR imaging systems and sequences.

Verhappen et al⁸ found TSE-DWI to be more reproducible among observers than EPI-DWI in a single-center, single-system study on primary tumors and lymph nodes of 12 patients with head and neck cancer. In the current multicenter, multisystem study, ADC values derived with the EPI-DWI-6b sequence were the most reproducible in healthy subjects with time, followed by EPI-DWI-2b. TSE-DWI-2b was the least reproducible sequence. These different findings may be attributed to the included subjects: healthy volunteers in the current study and patients with head and neck malignancies, which had diffusion restrictions in the study by Verhappen et al.⁸ TSE-DWI-2b has inherently lower SNR,²³ which limits the reproducibility in healthy tissue, whereas it does not have geometric distortion and is apparently sensitive

enough to detect diffusion restriction. In the current study, ROIs were drawn on $b=0 \text{ s/mm}^2$ images in visual correlation with anatomic T2 images. Because EPI-DWI has a higher SNR, small structures (eg, benign lymph nodes) are more easily visualized. EPI-DWI may therefore be more appropriate for the evaluation of small structures. In a study by Vandecaveye et al,²⁰ 57% of malignant lymph nodes had a diameter of $<1 \text{ cm}$; therefore, appropriate evaluation of small (apparently benign) structures is vital. Verhappen et al⁸ drew ROIs on ADC maps of malignant tissue that showed diffusion restriction. Especially, DWI of primary tumors in the head and neck area may have geometric distortion due to the tumor location at the air-tissue interface. In that case, geometric distortion of EPI techniques may reduce reproducibility among observers.⁸

There is also a difference in reproducibility among various tissues in the head and neck area. On all MR imaging systems and sequences, ADC values of the submandibular gland were the least precise (Table 4). An explanation for the relatively poor reproducibility might be the intrinsic physiologic changes in salivary glands during the time of day. ADC values in subdiaphragmatic lymph nodes have a relatively poor reproducibility (Table 4). Subdiaphragmatic lymph nodes are often too small for drawing reliable ROIs, particularly in healthy subjects. Moreover, lymph nodes are prone to changes with time (eg, due to frequently occurring inflammation in the head and neck area). In contrast, ADC values of the spinal cord and the tonsil are the most reproducible within subjects. In 87% of the images, a region of interest could be drawn on the tonsils; this percentage was lower than for the other tissues (range, 97%–98%) (Table 2). In healthy subjects, the tonsils are sometimes too small for reliably drawing a region of interest on

DWI. However, if the tonsils are large enough to allow the assessment of ADC values, these values appear to be relatively stable with time within a subject; this stability results in the relatively high precision and reproducibility of ADC measurements. The sternocleidomastoid muscle has intermediate reproducibility. Small changes in ADC values of muscle tissue may be explained by small differences in muscle tone with time.

Sasaki et al¹⁰ previously assessed the reproducibility of ADC measurements in the brain among MR imaging systems, imaging protocols on different time points, and different institutions. It was concluded that there was significant variability in ADC values depending on the coil systems, imagers, vendors, and field strengths. However, only 3 of 10 patients were imaged more than once on the same MR imaging system. In our study, all patients were imaged multiple times on the same MR imaging system, in different institutions, and with a time interval of at least a month between imaging. We found significant differences between MR imaging systems and sequences.

The present study shows that though the physiology of healthy subjects may change with time, ADC values obtained within 1 person and with the same MR imaging system, protocol, and sequences immediately after the first scan and with an interval of at least 1 month have a low variance (ie, the intrasubject variance is small) (Fig 5). This finding indicates that ADC measurements are reproducible and independent of time. The spinal cord and tonsil are the tissues with the lowest ADC variability when different MR imaging systems, protocols, and sequences are used.

This study had some limitations. We included only healthy subjects with a broad age range for whom a stable physiologic status with time for all normal tissues can only be assumed. On the basis of Fig 5, the influence of time appears to be limited, with mean ADC differences being less than 10×10^{-6} mm/s² among measurements. The stability of the MR imaging systems and sequences used also needs to be assumed. Furthermore, the study population was too small to calculate a conversion factor for different MR imaging systems. A group size of ≥ 50 subjects is needed to calculate such a conversion factor.¹³

CONCLUSIONS

The smallest range of ADC values can be obtained by imaging a subject on the same MR imaging system with an EPI-DWI with 6 b-values. Of the investigated tissues, the spinal cord shows the least variance and therefore should serve as reference tissue in the head and neck region.

REFERENCES

- Jemal A, Bray F, Center MM, et al. **Global cancer statistics.** *CA Cancer J Clin* 2011;61:69–90
- de Bree R, Castelijns JA, Hoekstra OS, et al. **Advances in imaging in the work-up of head and neck cancer patients.** *Oral Oncol* 2009;45:930–35
- Le Bihan D, Breton E, Lallemand D, et al. **Separation of diffusion and perfusion in intravoxel incoherent motion MR imaging.** *Radiology* 1988;168:497–505
- Chenevert TL, Meyer CR, Moffat BA, et al. **Diffusion MRI: a new strategy for assessment of cancer therapeutic efficacy.** *Mol Imaging* 2002;1:336–43
- Thoeny HC, De Keyzer F, King AD. **Diffusion-weighted MR imaging in the head and neck.** *Radiology* 2012;263:19–32
- Vandecaveye V, Dirix P, De Keyzer F, et al. **Predictive value of diffusion-weighted magnetic resonance imaging during chemoradiotherapy for head and neck squamous cell carcinoma.** *Eur Radiol* 2010;20:1703–14
- Kim S, Loevner L, Quon H, et al. **Diffusion-weighted magnetic resonance imaging for predicting and detecting early response to chemoradiation therapy of squamous cell carcinomas of the head and neck.** *Clin Cancer Res* 2009;15:986–94
- Verhappen MH, Pouwels PJ, Ljumanovic R, et al. **Diffusion-weighted MR imaging in head and neck cancer: comparison between half-Fourier acquired single-shot turbo spin-echo and EPI techniques.** *AJNR Am J Neuroradiol* 2012;23:1239–46
- Padhani AR, Liu G, Koh DM, et al. **Diffusion-weighted magnetic resonance imaging as a cancer biomarker: consensus and recommendations.** *Neoplasia* 2009;11:102–25
- Sasaki M, Yamada K, Watanabe Y, et al. **Variability in absolute apparent diffusion coefficient values across different platforms may be substantial: a multivendor, multi-institutional comparison study.** *Radiology* 2008;249:624–30
- Do RK, Chandarana H, Felker E, et al. **Diagnosis of liver fibrosis and cirrhosis with diffusion-weighted imaging: value of normalized apparent diffusion coefficient using the spleen as reference organ.** *AJR Am J Roentgenol* 2010;195:671–76
- Burdette JH, Elster AD, Ricci PE. **Calculation of apparent diffusion coefficients (ADCs) in brain using two-point and six-point methods.** *J Comput Assist Tomogr* 1998;22:792–94
- Carstensen B. *Comparing Clinical Measurement Methods: A Practical Guide.* Hoboken: John Wiley & Sons; 2010:59–67
- Carstensen B, Simpson J, Gurrin LC. **Statistical models for assessing agreement in method comparison studies with replicate measurements.** *Int J Biostat* 2008;4:Article 16
- Akaike H. **A new look at the statistical model identification.** *IEEE Trans Automat Contr* 1974;19:716–23
- Bryman, A, Cramer, D. *Quantitative Data Analysis with SPSS Release 12 and 13: A Guide for Social Scientist.* New York: Routledge; 2005:147–77
- Cianchetti M, Mancuso AA, Amdur RJ, et al. **Diagnostic evaluation of squamous cell carcinoma metastatic to cervical lymph nodes from an unknown head and neck primary site.** *Laryngoscope* 2009;119:2348–54
- Koh DM, Padhani AR. **Diffusion-weighted MRI: a new functional clinical technique for tumour imaging.** *Br J Radiol* 2006;79:633–35
- Sinkus R, Van Beers BE, Vilgrain V, et al. **Apparent diffusion coefficient from magnetic resonance imaging as a biomarker in oncology drug development.** *Eur J Cancer* 2012;48:425–31
- Vandecaveye V, De Keyzer F, Vander Poorten V, et al. **Head and neck squamous cell carcinoma: value of diffusion-weighted MR imaging for nodal staging.** *Radiology* 2009;251:134–46
- Vandecaveye V, De Keyzer F, Nuyts S, et al. **Detection of head and neck squamous cell carcinoma with diffusion weighted MRI after (chemo)radiotherapy: correlation between radiologic and histopathologic findings.** *Int J Radiat Oncol Biol Phys* 2007;67:960–71
- Pagani E, Hirsch JG, Pouwels PJ. **Intercenter differences in diffusion tensor MRI acquisition.** *J Magn Reson Imaging* 2010;31:1458–68
- Reiser M, Faber SC. **Recent and future advances in high-speed imaging.** *Eur Radiol* 1997;7:166–73

Impact of Model-Based Iterative Reconstruction on Image Quality of Contrast-Enhanced Neck CT

S. Gaddikeri, J.B. Andre, J. Benjert, D.S. Hippe, and Y. Anzai

ABSTRACT

BACKGROUND AND PURPOSE: Improved image quality is clinically desired for contrast-enhanced CT of the neck. We compared 30% adaptive statistical iterative reconstruction and model-based iterative reconstruction algorithms for the assessment of image quality of contrast-enhanced CT of the neck.

MATERIALS AND METHODS: Neck contrast-enhanced CT data from 64 consecutive patients were reconstructed retrospectively by using 30% adaptive statistical iterative reconstruction and model-based iterative reconstruction. Objective image quality was assessed by comparing SNR, contrast-to-noise ratio, and background noise at levels 1 (mandible) and 2 (superior mediastinum). Two independent blinded readers subjectively graded the image quality on a scale of 1–5, (grade 5 = excellent image quality without artifacts and grade 1 = nondiagnostic image quality with significant artifacts). The percentage of agreement and disagreement between the 2 readers was assessed.

RESULTS: Compared with 30% adaptive statistical iterative reconstruction, model-based iterative reconstruction significantly improved the SNR and contrast-to-noise ratio at levels 1 and 2. Model-based iterative reconstruction also decreased background noise at level 1 ($P = .016$), though there was no difference at level 2 ($P = .61$). Model-based iterative reconstruction was scored higher than 30% adaptive statistical iterative reconstruction by both reviewers at the nasopharynx ($P < .001$) and oropharynx ($P < .001$) and for overall image quality ($P < .001$) and was scored lower at the vocal cords ($P < .001$) and sternoclavicular junction ($P < .001$), due to artifacts related to thyroid shielding that were specific for model-based iterative reconstruction.

CONCLUSIONS: Model-based iterative reconstruction offers improved subjective and objective image quality as evidenced by a higher SNR and contrast-to-noise ratio and lower background noise within the same dataset for contrast-enhanced neck CT. Model-based iterative reconstruction has the potential to reduce the radiation dose while maintaining the image quality, with a minor downside being prominent artifacts related to thyroid shield use on model-based iterative reconstruction.

ABBREVIATIONS: ASiR30 = 30% adaptive statistical iterative reconstruction; BN = background noise; CNR = contrast-to-noise ratio; FBP = filtered back-projection; HU, Hounsfield units; MBIR = model-based iterative reconstruction; PM = pectoris muscle; SCM = sternocleidomastoid muscle; SVC = superior vena cava

Since the introduction of CT for medical imaging in the early 1970s, there has been tremendous advancement in overall image quality with concomitant shortening of requisite scan times.

Additional major effort has been undertaken to reduce the radiation dose to improve patient safety while maintaining image quality. In particular, image reconstruction algorithms have evolved from the traditional analytic algorithms such as filtered back-projection (FBP) to newer iterative reconstruction methods such as adaptive statistical iterative reconstruction (ASiR; GE Healthcare, Milwaukee, Wisconsin) and most recently model-based iterative reconstruction (MBIR; GE Healthcare), which models system noise statistics and optics.

Both phantom and clinical studies have confirmed that the application of the MBIR algorithm results in an improved contrast-to-noise ratio (CNR), lower background noise (BN),^{1–4} and reduction of helical conebeam artifacts.^{2,4} Clinical studies in the delineation of arteries in the posterior fossa on 3D brain CT angiography,¹ improved liver lesion detection,^{3,5} general evaluation

Received May 25, 2014; accepted after revision August 18.

From the Department of Neuroradiology (S.G., J.B.A., Y.A.), University of Washington Medical Center, University of Washington, Seattle, Washington; Department of Neuroradiology (J.B.), University of Washington and VA Puget Sound, Seattle, Washington; and Department of Radiology (D.S.H.), University of Washington, Seattle, Washington.

Paper previously presented as an abstract at: American Society of Neuroradiology Annual Meeting and the Foundation of the ASNR Symposium, May 17–22, 2014; Montreal, Quebec, Canada.

Please address correspondence to Santhosh Gaddikeri, MD, Department of Radiology, University of Washington Medical Center, 1959 NE Pacific St, Box 357115, Seattle, WA 98195-7115; e-mail: sg272@uw.edu

<http://dx.doi.org/10.3174/ajnr.A4123>

Table 1: Soft-tissue neck CT protocol

CT Protocol	
Scanned region	1 cm above the level of frontal sinus to aortopulmonary window
Type	Helical 0.5-second duration.
Pitch	0.984:1
Gantry tilt	0°
Section thickness and section interval	0.625-mm-thick/0.625 interval and 40-mm detector coverage
Reconstruction	Standard soft-tissue algorithm with 2.5-mm thickness
Matrix	512 × 512
Kilovolt(peak)	140
Noise index at 0.625-mm section thickness	40 HU

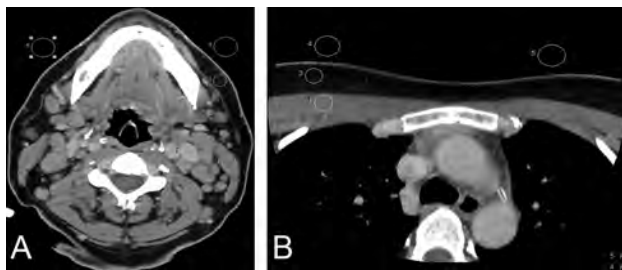


FIG 1. Assessment of objective image quality at the level of the mandible (A) and superior mediastinum (B). Region of interest drawn to measure the SD of air bilaterally (background noise), attenuation of the sternocleidomastoid and pectoralis major muscles, internal jugular vein and superior vena cava, and surrounding fat for the estimation of signal-to-noise ratio and contrast-to-noise ratio.

of abdominopelvic CT,² and pediatric chest CT⁶ all support the use of MBIR, with or without radiation-dose reduction. In this study, we compared objective and subjective image quality in neck CT images reconstructed with 2 different iterative reconstruction algorithms (MBIR versus 30% adaptive statistical iterative reconstruction [ASiR30]) by using the same raw dataset.

MATERIALS AND METHODS

Patients

The local institutional review board approved this Health Insurance Portability and Accountability Act–compliant retrospective study. Sixty-four consecutive contrast-enhanced CT neck examinations, performed during June and July 2013, were included in this study. There were 42 male (66%) and 22 female (34%) patients (median age, 61 years; age range, 20–84 years). The indications for neck CT examinations included initial head and neck cancer staging, lymphoma staging and surveillance, routine follow-up in the setting of treated tumor, and known or suspected soft-tissue neck infection.

Neck CT Protocol

Details of the contrast-enhanced CT neck protocols are described in Table 1. All CT examinations were performed on a 64–detector row multidetector CT (Discovery HD 75; GE Healthcare), with tube current modulation applied at a noise index of 40 Hounsfield units (HU) for 0.625-mm section thickness by using 0.5-second helical gantry rotation. Because the noise index varies with the section thickness, the predicted noise index for 2.5-mm section thickness was about 23.4 HU.⁷ For each diagnostic scan, 80 mL of

iohexol, 350 mg/mL (Omnipaque 350; GE Healthcare), was intravenously administered via a power injector (the initial 50 mL at a rate of 2 mL/s and the remaining 30 mL at 0.5 mL/s) followed by 30 mL of saline (0.9% NaCl) flush at a rate of 1.5 mL/s. The scan was acquired with a delay of 120 seconds following the commencement of contrast injection. A bismuth thyroid shield was placed over the lower neck in all patients as part of a radiation safety exercise at our institution.⁸

CT Data Reconstruction

The raw data from each subject's CT examination were reconstructed at the scanner, with a similar magnification, 2.5-mm section thickness at an interval of 2.5 mm in the axial plane, first with ASiR30 and then with MBIR. Details regarding specifically used reconstruction methods were omitted from the generated image sets to ensure complete blinding of the subjective imaging review. The images were sent to the PACS for analysis.

Quantitative Image Analysis

Quantitative image parameters were assessed by a neuroradiologist with a cumulative experience of 8 years (including 2 years of fellowship training in neuroradiology) in interpreting neck CT examinations (S.G.). Several region-of-interest measurements were performed on a PACS workstation by using a 0.5- to 10-mm-diameter circle tool. Mean attenuation values (V) and SD were measured and recorded in Hounsfield units. BN was also measured and recorded as the SD of air. The measurements on each image set were performed at 2 anatomic levels: level 1, the angle of the mandible (Fig 1A) and level 2, the superior mediastinum (Fig 1B). BN was assessed bilaterally at each level, and the mean was calculated. We placed ROIs on the following structures and recorded their respective measurements: The sternocleidomastoid muscle (SCM) (level 1), pectoralis major muscle (PM) (level 2), dominant internal jugular vein (level 1), superior vena cava (SVC) (level 2), and the surrounding fat (both levels) were measured. Signal-to-noise ratio and the CNR were calculated by using the following standard equations⁹:

$$SNR = V_{\text{muscle}} / BN,$$

$$CNR = V_{\text{vein}} - V_{\text{muscle}} / [(SD_{\text{vein}})^2 + (SD_{\text{muscle}})^2]^{1/2}.$$

Qualitative Image Analysis

Qualitative image analysis was performed at 4 predefined anatomic levels: 1) the nasopharynx (at the level of fossa of Rosenmuller); 2) the oropharynx (at the level of palatine tonsils); 3) the true vocal cords, and 4) the sternoclavicular junction. In patients with prior tonsillectomy or laryngectomy, images were selected at the level of the surgical bed. On a per-subject basis, identical anatomic levels were selected carefully from both the ASiR30 and MBIR image sets. These 4 anatomic levels were specifically chosen for their increased respective incidence of head and neck cancers and/or a proclivity for streak (due to dental amalgam) or beam-

Table 2: Quantitative assessment of image quality (N = 64 subjects)

	MBIR		ASiR		Difference (MBIR-ASiR)		P Value ^a
	Mean	(95% CI)	Mean	(95% CI)	Mean	(95% CI)	
Level 1 (angle of mandible)							
Mean of IJV (HU)	130.3 ± 19.6	(125.4–135.1)	131.0 ± 19.2	(126.2–135.8)	-0.7 ± 2.7	(-1.4 to -0.1)	.030
Mean of SCM (HU)	62.9 ± 5.0	(61.7–64.2)	64.4 ± 4.9	(63.2–65.6)	-1.5 ± 2.2	(-2.0 to -0.9)	<.001
Mean of fat (HU)	-81.4 ± 23.2	(-87.2 to -75.6)	-77.1 ± 23.3	(-82.9 to -71.3)	-4.2 ± 8.1	(-6.3 to -2.2)	<.001
SD of IJV (HU)	6.3 ± 2.6	(5.7–7.0)	7.3 ± 2.0	(6.8–7.8)	-1.0 ± 1.9	(-1.5 to -0.6)	<.001
SD of SCM (HU)	6.6 ± 1.4	(6.3–7.0)	7.1 ± 1.6	(6.7–7.5)	-0.5 ± 1.5	(-0.8 to -0.1)	.020
SD of air (BN) (HU)	6.3 ± 9.2	(4.0–8.6)	7.8 ± 9.2	(5.5–10.1)	-1.5 ± 4.8	(-2.7 to -0.3)	.016
SNR of SCM	16.2 ± 7.2	(14.4–18.0)	12.1 ± 4.3	(11.0–13.2)	4.1 ± 5.7	(2.7–5.5)	<.001
CNR of IJV and SCM	7.6 ± 2.6	(7.0–8.3)	6.8 ± 2.4	(6.2–7.4)	0.9 ± 1.4	(0.5–1.2)	<.001
Lower level 2 (superior mediastinum)							
Mean of SVC (HU)	119.8 ± 24.5	(113.7–125.9)	117.8 ± 23.7	(111.8–123.7)	2.0 ± 7.3	(0.2–3.9)	.030
Mean of PM (HU)	55.6 ± 11.0	(52.9–58.4)	53.3 ± 13.0	(50.1–56.5)	2.3 ± 7.9	(0.4–4.3)	.021
Mean of fat (HU)	-101.3 ± 19.4	(-106.2 to -96.5)	-98.9 ± 18.1	(-103.4 to -94.3)	-2.5 ± 7.7	(-4.4 to -0.6)	.012
SD of SVC (HU)	10.2 ± 4.5	(9.1–11.3)	13.7 ± 4.9	(12.5–14.9)	-3.5 ± 2.8	(-4.2 to -2.8)	<.001
SD of PM (HU)	8.5 ± 2.4	(7.9–9.1)	10.9 ± 2.9	(10.2–11.6)	-2.4 ± 3.0	(-3.2 to -1.7)	<.001
SD of air (BN) (HU)	32.1 ± 32.5	(23.9–40.2)	33.5 ± 30.5	(25.9–41.1)	-1.4 ± 23	(-7.1–4.2)	.61
SNR of PM	6.9 ± 8.1	(4.9–9.0)	3.9 ± 3.4	(3.0–4.7)	3.1 ± 6.4	(1.5–4.7)	<.001
CNR of SVC and PM	4.9 ± 2.0	(4.4–5.4)	3.7 ± 1.6	(3.3–4.1)	1.2 ± 1.3	(0.9–1.5)	<.001

Note:—IJV indicates internal jugular vein.

^a Paired *t* test.

hardening (due to shoulders) artifacts. In addition, readers subjectively evaluated all the images within an image stack (ASiR30 versus MBIR) to assess overall image quality.

Two experienced fellowship-trained neuroradiologists with 9 (J.B. [reader 1]) and 10 (J.B.A. [reader 2]) years of cumulative experience in interpreting neck CT examinations were blinded to the patient information and reconstruction methodology. On a per-patient basis, image stacks obtained from the 2 reconstruction algorithms were displayed side-by-side on each of 2 PACS monitors. Images were presented to reviewers with a prespecified window width and level of 350 and 50 HU, respectively, though reviewers were free to vary both at their discretion. In the absence of a focal lesion, the readers (1 and 2) were asked to evaluate the appearance of normal structures, with special attention paid to the delineation of fat planes, the internal architecture of soft tissues, and overall artifacts burden. In the presence of a focal lesion, readers were asked to evaluate lesion conspicuity, the margins, internal architecture of the lesion, and overall artifacts burden.

Overall image quality and image quality at each of the 4 preselected anatomic locations were graded on a scale of 1–5 (5 = excellent, no artifacts; 4 = good, minimal artifacts; 3 = acceptable, mild artifacts; 2 = suboptimal, moderate artifacts; and 1 = nondiagnostic, significant artifacts). Grades 1 and 2 were considered unacceptable for clinical interpretation. On the basis of the grades of qualitative assessment by each of the readers (1 and 2), the data were divided into 2 categories: category I (readers agree that ASiR > MBIR) and category II (readers agree that MBIR ≥ ASiR).

Statistical Analysis

The paired Student *t* test was used to assess differences in objective measures of image quality between the 2 reconstruction algorithms. Histograms were visually inspected to ensure that distributional assumptions were reasonable. The Wilcoxon signed rank test was used to test for differences in subjective image-quality ratings between the 2 reconstruction algorithms and readers. The percentage agreement of the 2 readers (1 and 2) for the categories I (readers agree that ASiR > MBIR) or II (readers agree that MBIR ≥ ASiR) was assessed at all 4 levels and for overall image

quality. All statistical calculations were conducted with the statistical computing language R (R statistical computing software; (<http://www.r-project.org/>)). Throughout, 2-tailed tests were used with *P* < .05 denoting statistical significance.

RESULTS

Quantitative Analysis

Objective image-quality measurement data are summarized in Table 2. At level 1, the mean BN was significantly lower (*P* = .016) for MBIR compared with ASiR30. The mean attenuation values of the internal jugular vein and SCM for the MBIR dataset were significantly lower (*P* = .03 and *P* < .001, respectively) in comparison with the ASiR30 dataset. At level 2, there was no statistically significant difference (*P* = .61) in the BN between the MBIR and ASiR30 image sets, whereas the mean attenuation values of SVC and PM for the MBIR dataset were significantly higher (*P* = .03 and *P* < .021, respectively) compared with the ASiR30 dataset.

The measured SNRs of the SCM and PM were significantly higher (*P* < .001 and *P* < .001, respectively) for the MBIR dataset compared with the ASiR30 dataset, likely due to reduced BN. The measured CNR of the internal jugular vein and SVC in relation to the SCM and PM was also significantly higher (*P* < .001 and *P* < .001, respectively) for MBIR compared with ASiR30.

Qualitative Analysis

Subjective image-quality assessment is summarized in Table 3. Both readers preferentially graded MBIR over ASiR30 for overall image quality (the entire stack of images) (*P* < .001) and at the levels of the nasopharynx and oropharynx (Figs 2 and 3). Readers preferentially graded ASiR30 over MBIR (*P* < .001) at the level of the vocal cords and sternoclavicular region (Fig 4).

The percentage of agreement and disagreement between the readers for categories I and II is presented as a bar graph (Fig 5). Reader agreement in preferring MBIR to ASiR30 was 83% for overall image quality, 100% at the level of nasopharynx, and 98% at the level of the oropharynx. The percentage of agreement between the 2 readers at the level of the vocal cords and sternoclavicular junction, however, was only 41% and 42%, respectively.

Table 3: Qualitative assessment of image quality, based on average ratings of 2 readers (N = 64 subjects)

	MBIR		ASiR		Difference (MBIR-ASiR)		
	Mean	(95% CI)	Mean	(95% CI)	Mean	(95% CI)	P Value ^a
Nasopharynx	4.80 ± 0.26	(4.74–4.87)	4.16 ± 0.31	(4.08–4.23)	0.65 ± 0.30	(0.57–0.72)	<.001
Oropharynx	3.74 ± 0.60	(3.59–3.89)	3.08 ± 0.64	(2.92–3.24)	0.66 ± 0.37	(0.56–0.75)	<.001
Vocal cord	3.73 ± 0.53	(3.59–3.86)	4.02 ± 0.37	(3.92–4.11)	–0.29 ± 0.53	(–0.42 to –0.16)	<.001
SC junction	3.41 ± 0.48	(3.29–3.53)	3.75 ± 0.25	(3.69–3.82)	–0.34 ± 0.52	(–0.47 to –0.21)	<.001
Overall IQ	3.85 ± 0.32	(3.77–3.93)	3.69 ± 0.28	(3.62–3.76)	0.17 ± 0.31	(0.09–0.24)	<.001

Note:—SC indicates sternoclavicular; IQ, image quality.

^a Wilcoxon signed ranked test.

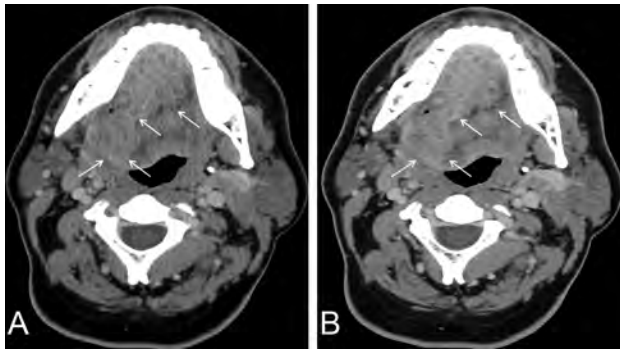


FIG 2. Axial images of contrast-enhanced neck CT at the level of oropharynx reconstructed by using 30% adaptive statistical iterative reconstruction (A) and model-based iterative reconstruction (B). Note better conspicuity and definition of tumor margins on MBIR (arrows) compared with ASiR30 (arrows).

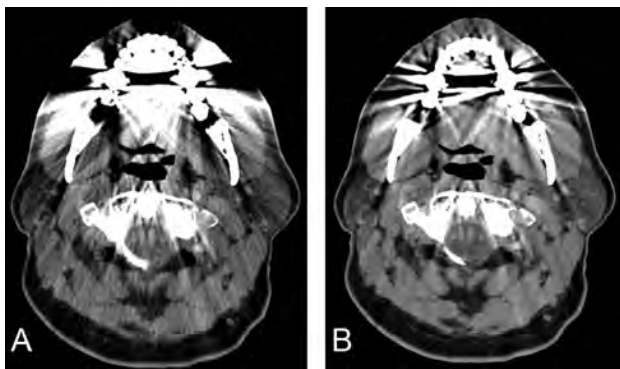


FIG 3. Axial images of contrast-enhanced neck CT at the level of oropharynx reconstructed by using 30% adaptive statistical iterative reconstruction (A) and model-based iterative reconstruction (B). Note a decrease in the streak artifacts related to dental amalgam particularly in the region of the base of the tongue, parotids, and foramen magnum and a poorer definition of fat planes in the parapharyngeal space on MBIR images.

DISCUSSION

CT, enabled by technologic advances and widespread availability, has become the imaging technique of choice in the assessment of numerous neck pathologies. Multidetector CT technology has brought a commensurate increase in the number of CT studies performed,¹⁰ leading to a significant increase in the radiation dose related to CT scanning.^{11,12} Although CT scanning is only approximately 15% of all radiologic examinations, it accounts for up to 70% of the radiation dose to the patient.¹³ Increasing media attention and public awareness regarding the potential risks of radiation exposure, particularly radiation-induced carcinogenesis, have encouraged development of strategies to further reduce the patient radiation dose. The radiation risk to children is of particular concern because the estimated lifetime

cancer risk for a 1-year-old child from the radiation exposure of a head CT is 0.07%.¹⁴ Radiation-induced carcinogenesis may be related to a linear no-threshold stochastic effect¹⁵ or a cumulative radiation effect,¹⁶ particularly in patients with a known history of cancer or other chronic head and neck diseases warranting repeat CT imaging.

There are several strategies for radiation-dose reduction in clinical CT examinations, including changing the CT acquisition parameters (tube current, tube rotation time, peak voltage, pitch, and collimation), use of tube current modulation,¹⁷ automatic exposure control,¹⁸ adjusting the kV on the basis of patient size,¹⁹ iterative reconstruction,^{20–22} and selective in-plane shielding²³ (thyroid, eye lens, breast, or gonadal shield). Developing appropriate CT protocols with an optimal compromise between diagnostic image quality and radiation dose is a team effort of technologist, physicist, and radiologist.²⁴

The FBP algorithm for CT image reconstruction has been the preferred reconstruction algorithm for CT images since its introduction in the 1970s. FBP is based on the assumption that the CT system is perfect and noise-free. However, FBP actually amplifies the quantum and electronic noise in the projection data.²⁵ Its main advantages include speed of image reconstruction due to single-pass direct calculation and production of CT images that are routinely considered clinically acceptable. To overcome the limitation of analytic FBP, iterative techniques for image reconstruction were introduced. ASiR (GE Healthcare) is a partially iterative method using a statistical model of noise that has been commercially available since 2008.^{20,21} It uses the information obtained by initial FBP reconstruction and then repeatedly compares the estimated pixel value with the ideal value predicted by the noise model, until the estimated and ideal values converge.²⁶

MBIR is a fully iterative method that not only models the statistics of noise (photon statistic and electronic noise) but additionally models the system optics (detector response to incident x-ray beam).^{4,27} Prior research has suggested that the MBIR algorithm generates CT images with better noise suppression, spatial resolution, conspicuity, and overall image quality compared with FBP, while maintaining similar uniformity and beam-hardening.²⁸ Several studies have reported clinically relevant radiation-dose reduction by using MBIR while still preserving diagnostic image quality.^{2,5,6,25} One notable drawback of the current version of the MBIR is that it can only reconstruct CT images by using a standard soft-tissue kernel and not a bone kernel; hence, this algorithm fails to provide images with requisite edge details for better assessment of bony lesions.

In this study, the neck CT images reconstructed by using MBIR showed significantly improved SNR and CNR while reduc-

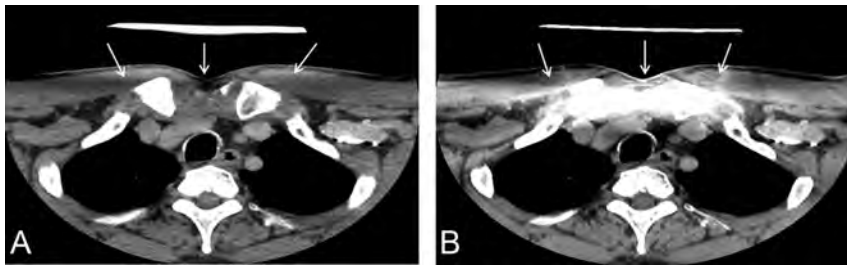


FIG 4. Axial images of contrast-enhanced neck CT at the level of sternoclavicular junction reconstructed by using 30% adaptive statistical iterative reconstruction (A) and model-based iterative reconstruction (B). Artifacts are due to a thyroid shield in the display FOV specific for MBIR (arrows). Note the absence of these thyroid shield artifacts on images reconstructed by using ASiR30 (arrows).

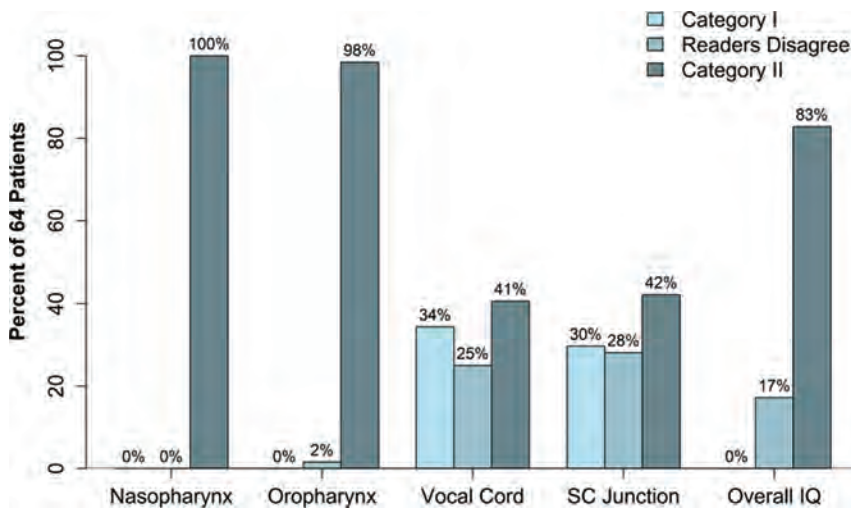


FIG 5. Bar graph showing the percentage of agreement and disagreement between the 2 independent readers (1 and 2) for the assessment of subjective image quality at various levels and overall image quality in both categories (category I: ASiR > MBIR and category II: MBIR ≥ ASiR).

ing the BN compared with images reconstructed by using ASiR30. The qualitative assessment by 2 blinded independent readers suggests that MBIR is superior to ASiR30 at the levels of nasopharynx and oropharynx. However, qualitative assessment at the levels of the vocal cords and sternoclavicular region suggests that ASiR30 is preferred over MBIR in these regions. This observation may, in part, be explained by the presence of a bismuth thyroid shield used for radiation-dose reduction to the thyroid gland. The bismuth shield resulted in artifacts projecting over the vocal cords and sternoclavicular region, which was more prominent on images reconstructed with MBIR, particularly when the shield was close to the skin surface. The exact cause of these artifacts in CT images reconstructed with the MBIR algorithm remains unknown, though we believe that it is at least partly related to the current noise model of the MBIR algorithm, which is not well-equipped to deal with the sharp changes in local attenuation and statistics in the projection sinogram produced at the edges of the bismuth shield. We also believe that these thyroid shield artifacts contributed to the underperformance of MBIR at the level of the vocal cords and sternoclavicular region.

It has been reported from various clinical studies that MBIR methods are better than analytic FBP and ASiR algorithms in providing acceptable image quality in the setting of a lower radiation dose.^{1-3,29-31} The major advantages of MBIR over ASiR in-

clude further improvement in CNR, decrease in BN, and decrease in artifacts while preserving the diagnostic image quality.^{1-3,5,6} In this study, overall image quality in neck CT examinations was improved with MBIR, potentially allowing the exchange of improved image quality for further radiation-dose reduction. A recent study applying MBIR to chest CT reported radiation-dose reductions approaching 70%–80%.¹⁶ In contrast, the expected dose reduction from using a bismuth thyroid shield is 28%.⁸ If a similar radiation-dose reduction can be achieved in contrast-enhanced neck CT examinations by applying a particular postprocessing algorithm, then one could argue that the use of a thyroid shield is less warranted.

The main drawback of MBIR in its present form over other reconstruction algorithms is the computing time, which is about 1 image per second as opposed to 15 images per second for FBP and 10 images per second for ASiR50. In our study, the average reconstruction time for individual soft-tissue neck CT examinations was approximately 45 minutes (range, 30–75 minutes). This time constraint for MBIR, however, should be reduced in the near future due to advancements in computational power.

Study Limitations

Our study has many limitations. First, we did not perform a quality comparison of the MBIR image algorithm with and without the use of a thyroid shield to more accurately compare the image quality of ASiR and MBIR. Second, the qualitative image analysis was a simultaneous assessment of image quality and artifacts burden. As such, this may explain lower subjective scores in areas covered by the thyroid shield. Third, patient data collection was performed in a consecutive fashion, without discrete inclusion criteria to evaluate a specific pathology; thus our study cannot assess the impact of MBIR on the detection of disease.

CONCLUSIONS

MBIR offers improved subjective and objective image quality for contrast-enhanced neck CT, suggesting that MBIR may further reduce the radiation dose while maintaining diagnostic image quality. Further studies are necessary to assess how much radiation-dose savings can be achieved with the application of newer and faster model-based iterative reconstruction algorithms, and further development will be required to bring image processing into clinically reasonable timeframes.

Disclosures: Daniel S. Hippe—UNRELATED: GE Healthcare, Philips Healthcare, Comments: research grants outside current work. Also, Society of Interventional Radiology Foundation award for statistical analysis work on another study.

REFERENCES

1. Machida H, Takeuchi H, Tanaka I, et al. **Improved delineation of arteries in the posterior fossa of the brain by model-based iterative reconstruction in volume-rendered 3D CT angiography.** *AJNR Am J Neuroradiol* 2013;34:971–75
2. Yasaka K, Katsura M, Akahane M, et al. **Model-based iterative reconstruction for reduction of radiation dose in abdominopelvic CT: comparison to adaptive statistical iterative reconstruction.** *Springerplus* 2013;2:209
3. Shuman WP, Green DE, Busey JM, et al. **Model-based iterative reconstruction versus adaptive statistical iterative reconstruction and filtered back projection in liver 64-MDCT: focal lesion detection, lesion conspicuity, and image noise.** *AJR Am J Roentgenol* 2013;200:1071–76
4. Thibault JB, Sauer KD, Bouman CA, et al. **A three-dimensional statistical approach to improved image quality for multislice helical CT.** *Med Phys* 2007;34:4526–44
5. Volders D, Bols A, Haspelslagh M, et al. **Model-based iterative reconstruction and adaptive statistical iterative reconstruction techniques in abdominal CT: comparison of image quality in the detection of colorectal liver metastases.** *Radiology* 2013;269:469–74
6. Miéville FA, Berteloot L, Grandjean A, et al. **Model-based iterative reconstruction in pediatric chest CT: assessment of image quality in a prospective study of children with cystic fibrosis.** *Pediatr Radiol* 2013;43:558–67
7. Kanal KM, Stewart BK, Kolokythas O, et al. **Impact of operator-selected image noise index and reconstruction slice thickness on patient radiation dose in 64-MDCT.** *AJR Am J Roentgenol* 2007;189:219–25
8. Gunn ML, Kanal KM, Kolokythas O, et al. **Radiation dose to the thyroid gland and breast from multidetector computed tomography of the cervical spine: does bismuth shielding with and without a cervical collar reduce dose?** *J Comput Assist Tomogr* 2009;33:987–90
9. Bodelle B, Bauer RW, Holthaus L, et al. **Dose and image quality of high-pitch dual source computed tomography for the evaluation of cervical lymph node status: comparison to regular 128-slice single source computed tomography.** *Eur J Radiol* 2013;82:e281–285
10. Kalra MK, Maher MM, Toth TL, et al. **Strategies for CT radiation dose optimization.** *Radiology* 2004;230:619–28
11. Wiest PW, Locken JA, Heintz PH, et al. **CT scanning: a major source of radiation exposure.** *Semin Ultrasound CT MR* 2002;23:402–10
12. Imhof H, Schibany N, Ba-Ssalamah A, et al. **Spiral CT and radiation dose.** *Eur J Radiol* 2003;47:29–37
13. Linton OW, Mettler FA Jr. **National conference on dose reduction in CT, with an emphasis on pediatric patients.** *AJR Am J Roentgenol* 2003;181:321–29
14. Brenner D, Elliston C, Hall E, et al. **Estimated risks of radiation-induced fatal cancer from pediatric CT.** *AJR Am J Roentgenol* 2001;176:289–96
15. Sodickson A, Baeyens PF, Andriole KP, et al. **Recurrent CT, cumulative radiation exposure, and associated radiation-induced cancer risks from CT of adults.** *Radiology* 2009;251:175–84
16. Katsura M, Matsuda I, Akahane M, et al. **Model-based iterative reconstruction technique for radiation dose reduction in chest CT: comparison with the adaptive statistical iterative reconstruction technique.** *Eur Radiol* 2012;22:1613–23
17. Gress H, Wolf H, Baum U, et al. **Dose reduction in computed tomography by attenuation-based on-line modulation of tube current: evaluation of six anatomical regions.** *Eur Radiol* 2000;10:391–94
18. Mulkens TH, Bellinck P, Baeyaert M, et al. **Use of an automatic exposure control mechanism for dose optimization in multi-detector row CT examinations: clinical evaluation.** *Radiology* 2005;237:213–23
19. McCollough CH, Primak AN, Braun N, et al. **Strategies for reducing radiation dose in CT.** *Radiol Clin North Am* 2009;47:27–40
20. Hara AK, Paden RG, Silva AC, et al. **Iterative reconstruction technique for reducing body radiation dose at CT: feasibility study.** *AJR J Roentgenol* 2009;193:764–71
21. Vachha B, Brodoefel H, Wilcox C, et al. **Radiation dose reduction in soft tissue neck CT using adaptive statistical iterative reconstruction (ASIR).** *Eur J Radiol* 2013;82:2222–26
22. Nuyts J, De Man B, Dupont P, et al. **Iterative reconstruction for helical CT: a simulation study.** *Phys Med Biol* 1998;43:729–37
23. Geleijns J, Salvado Artells M, Veldkamp WJ, et al. **Quantitative assessment of selective in-plane shielding of tissues in computed tomography through evaluation of absorbed dose and image quality.** *Eur Radiol* 2006;16:2334–40
24. Hamberg LM, Rhea JT, Hunter GJ, et al. **Multi-detector row CT: radiation dose characteristics.** *Radiology* 2003;226:762–72
25. Fleischmann D, Boas FE. **Computed tomography: old ideas and new technology.** *Eur Radiol* 2011;21:510–17
26. Silva AC, Lawder HJ, Hara A, et al. **Innovations in CT dose reduction strategy: application of the adaptive statistical iterative reconstruction algorithm.** *AJR J Roentgenol* 2010;194:191–99
27. Yu Z, Thibault JB, Bouman CA, Sauer KD, et al. **Fast model-based X-ray CT reconstruction using spatially nonhomogeneous ICD optimization.** *IEEE Trans Image Process* 2011;20:161–75
28. Gramer BM, Muenzel D, Leber V, et al. **Impact of iterative reconstruction on CNR and SNR in dynamic myocardial perfusion imaging in an animal model.** *Eur Radiol* 2012;22:2654–61
29. Kilic K, Erbas G, Guryildirim M, et al. **Lowering the dose in head CT using adaptive statistical iterative reconstruction.** *AJNR Am J Neuroradiol* 2011;32:1578–82
30. Niu Y, Wang Z, Liu Y, et al. **Radiation dose to the lens using different temporal bone CT scanning protocols.** *AJNR Am J Neuroradiol* 2010;31:226–29
31. Singh S, Kalra MK, Hsieh J, et al. **Abdominal CT: comparison of adaptive statistical iterative and filtered back projection reconstruction techniques.** *Radiology* 2010;257:373–83

Radiology Reports for Incidental Thyroid Nodules on CT and MRI: High Variability across Subspecialties

A.T. Grady, J.A. Sosa, T.P. Tanpitukpongse, K.R. Choudhury, R.T. Gupta, and J.K. Hoang



ABSTRACT

BACKGROUND AND PURPOSE: Variability in radiologists' reporting styles and recommendations for incidental thyroid nodules can lead to confusion among clinicians and may contribute to inconsistent patient care. Our aim was to describe reporting practices of radiologists for incidental thyroid nodules seen on CT and MR imaging and to determine factors that influence reporting styles.

MATERIALS AND METHODS: This is a retrospective study of patients with incidental thyroid nodules reported on CT and MR imaging between January and December 2011, identified by text search for "thyroid nodule" in all CT and MR imaging reports. The studies included CT and MR imaging scans of the neck, spine, and chest. Radiology reports were divided into those that mentioned the incidental thyroid nodules only in the "Findings" section versus those that reported the incidental thyroid nodules in the "Impression" section as well, because this latter reporting style gives more emphasis to the finding. Univariate and multivariate analyses were performed to identify radiologist, patient, and nodule characteristics that influenced reporting styles.

RESULTS: Three hundred seventy-five patients met the criterion of having incidental thyroid nodules. One hundred thirty-eight (37%) patients had incidental thyroid nodules reported in the "Impression" section. On multivariate analysis, only radiologists' divisions and nodule size were associated with reporting in "Impression." Chest radiologists and neuroradiologists were more likely to report incidental thyroid nodules in the "Impression" section than their abdominal imaging colleagues, and larger incidental thyroid nodules were more likely to be reported in "Impression" ($P \leq .03$). Seventy-three percent of patients with incidental thyroid nodules of ≥ 20 mm were reported in the "Impression" section, but higher variability in reporting was seen for incidental thyroid nodules measuring 10–14 mm and 15–19 mm, which were reported in "Impression" for 61% and 50% of patients, respectively.

CONCLUSIONS: Reporting practices for incidental thyroid nodules detected on CT and MR imaging are predominantly influenced by nodule size and the radiologist's subspecialty. Reporting was highly variable for nodules measuring 10–19 mm; this finding can be partially attributed to different reporting styles among radiology subspecialty divisions. The variability demonstrated in this study further underscores the need to develop CT and MR imaging practice guidelines with the goal of standardizing reporting of incidental thyroid nodules and thereby potentially improving the consistency and quality of patient care.

ABBREVIATION: ITN = incidental thyroid nodule

Incidental thyroid nodules (ITNs) are a common radiologic finding, seen in 1 in 6 patients undergoing CT and MR imaging examinations of the neck.^{1,2} Unlike nodules seen on sonography, there are no reliable signs of malignancy and no well-accepted guidelines for

reporting ITNs detected on CT and MR imaging. Consequently, the current practice of reporting thyroid nodules on CT and MR imaging by radiologists is highly variable.³ Some radiologists may report all ITNs because there is a chance that an ITN could be malignant. Other radiologists may not report any ITNs because thyroid cancers in ITNs are relatively uncommon⁴ and small thyroid cancers often have an indolent course.^{5,6} In particular, reporting an ITN in the "Impression" section of a radiology report provides more emphasis of the finding and may increase the chance of further work-up.

Different recommendations for patients with the same nodule characteristics and clinical history are problematic because they can lead to variation in practice patterns, potential variation in the quality of patient care, and anxiety for patients, and they can po-

Received June 1, 2014; accepted after revision July 7.

From the Departments of Radiology (A.T.G., T.P.T., K.R.C., R.T.G., J.K.H.), Surgery (J.A.S.), and Radiation Oncology (J.K.H.), Duke Cancer Institute (J.A.S.), and Duke Clinical Research Institute (J.A.S.), Duke University Medical Center, Durham, North Carolina.

Please address correspondence to Jenny K. Hoang, MBBS, Department of Radiology, Duke University Medical Center, Box 3808, Erwin Rd, Durham, NC 27710, e-mail: jennykh@gmail.com; @JennyKHoang

Indicates article with supplemental on-line table.

<http://dx.doi.org/10.3174/ajnr.A4089>

tentially increase health care costs from the performance of more imaging studies, biopsies, and diagnostic surgeries.^{2,7-9} Although some incidental cancers may be diagnosed and treated at an earlier stage, >50% of patients with ITNs that have surgery will ultimately be diagnosed with benign disease.^{10,11}

The variation in reporting styles for ITNs seen on CT and MR imaging has been measured in a recent study, which surveyed radiologists on how they reported different scenarios varying in nodule size and patient history.³ The study demonstrated high variability of ITN reporting, with an overall mean agreement in reporting style of 53% and lower rates of agreement for smaller nodules. A limitation of a survey, however, is that it may not accurately reflect what a radiologist actually does in practice. Another study evaluated reporting practices for ITNs based on radiology reports for cervical spine CT.¹² The authors found that recommendations for ITNs are made inconsistently and the type of management recommended is variable. However, variability in reporting may have been underestimated in their study because it was limited to CT reports issued only by emergency radiologists and did not encompass the reporting practices of abdominal, chest, and neuroimaging radiologists. In addition, the authors did not differentiate between ITNs reported in the “Impression” section of the report versus only the “Findings” section. To fully examine variability in reporting of ITNs, a study should evaluate the reporting style, encompass all radiology subspecialties, and include all CT and MR imaging studies that may lead to detection of ITNs.

The purpose of this study was to describe the reporting practices of radiologists for ITNs seen on CT and MR imaging and to determine the factors associated with reporting ITNs in the “Impression” section of the radiology report. We hypothesized that reporting styles would be influenced not only by nodule and patient characteristics but also by radiologist-specific factors, such as subspecialty training and years of experience. Understanding factors associated with variation in reporting practices among radiologists may help to standardize practice patterns, and demonstration of highly variable practices would support the need for guidelines for reporting ITNs seen on CT and MR imaging.

MATERIALS AND METHODS

Study Group

This was a retrospective study of 401 patients with thyroid nodules reported on CT or MR imaging between January 1, 2011, and December 31, 2011, at a single large academic institution with 8 subspecialty clinical divisions and 59 subspecialty radiologists. Patients were identified by performing a text search of CT and MR imaging reports for the phrase “thyroid nodule” by using the Duke Enterprise Data Unified Content Explorer, a Web application for cohort identification and data extraction. The search encompassed all CT and MR imaging examinations performed during the time of interest regardless of the body part/region imaged. The studies included CT and MR imaging of the neck, spine, and chest. To capture only ITNs, we excluded patients if the imaging study was performed to evaluate the thyroid, if they had prior evaluation of the thyroid (such as previous thyroid sonography or biopsy), or if they had a personal history of thyroid cancer. The study was approved by our institutional review board. Written informed consent was waived by the institutional review board.

Reporting Style

Reports were analyzed by 2 radiologists, each with 4 years’ experience, to determine the reporting style and factors that could influence the reporting style. The primary reporting style of interest was whether the nodule was reported in the “Impression” section of the report (versus only in the “Findings” section) because this action by the radiologist will highlight the finding to the clinician and is more likely to result in subsequent evaluation. Reports were also categorized on the basis of whether the radiologist specifically recommended further work-up with another examination, such as a thyroid sonography.

Factors Associated with Reporting Styles

Data were collected on factors that could influence reporting styles and included characteristics of the radiologists, patients, and nodules. Radiologist characteristics included years of experience after completion of training and radiology subspecialty division (chest imaging, abdominal imaging, neuroradiology, other). At our institution, diagnostic thyroid sonography and sonography-guided thyroid biopsy are performed by abdominal radiologists. Patient characteristics included sex and age and the study indication. Study indication was obtained directly from the dictated radiology report and was categorized into 1 of 5 groups: malignancy, trauma, nontraumatic vascular pathology, inflammation/infection, and other indication. Nodule characteristics consisted of size, morphology (calcified, cystic, hyperenhancing), and the presence of other nodules. Nodule sizes were obtained directly from the reports, and the longest reported dimension was recorded. For statistical analyses, an ITN reported as “subcentimeter” was converted to continuous data by assigning it a size of 8 mm. Eight millimeters was chosen because an ITN of <5 mm is less likely to be clearly seen on CT and MR imaging, while an ITN close to 10 mm would more likely be reported as a 10-mm nodule. Thus, 8 mm was chosen for the purpose of data analysis because it lies between 5 and 10 mm.

Outcome Measures and Statistical Analysis

We calculated the proportion of ITNs reported in the “Impression” section of the report and recommended for further evaluation. Patients with ITNs reported in the “Impression” section were compared with those with ITNs reported only in the “Findings” section of reports. Patients with ITNs recommended for work-up were compared with those without work-up recommendations. Either a χ^2 test or Fisher exact test was used for testing differences in these patients for categorical variables. The unpaired *t* test was used to test for differences for continuous variables. A multivariable logistic regression model was fitted to identify factors that were associated with ITNs that were reported in the “Impression” sections of reports and recommended for further evaluation. A *P* value < .05 was considered statistically significant.

Data were entered into an Excel spreadsheet (2007; Microsoft, Redmond, Washington). Statistical analyses were performed by using the SAS Enterprise Guide (Version 4.2; SAS Institute, Cary, North Carolina).

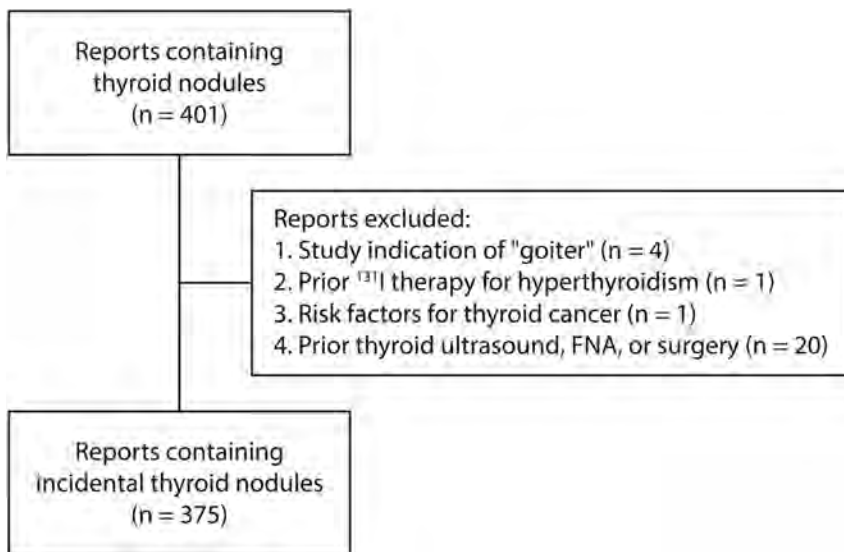


FIG 1. Flowchart of study patients. FNA indicates fine needle aspiration.

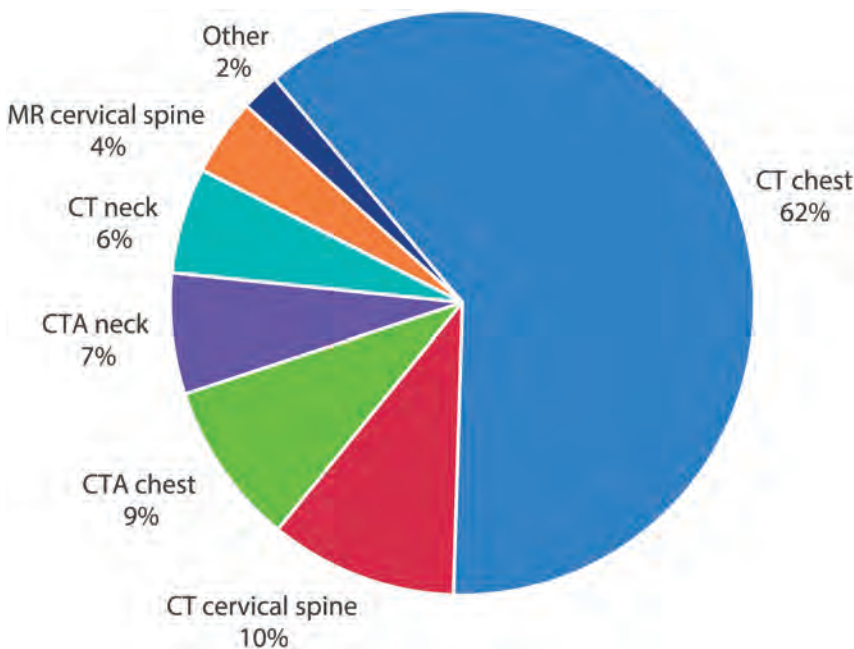


FIG 2. Source of imaging studies with reported incidental thyroid nodules.

RESULTS

Study Group

Three hundred seventy-five patients met the inclusion criteria of having ITNs in their radiology reports and no history of thyroid pathology (Fig 1). The mean patient age was 64 ± 14 years, and 250 (67%) patients were women (On-line Table). CT was the most common source of ITN detection and accounted for 353 (94%) patients, compared with 22 (6%) patients with ITNs on MR imaging studies (Fig 2). In patients who had ITNs discovered on CT, 231 (65%) were identified on chest CT, followed in frequency by cervical spine CT ($n = 39$, 11%) and chest CT angiography ($n = 34$, 10%). The most common study indication for CT or MR imaging was evaluation of malignancy (52%).

Reporting Style

One hundred thirty-eight of 375 (37%) patients had ITNs reported in the "Impression" sections of their reports, while 237 (63%) had ITNs reported only in the "Findings" section (On-line Table). No reports contained ITNs in the "Impression" without the ITNs also being described in the "Findings" section. All reports had both "Findings" and "Impression" sections. Sixty-nine of 375 (18%) patients had ITNs recommended for further work-up (On-line Table). There were no recommendations for investigations other than sonography.

Factors Associated with Reporting in the Impression Section

Univariate analysis found radiology division, study indication, and nodule size to be significantly associated with ITNs reported in the "Impression" sections of reports (P values $< .0001$) (On-line Table). Radiologist experience was not significantly associated with reporting ITNs in the "Impression" section. However, we observed that radiologists with 5–9 years' experience were less likely to report ITNs in the "Impression" (29%) than those with 0–4 years' experience (35%) and >10 years' experience (42%). On multivariate analysis, only radiology division and nodule size remained significant ($P \leq .03$).

Abdominal division radiologists were less likely to report ITNs in the "Impression" section of the report than radiologists in other divisions. ITNs were reported in the "Impression" section in 23% of the studies interpreted by abdominal radiologists compared with 43% for chest radiologists and 50% for neuroradiologists (On-line Table).

Larger nodules were more likely to be reported in the "Impression" sections of reports. The mean nodule size was $16.9 \pm$

9.8 mm for ITNs reported in the "Impression" compared with 15.4 ± 7.4 mm for ITNs not reported in the "Impression" section (On-line Table).

On subgroup analysis of nodule sizes, there was higher variability in reporting styles for ITNs measuring between 10 and 19 mm than for other sizes. Sixty-one percent of 10- to 14-mm nodules and 50% of 15- to 19-mm nodules were reported in the "Impression" (On-line Table and Fig 3). In contrast, there were less variability and more agreement in reporting styles for larger nodules and subcentimeter nodules. Seventy-three percent of ITNs of ≥ 20 mm and only 30% of ITNs < 10 mm were reported in the "Impression" section. Notably, 185 (49%) reports did not provide the nodule size, including 42 patients with ITNs reported in the



FIG 3. Three patients with incidental thyroid nodules that were similar in size but were reported differently. *A*, A 46-year-old man with a 12-mm incidental nodule in the left thyroid lobe detected on chest CTA performed to evaluate an abdominal aortic aneurysm. The nodule was reported only in the “Findings” section of the report without a recommendation. *B*, A 47-year-old woman with a 10-mm incidental nodule in the right thyroid lobe detected on chest CTA performed to evaluate chest pain. The nodule was reported in the “Impression” section without a recommendation. *C*, A 63-year-old man with several incidental thyroid nodules detected on cervical spine CT performed to evaluate neck injury. The largest was in the left thyroid lobe and measured 10 mm. The nodule was reported in the “Impression” section with a recommendation for sonography.

The Duke 3-tiered system for CT, MRI, or PET-detected thyroid nodules^{1,13,14,a}

Category	Criteria for Categories	Recommendations
Risk category 1: highly suspicious for malignancy	PET avid thyroid nodule Suspicious lymphadenopathy; ^b extrathyroid spread with or without signs of vocal cord palsy on side of nodule; lung metastases	Strongly consider work-up with ultrasound for any size nodule
Risk category 2: indeterminate with risk factor of young age	Age younger than 35 years	Consider work-up with ultrasound if ≥ 1 cm in adults Consider work-up with ultrasound for any size in pediatric patients
Risk category 3: indeterminate without risk factors	Age 35 years or older	Consider work-up with ultrasound if ≥ 1.5 cm

^a Intended for management of incidental thyroid nodules in low-risk patients.

^b Suspicious lymph nodes are defined as nodes >10 mm in the short axis (with the exception of jugulodigastric lymph nodes, which are permitted to be up to 15 mm in the short axis) or nodes that contain either calcifications, cystic components, or irregular margins.

“Impression” section of reports and 17 patients with recommendations for sonography.

Factors Associated with Recommendations for Further Work-Up

For factors that influenced recommendations for work-up, univariate analysis found radiology division, radiologist experience, and study indication significantly associated with ITNs recommended for work-up ($P \leq .03$) (On-line Table). On multivariate analysis, study indication and radiology division remained significant ($P < .05$).

Abdominal division radiologists were less likely to recommend work-up for ITNs than those in other divisions. Only 6% of reports generated by abdominal radiologists had recommendations for additional work-up, compared with 32% by chest radiologists and 24% by neuroradiologists (On-line Table). Although radiologist experience did not significantly influence recommendations on multivariate analysis, on univariate analysis, radiologists with 5–9 years’ experience were much less likely to recommend further work-up (10%) than those with 0–4 years’ experience (17%) and >10 years’ experience (24%).

Patients undergoing imaging for another malignancy were less likely to have recommendations for additional work-up of ITNs. Additional work-up for ITNs was recommended in 7% of patients

with known malignancy compared with 31% of patients having imaging for other indications (On-line Table).

DISCUSSION

Variability in reporting styles and recommendations for ITNs by radiologists can lead to confusion among clinicians and may contribute to inconsistent patient care. Ideally, recommendations in radiology reports should be uniform, and factors that influence further evaluation should be based only on nodule and patient characteristics. This study demonstrates that there is high variability for reporting of ITNs measuring 10–19 mm on CT and MR imaging, and that the subspecialty of radiologists is a major factor associated with ITNs being reported in the “Impression” section, independent of nodule size. This finding implies that the high variability in reporting styles is partially due to different practices among subspecialty radiologists.

Our study found that abdominal imaging radiologists were less likely to report ITNs in the “Impression” section of reports and were also less likely to specifically recommend work-up. There are 2 possible reasons for this finding. First, abdominal imaging radiologists are often reading CT examinations covering multiple body parts (such as the chest, abdomen, and pelvis) that may contain many significant findings. Small ITNs may be con-

sidered less important relative to other abnormalities and, therefore, are not included in the “Impression” section of the reports. Second, at our institution, abdominal imaging radiologists perform sonography-guided thyroid biopsies and observe firsthand the high number of benign biopsies, potentially making them less apt to recommend further work-up.

Another radiologist characteristic that was studied was years of experience. A prior study found that the overall rate of recommending additional imaging decreased as radiologists’ experience increased.⁸ However, we did not observe this trend. In fact, the more experienced radiologists were most likely to report ITNs in the “Impression” section and recommend work-up, and radiologists with 5–9 years’ experience were least likely to report ITNs in the “Impression” and recommend work-up. We believe this finding reflects the high baseline variability in ITN reporting irrespective of experience level and that a more influential factor is the tendency for radiologists to utilize a reporting style that is similar to others within their own local subspecialty group.

Lehnert et al¹² also retrospectively evaluated recommendations made in radiology reports for ITNs. Their study was limited to a subset of CT cervical spine scans reported by emergency radiologists, but it did highlight several deficiencies in current radiology reporting practices that are also present in our study. Our study and that of Lehnert et al found that a large proportion of ITNs did not have nodule size described anywhere in the report (49% and 23%, respectively). Size is a significant factor in the decision to further evaluate ITNs; therefore, it is an important feature to describe if the nodule warrants mentioning in the report. Additionally, recommendations were not commonly included in radiology reports. In our study, recommendations were not provided for half of the patients with ITNs reported in the “Impression” section. In the study of Lehnert et al, 43% of ITNs had no management recommendations. Some may argue that recommendations may not be necessary; however, this argument assumes that the clinician recognizes the significance of ITNs and is familiar with their work-up.

Our study also identified highly variable reporting practices for nodules measuring between 10 and 19 mm. These results concur with findings from a survey on how radiologists report ITNs on the basis of scenarios differing in patient age, sex, and nodule size.³ In this survey, the scenario with the highest variability in responses was that of a 60-year-old woman with a 10-mm ITN: Thirty-six percent of radiologists thought that the nodule should be left in the “Findings” section and not receive work-up, while 35% of radiologists would recommend additional work-up with sonography and 21% would report the nodule in the “Impression” without a recommendation.³ In our study, which evaluated actual reporting practices, the practices seen in radiology reports for 10- to 19-mm nodules were also almost equally split: Sixty-one percent of ITNs measuring 10–14 mm and 50% of those measuring 15–19 mm were reported in the “Impression.” This high variability suggests that radiologists are less certain of how to manage ITNs measuring 10–19 mm than they are for ITNs <1 cm or >2 cm, and this size range appears to be one for which future guidelines have the potential to significantly improve reporting consistency.

Although there are not yet any official guidelines from the professional societies within radiology, a categorization method for ITN

discovered on CT, MR imaging, and PET/CT has been proposed and is known as the 3-tiered system (Table).^{1,13,14} The 3-tiered system is based on nodule size, patient age, and suspicious imaging findings. Two retrospective studies found that the 3-tiered system had the potential to reduce radiographic and endocrinologic work-up by 35%–46% without missing a malignancy.^{1,14} In addition to reducing the costs, patient anxiety, and additional procedures that are associated with unnecessary ITN work-up, the advantage of such a system is standardization of radiology reporting and recommendations. From a medical-legal perspective, guidelines would also serve as a resource for radiologists when facing the dilemma of whether and how to report incidentalomas.¹⁵

There are several limitations to this study. First, this is a retrospective study performed at a single institution, and these results may not be generalizable to all radiology practices, particularly smaller, less subspecialized ones. We know that on the basis of prior survey results, radiologists at our institution describe fewer ITNs in the “Impression” section of their reports.^{3,16} In a published survey, a 15-mm nodule in a 60-year-old woman would be reported in the “Impression” section (with or without recommendation) by 78% of respondents³; in our study, 50% of nodules 15–19 mm were actually reported in the “Impression.” In the survey, a 10-mm nodule in a 60-year-old woman would be reported in the “Impression” section (with or without recommendation) by 56% of respondents; in our study, 50% of nodules measuring 10–14 mm were actually reported in the “Impression.” While ITNs may be reported differently at other institutions depending on their size and practice type,³ demonstrating variability even within 1 institution highlights the problem of not having guidance on managing ITNs.

Second, the text report search used likely underestimated the number of incidental thyroid findings by only searching for the phrase “thyroid nodule” and not including other related terms. However, using this single search term provided a sufficient sample size during the 12-month study period, and we do not believe that including all incidental thyroid findings would necessarily alter the results. Third, nearly half of reports did not include a description of the nodule size and were therefore excluded from the analyses examining the relationship between nodule size and reporting style. However, these nodules were included in the univariate analyses of other factors influencing reporting style. Finally, we did not verify the findings reported in the radiology reports by reviewing the images, nor did we examine other studies performed during the time of interest to identify patients who had ITNs on imaging that were overlooked or not reported by the radiologist. Because our aim was to study the factors that influenced reporting, it was only what the radiologist saw and interpreted that was relevant. Finally, we did not evaluate the outcomes of the reporting styles and recommendations because we were focused on radiologist reporting practices. These could be a topic of future study.

CONCLUSIONS

One in 3 patients with ITNs detected on CT or MR imaging has a thyroid nodule reported in the “Impression” section of the report, and half of these patients have recommendations for additional

evaluation. Whether an ITN is reported in the “Impression” versus left in the “Findings” section is predominantly influenced by the nodule size and the radiologist’s subspecialty. The variability demonstrated in this study further underscores the need to develop CT and MR imaging practice guidelines that can be used by all radiologists, with the goal of standardizing reporting of ITNs and thereby potentially improving the consistency and quality of patient care.

Disclosures: Rajan T. Gupta—UNRELATED: Consultancy: Bayer Pharma AG, Payment for Lectures (including service on Speakers Bureaus): Bayer Pharma AG.

REFERENCES

1. Nguyen XV, Choudhury KR, Eastwood JD, et al. **Incidental thyroid nodules on CT: evaluation of 2 risk-categorization methods for work-up of nodules.** *AJNR Am J Neuroradiol* 2013;34:1812–17
2. Yousem DM, Huang T, Loevner LA, et al. **Clinical and economic impact of incidental thyroid lesions found with CT and MR.** *AJNR Am J Neuroradiol* 1997;18:1423–28
3. Hoang JK, Riofrio A, Bashir MR, et al. **High variability in radiologists’ reporting practices for incidental thyroid nodules detected on CT and MRI.** *AJNR Am J Neuroradiol* 2014;35:1190–94
4. Smith-Bindman R, Lebda P, Feldstein VA, et al. **Risk of thyroid cancer based on thyroid ultrasound imaging characteristics: results of a population-based study.** *JAMA Intern Med* 2013;173:1788–96
5. Davies L, Welch HG. **Current thyroid cancer trends in the United States.** *JAMA Otolaryngol Head Neck Surg* 2014;140:317–22
6. Ito Y, Miyauchi A, Inoue H, et al. **An observational trial for papillary thyroid microcarcinoma in Japanese patients.** *World J Surg* 2010;34:28–35
7. Lee SI, Krishnaraj A, Chatterji M, et al. **When does a radiologist’s recommendation for follow-up result in high-cost imaging?** *Radiology* 2012;262:544–49
8. Sistrom CL, Dreyer KJ, Dang PP, et al. **Recommendations for additional imaging in radiology reports: multifactorial analysis of 5.9 million examinations.** *Radiology* 2009;253:453–61
9. Cho JS, Fulgham P, Clark A, et al. **Followup imaging after urological imaging studies: comparison of radiologist recommendation and urologist practice.** *J Urol* 2010;184:254–57
10. Bahl M, Sosa JA, Nelson RC, et al. **Imaging-detected incidental thyroid nodules that undergo surgery: a single-center experience over 1 year.** *AJNR Am J Neuroradiol* 2014;35:2176–80
11. Hobbs HA, Bahl M, Nelson RC, et al. **Applying the Society of Radiologists in Ultrasound recommendations for fine-needle aspiration of thyroid nodules: effect on workup and malignancy detection.** *AJR Am J Roentgenol* 2014;202:602–07
12. Lehnert BE, Sandstrom CK, Gross JA, et al. **Variability in management recommendations for incidental thyroid nodules detected on CT of the cervical spine in the emergency department.** *J Am Coll Radiol* 2014;11:681–85
13. Hoang JK, Raduazo P, Yousem DM, et al. **What to do with incidental thyroid nodules on imaging? An approach for the radiologist.** *Semin Ultrasound CT MR* 2012;33:150–57
14. Hobbs HA, Bahl M, Nelson RC, et al. **Journal club: incidental thyroid nodules detected at imaging—can diagnostic workup be reduced by use of the Society of Radiologists in Ultrasound recommendations and the three-tiered system?** *AJR Am J Roentgenol* 2014;202:18–24
15. Berlin L. **Medicolegal: malpractice and ethical issues in radiology—the incidentaloma.** *AJR Am J Roentgenol* 2013;200:W91
16. Johnson PT, Horton KM, Megibow AJ, et al. **Common incidental findings on MDCT: survey of radiologist recommendations for patient management.** *J Am Coll Radiol* 2011;8:762–67

A Prospective Longitudinal Brain Morphometry Study of Children with Sickle Cell Disease

R. Chen, M. Arkuszewski, J. Krejza, R.A. Zimmerman, E.H. Herskovits, and E.R. Melhem



ABSTRACT

BACKGROUND AND PURPOSE: Age-related changes in brain morphology are crucial to understanding the neurobiology of sickle cell disease. We hypothesized that the growth trajectories for total GM volume, total WM volume, and regional GM volumes are altered in children with sickle cell disease compared with controls.

MATERIALS AND METHODS: We analyzed T1-weighted images of the brains of 28 children with sickle cell disease (mean baseline age, 98 months; female/male ratio, 15:13) and 28 healthy age- and sex-matched controls (mean baseline age, 99 months; female/male ratio, 16:12). The total number of MR imaging examinations was 141 (2–4 for each subject with sickle cell disease, 2–3 for each control subject). Total GM volume, total WM volume, and regional GM volumes were measured by using an automated method. We used the multilevel-model-for-change approach to model growth trajectories.

RESULTS: Total GM volume in subjects with sickle cell disease decreased linearly at a rate of 411 mm³ per month. For controls, the trajectory of total GM volume was quadratic; we did not observe a significant linear decline. For subjects with sickle cell disease, we found 35 brain structures that demonstrated age-related GM volume reduction. Total WM volume in subjects with sickle cell disease increased at a rate of 452 mm³ per month, while the trajectory of controls was quadratic.

CONCLUSIONS: There was a significant age-related decrease in total GM volume in children with sickle cell disease. The GM volume reduction was spatially distributed widely across the brain, primarily in the frontal, parietal, and occipital lobes. Total WM volume in subjects with sickle cell disease increased at a lower rate than for controls.

ABBREVIATIONS: NIHPD = National Institutes of Health MRI Study of Normal Brain Development; SCD = sickle cell disease

Sickle cell disease (SCD) is one of the most common severe single-gene disorders in the United States.¹ SCD is a hemolytic disease characterized by abnormally shaped (sickled) red blood cells, leading to anemia.² Patients with SCD have at least

1 sickle cell hemoglobin chain and 1 other abnormal β globin chain. The most common type of SCD is sickle cell anemia (60%–70% of cases of SCD), characterized by 2 sickle cell hemoglobin genes. The pathophysiology of SCD includes hemoglobin polymerization, chronic anemia, hemolysis, and vasculopathy.

MR imaging provides in vivo structural or functional images of the brain. MR-based brain morphometry centers on neuro-anatomic changes. It could provide a method for demonstrating

Received May 14, 2014; accepted after revision July 16.

From the Department of Diagnostic Radiology and Nuclear Medicine (R.C., J.K., E.H.H., E.R.M.), University of Maryland, Baltimore, Maryland; Department of Neurology (M.A.), Medical University of Silesia, Katowice, Poland; Department of Radiology (R.A.Z.), Children's Hospital of Philadelphia, Philadelphia, Pennsylvania; and Department of Radiology (R.C., R.A.Z.), Raymond and Ruth Perelman School of Medicine, University of Pennsylvania, Philadelphia, Pennsylvania.

Some data used in the preparation of this article were obtained from the Pediatric MRI Data Repository created by the National Institutes of Health MRI Study of Normal Brain Development. This is a multisite, longitudinal study of typically developing children, from ages newborn through young adulthood, conducted by the Brain Development Cooperative Group and supported by the National Institute of Child Health and Human Development, the National Institute on Drug Abuse, the National Institute of Mental Health, and the National Institute of Neurological Disorders and Stroke (contract numbers N01-HD02-3343, N01-MH9-0002, and N01-NS-9-2314, -2315, -2316, -2317, -2319 and -2320).

This article reflects the views of the authors and may not reflect the opinions or views of the National Institutes of Health.

Rong Chen and Edward H. Herskovits were supported by National Institutes of Health grant R01 AG13743, R03 EB-009310 and the American Recovery and Reinvestment Act. Rong Chen was supported by an Institute for Translational Medicine and Therapeutics fellowship, University of Pennsylvania. Jaroslaw Krejza, Michal Arkuszewski, and Elias R. Melhem were supported by National Institutes of Health grant R01 NS 046717.

Please address correspondence to Rong Chen, PhD, MTR, Department of Diagnostic Radiology and Nuclear Medicine, University of Maryland, 22 South Greene St, Baltimore, MD 21201; e-mail: rchen@umm.edu

Indicates open access to non-subscribers at www.ajnr.org

Indicates article with supplemental on-line table.

<http://dx.doi.org/10.3174/ajnr.A4101>

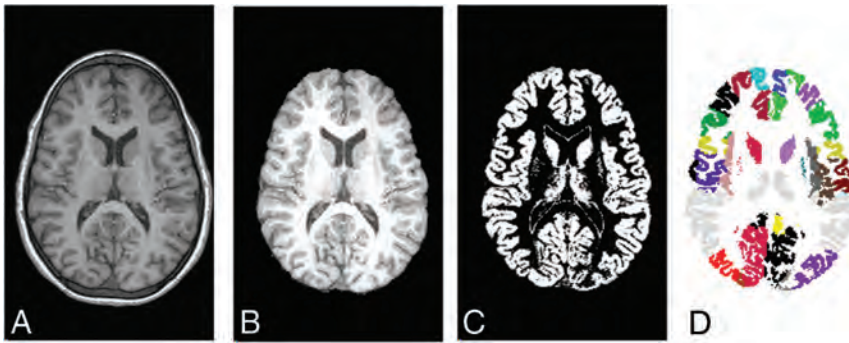


FIG 1. Image-processing pipeline: raw image (A), skull-stripped image (B), segmented gray matter (C), and brain parcellation (D).

brain injury in children with SCD, complementary to lesion-based analysis. Brain atrophy is defined as the abnormal loss of brain-tissue volume and manifests visually as lobar asymmetry, open sulci, or ventricular dilation.³ A quantitative approach to detecting atrophy is brain morphometry, which provides quantitative measurements of brain-tissue volumes. There have been several studies of SCD based on brain morphometry.^{4–7} Baldeweg et al⁴ performed whole-brain voxel-based morphometric analysis on 36 children and adolescents with SCD (9–24 years of age) and 31 controls (8–25 years of age). They found that in comparison with controls, subjects with SCD (with or without silent infarcts) demonstrated white matter density reduction and gray matter density changes. Kirk et al⁶ used surface-based morphometry to examine cortical thinning in children with SCD.

Studies have assessed age-related changes in neurocognitive functioning in children with SCD.⁸ In a longitudinal study of 373 children with SCD (6–18 years of age), Wang et al⁸ reported that the scores for verbal intelligence quotient, math achievement, and coding declined with increasing age.

Age-related changes in brain morphology are crucial to understanding the neurobiology of SCD. However, most previous morphometric studies have been only cross-sectional. No previous studies, to our knowledge, have assessed longitudinal MR-based morphometric changes in children with SCD. We addressed the problem of characterizing brain structure development in children with SCD in this study. We hypothesized that growth trajectories for total gray matter volume, total white matter volume, and regional gray matter volumes (normalized to total brain volume) are altered in children with SCD compared with controls. We tested this hypothesis on the basis of data from a prospective longitudinal study of children with SCD.

MATERIALS AND METHODS

Participants

This study included children with SCD and healthy children. The SCD population was drawn from the Comprehensive Sickle Cell Center at the Children’s Hospital of Philadelphia. The institutional review board of the Children’s Hospital of Philadelphia approved the protocol of this prospective study, which was also compliant with the Health Insurance Portability and Accountability Act. Written informed consent was given by subjects’ parents (with assent for subjects 7 years and older). The SCD group had 28

children with SCD. Inclusion criteria were the following: 1) sickle cell anemia genotype: homozygous SS, confirmed by isoelectric focusing with DNA-based confirmatory testing or parental studies, 2) no deficits on neurologic examination, 3) no history of stroke, and 4) transcranial Doppler sonography mean velocities <170 cm/s in a routine screening examination. Exclusion criteria were the following: 1) a history of major head injury requiring a visit to an emergency department; 2) a history of seizure disorder requiring anticonvulsant therapy; 3) chronic transfusion therapy; 4) occurrence of a sickle cell anemia pain episode, acute chest syndrome, or another significant medical problem in the period of laboratory blood testing, neuropsychological testing, and sonographic studies; 5) a history of prenatal or perinatal hypoxic-ischemic brain injury; and 6) evidence of HIV infection. The SCD group was selected from a larger cohort of 67 children with SCD without prior clinically overt stroke or transient ischemic attack.⁹ The subjects with SCD in the current study had longitudinal MR imaging examinations.

The control group included 28 healthy children selected from the National Institutes of Health MRI Study of Normal Brain Development (NIHPD).¹⁰ Subjects were excluded if they met criteria “established or highly suspected to adversely impact healthy brain development.” Informed consent was obtained from parents and adolescents, and assent was obtained from children. Protocols and procedures were approved by relevant institutional review boards. For each subject in the SCD group, we selected an age- and sex-matched child from the NIHPD data base. If there was no age- and sex-matched child in the NIHPD data base for a participant in the SCD group, we selected a healthy child whose age was close to that of the subject with SCD.

The control group included 28 healthy children selected from the National Institutes of Health MRI Study of Normal Brain Development (NIHPD).¹⁰ Subjects were excluded if they met criteria “established or highly suspected to adversely impact healthy brain development.” Informed consent was obtained from parents and adolescents, and assent was obtained from children. Protocols and procedures were approved by relevant institutional review boards. For each subject in the SCD group, we selected an age- and sex-matched child from the NIHPD data base. If there was no age- and sex-matched child in the NIHPD data base for a participant in the SCD group, we selected a healthy child whose age was close to that of the subject with SCD.

MR Imaging and Analysis

The 28 children in the SCD group were those who had a minimum of 2 yearly brain MR imaging examinations, including a baseline examination. All subjects with SCD underwent MR imaging by using a 3T Magnetom Trio scanner (Siemens, Erlangen, Germany) at the Children’s Hospital of Philadelphia. The T1-weighted MR imaging parameters were TR/TE/TI, 1380/2.15/800 ms; matrix, 256 × 256; voxel size, 1 × 1 × 1 mm. Among these 28 subjects, 16 children had 2 MR imaging examinations, 9 children had 3, and 3 children had 4. The total number of MR imaging examinations in this study was 71.

For the control group, a whole-brain 3D T1-weighted spoiled gradient recalled-echo sequence was acquired. The matrix was 256 × 256, and section thicknesses were 1 and 1.4–1.8 mm on the Siemens and GE scanners, respectively; MR image acquisition details are reported in the Brain Development Cooperative Group reference.¹¹ Each child in the control group underwent 2–3 biannual MR imaging examinations.

The MR image analysis procedures (Fig 1) were as follows: First, we used the FMRIB Brain Extraction Tool from FSL ([404 Chen Feb 2015 www.ajnr.org](http://</p>
</div>
<div data-bbox=)

Demographic characteristics of the study

	SCD	Controls	P Value
Mean age across all observations (mo)	113	116	.732
Age range across all observations (mo)	33–190	31–194	NA
Mean age at baseline (mo)	98 ± 37.6	99 ± 38.0	.947
Age range at baseline (mo)	33–156	31–157	NA
Sex (female/male)	15/13	16/12	.788

Note:—NA indicates not applicable.

www.fmrib.ox.ac.uk/fsl)¹² to exclude nonbrain tissues. Then we used SPM5 (Wellcome Department of Imaging Neuroscience, London, United Kingdom)¹³ to perform joint segmentation and registration, yielding GM, WM, and CSF by using labeled voxels, normalized to the standard Montreal Neurological Institute space. Automatic volume calculation was performed by using a software package called Individual Brain Atlases Using Statistical Parametric Mapping Software (<http://www.thomaskoenig.ch/Lester/ibaspm.htm>). We thus parcellated each individual brain into 90 brain structures defined in the brain template of Automated Anatomical Labeling (AAL).¹⁴ On the basis of the results of tissue segmentation and brain parcellation, we calculated total GM volume, total WM volume, total brain volume (defined as the sum of GM and WM volumes), and regional GM volumes for the 90 Automated Anatomical Labeling structures, measured in cubic millimeters. For regional GM volumes, we were interested in regional rather than global effects; therefore, we adjusted regional GM volumes for each subject's total brain volume in the same MR image. For a brain structure with index k , we defined relative volume as $10,000 \times [V_k / (\text{total brain volume})]$, where V_k is the raw regional volume of structure k ; we multiplied the fraction $V_k / (\text{total brain volume})$ by 10,000 because $V_k / (\text{total brain volume})$ was typically a very small number and not stable under numeric procedures. These regional volumes are relative measurements and dimensionless. This image-analysis pipeline had been used in other studies of pediatric populations.^{15–18}

Statistical Analysis: Modeling Trajectories

To analyze the trajectory of brain growth (for either children with SCD or for healthy children in the control group), we used the multilevel-model-for-change¹⁹ approach, which addresses simultaneously within-subject and between-subject questions about change rates. This method can handle varying numbers of measurements and variably spaced measurements. We used the *xtmixed* procedure in STATA 11 (StataCorp, College Station, Texas) to implement this analysis.

There are 2 components in the multilevel model for change: level 1 and level 2 submodels. The level 1 component (the individual growth model) represents the change that each member undergoes during the time under study. If one adopts an individual growth model in which change is a linear function of age, the level 1 model is

$$1a) \quad Y_{ij} = \pi_{0i} + \pi_{1i} \times \text{Age} + \varepsilon_{ij},$$

where Y_{ij} is the outcome variable of interest, such as total GM volume for subject i at time j , π_{0i} is the intercept of the growth curve, π_{1i} is the slope (rate of change) of the growth curve, and ε_{ij} is the random measurement error. We recentered *Age* so that its

mean was 9 years (108 months, the sample mean) to ensure that the value of *Age* associated with π_{0i} was within the observed range of *Age*.¹⁹

The level 2 model allows the value of each individual's growth parameters (π_{0i} and π_{1i}) to be distributed about the relevant population average. The level 2 model is

$$1b) \quad \begin{aligned} \pi_{0i} &= \gamma_{00} + \zeta_{0i} \\ \pi_{1i} &= \gamma_{10} + \zeta_{1i} \end{aligned}$$

where γ_{00} and γ_{10} represent the population average initial status and rate of change, respectively, and ζ_{0i} and ζ_{1i} are level 2 residuals. We assume that $\varepsilon_{ij} \sim N(0, \sigma_e^2)$ and ζ_{0i} and ζ_{1i} follow a joint Gaussian distribution with the mean zero and the covariance matrix Σ . We used the maximum-likelihood estimation procedure in STATA to estimate model parameters.

Sometimes the growth trajectory is quadratic. For this case, we added Age^2 to the level 1 model. For a quadratic change trajectory, the level 1 model is

$$2) \quad Y_{ij} = \pi_{0i} + (\pi_{1i} \times \text{Age}) + (\pi_{2i} \times \text{Age}^2) + \varepsilon_{ij},$$

where π_{0i} is the intercept of the growth curve, π_{1i} is the instantaneous rate of change, and π_{2i} is curvature. Note that π_{1i} in the linear change and quadratic change trajectories have different interpretations. We selected a suitable level 1 model (linear change or quadratic change) on the basis of the Bayesian information criterion.¹⁹

We constructed the multilevel models for changes (total GM and WM volume) for the SCD and control groups, respectively. If the growth curve was linear, our null hypothesis was that γ_{10} , the slope of the population-change trajectory, is zero. If the growth curve was quadratic, our null hypothesis was that γ_{10} , the instantaneous rate of change, is zero.

We constructed multilevel models for change for the 90 regional GM volumes for the SCD group to test whether γ_{10} is zero. We performed Bonferroni multiple-comparison correction; if the adjusted P value after multiple-comparison correction was $<.05$, we rejected the corresponding null hypothesis.

RESULTS

The demographic characteristics of the study are summarized in the Table. For the SCD group, each child underwent 2–4 annual examinations. At baseline, the mean age was 98 ± 37.6 months. The female/male ratio was 15:13. For the control group, each child underwent 2–3 biannual examinations. At baseline, the mean age was 99 ± 38.0 months; the female/male ratio was 16:12. There were no significant differences in the baseline age ($P = .947$ based on the 2-sample t test) or female/male ratio ($P = .788$ based on the χ^2 test) and the mean age across all observations ($P = .732$ based on the 2-sample t test). There were no significant differences in the age range across all observations and the age range at baseline.

We did not observe any neurologic clinical events such as a stroke or TIA during the period of observation in our patients with SCD. We did not find any Moyamoya disease syndrome in children with SCD.

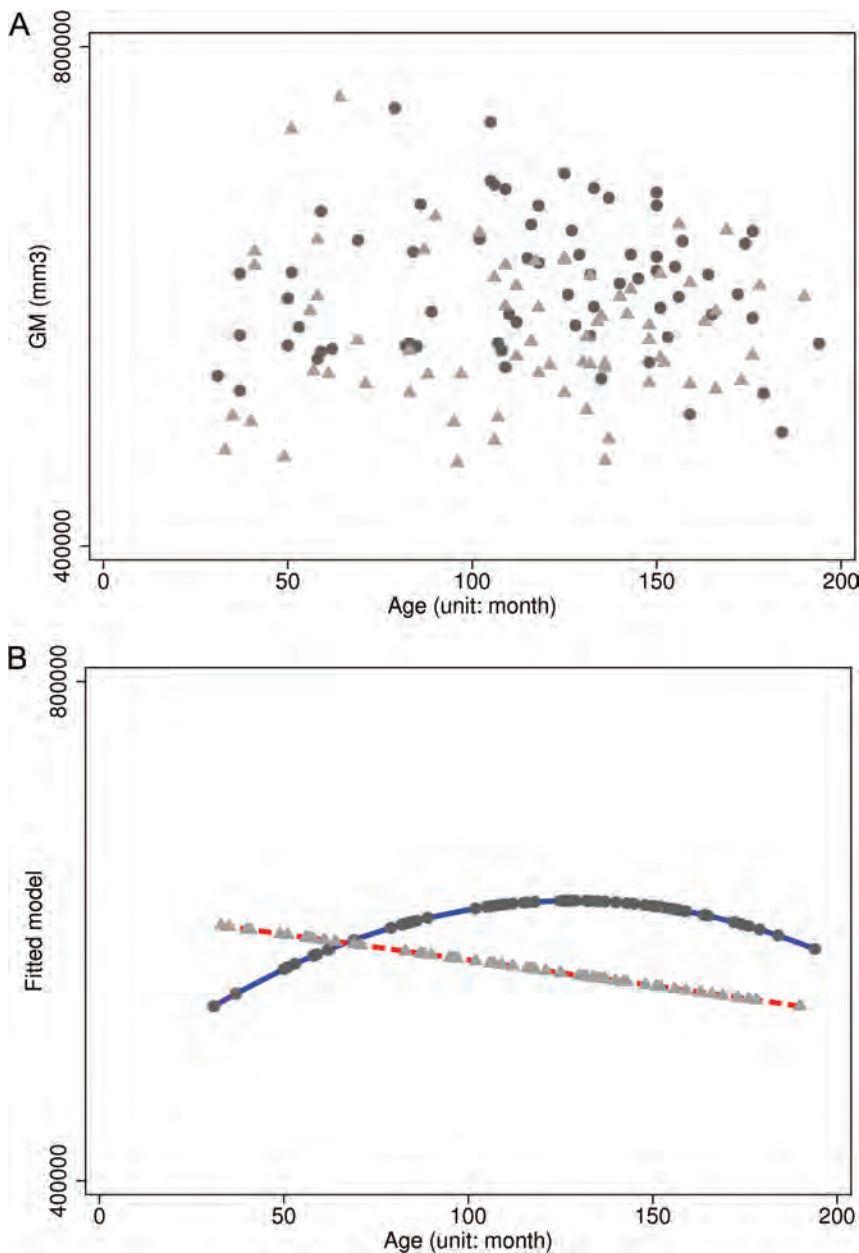


FIG 2. The population growth trajectory for total GM volume. *A*, the scatterplot of GM volumes versus age. *Triangles* represent data points for the SCD group, and *circles* represent data points for healthy control subjects. *B*, the fitted model. Red and blue curves are for the SCD and control groups, respectively.

All MR imaging and MRA examinations were analyzed by 2 experienced neuroradiologists (with 20 and 30 years of experience) blinded to patient data. Discrepancies were resolved by consensus. Silent infarct was defined as an area of abnormal hyperintensity on FLAIR images ≥ 3 mm in diameter and visible in at least 2 perpendicular planes.

In the first MRA examination, we found 3 stenoses in 2 children, including 1 child with isolated left terminal internal carotid artery (tICA) stenosis (25%–49%) and 1 child with mirror stenoses of both anterior cerebral arteries (25%–49%).

On the basis of MR imaging data, we found silent infarcts in 15 children, including 1 with stenosis of the left tICA. In 9 children, silent infarcts were observed in the first MR imaging examination

(the baseline) and in all following MR imaging examinations; whereas in the remaining 6 children, silent infarcts were recorded only in the follow-up studies. We did not observe significant changes in the total volume of silent infarcts. The median values of the volume of silent infarcts in the following years (years 1–4) were 29.5, 33, 54, and 32 mm³, respectively. The small number of subjects with silent infarcts did not allow us to perform trajectory analysis because of a lack of statistical power.

Total GM and WM Volumes

Figure 2 displays the multilevel model for change for total GM volume. For the SCD group, the best-fitting model of age-related changes in total GM was linear. The intercept γ_{00} , which was the volume at 9 years of age, was 573,602 mm³. The slope of the population change trajectory, γ_{10} , was -411 ; that is, total GM volume decreased at a rate of 411 mm³ per month. We rejected the null hypothesis ($\gamma_{10} = 0$) with $P = .014$. For the control group, the best-fitting model of age-related changes in total GM was quadratic. The intercept (the volume at 9 years of age), the instantaneous rate of change, and curvature were 620,691 mm³ ($P < .001$), 362 ($P = .001$), and -8.94 ($P < .001$), respectively. The trajectory was $-8.94\text{Age}^2 + 362\text{Age} + 620,691$. The average rate of change was 272 mm³ per month.

Figure 3 shows the multilevel model for change for total WM volume. For the SCD group, the best-fitting model of age-related changes in total WM was linear. The intercept γ_{00} was 363,260 mm³ ($P < .001$). The slope of the population change trajectory, γ_{10} , was 452 ($P < .001$); that is, total WM volume grew at a rate of 452 mm³ per month. For the control group, the best-fitting model of age-related changes in total WM was quadratic. The intercept (the volume at 9 years of age), the instantaneous rate of change, and curvature were 423,073 mm³ ($P < .001$), 1020 ($P < .001$), and -4.37 ($P < .001$), respectively. The trajectory was $-4.37\text{Age}^2 + 1020\text{Age} + 423,073$. The average rate of change was 976.3 mm³ per month.

Regional Volumes

The On-line Table summarizes results for the 90 regional volumes. Because the multilevel models for changes in the On-line Table are for relative regional volumes, the absolute value of rate of change does not have a clear interpretation. Most of brain structures in children with SCD underwent volume reduction (ie,

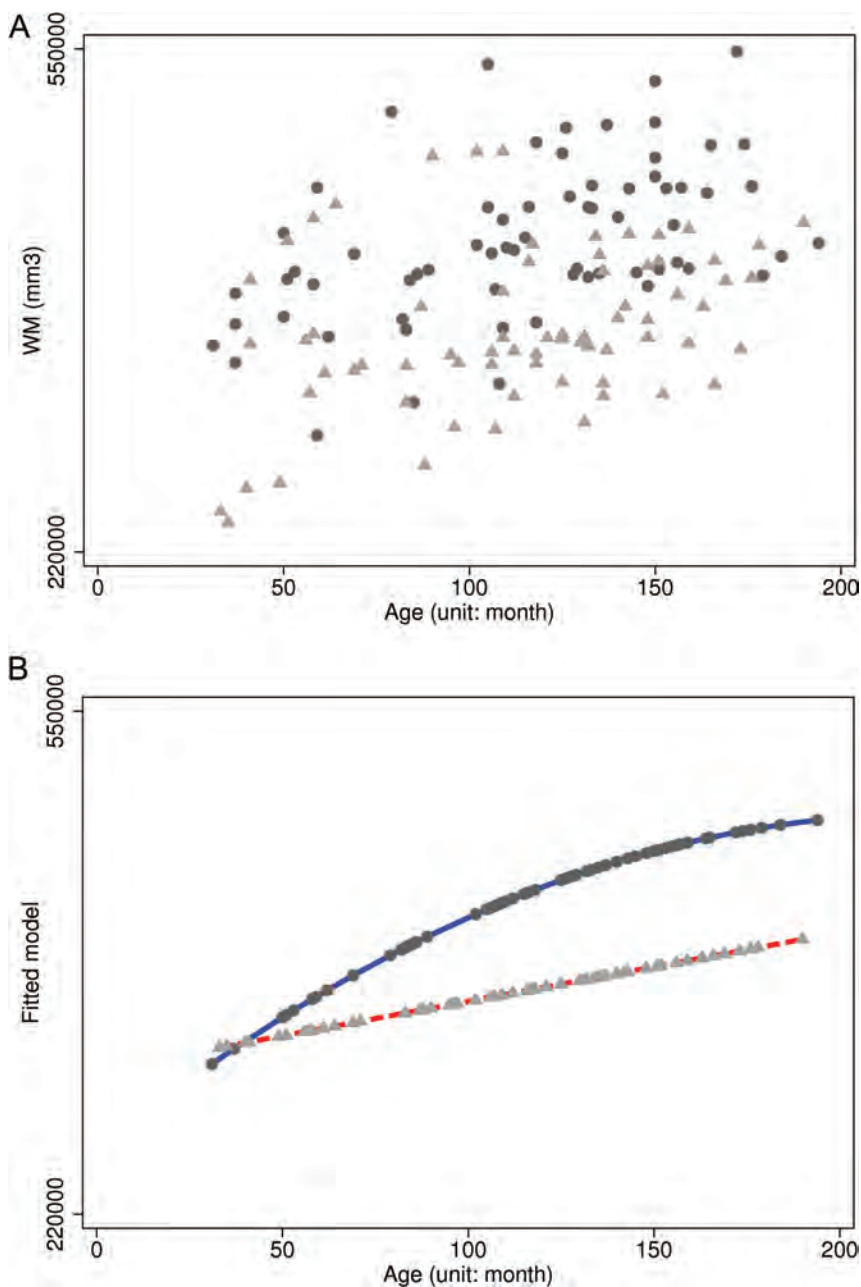


FIG 3. The population growth trajectory for total WM volume. *A*, the scatterplot of WM volumes versus age. *Triangles* represent data points for the SCD group, and *circles* represent data points for healthy control subjects. *B*, the fitted model. Red and blue curves are for the SCD and control groups, respectively.

negative slope); only 8 of 90 structures had a positive slope. After performing Bonferroni correction, we found that 35 structures had a nonzero slope (P value with the Bonferroni correction $< .05$).

Figure 4 shows slopes for these brain regions. Of note, slopes were negative for all of these structures; that is, these structures underwent volume reduction. The frontal, parietal, and occipital lobes demonstrated significant age-related volume reduction: 11 of 30 structures in the frontal lobes, 9 of 14 structures in the parietal lobes, and 8 of 14 structures in the occipital lobes had nonzero slopes. The temporal lobe and the limbic system demonstrated less age-related volume reduction: One of 12 struc-

tures in the limbic system and 4 of 12 structures in the temporal lobes had nonzero slopes.

DISCUSSION

Atrophy, stroke, and cognitive impairment are major consequences of SCD on the brain. Children with SCD have a high risk for a range of effects on the brain, including overt stroke, cerebral infarcts that occur without overt symptoms of stroke (silent infarct), and insufficient oxygen or glucose delivery or both that result in deficits in brain function without structural tissue damage. Infarct (both overt and silent) and atrophy are common MR imaging findings in children with SCD.²⁰

In this study, we found that the total GM trajectories for the SCD group and the control subjects group were different. The trajectory of total GM volume was linear: Total GM volumes decreased at a rate of 411 mm³ per month for children with SCD. For the age- and sex-matched control subjects, the trajectory of total GM volume was quadratic. As shown in Fig 2, total GM volume first increased, peaked at 11 years of age, and then decreased. We did not observe a significant linear decline in total GM volumes. Several MR imaging-based studies describe anatomic brain changes in healthy children and adolescents.²¹⁻²⁴ They found that total GM volume increases or stabilizes in healthy children as they develop from 3 to 15 years of age. For example, Matsuzawa et al²² reported that total GM volume gradually increased from 2 to 10 years of age. In a study of 35 normally developing children and adolescents between 7 and 16 years of age, Sowell et al²³ found that there was no significant change in absolute total GM volume. In contrast, we found a significant decline in

total GM volume for children with SCD between 3 and 16 years of age.

For the SCD group, we found 35 Automated Anatomical Labeling atlas structures demonstrated volume reduction with age; these structures were distributed across the entire brain, primarily in the frontal, parietal, and occipital lobes (Figure 4). In contrast, GM volumes of structures in the temporal lobes and limbic system did not change significantly.

The 2 events that occur in brain development for children between 3 and 16 years of age are synaptic pruning and myelination.²⁴ Both processes could result in the appearance of GM volume reduction. Synaptic pruning selectively prunes and refines

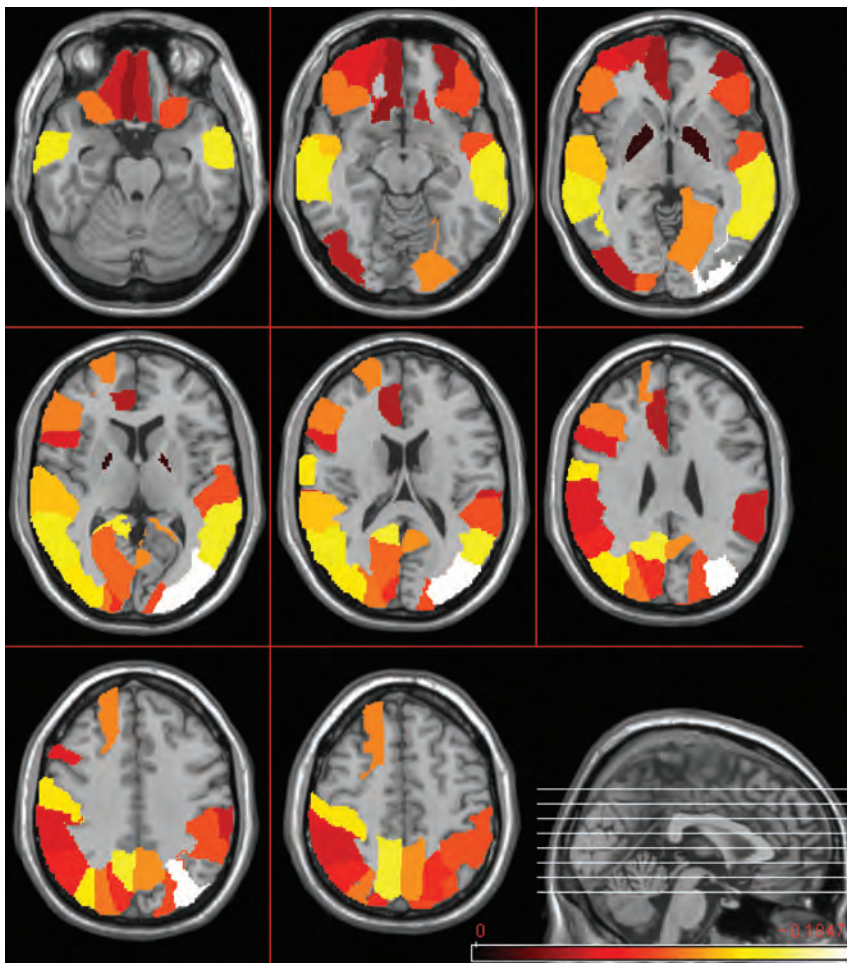


FIG 4. The slopes of the GM growth trajectories for different brain regions. Only regions with an adjusted P value $< .05$ are shown. Brighter color represents more severe volume reduction rate (red indicates less severe volume reduction; white, more severe volume reduction).

synapses that are components of GM. Nonmyelinated peripheral axonal and dendritic fibers do not have normal WM signal on T1-weighted MR images and may be volume-averaged with gray matter. Therefore, myelination could cause an apparent reduction in GM volume.²⁵ For healthy children 3–15 years of age, the interaction of synaptic formation, synaptic pruning, and myelination^{24,26} results in a pattern of total GM volume increase or stabilization.^{22–24} In contrast, we found that total GM volume decreases in children with SCD between 3 and 16 years of age and that this GM reduction is distributed across the brain, primarily in the frontal, parietal, and occipital lobes. Alternations in any of these developmental processes (synaptic formation, new cell generation, synaptic pruning, and myelination) could result in apparent or actual GM volume loss.

Many MR imaging–based studies have examined anatomic brain changes in healthy children.^{21,23} Giedd et al²¹ reported that total WM volume increased linearly with age in 145 healthy children and adolescents; the net increase across the age range of 4–22 years was 12.4%. Our findings are consistent with these results. Furthermore, we found that total WM volume increased in subjects with SCD at approximately half the rate of that seen in control subjects. This finding suggests that WM development is affected by SCD pathology.

In this longitudinal study, we found that the total GM and WM trajectories for the SCD group were different from those of controls. Other cross-sectional morphometric studies also suggested that brain morphologic features were changed in children with SCD. Baldeweg et al⁴ performed voxel-based morphometric analysis in a study including 36 children and adolescents with SCD (9–24 years of age) and 31 controls (8–25 years of age). They found that in comparison with controls, subjects with SCD (with or without silent infarcts) demonstrated WM density reduction. For subjects with silent infarcts, decreases in WM density were found along the ventricles bilaterally from the anterior frontal to parieto-occipital white matter. For subjects without silent infarcts, the pattern of WM decrease was similar to that for subjects with silent infarcts. Baldeweg et al⁴ also reported GM changes. For subjects with silent infarcts, areas with GM density decrease were found along the medial wall of the frontal and parietal lobes and areas with GM density decrease were found along the medial frontal surface. In a cross-sectional study including 83 children with SCD and 43 controls, Steen et al⁵ found that patients had 9% less GM than controls at 5.0 years of age and 5% less GM than controls at age 9.5 years. Kirk et al⁶ used surface-based morphometry to examine cortical thinning in children with SCD. They compared regional cortical thickness between the SCD group (12 subjects; mean age, 14.6 years) and the control group (15 subjects; mean age, 15.6 years) and found that the SCD group had significant bilateral thinning of the medial cortex, including the superior frontal regions, the precuneus, and the paracentral. The frontal areas were among the regions that showed significant thinning.

A possible explanation of the global effect of SCD on brain development is related to the abnormal hemoglobin, which has reduced oxygen affinity and low solubility in its deoxygenated form, which subsequently leads to aggregation and “sickling” of red blood cells.^{27,28} This process is at the core of the disease because sickled cells have greater stiffness, thereby becoming entangled when passing through capillaries and resulting in vaso-occlusive crises observed in this population.²⁹ In turn, sickled cells are prematurely destroyed (hemolysis), the consequence of which is anemia. The brains in these children, however, can be normally oxygenated due to a substantial compensatory increase in cerebral blood flow.³⁰ This increase in CBF, however, is still controversial because a few recent studies did not detect increased brain perfusion because of substantial compensatory peripheral vasodilation (perfusion paradox).^{31,32}

In anemia, oxygen transport is optimized at lower hematocrit levels and higher blood volume to counterbalance abnormal

rheologic behavior of less pliable sickle red blood cells and the high viscosity of blood, especially saturated with deoxygenated hemoglobin SS.²⁷ In a model,³³ oxygen diffusivity of the capillary bed could be adjusted with respect to perfusion, oxygen partial pressure, hematocrit, and level of vasodilation, thus playing a crucial role in regulating cerebral oxygen delivery in vivo. The autoregulation in children with SCD can also be affected via the alternate hemolytic pathway that begins with intravascular destruction of red blood cells and the release of free hemoglobin and arginase into the plasma. Free hemoglobin binds and inactivates nitric oxide, and concomitantly, free arginase converts L-arginine into ornithine, a nitric oxide substrate, reducing the production of nitric oxide.³⁴ Reduced levels of nitric oxide cause vasoconstriction and may interfere with vasodilation that is required as a response to an increase in wall shear stress and other stimuli. Severe hemodynamic disturbances during a period of dynamic brain development might lead to chronic ischemic brain injury and subsequent reduction of GM and WM volume.

We found that the GM volume reduction in children with SCD was primarily in the frontal, parietal, and occipital lobes, while the temporal lobes and limbic system did not change significantly. The exact process underlying this region-specific GM volume reduction in children with SCD is unknown. We speculate that it may be related to a region-specific manner of brain GM maturation. In normal brain development, GM maturation begins first in the dorsal parietal cortices and the spreads over the frontal lobe and caudally and laterally over the parietal and occipital lobes; finally, it spreads over the temporal lobe.³⁵ Therefore, we speculate that the frontal, parietal, and occipital lobes demonstrated more reduction in children with SCD because the maturation process in these lobes starts earlier and the accumulated effect of hemodynamic disturbances is more significant.

Recently, there have been several cross-sectional DTI studies of SCD.^{36,37} DTI uses MR imaging in different diffusion-sensitizing gradient directions. It is capable of detecting microstructural WM changes.³⁸ Balci et al³⁶ analyzed DTI data for 16 patients with SCD (mean age, 25.4 ± 11.1 years) and 14 age- and sex-matched healthy controls. They calculated fractional anisotropy and apparent diffusion coefficients for predefined regions of interest. Wide-ranging, bilateral changes in fractional anisotropy values were observed in patients with SCD. Significant reduced fractional anisotropy values, increased ADCs, or both were clustered in several brain regions, including the corpus callosum, frontal white matter, and centrum semiovale. Sun et al³⁷ analyzed DTI data for patients with SCD with no visible lesions (mean age, 15.19 ± 1.55 years), patients with SCD with mild gliosis (mean age, 15.38 ± 3.05 years), and age-matched controls. They performed tract-based spatial statistics analysis and found that both SCD populations exhibited reduced anisotropy and increased diffusivity compared with controls in several brain regions, including the corpus callosum and centrum semiovale. These 2 cross-sectional DTI studies suggest that WM is changed in patients with SCD. This finding is consistent with the results of our study.

In this study, we modeled neurodevelopmental trajectories in children with SCD. We found that trajectories of total GM and WM in children with SCD were different from those of healthy controls. In a longitudinal study of 373 children with SCD, Wang et al⁸ reported that scores for verbal intelligence quotient, math

achievement, and coding declined with increasing age. In a cross-sectional study, Chen et al⁷ found a linear association between intelligence quotient and regional GM volume in children with SCD. This finding suggests that some variance in intelligence quotient in children with SCD is accounted for by regional variability of GM volume.

One of the limitations of this study is that T1-weighted MR images provide little information about which processes contribute to abnormal GM development. Multimodality imaging could partially solve this problem. For example, DTI could provide additional information about myelination (eg, on the basis of diffusion anisotropy). Another limitation is that we did not monitor continuously flow in small vessels during the period of observation. Therefore, we cannot determine the frequency and extent of focal brain lesions corresponding to small-vessel ischemia.

Our future work will focus on the following: 1) determining whether age-related changes in brain morphology are associated with changes in neurocognitive functioning with time. We hope to determine the extent to which variability in neurocognitive functioning can be explained by age-related brain anatomic changes. 2) Using longitudinal DTI to examine white matter development in children with SCD could provide additional information about white matter integrity and myelination.

CONCLUSIONS

To our knowledge, ours is the first longitudinal morphometry study to investigate brain development in children with SCD. Using a multilevel-model-for-change approach to investigate brain development of children with SCD, we found a significant decline in total GM volume for children with SCD between 3 and 16 years of age. This GM volume reduction is distributed broadly across the brain, primarily in the frontal, parietal, and occipital lobes, largely sparing the limbic system and temporal lobes. The findings of this study may provide valuable information about the neuropathology of SCD.

Our longitudinal morphometric study supports the notion that reduced cerebral GM and WM volumes in neurologically intact children with SCD can be an effect of chronic hemodynamic complications and subsequent insufficient oxygen delivery to neuronal tissue. Early detection of alterations in the delivery and metabolism of oxygen is important because blood transfusion or hydroxyurea therapy can reverse these functional deficits before the structural changes become evident.

Disclosures: Rong Chen—RELATED: Grant: National Institutes of Health. Edward H. Herskovits—UNRELATED: Expert Testimony: medicolegal; Grants/Grants Pending: Center for Health-Related Informatics and Bioimaging.

REFERENCES

1. Rees DC, Williams TN, Gladwin MT. **Sickle-cell disease.** *Lancet* 2010;376:2018–31
2. Bunn HF. **Pathogenesis and treatment of sickle cell disease.** *N Engl J Med* 1997;337:762–69
3. Steen RG, Emudianughe T, Hankins GM, et al. **Brain imaging findings in pediatric patients with sickle cell disease.** *Radiology* 2003;228:216–25
4. Baldeweg T, Hogan AM, Saunders DE, et al. **Detecting white matter injury in sickle cell disease using voxel-based morphometry.** *Ann Neurol* 2006;59:662–72
5. Steen RG, Emudianughe T, Hunte M, et al. **Brain volume in pediatric**

- patients with sickle cell disease: evidence of volumetric growth delay? *AJNR Am J Neuroradiol* 2005;26:455–62
6. Kirk GR, Haynes MR, Palasis S, et al. **Regionally specific cortical thinning in children with sickle cell disease.** *Cereb Cortex* 2009; 19:1549–56
 7. Chen R, Pawlak MA, Flynn TB, et al. **Brain morphometry and intelligence quotient measurements in children with sickle cell disease.** *J Dev Behav Pediatr* 2009;30:509–17
 8. Wang W, Enos L, Gallagher D, et al. **Neuropsychologic performance in school-aged children with sickle cell disease: a report from the Cooperative Study of Sickle Cell Disease.** *J Pediatr* 2001;139:391–97
 9. Arkuszewski M, Krejza J, Chen R, et al. **Sickle cell anemia: intracranial stenosis and silent cerebral infarcts in children with low risk of stroke.** *Adv Med Sci* 2014;59:108–13
 10. Evans AC, for the Brain Development Cooperative Group. **The NIH MRI Study of Normal Brain Development.** *Neuroimage* 2006; 30:184–202
 11. Brain Development Cooperative Group. **Total and regional brain volumes in a population-based normative sample from 4 to 18 years: the NIH MRI Study of Normal Brain Development.** *Cereb Cortex* 2012;22:1–12
 12. Smith SM. **Fast robust automated brain extraction.** *Hum Brain Mapp* 2002;17:143–55
 13. Ashburner J, Friston KJ. **Unified segmentation.** *Neuroimage* 2005; 26:839–51
 14. Tzourio-Mazoyer N, Landeau B, Papathanassiou D, et al. **Automated anatomical labeling of activations in SPM using a macroscopic anatomical parcellation of the MNI MRI single-subject brain.** *Neuroimage* 2002;15:273–89
 15. Tzarouchi LC, Astrakas LG, Xydis V, et al. **Age-related grey matter changes in preterm infants: an MRI study.** *Neuroimage* 2009; 47:1148–53
 16. Yamashita K, Yoshiura T, Hiwatashi A, et al. **Volumetric asymmetry and differential aging effect of the human caudate nucleus in normal individuals: a prospective MR imaging study.** *J Neuroimaging* 2011;21:34–37
 17. Widjaja E, Yeung R, Geibprasert S, et al. **Longitudinal brain volumes in children with intractable partial seizures.** *Pediatr Neurol* 2010; 42:315–19
 18. Tzarouchi LC, Astrakas LG, Zikou A, et al. **Periventricular leukomalacia in preterm children: assessment of grey and white matter and cerebrospinal fluid changes by MRI.** *Pediatr Radiol* 2009;39:1327–32
 19. Singer JD, Willett JB. *Applied Longitudinal Data Analysis: Modeling Change and Event Occurrence.* Oxford: Oxford University Press; 2003
 20. Loneragan GJ, Cline B, Abbondanzo SL. **Sickle cell anemia.** *Radiographics* 2001;20:971–94
 21. Giedd JN, Blumenthal J, Jeffries NO, et al. **Brain development during childhood and adolescence: a longitudinal MRI study.** *Nat Neurosci* 1999;2:861–63
 22. Matsuzawa J, Matsui M, Konishi T, et al. **Age-related volumetric changes of brain gray and white matter in healthy infants and children.** *Cereb Cortex* 2001;11:335–42
 23. Sowell ER, Trauner DA, Gamst A, et al. **Development of cortical and subcortical brain structures in childhood and adolescence: a structural MRI study.** *Dev Med Child Neurol* 2002;44:4–16
 24. Lenroot RK, Giedd JN. **Brain development in children and adolescents: insights from anatomical magnetic resonance imaging.** *Neurosci Biobehav Rev* 2006;30:718–29
 25. Paus T. **Mapping brain maturation and cognitive development during adolescence.** *Trends Cogn Sci* 2005;9:60–68
 26. Gould E, Reeves AJ, Graziano MS, et al. **Neurogenesis in the neocortex of adult primates.** *Science* 1999;286:548–52
 27. Vayo MM, Lipowsky HH, Karp N, et al. **A model of microvascular oxygen transport in sickle cell disease.** *Microvasc Res* 1985;30: 195–206
 28. Eaton WA, Hofrichter J. **Hemoglobin S gelation and sickle cell disease.** *Blood* 1987;70:1245–66
 29. Christoph GW, Hofrichter J, Eaton WA. **Understanding the shape of sickled red cells.** *Biophys J* 2005;88:1371–76
 30. Prohovnik I, Hurler-Jensen A, Adams R, et al. **Hemodynamic etiology of elevated flow velocity and stroke in sickle-cell disease.** *J Cereb Blood Flow Metab* 2009;29:803–10
 31. Nath KA, Katusic ZS, Gladwin MT. **The perfusion paradox and vascular instability in sickle cell disease.** *Microcirculation* 2004;11: 179–93
 32. van den Tweel XW, Nederveen AJ, Majoie CB, et al. **Cerebral blood flow measurement in children with sickle cell disease using continuous arterial spin labeling at 3.0-Tesla MRI.** *Stroke* 2009;40:795–800
 33. Hyder F, Shulman RG, Rothman DL. **A model for the regulation of cerebral oxygen delivery.** *J Appl Physiol (1985)* 1998;85:554–64
 34. Kato GJ, Hebbel RP, Steinberg MH, et al. **Vasculopathy in sickle cell disease: biology, pathophysiology, genetics, translational medicine, and new research directions.** *Am J Hematol* 2009;84:618–25
 35. Gogtay N, Giedd JN, Lusk L, et al. **Dynamic mapping of human cortical development during childhood through early adulthood.** *Proc Natl Acad Sci U S A* 2004;101:8174–79
 36. Balci A, Karazincir S, Beyoglu Y, et al. **Quantitative brain diffusion-tensor MRI findings in patients with sickle cell disease.** *AJR Am J Roentgenol* 2012;198:1167–74
 37. Sun B, Brown RC, Hayes L, et al. **White matter damage in asymptomatic patients with sickle cell anemia: screening with diffusion tensor imaging.** *AJNR Am J Neuroradiol* 2012;33:2043–49
 38. Feldman HM, Yeatman JD, Lee ES, et al. **Diffusion tensor imaging: a review for pediatric researchers and clinicians.** *J Dev Behav Pediatr* 2010;31:346–56

Comparison of Spin-Echo and Gradient-Echo T1-Weighted and Spin-Echo T2-Weighted Images at 3T in Evaluating Term-Neonatal Myelination

A.E. Tyan, A.M. McKinney, T.J. Hanson, and C.L. Truwit

ABSTRACT

SUMMARY: A prior clinical report of 3T MR imaging in subsequently healthy very premature neonates imaged at term-equivalent age found that both gradient recalled-echo-T1WI and spin-echo-T2WI showed higher rates of myelinated structures, compared with spin-echo-T1WI. The current study set out to assess those rates on the same sequences at 3T in term neonates and thus consisted of 16 term neonates with normal-appearing MR imaging findings who subsequently had normal findings at clinical follow-up. Two neuroradiologists independently assessed 19 structures in those infants on all 3 sequences. Gradient recalled-echo-T1WI showed a slightly higher rate of myelination (57.2%–72.4% of all structures) and interobserver agreement ($\kappa = 0.546, P < .0001$) than spin-echo-T2WI (58.2%–64.8%; $\kappa = 0.468, P < .0001$), while spin-echo-T1WI had the lowest myelination rate and agreement (25.0%–48.4%; $\kappa = 0.384, P < .0001$). Both observers noted that the following structures were myelinated in 88%–100% of patients on gradient recalled-echo-T1WI: the brachium of the inferior colliculus, decussation of the superior cerebellar peduncle, habenuar commissure, medial lemniscus, pyramidal decussation, posterior limb of the internal capsule, and superior cerebellar peduncle; on spin-echo-T2WI, there was myelination in 88%–100% of the following structures: the brachium of the inferior colliculus, decussation of the superior cerebellar peduncle, inferior cerebellar peduncle, medial lemniscus, and posterior limb of the internal capsule. In conclusion, this study confirmed that similar to the findings in term-equivalent-age premature infants, myelination changes in term neonates may be best assessed on both gradient recalled-echo-T1WI and spin-echo-T2WI at 3T, and not on spin-echo-T1WI.

ABBREVIATIONS: BIC = brachium of the inferior colliculus; CST = corticospinal tracts; DSCP = decussation of the superior cerebellar peduncle; GRE = gradient recalled-echo; ICP = inferior cerebellar peduncle; PLIC = posterior limb of the internal capsule; SCP = superior cerebellar peduncle; SE = spin-echo

MR imaging is often used in term neonates to assess myelination and to evaluate hypoxic-ischemic injury, developmental malformations, metabolic diseases, intracranial infections, and vascular injuries such as stroke or venous sinus thrombosis.¹ While the process of myelination in term neonates has been well-documented histologically, there is a need to confirm such myelination by MR imaging; thus, previous studies at lower field strengths ($\leq 1.5T$) have described normal myelination patterns in both term and preterm neonates on conventional spin-echo (SE)-T1WI and SE-T2WI sequences.^{2,3} However, these patterns could differ at higher field strengths, where there are expectable gains in signal-to-noise and contrast-to-noise ratios, and the gray-white matter differentiation on

SE-T1WI may worsen.^{4,5} Thus, there are few data comparing term-neonatal myelination among gradient recalled-echo (GRE)-T1WI, SE-T1WI, and SE-T2WI at 3T in subsequently healthy term neonates. However, a recent preliminary study of subsequently developmentally healthy very preterm neonates evaluated by 3T MR imaging at term-equivalent age showed that both GRE-T1WI and SE-T2WI had much higher rates of myelinated structures than SE-T1WI, with certain structures being visible on both GRE-T1WI and SE-T2WI in all infants: namely, the decussation of the superior cerebellar peduncle (DSCP), inferior cerebellar peduncle (ICP), and lateral lemniscus.⁶ That study also found that there was myelination in 90%–100% of these term-equivalent patients in the medial lemniscus, pyramidal decussation, posterior limb of the internal capsule (PLIC), and superior cerebellar peduncle (SCP) based solely on GRE-T1WI, and within the spinal tract of V (ie, the spinal trigeminal tract) based solely on SE-T2WI.

The purpose of this study was to assess the rates of myelination as determined by using these 3 sequences in a group of subsequently healthy term neonates who were initially evaluated for suspected hypoxic-ischemic injury and had normal MR imaging findings according to 2 pediatric neuroradiologists. Our goal was

Received April 28, 2014; accepted after revision July 8.

From the Department of Radiology, University of Minnesota-Fairview and Hennepin County Medical Centers, Minneapolis, Minnesota.

Paper previously presented as an oral presentation at: Annual Meeting of the American Society of Neuroradiology and the Foundation of the ASNR Symposium, April 21–16, 2012; New York, New York.

Please address correspondence to Alexander M. McKinney, MD, Department of Radiology, University of Minnesota-Fairview and Hennepin County Medical Centers, Minneapolis, MN 55455; e-mail: mckinrad@umn.edu

<http://dx.doi.org/10.3174/ajnr.A4099>

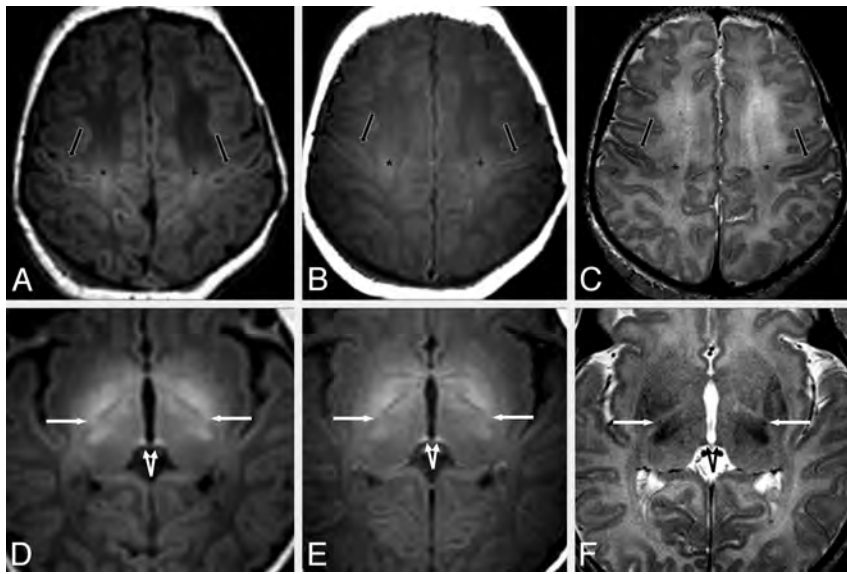


FIG 1. A 3-day-old male neonate with respiratory depression. A–C, MR images at the level of the centrum semiovale demonstrate mildly bright signal of the perirolandic cortex (*black arrows*) on GRE-T1WI (A) and SE-T1WI (B). The perirolandic cortex appears darker on SE-T2WI (C) relative to the remainder of the frontal and parietal cortices in most, but not all, infants in this study. The CST (*asterisk*) are also quite bright on both T1WI sequences and are mildly dark on SE-T2WI. D–F, On images at a lower level through the basal ganglia, the PLIC (*arrows*) and the habenuular commissure (*split arrows*) appear visibly myelinated (ie, bright) on GRE-T1WI (D), SE-T1WI (E), and on SE-T2WI (F), though the PLIC appears much smaller on SE-T2WI. Both the habenuular commissure and the PLIC appear myelinated on GRE-T1WI in all term neonates in this study.

to determine whether the degree of myelination on those 3 sequences at 3T matched that of prior studies at lower field strengths and matched the findings of a prior 3T study of preterm neonates imaged at term-equivalent age.^{2,3,6}

MATERIALS AND METHODS

Institutional review board approval was obtained. PACS data base and clinical record reviews identified all term neonates younger than 21 days of age with a 3T MR imaging to evaluate for hypoxic-ischemic injury between July 2006 and July 2012 ($n = 49$), with the intent of including only subsequently developmentally healthy children. Of the 49 term neonates, we excluded 33 on the basis of the following: cerebral structural pathology, hypoxic-ischemic injury, or parenchymal hematoma on MR imaging ($n = 15$); 1 of the 3 sequences missing ($n = 9$); neurologic deficit on clinical follow-up ($n = 3$); parenchymal calcification ($n = 1$); meningitis ($n = 1$); no clinical follow-up at older than 6 months of age ($n = 3$); or motion precluding evaluation ($n = 1$). Thus, we included 16 term neonates with normal initial MR imaging findings who were considered subsequently developmentally healthy on the basis of clinical evaluations at older than 6 months of age. At 3T, 3-mm axial GRE-T1WI, SE-T1WI, and SE-T2WI sequences are standard in our noncontrast MR imaging evaluation for suspected hypoxic-ischemic injury. Of the 16 remaining patients included for analysis, 10 were male and 6 were female. The recorded 5-minute Apgar scores of those patients ranged from 3 to 9, with a median score of 7.

MR Imaging Technique

All patients were scanned on a single 3T magnet (Intera; Philips Healthcare, Best, the Netherlands), with patients sedated by a pe-

diatric intensivist. The parameters were identical to those of a prior study of very preterm neonates at 3T, which, for GRE-T1WI, were the following: a volumetric acquisition of 9.8/4.6 ms/8°/15–20 cm/1 (TR/TE/flip angle/FOV/NEX), a $169 \times 169 \times 240$ matrix, 1-mm-thickness reconstructed axially at 3 mm (0-mm gap), and an acquisition time of 5 minutes. For SE-T1WI, the parameters were the following: 353–734/10 ms/14–20 cm/1 (TR/TE/FOV/NEX), a $168 \times 132 \times 265 \times 205$ matrix, an axial thickness of 3 mm (0.3-mm gap), and an acquisition time of 5 minutes. For SE-T2WI, the parameters were the following: a turbo factor of fourteen, 3000/80–122 ms/14–20 cm/2 (TR/TE/FOV/NEX), a $268 \times 190 \times 400 \times 312$ matrix, an axial thickness of 3 mm (0.3-mm gap), and an acquisition time of approximately 2.5 minutes.⁶

Image Interpretation

Two staff neuroradiologists (A.M.M., C.L.T., each with at least 10 years' experience in interpreting neonatal MR imaging) independently assessed each of

the 19 structures, evaluating each sequence separately. The structures assessed were based on previous studies and included the following: brachium of the inferior colliculus (BIC), callosal splenium, cranial nerve V fascicle, corticospinal tracts (CST) within the brain stem, CST within the centrum semiovale, DSCP, habenuular commissure, ICP, lateral geniculate nucleus, lateral lemniscus, medial lemniscus, medial longitudinal fasciculus, optic nerves, optic tracts, pyramidal decussation (being in close proximity to the decussation of the medial longitudinal fasciculus), PLIC, perirolandic cortex, SCP, and the spinal tract of V.^{2,3,6} The 2 staff reviewers consulted a dedicated imaging atlas to confirm the location of smaller brain stem structures before review.⁷ Each of the 19 structures was recorded as being “definitely myelinated” (+, being relatively hyperintense on GRE-/SE-T1WI or hypointense on SE-T2WI compared with surrounding structures or periventricular white matter), “nonmyelinated” (–), or “equivocal” (\pm), identical to the method of the prior study of very preterm neonates at 3T.⁶ Representative examples of myelination assessment in 16 of the 19 structures are demonstrated in Figs 1–4, with the exception of the callosal splenium and the medial longitudinal fasciculus because those 2 structures had very low rates of myelination in this study (see the “Results” section).

Regarding statistical analysis, the overall percentage of myelination rates of all structures and the interobserver reliability (κ) for each structure were calculated on the basis of each sequence. Later, after reviewing the medical records to determine which patients had undergone therapeutic head cooling within the first 72 hours, a Mann-Whitney U test was implemented to determine whether there were overall any significant differences between

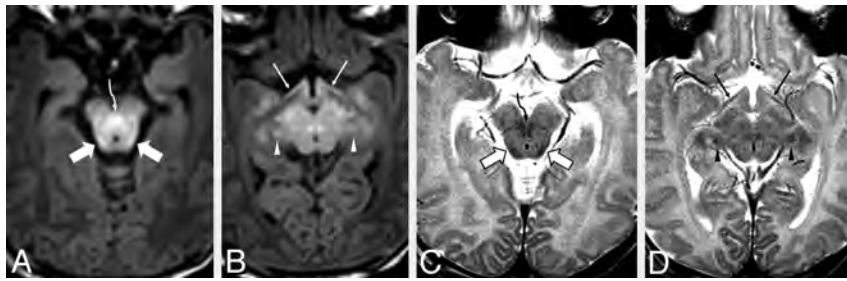


FIG 2. A 3-day-old male neonate with respiratory depression. MR images demonstrate clearly visible bright signal on GRE-T1WI (A and B) and clearly visible dark signal on SE-T2WI (C and D), indicative of normal early myelination within the BIC (wide arrows) and the DSCP (curved arrows). The optic tracts (thin arrows) are visibly myelinated on GRE-T1WI but are questionably myelinated on SE-T2WI. The BIC and the DSCP were both clearly myelinated in at least $\geq 88\%$ of patients on both GRE-T1WI and SE-T2WI, while the SCP was myelinated in $\geq 88\%$ of patients on GRE-T1WI only. Note the apparently myelinated lateral geniculate nuclei (arrowheads).

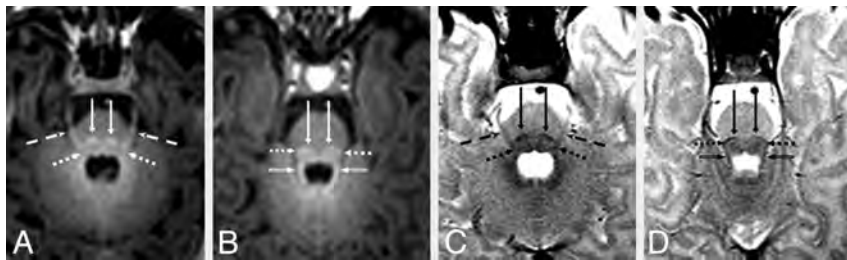


FIG 3. A 6-day-old male neonate with respiratory depression. Axial MR images illustrate bright myelination of the medial lemnisci (long arrows), lateral lemnisci (dotted arrows), cranial nerve V fascicle (dashed arrows), and SCP (beveled arrows) on GRE-T1WI (A and B), which were not clearly visible on SE-T1WI (not shown), but all appeared dark (myelinated) on SE-T2WI (C and D). The medial lemnisci were visibly myelinated in $\geq 94\%$ of neonates on both GRE-T1WI and SE-T2WI. In most patients, the lateral lemnisci and cranial nerve V fascicle were best visualized as being myelinated on GRE-T1WI.

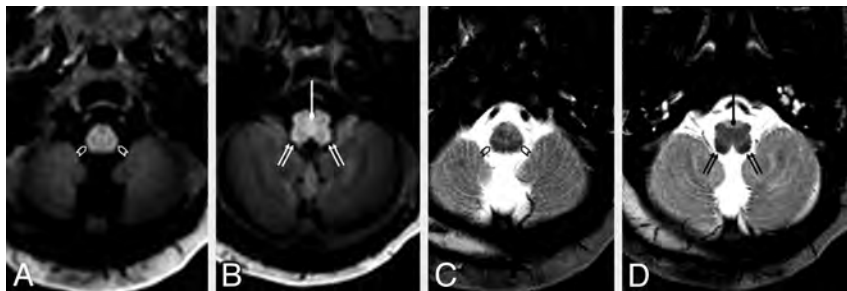


FIG 4. A 4-day-old female neonate with respiratory depression and possible seizures. The pyramidal decussation (circle tipped arrows) is visibly myelinated (bright) on GRE-T1WI (A and B) but was rated as “questionably myelinated” (ie, scored \pm by both reviewers on SE-T2WI (C and D). In contrast, the spinal tract of V (open arrowheads) was considered to be “definitely myelinated” (ie, scored $+$) by both reviewers on SE-T2WI, while it was considered to be only “questionably myelinated” on GRE-T1WI. The ICP (double arrows) appeared clearly myelinated on both sequences. On SE-T1WI (not shown), myelination was not visible (ie, scored as $-$) by either reviewer in the aforementioned structures in this patient. The ICP was the 1 structure that was clearly myelinated in all neonates on SE-T2WI and was better visualized as being “definitely myelinated” (ie, scored $+$) on SE-T2WI compared with both GRE-T1WI and SE-T1WI.

cooled ($n = 9$) and noncooled ($n = 7$) patients for each of the 3 sequences. Statistical significance was set to $P < .05$ for each of the above-mentioned calculations.

RESULTS

Overall, with regard to all structures in all 16 patients, the number of regions counted as “definitely myelinated” ($+$) was a mean of 64.8% on GRE-T1WI (range, 57.2%–72.4% by observer), 61.5%

on SE-T2WI (range, 58.2%–64.8%), and 36.7% on SE-T1WI (range, 25.0%–48.4%). The percentages of each structure counted as “ $+$ ” for myelination based on each sequence are shown in the Table. Both observers found the following structures to be “definitely myelinated” in $\geq 88\%$ of all patients on GRE-T1WI: the BIC, DSCP, habenular commissure, medial lemniscus, pyramidal decussation, PLIC, and SCP. In addition, both reviewers noted that the optic tracts were definitely $+$ for myelination in $>80\%$ of patients on GRE-T1WI. On SE-T2WI, myelination was definitely $+$ in $\geq 88\%$ of patients within the following structures: BIC, DSCP, ICP, medial lemniscus, and PLIC; both reviewers noted that on SE-T2WI, the SCP appeared dark (definitely $+$) in $\geq 75\%$ of patients. Regarding SE-T1WI, the only structure that both observers deemed definitely $+$ for myelination in $>88\%$ of patients was the habenular commissure. Note that 3 structures had a low rate of being $+$ for myelination on all 3 sequences (a $<40\%$ myelination rate on each sequence): the callosal splenium, the CST within the brain stem, and the medial longitudinal fasciculus. Examples of myelinated structures on the 3 sequences used are provided in Figs 1–4.

The reviewers agreed overall on 64.0% of all scores. The interobserver κ was moderate-strong for GRE-T1WI ($\kappa = 0.546$, $P < .0001$), moderate for SE-T2WI ($\kappa = 0.468$, $P < .0001$), and fair-moderate for SE-T1WI ($\kappa = 0.384$, $P < .0001$). The structures with the highest rate of disagreement between observers were the ICP on GRE-T1WI and SE-T1WI, the PLIC on SE-T1WI, and the pyramidal decussation on SE-T2WI (Table).

Nine patients had undergone head cooling within the first 72 hours of life; 7 had not. A Mann-Whitney U test showed that overall, there were no significant differences (each $P > .05$)

among all scores of the cooled-versus-noncooled patients for either reviewer, based on GRE-T1WI ($P = .124-.923$), SE-T1WI ($P = .794-.884$), or SE-T2WI ($P = .316-.837$).

DISCUSSION

Because the process of myelination is dynamic in the neonate and infant, the determination of the degree of myelination is perhaps

Percentages and numbers of term infants with myelination

Structure	GRE-T1WI		SE-T1WI		SE-T2WI	
	Observer 1	Observer 2	Observer 1	Observer 2	Observer 1	Observer 2
BIC	100%, ^a 16/16	94%, ^a 15/16	75%, 12/16	50%, 8/16	100%, ^a 16/16	88%, ^a 14/16
CCS	0%, 0/16	0%, 0/16	0%, 0/16	0%, 0/16	6%, 1/16	38%, 6/16
CNV	94%, ^a 15/16	56%, 9/16	50%, 8/16	6%, 1/16	44%, 7/16	13%, 2/16
CST-BS	25%, 4/16	0%, 0/16	0%, 0/16	0%, 0/16	0%, 0/16	0%, 0/16
CST-CS	75%, 12/16	63%, 10/16	75%, 12/16	31%, 5/16	6%, 1/16	6%, 1/16
DSCP	100%, ^a 16/16	100%, ^a 16/16	81%, 13/16	31%, 5/16	100%, ^a 16/16	94%, ^a 15/16
HC	100%, ^a 16/16	100%, ^a 16/16	100%, ^a 16/16	94%, ^a 15/16	69%, 11/16	63%, 10/16
ICP	88%, ^a 14/16	31%, 5/16	56%, 9/16	0%, 0/16	100%, ^a 16/16	100%, ^a 16/16
LGN	38%, 6/16	25%, 4/16	6%, 1/16	0%, 0/16	50%, 8/16	56%, 9/16
LL	94%, ^a 15/16	69%, 11/16	38%, 6/16	56%, 9/16	75%, 12/16	44%, 7/16
ML	100%, ^a 16/16	94%, ^a 15/16	88%, ^a 14/16	25%, 4/16	100%, ^a 16/16	100%, ^a 16/16
MLF	25%, 4/16	0%, 0/16	0%, 0/16	0%, 0/16	19%, 3/16	31%, 5/16
ON	44%, 7/16	44%, 7/16	0%, 0/16	0%, 0/16	19%, 3/16	44%, 7/16
OT	88%, ^a 14/16	81%, 13/16	69%, 11/16	56%, 9/16	56%, 9/16	56%, 9/16
PD	94%, ^a 15/16	88%, ^a 14/16	31%, 5/16	6%, 1/16	88%, ^a 14/16	38%, 6/16
PLIC	100%, ^a 16/16	100%, ^a 16/16	100%, ^a 16/16	44%, 7/16	88%, ^a 14/16	88%, ^a 14/16
PRC	56%, 9/16	19%, 3/16	31%, 5/16	6%, 1/16	88%, ^a 14/16	63%, 10/16
SCP	100%, ^a 16/16	100%, ^a 16/16	75%, 12/16	44%, 7/16	88%, ^a 14/16	75%, 12/16
STV	56%, 9/16	25%, 4/16	44%, 7/16	25%, 4/16	81%, 13/16	69%, 11/16

Note:—CCS indicates callosal splenium; CNV, cranial nerve V fascicle; CST-BS, CST in the brain stem; CST-CS, CST in the centrum semiovale; HC, habenular commissure; LGN, lateral geniculate nucleus; LL, lateral lemniscus; ML, medial lemniscus; MLF, medial longitudinal fasciculus; ON, optic nerve; OT, optic tract; PD, pyramidal decussation; PRC, perirolandic cortex; STV, spinal tract of V.

^a Structures with ≥88% of patients with myelination.

the most important indicator of brain maturation on MR imaging.³ The current study confirms that GRE-T1WI seems to “lead” SE-T1WI in regard to the degree of myelination and has a higher interobserver reliability in subsequently healthy term neonates; this finding is in accordance with a prior 3T study that used the same sequences in subsequently healthy very preterm neonates imaged at term-equivalent age.⁶ However, the current study found slightly higher rates of myelination changes on GRE-T1WI than on SE-T2WI, while the prior analysis of very preterm neonates suggested that SE-T2WI detected myelination as well as or better than GRE-T1WI.⁶ The current results confirm that at 3T, GRE-T1WI and SE-T2WI should be preferred to SE-T1WI in the assessment of term-neonatal myelination maturation.

While prior studies at lower field strengths have shown that myelination is usually visible on SE-T1WI before SE-T2WI, the findings of this study of myelination on GRE-T1WI and SE-T2WI, compared with SE-T1WI, could be due to several factors, including field strength.^{8,9} First, compared with the adult brain, the healthy neonatal brain generally demonstrates T1 prolongation, thought due to a lack of myelin-based lipids such as galactocerebrosides and cholesterol, along with increased water content.^{8,10-12} The high concentration of free water at birth also contributes to the prolonged T2 signal seen in both term and preterm neonate brains at lower field strengths; the absence of certain hydrocarbon elements, such as those found in adult myelinated tissue, may also contribute to such T2 prolongation in early infancy, which could be more pronounced at 3T.^{8,12-16}

As regions mature, the decrease in free water could be less apparent on SE-T1WI at 3T because the bright, T1-shortened signal from maturation is offset by a decrease in spin attenuation.⁸ Also, at 3T, conventional spin-echo sequences are often replaced by an FSE acquisition to decrease scanning time, while attempting to preserve the precision of the myelination evaluation; thus, it is plausible that the increased visibility of dark signal on SE-T2WI at

3T may partially relate to the increasing magnetization transfer effects that occur with an FSE acquisition.^{17,18} Additionally, a GRE-T1WI acquisition at 3T may offer other advantages over SE-T1WI; for example, GRE-T1WI has shown a higher SNR gain compared with FSE T1WI techniques at 3T in adult brains.¹⁹ Hence, such known effects may account for the greater visibility of myelination on GRE-T1WI and SE-T2WI at 3T in neonates, compared with SE-T1WI, based on the results of this study and the prior one.⁶ However, such theoretic benefits in evaluating myelination at higher field strengths are speculative, without direct comparison among field strengths or corroboration by histology.

The noted differences in the frequency of maturation of structures among sequences, as exemplified in the current study by the habenular commissure, ICP, and perirolandic cortex, could be explained by some of the complex interactions mentioned above, including the use of FSE acquisitions, the concentration of free water surrounding a structure, and other factors related to the composition of myelin or its precursors.^{18,20-23} Unfortunately, many MR imaging studies of myelination in neonates do not consistently evaluate the same set of structures, particularly the habenular commissure, for example. It has been noted previously that there can be substantial discrepancies both among the literature and among sequences regarding myelin maturation; for example, 1 noted factor has been that magnetization transfer effects may augment the visualization of maturation on FSE-T2WI versus conventional SE-T2WI.^{18,21,22} While conventional knowledge is that T1WI is more useful for early myelination changes and T2WI is better for later myelination changes, there are studies that suggest that certain structures may preferentially manifest the initial changes of maturation on T2WI; also, Barkovich² has suggested that myelination of gray matter structures may be best demonstrated on T2WI, whereas white matter structures may be better visualized on T1WI.^{2,14,23} Given such variations in myelination among sequences and among the literature at lower field

strengths, it is conceivable that such differences would theoretically be exacerbated at higher field strengths such as 3T.

An important finding in the current study was that the apparent discrepancy regarding the frequency of T1-bright myelination of the CST within the brain stem was less than that of the PLIC, though maturation is known to occur earlier within the CST within the brain stem both histologically and at lower field strengths (eg, 0.6T, 1T).^{14,24} This appearance could be due to a complex interaction of various factors in the current 3T study: the composition of myelin (or its precursors) in that location, the presence of free water, the “compactness” of fibers, or the field strength. As stated above, the T1-bright, T2-dark appearance of the dynamic process of myelination likely relates to a complex interaction of the progressively decreasing free water content along with cholesterol, galactocerebrosides, and proteins of the myelin membrane.^{8,10,11,20,21} It is conceivable that a site with a higher degree of “compactness” of fibers, as evidenced by the described higher fractional anisotropy in the PLIC relative to the CST within the brain stem, could have brighter T1 signal due to a higher concentration of myelin or myelin precursors.^{25,26} Such lower “compactness” of fibers in the CST within the brain stem, albeit being myelinated earlier, in tandem with the known surrounding higher free water content of the ventral pons in general, could theoretically obscure what should appear as T1-bright signal intensity. This appearance may be even more profound at higher field strengths such as 3T, due to its increasing ability to depict free water.^{14,20,24} Thus, this discrepancy between the current study and histology is likely an MR imaging discrepancy at 3T that radiologists and clinicians should be aware of. Therefore, because the CST within the brain stem is known to be myelinated earlier than the PLIC, the lack of T1-bright signal within the CST within the brain stem on 3T MR imaging should not be misconstrued as a lack of maturation in this location.

Another interesting finding of this study was that on all sequences, the callosal splenium exhibited a much lower rate of myelination (<40%) on SE-T2WI compared with the rate in the prior study of very preterm neonates at term-equivalent age (>90%).⁶ The difference between these cohorts deserves some discussion as to possible factors. One is that, while the growth of the callosal genu slows after birth, in contrast, splenial growth accelerates after birth; perhaps this finding could represent accelerated myelination in the cohort of very preterm neonates.²⁷ However, diffusion tensor imaging studies that have focused on the callosal splenium have shown disparate results; 1 study of preterm infants at term-equivalent age found significant differences compared with term infants, while another found no definite relationship between gestational age and changes in various DTI parameters.^{28,29} Theoretically, another possibility may relate to a phenomenon called the “visual experience” hypothesis, which essentially states that because preterm infants are “out” of the mother longer by the time of term-equivalent imaging (relative to full-term neonates), healthy premature infants would have experienced a greater degree of visual stimulation and thus would have accelerated maturation of visual pathways by the same postnatal gestational age.³⁰ Most interesting, studies using visual-evoked potentials and contrast sensitivities have suggested accelerated maturation of the visual cortices in preterm relative to term

infants, which might have manifested in the current study as earlier visualization of callosal splenium maturation in the preterm infants imaged at term-equivalent age.^{30,31} However, this finding on MR imaging is difficult to prove without correlating it with other clinical tests.

Regarding the interobserver reliability, a potential criticism of this study would be that the interobserver reliability was not high, because GRE-T1WI was moderate-strong ($\kappa = 0.546$), SE-T2WI was moderate ($\kappa = 0.468$), and SE-T1WI was fair-moderate ($\kappa = 0.384$). We opine that the findings of moderate-strong interobserver reliability highlight how the task of assessing myelination in young infants can be challenging, which has been mentioned previously.²¹ Such variability is quite similar to that in the prior study of very preterm neonates at term-equivalent age, in which GRE-T1WI was moderate-high ($\kappa = 0.56$) and both SE-T2WI ($\kappa = 0.43$) and SE-T1WI ($\kappa = 0.40$) were moderate.⁶ Our review of the limited available literature on the subject of interobserver reliability in term neonates found only a few reports even at lower field strengths, with the interobserver κ ranging from 0.21 to 0.40 by using routine sequences in early infancy.^{3,6,22,32} One study of solely very preterm neonates found a much higher interobserver reliability ($\kappa = 0.72$) when using SE-T1WI, SE-T2WI, and inversion recovery T1WI at 1T, but that study analyzed fewer structures and did not provide the κ for each sequence; thus, their results are difficult to extrapolate onto the current study.³ It is also plausible that there is lower interobserver reliability at 3T compared with lower field strengths, but this aspect was not explored by the current study. Hence, we opine that such interobserver variability is likely present even among experienced pediatric neuroradiologists who routinely assess myelination, due to subtle changes in early infancy, but this phenomenon is perhaps underreported. Therefore, we think that such variability underscores the need to use GRE-T1WI at a minimum when assessing myelination at 3T.

The limitations of this study include those inherently involved with retrospective analyses. Also, a qualitative analysis based on subjective scoring was used, in the fashion of the prior report of preterm neonates.⁶ Additionally, the number of participants was limited, because MR imaging was only performed when there was clinical concern for hypoxic-ischemic injury; this limitation could have caused selection bias because 9 of the 16 patients had undergone head-cooling therapy before the MR imaging. Thus, it is plausible that a difference in myelination may exist between cooled and noncooled patients; however, we found no significant difference between those 2 groups regarding the degree of myelinated structures. Finally, another potential limitation is that a minimum clinical follow-up of 6 months may not have been enough to entirely ensure a lack of mild neurologic sequelae.

CONCLUSIONS

GRE-T1WI depicts a higher degree of myelination than SE-T1WI and has a higher interobserver reliability than both SE-T2WI and SE-T1WI. Compared with a prior 3T study of very preterm infants at term-equivalent age, in which SE-T2WI showed a slightly higher overall rate of myelination in very preterm infants, our study found that GRE-T1WI had a slightly higher rate of myelination than SE-T2WI. These findings confirm that in both term

neonates and term-equivalent age infants, myelination changes are best evaluated on GRE-T1WI and SE-T2WI at 3T, while the performance of SE-T1WI at 3T is inferior in assessing the degree of neonatal myelination.

REFERENCES

1. Sie LT, van der Knaap MS, van Wezel-Meijler G, et al. **MRI assessment of myelination of motor and sensory pathways in the brain of preterm and term-born infants.** *Neuropediatrics* 1997;28:97–105
2. Barkovich AJ. **MR of the normal neonatal brain: assessment of deep structures.** *AJNR Am J Neuroradiol* 1998;19:1397–403
3. Counsell SJ, Maalouf EF, Fletcher AM, et al. **MR imaging assessment of myelination in the very preterm brain.** *AJNR Am J Neuroradiol* 2002;23:872–81
4. Lu H, Nagae-Poetscher LM, Golay X, et al. **Routine clinical brain MRI sequences for use at 3.0 Tesla.** *J Magn Reson Imaging* 2005;22:13–22
5. Schmitz BL, Grön G, Brausewetter F, et al. **Enhancing gray-to-white matter contrast in 3T T1 spin-echo brain scans by optimizing flip angle.** *AJNR Am J Neuroradiol* 2005;26:2000–04
6. Sarikaya B, McKinney AM, Spilseth B, et al. **Comparison of spin-echo T1- and T2-weighted and gradient-echo T1-weighted images at 3T in evaluating very preterm neonates at term-equivalent age.** *AJNR Am J Neuroradiol* 2013;34:1098–103
7. Naidich TP, Duvernoy HM, Delman BN, et al. *Duvernoy's Atlas of the Human Brain Stem and Cerebellum.* New York: Springer-Verlag; 2009
8. Barkovich AJ, Kjos BO, Jackson DEJ, et al. **Normal maturation of the neonatal and infant brain: MR imaging at 1.5 T.** *Radiology* 1988;166:173–80
9. Martin E, Kikinis R, Zuerrer M, et al. **Developmental stages of human brain: an MR study.** *J Comput Assist Tomogr* 1988;12:917–22
10. Koenig SH, Brown RD 3rd, Spiller M, et al. **Relaxometry of brain: why white matter appears bright in MRI.** *Magn Reson Med* 1990;14:482–95
11. Kucharczyk W, Macdonald PM, Stanisiz GJ, et al. **Relaxivity and magnetization transfer of white matter lipids at MR imaging: importance of cerebroside and pH.** *Radiology* 1994;192:521–29
12. Dobbing J, Sands J. **Quantitative growth and development of human brain.** *Arch Dis Child* 1973;48:757–67
13. Thornton JS, Amess PN, Penrice J, et al. **Cerebral tissue water spin-spin relaxation times in human neonates at 2.4 Tesla: methodology and the effects of maturation.** *Magn Reson Imaging* 1999;17:1289–95
14. Counsell SJ, Kennea NL, Herlihy AH, et al. **T2 relaxation values in the developing preterm brain.** *AJNR Am J Neuroradiol* 2003;24:1654–60
15. Williams LA, Gelman N, Picot PA, et al. **Neonatal brain: regional variability of in vivo MR imaging relaxation rates at 3.0 T: initial experience.** *Radiology* 2005;235:595–603
16. Holland BA, Haas DK, Norman D, et al. **MRI of normal brain maturation.** *AJNR Am J Neuroradiol* 1986;7:201–08
17. Prenger EC, Beckett WW, Kollias SS, et al. **Comparison of T2-weighted spin-echo and fast spin-echo techniques in the evaluation of myelination.** *J Magn Reson Imaging* 1994;4:179–84
18. Shaw DW, Weinberger E, Astley SJ, et al. **Quantitative comparison of conventional spin echo and fast spin echo during brain myelination.** *J Comput Assist Tomogr* 1997;21:867–71
19. Wintersperger BJ, Runge VM, Biswas J, et al. **Brain tumor enhancement in MR imaging at 3 Tesla: comparison of SNR and CNR gain using TSE and GRE techniques.** *Invest Radiol* 2007;42:558–63
20. Barkovich AJ. **Concepts of myelin and myelination in neuroradiology.** *AJNR Am J Neuroradiol* 2000;21:1099–109
21. Welker KM, Patton A. **Assessment of normal myelination with magnetic resonance imaging.** *Semin Neurol* 2012;32:15–28
22. Kizildağ B, Düşünceli E, Fitoz S, et al. **The role of classic spin echo and FLAIR sequences for the evaluation of myelination in MR imaging.** *Diagn Interv Radiol* 2005;11:130–36
23. Murakami JW, Weinberger E, Shaw DW. **Normal myelination of the pediatric brain imaged with fluid-attenuated inversion-recovery (FLAIR) MR imaging.** *AJNR Am J Neuroradiol* 1999;20:1406–11
24. McArdle CB, Richardson CJ, Nicholas DA, et al. **Developmental features of the neonatal brain: MR imaging. Part I. Gray-white matter differentiation and myelination.** *Radiology* 1987;162:223–29
25. Partridge SC, Mukherjee P, Berman JJ, et al. **Tractography-based quantitation of diffusion tensor imaging parameters in white matter tracts of preterm newborns.** *J Magn Reson Imaging* 2005;22:467–74
26. Partridge SC, Vigneron DB, Charlton NN, et al. **Pyramidal tract maturation after brain injury in newborns with heart disease.** *Ann Neurol* 2006;59:640–51
27. Kier EL, Truwit CL. **The normal and abnormal genu of the corpus callosum: an evolutionary, embryologic, anatomic, and MR analysis.** *AJNR Am J Neuroradiol* 1996;17:1631–41
28. Hasegawa T, Yamada K, Morimoto M, et al. **Development of corpus callosum in preterm infants is affected by the prematurity: in vivo assessment of diffusion tensor imaging at term-equivalent age.** *Pediatr Res* 2011;69:249–54
29. De Bruïne FT, van Wezel-Meijler G, Leijser LM, et al. **Tractography of developing white matter of the internal capsule and corpus callosum in very preterm infants.** *Eur Radiol* 2011;21:538–47
30. Bosworth RG, Dobkins KR. **Effects of prematurity on the development of contrast sensitivity: testing the visual experience hypothesis.** *Vision Res* 2013;82:31–41
31. Leaf AA, Green CR, Esack A, et al. **Maturation of electroretinograms and visual evoked potentials in preterm infants.** *Dev Med Child Neurol* 1995;37:814–26
32. Maricich SM, Azizi P, Jones JY, et al. **Myelination as assessed by conventional MR imaging is normal in young children with idiopathic developmental delay.** *AJNR Am J Neuroradiol* 2007;28:1602–05

Time-Resolved Contrast-Enhanced MR Angiography of Spinal Vascular Malformations

M. Amarouche, J.L. Hart, A. Siddiqui, T. Hampton, and D.C. Walsh



ABSTRACT

BACKGROUND AND PURPOSE: The diagnosis of spinal vascular malformations may be challenging on conventional MR imaging because neither the location of the signal abnormality in the spinal cord nor the level of the abnormal flow voids correlates with the level of the fistula. We conducted a retrospective evaluation of the utility of using a time-resolved imaging of contrast kinetics sequence in the diagnosis, characterization, and localization of spinal vascular malformations, comparing it with the criterion standard of spinal DSA.

MATERIALS AND METHODS: Fifty-five consecutive patients with a suspected diagnosis of spinal vascular malformation underwent time-resolved imaging of contrast kinetics followed by spinal DSA. All scans were performed on a 1.5T scanner by using a standard 8-channel spine coil and were reported by a neuroradiologist before the DSA was performed.

RESULTS: Forty-seven lesions were confirmed on time-resolved imaging of contrast kinetics and classified as spinal dural arteriovenous fistulas ($n = 33$, with 1 patient having a type 1b fistula), perimedullary spinal cord arteriovenous fistulas ($n = 10$), and intramedullary arteriovenous malformations ($n = 3$). One patient had an extradural spinal vascular malformation. Time-resolved imaging of contrast kinetics identified the location of the arterial feeder to within 1 vertebral level in 27/33 patients (81.8%) with spinal dural arteriovenous fistulas and correctly predicted the side in 22/33 (66.6%) patients. Perimedullary spinal cord arteriovenous fistulas were erroneously considered to represent spinal dural arteriovenous fistulas before spinal DSA. The anatomy of the arterial supply to intramedullary arteriovenous malformations was also poorly characterized on time-resolved contrast-enhanced MR angiography.

CONCLUSIONS: It has been our experience that time-resolved imaging of contrast kinetics is a useful confirmatory tool when a spinal vascular malformation is suspected on the basis of clinical and conventional MR imaging findings. As experience with the technique grows and sequences are refined, it may be possible to rely on time-resolved imaging of contrast kinetics as a screening tool for the diagnosis of spinal vascular malformations.

ABBREVIATIONS: PMAVF = perimedullary spinal cord arteriovenous fistula; SCAVM = intramedullary arteriovenous malformation; SDAVF = spinal dural arteriovenous fistula; SVM = spinal vascular malformation; TRICKS = time-resolved imaging of contrast kinetics; TR-MRA = time-resolved contrast-enhanced MR angiography

Spinal vascular malformations (SVMs) are an uncommon and heterogeneous group of vascular abnormalities.¹⁻⁴ Early diagnosis is important because SVMs are a treatable cause of a potentially reversible myelopathy. Unfortunately, there is often considerable delay between symptom onset and treatment: The diagnosis of SVM may be challenging on conventional MR

imaging because the associated spinal cord intramedullary T2WI hyperintensity may mimic a tumor, an inflammatory pathology, or an infection. Moreover, neither the location of the signal abnormality in the spinal cord nor the level of the abnormal flow voids correlates with the level of the fistula.

Catheter-based spinal digital subtraction angiography is considered the criterion standard diagnostic technique to describe the angioarchitecture of SVMs. However, it is an invasive and potentially lengthy undertaking, requiring selective catheterization of all the arteries supplying the spinal cord. It will sometimes require general anesthesia to ensure that the patient is still during the procedure. If not, it may require staging to a second examination. The contrast and radiation doses can be higher than preferable.

It is therefore desirable that a noninvasive imaging technique to characterize these lesions either replace or allow targeted conventional angiography of SVMs. Time-resolved contrast-

Received April 3, 2014; accepted after revision July 2.

From the Departments of Neurosurgery (M.A., D.C.W.) and Neuroradiology (J.L.H., A.S., T.H.), King's College National Health Service Foundation Trust, London, United Kingdom; and Department of Clinical Neurosciences (D.C.W.), Institute of Psychiatry, King's College, London, United Kingdom.

Please address correspondence to Jonathan L. Hart, MD, King's College National Health Service Foundation Trust, Denmark Hill, London SE5 9RS, United Kingdom; e-mail: jonathanhart@nhs.net

Indicates article with supplemental on-line table.

<http://dx.doi.org/10.3174/ajnr.A4164>

enhanced MR angiography (TR-MRA) techniques have shown particular promise. In this article, we describe their application in our institution to SVMs during a 7-year interval.

First described in the 1980s,⁵ TR-MRA techniques allowed the acquisition of images with good spatial and contrast resolution, but they were too slow to follow the uptake of the contrast agents, resulting in poorer temporal resolution images than DSA. The keyhole method proposed by van Vaals et al⁶ in 1993 accelerated the contrast uptake severalfold, resulting in better quality images. Three years later, Korosec et al⁷ introduced the time-resolved imaging of contrast kinetics (TRICKS). They described a method in which the *k*-space is sampled more frequently than the peripheral regions and timeframes are formed by temporal interpolation, continuously updating the spatial frequency uptake and significantly improving the image quality compared with the keyhole technique. TR-MRA techniques continue to progress with the most recent TRICKS techniques offering the ability to temporally resolve the arterial and venous phases of an MRA study. These are being used increasingly for evaluation of the vasculature in the extremities,^{8,9} brain,^{10,11} and spine.^{11,12}

Our institution adopted TR-MRA by using the TRICKS sequence as part of our standard evaluation of suspected SVMs in 2005. We conducted a retrospective evaluation of the utility of using the TRICKS technique in the diagnosis, characterization, and localization of SVMs, comparing it with the criterion standard of spinal DSA.

MATERIALS AND METHODS

Patient Population

Between May 2006 and January 2014, 55 patients with a suspected diagnosis of SVM (on clinical and conventional MR imaging grounds) underwent TRICKS followed by spinal conventional angiography.

Five patients were excluded from the study because both TRICKS and DSA had negative findings. The final clinical diagnosis in these patients was transverse myelitis, spinal cord tumor, spinal cord cavernoma, and idiopathic superficial siderosis. In 1 case, no definitive diagnosis was made (though an inflammatory cause was strongly suspected). DSA was unsuccessful in 4 patients due to technical difficulties, mainly related to aortoiliac ectasia and tortuosity, which precluded an adequate examination. These cases were explored surgically, guided by the TRICKS imaging and, in 1 case, additional CTA imaging.

Conventional MR imaging was performed without contrast in 57% of the remaining 50 patients. The diagnosis of SVM was suspected on initial MR imaging in 88% of patients.

MR Imaging Technique

All scans were performed on a Signa 1.5T scanner (GE Healthcare, Milwaukee, Wisconsin) by using a standard 8-channel spine coil. A counting whole-spine sagittal T1WI was performed followed by a sagittal T2WI on which a coronal 4- to 5-cm slab was positioned covering the vertebral body and spinal canal. The image volume was centered on the lower thoracic level to cover T6 to L2. This was modified in some circumstances when spinal cord swelling and signal change were located outside this standard FOV or focal hemorrhage was present (eg, in the context of intramedullary ar-

teriovenous malformation [SCAVM] or perimedullary spinal cord arteriovenous fistula [PMAVF]). In cases in which the point of fistulation was outside the FOV, diagnostic confirmation was nevertheless obtained on the basis of identification of filling of median spinal cord veins in the arterial phase.

The TRICKS sequence parameters were FOV = 34 (length/craniocaudal), 3.2-mm section thickness, 1.6-mm section gap, 256 × 128 matrix, NEX = 1, TR = 3.14 ms, TE = 0.8 ms. Twenty-seven phases were obtained with 14 scan locations in each phase. The total scan time was 59 seconds with a temporal resolution of 1.8 seconds.

Following the acquisition of a mask, 20 mL of gadolinium-based contrast agent was administered intravenously at 3 mL per second by a pump injector followed by a 50-mL saline bolus “chaser.” Triggering was performed manually after the mask acquisition with minimal or no delay.

Catheter Angiography

Selective intra-arterial spinal DSA was performed via a femoral approach in a dedicated biplanar neuroangiographic suite within 7 days of the MR imaging examination. Procedures were performed with the patient under local anesthetic. Iodinated non-ionic contrast medium (3–5 mL of 300 mg/mL) was injected selectively into the intercostal or lumbar radicular artery, expected to be supplying the lesion on the basis of TR-MRA findings, and into the contralateral radicular artery at the same level. Further bilateral injections were performed to include 2 levels above and below the identified fistula. If a fistula was not identified at the anticipated level, complete spinal angiography was undertaken, usually with the patient under general anesthesia.

Imaging was performed in the anteroposterior plane at 3 frames per second. Oblique, lateral, and magnified views were obtained as necessary to fully delineate the anatomy of the fistula.

Image Processing and Review

Fully automated postprocessed images were available for review as in-line subtracted coronal 3.2-mm datasets for each of the 27 MRA phases acquired and also as coronal maximum intensity projections. 3D volume reconstructions for the phases with maximal lesional conspicuity were also generated.

MR imaging and TRICKS scans were all reported by a neuro-radiologist before DSA was performed. TRICKS findings were deemed positive if there was early filling of abnormal tortuous midline vessels (representing enlarged intradural longitudinal veins). The level of the feeding vessel was identified by the site of the earliest appearance of the abnormal midline vessel and by the lateral connection of the earliest appearing vessels to the radiculomedullary or segmental branches.

For this retrospective review, TRICKS findings were correlated with the subsequent angiographic results to assess the accuracy of the technique in identifying, characterizing, and localizing SVMs.

Classification of SVM

Several classification schemes have been described on the basis of the anatomic characteristics of these lesions or emphasizing their hemodynamic properties.^{1–4} One of the most widely used classi-

fications⁴ groups these lesions into 4 different categories (summarized in Table 1): spinal dural arteriovenous fistulas (type I), intramedullary arteriovenous malformations (type II), extensive juvenile or metamerismic malformations (type III), and perimedullary spinal cord arteriovenous fistulas (type IV). SDAVFs are the most commonly identified type, comprising approximately 80% of SVMs. They are usually located on a nerve root sleeve within the neural foramen and are supplied by a dural branch of the segmental radicular artery.

RESULTS

Of 50 patients (age range, 5–83 years; median, 61 years; 24 females, 26 males), 46 had both TRICKS-MRA and DSA available for comparison and 4 were managed on the basis of TRICKS findings with additional CTA findings in 1 patient. The suspected diagnosis of SVM, based on the finding of early-filling, median longitudinal venous structures on TRICKS, was confirmed with DSA in 41 cases. In 3 cases, TRICKS failed to show an SVM that was subsequently identified by DSA. In 3 other cases, the initial TRICKS was reported as suggestive of an SVM but subsequent comprehensive spinal angiography failed to demonstrate an arteriovenous shunt. The final diagnosis for these patients was subsequently reported as long-standing arachnoiditis with syrinx and primary spinal cord neoplasm in 2 patients. The third patient had repeat TRICKS 4 months after the initial study showing no arteriovenous shunting. Including all 54 studies, sensitivity, specificity, positive predictive value, and negative predictive value for the

detection of a spinal vascular malformation on TRICKS in comparison with the criterion standard DSA were 98%, 63%, 93%, and 83%, respectively. The low negative predictive value is probably due to a low data sample of studies with negative findings.

The 47 lesions confirmed on TRICKS were classified as SDAVF ($n = 33$, with 1 patient having a type Ib fistula), PMAVF ($n = 10$), and SCAVM ($n = 3$) (Table 1). One patient had an extradural SVM. Patient imaging findings are recorded in the Online Table and Table 2.

In the SDAVF group (33/47, 70.2%), the segmental level of fistulation identified on TRICKS was concordant with conventional angiography findings in 21 of 33 patients (63.6%) (Fig 1). In 6 patients, it was within 1 predicted level, and in 3 patients, within 2 predicted levels. The correct side was predicted in 22 of 33 patients (66.6%). One patient with an SDAVF had cervical spinal cord signal change on MR imaging and was found to have a posterior fossa fistula with reflux into cervical spinal cord veins. In this case, cervical spine intramedullary signal change was evident. The TRICKS was centered on this level and duly confirmed filling of median spinal veins in the arterial phase. The arterial supply to the fistula was not evident on this acquisition and was delineated on DSA.

In the PMAVF group (10/47, 21.27%), TRICKS and the DSA level were concordant in 1 patient, within 1 predicted level in 2 patients, and within 2 predicted levels in 3 patients (Fig 2). The correct side was identified in 2 patients. Additional feeding vessels were also demonstrated on DSA in 2 of 3 patients with PMAVFs; these lesions were also initially erroneously characterized as SDAVFs following TRICKS.

In the SCAVM group (3/47, 6.38%), the nidus was accurately located on TRICKS and the extent of draining veins was demonstrated in 1 patient (Fig 3). However, feeding vessels were not identified and characterized reliably: Conventional angiography confirmed the presence of multiple feeders in these lesions, 2 of which had not been resolved on TRICKS. In the case of the sacral fistula, TRICKS centered on T6 to L2 showed arterial phase filling of the spinal cord venous plexus. A feeder was suspected at L2 on TRICKS but was not seen on conventional angiography. Selective catheterization of the median sacral artery demonstrated the fistula.

Table 1: Classification of spinal vascular malformations and the number of patients included in our study^{4,13}

Type	Description	No.
I	SDAVF:	33
	Ia) Single fistula Ib) Polyfistulous	
II	SCAVM	3
III	Juvenile/metameric malformations	0
IV	PMAVF ¹³ :	10
	A) Single fistula	
	B) Often multiple, intermediate flow C) Polyfistulous, large lesions	

Table 2: TRICKS, DSA findings, and treatment of patients with intramedullary arteriovenous malformations, perimedullary spinal cord arteriovenous fistulas, and extradural SVMs

Age (yr)	Sex	Side and Level of Feeding Vessel		Treatment	Classification
		TRICKS	Angiogram		
24	M	Conus midline	L T10	Surgery	II
46	M	L C5/6	R C5/6	Awaiting radiosurgery	II
58	F	SVM but no level or side identified	Left vertebral artery just beyond the PICA origin	Surgery	II
78	M	T11/T12, no side identified	L L1	Surgery	IV
73	M	R L3/L4	R L1	Surgery	IV
33	M	R T11	R T11	Surgery	IV
71	F	L L2, postembolization to coccyx	Distal coccyx, branches of the median sacral artery	Multiple embolizations and surgery	IV
45	M	R T6	L T7	Radiosurgery	IV
17	M	T9, no side identified	L T7	Awaiting radiosurgery	IV
82	F	Bilateral T12	Unsuccessful	Surgery	IV
79	F	L T11	Unsuccessful	Surgery	IV
74	F	R L3/L4	Unsuccessful	Surgery	IV
32	F	No SVM identified	R C2	Conservative	IV
65	M	R L3/L4	R L3/L4	Embolization	Extradural

Note:—L indicates left; R, right; PICA, posterior inferior cerebellar artery.

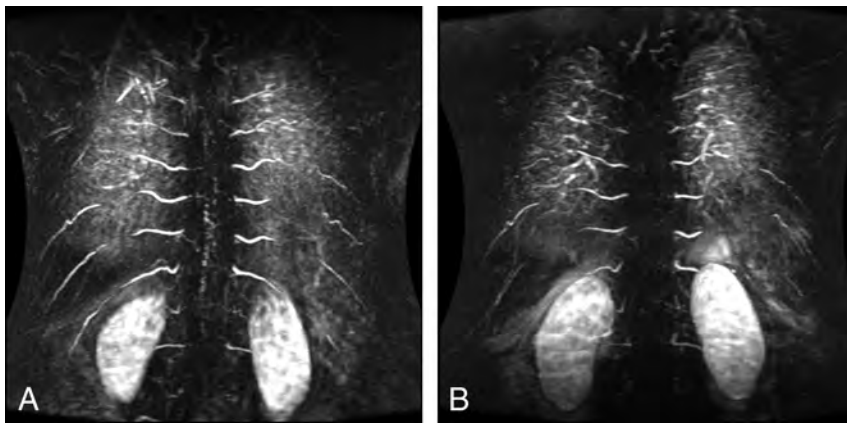


FIG 1. Preoperative (A) and postoperative (B) TRICKS sequences of a patient with an SDAVF (type I).

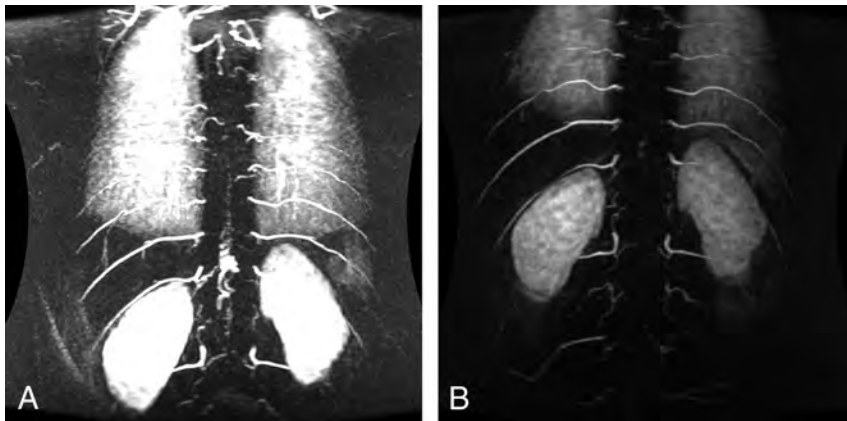


FIG 2. Preoperative (A) and postoperative (B) TRICKS sequences of a patient with a PMAVF (type IV).

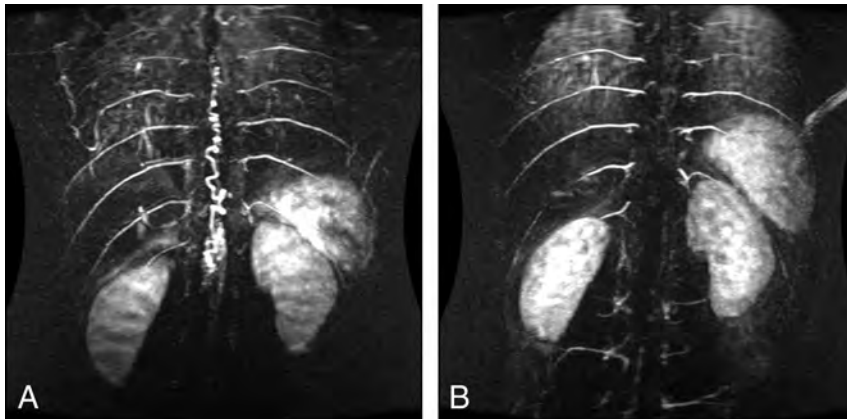


FIG 3. Preoperative (A) and postoperative (B) TRICKS sequences of a patient with SCAVM of the conus (type II).

Patients were treated surgically in most cases. Three patients underwent endovascular treatment, but 2 attempts at embolization with Onyx (Covidien, Irvine, California) of 1 sacral dural arteriovenous fistula were unsuccessful in closing all supplying arteries and surgical treatment was necessary to achieve complete obliteration of the fistula. In 3 cases of SCAVM, the lesion anatomy (in particular the relationship to a major anterior spinal artery radiculomedullary supply) precluded safe endovascular or surgical treatment. One patient has been treated by using

radiosurgery, and 2 patients are awaiting the same treatment. One patient refused treatment and is being managed conservatively.

DISCUSSION

TRICKS is increasingly used for noninvasive vascular imaging. Fast, time-resolved imaging of the spine increases temporal resolution, permitting hemodynamic assessment of SVMs over a relatively large FOV (with relatively little compromise in spatial resolution or signal-to-noise ratio). The TRICKS sequence acquires central k -space data in all sections, but the remaining peripheral data are split and shared among sections. Combining this k -space data acquisition with a very low TR, on the order of approximately 3 ms, allows rapid data acquisition and provides dynamic, multiphase real-time angiographic information. The increased temporal resolution achieved is of particular value in the evaluation of arteriovenous shunts, and preliminary results have also been described in studies of intracranial AVMs and dural fistulas.^{10,11,14} Other advantages include a shorter acquisition time and lack of requirement for contrast bolus timing.¹⁵

Standard TOF MRA techniques lack sufficient temporal resolution to identify SVMs, and phase-contrast methods are not suited to the detection of these often relatively low-flow shunts. Contrast-enhanced MRA techniques with 3D TOF acquisition have been described by a number of authors, who report a reasonable degree of success in identifying the level of the SDAVF (on the order of 50%–75%).^{16–18} Elliptic-centric contrast-enhanced MRA 3D techniques have also proved useful in demonstrating the presence and level of SDAVFs,^{19,20} but again they do not demonstrate the actual fistula or resolve arterial and venous phases to allow differentiation of the fistula and draining radiculomedullary vein from the engorged coronal venous plexus. The level of fistula was inferred in these studies by tracing an engorged medullary vein retrogradely to the neural foramen. Without the ability to distinguish this vein from veins draining away from the coronal venous plexus, there is the potential for false localization. CTA is similarly limited by the inability to temporally resolve arteries and veins.^{21,22} Images with high spatial resolution can be obtained, but interpretation is hampered by the adjacent bony

anatomy. In the recently published article by Saindane et al,¹⁵ a higher number of studies with negative findings were reported, explaining the higher negative predictive value compared with our study.

Our results demonstrate that the TRICKS technique is reliable in confirming the presence of a suspected SVM, though there was a high pretest probability based on the clinical and MR imaging findings. As experience with the technique grows and sequences are refined, it may become possible to rely on TRICKS as a screening tool, but it cannot currently be depended on as a “rule-out” test in cases of a suspected SVM.

While the temporal resolution of the 2 techniques is not substantially different, the difference in spatial resolution remains considerable and largely accounts for the difficulty in distinguishing SDAVF from PMAVF and in adequately characterizing SCAVM with TRICKS. For SDAVF, TRICKS identified the location of the arterial feeder to within 1 vertebral level in 27 of 33 patients, and in most cases, a targeted spinal DSA (performed with the patient under local anesthetic) could be performed following TRICKS, minimizing radiation exposure and contrast dose. Cases of sacral SDAVF ($n = 1$) and rather small bilateral thoracic SDAVF ($n = 1$) necessitated more comprehensive DSA examination. The 3 cases of PMAVF were erroneously considered to represent SDAVF before spinal DSA, which also identified additional supplying arteries. The anatomy of the arterial supply to SCAVM was also poorly characterized on TRICKS, and we were unable to resolve the angioarchitecture of this type of SVM. On this basis, spinal DSA remains mandatory to accurately characterize SVMs. Conventional angiography also demonstrates the level of origin of the artery of Adamkiewicz or other radiculomedullary branches; this demonstration is essential when considering treatment of these lesions.

Interpretation of the technique requires some experience on the part of the reporting neuroradiologist, but common pitfalls can generally be avoided by the appropriate use of the cross-referencing tools and scrutinizing individual arterial phase datasets in addition to MIP images. Although 3 studies were initially reported as having positive findings, on retrospective review, no false-positive studies were identified. One case, reported early in the series, was due to misinterpretation of an extraspinal longitudinal venous structure as a median longitudinal spinal vein. The 2 other cases were rather equivocal, with no clear level of supply or fistulation to the potentially abnormal median veins identifiable on TRICKS. There was only 1 case in which TRICKS failed to identify a SVM. The patient had a high cervical PMAVF.

Our results are consistent with findings reported by a number of other investigators. Ali et al²³ described the use of a TR-MRA (TRICKS) sequence to predict the level of SDAVF to within 1 vertebral level in 6 patients. The authors also suggested that the technique was accurate for excluding the presence of SDAVFs and in confirming successful fistula occlusion following treatment. Tapping et al¹² described the use of the TRICKS sequence after a technically difficult spinal catheter angiogram (due to aortic tortuosity and atherosclerosis), which did not locate the anticipated SDAVF. It was subsequently located on 3T TR-MRA. In a second case, it was impossible to obtain a stable catheter position at the level of the known fistula; therefore, 3T TRICKS was used to fur-

ther characterize the lesion before surgery. We have also encountered a small number of patients ($n = 4$) in whom adequate DSA could not be completed due to technical difficulties and who underwent surgery solely on the basis of information from the TRICKS.

Limitations of the study include the small number of patients having a rare condition and its retrospective design. Although images were analyzed by only a single neuroradiologist, assessment preceded the DSA in all cases; thus, the neuroradiologist was blinded to the nature and level of the lesion. Further evaluation of the technique might incorporate an assessment of interobserver agreement.

CONCLUSIONS

The infrequency of these cases precludes large studies. Consequently, conclusions have to be drawn from pooled case series similar to the present study. It has been our experience that TRICKS is a useful confirmatory tool when an SVM is suspected on the basis of clinical and conventional MR imaging findings. The frequent ability to identify the level of arteriovenous shunting on TRICKS allowed the subsequent spinal catheter angiography to be directed to the level of interest and involved less contrast load and radiation exposure; these features abbreviated an otherwise lengthy and potentially difficult procedure.

DSA remains necessary to characterize SVMs and, particularly in the case of PMAVF and SCAVM, to identify important radiculomedullary feeders before consideration of treatment.

REFERENCES

1. Black P. **Spinal vascular malformations: an historical perspective.** *Neurosurg Focus* 2006;21:E11
2. Spetzler RF, Detwiler PW, Riina HA, et al. **Modified classification of spinal cord vascular lesions.** *J Neurosurg* 2002;96:145–56
3. Qureshi AI. **A new classification scheme for spinal vascular abnormalities based on angiographic features.** *J Neuroimaging* 2013;23:401–08
4. Anson JA, Spetzler RF. **Classification of spinal arteriovenous malformations and implications for treatment.** *BNI Quarterly* 1992;8:2–8
5. Grist TM, Mistretta CA, Strother CM, et al. **Time-resolved angiography: past, present, and future.** *J Magn Reson Imaging* 2012;36:1273–86
6. van Vaals JJ, Brummer ME, Dixon WT, et al. **“Keyhole” method for accelerating imaging of contrast agent uptake.** *J Magn Reson Imaging* 1993;3:671–75
7. Korosec FR, Frayne R, Grist TM, et al. **Time-resolved contrast-enhanced 3D MR angiography.** *Magn Reson Med* 1996;36:345–51
8. Andreisek G, Pfammatter T, Goepfert K, et al. **Peripheral arteries in diabetic patients: standard bolus-chase and time-resolved MR angiography.** *Radiology* 2007;242:610–20
9. Ruhl KM, Katoh M, Langer S, et al. **Time-resolved 3D MR angiography of the foot at 3 T in patients with peripheral arterial disease.** *AJR Am J Roentgenol* 2008;190:W360–64
10. Petkova M, Gauvrit JY, Trystram D, et al. **Three-dimensional dynamic time-resolved contrast-enhanced MRA using parallel imaging and a variable rate k-space sampling strategy in intracranial arteriovenous malformations.** *J Magn Reson Imaging* 2009;29:7–12
11. Saleh RS, Lohan DG, Villablanca JP, et al. **Assessment of craniospinal arteriovenous malformations at 3T with highly temporally and highly spatially resolved contrast-enhanced MR angiography.** *AJNR Am J Neuroradiol* 2008;29:1024–31

12. Tapping CR, Thackeray AT, Bartlett RJ, et al. **Evaluation of spinal dural arteriovenous fistulae with gadofosveset trisodium at 3 T (TRICKS and LAVA).** *Clin Radiol* 2011;66:865–68
13. Merland JJ, Reizine D. **Embolization techniques in the spinal cord.** In: Dondelinger RF, Rossi P, Kurdziel JC, et al, eds. *Interventional Radiology*. New York: Thieme; 1990:433–42
14. Kunishima K, Mori H, Itoh D, et al. **Assessment of arteriovenous malformations with 3-Tesla time-resolved, contrast-enhanced, three-dimensional magnetic resonance angiography.** *J Neurosurg* 2009;110:492–99
15. Saindane AM, Boddu SR, Tong FC, et al. **Contrast-enhanced time-resolved MRA for pre-angiographic evaluation of suspected spinal dural arterial venous fistulas.** *J Neurointerv Surg* 2015;7:135–40
16. Binkert CA, Kollias SS, Valavanis A. **Spinal cord vascular disease: characterization with fast three-dimensional contrast-enhanced MR angiography.** *AJNR Am J Neuroradiol* 1999;20:1785–93
17. Bowen BC, Fraser K, Kochan JP, et al. **Spinal dural arteriovenous fistulas: evaluation with MR angiography.** *AJNR Am J Neuroradiol* 1995;16:2029–43
18. Saraf-Lavi E, Bowen BC, Quencer RM, et al. **Detection of spinal dural arteriovenous fistulae with MR imaging and contrast-enhanced MR angiography: sensitivity, specificity, and prediction of vertebral level.** *AJNR Am J Neuroradiol* 2002;23:858–67
19. Farb RI, Kim JK, Willinsky RA, et al. **Spinal dural arteriovenous fistula localization with a technique of first-pass gadolinium-enhanced MR angiography: initial experience.** *Radiology* 2002;222:843–50
20. Luetmer PH, Lane JJ, Gilbertson JR, et al. **Preangiographic evaluation of spinal dural arteriovenous fistulas with elliptic centric contrast-enhanced MR angiography and effect on radiation dose and volume of iodinated contrast material.** *AJNR Am J Neuroradiol* 2005;26:711–18
21. Lai PH, Weng MJ, Lee KW, et al. **Multidetector CT angiography in diagnosing type I and type IVA spinal vascular malformations.** *AJNR Am J Neuroradiol* 2006;27:813–17
22. Terae S, Kudo K, Asano T, et al. **CT angiography with multidetector-row helical CT in spinal arteriovenous malformation.** *Clin Imaging* 2004;28:23–27
23. Ali S, Cashen TA, Carroll TJ, et al. **Time-resolved spinal MR angiography: initial clinical experience in the evaluation of spinal arteriovenous shunts.** *AJNR Am J Neuroradiol* 2007;28:1806–10

Driving practice innovation.

The AMA is transforming the health of patients through practice advancements. I belong so that I can help move medicine forward.

Diana E. Ramos, MD
Member since 1990



I am a doctor. We are the AMA.

Visit www.ama-assn.org to activate
your membership today!



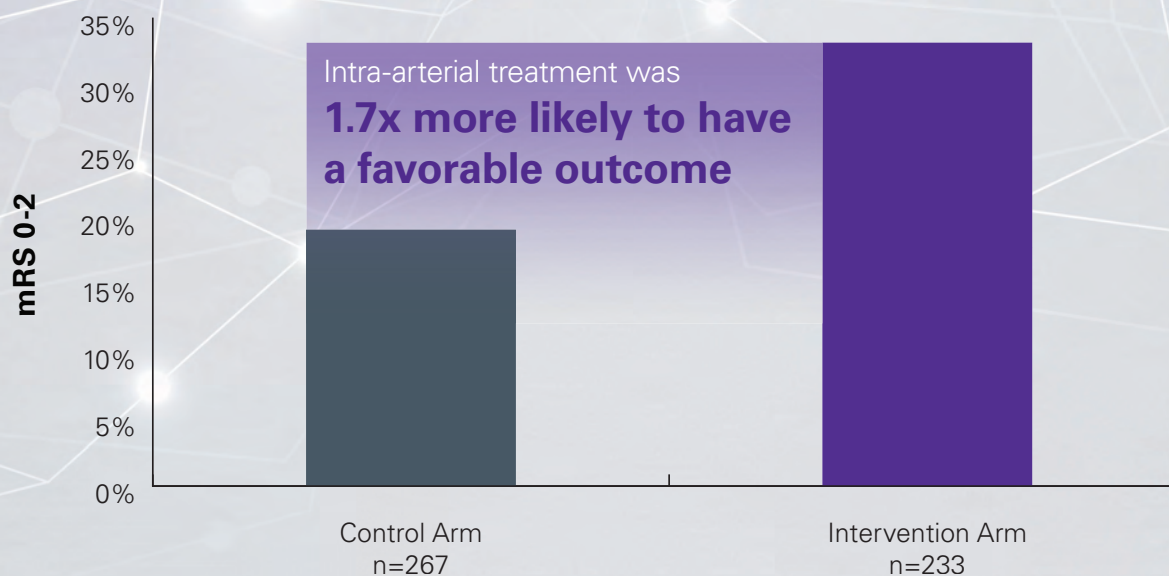
Congratulations to the MR CLEAN Investigators!

stryker[®]
Neurovascular

Intra-arterial treatment plus usual care results in better outcomes than usual care alone^{*†}

- Increase in functional independence in daily life, with no increase in mortality at 90 days
- **Stent retrievers were used in 97% of patients** (190/196) treated with intra-arterial therapy

Effect of Intervention on Primary Outcome at 90 days¹



* Intra-arterial treatment included mechanical thrombectomy (stent retrievers, Merci Retriever[®], wire disruption, thromboaspiration) and IA lytic. Usual care defined as intravenous administration of alteplase.

† In patients with acute ischemic stroke caused by proximal intracranial occlusion of the anterior circulation, treated within 6 hours after stroke onset.

1. O.A. Berkhemer et. al. A Randomized Trial for Intraarterial Treatment for Acute Ischemic Stroke. *N Eng J Med* 2014.



Trevo[®] XP

PROVUE RETRIEVER

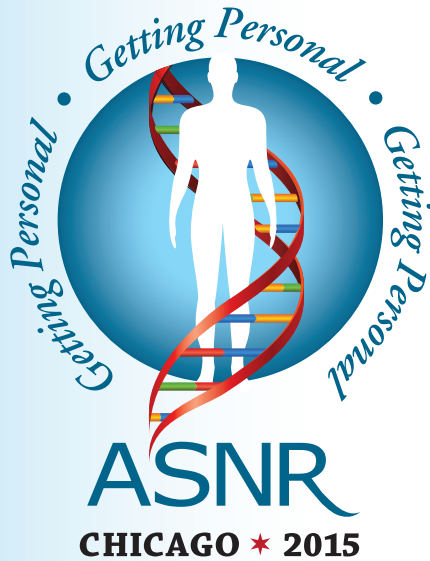
Take Control. Capture More.

The newly designed Trevo[®] XP ProVue Retriever takes proven Trevo Retriever performance to new levels for **easy delivery**, **easy placement**, and **easy visualization**.

When you're in control, it's amazing what you can capture.

stryker[®]
Neurovascular

ASNR 53rd Annual Meeting & The Foundation of the Symposium 2015 in Chicago, April 25-30, 2015



ASFNR ASHNR ASPNR ASSR SNIS

THE FOUNDATION OF THE ASNR



**Stay connected with friends and colleagues.
Get value-based neuroradiology that
addresses best practices. Visit the ASNR
2015 Meeting website to see the program!**

Laurie A. Loevner, MD
ASNR 2015 Program Chair and President-Elect

Request Programming and Registration Materials for the ASNR 53rd Annual Meeting, Contact:

ASNR 53rd Annual Meeting
c/o American Society of Neuroradiology
800 Enterprise Drive, Suite 205
Oak Brook, Illinois 60523-4216
Phone: 630-574-0220
Fax: 630-574-0661
Email: meetings@asnr.org
Website: www.asnr.org/2015

**Scan now to
visit our website**



An exceptional Symposium and Meeting at the newly renovated Sheraton Chicago Hotel & Towers.

The weekend Symposium: The Skull Base, will bridge the gap between the head and the spine. It will cover:

- Pertinent anatomy
- Optimization of imaging techniques
- Development and function of all the cranial nerves using a symptom-based approach
- Cutting edge intraoperative footage of transnasal endoscopic techniques which have redefined "surgical resectability", and have revolutionized the role of the neuroradiologist
- The posterior fossa, central hypertension and hypotension, and the craniovertebral junction

Sunday afternoon, the symposium continues with "Neuroradiologist-Clinician-Patient" Seminars. Breakout sessions include:

- Brain Tumors
- Head & Neck Cancer
- Thyroid Cancer
- Mild Traumatic Brain Injury
- MCI-Alzheimers Disease

Following these symposiums join us for an engaging game of Neuroradiology Jeopardy featuring Doctor-Patient teams, followed by a "mocktail reception" and Broadway entertainment!

ASNR Annual Meeting will provide informative updates on Neuroradiology and showcase specialty programming.

Monday morning "Keynote Symposium: Getting Personal" features Beth Daley Ullem, nationally-recognized Governance Expert; Grant Achatz, American chef, restaurateur, and head & neck cancer survivor; and Julian E. Bailes, Jr., MD, Neurosurgeon, consultant to NFL Players' Association, and advisor to NCAA Concussion Task Force.

Attend 5 Mini-Symposia throughout the week:

- Connectome and Genomics: Omics and Big Data for Neuroradiology
- Emergency Room Triage: Traumarama and Other Urgencies
- Neuroimaging Gently: Creating a Safe and Quality Environment for Neurodiagnostics & Neurointerventions
- Neuro-Nuclear Immersion
- Functional Neuroimaging Biomarkers of Psychiatric Disorders

SAVE THE DATES....April 25-30, 2015